

Epo, by any other name

Regulators must be given ways to approve follow-on 'biosimilars' when proteins fall out of patent if the fruits of molecular biology are to have the greatest possible effect on health care.

Late last month, the European Commission granted marketing authorizations to three companies for generic versions, or 'biosimilars', of the hormone erythropoietin. Amgen, the world's largest biotechnology company by sales, started selling Epogen ('Epo'), its recombinant version of this naturally occurring hormone, in 1989, producing it from cells into which the relevant gene had been engineered. The drug's ability to boost red blood-cell production has led to its widespread use to treat the anaemia associated with some diseases. Epogen and its newer incarnation, Aranesp, earned nearly US\$7 billion for Amgen last year, and more than \$3 billion for Johnson & Johnson, which has licensed the drug from Amgen and markets it in the United States, Europe and elsewhere. Now that the commission has allowed other companies to market their own version, revenues from Johnson & Johnson's estimated 250,000 European customers look set to erode. Sandoz, the generic-drugs branch of Novartis, said on 10 September that it will have its version of the drug on the market in the United Kingdom and Germany as soon as October, and that it will cost 25–30% less than Johnson & Johnson is charging.

The approvals bring to five the number of follow-on biological drugs to which the commission has given the go-ahead since it opened up a regulatory path for their approval last year. Eleven more applications are in a lengthening queue at the European Agency for the Evaluation of Medicinal Products. In the United States, though, the situation is very different. When the US patents on Epo expire, Amgen will not, as things stand now, face any new competition. The US Food and Drug Administration (FDA) doesn't have the authority to designate subsequent versions of biologicals — drugs consisting of proteins made using biotechnology — as interchangeable with currently marketed products. The potential for such products is large (see News Feature, page 274); sales of biological drugs no longer protected by patents in the United States were worth \$11.5 billion in 2006. But at the moment the United States does not have an abbreviated regulatory system for

biosimilars, which seek simply to mimic the drugs already on sale, so — with rare exceptions — there is no way into that market.

This year Congress vowed to put this matter right. A bill drafted by leading liberal Democrats and conservative Republicans in the Senate and backed by the Senate health committee would give biotech companies twelve years of market exclusivity on any new biological drug from the time that it is approved. This is longer than they might get from patent protection alone, which starts to run out as soon as the patent is granted even if the drug has not been approved. Companies with an interest in making biosimilars would, for their part, receive an abbreviated pathway to FDA approval of their follow-on products once that twelve-year period is up.

But neither the generics industry nor the biotech industry seem to be pushing to have this compromise passed by the House. Why? Because, compromise that it is, neither side is entirely happy. The generics industry is assuming that it will get a better deal in 2009, under a new US president. The biotech industry, although willing to stomach the compromise, is not going to go to bat for it. And so American health-care providers will continue to pay exorbitant prices for drugs such as Genentech's Cerezyme (imiglucerase) for Gaucher's disease, which is off patent but still costs up to \$200,000 per patient per year. The US biotech industry will continue to operate under a cloud of uncertainty that does not hamper its European competitors.

No one is suggesting that biosimilars will ever be marketed with the large discounts — 70% or more — that consumers enjoy when they buy generic versions of small-molecule drugs. But given current prices, regulation that facilitates generic competition on pricey biologicals while duly protecting innovators would still help health-care providers greatly. It's fair, it's possible, and Congress should make it happen now. ■

"Congress should make it happen now."

Regulatory failures

Outbreaks of foot-and-mouth disease have revealed unacceptable shortcomings in UK regulation.

Nothing gets a British prime minister to the emergency-response table quicker than a security threat, and biosecurity is no exception. Gordon Brown has already found himself having to respond promptly to outbreaks of foot-and-mouth disease, as did his predecessor Tony Blair. Unless the proper lessons are learned from these outbreaks, he could face more, and more serious, such emergencies in the future.

An outbreak in 2001 led to widespread culls of British livestock and

devastating financial losses to farmers and the economy. Two more outbreaks this year, in which the virus escaped from a research site in Surrey, have been much more contained. Reports by the Health and Safety Executive and by a group of scientists led by Brian Spratt, a bacteriologist from Imperial College London, revealed that the site, in Pirbright, had critical problems with its effluent systems. The government has responded to the report, and set up more reviews to correct regulatory shortcomings.

These shortcomings are glaring enough. The site has two occupants, the publicly funded Institute for Animal Health (IAH) and Merial, a company that produces vaccines against foot-and-mouth disease. The reports conclude that Merial had not breached the terms of its biosecurity licence, awarded by the Department for Environment, Food and Rural Affairs (DEFRA). But they acknowledge that

Prospects power up for nuclear energy

American energy utility NRG Energy is planning to build two reactors for nuclear power in Texas. Its application to the US Nuclear Regulatory Commission for permission to construct the reactors marks the first such request in the United States for three decades.

Meanwhile, Italy is reversing a 20-year post-Chernobyl moratorium on nuclear fission research to participate in the scientific development of 'Generation IV' nuclear reactors. How exactly the country will contribute to the Generation IV research has not yet been revealed. The planned next generation of nuclear power plants is intended to improve nuclear safety and to minimize waste and natural-resource use compared with the current generation of plants.

Europe plots course for funding navigation system

The European Commission is launching a bid to save Galileo, the continent's troubled satellite navigation system. It has asked the European Parliament to back its plan to foot the whole bill for the 30-satellite system. The cost would be some €3.4 billion (US\$4.8 billion) over the next six years.

Galileo would see Europe break free from its dependence on the US-based Global Positioning System (GPS). But the project suffered a serious setback earlier this year when a public-private deal to fund the system collapsed (see *Nature* 447, 765; 2007).

If the commission manages to salvage Galileo, it would get the extra cash from surplus monies in the agricultural and administration budgets. Member states will take the first steps to making a decision on the proposals in early October.

Meanwhile, President George W. Bush has announced that the United States will permanently leave the capability

Meteorite proves to be a hit in Peru

Researchers are examining a 17-metre-wide crater in southern Peru, looking for fragments of what is believed to be one of the largest meteorites to hit land in years.

The meteorite apparently plummeted to Earth on 15 September near the village of Carancas, west of Lake Titicaca on the Bolivian border. Scientists from Peru's Geological, Mining and Metallurgical Institute in Lima last week checked the crater (pictured), now filled with water, for debris from the object they described as a chondrite or stony meteorite.

People living near the impact complained of odd smells and illnesses, but some scientists speculated that the reported sickness may be group hysteria. They noted that objects that come from the sky have deep cultural significance to villagers.



LA REPUBLICA/AP

of distorting signals off any future GPS satellites. This feature was designed to give the US government a better working version of GPS than civilians, but has not been used since 2000.

HIV vaccine failure prompts Merck to halt trial

An HIV vaccine being developed by Merck has apparently failed, causing the company to halt a large and once-promising clinical trial last week.

Merck's STEP vaccine used a mixture of components from three weakened adenoviruses to carry three synthetically produced HIV genes. The hope was that each gene would stimulate an immune response against the virus, as earlier trials had suggested.

The latest trial began in 2004 and enrolled 3,000 people considered to be at high risk of infection. But a group of 741 volunteers who received the vaccine saw 24 HIV infections, compared with the control group of 762 people who saw 21 infections. Furthermore, the vaccine did not reduce the amount of HIV in the bloodstream of those infected.

FDA poised for broader powers over drugs on sale

The US Congress last week passed a bill significantly increasing the powers of the Food and Drug Administration (FDA) to police the safety of marketed drugs (see *Nature* 446, 844–845; 2007). President George W. Bush is expected to sign the bill by 30 September, when a current law expires.

Under the new law, the FDA will for the first time be able to order companies to make label changes on marketed drugs; to run new clinical trials when

safety issues emerge; and to fine non-compliant companies up to \$10 million. It also includes \$225 million in new drug-company-paid user fees that the agency will spend on post-market drug safety.

The bill requires the FDA to cut by 25% the number of waivers it grants to external experts with financial interests in matters on which they are advising the agency. Such waivers allow them to serve on committees that advise the agency on drug approvals, withdrawals and label changes — advice it almost always follows.

California universities maintain tobacco habit

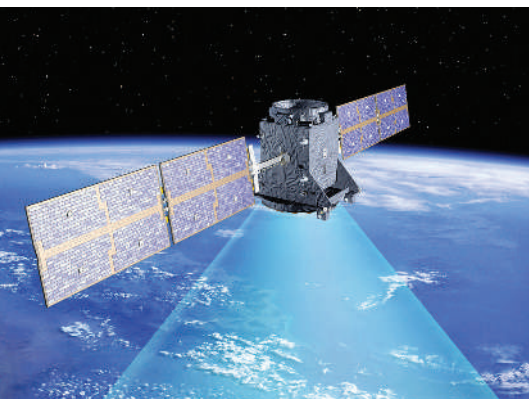
Under a policy adopted last week, scientists at the University of California's ten campuses can continue to accept research grants from tobacco firms. But new grants coming from the industry will undergo added scrutiny.

The University of California's governing board approved the policy on 20 September after several years of intense debate — spurred by a core of outraged scientists (see *Nature* 446, 242; 2007). Under the new policy, proposed tobacco-firm grants will undergo peer review by panels of scholars at each campus, where the chancellors will oversee the monitoring process. There will also be an annual report on all research funded by the tobacco industry, describing both submitted and approved projects.

Last year, seven of the university's campuses received a total of \$16 million for 23 projects, all funded by Philip Morris of Richmond, Virginia.

Correction

The Editorial 'Epo, by any other name' (*Nature* 449, 259; 2007) incorrectly stated that the drug Cerezyme is produced by Genentech. It is, in fact, produced by Genzyme Therapeutics.



Up in the air: Europe's planned Galileo navigation system has yet to secure full funding.

even though the firm had used chemical treatments to clean up 12,000 litres of fluid containing an estimated 10^{14} infectious units of virus in its category 4 containment facility, there was every possibility that the outbreak was caused by effluent from the facility. That such a possibility could meet the terms of a licence beggars belief. DEFRA's licensing standards are in urgent need of review; the government response rightly, if belatedly, acknowledges that the company probably needs to install sterilizing heat treatment.

Another belated government response is its recognition of two glaring conflicts of interest that bedevil biosecurity at the site: that the person responsible for Merial's biosecurity was also its site director; and that the site's other occupant, the IAH, is not only licensed by DEFRA but is also in large part funded by it. Such financially conflicted dual responsibilities are a recipe for underspending on security.

But there is no public sign, either from the government or elsewhere, of a more fundamental concern. The IAH is central to Britain's ability to protect itself against future outbreaks of animal disease, whether unleashed by natural causes, human error or enemy action. It also has a vital role in these issues internationally. To fulfil these roles the institute requires (and indeed has) a world-class research base that lets it address key scientific questions and at the same time maintain and develop the techniques needed to identify and deal with diseases. It also requires infrastructure to support

both research and surveillance. Spratt's committee mentions chronic shortcomings in lab conditions at the IAH, although they are not blamed for the outbreak.

Here DEFRA is yet again in the frame. The IAH's core funding is provided by the United Kingdom's Biotechnology and Biological Sciences Research Council (BBSRC). Its surveillance obligations and other practical duties mean that it struggles for funding against other institutes with roles that lie squarely within the BBSRC's research remit. DEFRA is supposedly obliged to uphold a government principle to fully fund the institute's infrastructure costs. This it has failed to do — a failure that has become marked, as it has cut its support for the IAH at a time when such support seems more important than ever.

The IAH's role was last reviewed in 2002. At that time, the review committee emphasized the need for biological and regulatory research to be strengthened at the IAH, and for its funders to develop a coherent approach.

Recently, the relevant bodies have seen a wave of turnover in their key players — ministers and the chief scientists of both the government at large and DEFRA in particular have changed, as has the head of the BBSRC (which, for good measure, is now supported through a new department). If he wants to minimize the frequency of future emergency committee meetings, Gordon Brown should bang all these new heads together and ensure that the 2002 funding recommendations for the IAH are implemented by all key players, and soon. ■

Drill often, drill deep

Splice the mainbrace: the greatest scientific ocean-drilling vessel ever built is going to sea.

After 18 years, 1,800 boreholes, some 36,000 cores and a host of impressive scientific discoveries, the international Ocean Drilling Program came to a close in 2003. Its successor, the Integrated Ocean Drilling Program (IODP), has hired some ships for drilling expeditions to sites of scientific importance, but has been waiting for a new flagship before going full steam ahead. The wait is now over. This week marks the research debut of the mammoth Japanese research vessel *Chikyu* (see News Feature, page 278). Japan has spared no expense in providing its riser-protected drilling pipe, its elaborate laboratories, its cushy cabins and all the other amenities a world-travelling scientist at sea might need. There is unlikely to be a research drilling ship in the near, or not-so-near, future to match it.

The ship's future will not be plain sailing, though, unless both Japan and the international community learn from the past. Japan is not the only country to plop down money for a big science project without providing the resources — especially the human resources — to make best use of it. But this it has done, and its government must now cultivate scientists who can use *Chikyu* to answer big questions in creative and effective ways. Japanese researchers will be competing with the international community for the IODP funding pot, and if they wish to play a leading role aboard *Chikyu* they must have the type of high-calibre proposals that will win respect in the international arena. This may not be easy: at Japan's sole academic oceanographic institution

— the Ocean Research Institute at Tokyo University — the number of graduate students and postdoctoral fellows has dropped dramatically over the past five years. Japan's science ministry needs to support new faculty positions, new postdoctoral positions, more graduate students and more positions for visiting Earth scientists from abroad.

And as magnificent as it is, *Chikyu* cannot do everything that the IODP needs done. The programme has two other 'pillars' that have run into problems. The US-led contribution is a vessel meant to complement *Chikyu*, but this veteran of the Ocean Drilling Program, *JOIDES Resolution*, continues to languish at a dock in Singapore because of lack of funding and skilled workers to refurbish it. European organizers of the third pillar — mission-specific platforms — must cope with the fact that the oil industry's appetite for ships and staff leaves little capacity for equipment and staffing for scientific expeditions. The IODP has struggled just to rent mission-specific platforms for individual cruises, even though member countries have paid their dues and invested the time of their leading scientists.

A downturn in the oil price after investment in new fields might alleviate those problems by reducing the incentives for exploration (although don't bet on it). Even if it does, though, and especially if it doesn't, IODP managers must do what they can to get *JOIDES Resolution* refitted and back at sea. It would be a shame if, after all the scientific and diplomatic work that has gone into the exemplary international setting up of the IODP, the efforts ended up wasted by the budgetary stress of an oil crisis that was not predicted when the IODP started its planning. The launch of *Chikyu* should serve as a wake-up call for scientists, mission planners, and policymakers to redouble their efforts to keep this exciting programme moving in the right direction. Onwards and downwards! ■

RESEARCH HIGHLIGHTS

CLIMATE SCIENCE

Water, water, in the air

Proc. Natl Acad. Sci. USA doi:10.1073/pnas.0702872104 (2007)

Satellite observations show that the total atmospheric moisture content above the oceans has increased by 0.41 kilograms per square metre per decade since 1988. Statistical analyses now show that this is a climate 'fingerprint' of human greenhouse gas emissions.

The analysis, led by Benjamin Santer of the Lawrence Livermore National Laboratory in California, shows that the observed increases in atmospheric moisture levels are consistent with models that take into account a human-induced greenhouse effect. Furthermore, they could not be fully explained by other proposed causal factors such as increased solar activity or recovery from the 'global dimming' effects of the 1991 Mount Pinatubo eruption.

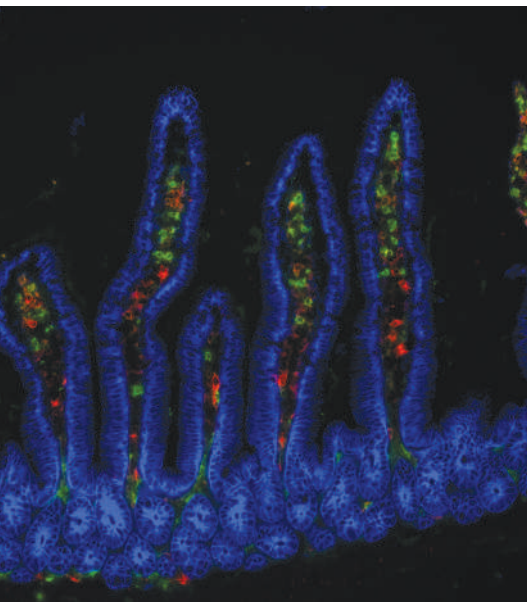
IMMUNOLOGY

A gut decision

Nature Immunol. doi:10.1038/nri1511 (2007)

In the gut, the immune system must attack deadly pathogens such as *Salmonella*, while tolerating the billions of harmless bacteria that live there. Bali Pulendran and his colleagues at Emory University in Atlanta have discovered two types of immune cell in the guts of mice that may help to determine which response a microbe meets.

The cells seem to wage a tug-of-war. On one side are a type of macrophage (stained green in the section of small intestine pictured) that acts to suppress the immune



The scent collectors

Proc. R. Soc. B doi:10.1098/rspb.2007.0727 (2007)

Researchers have traced how male neotropical orchid bees (pictured) concoct a perfume that they may use to seduce their mates.

The bees collect scents by spitting fatty secretions onto everything from flowers to faeces. The secretions absorb the smell, and are then stashed in pockets on the bees' hind legs. Thomas Eltz at the University of Düsseldorf in Germany and his colleagues isotopically labelled a component of these secretions and added it to the hind-leg pockets of male *Euglossa viridissima*. Four days later, the bees had recycled most of the compound, moving it from the legs to glands in the head.

The researchers note that *E. viridissima* glands and secretions resemble those of bumblebees that spread their own scent, suggesting an evolutionary link between the two behaviours.



T. ELTZ

response. On the other, a type of dendritic cell that the team showed turns up mouse defences. Their interplay may be what shifts the overall response of the immune system in the gut. The researchers also suggest that imbalances in the cells' effects could explain inflammatory bowel disease.

NEUROBIOLOGY

Cycling in tune

Nature Neurosci. doi:10.1038/nn1974 (2007)

Auditory neurons, which transmit acoustic information into the brain, need to encode sounds ranging from the very quiet to the very loud. New observations show that the number of one type of receptor at a neuron's surface drops temporarily after exposure to a loud sound, decreasing the neuron's sensitivity to subsequent noise.

William Sewell and his colleagues at the Massachusetts Eye and Ear Infirmary and Harvard Medical School in Boston saw this happening for AMPA receptors. Researchers have previously seen AMPA receptors coming and going in cultured hippocampal neurons. The function of such recycling in a part of the brain associated with learning and memory is not clear, but the researchers suggest that in auditory neurons it may optimize the handling of sound's large dynamic range.

OPTICS

Bumps in the night

Appl. Phys. Lett. 91, 101108 (2007)

Some nocturnal insects such as moths enhance their vision with an antireflective coating of tiny bumps on their compound eyes. Peng Jiang of the University of Florida in Gainesville and his co-workers offer a cheap route to copying the coating's design.

Antireflective coatings are useful in industry, for example on car dashboards or solar cells. But patterns that mimic the small moth-eye bumps are difficult to make over large areas using standard lithographic patterning methods. Jiang and colleagues' approach is to cover a surface with a layer of 360-nm silica beads, which pack into an ordered array. This acts as the template for a mould made from a soft polymer, from which endless replicas of the bead layer can be made.

CELL BIOLOGY

Out of shape

Cell 130, 837-850 (2007)

Proteins known as septins form part of a signalling pathway that links a human cell's scaffolding to its DNA-damage response, researchers report.

Ian Macara and his team at the University of Virginia School of Medicine in Charlottesville

found that silencing expression of three septins caused human cells to lose their shape, because their scaffolding of actin fibres broke down. They showed that the effect depends on the interaction of septins with a signalling protein called SOCS7, and that loss of that interaction triggers SOCS7 to recruit another protein, known as NCK, to the cell's nucleus.

Further experiments revealed that NCK also collects in the nucleus of cells exposed to DNA-damaging stresses such as ultraviolet light, helping to stop the cells' growth. Macara says that many details of how and why the link operates remain to be explored.

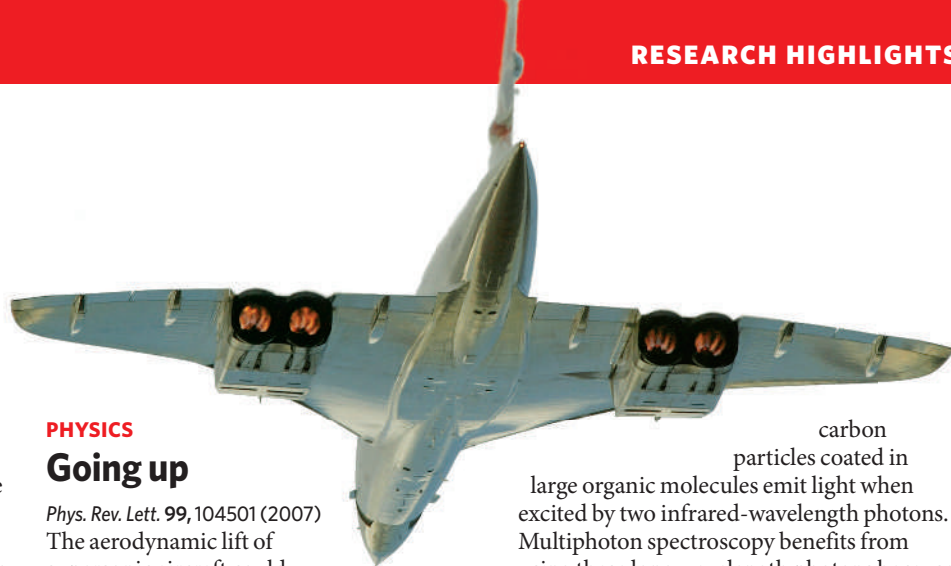
CANCER BIOLOGY

Alternative remedy

Cancer Cell 12, 230–238 (2007)

New research challenges the long-held idea that antioxidants fight tumours primarily by preventing DNA damage. Tests involving vitamin C and another antioxidant, *N*-acetylcysteine, suggest that they inhibit tumour growth by destabilizing the protein hypoxia-inducible factor 1 (HIF-1). This protein stimulates blood-vessel development and glucose metabolism in tumours.

Chi Dang of Johns Hopkins University School of Medicine in Baltimore, Maryland, and his colleagues found that *N*-acetylcysteine reduced tumour growth in mice and in human cell cultures without affecting the frequency of genome rearrangements due to DNA damage. They also found that both *N*-acetylcysteine and vitamin C increased the degradation of HIF-1. The researchers confirmed the link with the finding that tumours expressing a mutant form of HIF-1 that resists degradation were less affected by the two antioxidants than those expressing a normal form.



PHYSICS

Going up

Phys. Rev. Lett. 99, 104501 (2007)

The aerodynamic lift of supersonic aircraft could be boosted by roughening the undersurface of their wings, Guang Lin and his colleagues at Brown University in Providence, Rhode Island, suggest.

The researchers' computational models predict that the amount of lift generated by an aerofoil wing over which air flows at supersonic speeds increases when the wing's bottom edge has a randomly rough surface. This offers a theoretical validation of an idea that emerged from experiments in the 1990s.

The effect is caused by complex reflections of the shock waves generated at the wing surface, and the increase in lift can be comparable to that produced by a smooth aerofoil. But the authors stress that any attempt to exploit the effect in aircraft (should there be a successor to Concorde, pictured, for example) would have to balance the gain in lift against the increased drag the roughness causes.

METHODS

Dot to dot

J. Am. Chem. Soc. doi:10.1021/ja0735271 (2007)

Carbon nanoparticles can be used in a technique known as multiphoton imaging to light up the inside of cells, researchers report.

Ya-Ping Sun and his colleagues at Clemson University in South Carolina found that

carbon particles coated in

large organic molecules emit light when excited by two infrared-wavelength photons. Multiphoton spectroscopy benefits from using these long wavelength photons because they can penetrate tissue more deeply and are less damaging to biological material than shorter wavelength light. The team tested the particles in human cancer cells. Carbon-based imaging agents are non-toxic and are unlikely to bioaccumulate.

IMMUNOLOGY

Collateral damage

J. Clin. Invest. doi:10.1172/JCI31344 (2007)

A type of therapy being tested against HIV may carry a risk of boosting coronary artery disease, if results from a mouse study hold true in humans.

Previously, researchers have shown that a protein known as programmed death 1 (PD-1) is displayed at high levels on T cells in patients with HIV. PD-1 seems to interact with partner proteins PD-L1 and PD-L2 to exhaust the body's response to the virus, so scientists are testing whether blocking this interaction could help patients to fight HIV.

But Andrew Lichtman and his team at the Brigham and Women's Hospital and Harvard Medical School in Boston, Massachusetts, have found that if mice with high cholesterol lack PD-L1 and PD-L2, they have larger plaques in their arteries with more T cells than do mice with high cholesterol that have both proteins.

JOURNAL CLUB

Eörs Szathmáry
Collegium Budapest, Hungary,
and The Parmenides Foundation
for the Study of Thinking,
Munich, Germany

A theoretical biologist recommends thought-provoking reading on the origin of translation and the genetic code.

As Francis Crick and his co-workers once noted, "the origin of protein synthesis is a notoriously difficult problem". Our best hopes of resolving this problem begin, in my opinion, in an RNA world.

The RNA-world hypothesis holds that RNA emerged before DNA and proteins, neatly separating the origin of life from that of the genetic code and its translation. The question then becomes: how did RNA evolve to make proteins?

In a recent paper, Yuri Wolf and Eugene Koonin of the National Institutes of Health in Bethesda, Maryland, present one scenario (*Biol. Direct* 2, 14; 2007).

They rightly call attention to studies that suggest that protein-based aminoacyl-tRNA synthetases, which are involved in the first steps of assembling

amino acids into proteins, are relatively late evolutionary inventions. This forces us to accept the idea that protein synthesis is older than such synthetases.

Before the evolution of synthetases, the only agents that could conceivably have marshalled amino acids are RNA enzymes, or ribozymes. Wolf and Koonin share my view that the recruitment of amino acids was driven by selection for enhanced catalytic activity, and that the ancestor of the large ribosomal RNA that catalyses protein synthesis in today's cells — a

molecular 'fossil' — was a catalyst that linked only two amino acids.

I am less happy with these authors' suggestion of a relatively late switch from peptide-specific proto-ribosomes to those that could use an external template such as mRNA to synthesize peptides with arbitrary sequence — but they may well be right.

They lay out an evolutionary sequence that is more complete than the scenario I once proposed. I highly recommend this well-written, thought-provoking paper.

Discuss this paper at <http://blogs.nature.com/nature/journalclub>

NEWS

Fusion project faces axe

A major US experiment that might open a more commercially attractive route to fusion is facing the prospect of closure after running into heavy cost overruns and scheduling delays.

On 15 September, a panel of independent scientists travelled to Princeton Plasma Physics Laboratory in New Jersey to determine whether to shut down the National Compact Stellarator Experiment (NCSX). Raymond Orbach, the Department of Energy's undersecretary for science, called for the review after discovering that the project was nearly US\$40 million over budget and two years behind schedule. "Given the magnitude of the increases projected," Orbach wrote in a 9 August letter to the panel, "all options, including termination of the project, must be considered."

Whereas nuclear fission derives its energy from the splitting of heavy nuclei such as uranium, fusion produces energy from the fusing of lightweight elements, usually hydrogen isotopes. The dream is to produce energy from abundant materials such as sea-water without generating long-lived radioactive waste. Most of the world's current efforts to show that fusion could be a feasible energy option is focused on ITER, a massive reactor now under construction in Cadarache, France, and slated to cost \$6 billion in construction and \$6 billion in operating costs until 2026.

Fusion only takes place when hydrogen is heated to hundreds of millions of degrees to form a plasma, and so fusion reactors must contain their hydrogen fuel inside a magnetic field. ITER's design, known as a tokamak, will generate that field by a combination of external superconducting magnets and an internal current through the core (see *Nature* **436**, 318; 2005). This design is relatively simple to build, but the internal current can disrupt the confinement.

Tokamaks hold on

South Korea has just completed its own large tokamak fusion reactor. Located in Daejeon, the Korean Superconducting Tokamak Advanced Research (KSTAR) reactor opened on 13 September after 12 years construction at a cost of US\$330 million.

KSTAR is an important precursor to the ITER fusion project, says Francesco Romanelli, who directs the Joint European Torus — the world's largest operating tokamak, located in Oxfordshire, UK. KSTAR is the first machine to have magnets made from a niobium-tin (Nb_3Sn) alloy rather than copper — Nb_3Sn will also be used in ITER. The superconducting magnets will allow KSTAR to hold its plasma for relatively long pulses, perhaps up to 5 minutes: good for a tokamak, Romanelli says.

With a radius of 1.8 metres, KSTAR is one-third the size of ITER. Korea is also involved in the ITER project, contributing nearly one-tenth of its costs.

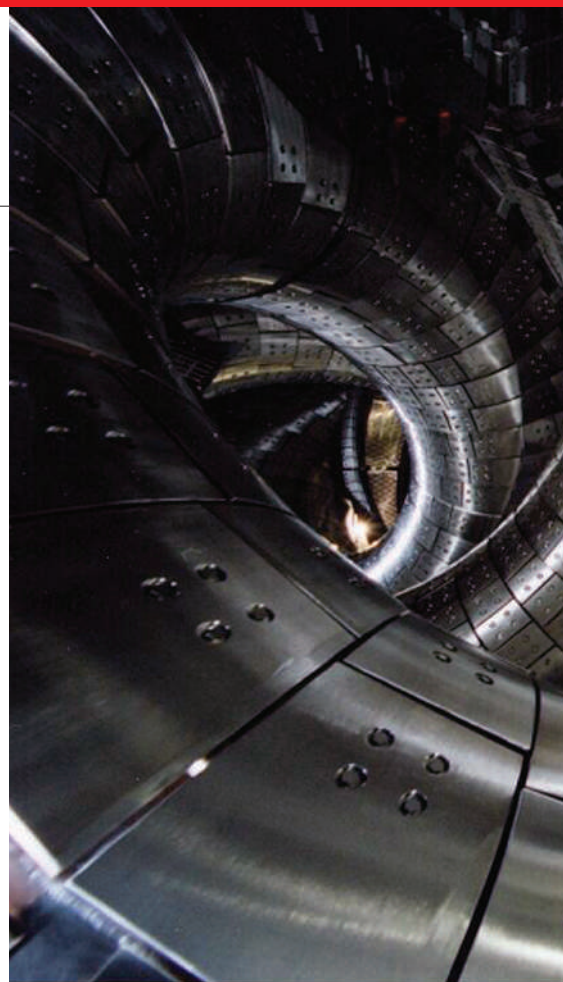
G.B.

The Princeton experiment hopes to get round those problems using an alternative set-up called a stellarator. Unlike tokamaks, stellarators use only external magnets to confine the plasma. The lack of an internal current makes the plasma more stable and, in theory at least, allows stellarators to run for longer than tokamaks. Stellarators cannot yet operate at the temperatures and pressures of tokamaks, but the results of early experiments are impressive: a Japanese stellarator known as the Large Helical Device, in Toki City, has held its plasma for more than an hour. Current tokamaks, by contrast, can hold their plasmas for a few minutes at most.

But the promise of stability comes at a cost, says Thomas Klinger of the Max Planck Institute for Plasma Physics in Greifswald, Ger-

many. To hold plasma without an internal current requires much more complex magnetic-field geometry. That must be created with unusually shaped magnetic coils, which are difficult to manufacture. "A stellarator is much simpler to operate, but much more difficult to build," he says.

Construction seems to be at the core of the NCSX's woes. The project was originally budgeted at about \$92 million with completion in 2009, but a review this July found that costs had ballooned to \$130 million and completion date had been pushed back to 2011. "As we came into the assembly phase, it turned out to be more complicated than we anticipated," says Stewart Smith, dean of research at Princeton University, which oversees the lab and



Florida courts German life-sciences institute

Germany's Max Planck Society is to open its first non-European institute in Florida. On 11 September, the state's Palm Beach County commission voted to spend \$87 million over the next 10 years building a Max Planck Institute adjacent to the planned site of Scripps Florida on the Jupiter campus of Florida Atlantic

University. The state of Florida is expected to contribute the remaining \$103 million needed to fund the institute, which will focus on bioimaging.

Max Planck Society president Peter Gruss says current plans are for the new institute to house three senior department heads and their labs, five junior faculty

and six labs for visiting professors, in all a total of about 150 staff. He says that if the state commits to giving its share of funds soon, as is expected, administrative operations could begin as early as 2008. Gruss says the idea to set up in Florida stemmed from the efforts of former Florida governor Jeb Bush, who visited Munich to

court a partnership in 2005.

Gruss' friendship with Scripps president Richard Lerner also played a part. The prospect of being next door to Scripps Florida was a huge draw, says Gruss. "We are quite strong in bioimaging, and we thought this would complement Scripps' expertise in biological chemistry very well,"



NIFS, JAPAN

Japan's fusion machine, the Large Helical Device, has produced impressive results.

the experiment. Smith declined to comment further on the reasons for the delay, except to say that the cost underestimation was being taken "very seriously".

The review of the NCSX comes at a crucial time for the US fusion programme, according to Stephen Dean, the head of Fusion Power Associates, a non-profit group in Washington, Seattle, that advocates the development of fusion. The fusion-research community has long feared that US participation in ITER would starve other programmes of funds. As all planned fusion budget increases are to go towards the American contribution to ITER, that leaves no contingency for cost overruns in other programmes such as the NCSX, says Dean. "I think there's a fair possibility that the Department of Energy

will cancel the programme," he says.

"In my opinion, that would be a sin," says Klinger, who heads Wendelstein 7-X, a €300-million (\$416 million) German stellarator project under construction in Greifswald. Unlike the German reactor, the NCSX was to use a unique hybrid of stellarator and tokamak technology. If it worked, Klinger says, it could lead to tokamaks that could operate continuously, which would be far more commercially attractive than the ITER design. "It is a very important experiment," he says.

The fate of the programme will probably be determined after the current review is completed. The committee is expected to deliver its report at the end of October.

Geoff Brumfiel

Gruss adds. "We thought a unit in the vicinity of Scripps would create an entity that would be more than the sum of its parts."

Scripps Florida has encountered some roadblocks since the agreement with the state to set up an institute in Palm Beach County was signed in 2003. Tussles over siting of the institute delayed its opening (see *Nature* 431,

5; 2004), and some Florida lawmakers objected to the terms of the deal between Scripps and Florida. But construction is now under way, while about 260 employees work in temporary space. Lerner says the new campus should be operational in 2009.

Gruss has big plans. "Our business is running high-class, cutting-edge research institutes, and we

want to spread our wings," he says. The institute has two 'partnerships' with universities in Buenos Aires and Shanghai, but these are not full-fledged institutes. Should the Florida venture be successful, Gruss says the society will look to open more institutes elsewhere: "I am optimistic that this is not going to be the last." Erika Check

ON THE RECORD

"I think [Lisa] Nowak should be admired for travelling across the country at night and not getting out of her car to put in gas or go to the restroom."

Former moonwalker Buzz Aldrin tries to take the positives from astronaut Lisa Nowak's arrest for attempted kidnapping.

3 GOOD REASONS...

Yet more NASA fun as *Wired's* bloggers have been asking readers to suggest a new slogan for the world's best-loved space agency. Our favourites are:

1 NASA: In 100 years, you'll wish you'd given us more funding.

2 NASA: Actually, this is rocket science.

3 NASA: The budget is the limit.

SCORECARD



Electric motorbikes

The search for high-performance non-petroleum bikes took a lurch forward in Los Angeles last week, as inventor Bill Dube unveiled his 'KillaCycle', which, he says, can go from zero to 100 kilometres per hour in less than a second.



Electric motorbikes

Unfortunately for Dube, the KillaCycle almost lived up to its name during the demonstration, as he accidentally hurtled straight into a van.

Sources: Associated Press, *Wired*, *TGdaily.com*, *Grist*

WWW.KILLACYCLE.COM

SIDELINES

Debt collectors channel cash to corals

Damaged by divers, pollution and climate change, coral reefs may soon be protected through debt forgiveness. The US Congress is expected to approve a bill that would cancel foreign debt in developing countries in exchange for coral reef and rainforest conservation.

The Tropical Forest and Coral Conservation Act of 2007 sailed through the Senate's foreign-relations committee on 11 September. The full Senate and House of Representatives should take up the bill soon, and it could reach President George W. Bush — a supporter — by the end of 2007, says Mark Helmke, a senior adviser for Senator Richard Lugar (Republican, Indiana), one of the bill's sponsors. The bill provides \$75 million to pay off debts owed to the United States over the next three years.

Congress passed a similar bill in 1998 that has channelled \$137 million to protect rainforests in developing countries such as Panama,



Indonesia could be the first country to swap national debt for corals.

Bangladesh and Botswana. Under the deal, countries in debt to the US Agency for International Development give money to local conservation groups. In return, the United States cancels the same amount of debt. For example, in 2003, the US government cancelled \$10 million in debt owed by Panama to pro-

tect the Chagres National Park. The money is being spent on projects such as park-boundary enforcement to stem illegal farming and training locals as ecotourist guides.

Indonesia is likely to be the first country to take up the debt-for-coral swap. Its Coral Triangle, home to more than 600 species of coral and 3,000 species of fish, is under threat from pollution, overfishing and bleaching — a situation exacerbated by global warming.

"Corals are in a tricky position because of climate change," says Lara Hansen, chief scientist for climate change with the conservation group WWF

in Washington DC, which has helped to broker rainforest protection. "Even if you protect a coral spatially, you still have this massive threat." But any measure that relieves stress on reefs will buffer against damage from warming, she adds.

Ewen Callaway

B. COLE/NATUREPL.COM

Malaria research should go 'back to basics'

Efforts to wipe out malaria must stop squandering resources on trials of ineffectual vaccines and focus instead on generating better candidates, according to a report released on 17 September by the George Institute for International Health in Sydney, Australia.

The report looked at the status and future prospects of 47 vaccines and 21 drugs in various stages of development. The vaccine furthest along is one developed by GlaxoSmithKline (GSK). It should enter large-scale, phase III trials in 2008, with licensing pegged for 2012. The vaccine nearly halved severe malaria in a 2005 trial in 2,000 children younger than 5 years in Mozambique (P. L. Alonso *et al. Lancet* 366, 2012–2018; 2005). But the report comes down hard on the other vaccines. Far too many have been tested in clinical

trials, in which most are certain to fail, eating up resources, says lead author Mary Moran, director of health policy at the George Institute. "You can't have all this stuff going to the field, you have to start weeding them out," she says.

But GSK's vice-president of clinical development, Ripley Ballou, argues that clinical tests are the only way to determine whether a vaccine works or not, and says that the trials can be done relatively cheaply. "For a couple of million dollars you can do a clinical study and kill a product if it doesn't work," he says.

Moran's team is calling for more basic research into malaria and the *Plasmodium* parasites that cause the disease. "There's not much new science coming into the field," agrees Stephen Matlin of the Geneva-based Global Forum for Health Research. Researchers

barely know how humans fend off malaria, he points out, an insight that would help vaccine-makers to focus their efforts.

But Pedro Alonso, a researcher at the University of Barcelona in Spain who led trials of the GSK vaccine, says that the world shouldn't wait for science to catch up before going forward with malaria vaccines. "I worry that other vaccines aren't

doing as well," he says. But they shouldn't be abandoned. "It is not healthy to rely on just one candidate. Things can go wrong."

Despite large donors such as the US National Institutes of Health and the Gates Foundation infusing the field with cash, much more money is needed, the report claims. At least \$560 million will be required over the next five years to see current vaccines and drugs through development and clinical trials, Moran's team says. The report also calls for more cooperation between people who talk regularly but don't often work together. Such coordination would make more efficient use of the 23 clinical test sites for malaria vaccines in Africa. With so many vaccines moving forward, researchers could end up fighting for access to patients.

Ewen Callaway



Malaria kills at least 1 million a year.

O. ANDERSEN/AFP/GETTY



SNAPSHOT

Beneath the skin

Anatomy was rediscovered during the Renaissance when artists such as Leonardo da Vinci needed to be scientists — and scientists, such as Andreas Vesalius, needed to be artists. They measured proportions and features with mathematical precision. And when dissecting corpses, they systematically drew what they saw — there was no alternative method. The results were practical: precise anatomical knowledge informed both painting and the early studies in physiology. These paintings and studies were also beautiful. The presentation of human anatomy continued to be highly aestheticized over the centuries — and now, it seems, it is highly collectable.

A remarkable collection of more than 200 books, prints, drawings and wax models depicting human anatomy is being auctioned by Christie's in New York on 5 October. Put together by the US physician-broadcaster Dean Edell, the collection includes items from the sixteenth to the twentieth centuries.

Included, for example, is a 1528 edition of Albrecht Dürer's *Hierinn sind begriffen vier Bücher von menschlicher Proportion* (*Four Books on Human Proportions*) which is reserved at \$20,000, a 1543 edition of Vesalius' seven-volume *De humani corporis fabrica* (*On the Fabric of the Human Body*) which is expected to go for at least \$250,000 and a series of photographs of brain preparations dissected and stained by the nineteenth-century neuroanatomist Carl Wernicke, at just a few hundred dollars.

The collection also includes several rare books and prints by the eighteenth-century illustrator Jacques Gautier d'Agoty — a pioneer of colour printing. The picture here (left) is typical of the d'Agoty style of exposed internal anatomy in an otherwise quiet, everyday composition. ■

Alison Abbott

Arctic melt opens Northwest passage

The most direct shipping route between the Atlantic and Pacific oceans, connecting Asia and Europe, is fully navigable for the first time since records began, data show. Warming has led to a record retreat of Arctic sea ice, which covers about 16 million square kilometres during March each year and melts to a minimum sometime in September or October. The previous record minimum was 5.32 million square kilometres, set in 2005, but this year it has already reached a low of 4.24 million square kilometres, according to the US National Snow and Ice Data Center in Boulder, Colorado.

The drop may have been caused by warmer ocean waters over the past few summers, says John Walsh, a climate scientist at the University of Illinois in Urbana-Champaign. This summer has been unusually cloud-free, and spring temperatures over the Russian part of the Arctic were higher than usual, he says. Lack of sea ice itself contributes to warming, since ice reflects the Sun's heat better than the sea. The Intergovernmental Panel on Climate Change predicts that if current trends continue, a summer without sea ice will occur in the next 40 to 100 years. ■

Daniel Cressey

SPECIAL REPORT

Opiates for the masses

Afghanistan produces almost all of the world's illegal opiates. Should it eradicate the poppy trade or experiment with legalizing it to make painkillers for the developing world? **Katharine Sanderson** reports.

During the next few weeks farmers in one of the world's poorest countries will begin sowing seeds for what is expected to become the biggest and most lucrative opium crop yet. Field upon field of beautiful blooms belie a dark legacy that wends a destructive path from the growing fields of Afghanistan to individuals in cities thousands of miles away.

Yet opium and its derivative heroin are the biggest cash exports in a country ravaged by war — the livelihoods of whole communities depend on the crop, which represents more than 40% of the country's gross domestic product. And it's not just Afghan villagers earning from the crops — insurgents, warlords, the Taliban and terrorist groups obtain a large part of their funding through trade in illicit narcotics, according to the United Nations Office on Drugs and Crime (UNODC), headquartered in Vienna, Austria. The nation's opium production — accounting for 93% of global illegal production — exceeds the world's demand for illicit opiates by more than 3,000 tonnes, according to a UNODC report released last month.

Opium poppy (*Papaver somniferum*) cultivation in Afghanistan is up 17% on last year, to 193,000 hectares. Good weather meant that each hectare yielded more opium — the crop in 2007 was up by more than one-third from 2006. It is an attractive crop for farmers in times of insecurity — opium lasts for a long time without spoiling, unlike other perishables. And, of course, it attracts high prices. In 2007 the average 'farm-gate' price of opium was US\$122 per kilogram. The southern province of Helmand, where there is little security and Taliban insurgents exert a huge influence, is now the world's biggest supplier of illicit drugs — the total opium income for farmers in that province was \$528 million. In 2006, according to the US state department, the export value of opium from Afghanistan was \$3.1 billion (for 6,100 tonnes), but by the time it reaches the streets of London, UK, for example, its price rises to about £20 billion (\$38 billion).

Internationally, the consensus is that the situation is at crisis point, but there remains intense disagreement on the best course of action. The United Nations and the Afghan government

have both called for assistance from North Atlantic Treaty Organization (NATO) troops to help to eradicate poppies. But last week NATO reiterated its opposition to direct action, saying: "The NATO International Security Assistance Force (ISAF) does not allow for ISAF to be directly involved in poppy eradication." Many fear that the sight of NATO troops ripping up crops would damage relations with ordinary Afghans and drive them towards the Taliban.

To spray or not to spray?

So what should be done? Many argue that indiscriminate aerial crop-spraying will be the only effective option. "Very strong pressure is now building up in favour of aerial eradication," UNODC's executive director, Antonio Maria Costa said recently. The United States also strongly supports this stance, and is leading the push to spray the growing poppy fields. But Afghan president Hamid Karzai is opposed to the idea. However, in a direct contradiction, Ahmad Zia Massoud, one of Afghanistan's vice-presidents, recently called for spraying.

His view is not shared by a number of other bodies. "We are against the policy of aerial spraying," says the British Embassy in Afghanistan's counter-narcotics expert. "We would likely be handing the insurgents a propaganda tool." Every subsequent birth defect, or "two-headed cow" would immediately be blamed on the spraying, he argues.

With the population so financially dependent on the crop, international bodies are increasingly looking at alternatives to eradication to address the illicit drugs trade problem, including introducing a legal, licensing scheme. On 12 September, the European Parliament's Committee on Foreign Affairs issued a report calling for its council to put a proposal to the Afghan government for turning part of the poppy crop into legal analgesics, such as morphine and codeine.

The Senlis Council, an international think tank with an office in Kabul, has its own scheme, called the Poppy for Medicine programme, which would give control of opium production to local communities, and would license them to produce morphine powder from their crop. "It's not just a policy choice, it symbolizes

"Legalizing trade symbolizes what sort of relationship you want to have with the Afghan people."



Heads in the clouds: heroin and morphine can be derived from the gum in opium poppy seed heads.

what sort of relationship you want to have with the Afghan people," says Norine MacDonald, president of the scheme. Opium-licensing schemes in Turkey, introduced in the 1970s, and a longer-running scheme in India have proved successful, MacDonald points out.

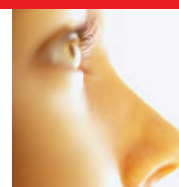
Law and order needed

But the proposal has its critics. "Legalizing is not an option," says Susan Pittman, from the US state department. And the British agree: "In order to have licit cultivation you need to have law and order," and Afghanistan is not in that situation. "You'd be putting the Afghanistan government in competition with the narcotics traders," the British Embassy spokesman says.

The Embassy's view is that producing morphine in Afghanistan would be uneconomic because of cheaper fertilizers and automated systems in other countries. The Senlis Council claims that in its Poppy for Medicine schemes, groups of farmers would sell their morphine to the Afghan government for \$3,100 per kilogram — a significant mark-up on the current gate-price of opium — and the government could then sell it on for \$4,300 per kilogram.

Opium is first processed to a crude morphine base, morphine hydrochloride. This can then be converted to either morphine powder, or heroin (see 'From flower to needle').

A. MASSOUD/REUTERS



BEAUTY IS IN THE NOSE OF THE BEHOLDER

Gene found that determines whether human pheromone smells nasty or nice.

www.nature.com/news

expert says that this is a misconception. "There may be fundamental problems with supply," he says, and problems with distribution, but "there is not a worldwide morphine shortage."

"For the past two decades morphine has been available in sufficient quantities at the global level to cover the demand," says Margarethe Ehrenfeldner from the International Narcotics Control Board (INCB) in Vienna, Austria. That morphine comes from licit opium, produced mainly in India, Turkey, Australia, France, Spain and the United Kingdom. GlaxoSmithKline, for example, supplies 25% of the world's medicinal opiates from poppies grown in Tasmania in Australia.

But the Senlis Council claims that the INCB's data are skewed. It says that the market demand defined by the INCB is not the same as the actual need for morphine and other poppy-derived medicines, such as codeine. The need for morphine in developing countries is underestimated because of a self-perpetuating cycle of under-prescription and inhibitory import regulations, the Senlis Council says. And Ehrenfeldner admits that some governments report low levels of morphine consumption. "The INCB and WHO are taking measures to increase accessibility of analgesics worldwide," she says, "however, this cannot be accomplished in the short run."

The Senlis Council had hoped to have its pilot scheme up and running by the October growing season, but this is looking "unlikely", it now says. The plan for a new Afghan industry in legal opium production could be thrown into jeopardy if aerial spraying is carried out during the February 2008 harvest. "The deal was essentially that if cultivation was up next season on 2007's, the United States would absolutely spray this coming year," says Senlis's Brigitte Scheffer. ■

To produce 1 kilogram of morphine takes around 8 kilograms of opium. According to the UNODC, this year's opium crop in Afghanistan — 8,200 tonnes — would produce 1,170 tonnes of heroin. Most of Afghanistan's opium is converted to heroin within the country, mainly in labs set up near the border with Iran. Surveyors reports showed that the number of these labs increased in 2007. The trafficking process includes bringing the chemicals needed to convert opium to heroin into Afghanistan. Under the Senlis Council proposal labs would be set up locally to produce morphine powder directly.

One of the Poppy for Medicine programme's strongest arguments is the need to provide painkillers to countries where there is a shortage, including Afghanistan itself. In North America, average annual morphine consumption is 55 milligrams per person, in north Africa and the Middle East this plummets to 0.29 milligrams per person, and in the Asia Pacific region it is 0.67 milligrams per person. "Afghans don't know what painkillers are; it's a rich person's idea," says MacDonald, who says that there is a large unmet need for painkillers. But the British Embassy counter-narcotics

From flower to needle

Opium comes from the poppy's seed pod. When first extracted it is a white gum, which turns into a black tar over a short period of time once it is released from the pod. This crude opium gum contains more than 20 alkaloid compounds. Morphine is one of those alkaloids, and makes up 10–20% of the gum, depending on the plant and the growing conditions. The amount of morphine is also related to the gum's codeine content, which varies from 1% to 3%. Heroin is not present in the opium gum but is produced through further

chemical reactions on morphine.

Morphine can be extracted easily: the opium gum is usually placed in a large drum filled with boiling water and lime (calcium hydroxide). This converts the morphine into calcium morphenate, making it water-soluble. Other organic molecules remain insoluble, and can be removed. As the solution cools, the calcium morphenate can be scraped out of the barrel, filtered, washed with ammonia, and dried to form a crude morphine clay. The conversion to heroin is a two-step process, and involves heating



An Afghan farmer collects poppy gum.

the morphine clay with acetic anhydride to replace both hydroxyl (OH) groups with acetyloxy (OCOCH₃) groups, leaving a crude form of diacetylmorphine (heroin). Further purification is needed to get

a sellable heroin base.

One kilogram of opium will produce 100–200 grams of morphine and 10–30 grams of codeine. More codeine can be made by replacing one of morphine's OH groups with a methoxyl (OCH₃) group.

And as the yield for the transformation to heroin is around 68%, depending on the production method, that single kilogram of opium, transformed to morphine, will produce about 60–70 grams of heroin.

K. S.

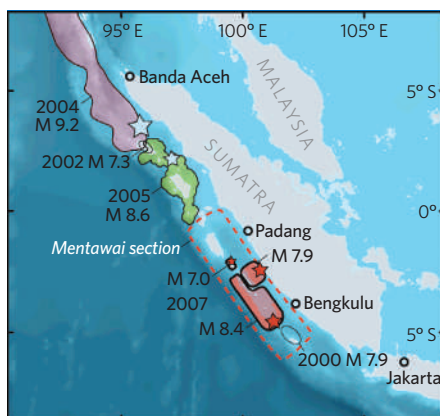
R. GUL/AP

Worse quake to come, Indonesia warned

A week after a series of powerful earthquakes rocked Indonesia, killing more than 20 people, geologists are warning that “the big one” may be yet to come. The region might still hold enough energy to release a magnitude-9.0 tremor that could produce a deadly tsunami, echoing the 2004 tsunami that killed more than 230,000 people in southeast Asia.

The trio of quakes, of magnitudes 8.4, 7.9 and 7.0, occurred off the coast of Padang in southwest Sumatra on 12 and 13 September, along a subduction zone where the Australian tectonic plate dives under the Sunda plate. The plates are sliding past each other, but in some patches they stick, building pressure, which is released when the plates slip in an earthquake. Last week’s earthquakes released pressure from a 700-kilometre-long region, known as the Mentawai section, which had been building since the last quake, an event of magnitude 8.6–8.9 in 1833.

Kerry Sieh, an earthquake geologist at the



A magnitude-9.0 quake is predicted to hit the top of the Mentawai section, left unruptured last week.

California Institute of Technology in Pasadena, has spent the past 15 years studying the history of Indonesian earthquakes from the patterns the tremors leave in coral growth. His data

suggest that this area has ruptured every 200 to 230 years since the fourteenth century.

Based on Sieh’s study of the uplift of fossil corals, a preliminary analysis suggests that last week the plates slipped far less (around 2 metres) than they did in 1833 (10–18 metres). If that is the case, not all the pressure may have been released, and part of last week’s rupture zone could ‘re-rupture’ in conjunction with a 200-kilometre patch off the coast of Padang (see image) that has not ruptured since 1797. That would produce a magnitude-9.0 quake, he says — enough to spawn a deadly tsunami.

Jim Mori, an earthquake specialist at Kyoto University’s Disaster Prevention Research Institute, says Sieh’s ‘seismic gap’ theory is plausible. “It is similar to the geological trough at Nankai in Japan in that earthquakes are now expected where they have not occurred in a long time,” he says.

David Cyranoski

See News Feature, page 278.

Gene therapy might not have caused patient’s death

A patient with arthritis who died in July during a gene-therapy trial may have succumbed to an infection she had before the viral vector was administered, experts said on Monday at a meeting of an advisory panel in Bethesda, Maryland, investigating the incident.

Little of the evidence presented to the panel seemed to indicate that the injected viral vector had a key role in 36-year-old Jolee Mohr’s demise. Although DNA sequences from the vector were found in her liver and spleen, “the detection of the sample is very low and below the limit of quantification in these assays”, said Jeffrey Bartlett, a member of the National Institutes of Health (NIH) Recombinant DNA Advisory Committee (RAC). “It really indicates the absence of ongoing replication of the vector in these tissues.”

The panel is still awaiting the results of tests on Mohr’s tissue samples, expected by December, and the results of blood studies looking for the vector and protein

produced by the transgene. It will then reach a firmer conclusion about whether the gene therapy she received three weeks before her death was in any way responsible for it. But even with all the information in hand, “there will I think still be some uncertainty”, said RAC chair Howard Federoff.

Mohr died on 24 July, 22 days after her right knee was injected with an adeno-associated virus (AAV) vector made by Targeted Genetics, a Seattle company. This vector was engineered to contain a gene for an anti-inflammatory protein, TNFR:Fc, which inhibits tumour-necrosis factor- α (TNF- α). TNF- α causes inflammation in rheumatoid arthritis.

Autopsy results and the clinical history of the patient presented at the 17 September meeting indicated that the immediate cause of her death was massive bleeding of unknown origin in the tissue space behind the kidneys. This displaced her abdominal organs and ultimately

compressed her lungs, making them unable to function. She was also overwhelmingly infected with histoplasmosis, an environmental fungus that can cause serious infections in immunocompromised individuals. She began to feel ill with fatigue and a low-grade fever three days before the gene therapy was administered, the panel heard.

TNFR:Fc suppresses the immune system, and so it is possible that the gene therapy caused the infection. However, the design of the trial, in which some patients were also taking similarly acting immunosuppressant drugs, means that it will be difficult to ascertain what caused the infection to take hold. Mohr was also taking a TNF- α -inhibitor drug for the arthritis, which suppresses the immune system. Carol Kauffman, an infectious-disease specialist at the University of Michigan, Ann Arbor, told the panel that overwhelming histoplasmosis infection had killed several patients taking such TNF-inhibitory drugs.

Of the 871 gene-therapy trials

registered with the NIH, 4% have used AAV. Officials at the NIH and the US Food and Drug Administration reported at the meeting that they had reviewed all the AAV trials to date and found no pattern of adverse events associated with AAV, or any increased incidence of adverse events compared with trials using other gene-therapy vectors. The trial Mohr took part in was unusual in that it involved repeated injections. It was halted after her death.

Meredith Wadman

Correction

In the News story ‘Borysiewicz to head UK medical council’ (*Nature* **449**, 121; 2007), we misquoted Colin Blakemore, chief executive of the Medical Research Council (MRC), in a way that suggested he knew that there would be a substantial increase in the MRC’s budget. Professor Blakemore said that he hoped there would be a substantial increase in the MRC’s budget, and points out that he is not in a position to declare a definite funding increase. We apologize to Professor Blakemore.

Japan names institutes in search for global excellence

Japan has selected its five World Premier International Research Centers (WPIs), a group of institutes that will share US\$70 million per year for up to ten years (see *Nature* 447, 362–363; 2007).

A central goal of the WPI initiative is to create world-leading research organizations by attracting foreign scientists and collaborating with foreign institutions. For instance, the National Institute for Materials Science in Tsukuba, named as a WPI, aims to make materials for sustainable development through a new technology called nanoarchitectonics. It already has collaborators lined up in the United States, South Korea, China and the Czech Republic.

But there were few surprises among the chosen five, or in the fact that Japan's most prestigious national universities — Tokyo, Kyoto, Osaka and Tohoku — each has one designated WPI.

California gets Australia's top stem-cell scientist

California's \$3-billion stem-cell research programme has finally acquired a new leader.

Australian Alan Trounson was named last week as the president of the San Francisco-based California Institute for Regenerative Medicine (CIRM). He currently works at Monash University in Victoria, Australia, and has done pioneering work on *in vitro* fertilization and stem cells.

Trounson's appointment has taken some by surprise. When the board of the CIRM appointed Richard Murphy as interim president in August this year, it was suggested he could stay until March 2008.



Alan Trounson will be the next president of the California Institute for Regenerative Medicine.

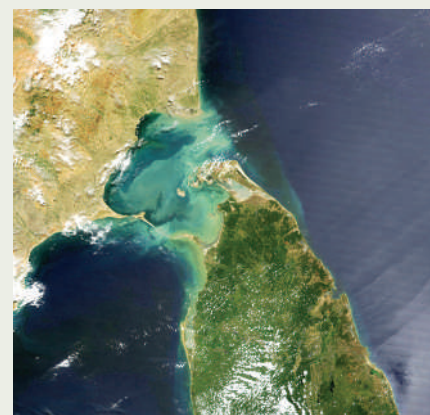
NASA photos are used in court case over divine bridge

A high-profile Indian court case has invoked NASA imagery to help clarify whether a submerged chain of sandbanks is a bridge of legend or not.

The religious text Ramayana recounts how the Hindu god Ram, with an army of monkeys, built a stone bridge from India to Sri Lanka to rescue his kidnapped wife Sita from a demon king. Last week, India's Supreme Court heard arguments over whether the 48-kilometre-long underwater ridge visible in satellite photos (right, as seen by the Terra satellite) is in fact the Hindu relic.

The suit, brought by the opposition Bharatiya Janata Party, aims to stop a US\$600-million project to convert the narrow strait between India and Sri Lanka into a shipping lane. Meanwhile, the Congress Party in power has argued that the project is vital for the country's economy — and also cited NASA's own clarification that satellite photos give no proof that the so-called Ram's bridge was man-made.

On 14 September, the court postponed its verdict until January 2008. The government has agreed to re-examine the project to see whether the shipping channel can be created without boring through the controversial ridge.



J. DESCLOTRES, MODIS LAND RAPID RESPONSE TEAM, NASA/GSFC

The institute had been without a permanent president since Zach Hall resigned in April.

The first \$250 million in bonds to fund the research programme is due to be issued by California state shortly.

Judge backs US states' bid to curb exhaust emissions

A federal judge in Vermont has ruled in favour of California's efforts to restrict the levels of greenhouse gases spewing from automobile exhaust pipes.

Under the US Clean Air Act, California has special provision to make its air-pollution rules stronger than federal rules. At least 11 states have joined California since 2002 in its quest to regulate greenhouse gases. Car makers sued, saying that the states were usurping the role of the federal government to set standards for fuel economy — the most obvious way to limit greenhouse-gas emissions. The case came to trial first in Vermont.

But environmentalists aren't ready for their low-carbon victory lap yet. The US Environmental Protection Agency has still not given California official permission to go ahead with the new regulations, despite a 2 April Supreme Court decision ordering the agency to consider the request.

Climate-change science programme 'lacks impact'

Federal research into climate change has a long way to go in informing US policy decisions, says a new independent analysis.

The United States spends \$1.7 billion each year on climate-change research,

spread among different agencies under the rubric of the US Climate Change Science Program. One of its main tasks is to produce 21 federally approved reports on the state of climate science (see *Nature* 436, 890; 2005), but because of bureaucratic hold-ups, only two of these long-delayed reports have appeared.

A panel convened by the US National Research Council has now evaluated the programme and found it lacking in several areas, including the evaluation of mitigation of and adaptation to climate change and in helping policy-makers incorporate climate science into their decisions.

The programme has done well in some areas, the panel added — such as documenting temperature increases and other climate-related changes on a global scale.

Fly to the Moon and land \$20 million, urges Google

The 'Google Lunar X Prize' aims to extend private space travel well out of Earth's orbit.

The US\$20-million prize, sponsored by Google and run by the X Prize Foundation in Santa Monica, California, will go to the first privately funded group that sends a rover to the lunar surface and accomplishes tasks that include roving for at least 500 metres and beaming images and videos back to Earth. In 2004, the foundation awarded \$10 million to the team that developed the first private piloted craft that went into suborbital space.

The total prize money is available until the end of 2012, then the purse drops to \$15 million until the end of 2014 — after which the competition will be cancelled.

BUSINESS

The shipping forecast

Although cargo vessels are currently spared emissions restrictions, the industry is planning ahead. **Kurt Kleiner** looks at the ideas being floated to improve energy efficiency on the high seas.

When the ship *MV Beluga SkySails* weighs anchor later this year it will do something unusual for a modern cargo ship: it will hoist a sail. The 140-metre vessel is being equipped with a kite-like sail that will fly from its bow, offering it extra propulsion and potentially cutting the amount of fuel needed for its voyage by up to 35%.

The sail is just one example of the ways in which the shipping industry is trying to tackle the question of energy efficiency. Partly motivated by rising costs of fuel oil, ship designers and operators are also hoping to pre-empt the inevitable clampdown on the greenhouse gases their vessels emit.

When it comes to transporting freight around the world, ships move by far the greatest amount — about four times more than lorries, six times more than rail and 400 times the weight carried by planes each year. But shipping has so far been exempt from emissions restrictions. It is, in fact, comparatively efficient, as it uses 25–50% as much fuel as lorries to move a tonne of cargo a given distance (see graph).

James Corbett, an engineer at the University of Delaware in Newark who studies transportation and pollution, estimates that cargo ships emit some 2.7% of the global total of greenhouse gases. This equates to 800 million tonnes of emissions per year — a figure that could double by 2030 as global trade increases, Corbett warns.

The International Maritime Organization (IMO), which regulates the shipping industry, is compiling a survey of greenhouse-gas emissions from cargo vessels, as the first step in deciding whether to impose limits. The results are expected early in 2008.

Meanwhile, the European Commission is considering whether to include shipping in a future cap-and-trade system for greenhouse-gas emissions. Shipping and aviation are not included in the European carbon market, and both industries face similar challenges: their emissions are likely to be regulated in the future, and they want to be seen doing something about the problem now (see *Nature* 448, 120–121; 2007).

“There is pressure on all industries not only from regulators, but also from the general public, to reduce emissions of greenhouse gases,” says Alfons Guinier, secretary-general of the European Community Shipowners’ Association,

which is based in Brussels.

One of the easiest ways to make shipping more efficient would be to slow the ships down. Fuel consumption increases rapidly with speed: doubling a ship’s speed means using eight times as much fuel. With the amount of freight to be shipped on the rise, and shippers demanding quick transit times, ship owners are under pressure to accelerate their vessels.

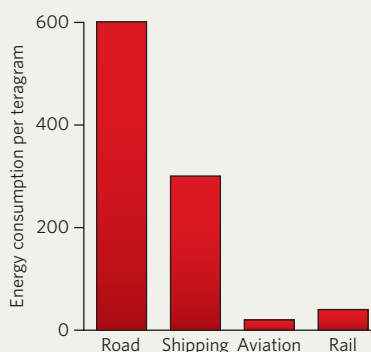
So engineers and designers are looking for ways to squeeze more efficiency out of traditional ship designs. “Until two years ago very few in the shipping industry were interested in this,” says Per Brinchmann, a naval architect with Wallenius Wilhelmsen Logistics in Lysaker, Norway. “Now everybody is talking about it.”

The IMO has set out a number of options for improving energy efficiency. These range from engine optimization to better hull and propeller designs. Improving hull design, for example, could increase energy efficiency by an average of 15%, the IMO says.

Some designers are proposing more radical solutions: the sail being tested on the *Beluga SkySails*, for instance. These sails have been dreamt up by SkySails, a small firm based in Hamburg, Germany, and set up in 2001 by an economic engineer and a naval architect. Attached to the hull with carbon-fibre rope, the kite-like sails have an area of up to 5,000 square metres and can be steered to provide pull even when the ship is travelling at a steep angle into the wind. They act like parafoils — wing-like structures that fill with air and generate lift.

SkySails says the kite can provide propulsion equivalent to a 5,000-kilowatt engine,

ENERGY USAGE FOR CARGO TRANSPORT



saving 10–30% in fuel costs. Such savings, the company says, would recoup the cost of the kites — between €500,000 (US\$700,000) and €2 million — in three to five years.

Bremen-based Beluga Shipping, which owns the *Beluga SkySails*, plans to test the system over the next year. “We’ll collect data and experiment,” says Verena Frank, a spokeswoman for the company. “Most probably we will equip another ship.”

Turning the tide

A company in the Netherlands, meanwhile, is planning to harness the power of air in a different way — by pumping it under the ship’s hull to reduce friction with the water.

Jörn Winkler, founder of the Rotterdam company DK Group, has developed a design that uses some of the ship’s power to pump air into cavities built into the bottom of the vessel. This means that a good portion of the hull floats on a cushion of air, rather than coming into contact with water. “On a standard tanker, we have 8,000 square metres of wetted surface that we can actually remove from the equation,” says Winkler. “That’s a standard football field.”

The DK Group is rebuilding a 2,500-tonne vessel to demonstrate the system. Preliminary tests suggest that it will reduce fuel use by 15%, while consuming only about 1% of the ship’s power. The system would cost roughly 2–3% of the total cost of the vessel, Winkler says.

Another possible way to reduce greenhouse-gas emissions would be to switch to alternative fuels such as natural gas, which emits much less carbon dioxide than the fuel oil burned by most cargo ships.



Plain sailing: kite-like sails, such as this test model, may offer cargo ships fuel savings of some 15%.

Per Magne Einang, a research director at the Norwegian Marine Technology Research Institute in Trondheim, is studying whether natural-gas-burning combustion engines could efficiently power short-haul ships. Natural gas would be an affordable fuel, he says, especially as regulations against emissions of sulphur and nitrogen oxides become stiffer. Unfortunately, natural gas is only a little better than fuel oil when it comes to greenhouse-gas emissions — although it emits much less CO₂, not all of the methane gets burned and this, when emitted, is a much more potent greenhouse gas than CO₂.

A way around this might be to put the natural gas in fuel cells, says Tomas Tronstad, a project manager at DNV Research and Innovation in Oslo. DNV is fitting a 100-metre supply ship with a fuel cell made by the Munich company CFC Solutions that can run directly on natural gas. Tronstad says that this will result in 50% fewer greenhouse-gas emissions than a diesel engine. The fuel cell will be an auxiliary engine, complementing a conventional natural-gas combustion engine that drives an electric motor. But Tronstad says that eventually, similar fuel cells might be able to power a ship's engine completely.

Brinchmann says that such green innovations probably aren't affordable at the moment. But if fuel prices continue to rise as expected, he thinks the new designs may start looking much more attractive.

And with the possibility of emissions restrictions on the horizon, even more explosions in innovation may be coming, says Brinchmann: "We're still waiting for the big bang in this." ■

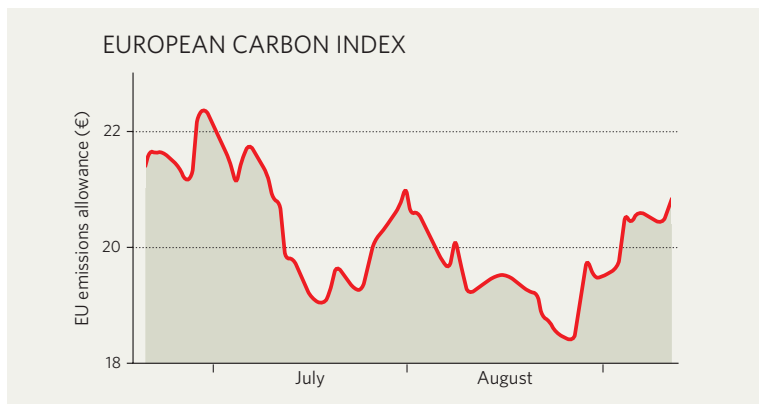
IN BRIEF

CRASH LANDING Rocketplane Kistler, a company in Oklahoma City that hopes to put tourists into space, is on the verge of losing up to \$207 million in government support. The company is one of two firms with which NASA has signed a Commercial Orbital Transportation Services agreement, which the space agency hopes will lead to alternative methods of flying cargo to the International Space Station (see *Nature* 448, 988–991; 2007). But Rocketplane has struggled to raise private financing as required by the deal, and NASA has now told it that if it cannot do so then its agreement may be terminated next month.

BLOOD BATTLE Biotech giant Amgen, which has suffered flagging sales and employee lay-offs in recent months, has been given a bit of a breather by the US Food and Drug Administration (FDA). An advisory panel has voted against requiring the company to add a label to several of its drugs to treat anaemia that would have specified the level of red blood cells patients should have before using the treatments. Had the change been enforced, it would probably have cut sales of the drugs. FDA regulators will make a final decision on the labelling later, but they usually take the advice of the advisory panels.

ENERGY SPIKE Crude-oil prices have topped \$80 a barrel on the New York Mercantile Exchange for the first time ever. Early last week, two reports from the US Energy Information Administration suggested that inventories of gasoline and crude oil were lower than expected. And six attacks on pipelines in Mexico, possibly by leftist rebels, have made the market nervous. The price spike comes even as the Organization of Petroleum Exporting Countries said it would increase production by half-a-million barrels a day from November.

MARKET WATCH



The price of the right to emit a tonne of carbon has floated lazily around the €20 (US\$28) mark this summer. But one announcement did create a bit of a buzz at the five European carbon exchanges that trade the right to emit, including the European Energy Exchange in Leipzig, Germany (above).

On 30 August, the United Nations announced that the 'international transaction log' will be up in time for the markets' second phase, which starts in 2008. This will make it possible to transfer certified emission reductions (CERs) bought through the Clean Development Mechanism of the Kyoto Protocol to trading registries of the various Kyoto countries. Under the mechanism, credits for emissions-reduction projects in poorer countries can be bought by those in richer countries.

Before the announcement, trading in CERs was already brisk (see *Nature* 448, 974–975; 2007). But afterwards, even more players switched to dealing in CERs, leaving the allowances market flailing. The setback was short-lived, however, and overall, the spread in price between allowances and CERs has tightened in the past two months.

One factor putting downward pressure on the price of carbon emissions is rising coal prices, says analyst Milo Sjardin of New Carbon Finance in London. "The choice of either running a coal plant or a gas plant has gone more in favour of gas," says Sjardin. And when a company is looking to reduce emissions, switching to lower-emission natural gas from coal is an alternative to buying allowances, which lessens demand for these allowances.

Emma Marris

THE SAME BUT DIFFERENT

As several lucrative protein-based drugs are poised to go off patent, makers of biopharmaceuticals argue that their products are too complex to be reproduced as generics. **Heidi Ledford** investigates how close 'biosimilar' drugs can get to the original.



In 2006, Craig Wheeler, then president of Chiron BioPharmaceuticals in Emeryville, California, received a call from across the country that would challenge his perspective on the biotechnology industry. Momena Pharmaceuticals, a small firm in Cambridge, Massachusetts, was looking for a new chief executive. The company planned to develop new drugs, in part relying on its ability to detect and manipulate the carbohydrate molecules that decorate proteins. But Momena also intended to create generic versions of therapeutic proteins, something that Wheeler says he thought was impossible.

Unlike the straightforward industrial chemistry techniques used to make small-molecule drugs, the methods of producing and isolating 'biologics' — complex drugs, vaccines or antitoxins made by or from living cells — can be complex and fickle. "The process is the product" was the mantra of the biopharmaceutical world, says Wheeler. Even those who developed drugs in the first place were loath to play around with their methods. "We were deathly afraid of changing anything because we couldn't tell where it would lead," he says.

Debate has flared over whether proteins are too complex to be copied. Even nomenclature for the replicants has changed as a result. Many have discarded the term 'biogenerics' in favour of 'biosimilars', saying that the word 'generic' unfairly implies a perfect replication. And

companies and lobbyists on both sides are battling over whether biosimilars should be allowed to follow the fast track to approval available for small-molecule generics, or whether they should undergo expensive clinical trials beforehand. Pending US legislation on the matter could result in billions of dollars being won or lost by companies such as Momena and the larger biotechnology and pharmaceutical companies that own the ageing patent rights to biologic drugs.

Epoetin alpha or 'EPO', for example, is a recombinant form of the protein erythropoietin used to treat anaemia. It is marketed by several companies under different names, and currently commands a \$12-billion market. EPO has already lost patent protection in Europe, and European regulators approved the first epoetin biosimilar in August. EPO and other drugs set to lose patent protection in the near future (see table, overleaf) are attractive targets for the generics market. Europe has only recently determined a regulatory pathway for such generics, reaching the conclusion that the expedited path for small-molecule drugs is not directly applicable to protein-based therapeutics. Neither the United States nor Japan has a policy in place, and expectations of US legisla-

tive action during this session of Congress are fading. Ultimately generics companies want to leave the door open for accelerated reviews that would decide on a case-by-case basis.

Complex challenge

Wheeler certainly had his doubts both about biosimilars and Momena. The sheer complexity of proteins presents a challenge. For small-molecule drugs, structure can be determined with certainty, and 'the process' is not in itself crucial. As long as the end product is the same as the original and there are no worrisome contaminants, the generic form of a small-molecule drug may often proceed to market without clinical trials.

But proteins are much bigger — sometimes hundreds to thousands of times as large. In some cases the precise structure made by the atoms

in the protein and the various chemical adornments it may have picked up cannot be determined. Moreover, the cells that are used to produce the protein sometimes leave a unique fingerprint of sugars and phosphate patterns reflective not only of the cell type but also the conditions under which they are grown (M. Gawlitzek, U. Valley, M. Nimtz, R. Wagner and H. S. Conradt *J. Biotechnol.* **42**, 117–131; 1995). Genzyme for

"You first need to establish that you at least chemically understand the molecule." — Ganesh Venkataraman

D. MARTINEZ/REUTERS/CORBIS

example, another Cambridge biotechnology company with a number of biologic products, recently struggled to gain regulatory approval to scale up production for one of its own drugs. Growing the cells in large tanks was found to change the drug's carbohydrate composition.

A change in the arrangement or type of these sugars can profoundly affect protein activity, directing it to a new tissue, altering its function or alerting the immune system to its presence. Momenta claims that its generics will be aided by new methods to precisely monitor the sugars that decorate many protein surfaces. Understanding the arrangement of these sugars can be crucial to creating a copy of a protein that bears them, but they have been notoriously difficult to study, says Wheeler. "I said, 'They can't know this stuff.'" Nevertheless, on a whim, he decided to pay the company a visit.

Wheeler studied the approach, toured the laboratories and came away convinced. Having made the leap to become Momenta's chief executive, he knows he is a rarity among his peers. "The generics people still really hate me because I was on the other side," says Wheeler with a laugh. "I know all the counter arguments."

The dangers of change

The arguments can be compelling, as even small changes in biopharmaceutical production have resulted in tragic consequences. In 1998, European regulators asked Johnson & Johnson, based in New Jersey, to remove human serum albumin from its brand of EPO, called Eprex. Serum albumin, which was purified from human blood at the time, was there only to stabilize the protein during storage, and regulators wanted to eliminate the risk that Eprex might spread infectious agents. So Johnson & Johnson replaced it with

polysorbate 80 (also known as Tween 80), a detergent and emulsifier commonly used to keep proteins in solution. Around the same time, the company also introduced a line of pre-loaded syringes.

Nicole Casadevall, a haematologist at Hôtel-Dieu Hospital in Paris, remembers when the first Eprex patients began to get sick. Doctors shipped blood samples to her so that she could test for antibodies against the drug. "I began to see one case, then another, and then I was receiving cases from all of Europe," says Casadevall. In some patients, the immune system branded Eprex a foreign invader and produced antibodies to neutralize the drug. The antibodies not only rendered the therapy useless, they also attacked the endogenous protein — erythropoietin — causing a life-threatening anaemia in at least 200 patients.

It has taken years to determine just what went wrong with Eprex. Johnson & Johnson says that polysorbate 80 caused compounds to leach from rubber stoppers in some of the pre-loaded syringes. Those compounds, the company argued, may have served as an adjuvant, boosting the recipients' immune response to the protein.

In the United States, the original legislation covering generic drugs simply did not anticipate biological therapies, says Janice Reichert, a research fellow at Tufts Center for the Study of Drug Development in Boston, Massachusetts. The only protein therapeutics on the market in that era were insulin and growth hormone. "There was no reason to believe that they would have EPO on the market," says Reichert. "Now we're sort of reaching a critical mass."

"The generics people still really hate me because I was on the other side."

— Craig Wheeler

Biopharmaceuticals represented a \$30-billion market in 2005 and are expected to net \$70 billion by the end of this decade.

The US Congress introduced legislation to carve out a regulatory path for biosimilars but has been slow to act on it. Patent-holding companies have vigorously opposed the legislation, which is intended to assess biosimilars on a case-by-case basis rather than require trials

for every drug. Meanwhile, Europe has approved only two drugs, EPO and human growth hormone, via its biosimilars pathway. Insulin and growth hormone, the only biosimilars marketed in the United States, are covered under present generics legislation because of their long history of use and their relative

structural simplicity. All eyes are looking to companies such as Momenta to see what will happen to their first applications for approval in Europe and, eventually, the United States.

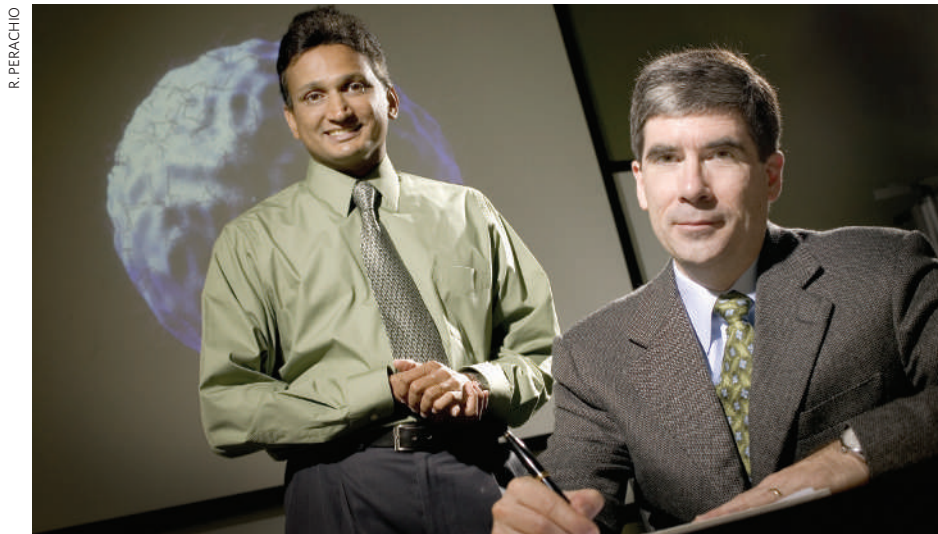
Three steps

Momenta Pharmaceuticals occupies a building in Cambridge's Kendall Square, just a stone's throw from the Massachusetts Institute of Technology, where the company's founders first developed the carbohydrate technology.

On a recent summer afternoon, one of those founders, senior vice-president of research Ganesh Venkataraman, leans against a fume hood and outlines the company's three-step plan to introduce its technology to the US Food and Drug Administration.

The first step is M-Enoxaparin, he explains, a generic form of Sanofi-Aventis's Lovenox. Lovenox is a complex mixture of sugars — but no protein — produced when the long carbohydrate polymer heparin is isolated from pig intestines and chemically shattered into short sugar chains. The resulting fragments are used to treat deep-vein thrombosis and pulmonary embolism, and Lovenox pulled in €2.4 billion in sales in 2006. Venkataraman says that Sanofi-Aventis declared it impossible to determine more than 70% of the carbohydrate composition of Lovenox. "We can account for every species in that mixture," says Venkataraman. Momenta chemically recreated that blend, and submitted the drug for approval in August 2005. Lovenox is not considered a biopharmaceutical, however. So Momenta's partner, Sandoz — the biogenerics arm of the Swiss pharmaceutical company Novartis — based in Holzkirchen, Germany, has filed for approval under the standard, existing generics pathway. That application, originally projected to take two years or less, is still pending.

The second step is a generic version of



Creating the impossible: Ganesh Venkataraman (left) and Craig Wheeler of Momenta.

Copaxone, a complex peptide mix marketed by Teva Pharmaceuticals in Petach Tikva, Israel for the treatment of multiple sclerosis. Momenta, together with Sandoz, will also file for approval of its version of Copaxone under the existing generics pathway. But after that comes the challenge: the third step involves two protein biologics, still in development, both of them complex proteins, complete with their adorning sugars and other modifications. By then Momenta will have walked through the entire regulatory process, says Venkataraman.

For now, the researchers are working on characterizing complex mixtures and proteins. Using enzymes that cut sugars in specific places, they feed the fragments into one of the whirring mass spectrometers scattered throughout the lab, ready to pick apart a protein's knots of amino acids and forking carbohydrate chains. "These instruments can give you femtomolar resolution," says Venkataraman, proudly indicating the mass spectrometers. Momenta has also developed a computer algorithm that allows its researchers to feed in results as they are revealed. The algorithm then calculates all the structural possibilities, which can then be narrowed down and confirmed through additional experiments.

Momenta is counting on its in-depth structural analysis to promote acceptance of its biosimilars. "We think that chemical characterization is a door opener," says Venkataraman. "You first need to establish that you at least chemically understand the molecule." Both Wheeler and Venkataraman are quick to note that they are not opposed to clinical trials of biosimilars. But whether a trial is necessary and what form that trial must take should be decided on a case-by-case basis, they say, not made mandatory.

Original variability

Biopharmaceuticals are often a mixture of protein variants, differing from batch to batch. "One of the key things that one has to do is to accumulate enough information on the original product to understand its own variability," says Cartikeya Reddy, head of the biologics division at Dr Reddy's Laboratories, a pharmaceutical company based in Hyderabad, India. Since 2001, Dr Reddy's has been producing a biosimilar version of granulocyte-colony stimulating factor (G-CSF), a protein drug used primarily to stimulate white blood cell production after chemotherapy or bone-marrow transplants.

Understanding the variability in the original product is crucial but reproducing the precise mixture poses another challenge. Generics

PATENT EXPIRATIONS FOR PROMINENT BIOLOGIC DRUGS

Product class	Leading brands	Company	EU patent expiry	US patent expiry
Erythropoietin alpha	Epogen/Procrit/Eprex/Erypo	Amgen/Johnson & Johnson	Expired ¹	2012 ²
Erythropoietin beta	NeoRecormon	Roche/Wyeth/Chugai	Expired ³	Expired
Interferon- β 1-a	Avonex, Rebif	Biogen Idec, Serono	2012	2008 & 2013
Interferon- β 1-b	Betaferon	Bayer (Schering)	Expired ⁴	Expired
Granulocyte-colony stimulating factor	Neupogen	Amgen	Expired	2013
Interferon- α -2b	Intron A	Schering-Plough	Expired	Expired
Interferon- α -2a	Roferon-A	Roche	Expired ⁵	NA
Interleukin-2	Proleukin	Chiron	2007	2012
Soluble TNF- α receptor	Enbrel	Amgen/Wyeth	2010	2009
TNF- α antibody	Remicade	Centocor, Schering-Plough and Tanabe	2010/2011/2012	2011
CD20 antibody	MabThera/Rituxan	Genentech/Roche	2013 ⁶	2015
ErbB2 receptor antibody	Herceptin	Genentech/Roche	2014	2014
EGFR antibody	Erbix	Bristol-Myers Squibb	2010	2015
VEGF antibody	Avastin	Roche	2019	2017

1 November 2007 in France, July 2008 in Spain
2 Possibly extending to 2013 or 2015

3 July 2008 in Italy
4 October 2008 in France, Germany and the UK
Source: Datamonitor, Thomson Database of all pharmaceutical inventions, August 2007

5 2008 in Spain
6 Possibly extending to 2018 in the UK

companies may know only the sequence of the protein of interest, and what they can glean from published material, says Reddy. Whenever possible, Reddy says his company uses the same cell line, or another cell line from the same species used by the innovator.

Wheeler says that Momenta's intensive characterization ahead of time gives it a competitive advantage when it comes to making the drug. "We would have a far greater ability to design a work-around than others because of our analytical capability," he says. But Venkataraman admits that the company has not yet worked out a rational design for how to, for example, force a cell to reproduce a particular sugar pattern once it has been identified. "We're trying to get to it," says Venkataraman. "It's a frontier that hasn't been tackled."

Venkataraman's ultimate goal is to use the structural information about a product and its biosimilars to rationally predict whether the differences between the two are likely to have an impact on toxicity or efficacy. Nevertheless Momenta's analyses will easily be overshadowed by real-world examples of the dangers involved. Johnson & Johnson's Eprex is so often cited in reference to biosimilars that the details of the incident sometimes get forgotten. Eprex was not a biosimilar, and problems associated with manufacturing changes are endemic to all biopharmaceuticals, not just biosimilars.

Moreover, a clinical trial wouldn't have revealed Eprex's problems. But a simple chemical analysis might have shown the presence of the leachates in the syringes. "Eprex is an example that's good to scare people," says Venkataraman. "It raises this fear of the unknown."

But the tale of Eprex also highlights the unpredictability of the human immune system. With the exception of G-CSF, every known protein-based drug tested prompts antibody production, usually at a subclinical level. Models that aim to determine whether a particular change in protein structure will tip the immune response from subclinical, to clinical, have performed poorly. "There doesn't seem to be any underlying pattern to what's immunogenic and what's not," says Robin Thorpe, head of the biotherapeutics group at the National Institute for Biological Standards and Control in Potters Bar, UK. "You're going to have to do some kind of study in humans." Because of the low frequency of immunogenic responses, as seen in the Eprex case, such trials are likely to include post-marketing surveillance.

Venkataraman agrees that post-marketing surveillance will be important for biosimilars. "There are still several leaps that have to happen to get to the same level as small molecules," says Venkataraman. "The science is evolving to get there, but the lawmakers need to create the incentives. They shouldn't base legislation on today's technology."

Heidi Ledford writes for *Nature* from Boston.
See Editorial, page 259.

"You're going to have to do some kind of study in humans."
— Robin Thorpe

IN THE ZONE

The world's biggest, best-equipped research drilling vessel is about to set off on its first scientific voyage.

David Cyranoski previews its quest to catch a formidable earthquake in the act.



When it comes to natural disasters, the Japanese government is good with numbers. It expects, for instance, a magnitude-8.1 quake to strike in the next 30 years with an epicentre in the Nankai trough — a depression in the sea-floor 100 kilometres off the country's east coast. And when it hits, it is likely to kill between 12,000 and 18,000 people.

The Nankai trough lies in a subduction zone, a perilous region in which one tectonic plate dives under another, building up the sort of rock strain that can unleash the world's most powerful earthquakes. All earthquakes with a magnitude of greater than 9 have occurred in these zones. And although the next earthquake at Nankai is not expected to be quite this big, the region could prove key in understanding why earthquakes in subduction zones release such vast amounts of energy.

On 21 September, a brand new research ship is due to depart from the city of Shingu in Japan on the first leg of a five-year project. The initiative, called the Nankai Trough Seismogenic Zone Experiment (NanTroSEIZE), is the latest and most ambitious of a series of deep-drilling research projects that stretch back decades (see 'Staying afloat'). Everything about the ship, named *Chikyu* for 'Earth', is large: its 210-metre length, its 10 kilometres of drill string and its ¥60-billion (US\$526-million) price tag. *Chikyu* is the first research ship to use a massive pipe known as a 'riser' to encompass the main drill

pipe — making the rig more stable and enabling it to drill more than three times deeper than any other scientific drill ship¹.

But once *Chikyu* gets down to its ultimate goal — an earthquake-generating zone some six kilometres below the sea-floor — its work will become very small-scale. Scientists onboard the vessel will be looking at minute changes in the porosity and other characteristics of the rocks drilled from the depths. Eventually, they will place instruments in a deep borehole that will gather data over several years. The goal is to monitor the build up of strain in the rocks — to see an earthquake in the making.

Down under

Previous attempts have been made to monitor earthquake zones — for instance, at the Parkfield site in California atop the infamous San Andreas fault — but *Chikyu* will be the first to take such a precise look in a subduction zone. "It will be the first chance to see how such an earthquake is being prepared," says Asahiko Taira, director-general of the Center for Deep Earth Exploration in Yokohama, Kanagawa, which manages *Chikyu* and its attempts to unearth the very origins of earthquakes. "Having an exposed system to observe is like being able to examine a live squid rather than a dried one to understand its biology," he says.

Japan, which footed the bill for building *Chikyu*, has a good reason to focus on the Nankai trough. Here, the Philippine tectonic plate dives beneath the Eurasian plate, on which Japan sits, at a rate of about four centimetres per year. But at some points along the boundary, the plates 'stick' together and pressure builds. Two of these sticky patches, both roughly 100 kilometres wide, were responsible for earthquakes in 1944 and 1946 (ref. 2) that each killed around 1,300 people. And it is these patches that are thought to be where pressure is building for the next big quake. It's a good bet. For the past 1,300 years the Nankai trough has unleashed a large earthquake, of magnitude 8 or greater, every 90 to 210 years.

This regularity offers scientists an opportunity for a before-and-after look at an earthquake in a subduction zone. "There's no place in the world like it," says Taira.

Going deep is the best way to study the trough. Using the riser system, *Chikyu* scientists intend to dig the 'ultimate' borehole. (The record for the deepest scientific hole in the ocean is held by the *JOIDES Resolution* vessel, which drilled to a depth of 2,111 metres in 1993.) *Chikyu* will also drill at least 5 other boreholes along a 70-kilometre line, spanning a range of depths above the plate boundary

"Having an exposed system to observe is like being able to examine a live squid rather than a dried one." — Asahiko Taira

JAMSTEC

(see graphic). “We can look at temperature, pressure, material composition, as well as the degree of dehydration, and see how these properties change from the shallow part of the plate boundary into the deep,” says Masataka Kinoshita, a researcher at the Japan Agency for Marine-Earth Science and Technology (JAMSTEC) in Yokosuka and a chief project scientist for NanTroSEIZE.

But those comparisons will have to wait until the project is completed, which won't be before 2012. The leg starting on 21 September is an 8-week-long rapid survey of the six planned borehole sites. The 16 scientists on board will use sensors attached above the drill bit to pick up signals such as γ -radiation, electric currents, and sound waves transmitted from the drill to obtain information about the porosity and density of the surrounding rock. “We can record information about the rock types before we've disturbed them,” says Harold Tobin of the University of Wisconsin in Madison, the project's other chief scientist. “This is about as close to pristine conditions as you can get.”

To keep the project moving at a fast pace, no cores will be taken. That will be the task of the next leg — a 4–5 week mission scheduled for late November. One of the cores will go down to 1,000 metres, and they will all be analysed with *Chikyu*'s plush scientific facilities, which include a computed-tomography (CT) scanner that can reveal the internal structure of the core without destroying it. In late December, a third



***Chikyu*'s cores will provide unprecedented information about earthquakes around Japan.**

leg will involve penetrating to a depth of 1,000 metres at two other sites.

After that, *Chikyu* will be temporarily sidelined, partly because of an agreement with Japan's fisheries, partly to save money and partly to do maintenance work. Drilling is slated to resume again in October 2008, when the massive riser system will come into play. A riser, common on oil-drilling vessels but rare for scientific missions, surrounds the drill pipe all the way from the ship down to the sea-floor and below. Heavy mud

is circulated at high pressure between the riser and the drill pipe to stabilize the rocks and stop them from collapsing.

The ship will recover cores in continuous nine-metre stretches, which

will provide valuable information about the geological history of the region. The layers within the cores “are like tree rings”, says Tobin. “You don't want to miss any dates.” But coring is a slow process — every nine-metre section must be hoisted up into the ship before drilling can continue. Raising a core can take as little as 15 minutes, to more than an hour, depending on the depth of the water at the drill site.

Because of the premium on ship time, the crew will work around the clock. A helicopter will make runs every two weeks from the shore to exchange scientists and drilling crews. In the end, Tobin says, it will take six or more legs of concentrated eight-week drill stints to reach all the way down to six kilometres.

Half of the cores will be analysed on board; the other half will be stored in a facility at Kochi University, on the island of Shikoku, for permanent archiving. Onboard researchers get first dibs at studying them, but a year after being extracted anyone can apply to study them.

Detectors in the depths

But many scientists are more excited about the possibilities once the drilling has finished. Project scientists plan to place long-term observatories down some of the boreholes to measure rock tilt, seismic activity, strain, pore pressure and temperature — key variables for understanding how the rocks behave. The sensors must be designed to withstand very high temperatures, and will cost around ¥1.5 billion over the next five years to develop. It's not yet clear whether they will be ready before *Chikyu* finishes its drilling. The researchers

hope to operate the sensors for at least five years after they have been installed, perhaps uploading their data to remotely operated submersibles or sending them back to shore via cables on the bottom of the ocean.

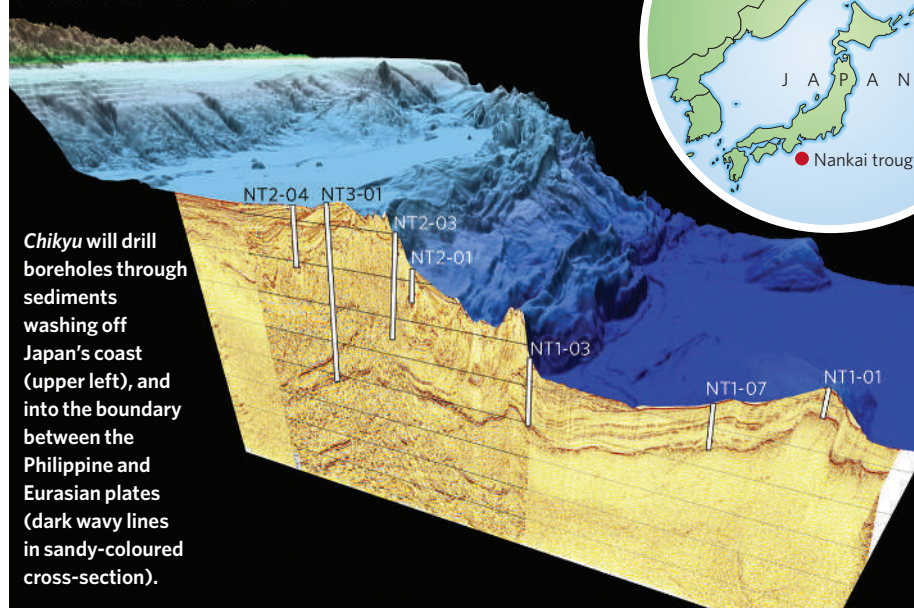
The observatories will measure changes that are surprisingly small given what can be felt on the ground during earthquakes. But “these measurements will be the key to getting a quantitative description of how the earthquake is building its energy,” says Kinoshita. Over the long term, Taira adds, the observatories might even be able to provide a way to identify the very start of earthquakes, and perhaps even to warn areas that have not yet been hit.

The measurements should also shed light on some important research questions. What happens to the rocks, and the water they carry, in the subducting plate? How does the strain released during an earthquake propagate to the surface? Under what conditions do earthquakes trigger tsunamis? Previous drilling has helped to answer other questions about the behaviour

“We can record information about the rock types before we've disturbed them.”

— Harold Tobin

DRILLING DEEP



Staying afloat

The arrival of *Chikyu*, Japan's massive ocean-drilling vessel, has come with some financial headaches.

Japan paid for *Chikyu* to be built, but running it will take another ¥10 billion (US\$90 million) per year. Most of these costs will be met by Japan and America, as members of the Integrated Ocean Drilling Program (IODP), headquartered in Washington DC. But research funders struggle to compete with the rich coffers of oil-drilling firms and their demands for ship crews and shipyard time. Last year, *Chikyu* was chartered by an Australian company to look for oil off Kenya.

But the greatest casualty so far has been America's *JOIDES Resolution*. For years the *Resolution* was the workhorse of the ocean-drilling community. In 1985 it was converted to a research vessel for the IODP's predecessor, the Ocean Drilling Program, and since then it

has pulled up some 35,772 cores from 1,797 boreholes. The IODP had originally planned for *Chikyu* and the *Resolution* to be working at the same time along the Nankai trough, 100 kilometres off the coast of Japan.

The *Resolution* was taken out of service in 2003 when the Ocean Drilling Program ceased to exist. The intention was to upgrade it for the IODP, but it has languished at a shipyard in Singapore ever since. High demand for the construction of oil rigs has funnelled potential workers off to other projects, and it is not certain when or if the *Resolution* will ever take part in the Nankai trough work. "It's a pity, especially because it would



The *JOIDES Resolution* started life drilling for oil.

have been nice symbolically to work together," says Greg Moore of the Japan Agency for Marine-Earth Science and Technology in Yokosuka.

The Nankai-trough drilling project has already been deferred from a start date of 2006 to September this year to help defray the effect of ever-inflating costs. With the *Resolution* also out of action, the project is now expected

to last into 2012 instead of 2009.

In addition to the *Chikyu*, the IODP funds drilling tasks on mission-specific platforms. But some worry that the huge sums of money needed for *Chikyu* could jeopardize other drilling projects. If the *Chikyu* cannibalizes money from IODP's other missions, then "community support for the IODP could diminish significantly", says Mike Coffin, a marine geologist at Tokyo University and former chair of the IODP's science planning committee.

Other IODP projects are already facing challenges. This July, a project that had planned to drill into the continental shelf off the coast of New Jersey had to be delayed because of issues over the availability of the drilling platform. The next IODP expedition after *Chikyu* gets going will now not take place until next March, in the equatorial Pacific. **D.C.**

of plate boundaries. At the Parkfield site, for instance, scientists have drilled three kilometres into the San Andreas fault and found that rocks there contain talc, which could explain the ease with which the plates slide along each other at those points³.

At Nankai, excitement has grown in the past five years, after seismologists there discovered earthquakes that generate very-low-frequency waves. Before that, it was generally thought that a subduction system had 'creeping' regions that slid past other, and 'locked' zones in which pressure builds up. But using broadband seismometers, Japanese scientists found seismic events at lower frequencies than had previously been detected, and in places thought to be devoid of seismic activity. Taira speculates that these low-frequency earthquakes, which are typically of magnitude 3 or 4, relieve strain over the long term. "It is clear they have something to do with the earthquake cycle," he says.

The new-found earthquakes could be partly caused by water carried by the subducting tectonic plate, says Kazushige Obara, at the National Research Institute for Earth Science and Disaster Prevention in Tsukuba. The water creates a clay-like formation that "acts like a cushion" to slow the action of the earthquakes, he says.

When Obara and his colleague Yoshihiro Ito discovered these low-frequency earthquakes in the shallower region of *Chikyu*'s drilling area, it gave the mission a whole new target to study⁴.

In 2001, when *Chikyu*'s drilling was being planned, "no one had heard of these earthquakes", says Greg Moore, also of the JAMSTEC. "We now know there is a lot of seismic activity."

By 2012, *Chikyu* may have spent as much time as it needs to study these and other details of the Nankai trough. After that, project managers expect that the ship will be in high demand for other missions. Two vying to be next are a

palaeoclimate study in the Indian Ocean, and a seismogenic study in the Middle America trench off Costa Rica. Both require such deep drilling that only *Chikyu* can do it.

And eventually, *Chikyu* could achieve one of scientific ocean-drilling's greatest dreams. In the 1960s, scientists envisioned an ocean drilling project that could pierce Earth's mantle. The project, called 'Mohole', never got deeper than 200 metres beneath the sea-floor — let alone to 10 kilometres, where the crust borders the mantle. But one day *Chikyu* might try its own version of Mohole. To do so, it would need a costly extension of the riser from its current 2.5 kilometres to 4 kilometres so that it could operate in the deep waters where the mantle is closest. But it would be worth it, says Kinoshita. "This is a long-held dream of all mankind, or at least of all Earth scientists." ■

David Cyranoski is Nature's Asia-Pacific correspondent, based in Tokyo.



A riser system will hopefully allow *Chikyu* to drill into Earth's mantle.

See Editorial, page 260.

1. Dalton, R. & Cyranoski, D. *Nature* **426**, 492–494 (2003).
2. Ichinose, G. A., Thio, H. K., Somerville, P. G., Sato, T. & Ishii, T. *J. Geophys. Res.* **108**, 2497 (2003).
3. Moore, D. E. & Rymer, M. J. *Nature* **448**, 795–797 (2007).
4. Ito, Y. & Obara, K. *Geophys. Res. Lett.* **33**, L02311 (2006).

Doping destroys the story at the heart of cycling

SIR — Suggesting that the Tour de France should lead the way for other sports by permitting drug enhancement, as your recent Editorial 'A sporting chance' (*Nature* **448**, 512; 2007) does, misses an important point. You fail to recognize the reason why people drive 10 hours to watch the regional final of college basketball, wake up in the middle of the night to watch the inevitable penalty shoot-out at the end of an England World Cup football match or even hop on the fast train to see the yellow jersey lead the Tour de France on to the Champs-Élysées. Genuine fans of sport don't just follow their teams to see sportsmen and sportswomen make great plays; they do so to see stories unfold.

To understand why pharmacological enhancements should never be allowed in cycling, you need to understand that all spectator sports thrive by selling simple stories to their fans. The cycling story is that, with great talent and after years of training, the best riders ride faster than the others at the very limits of natural human endurance. In the Tour de France, this story has been told and retold for 100 years — over stages, tours and careers. It describes the overall winner, the best hill climber and even the failed solo breakaway.

How could cycling's story survive if pharmacological enhancements were allowed? Even if the time comes when botulinum toxin injections are available from vending machines, doping should never be allowed in cycling.

Steven Riley

Department of Community Medicine and School of Public Health, Faculty of Medicine, University of Hong Kong, Hong Kong Special Administrative Region, People's Republic of China

Doping: drugs misused for sports put athletes at risk

SIR — While suggesting that we allow the use of performance-enhancing drugs in competition sports, your Editorial 'A sporting chance' (*Nature* **448**, 512; 2007) assumes that by the end of this century the unenhanced body and mind may be "vanishingly rare" in the general population. As a pharmacologist I disagree. Most pharmaceutical compounds in current use are, or have been, developed to correct pathological processes and not to enhance body functions.

There is no accepted drug treatment to improve superior intellectual activities. Most drugs that increase physical performance in sports do so with serious side effects. For example, liver and heart damage can result from chronic use of anabolic steroids to build

muscle, erythropoietin (manufactured to treat anaemia but misused to increase endurance) can cause thrombosis, and the use of stimulants or fatigue retardants can lead to cardiovascular problems.

Given the economic and societal pressure pushing athletes to victory at all costs, introducing leniency towards drug treatment would create wild drug experimentation in all sports, exposing athletes (and possibly young people involved in non-competitive sports) to unknown and potentially severe health risks. To my knowledge, the rule *primum non nocere* — first, do no harm — has not yet been abolished for the medical professions.

Piero Dolara

Department of Pharmacology, University of Florence, Viale Pieraccini 6, 50139 Firenze, Italy

Life on Mars may be hidden like Earth's extremophiles

SIR — Your News Feature 'Secrets of the martian soil' (*Nature* **448**, 742–744; 2007) addressed the implications of the next Mars mission finding organic molecules, or not, on the surface of Mars. But the question of whether there are organics on the planet's surface, although important, is not necessarily relevant to whether there is, or was, microbial life on Mars.

With an absolute maximum reach of a metre, the Phoenix mission may do better than Viking (which in 1976 dug down about 6 centimetres). But even if the top metre is sterile, that doesn't indicate whether the planet as a whole is bereft of life.

If life had developed during the planet's first billion years, it and any accompanying organics would have had to survive billions of years of meteorite bombardments, exposure to high levels of ultraviolet and cosmic radiation, and perhaps a highly oxidizing environment. Even if life evolved to withstand such extreme conditions and managed to survive near the surface in some regions, Phoenix is surveying only one point on a planet with a dry-land area equal to that of Earth's.

Only in the past couple of decades has the extent to which life on Earth has colonized, evolved and thrived in a variety of deep ecosystems become evident. For example, recently a thermophilic anaerobic member of the genus *Bacillus* was obtained from a depth of about 2,700 metres below the surface in Virginia. If Earth is any guide, the question of life on Mars will remain very open until we have at least explored all the areas on Mars equivalent to those on Earth where life has been found.

Samuel Kounaves

Phoenix Mars Scout Mission and Department of Chemistry, Tufts University, Medford, Massachusetts 02155, USA

Turning up the heat on scientific accuracy

SIR — In your News Feature on the search for organic molecules in martian soil 'Secrets of the martian soil' (*Nature* **448**, 742–744; 2007), you say that the mass spectrometer on NASA's Phoenix lander will be used on "samples heated as high as 1,000 °C — twice the temperature of Viking's ovens", which is defined as 500 °C. Of course, the former temperature is only about 65% higher than the latter, since absolute zero is –273 °C. Although this is not a big mistake, it does not aid the understanding of scientific fundamentals by the general public.

Alexandros Kiupakis

Institute of Molecular Biology and Biotechnology, Foundation for Research and Technology Hellas, Vassilika Vouton, PO Box 1527, Iraklio, Crete 71210, Greece

Olduvai fossils need more than one research team

SIR — Your News story 'War of words erupts over fossil dig' (*Nature* **448**, 12; 2007) about the conflict between two research teams at the Olduvai Gorge site in Tanzania gives a partial account of the situation. Contrary to what it states, our team never probed trenches that the Olduvai Landscape Paleanthropology Project (OLAPP) group had already dug.

The article also fails to clarify that in August 2006, a commission including Tanzanian academics and representatives from the Tanzanian Commission for Science and Technology, the Department of Antiquities and the Ministry of Natural Resources and Tourism declared that there was no scientific overlap between our project and that of the OLAPP group, and that both teams should be allowed to work at the gorge.

Every year erosion exposes hundreds of new fossils that will be lost to science for ever because of the limited power of a single team to undertake proper research along 25 km of deposits spanning 100 m of depth. Twenty-first-century palaeoanthropology must overcome this feudal approach to sites if it is to provide knowledge and preserve the human evolutionary heritage for future generations.

Manuel Domínguez-Rodrigo*, **Audax Mabulla†**, **Henry Bunn‡**

*Department of Prehistory, Complutense University, c/Prof. Aranguren s/n, 28040 Madrid, Spain

†Archaeology Unit, University of Dar es Salaam, PO Box 35050, Dar es Salaam, Tanzania

‡Department of Anthropology, 5240 Social Science Building, 1180 Observatory Drive, University of Wisconsin, Madison, Wisconsin 53706, USA

BOOKS & ARTS

Real science on show

The revamped museum at the Massachusetts Institute of Technology will offer the public access to science in action, as more museums should, argues director John Durant.

MIT MUSEUM

The Massachusetts Institute of Technology (MIT) used to run a small, almost hidden museum that had one really big asset: MIT. A wealth of exemplary scientific and technological research was directly accessible to the museum, an advantage not enjoyed by many, much larger, national and independent museums. Later this month, MIT will open a greatly expanded museum that seeks to exploit this advantage by engaging visitors directly with some of the institute's current research.

There are good reasons to care about public engagement with research. It is science-in-the-making that holds the key to many of the most pressing challenges we face. Today the public is confronted with conflicting claims about what science has to say and what it doesn't have to say, for example, on the role of rising carbon dioxide emissions in global climate change, on the potential value of experiments with human embryonic stem cells, or even about the history of life on Earth (as in the new Creation Museum in Petersburg, Kentucky). So it is crucial that citizens should acquire a feel for the real thing, for scientific and technological practice.

One or two independent museums of science and technology have recognized and acted on the importance of public engagement with research. In London, visitors to the Wellcome Wing at the Science Museum encounter contemporary science and technology news displays in the Antenna exhibition, and can even volunteer as research subjects in the Live Science section of the Who Am I? gallery; and visitors to the Darwin Centre at the Natural History Museum can engage with curators working with the museum's collections. Similarly, the Science Museum of Minnesota offers the public access to science news and views through its Science Buzz initiative; and the Exploratorium in San Francisco regularly links visitors directly by live webcast to scientifically important research sites around the world.

There's no one right way of giving the public access to the business of science. Offering people the chance to volunteer as research subjects can work well in some areas of biomedical science. Some natural-history disciplines



MIT Museum will display for the first time devices invented by information theorist Claude Shannon, such as this juggler.

provide opportunities for 'citizen science', whereby non-professionals contribute directly to the collection of data — on, for example, the distribution of particular species, or the timing of seasonal phenomena such as budding and flowering. But it's difficult to offer citizens science opportunities in, say, particle physics or quantum chemistry.

This is where university museums of science and technology have a role. For the most part, university museums are relatively small and short of resources (space, staff, funds). But what they may lack in resources, they can more than make up for in access to the people and processes of science and technology, which gives them the opportunity — and the responsibility — to contribute to the public's engagement with these things.

Visitors to the new MIT Museum will encounter an introductory gallery that showcases a range of live projects across the institute. For the opening, there is a collaborative

project between MIT and the Woods Hole Oceanographic Institution to build the next generation of remotely operated vehicles for underwater ocean exploration; a cancer research programme using the familiar zebrafish as a model to understand genetic developmental processes; and an MIT Media Lab project to build an urban concept car for the twenty-first century. In the future, we hope to present a much larger and more representative array of MIT research projects, and even to create a laboratory within the museum that scientists and engineers can use if they are willing to conduct their day jobs in public.

The introductory gallery will also feature 'MIT 360', a dedicated space with the capacity to connect audiences directly with researchers by video conference. In MIT 360, we plan to link visitors with oceanographers on Cape Cod as they receive data feeds from remotely operated vehicles out at sea. Similarly, we could enable visitors to interact with neuroscientists as they record brain images from awake human subjects. None of this is technically difficult — it's simply a matter of using appropriate ethical frameworks and communication technologies to link citizens directly with science-in-the-making.

All this depends on one scarce and ultimately limiting resource: scientists' time. Research scientists and engineers are busy people, and they need to be willing to carve out space in their crowded calendars to talk to interested or concerned members of the public about what they're doing. We find that most of our colleagues at MIT are willing to do this, provided the demands are reasonable. Long may this continue. Both scientists and the public will benefit from greater mutual understanding. If scientists close off, they risk at best not being understood and at worst not being trusted or supported. The stakes — for science and for the rest of society — have never been higher. ■

John Durant is director of the MIT Museum, Building N51-201, 265 Massachusetts Avenue, Cambridge, Massachusetts 02139, USA.

The MIT Museum re-opens on 29 September 2007
(<http://web.mit.edu/museum/>).

Earth's green heroes

Eating the Sun: How Plants Power the Planet

by Oliver Morton*

Fourth Estate: 2007. 384 pp. £25

Richard Fortey

All the greatest monsters are green. The Incredible Hulk had to turn green before going on the rampage and the *Eagle* comic featured a supremely evil green being called the Mekon, who was opposed in almost every issue by the chisel-jawed space hero, Dan Dare. One explanation for this odd association of colour with character is that green belongs to the vegetable kingdom. Humanoids have no right to have chloroplasts in their tissues — and if they do have them, well, they are probably not quite right. In the plant world, green is a heroic tint. It's a measure of the presence of chlorophyll and a sign that an organism captures energy from the Sun to convert it into organic matter. This is the basis of almost all life on the planet, and is arguably the single most important biochemical pathway there is.

Oliver Morton has written a biography of this organic greenery. He takes us on a grand tour from molecules to biosphere, and a very impressive journey it is. He tackles the difficulties of explaining how photosynthesis works, and teases out the exciting story of how electrons hop from one molecule to another along their complex pathways. If you thought that photosynthesis simply 'splits' carbon dioxide into its constituent elements in order to build organic molecules and release oxygen, you will soon be disabused. The oxygen is derived from water molecules, as part of the elaborate atomic trade-offs that power cells.

These complexities might have benefited from a few more diagrams to help the less biochemically literate, although to the uninitiated, looking at folded proteins can be as confusing as contemplating a plate of tagliatelle. And Morton's writing is exemplary in its clarity, drawing an analogy where it will help, and grasping conceptual nettles where it won't.

Morton goes on to outline the 3.5-billion-year-plus history of photosynthesis on Earth. It is by now a familiar fact that we owe our oxygenated atmosphere to the early and relentless activity of photosynthetic cyanobacteria and, subsequently, of algae. These small organisms converted the seas into something that could be colonized by respiring animals by harnessing the Sun's energy over three-quarters of geological time. There is simply no escaping a kind of modified Gaia outlook here: life, nutrient cycles and rock weathering are all locked together in one inescapable dance.

Less familiar to most readers will be some of the crucial episodes during this long history. There were times when Earth is thought to



The ability of green plants to harness the Sun's energy is the basis of almost all life on Earth.

have almost completely frozen over, for example. The Precambrian was not one slow story of advance towards the emergence of animal life. During the mid-Proterozoic, there was a period dubbed the 'boring billion' when nothing much happened in the way of biological innovation, at least according to many palaeontologists — life simply ticked over. It is not certain whether this stasis was linked to a shortage of available nitrogen or to the absence of animals to provide a fillip to innovation.

Whatever the reason, when animals did appear after about 1 billion years ago, the pace of evolution sped up dramatically. Morton is very good on what is needed to turn an alga into a land plant, and then to prop up that plant so that it can bathe in air and light to make a tree. The greening of the ancient continents was the final triumph of the chloroplast.

Eating the Sun proceeds smoothly to an account of climate history. Plants have influenced, and been gripped by, climatic fluctuations that have produced alternations of a 'greenhouse' and an 'icehouse' world. The climatic changes that seem inevitable to us now have, in all likelihood, been paralleled at one time or another in geological history. What is unprecedented is the burning of so much

photosynthetically fixed carbon that had been sealed away in rocks. What time had sequestered so securely is now being blasted into the atmosphere by thousands of power stations.

The book describes with admirable dispassion the different hypotheses detailing how the biological and human world might cope with this challenge. It is good to have a proper acknowledgement of the difficulties of predictive climate modelling, where there are so many unknowns — particularly in biotic responses to increased carbon dioxide availability. Theoretical mitigation possibilities — such as seeding some parts of the ocean with iron to stimulate plankton blooms — are carefully considered and then given short shrift. The problem is that we cannot simply wait around for the science to improve just so that we might better appreciate the particular flavour of our doom. Unfortunately, quite a few of the precautions that should have been taken against this have already been surpassed.

If we want to see just how bad things might become, we can contemplate the dreadful object lesson of the biological world after the mass extinction at the end of the Permian period, when a sick and enfeebled biosphere took millions of years to recover — indeed,

F. LANTING/FLPA

nothing as bad followed even the extinction of the dinosaurs. Morton briefly reviews the alternative sources for the energy consumption to which humankind is so addicted. The problem with such sensible words is that the reader still feels that no rational course will ever be adopted until the very tragedies that we seek to avert have come to pass. Of several recent accounts of what might happen to

climate in the next decades, Morton's is among the most balanced, but I am still left crossing my fingers and recycling a few plastic bags. As T. S. Eliot remarked, humankind cannot bear very much reality.

Morton's account of the ubiquitous importance of photosynthesis is an original viewpoint for looking at the world. It is written with verve and an eye for detail. His breadth

of scholarship could leave other science writers green — with envy.

Richard Fortey is visiting professor of palaeobiology at Oxford University, and research associate at the Natural History Museum, Cromwell Road, London SW7 5BD, UK.

*Oliver Morton is *Nature's* chief News and Features editor.

Science and the Supreme Court

The Nine: Inside the Secret World of the Supreme Court

by Jeffrey Toobin

Doubleday: 2007. 384 pp. \$27.95

Henry T. Greely

The United States Supreme Court is one of the more unusual aspects of a very unusual country. An unelected body that is expressly non-political, its membership is subject to bitter political struggles and its decisions can have profound political consequences — sometimes even changing history. Its nine members are famous but faceless, oddly impersonal in the midst of a culture of celebrity. These nine people work painstakingly at a difficult job that is usually routine and often obscure.

Jeffrey Toobin is a staff writer at *The New Yorker* and a legal analyst for CNN. His latest, very readable book is one of several efforts in the past few decades to personalize the Supreme Court and its members. He does so through a close examination of the past 20 years of its membership and decisions. The inside stories of the famous cases he discusses are not shocking, they are intriguing — particularly the discussion of *Bush vs Gore*, which prematurely ended Al Gore's challenge to George W. Bush's 2000 election. The book's strength, though, is not its account of the court's history, but what it reveals about the men and women who wear the robes. It is enlightened and enlivened by insights gleaned from Toobin's many interviews. Toobin focuses particularly on the rise to prominence of Justice Sandra Day O'Connor and the likely conservative future of the Supreme Court after her 2006 retirement.

Nearly 30 years ago, I had the good luck, and honour, to serve as a law clerk for a justice of the Supreme Court. Toobin's portrayal of the court generally feels right to me,

although he overemphasizes the influence of public opinion on it and slights its less dramatic aspects. Many of the cases have no liberal or conservative side, which may help to explain why even the deeply divided court of recent years decides about a third of its cases unanimously.

Just as science clocks up more drudgery than 'Eureka!' moments, Supreme Court justices spend most of their working lives reading yet another claim that a prisoner's attorney was incompetent, or writing and rewriting another background paragraph for a case that will attract no attention. In some ways,



George W. Bush nominated two of the current nine Supreme Court judges.

a justice's work resembles a scientist's. Both examine lots of inputs — laws, precedents and arguments for the justice; data and hypotheses for the scientist. And they try to make sense of them, to find a solution that will work. Both know they will have to defend their solution by the authority of their positions and by their reasoning. Scientists' papers are scrutinized for any weaknesses by friends and rivals; justices face external and internal critics, sometimes being the targets of stinging dissent from their colleagues on the Supreme Court.

In most cases, no verifiable (or falsifiable) truth underlies the Supreme Court's decisions. As Toobin illustrates nicely, every justice has a different view of the law, and the world. The

justices (and their law clerks) are intelligent, hard-working and dedicated, weighing and reweighing every word. Technically, 30 years ago and today, the justices usually do an excellent job, but their different perspectives often lead to different decisions. The book shows that these views are complex and can be only poorly summarized as 'conservative' or 'liberal'; the effects of those views are also complicated.

In ways that non-lawyers do not always understand, the Supreme Court is the weakest part of the US government. It has no power over the laws of the 50 states unless those laws run foul of the regulations, statutes or Constitution of the federal government. It cannot overturn actions by Congress unless they violate the Constitution, or of the president unless they

violate the Constitution or statutes. Even when such issues arise, the court is forced to be responsive, not active. Justices who want to decide an important issue have to wait for it to be argued in a real case that reaches them through a chain of lower courts. Then they have to hope that they can persuade at least four colleagues to agree with them, on both the result and the reasoning.

Still, the Supreme Court has plenty of power and that power will sometimes involve science. It applies patent and copyright laws in ways that affect high-tech industries and universities. It can interpret the First Amendment to judge attempts to limit the teaching of evolution. It can decide what kind of scientific evidence a court can admit. But most of what is important to 'science' itself is not within the Supreme Court's jurisdiction. For example, President Bush's restrictive stem-cell funding policy or California's expansive policy could come before the court only on claims that they violated the Constitution, but no such claim is plausible. The Supreme Court will not rule on whether human actions are changing the climate: at most, it might decide whether state regulation of industries to limit climate change interferes with powers reserved to the federal government.

Crucial disputes about the funding of science, or on the influence of industry on agency actions supposedly based on science, simply will not come within the Supreme Court's reach. Its decisions about abortion and sexual freedom will influence public health, but will not, on either side, involve much science. I am unhappy about the Bush administration's general attitude towards science and its selection of Supreme Court justices, as two separate harms; a conservative counter-revolution on the Supreme Court would change the United States (for the worse, in my view) but is unlikely to have a major effect on science.

Will that counter-revolution take place? Observers have proclaimed its coming since at least 1969, when Chief Justice Burger replaced

Chief Justice Warren — Toobin himself details other such failed reversals in the past 20 years. The Supreme Court's future course depends largely on its future members, who in turn depend on future presidents and senators — and the public opinion to which they all, in part, respond. It also depends on the current 'nine' and how (not if) they change during their years on the court.

Toobin's book is an excellent introduction to today's Supreme Court, but readers must bear in mind that part of the "secret world" of the court is its own future course.

Henry T. Greely is professor of law, professor (by courtesy) of genetics and director of the Center for Law and the Biosciences, Stanford University, California 94305-8610, USA.

scientific ideas as an alternative to feverishly memorizing the technical details in the hope of passing an exam or sounding clever at a conference — then thermodynamics is a good place to start.

The development of thermodynamics in the nineteenth century was the most wide-reaching and fundamental advance since Newton's mechanics. It underpinned (albeit some time after the event) the Industrial Revolution, and led the way to statistical mechanics (and hence to statistical quantum mechanics) and to an understanding of phase behaviour, chemical reactions, the astrophysics of stars... to everything, in other words.

Or almost everything. Atkins never treads beyond the limitations of nineteenth-century thermodynamics, which can be summed up in three words — equilibrium, isolation and big. His 'four laws' work for systems at (or very near) equilibrium, systems isolated from (or at least connected in a very controlled way to) their surroundings, and systems that are, well, big. Big enough that the averages of macroscopic thermodynamics tell the whole story, big enough that fluctuations from the average don't matter.

A flavour of the subject beyond these limitations would have rounded out the book — highlighting the striking fact that, in this centenary year of the death of its great pioneer Lord Kelvin, thermodynamics is still very much in business. For instance, the latest research into the energetics of small systems, such as proteins, is potentially revolutionary. Proteins do the same job for life that steam engines did for Victorian industry. Unlike a railway engine, however, the cell is a profoundly non-equilibrium place. And proteins are not isolated but inextricably bound to the world around them, inescapably prey to brownian motion.

Understanding the microscopic, non-equilibrium, open-system thermodynamics of these 'life engines' could usher in fascinating discoveries: how life works as a physical process, how we might borrow life's technology to make our own nanoengines, and how we might transform medicine by replacing broad-spectrum chemical cocktails with medical engineering of proteins. All this requires twenty-first-century developments in thermodynamics that are no less revolutionary than the nineteenth-century theory.

Even without this excursion into the future, Atkins has written an engaging book, just the right length (and depth) for an absorbing, informative read. Those for whom the word 'entropy' still induces cold sweats may at last get a proper glimpse of the real 'theory of everything'.

Mark Haw lectures in the School of Chemical and Environmental Engineering, University of Nottingham, University Park, Nottingham NG7 2RD, UK. He is author of *Middle World: The Restless Heart of Matter and Life*.

The real 'theory of everything'

Four Laws that Drive the Universe

by Peter Atkins

Oxford University Press: 2007. 128 pp.

\$19.95

Mark Haw

Ask a science graduate to name their favourite subject, and few will say thermodynamics. My own undergraduate memories of the subject include a baffling proliferation of nineteenth-century science grandees — James Clerk Maxwell, Lord Kelvin and James Prescott Joule — some exhaustively squeezed gases and a forest of incomprehensible partial derivatives I couldn't imagine how to measure.

Thermodynamics ought to be the cornerstone of any scientist's understanding of nature. Forget superstrings and grand unified theories: thermodynamics is the original 'theory of everything'. Or perhaps the 'theory of what everything does and how it does it'. Thermodynamics explains the transformation of energy, and nothing happens without that.

In his new book *Four Laws that Drive the Universe*, Peter Atkins aims squarely at the fundamental logical and physical structure of thermodynamics. Atkins's systematic foundations should go a long way towards easing confusion about the subject. He dissects the laws one by one, tying each firmly to its partner fundamental quantity, be it temperature, internal energy or entropy.

There is no shortage of books on thermodynamics — indeed Atkins himself is a veteran of this particular publishing niche. The thing that distinguishes this quasi-textbook (for popular science it definitely isn't) from the others is its almost complete absence of mathematics. Hang on, where are the partial derivatives? Where are Maxwell's relations? This is Atkins's masterstroke: without the encumbrance of equations that are never

actually going to be applied, readers may begin to grasp what energy and entropy are really about.

Therein lies a difficulty: should you need to derive the back legs off the thermodynamic donkey, *Four Laws* would have to be supported by a more traditional text. If deep understanding is what you want, this book is the better choice. There is a need in many fields, from atomic physics to cell biology, for books with a similar brief to this one. Too many prime their readers with facts and figures to avoid the challenge of properly illuminating the underlying concepts.

And just suppose you were setting out on such a crusade, to promote understanding of



Entropy increases as order collapses in melting ice.

NEWS & VIEWS

COMPUTING

The wireless epidemic

Jon Kleinberg

As wireless communication technologies spread, so the potential for viruses to exploit them grows. Biological models of virus transmission will assume new relevance for assessing the emerging threat.

Ever since the first appearance of computer viruses on the digital landscape, our understanding of them has drawn on parallels with biology. Analogues of mutation, phylogenetic reconstruction and computational 'immune systems'¹ have all been investigated. But the central analogy has come from the use of epidemiological models to track how a computer virus spreads. A crucial ingredient in these models is a description of the contact network through which the epidemic propagates, where the links represent who has the potential to infect whom. Traditionally, computer viruses have propagated on networks that bear little resemblance to the networks of physical contact through which their biological counterparts spread. But a growing body of research²⁻⁸ shows that the increasing use of short-range wireless communication networks might cause the two models to converge.

Accurately modelling the network through which a disease epidemic spreads is difficult in almost any setting. Diseases in plant populations, or animal diseases such as rabies, are heavily constrained by geographical proximity and the relatively fixed physical locations of the infected individuals⁹. Models of these diseases have been extended using detailed data on patterns of travel within cities^{10,11} and by air worldwide¹² in attempts to analyse disease outbreaks in human populations.

Epidemics on the Internet are even more diverse. At the most general level, there is a distinction between computer viruses, which 'piggyback' on data exchanged between users, and computer worms, which more actively direct their own transmission through a network¹³. The networks on which these types of malicious code spread are based on patterns of file transfer or e-mail communication, or even on structures that evolve implicitly as a computer worm scans the Internet for targets.

Mathematical models of these different networks lie at various points on a broad conceptual spectrum. At one end are network models that reflect strong spatial effects, with nodes at fixed positions in two dimensions, each connected to a small number of other nodes a short distance away⁹. At the other end are 'scale-free' networks, which are essentially



Human mobility and wireless networking could combine to abet the spread of computer viruses.

unconstrained by physical proximity, and in which the number of contacts per node are widely spread¹⁴. Models based on human travel data occupy an intermediate position in this spectrum of spatial constraints. The different network structures lead in turn to qualitative differences in the way epidemics spread: whereas epidemics can persist at arbitrarily low levels of virulence in scale-free networks^{14,15}, epidemics in simple two-dimensional models need a minimum level of virulence to prevent them from dying out quickly⁹.

Very roughly, then, one could view models of biological epidemics as rooted in spatial networks, and expanding into less spatial realms to model the technologies that have accelerated human travel. Meanwhile, research on cyber-epidemics has occupied the non-spatial end of the spectrum, with its diverse and far-flung connections, when modelling global communication technologies such as the Internet.

But the spread of short-range wireless communication technologies such as Bluetooth, and the emergence of worms that exploit these systems²⁻⁴, is disrupting this dichotomy by making possible computer-virus outbreaks whose progress closely tracks human mobility patterns. These types of wireless worm are designed to infect mobile devices such as cell phones, and then to continuously scan for other devices within a few tens of metres or less, looking for new targets. A computer virus thus becomes something you catch not necessarily from a compromised computer halfway around the world, but possibly from the person sitting next to you on a bus, or at a nearby table in a restaurant.

Wireless worms can also be used to attack 'mobile ad-hoc networks' (MANETs), which are designed to connect devices such as cheap, low-powered sensors using short-range wireless communication⁵. These networks have applications in environmental monitoring, disaster relief and military operations; when the nodes of such a system are placed in relatively fixed positions, there is a close analogy to some of the oldest and best-studied models of disease epidemics, based on short-range spatial contacts in two dimensions⁹.

Although these types of worm have not yet achieved widespread penetration, prototypes have successfully exploited vulnerabilities in wireless protocols including Bluetooth, and it is to be expected that mobile devices will be increasingly targeted by malicious code. In assessing the risks of such attacks, and developing countermeasures against them, it is intriguing to contemplate how we might draw on expertise from the field of human epidemiology in understanding how contagion spreads.

These analogies will, of course, always be incomplete. In particular, the timescales over which highly successful mobile worms operate will probably be shorter than those of their biological counterparts. The initial outbreak, and the opportunities for recovery, will potentially

progress much more quickly. Mobile worms are also restricted in a way that has no obvious biological analogy by the limited communication rates of the devices they infect. Particularly aggressive worms will also be confronted with the 'self-throttling' effects of many infected devices competing for limited wireless bandwidth^{5,6}.

Analogies to biological epidemics can also be exploited for beneficial purposes, in the design of computer-network protocols¹⁶. For mobile devices, epidemiology helps in dealing with the problem of intermittent connectivity: that the routing of traffic must conform to a dynamic and unpredictable network structure as the owners of mobile devices move around. The result is a growing interest in opportunistic routing, in which messages are passed between devices that come into physical proximity, with the goal of eventually reaching a specified recipient⁷. The development of such protocols has drawn on detailed data concerning human mobility and contact patterns⁸.

These lines of work reinforce how the evolution of computer viruses and worms has always been closely linked with the legitimate concerns of computer networking. As that relationship extends into the domain of mobile devices, we are taking further steps towards a world where digital traffic flows not just over the wired backbone of the Internet, but also in

small leaps through physical space as people pass one another on the street.

Jon Kleinberg is in the Department of Computer Science, Cornell University, Ithaca, New York 14853, USA.

e-mail: kleinber@cs.cornell.edu

1. Kephart, J., Sorkin, G., Chess, D. & White, S. *Sci. Am.* 88-93 (Nov. 1997).
2. Mickens, J. W. & Noble, B. D. *Proc. ACM Workshop Wireless Security* 77-86 (ACM, New York, 2005).
3. Su, J. et al. *Proc. 4th ACM Workshop Rapid Malcode* 9-16 (ACM, New York, 2006).
4. Cheng, J., Wong, S., Yang, H. & Lu, S. *Proc. 5th ACM Int. Conf. Mob. Syst. Appl. Serv.* (ACM, New York, 2007).
5. Nekovee, M. *New J. Phys.* **9**, 189 (2007).
6. Cole, R. G., Phamdo, N., Rajab, M. A. & Terzis, A. *Proc. 19th IEEE Workshop Parallel Distr. Simul.* 207-214 (IEEE, New York, 2005).
7. Hui, P. et al. *Proc. ACM SIGCOMM Workshop Delay-Tolerant Networks* 244-251 (ACM, New York, 2005).
8. Chaintreau, A. et al. *IEEE Trans. Mobile Comput.* **6**, 606-620 (IEEE, New York, 2007).
9. Durrett, R. *SIAM Rev.* **41**, 677-718 (1999).
10. Eubank, S. et al. *Nature* **429**, 180-184 (2004).
11. Meyers, L. A., Pourbohloul, B., Newman, M. E. J., Skowronski, D. M. & Brunham, R. C. *J. Theor. Biol.* **232**, 71-81 (2005).
12. Colizza, V., Barrat, A., Barthélemy, M. & Vespignani, A. *Proc. Natl Acad. Sci. USA* **103**, 2015-2020 (2006).
13. Weaver, N., Paxson, V., Staniford, S. & Cunningham, R. *Proc. 1st ACM Workshop Rapid Malcode* 11-18 (ACM, New York, 2003).
14. Pastor-Satorras, R. & Vespignani, A. *Phys. Rev. Lett.* **86**, 3200-3203 (2000).
15. Berger, N., Borgs, C., Chayes, J. T. & Saberi, A. I. *Proc. 16th ACM Symp. Discr. Algor.* 301-310 (ACM, New York, 2005).
16. Demers, A. J. et al. *Proc. 6th ACM Symp. Princip. Distr. Comput.* 1-12 (ACM, New York, 1987).

AGEING

From stem to stern

Anne Brunet and Thomas A. Rando

Immortality is the stuff of myth and legend, but lifespan extension is the subject of serious scientific inquiry. Exploring the causes and effects of ageing in stem cells should aid this quest.

The explosion of research on stem cells has given the promise of treatments for degenerative diseases of ageing, enhancement of the repair of damaged tissues and possibly even slowing of decline-in-function that occurs with advancing age. But how stem cells are affected by the ageing process, and whether such changes are a cause or a consequence of organismal ageing, remain unclear¹. Three research teams²⁻⁴ have recently reported their findings on how age-related accumulation of DNA damage and changes in global patterns of gene expression might lead to the decline of stem-cell function.

In mammals, stem cells reside in many adult tissues and either continually produce new cells for tissues with a high turnover (blood, skin and gut) or serve as a reservoir for gradual cellular replacement or repair in the more stable tissues (liver, muscle and brain)¹. Stem-cell function, just like that of other cells, declines with age. However, to what extent age-related changes in

stem-cell function are due to intrinsic ageing of the cells or due to changes in the environment in which they reside⁵ is still unclear.

Many theories have been put forth to explain the decline of cell and tissue function with age, but a main challenge for researchers who study ageing is to distinguish among potential causal influences, virtually all of which interact with one another and lead to organismal ageing (Fig. 1). The free-radical theory of ageing proposes that reactive oxygen species, which are by-products of normal metabolism, are responsible for damage to many cellular components, including DNA⁶.

Several mechanisms of DNA repair that are essential for healthy tissues and long life⁷ have evolved in cells of higher organisms. In humans or mice, mutations in genes encoding DNA-repair enzymes may lead to dramatic increases in the incidence of cancer and the shortening of lifespan. What has remained unclear is how susceptible adult stem cells are to the age-

related accumulation of DNA damage, how effective DNA-repair activities are in these cells, and to what extent this balance contributes to the characteristics of tissue ageing.

Nijnik *et al.*² and Rossi *et al.*³ tested the hypothesis that accumulation of DNA damage is an essential mechanism underlying age-related decline in the function of haematopoietic stem cells (HSCs). These cells reside in the bone marrow and give rise to all cellular components of blood — from red blood cells to cells of the immune system⁸. For this, Rossi *et al.* studied mice that carry mutations in various DNA-repair pathways and show signs of accelerated ageing, whereas Nijnik *et al.* discovered and studied a mouse strain with a mutation in a gene encoding a DNA-repair enzyme, which models a human syndrome characterized by immunodeficiency and developmental abnormalities.

Both teams found that HSC function was severely impaired in rapidly ageing mutant mice. Moreover, HSCs from the mutant mice had compromised ability to generate blood cells even when they were transplanted into normal mice, indicating that the defects were intrinsic to the stem cells. Intriguingly, although the types of DNA defects that would be expected to accumulate in the various mouse mutants studied are different, the altered HSC functions observed in all of these mutants were similar. This suggests that HSCs have a limited repertoire of potential responses to intrinsic damage.

Do these results pertain to HSC ageing and the age-related decline of immune responses in normal mice? That partially depends on how accurately biological processes in the genetic mutants studied reflect those of normal ageing. Clearly, there are limitations in extrapolating results from a mouse or human with a single gene mutation, even if the outcome of the mutation resembles normal ageing. Thus, it is crucial to investigate the relationship between accumulation of DNA damage and ageing in genetically normal HSCs and their progeny.

Rossi *et al.*³ did find that HSCs from normal old mice have more DNA damage than those from younger animals, hinting that increased DNA damage may be responsible for limited stem-cell function in aged organisms. However, these authors also found that, in old mice, the DNA of HSC progeny was less damaged than HSCs themselves. This could be either because the progeny with high levels of DNA damage are selectively eliminated, because only HSCs without DNA damage successfully divide, or because the committed progenitors that are derived from HSCs can repair the lesions more efficiently than can HSCs themselves.

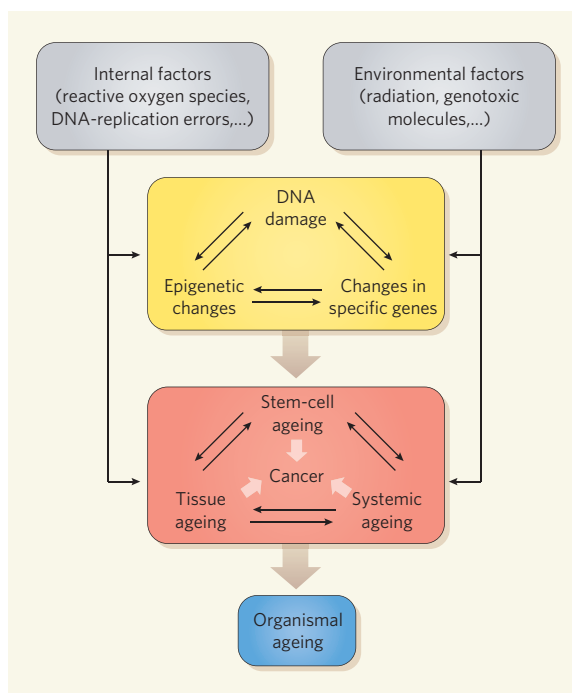


Figure 1 | Interplay between factors and networks influencing ageing. As stem cells are essential for tissue homeostasis and repair throughout life, three groups^{2–4} have explored what factors influence alterations in their function with age. These studies, together with previous work, suggest that the story is complex, involving interactions between different networks and at several levels. At the genomic level, both internal and environmental factors cause alterations in individual genes, groups of genes through epigenetic changes, and chromosomes, at least some of which arise from direct damage to DNA. At the levels of cells and tissues, functional changes in stem cells and other cells in the tissue influence each other and are, in turn, influenced by systemic changes that may be conveyed from one tissue to another via the circulation. All of these may contribute to the possible development of cancer in tissues throughout the body. The ultimate outcome is organismal ageing.

Can mechanisms other than accumulation of damaged DNA underlie stem-cell ageing? Chambers *et al.*⁴ asked whether the overall pattern of cellular gene expression was altered in aged HSCs. Looking for changes across the whole genome, they found that, indeed, old HSCs show high-order changes in gene expression: groups of genes, or entire chromosomal regions, which were normally silenced in young HSCs, were now turned on, whereas other genes and genomic regions were expressed at lower levels than in young cells.

Among the genes with reduced expression were those involved in modulating chromatin, which is the complex formed by DNA and histone proteins. Epigenetic changes — changes in chromatin structure without mutations in the DNA sequence — influence gene expression. The authors⁴ suggest that such epigenetic changes may underlie altered HSC function in aged animals. In agreement with the observations of Nijnik *et al.*² and Rossi *et al.*³, Chambers and colleagues also found that the expression of genes involved in DNA repair was reduced in aged HSCs. Intriguingly, studying a mutant mouse strain with features of premature ageing,

they found that HSCs had a ‘molecular signature’, defined as a distinct pattern of gene expression, that was similar to that of HSCs from young animals⁴, even though there is a marked decline in HSC regenerative potential in this strain⁹. Although this finding is interesting as a possible example of how a molecular signature of ageing may be uncoupled from cellular function, it may also highlight how a rapidly ageing mouse mutant might not mimic the characteristics of normal ageing.

The work of Chambers *et al.*⁴ brings into perspective the complexities of the ageing process and how single-gene mutations or single biological processes are unlikely to account for the myriad of cellular, tissue and organismal changes associated with ageing. Even if epigenetic changes are a hallmark of ageing, what are the processes that initially lead to them in old cells? The juxtaposition of these studies raises a conundrum similar to that of ‘chicken or egg’: do age-related epigenetic changes render DNA more susceptible to damage, or does DNA damage underlie epigenetic changes? And how do general epigenetic modifications fit in with specific genes that have been shown to limit HSC function¹⁰ or maintain HSC potential¹¹ during ageing? More importantly for regenerative medicine, are these epigenetic changes (and thus possibly ageing) reversible?

The authors^{2–4} converge in their general conclusions that, with age, adult HSCs decline in function but not number, and that DNA damage and epigenetic modifications may limit the regenerative potential of these cells. They also agree that HSCs are not protected from age-induced damage and, in fact, ageing may result in an accumulation of DNA mutations in these cells, thereby increasing the risk of cancer.

Their findings also raise further questions. Are these observations true for adult stem cells in other tissues, particularly tissues with much lower cellular turnover than the blood? Would stem-cell ‘enhancement’, whether genetic or epigenetic, delay the ageing characteristics of a particular tissue or even lead to an extension of lifespan? Understanding what limits stem-cell function during ageing will be essential for the field of regenerative therapeutics, which proffers the hope that the remarkable potential of stem cells will be harnessed for the repair of injury and the treatment of diseases. ■

Anne Brunet is in the Department of Genetics, and Thomas A. Rando is in the Department of Neurology and Neurological Sciences, Stanford University School of Medicine, Stanford, California 94305, USA.
e-mails: anne.brunet@stanford.edu;
rando@stanford.edu

1. Rando, T. A. *Nature* **441**, 1080–1086 (2006).
2. Nijnik, A. et al. *Nature* **447**, 686–690 (2007).
3. Rossi, D. J. et al. *Nature* **447**, 725–729 (2007).
4. Chambers, S. M. et al. *PLoS Biol.* **5**, e201 (2007).
5. Brack, A. S. et al. *Science* **317**, 807–810 (2007).
6. Finkel, T. & Holbrook, N. J. *Nature* **408**, 239–247 (2000).
7. Lombard, D. B. et al. *Cell* **120**, 497–512 (2005).
8. Shizuru, J. A., Negrin, R. S. & Weissman, I. L. *Annu. Rev. Med.* **56**, 509–538 (2005).
9. Dumble, M. et al. *Blood* **109**, 1736–1742 (2007).
10. Janzen, V. et al. *Nature* **443**, 421–426 (2006).
11. Tothova, Z. et al. *Cell* **128**, 325–339 (2007).

PALAEOANTHROPOLOGY

Homing in on early *Homo*

Daniel E. Lieberman

Newly described fossils from Georgia in Eurasia and from Kenya shed more light on the earliest members of the genus *Homo*. These finds indicate that there was considerable variability in their size and shape.

The fossil record of human evolution is like a pointillist painting: one sees a different picture close up from when one stands back. For years, students of human evolution have tended to prefer standing back when considering the evolution of the genus *Homo* from the genus *Australopithecus*, by contrasting what came before with what came after. Two sets of discoveries now help us to look more closely at the complex transition from *Australopithecus* to *Homo*. One of the papers concerned is by Lordkipanidze and colleagues (page 305 of this issue)¹, and deals with postcranial bones (those other than the cranium) from Georgia, Eurasia. The other, by Spoor and colleagues², was published in *Nature* on 9 August and describes cranial material from Kenya.

In terms of the big picture, the transition to *Homo* was one of the most substantial in human evolution. The time before then was the era of the australopiths. This diverse group of species had brains 400–550 cm³ in volume (only slightly larger than that of a chimpanzee), big cheek teeth, and massive faces adapted to generate and withstand large chewing forces. Australopiths also had many adaptations for upright bipedalism. But they were chimpanzee-sized (100–150 cm tall, weighing 30–50 kg), and retained some features useful for climbing trees, such as relatively long arms, upwardly oriented shoulders and long, curved digits.

Sometime after the transition came *Homo erectus*. This species first appeared in Africa about 1.9 million years ago, and quickly moved out of Africa by 1.8 million years ago. It had a bigger brain, a less snout-like, vertical face, and small, nearly human-sized teeth. A spectacular skeleton, of a juvenile male from Nariokotome, Kenya, dating to 1.5 million years ago, came to epitomize our view of the species as having a very modern body: tall (160–185 cm), large (50–70 kg), with long legs, and otherwise only subtly different from your body or mine³. *Homo erectus* also seems to have resembled modern humans in having low levels of sexual dimorphism, with males being about 10–20% larger than females.

When viewed up close, however, the *Australopithecus*–*Homo* transition has always been murky. One problem is that we don't know enough about *Homo habilis*, the putative ancestor of *H. erectus*. In addition, early *H. erectus* fossils are quite variable, and the more we look, the more we find contrasts with later hominins (the formal term for a species in the human lineage). For example, their rate of development was rapid and chimp-like, rather than slow and extended as in modern humans⁴. Also, brain size relative to body size in the earliest *H. erectus* fossils is not much different from that of many australopiths or *H. habilis*⁵. Finally, the earliest non-African fossils of *Homo* from Dmanisi, Georgia, which are dated to 1.77 million years ago, resemble *H. erectus* in many respects. But they are highly variable, and more in the size range of *H. habilis* than of *H. erectus*^{6,7}.

The new discoveries^{1,2} further highlight the transitional and variable nature of early *Homo*. Lordkipanidze and colleagues¹ describe several postcranial fossils from Dmanisi, including partial skeletons of an adolescent associated with a previously reported cranium (D 2700), some limb bones from an adult associated

with a massive, previously reported jaw (D 2600), and some foot bones from two smaller adults. In many respects, the fossils resemble modern humans and the Nariokotome *H. erectus* skeleton. The adult's limb proportions are quite modern, with a relatively long femur compared with the humerus, and a tibia/femur ratio similar to that of modern humans from Europe. The feet have a well-developed arch and are at least as modern as those of another early *Homo* foot, OH 8, from Olduvai Gorge in Tanzania⁸.

Other details, however, are less human-like. Most importantly, the Dmanisi individuals' stature and body mass are smaller than those of the Nariokotome boy. The larger adult would have weighed 48–50 kg and stood 147–166 cm tall. The adolescent would have weighed 40–43 kg and been 145–161 cm tall, so its adult weight and stature would have been even greater. Estimates of relative brain size are in the range of *Australopithecus*, well below those of later *H. erectus* and modern humans.

Other differences are also apparent. In modern humans, the elbow joint is typically rotated relative to the shoulder joint, so that the forearm naturally hangs with the palms facing inwards; but the new Dmanisi humeri lack torsion, so their palms would have been oriented more forwards. Lack of humeral torsion, a highly plastic and variable feature, suggests something different about the shoulder in these specimens. In addition, although the adolescent's collar-bone is of normal length for a 15–16-year-old human⁹, and the shoulder joint faces sideways (though at the more vertical end of human variation), other aspects of shoulder-blade shape seem to be primitive. New analyses of the Nariokotome boy also suggest a lack of humeral torsion¹⁰.

Evidence that early *Homo* was less modern and more variable than sometimes supposed is also bolstered by Spoor and colleagues' finds from Lake Turkana, Kenya². One of the fossils, KNM-ER 42700, is a beautiful

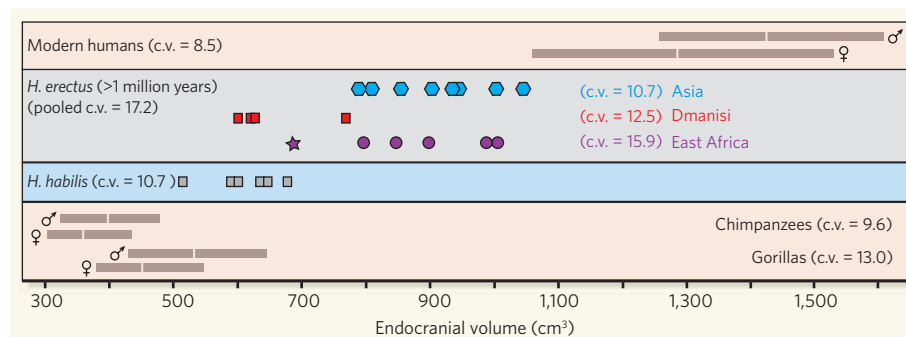


Figure 1 | The wide range of brain sizes in early *Homo*. Brain sizes (as endocranial volume) of *Homo habilis*, and of *Homo erectus* fossils more than 1 million years old, compared with those of modern humans and extant great apes (chimpanzees and gorillas). Data are from refs 1, 13 and 14. The Dmanisi crania and the new KNM-ER 42700 *H. erectus* cranium from Kenya (star)² have smaller brains than most other *H. erectus* specimens. Furthermore, including them in the same species as other fossils attributed to *H. erectus* yields a coefficient of variation (c.v.) of 17.2, much higher than those of modern humans and great apes, even in highly sexually dimorphic species such as gorillas. Grey bars indicate the 95% confidence interval around the means for each sex in the modern human and great ape samples. Values for c.v. are standard deviations as a percentage of the mean, and are corrected for sample size.

partial cranium, lacking most of the face, dated to 1.55 million years ago. The fossil's endocranial volume (the volume occupied by the brain inside the cranium) is only 691 cm³, but its shape is mostly typical of larger *H. erectus* crania when adjusted for size. Comprehensive comparative analyses have yet to be undertaken, but the fossil's similarity in size and shape to Dmanisi crania such as D 2700 and to other African fossils attributed to *H. erectus* suggests that these fossils belong to the same species. If so, then early *H. erectus* was not only quite widespread but also unusually variable in both body and brain size (Fig. 1).

Explaining the variation is a challenge. One possibility is that some of it is ecogeographic — that the Dmanisi specimens were simply smaller than their African relations. Alternatively, the Dmanisi fossils may be examples of a different species. In either case, early *Homo* probably had substantial levels of sexual dimorphism, as we see in *Australopithecus*. My hunch is that the Dmanisi and early African *H. erectus* fossils represent different populations of a single, highly variable species. But this hypothesis needs to be tested with comprehensive three-dimensional analyses of scaling and variation (something that will be expedited once computed tomography scans and casts of the fossils are made public).

New discoveries are often most valuable because of the research they stimulate. Basic questions include how many species are represented by the various fossils and how they are related to each other. In some respects, *H. habilis* looks like a good candidate as the ancestor of *H. erectus*: it has a vertical face, teeth of intermediate size between those of *Australopithecus* and *H. erectus*, and an intermediate-sized brain. But the oldest fossils definitively attributed to *H. habilis* are 1.9 million years old, and thus no older than the oldest *H. erectus* fossils. Moreover, Spoor *et al.*² also report a new *H. habilis* upper jaw dated to 1.44 million years ago, extending the species' temporal overlap with *H. erectus*. Clearly, we need to find and focus more on other fossils older than 2 million years, such as a 2.33-million-year-old upper jaw (AL 666) from Hadar, East Africa, that is possibly *H. habilis*¹¹.

In addition, how behaviourally modern was early *H. erectus*? The species had small teeth suggesting a more human-like diet, and relatively long legs and other features suited to walking and running¹². But they matured more rapidly than we do, and big increases in absolute and relative brain size evolved well after the species originated, perhaps as they became more proficient hunters. *Homo erectus* also might have been more sexually dimorphic. This has implications for reconstructing how much energy this species spent on reproduction, how frequently they spaced births, and aspects of social organization such as levels of male–male competition. Finally, there are other anatomical differences in the upper body and elsewhere that need to be studied for their significance. Looking more closely

at details of the long, complex, but highly consequential transformation from *Australopithecus* to *Homo* promises to reveal a rich and intriguing picture. ■

Daniel E. Lieberman is in the Departments of Anthropology, and Organismic and Evolutionary Biology, Harvard University, Cambridge, Massachusetts 02138, USA.

e-mail: danlieb@fas.harvard.edu

1. Lordkipanidze, D. *et al.* *Nature* **449**, 305–310 (2007).
2. Spoor, F. *et al.* *Nature* **448**, 688–691 (2007).
3. Walker, A. & Leakey, R. E. F. (eds) *The Nariokotome Homo erectus Skeleton* (Harvard Univ. Press, 1993).
4. Dean, C. *et al.* *Nature* **414**, 628–631 (2001).

5. Wood, B. A. & Collard, M. *Science* **284**, 65–71 (1999).
6. Rightmire, G. P., Lordkipanidze, D. & Vekua, A. *J. Hum. Evol.* **50**, 115–141 (2006).
7. Lordkipanidze, D. *et al.* *Anat. Rec.* **288A**, 1146–1157 (2006).
8. Harcourt, W. E. & Aiello, L. *J. Anat.* **204**, 403–416 (2004).
9. Scheuer, J. L. & Black, S. M. *Developmental Juvenile Osteology* (Academic, London, 2000).
10. Larson, S. G. *et al.* *J. Hum. Evol.* doi:10.1016/j.jhevol.2007.06.003 (2007).
11. Kimbel, W. H., Johanson, D. C. & Rak, Y. *Am. J. Phys. Anthropol.* **103**, 235–262 (1997).
12. Bramble, D. M. & Lieberman, D. E. *Nature* **432**, 345–352 (2004).
13. Holloway, R. L., Broadfield, D. C. & Yuan, M. S. *The Human Fossil Record Vol. 3. Brain Endocasts: The Paleoneurological Evidence* (Wiley-Liss, New York, 2004).
14. Tobias, P. V. *The Brain in Hominid Evolution* (Columbia Univ. Press, New York, 1971).

CATALYSIS

Raising the gold standard

A. Stephen K. Hashmi

Gold is the current star of metal catalysis, but most gold catalysts cannot control which mirror-image version of a molecule forms during a reaction. The answer lies with the positive catalyst's negative counter-ion.

Catalysts are crucial to almost every area of chemistry, often enabling reactions to occur that would otherwise be impossible. Even better, some catalysts can control molecular chirality — they determine which of two mirror-image versions a reaction product will take. Most soluble catalysts of this type are complexes, in which ligand molecules bind tightly to a transition metal; if these complexes are positively charged, the negative counter-ion generally has little effect on the chiral outcome of the reaction. But reporting in *Science*, Toste and colleagues¹ describe excellent chiral control in organic reactions catalysed by cationic gold complexes that have chiral counter-ions. If the same principle can be extended to other metals, this discovery could spark a revolution in catalysis, with potential applications for synthesis and the chemical industry.

Many three-dimensional molecules are chiral — they can exist in two forms known as enantiomers that are not superimposable on each other. Each enantiomer may have different properties, which is often of great significance in biology, medicine or materials science. This creates a challenge for chemists: how to devise enantioselective syntheses of such compounds in which the formation of one of the enantiomers is highly preferred. Nature uses enzymes for this purpose, and antibodies can also be developed as catalysts for synthetic reactions. But enzymes and antibodies are complex molecules with high molecular weights. Chemists prefer to use smaller, more easily available catalysts, such as transition-metal complexes or small organic molecules (organocatalysts).

Gold is the latest metal to enter the arena of transition-metal catalysis^{2,3}. Gold catalysts have developed impressively over the past few

years, and have already provided some valuable contributions. Early examples^{4,5} used cationic gold complexes that incorporated phosphorus-containing ligands known as phosphines, in combination with non-chiral counter-ions. Most gold catalysts still conform to this design. Despite the success of gold catalysts, surprisingly few enantioselective gold-catalysed reactions have been reported.

Toste and colleagues¹ now describe cationic gold complexes with chiral, negatively charged counter-ions that are based on a phosphate group. In several different reactions commonly catalysed by gold complexes, the authors used their catalysts to obtain chiral products with large excesses of one enantiomer over the other (Fig. 1a). The yields and enantiomeric ratios of these reactions far exceed the high standards required for successful chiral reactions, even when 'problematic' reagents were used that do not react under previously available conditions. This impressive chiral induction is a direct result of using a chiral counter-ion.

The authors found that the enantioselectivity of their reactions was enhanced if the cationic gold complex incorporated a chiral ligand — but only if the 'correct' enantiomer of that ligand was used. Perhaps most strikingly, the authors observed that the influence of the counter-ion can be stronger than the influence of chiral ligands covalently bound directly to the gold centre, which flies in the face of accepted chemical wisdom.

The idea of using counter-ions in catalysts to induce chirality is not new — the strategy has already been successfully used in organocatalysis⁶. The basic principle has even been established in transition-metal catalysis with copper complexes, although the

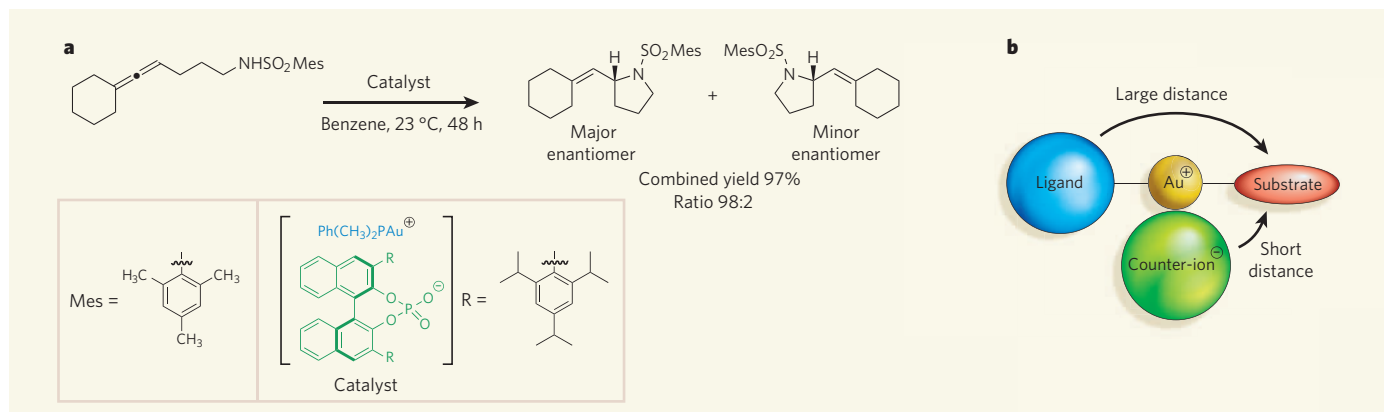


Figure 1 | Chiral counter-ions in gold catalysis. Chiral compounds can exist as one of two mirror-image forms (enantiomers). Certain catalysts can control which of these enantiomers forms during a reaction. **a**, In reactions such as the one shown at the top, Toste and colleagues¹ find that a cationic gold complex (blue), which ordinarily does not induce chirality, can promote the formation of a desired enantiomer in the presence of a

chiral counter-ion (green). **b**, During catalysis, reaction substrates and ligand molecules bind to gold (Au) cations on opposite sides of the metal, so the ligands are too distant to induce chirality on the substrate. The authors propose¹ that counter-ions associate with the gold complex by charge attraction. This brings them close enough to the substrate to control the enantiomeric outcome of the reaction.

enantioselectivity obtained was so low as to be practically useless^{7–9}. Gold and copper are from the same family of elements, and might therefore be expected to exhibit similar catalytic behaviour. So why are gold catalysts so much better at chiral induction in these systems?

The gold ions — known as gold(I) ions — used in gold catalysts¹ differ from most other metal centres because usually only two molecules can bind to them at once; most metals can accommodate four or six molecules. During catalysis, the gold ion binds to the reaction substrate and to another ligand, with the two molecules arranged as far apart as possible on opposite sides of the metal (Fig. 1b). In transition-metal catalysis, good chiral induction occurs only when the ligand and the substrate are close together on the metal. But on gold(I) ions the bound molecules are so far apart that only low enantioselectivity can generally be obtained.

Toste and colleagues' catalysts overcome this problem by using a counter-ion to induce chirality. The authors' spectroscopic studies¹ indicate that the cationic gold complex associates closely with the counter-ion in solution, as a result of charge interactions. As long as solvent molecules do not interfere, the chiral counter-ion can occupy the free space between the ligand and the substrate (Fig. 1b). The counter-ion thus probably ends up close to the substrate and so can induce chirality during the reaction. This is similar to a previously reported effect¹⁰ in which two independent ligand units cooperate to induce excellent chiral control in transition-metal-catalysed reactions.

The coming months will show how far this concept can be extended to other metals, but there will undoubtedly be difficulties to overcome. For example, because other metals can bind to more ligands than gold(I) ions, this will make it more difficult for a counter-ion to approach the metal centre and occupy a defined position close to the substrate. Nevertheless, the simple conditions developed by Toste and

colleagues¹ should allow a broad range of counter-ions and ligands to be screened rapidly. Perhaps a catalytic revolution is just around the corner.

A. Stephen K. Hashmi is at the Organisch-Chemisches Institut, Universität Heidelberg, Im Neuenheimer Feld 270, D-69120 Heidelberg, Germany.

e-mail: hashmi@hashmi.de

1. Hamilton, G. L., Kang, E. J., Mba, M. & Toste, F. D. *Science* **317**, 496–499 (2007).

2. Hashmi, A. S. K. & Hutchings, G. J. *Angew. Chem. Int. Edn* **45**, 7896–7936 (2006).
3. Hashmi, A. S. K. *Chem. Rev.* **107**, 3180–3211 (2007).
4. Ito, Y., Sawamura, M. & Hayashi, T. *J. Am. Chem. Soc.* **108**, 6405–6406 (1986).
5. Teles, J. H. et al. *Angew. Chem. Int. Edn* **37**, 1415–1418 (1998).
6. Mayer, S. & List, B. *Angew. Chem. Int. Edn* **45**, 4193–4195 (2006).
7. Llewellyn, D. B. & Arndtsen, B. A. *Tetrahedron: Asym.* **16**, 1789–1799 (2005).
8. Llewellyn, D. B. et al. *Org. Lett.* **26**, 4165–4168 (2000).
9. Lacour, J. & Hebbe-Viton, V. *Chem. Soc. Rev.* **32**, 373–382 (2003).
10. Reetz, M. T. et al. *Angew. Chem. Int. Edn* **42**, 790–793 (2003).

STRUCTURAL BIOLOGY

Unexpected opening

Cecilia M. Canessa

Cell membranes contain channels that open to allow ions into cells. The structure of a sodium ion channel helps explain how it opens in response to protons, and settles a long-standing debate about its composition.

What do humans have in common with worms, flies, hydra and sea urchins? One answer is that they all have proteins known as degenerins¹ that form pores in cell membranes for the passage of sodium ions. The acid-sensing ion channels (ASICs) belong to this family of proteins. They have been found in all vertebrates examined to date; even organisms with rudimentary nervous systems express at least one kind of ASIC. On page 316 of this issue, Gouaux and colleagues² report the first crystal structure of one of these intriguing proteins. The structure turns out to be unlike that of any other known ion channel, and provides some surprising answers to questions about the shape and behaviour of ASICs.

Degenerins all share certain structural features: two regions (TM1 and TM2) that cross the cell membrane; short terminal sections that face the cytoplasm; and a large domain that lies

outside the cell. Although their constituent amino-acid sequence varies between different degenerins, the extracellular section always contains cysteine amino acids at certain positions. Furthermore, the amino-acid sequence of TM2 — an essential component of the pore through which the ions pass — is remarkably similar in all degenerins. The evolutionary conservation of the TM2 structure makes these channels highly selective for sodium ions. Indeed, they have the highest sodium selectivity of all known ion channels, with a ratio of greater than 100:1 for sodium over potassium.

But the similarities between degenerins end there, as these ion channels have highly diverse functions and means of activation. Channels of the ASIC1 subclass found in the neurons of higher vertebrates open in response to extracellular hydrogen ions (protons, H⁺)³. The degenerins MEC-4 and MEC-10 in the

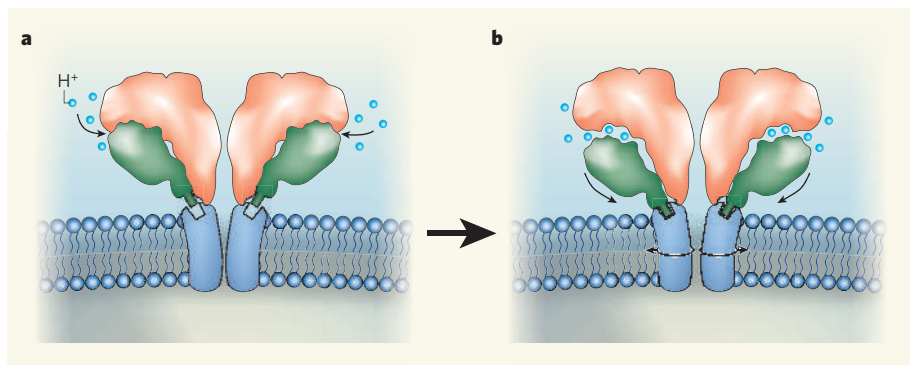


Figure 1 | Proposed mechanism for sodium-ion channel opening. Gouaux and colleagues² report the crystal structure of the chicken ASIC1 protein, which forms a channel across cell membranes. The channel opens in response to hydrogen ions (protons, H^+), so allowing sodium ions into cells. The authors propose the following mechanism. **a**, Protons bind to a cleft next to a thumb-shaped region (green) of the extracellular part of the protein. **b**, The proton-binding slightly displaces the thumb, which causes a conformational change that opens the channel.

worm *Caenorhabditis elegans* are mechano-transducers — slight mechanical stimulation of the worm's body surface induces a current in touch-responsive sensory neurons, an effect that is absent in animals lacking the *mec-4* and *mec-10* genes (ref. 4). Neurons in the garden snail *Helix aspersa* express a degenerin that is the only ion channel directly 'gated' by a peptide⁵. At the other end of the activation spectrum is ENaC (ref. 6), a sodium channel found in organs that regulate body sodium (such as the kidney, lung and the ducts of sweat glands). ENaC does not require a specific stimulus to open, but is constantly active.

A host of ions, toxins, small molecules, and enzymes and other proteins has been reported to bind to the extracellular domains of degenerins to modulate these channels' activities. Cations with two positive charges — particularly calcium ions (Ca^{2+}) — are crucial in this respect, because they stabilize a conformation of ASICs that makes the channels sensitive to protons.

Gouaux and colleagues² now provide the first three-dimensional structure of one of these functionally eclectic ion channels. They report the structure of chicken ASIC1 in the 'desensitized' state. This is a conformation adopted by the channel after it has opened, when it has ceased to conduct ions because the pore has closed up again, even though protons remain bound to the extracellular domain. Many of the observed structural features support previous experimental results, but the authors report several remarkable findings.

Perhaps one of the most unexpected discoveries is the number of subunits forming the channel. Previously, there were two schools of thought, one favouring four subunits and the other nine. Gouaux and colleagues' structure settles the matter once and for all: there are three. This means that all the other proteins in the degenerin family also have three subunits. In ASIC1, these subunits are of all the same type, but ENaC is known to have three different kinds of subunit; it can therefore now be concluded that ENaC is a heterotrimer.

The overall shape of the extracellular domain

is also surprising. It was expected to have a funnel shape that would concentrate sodium ions around the mouth of the pore, but in fact its rather compact mass provides no direct passage for ions. The only access points for sodium ions entering the pore are small windows formed by short loops that tether the extracellular domain to the transmembrane regions. As previously predicted, two transmembrane helices, mostly in TM2, line the pore itself.

The structure also shows that, in the desensitized state, the pore collapses without any ions trapped inside. This finding agrees with the notion that the pores of degenerins are narrow and able to hold only one ion at a time. Such narrow pores would strip water molecules from sodium ions before the ions enter the channel; the pores' narrow shape would also account for the relatively low flow of ions through the channels, and for the fact that the channels select small metal ions — so sodium ions are preferred over the larger potassium ions.

The most intriguing part of ASIC1 is its large extracellular region — its size, 'stickiness' for other molecules and crucial role in channel opening have attracted much attention. Nevertheless, attempts to understand the gating mechanism of degenerin channels have been

frustrated by the paucity of structural information about the extracellular domain. Gouaux and colleagues' structure² provides some much-needed data. The authors identify a cluster of negatively charged amino-acid residues that form the proton sensor; these residues are brought together from distant parts of the protein by an appropriate fold.

Gouaux and colleagues propose that binding of protons to the sensor displaces a thumb-shaped region of the protein; this nudges a short loop that connects the bulk of the extracellular domain to the transmembrane helices, so opening the pore (Fig. 1). This conformational-switch mechanism might not apply to every degenerin because not all of them respond to protons, even though a proton sensor is present. It is therefore reasonable to assume that the proton sensor is necessary, but not sufficient, to elicit conformational changes extending beyond the thumb region.

Thanks to Gouaux and colleagues' channel structure², these and other hypotheses can now be tested experimentally. It might also be possible to discover how the different channels can be gated by such diverse stimuli despite sharing a fundamentally common structure. The next task is to obtain the crystal structure of a channel in the open state, where sodium ions are found in the selectivity filter of the pore. This is an even greater technical challenge, but is essential if we are to observe the different conformations of the extracellular domain and so further elucidate the gating mechanism of these ubiquitous ion channels.

Cecilia M. Canessa is in the Department of Cellular and Molecular Physiology, Yale University School of Medicine, New Haven, Connecticut 06520, USA.

e-mail: cecilia.canessa@yale.edu

1. Kellenberger, S. & Schild, L. *Physiol. Rev.* **82**, 735–767 (2002).
2. Jasti, J., Furukawa, H., Gonzales, E. B. & Gouaux, E. *Nature* **449**, 316–322 (2007).
3. Waldmann, R., Champigny, G., Bassilana, F., Heurteaux, C. & Lazdunski, M. *Nature* **386**, 173–177 (1997).
4. Chelur, D. S. et al. *Nature* **420**, 669–673 (2002).
5. Lingueglia, E., Champigny, G., Lazdunski, M. & Barbry, P. *Nature* **378**, 730–733 (1995).
6. Canessa, C. M. et al. *Nature* **367**, 463–467 (1994).

GEOCHEMISTRY

Earth holds its breath

Chris J. Ballentine

Some inert-gas isotopes in Earth's atmosphere can only have come from deep inside the planet. We thought we knew how much gas Earth gives up, and how it does it — but a challenge has emerged to the prevailing model.

Slowly, Earth is cooling. The culprit is solid convection, which transports hot, buoyant material to Earth's surface from as far down as the core–mantle boundary, 2,900 kilometres beneath us. When this material reaches the

surface, some of it melts, and 'incompatible' elements that are of the wrong size, or the wrong ionic charge, to fit into the remaining solid mineral crystal diffuse into the molten rock. These elements become highly concentrated in

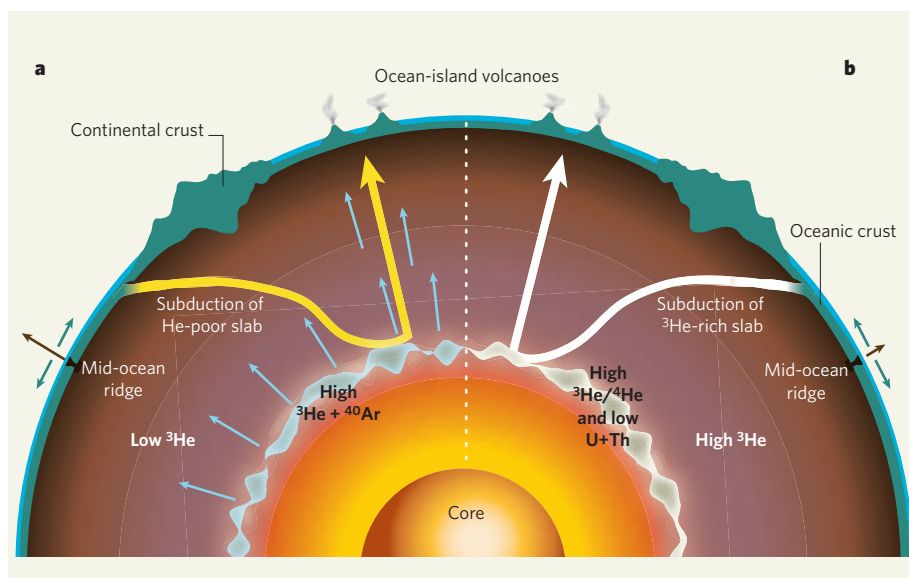


Figure 1 | Two inside views. Oceanic crust (grey) is subducted into Earth's interior at continental boundaries and, after residing in the deep mantle for a while, either mixes back into the convecting mantle or rises in plumes (large arrows) from the core–mantle boundary. **a**, If, as in the conventional view, the concentration of the helium isotope ^3He is low in the convecting mantle, a supply of ^3He (small arrows) would be needed from a volatile-rich reservoir in the deep mantle to maintain the observed $^3\text{He}/^4\text{He}$ ratios observed at mid-ocean ridges (^4He is continuously produced in the mantle by radioactive decay of uranium and thorium)⁹. Low mantle ^3He requires low mantle argon (^{40}Ar) levels, so a deep ^{40}Ar source is also required to balance the observed atmospheric argon concentration¹⁰. In this model, ocean-island basalts pick up some of this deep ^3He -rich reservoir, explaining their high $^3\text{He}/^4\text{He}$ ratios. **b**, But if, as Watson *et al.* suggest⁵, the inert gases are highly compatible and so the concentration of ^3He in the mantle is high, no ^3He flux into the convecting mantle or hidden ^{40}Ar reservoir is required to explain either high $^3\text{He}/^4\text{He}$ ratios at the mid-ocean ridges or the ratio of mantle argon to atmospheric argon. The high $^3\text{He}/^4\text{He}$ ratios of the ocean-island basalts might arise because they sample a deep reservoir that was depleted of uranium and thorium at an early stage in Earth's evolution, and is therefore ^4He -poor¹¹.

the oceanic crust that forms as the melt cools. Volatile elements that are highly incompatible — the inert gases such as helium and argon are generally counted among these^{1–3} — also escape the melt, being 'degassed' into Earth's atmosphere. These elements take little further part in subsequent processes such as continental-crust formation, and are not recycled back into the mantle.

Because their history seems so simple, inert-gas isotopes are widely used to define our understanding of deep-Earth processes: whether there is a volatile-rich reservoir that has been trapped deep in the mantle since Earth's accretion; how efficient mantle convection has been during Earth's history; and the details of the processes controlling the physical and chemical evolution of our planet⁴. On page 299 of this issue⁵, Watson *et al.* present new data that — if their interpretation is correct — would blow apart the basic assumption of all previous inert-gas studies. They argue that argon is between 10,000 and 10 million times more compatible than was previously thought.

Argon is a particularly useful tracer of Earth's mantle convection. Its most significant isotope by far, ^{40}Ar , is produced exclusively by the β -decay of the potassium isotope ^{40}K . Whereas in Earth's early history the amount of ^{40}Ar present was insignificant, today almost 1% of

the atmosphere consists of ^{40}Ar , representing about half of the ^{40}Ar produced since Earth formed. The atmospheric level of ^{40}Ar is thus a measure of the efficiency of mantle convection in bringing it from the depths to Earth's surface^{6,7}. The amount of ^{40}Ar in the mantle and the atmosphere must also add up, and so low ^{40}Ar concentrations in the parts of the mantle we can see might mean that hidden parts have higher concentrations⁸ — an essential detail in reconstructing which parts of the mantle are convecting.

Most mantle melting, and so degassing, takes place at mid-ocean ridges, where oceanic crust is formed as two tectonic plates move apart. Only 10–15% of the available material is actually melted, and argon degasses from this material when it migrates to the surface in what amounts to a continual planetary exhalation. Numerical simulations assuming argon's almost total incompatibility and a vigour of mantle convection similar to that of today calculate a release of the gas over time in good agreement with the proportion of argon in today's atmosphere⁶.

But on the basis of laboratory tests on olivine and enstatite, two closely related silicate minerals that form the bulk of Earth's upper mantle, Watson and colleagues⁵ argue that at most only 10–15% of the argon contained in the same volume of melt would be released — rather as

if the planet were holding its breath. The corollary is that, to supply the amount of argon that is currently in the atmosphere, convection in the mantle must have been much more vigorous in the past⁷.

The consequences go further. The helium–argon ($^4\text{He}/^4\text{Ar}$) ratios in basalt samples unaffected by degassing are similar to those predicted from the concentrations of their parent isotopes (potassium for argon, and the α -particle emitters uranium and thorium for helium) in the mantle⁴; so there can be little separation of helium from argon during melting. Thus, if Watson *et al.*⁵ are correct and argon is highly compatible, helium must be compatible too, and must also be only inefficiently extracted from solid minerals. The entire budget of inert gases in the mantle, including ^{40}Ar , is currently calculated from the present-day flux of ^3He into the oceans. This helium isotope was trapped in the Earth on its accretion and, in contrast to ^{40}Ar , has no significant production sources in Earth's interior. If helium is compatible, the concentration of ^3He in the mantle that maintains the observed outflow rate must also be significantly higher than was assumed.

If ^3He levels are low in the convecting mantle, the background production of ^4He by uranium and thorium decay in the convecting mantle would rapidly lead to much lower $^3\text{He}/^4\text{He}$ ratios than those observed in the mantle material that is exposed at mid-ocean ridges. The conventional picture thus requires a ^3He flux from a volatile-rich geochemical reservoir to balance things out⁹ (Fig. 1a). Ocean-island basalt rocks from isolated volcanoes that usually form away from ocean ridges can have even higher $^3\text{He}/^4\text{He}$ ratios, and are thought to 'sample' this reservoir directly. Similarly, if the ^{40}Ar concentration in the convecting mantle is low, the total amount of argon in the atmosphere and convecting mantle combined is less than that produced by potassium decay in the Earth. A hidden reservoir with high ^{40}Ar is thus also needed for 'mass balance'⁸.

Although Watson *et al.*⁵ predict high concentrations of inert gases in the mantle, those levels cannot be more than about 3.5 times higher than current estimates¹⁰. This is the 'zero-paradox' reference concentration: the point at which, for argon, the amount of the gas in the whole convecting mantle and the atmosphere summed up would balance the total amount produced in the Earth. Zero-paradox ^3He concentrations are the point at which the observed mid-ocean-ridge $^3\text{He}/^4\text{He}$ values balance with the estimated concentrations of uranium and thorium in the convecting mantle — and an external source of ^3He (Fig. 1a) is no longer required. The high compatibility of the inert gases opens the way for helium-rich material to be recycled back into the mantle, without the uranium and thorium that would produce ^4He (Fig. 1b). This has been suggested as an alternative explanation for the high $^3\text{He}/^4\text{He}$ values measured in ocean-island

basalt rocks (see, for example, ref. 11).

So should we rush out to buy this new model? Not yet. With such high compatibility, getting the noble gases out of the mantle at all becomes a significant problem. If we can indeed directly scale ^{40}Ar concentrations in the convecting mantle to the ^3He flux into the oceans, ^{40}Ar concentrations in the convecting mantle today would be two to three times higher than the zero-paradox reference value — we would have more ^{40}Ar in the combined convecting mantle plus atmosphere than the Earth has produced since its formation. Watson and colleagues' results⁵ also point to ultra-slow argon diffusion rates even at mantle temperatures. This would mean that it is very hard for olivine, which is the dominant mineral of the upper mantle, to release its helium or argon at all unless melted. A simple, testable prediction of the model would be that freshly exhumed mantle olivine should contain ^3He and ^{40}Ar concentrations somewhere between currently accepted average mantle values and the zero-paradox values.

Like many such laboratory studies, the question arises as to how relevant the results truly are to the mantle. Watson *et al.*⁵ exposed the surfaces of their crystals of olivine and enstatite to hot, pressurized argon gas, and deduced high argon compatibility from the high argon concentration at the surface, and very slow diffusion rates from its low penetration into the rest of the crystal. Such surface effects have been observed, in less detail, in other minerals before¹². But work on natural glass-olivine samples¹, theoretical lattice-accommodation models² and laboratory experiments^{2,3}, involving crystals grown from a melt containing inert gases, have all resulted in the opposite conclusion — inert-gas incompatibility.

So does the Earth hold its breath? Someone has got it wrong. Let's hope we don't have to hold our own breath too long to find out who. ■

Chris J. Ballentine is at the School of Earth, Atmospheric and Environmental Sciences, University of Manchester, Manchester M13 9PL, UK.
e-mail: chris.ballentine@manchester.ac.uk

CONDENSED-MATTER PHYSICS

Relaxation after a tight squeeze

Ehud Altman and Eugene Demler

Are the rules that determine relaxation to equilibrium the same in the classical and quantum worlds? Recent experiments supported the idea that they are — but an investigation with ultracold atoms now contradicts that.

Our everyday experiences lead us to expect things to seek equilibrium quickly when perturbed from rest. Cold milk poured into hot coffee, for example, soon distributes itself evenly, equalizing the temperature throughout the liquid. This kind of system, which over time samples every state available to it and so can relax to a true equilibrium state, is called ergodic. But unlike the milk-in-coffee example, not all systems that are governed by classical mechanics are ergodic, and it is difficult to push a system that is not naturally ergodic into an ergodic, equilibrium-seeking state. On page 324 of this issue¹, Hofferberth and colleagues report experiments that seem to indicate that a similar operation is much easier in the quantum world.

In classical statistical mechanics, concepts of ergodicity and thermodynamic irreversibility were originally addressed by Ludwig Boltzmann. His celebrated 'H-theorem' of 1872 states that an ideal gas will reach equilibrium starting from an arbitrary initial state. But even in classical mechanics, equilibration and the equalization of temperature are not guaranteed. One class of many-body systems, described by so-called integrable models, follows very different, non-ergodic dynamics, which does not allow relaxation to true equilibrium. Such systems have an infinite number of conservation laws, which prevents the sampling of the entire phase space, meaning that true equilibrium cannot be attained.

In fact, according to a well-founded

hypothesis of classical dynamics, the Kolmogorov–Arnold–Moser (KAM) theorem, a classical system does not even have to be exactly integrable to be non-ergodic; being nearly integrable is enough. For example, coupled nonlinear oscillators in a linear array do not equilibrate (share their energy equally), even though this system is integrable only when the distance between the oscillators tends to zero². Theorists continue to argue whether the KAM theorem has an equivalent in quantum dynamics, but others have set out to address the question experimentally. Their chosen proving-ground is the dynamics of one particular near-integrable quantum system — a condensate of cold atoms caught in a one-dimensional trap.

Just last year, the momentum distribution of a condensate of atoms confined to a one-dimensional tube and then kicked out of equilibrium was measured³. It did not re-equilibrate for a very long time — instead, individual atoms passed through each other repeatedly without ever coming to rest. This 'quantum Newton's cradle' was interpreted as a signature of non-ergodic dynamics in a near-integrable system, exactly as seen in the classical case.

Hofferberth *et al.*¹ investigated a similar system brought out of equilibrium in a different way, and came to precisely the opposite conclusion. They took a single condensate of ultracold rubidium atoms, caught in a one-dimensional magnetic trap, and split it along its length into two identical halves. After holding the atomic clouds separate for a certain time, the



Seeking equilibrium — cold milk in hot coffee.

- Heber, V. S., Brooker, R. A., Kelley, S. P. & Wood, B. J. *Geochim. Cosmochim. Acta* **71**, 1041–1061 (2007).
- Marty, B. & Lussiez, P. *Chem. Geol.* **106**, 1–7 (1993).
- Brooker, R. A. *et al. Nature* **423**, 738–741 (2003).
- Porcelli, D. & Ballentine, C. J. *Rev. Mineral. Geochem.* **47**, 411–480 (2002).
- Watson, E. B., Thomas, J. B. & Cherniak, D. J. *Nature* **449**, 299–304 (2007).
- van Keken, P. E. & Ballentine, C. J. *J. Geophys. Res.* **104**, 7137–7151 (1999).
- Huang, J. & Davies, G. F. *Geochem. Geophys. Geosyst.* **8**, Q03017 (2007).
- Hart, R., Dymond, J. & Hogan, L. *Nature* **278**, 156–159 (1979).
- O'Nions, R. K. & Oxburgh, E. R. *Nature* **306**, 429–431 (1983).
- Ballentine, C. J., van Keken, P. E., Porcelli, D. & Hauri, E. H. *Phil. Trans. R. Soc. Lond. A* **360**, 2611–2631 (2002).
- Parman, S. W. *Nature* **446**, 900–903 (2007).
- Wartho, J.-A. *et al. Earth Planet. Sci. Lett.* **170**, 141–153 (1999).

authors released them and observed the fringes formed as the matter waves of each condensate interfered. Repeating these experiments many times, Hofferberth *et al.*¹ noted that the position of interference fringes becomes more random with increasing 'hold time'.

The explanation for this observation is that, after splitting, the initially identical phases of the two condensates evolve independently. The relative phase between the two condensates becomes scrambled as the atoms within each condensate interact, and this loss of coherence expresses itself in a randomization of the interference fringes. From a classical point of view, this argument might seem surprising: identical systems prepared in the same state should surely evolve in the same way. But with a quantum system, identical measurements on identical wavefunctions can give different results.

More precisely in this case, the wavefunction describing the relative phase between the two condensates is in a 'squeezed' state just after splitting, because there is a very small uncertainty in the relative phase. But as time progresses after the separation, the wavefunction spreads out to form a wider probabilistic distribution. In any individual measurement, the relative phase will have a non-zero value somewhere within the spread of values covered by the wavefunction, even though its average value after many measurements remains zero.

This kind of analysis was first applied to the single-wave mode that describes a large, three-dimensional condensate^{4,5}, where it predicted a 'diffusion' of phase over time that was indeed observed⁶. In one-dimensional condensates, rigorous theorems forbid the existence of long-range order, and the multi-mode character of phase diffusion must be considered⁷. This analysis was extended by suggesting that degrees of freedom other than the relative phase — in particular, the summed phase of both condensates — might act as a heat reservoir⁸, resulting in a characteristic 'subexponential' decay of the coherence with hold time. This theoretically predicted signature of a system relaxing to thermal equilibrium is exactly that reported by Hofferberth and colleagues¹, suggesting that the dynamics they observe are indeed ergodic.

The idea of modelling a subset of the degrees of freedom by an effective heat bath is common to many areas of physics. But in the particular case of atoms in a one-dimensional trap this is hardly an obvious assumption, because such a system is very nearly integrable. It would be exactly integrable, were it not for the shallow trapping potential along the axis of the condensate. A common assumption is that as the potential varies little on the scale of interatomic distances, equilibration should still be prevented. Whereas the previous result³ supported this point of view, Hofferberth *et al.* seem to present a different answer.

What caused this difference? Perhaps it comes from the initial states or the degree of radial confinement, which was much greater in the earlier experiment³, and which affects

the accuracy with which the system can be described by an integrable model. Perhaps it originates in the temperature of the initial state, which was much higher relative to the chemical potential of the system in the new experiment¹. This experiment might also have been subject to a weak potential caused by low levels of magnetic-field disorder. It is a fundamental open question exactly what kind or magnitude of perturbations of an integrable quantum model are needed to effectively restore ergodicity, and to allow a system to reach equilibrium. A resolution of these two experimental results^{1,3} would provide a strong boost to our understanding of these fundamental questions.

Meanwhile, a practical lesson to be learnt from the experiments of Hofferberth and colleagues¹ is that the multi-mode character of quantum dynamics in low-dimensional systems might put fundamental limits on applications of cold-atom interferometers for metrology and spectroscopy, as it would accelerate the scrambling of interference fringes. But the worth of their investigation lies, above

all, in showing how systems of ultracold atoms can address fundamental questions in the non-equilibrium quantum dynamics of many interacting particles. The results will provoke heated debate, with implications beyond cold-atom research. ■

Ehud Altman is in the Department of Condensed Matter Physics, Weizmann Institute of Science, Rehovot 76100, Israel. Eugene Demler is in the Department of Physics, Harvard University, Cambridge, Massachusetts 02138, USA.
e-mails: ehud.altman@weizmann.ac.il;
demler@cmt.harvard.edu

1. Hofferberth, S., Lesanovsky, I., Fischer, B., Schumm, T. & Schmiedmayer, J. *Nature* **449**, 324–327 (2007).
2. Fermi, E., Pasta, J. & Ulam, S. *Studies in Nonlinear Problems I* Rep. LA-1940 (1955).
3. Kinoshita, T., Wegner, T. & Weiss, D. *Nature* **440**, 900–903 (2006).
4. Sols, F. *Physica B* **194–196**, 1389–1390 (1994).
5. Leggett, A. J. & Sols, F. *Phys. Rev. Lett.* **81**, 1344 (1998).
6. Shin Y. *et al.* *Phys. Rev. Lett.* **92**, 050405 (2004).
7. Bistrizter, R. & Altman, E. *Proc. Natl Acad. Sci. USA* **104**, 9955–9959 (2007).
8. Burkov, A. A., Lukin, M. D. & Demler, E. *Phys. Rev. Lett.* **98**, 200404 (2007).

FERTILIZATION

Calcium's double punch

Catherine Jessus and Olivier Haccard

Fertilization promotes a calcium surge necessary to ensure the success of embryonic development. It seems that calcium activates apparently opposite molecular signalling pathways to achieve that end.

Sexual reproduction relies on two cellular processes: meiosis, through which two cellular divisions produce gametes (sperm and egg), and fertilization, whereby male and female gametes fuse to form a zygote. In most organisms, the egg must halt meiosis to prevent embryonic development in the absence of fertilization. So a vertebrate egg remains arrested at the metaphase stage of the second meiotic division for many hours, awaiting the sperm. If sperm arrives, this breaks the arrest by increasing the intracellular concentration of calcium ions (Ca^{2+}), allowing cell divisions that ultimately produce a multicellular organism. Two reports^{1,2} published in this issue show that the enzyme calcineurin has a previously unidentified function that is triggered by the sperm-induced Ca^{2+} surge and is essential for overcoming the meiotic arrest.

Entry of cells into the division phase of the cell cycle (M phase) is mediated by a protein known as M-phase-promoting factor (MPF)³, which consists of a catalytic subunit, Cdk1, and a regulatory subunit, cyclin B. To overcome meiotic arrest, eggs must destroy cyclin B, thereby inactivating MPF. In vertebrate eggs, an unidentified agent dubbed cytosolic factor (CSF) mediates meiotic arrest³ by inhibiting a protein complex known as APC/C,

which would otherwise destroy cyclin B.

Meiotic arrest mediated by CSF is ensured through the activity of the Mos enzyme, which is present only during meiosis, and its downstream targets, MEK, MAPK and p90^{Rsk} (ref. 4). The relationship between the Mos–MEK–MAPK– p90^{Rsk} pathway and APC/C was clarified⁵ by the discovery of an egg-specific APC/C inhibitor, Erp1 (also known as Emi2), which, when phosphorylated by p90^{Rsk} , leads to meiotic arrest^{6,7}. This suggests that CSF consists of Mos, its downstream enzymes and their effector, Erp1, inhibiting APC/C to stabilize MPF (Fig. 1, overleaf).

So where does calcium come into the picture? For more than a decade, the only known function of Ca^{2+} waves in meiotic exit was in activation of the enzyme Ca^{2+} /calmodulin-dependent protein kinase II (CaMKII)⁸. Kinases regulate the activity of other proteins by phosphorylating them. CaMKII was shown^{9,10} to add an additional phosphate group to Erp1, allowing its subsequent phosphorylation by the Plx1 enzyme, which targets Erp1 for degradation. Free of Erp1, APC/C induces cyclin-B degradation, inactivating the kinase activity of MPF and thereby breaking meiotic arrest.

Nishiyama *et al.*¹ (page 341) and Mochida

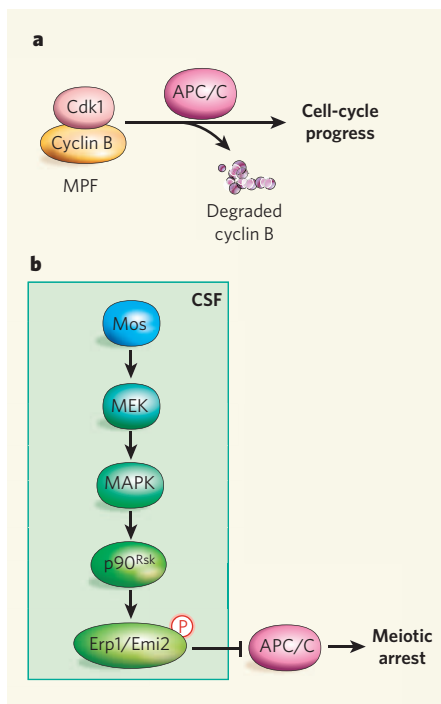


Figure 1 | Events leading to meiotic arrest. **a**, For cell-cycle progress, the APC/C complex mediates the degradation of the cyclin-B component of MPF, the sustained activity of which is responsible for cell-cycle arrest. **b**, In vertebrate eggs, however, premature cell-cycle progress is prevented by the Mos–MEK–MAPK–p90^{Rsk}–Erp1/Emi2 pathway, which is collectively known as CSF. Specifically, phosphorylated Erp1/Emi2 inhibits APC/C, leading to meiotic arrest.

and Hunt² (page 336) now show that another enzyme is also essential for overcoming meiotic arrest. This is a Ca²⁺-dependent phosphatase known as calcineurin. Phosphatases regulate other proteins by dephosphorylating them. Working with frog eggs, the authors show that, after Ca²⁺ release, calcineurin is quickly and transiently activated, independently of CaMKII. Moreover, calcineurin inhibition impairs several events that normally occur in response to Ca²⁺ (Fig. 2). These include cyclin-B degradation, dephosphorylation of proteins phosphorylated during M phase, migration of pronuclei (gamete nuclei seen after sperm enters the egg but before the two nuclei fuse) and rearrangement of the cytoskeleton in the cortical areas of the cell — that is, areas immediately beneath the cell membrane.

Both groups^{1,2} therefore conclude that, in addition to the CaMKII spike, activation of calcineurin is required to break meiotic arrest imposed by the Mos–MEK–MAPK–p90^{Rsk}–Erp1 signalling pathway, as well as for the completion of other cytoplasmic events that characterize fertilization (Fig. 2). Also noteworthy are observations¹ that indicate that, to allow both the growth of sperm aster — the array of sperm microtubules that mediates chromosome separation — and the migration of male and female pronuclei towards each other to fuse and form the nucleus of

the zygote, calcineurin activation must be transient.

In contrast to CaMKII, the molecular targets of which are well defined, proteins dephosphorylated by calcineurin to break CSF-mediated meiotic arrest have not been identified. Calcineurin could promote CaMKII-independent cyclin-B degradation by regulating Erp1 or APC/C, or both. As meiotic arrest by Erp1 depends on its phosphorylation by p90^{Rsk} (refs 6, 7), calcineurin could also dephosphorylate p90^{Rsk}-phosphorylated sites on Erp1, allowing its inactivation before it is degraded by the CaMKII-mediated pathway.

Other substrate candidates for calcineurin include APC/C components. Mochida and Hunt² show that, after the addition of Ca²⁺ to egg extracts, calcineurin quickly dephosphorylates an APC/C component, Apc3, as well as the APC/C activator Cdc20. Whether, in addition to Erp1 degradation, activation of APC/C depends on dephosphorylation of its subunits by calcineurin remains to be determined.

It is not unlikely that calcineurin also directly affects MPF. Mochida and Hunt show that this phosphatase promotes cyclin-B dephosphorylation, which could rapidly inactivate MPF before Erp1 is degraded. One could also imagine that, by directly or indirectly controlling Cdk1 phosphorylation, calcineurin would inhibit the catalytic activity of MPF without affecting cyclin B. Thus, simultaneous and parallel activities of a phosphatase (calcineurin) and a kinase (CaMKII) — both activated by Ca²⁺ and converging to inactivate MPF — would ensure rapid and irrevocable exit from meiosis.

Mochida and Hunt² find that calcineurin is also essential for reversing the phosphorylation state of other proteins specific to the second meiotic division. They add another twist to the story, showing that, shortly after the calcineurin spike, a second (non-calcineurin) wave of phosphatase activity fluctuates in a cell-cycle-dependent manner, presumably to dephosphorylate proteins common to meiotic and mitotic M phase. So whereas calcineurin and/or CaMKII might not be required for mitotic exit, the rapid embryonic cell cycles that follow fertilization must be controlled by other mitotic kinases and phosphatases.

Because in vertebrates both CaMKII and calcineurin are devoted to breaking the meiotic arrest at metaphase, these enzymes must have fertilization-specific substrates. These could include protein(s) that suppress a premature second wave of phosphatase activity before calcineurin activity peaks, and probably cytoskeletal proteins and their regulators. Fertilization triggers dramatic changes in the cytoskeleton and induces migration of pronuclei, which, as Nishiyama and colleagues¹ find, are also under calcineurin control (Fig. 2).

Depending on the species, eggs await fertilization either in the M-phase or the interphase stage of the cell cycle. Therefore, molecular

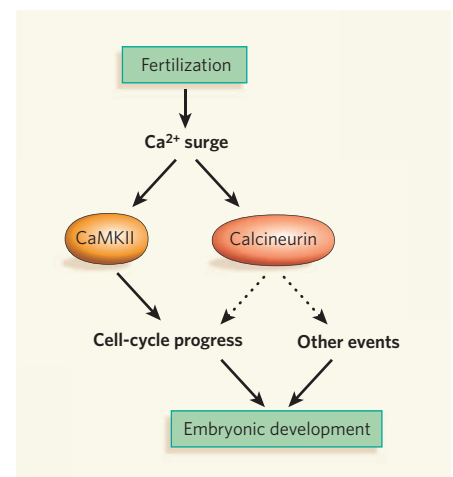


Figure 2 | Fertilization, calcium surge and calcineurin. Fertilization leads to cytoplasmic Ca²⁺ release that independently activates a kinase (Ca²⁺/calmodulin-dependent protein kinase II, or CaMKII) and — as Nishiyama *et al.*¹ and Mochida and Hunt² show — a phosphatase (calcineurin). Calcineurin, which seems to be essential for the release of meiotic arrest and cell-cycle progress, might directly or indirectly target the p90^{Rsk}-phosphorylated residues of Erp1, dephosphorylate essential partners or components of APC/C, dephosphorylate proteins phosphorylated during M phase, dephosphorylate cyclin B, or inhibit the activity of Cdk1 (see Fig. 1). Independently of this cell-cycle control, calcineurin might also be essential for the beginning of embryonic development by controlling chromatin decondensation, nuclear-envelope formation, migration of pronuclei and remodelling of the cortical cytoskeleton.

pathways ensuring meiotic arrest could be active both in the presence and in the absence of MPF activity. In both cases, however, the Mos–MEK–MAPK–p90^{Rsk} pathway and fertilization-associated Ca²⁺ surge remain essential for releasing meiotic arrest. Among the questions that the work of Nishiyama *et al.*¹ and Mochida and Hunt² raises, is whether, although CaMKII and Erp1 seem to be specific to eggs arrested in the M phase, calcineurin is universal in initiating embryonic development throughout the animal kingdom.

Catherine Jessus and Olivier Haccard are at CNRS, UMR7622 (Biologie du Développement), Université Pierre & Marie Curie, 9 quai Saint-Bernard, 75005 Paris, France. e-mails: jessus@ccr.jussieu.fr; olh@ccr.jussieu.fr

1. Nishiyama, T., Yoshizaki, N., Kishimoto, T. & Ohsumi, K. *Nature* **449**, 341–345 (2007).
2. Mochida, S. & Hunt, T. *Nature* **449**, 336–340 (2007).
3. Masui, Y. & Markert, C. L. *J. Exp. Zool.* **177**, 129–145 (1971).
4. Sagata, N., Watanabe, N., Vande Woude, G. F. & Ikawa, Y. *Nature* **342**, 512–518 (1989).
5. Schmidt, A. *et al. Genes Dev.* **19**, 502–513 (2005).
6. Inoue, D., Ohe, M., Kanemori, Y., Nobui, T. & Sagata, N. *Nature* **446**, 1100–1104 (2007).
7. Nishiyama, T., Ohsumi, K. & Kishimoto, T. *Nature* **446**, 1096–1099 (2007).
8. Lorca, T. *et al. Nature* **366**, 270–273 (1993).
9. Rauh, N. R., Schmidt, A., Bormann, J., Nigg, E. A. & Mayer, T. U. *Nature* **437**, 1048–1052 (2005).
10. Liu, J. & Maller, J. L. *Curr. Biol.* **15**, 1458–1468 (2005).

^{40}Ar retention in the terrestrial planets

E. Bruce Watson¹, Jay B. Thomas¹ & Daniele J. Cherniak¹

The solid Earth is widely believed to have lost its original gases through a combination of early catastrophic release and regulated output over geologic time. In principle, the abundance of ^{40}Ar in the atmosphere represents the time-integrated loss of gases from the interior, thought to occur through partial melting in the mantle followed by melt ascent to the surface and gas exsolution. Here we present data that reveal two major difficulties with this simple magmatic degassing scenario—argon seems to be compatible in the major phases of the terrestrial planets, and argon diffusion in these phases is slow at upper-mantle conditions. These results challenge the common belief that the upper mantle is nearly degassed of ^{40}Ar , and they call into question the suitability of ^{40}Ar as a monitor of planetary degassing. An alternative to magmatism is needed to release argon to the atmosphere, with one possibility being hydration of oceanic lithosphere consisting of relatively argon-rich olivine and orthopyroxene.

Most of our knowledge about the timing of atmosphere formation on Earth and the extent of planetary degassing in general has come from studies of noble-gas abundances and isotope ratios in natural samples. Information on timing is provided mainly by radiogenic noble-gas isotopes, and, because the half-lives of relevant parent isotopes span a range from 15.7 million years (Myr) (^{129}I decaying to ^{129}Xe) to 1.251 billion years (Gyr) (^{40}K decaying to ^{40}Ar), the potential exists to identify both early degassing episodes and gradual processes that have operated over much of Earth history. Present-day xenon isotope ratios (for example, $^{129}\text{Xe}/^{130}\text{Xe}$) in the mantle point to extensive degassing within the first 50–100 Myr of the Earth's history¹, perhaps as a consequence of the Moon-forming collision event 30–50 Myr after the Earth's formation^{2,3} and/or an early episode of extensive melting⁴. Information from other noble gases complicates this simple picture. Helium isotope ratios ($^3\text{He}/^4\text{He}$) of some ocean-island basalts and entrained mantle xenoliths, for example, have been interpreted to mean that early degassing of the Earth was incomplete and that portions of the mantle (a deep, geodynamically isolated reservoir?) still retain primordial ^3He (ref. 5).

Argon isotopes are a powerful complement to Xe and He because essentially all ^{40}Ar has been produced over Earth's history from decay of ^{40}K , and ^{36}Ar and ^{38}Ar are stable and almost exclusively primordial. If the K content of the bulk Earth were accurately known, the time-integrated extent of terrestrial degassing could be assessed directly from the abundance of ^{40}Ar in the atmosphere. A widely accepted estimate of the potassium abundance in the bulk silicate Earth (~250 p.p.m.; based on a K/U ratio of 12,700; ref. 6) leads to the conclusion that the present-day Earth is only ~50% degassed. The plausibility of this (low) value has been questioned because of the perceived efficiency of mantle convection and partial melting at removing volatiles from the solid Earth⁷. Incomplete ^{40}Ar degassing is consistent with the notion of a deep, isolated ^3He reservoir, but how such a reservoir is sustained in the presence of mass exchange between the upper and lower mantle is unclear^{7,8}. Support for the existence of such a reservoir may also be weakened by the suggestion that the ^3He -rich reservoir sampled by some ocean-island basalts is not so much rich in ^3He as poor in ^4He (ref. 9), possibly owing to early depletion in U and Th¹⁰.

Terrestrial ^{40}Ar production occurs mainly in the mantle owing to its volumetric dominance over the K-rich continental crust. The probable setting of most argon loss from the mantle is divergent plate

boundaries^{11,12}, but there is significant uncertainty in the factors that affect the efficiency with which mantle convection and magma production in these settings can extract noble gases. Degassing is thought to proceed through decompression melting of upwelling mantle (5–20%; refs 13, 14), transfer of noble-gas atoms to the melt phase, and subsequent loss of the gases to sea water and atmosphere on melt extrusion. Here we focus mainly on the crystal-to-melt transfer aspect: this is where the greatest uncertainty lies and also where additional experimental constraints can help clarify the overall behaviour of Ar in the mantle–melt system.

The efficiency of ^{40}Ar transfer from mantle minerals to partial melt is governed by the compatibility of Ar atoms in the relevant minerals (relative to the melt with which they interact) and the diffusivity of Ar in the mineral lattices, which affects the rate at which the system can approach partitioning equilibrium. We present experimental data on diffusion and solubility of Ar in the principal upper-mantle minerals olivine ($[\text{Mg,Fe}]_2\text{SiO}_4$) and enstatite ($[\text{Mg,Fe}]\text{SiO}_3$) obtained using a direct profiling method. Because the mantles of the terrestrial planets in general are dominated by olivine and enstatite, our data bear on the ^{40}Ar degassing of Venus and Mars as well as of Earth.

The solubility and diffusivity of argon

Most of the experiments were conducted with nominally pure synthetic Mg olivine (Mg_2SiO_4) grown commercially by Linde (Union Carbide) and natural enstatite from Sri Lanka (MgSiO_3 containing ~0.9 wt% FeO plus other minor impurities). These low-Fe materials were chosen to keep the background to a minimum during Ar analysis (see below). The crystals were cut into ~3 mm × 2 mm × 0.5 mm slabs and polished mechanically with alumina (down to 0.3 μm), then polished 'chemically' with colloidal silica to remove any abrasion damage that might have been introduced during the earlier polishing steps. Some samples were annealed at 1,000 °C for 16 h before use, as further assurance that preparation-introduced defects played no part in Ar uptake.

The polished olivine and enstatite samples were placed in small alumina boxes and inserted into cold-seal type René 41 or Ti–Zr–Mo superalloy pressure vessels connected to an argon pressure line. Following cold pressurization with Ar to about two-thirds of the final desired run pressure, the vessel was inserted into a preheated furnace and stabilized near the desired conditions of temperature and Ar pressure within ~15 min. Experimental temperatures ranged from

¹Department of Earth and Environmental Sciences, Rensselaer Polytechnic Institute, Troy, New York 12180, USA.

~690 to 1,340 K, establishing a robust basis for extrapolation to the somewhat higher temperatures of Earth's upper mantle. Oxygen fugacities are believed to have been buffered by the pressure vessel walls at about Ni–NiO (René 41 pressure vessel) or Mo–MoO₂ (Ti–Zr–Mo superalloy vessel). The temperature of a given experiment was maintained for 120 to 716 h, after which the pressure vessel was removed from the furnace and cooled to room temperature within ~5 min. To extend the results to low Ar pressure, one experiment was run in a tube furnace through which Ar gas flowed at a pressure of just over 1 bar. Conditions and materials used for all experiments are summarized in Supplementary Table 1.

Argon-uptake profiles in the olivine and enstatite samples were characterized using Rutherford backscattering spectroscopy, which has a relatively high detection limit (~200 p.p.m.) but excellent depth resolution (5–10 nm) and effective averaging over a large surface area (~1 mm²) of the samples¹⁵. The Rutherford backscattering spectra were converted into profiles of Ar concentration versus depth in the sample (Fig. 1); these profiles were then fitted to the appropriate solution to the non-steady-state diffusion equation for diffusive uptake into a semi-infinite medium held at constant surface concentration: $C_x/C_0 = 1 - \text{erf}[x/(Dt)^{1/2}]$, where C_x is Ar concentration in the mineral lattice at distance x from the surface (at $x = 0$), D is Ar diffusivity and t is experiment duration. The concentration at the surface, C_0 , is taken as the solubility of Ar in the lattice at the temperature and Ar pressure of the experiment (Fig. 1).

We pursued additional experimental strategies to validate two key premises of this study: first, that the Ar-uptake behaviour of the synthetic Mg olivine is representative of natural upper-mantle material; and, second, that our results are not compromised by surface adsorption of Ar. We ran two experiments using natural olivine from San Carlos, Arizona to confirm that the synthetic Mg olivine was a valid proxy for natural Mg olivine. These were conducted in an internally heated pressure vessel to achieve higher Ar pressures (the resulting higher solubilities enabled characterization of Ar uptake despite the higher Fe background). We addressed the surface adsorption issue in two ways, the first being to establish that the diffusivities obtained from Ar uptake experiments are independent of run

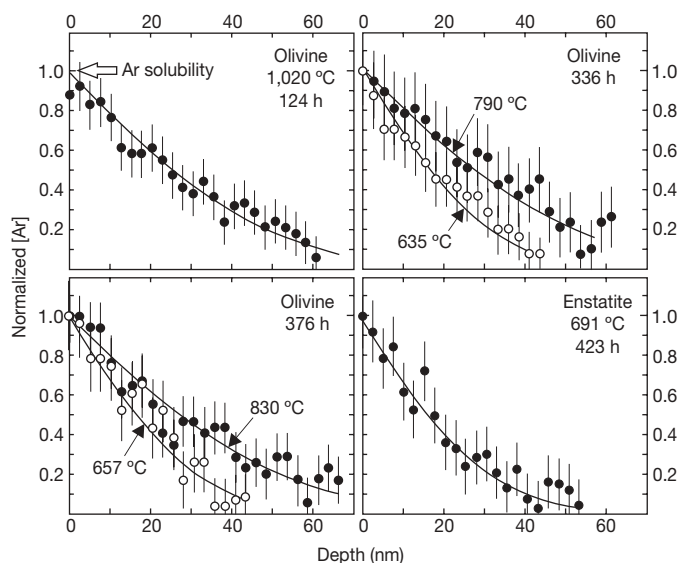


Figure 1 | Ar diffusive-uptake profiles in olivine and enstatite. Data produced by diffusion of Ar into the crystals from a pressurized gas source and characterized using Rutherford backscattering spectroscopy. The smooth curves are least-squares fits to a presumed error-function diffusion model (see text); the concentration of Ar at the sample surface is taken as the solubility. At the upper left is one of the best profiles in terms of uncertainty in the resulting diffusivity; the rest are more typical. Conditions of the experiments are shown on each panel. Error bars represent $\pm 1\sigma$ counting statistics.

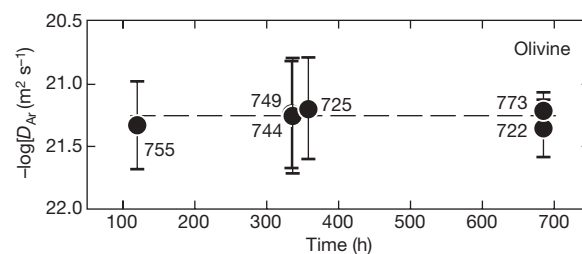


Figure 2 | Diffusivities of Ar in olivine at $T \approx 750^\circ\text{C}$ from experiments of differing duration. The similarity of D values extracted from experiments of markedly different duration eliminates surface control as a factor in the diffusive uptake of Ar. Error bars as in Fig. 1.

duration (Fig. 2). The second approach involved step-wise heating, in air, of a Mg-olivine sample recovered from a high-pressure Ar-uptake experiment. This sample was heated to a predetermined temperature (initially 100 °C), held for 30–60 min, allowed to cool, and profiled for Ar by Rutherford backscattering spectroscopy. This procedure was repeated at 200° increments up to a maximum temperature of 700 °C. No significant diminution in near-surface Ar concentration occurred during this aggressive thermal treatment, confirming its lattice-bound nature¹⁶.

The Ar diffusion and solubility results for olivine and enstatite are summarized in Figs 3 and 4, which reveal two striking aspects. The solubilities of Ar in both minerals are substantial (mean values are 1,830 p.p.m. in olivine and 3,230 p.p.m. in enstatite), and the lattice

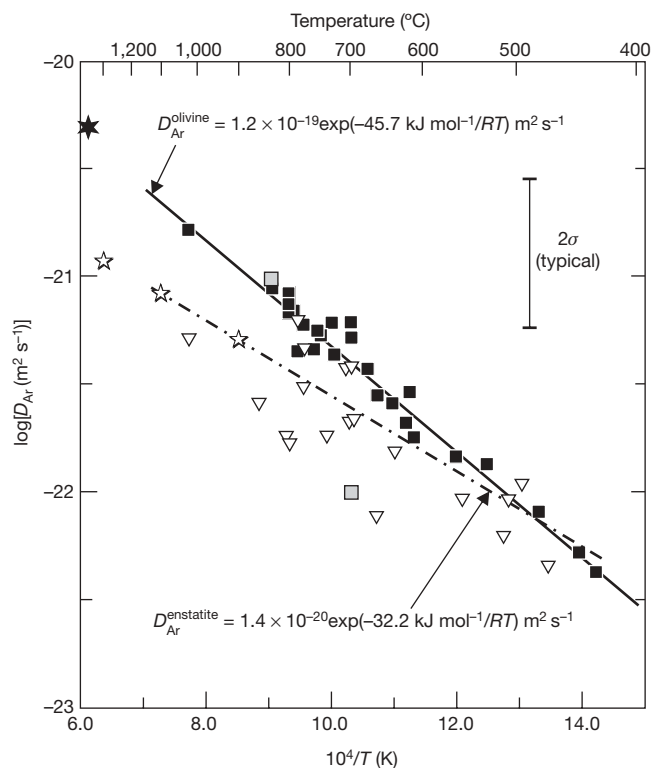


Figure 3 | Summary of diffusion data for olivine and enstatite. Black squares, pure Mg-olivine; grey squares, San Carlos olivine; triangles, enstatite. The lines represent least-squares fits to the olivine and enstatite data assuming Arrhenius behaviour (that is, $D = D_0 \exp[-E_a/RT]$, where R is the gas constant, E_a is the activation for diffusion and T is absolute temperature; equations on figure). The $\pm 2\sigma$ uncertainty in D_0 is ~0.4% for olivine and ~1.7% for enstatite; uncertainties in E_a are ~4% and 19%, respectively. Stars represent the diffusivities used in modelling diffusion in olivine (black star) and pyroxene (white stars); see Fig. 6. The diffusion law for enstatite (orthopyroxene) is assumed to apply to clinopyroxene as well (see text and Fig. 5).

diffusivities are not only low but also very weakly dependent on temperature: the apparent activation energies are ~ 46 and 32 kJ mol^{-1} for olivine and enstatite, respectively. The observed high solubilities show no discernible dependence on temperature (Supplementary Table 1) or Ar fugacity (f_{Ar} ; Fig. 4) suggesting that Ar atoms occupy point defects¹⁶, as has been predicted¹⁷ for MgO. A suitable model to describe a solubility phenomenon involving saturation of a fixed population of pre-existing sites is the Langmuir isotherm, which is shown in Fig. 4 and discussed in more detail in ref. 16. The form of the Langmuir isotherm is $k_L = [n/(M - n)]/f_{\text{Ar}}$, where k_L is the Langmuir equilibrium constant, n is the number of dissolved Ar atoms, and M is the number of available sites that can accommodate Ar atoms.

Within the uncertainty of our data, Ar solubility in olivine and enstatite is independent of Ar fugacity for values ranging from at least as low as 1 bar (the minimum we examined) to values in excess of 10^4 bar. As portrayed by the Langmuir isotherm model curve in Fig. 4, however, the equilibrium concentration of Ar in these minerals must drop to zero at $f_{\text{Ar}} = 0$. When considering the behaviour of Ar in the Earth, it is important to bear in mind that our data and the model curve represent equilibrium of minerals with pure Ar gas: they do not by themselves characterize the behaviour of Ar during melting in the Earth, where noble gases are present at only trace levels and dispersed in major phases. Argon partition coefficients—equilibrium concentration ratios of Ar in crystals relative to coexisting melt, $k_{\text{Ar}}^{\text{min/melt}}$ —can be estimated from our data by dividing our solubilities for minerals by those for Ar in relevant melts, for which the agreement among existing data are reasonably good^{18–24}. The form of the dependence

of Ar solubility on f_{Ar} is very different for minerals and melts (Fig. 4), so the value of $k_{\text{Ar}}^{\text{min/melt}}$ depends critically on choice of f_{Ar} . Figure 4 reveals, however, that for any plausible choice of terrestrial f_{Ar} , $k_{\text{Ar}}^{\text{min/melt}} \gg 1$ for both olivine and enstatite. Contrary to the traditional view of Ar as a quintessentially volatile and incompatible element, we conclude that it is in fact moderately to extremely compatible in its behaviour towards the dominant minerals of the upper mantle. The attribution of this compatibility to Ar siting in point defects¹⁶ does not alter the fundamental significance of the conclusion. Broadhurst *et al.*²¹ also concluded that Ar is somewhat compatible in minerals, but we believe their $k_{\text{Ar}}^{\text{min/melt}}$ value for olivine of ~ 1 – 30 must be adjusted upward for failure of the olivine grains to fully equilibrate with the surrounding Ar gas: on the basis of our measured Ar diffusivities, the extent of equilibration in their experiments ranged from ~ 0.5 to 5% . Our $k_{\text{Ar}}^{\text{ol/melt}}$ value is also qualitatively consistent with the concentration ratios measured by ref. 25 on natural olivines and glasses, although those authors suspected Ar loss from the melts on eruption onto the sea floor.

The partition coefficients implied by our new solubility data are at odds, to varying degrees, with partitioning information from other previous studies, including experimental investigations^{26–28} as well as analyses of natural crystal/glass pairs^{29,30}. Some of the discrepancy may be explained by the fact that Ar—because it diffuses so slowly—must be tenaciously retained in olivine and pyroxene during attempted laboratory release. More generally, we believe that the inconsistency of our results and those of Broadhurst *et al.*²¹ with other experimental studies^{26–28} is due to the different experimental protocols used. The crystal-growth procedures used in other studies may underestimate the uptake of Ar simply because noble-gas atoms in an ionic growth medium are unable to bond to the surface of a growing crystal, which is a necessary step for incorporation of any atom into a lattice site, point defect or otherwise. The contrasting solid-state approach used by ourselves and by Broadhurst *et al.*²¹ involves ‘in-diffusion’ from a pure gas, and thus circumvents the need for Ar to displace ions on an advancing crystal interface to gain entry into the lattice.

The disparity among existing partitioning data aside, Ar compatibility in ferromagnesian silicates is consistent with the common presence of unsupported (excess) ^{40}Ar in olivine and pyroxene phenocrysts and xenocrysts (and mantle xenoliths composed of these minerals) from a variety of geologic and tectonic settings^{31–34}. This excess Ar is sometimes attributed to fluid inclusions, but the question of how it enters the inclusions (and why it does not diffuse out) cannot be fully addressed without diffusion and solubility data. As discussed below, our diffusion data reveal that mafic xenocrysts entrained from the mantle can retain lattice ^{40}Ar through the melt transport and eruption process.

The observed compatible behaviour of Ar (that is, $k_{\text{Ar}} \gg 1$) in the principal minerals of Earth’s upper mantle leads to the realization that incomplete degassing of mantle Ar is not only plausible but expected, although the degree of Ar retention depends on the extent to which crystal/melt partitioning equilibrium is approached. The degree of equilibration may depend on the rate of melt production and extraction relative to lattice diffusion^{35–38}.

Implications for behaviour of mantle Ar

Our diffusion data enable quantitative assessment of Ar behaviour in the solid mantle as well as during potential degassing scenarios that involve partial melt. In a nominally anhydrous mantle, the primary host of parent ^{40}K is clinopyroxene, so this phase is the principal site of ^{40}Ar generation. Our analytical technique (Rutherford backscattering spectroscopy) cannot resolve small amounts of Ar in the presence of abundant Ca, so we cannot characterize Ar diffusion in calcic pyroxenes directly. However, unless Ar transport is very much slower in clinopyroxene than in orthopyroxene or olivine, the site of ^{40}Ar generation is immaterial: at near-solidus upper-mantle temperatures ($\sim 1,300^\circ\text{C}$), Ar will disperse throughout all phases on a

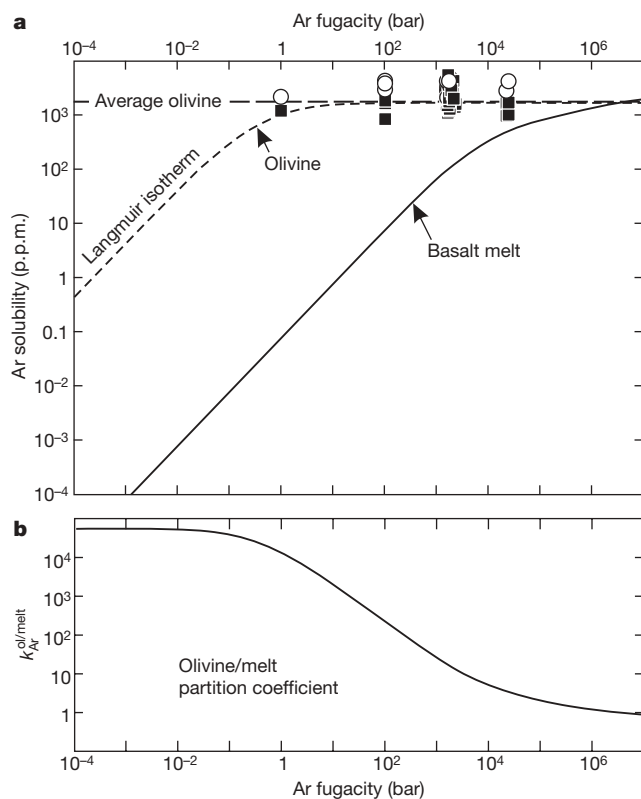


Figure 4 | Summary of Ar solubility measurements for olivine and enstatite compared with basaltic melt. **a**, The ‘Basalt melt’ curve represents predicted behaviour at $1,300^\circ\text{C}$ based on experimental measurements²⁴. Olivine (forsterite) (black squares) and enstatite (white circles) data span 430°C to $1,020^\circ\text{C}$ with no discernible temperature dependence. The Langmuir isotherm ‘fit’ (see text) is based on olivine alone because the enstatite data are scattered (see Supplementary Table 1). M in the Langmuir expression was assigned the maximum solubility in Mg olivine (San Carlos values were not used, being anomalously high owing to sample oxidation¹⁶). **b**, Olivine/melt partitioning behaviour implied by the information in **a**.

geodynamically short timescale (Fig. 5). Because Ar is soluble in olivine and orthopyroxene, these major phases will become the dominant hosts of (unsupported) ^{40}Ar .

The behaviour of Ar between the onset of melting and the removal of melt from the solid residue can also be evaluated, but assumptions about the mechanism of solid–liquid equilibration and the rate of melting and extraction are necessary. Extensive dissolution and reprecipitation of olivine and orthopyroxene—essentially ‘processing’ the solids through the melt—would probably assure crystal–melt equilibration. Deformation of the solid matrix could achieve the same end by introducing fast diffusion pathways in the lattices. More specific calculations require choice of a bulk crystal/melt partition coefficient ($k_{\text{Ar}}^{\text{bulk}}$), which is not well constrained by Fig. 4 because of the uncertainty in f_{Ar} of natural systems. Our approach is to use a conservative $k_{\text{Ar}}^{\text{bulk}}$ value of ten. Substantially higher values are ‘allowed’ at $f_{\text{Ar}} < 1,000$ bar, but the behaviour would differ only qualitatively and the general conclusions would be the same.

If equilibrium melting prevails with $k_{\text{Ar}}^{\text{bulk}} = 10$ (Fig. 6), then a very small fraction (0–2%) of the ^{40}Ar initially hosted by olivine and orthopyroxene is transferred to the melt over the range of plausible melt fractions F . Fractional melting yields a similar result, and together these simple melting scenarios give the lower bound, in terms of effectiveness, of possible solid-to-melt transfer of ^{40}Ar (Fig. 6a). The upper bound is the case of instantaneous batch melting and segregation with no diffusive equilibration. In this case, the fraction of ^{40}Ar transferred to the melt is equal to F (Fig. 6a). Assuming an upper limit on F of 0.2, the maximum amount of mantle ^{40}Ar that could conceivably be transferred to the liquid during a single melting episode—and thus lost from the solid Earth on eruption—is ~20%.

Our diffusion data can be used to evaluate partial equilibration scenarios lying in between these extremes as shown in Fig. 6b. This diagram was constructed for simplistic scenarios involving 15% total melting with the melt remaining in the system until melting is complete. For melting rates believed to operate today in divergent plate-boundary settings ($\sim 1.5 \times 10^{-14} \text{ s}^{-1}$)³⁸, near-equilibration between residual minerals and melt is expected for any reasonable grain size,

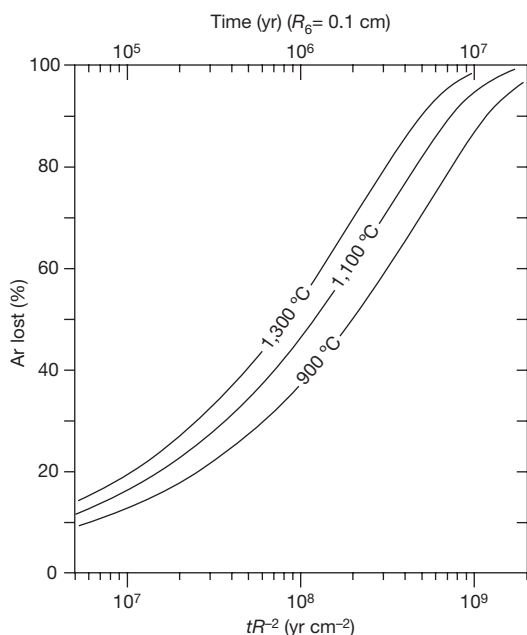


Figure 5 | Diffusive loss of Ar from spherical pyroxene grains. The diffusion law for enstatite (Fig. 3) is assumed to apply to clinopyroxene (the phase where most Ar is generated in the Earth’s upper mantle). Percentage loss is shown as a function of time for three temperatures. The top scale assumes a realistic grain radius R of 0.1 cm; the bottom scale is general for a range of time–radius combinations.

which would ensure only minor transfer to the melt (2–3%) at 15% melting. Depending on grain size, melting rates greater than 10^{-13} s^{-1} lead to substantial disequilibrium and somewhat more effective transfer of Ar to the melt. If melting rates were higher in the geologic past, the efficiency of Ar degassing may have exceeded Earth’s present-day capability, especially if the extent of melting was also higher. Cumulative Ar loss from a specific volume of mantle over the age of the Earth depends, furthermore, on the number of melting cycles experienced by that volume, which could be as many as three⁷. In summary, the conceivable range of mantle Ar degassing efficiencies based on our data lies between ~2% (a single 15% melting cycle with complete solid–melt equilibration) and perhaps ~30% (three melting cycles with substantial disequilibrium), though the high end of this range seems relatively unlikely.

The apparent inefficiency of magmatism as a means of ridding the Earth of ^{40}Ar raises the question of how ^{40}Ar got into the atmosphere at all. If, as our data and models suggest, most of the ^{40}Ar in materials processed through divergent plate boundaries is largely retained in

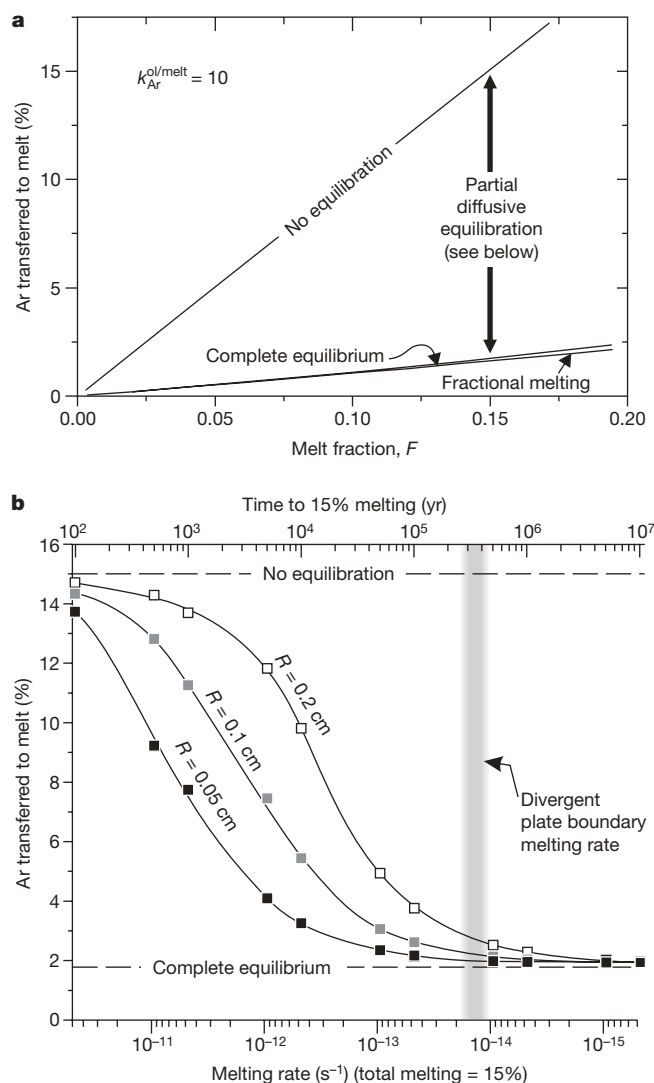


Figure 6 | Transfer of Ar from olivine to melt for various equilibration scenarios. In **a**, complete equilibrium and fractional melting are contrasted with the (unrealistic) case of no diffusive equilibration. In **b** are shown finite-difference calculations of partial equilibration during melting to 15% at various rates, with melt remaining in contact with solid. The vertical grey bar represents the estimated melting rate at divergent plate boundaries³⁸ ($\sim 10^{-14} \text{ s}^{-1}$); higher values are required for significant retention of Ar due to failed diffusive equilibration. The olivine/melt partition coefficient, $k_{\text{Ar}}^{\text{ol/melt}}$, was assumed to be ten in all cases (see text and Fig. 4).

olivine and orthopyroxene, then one possibility is Ar release during hydration of oceanic lithosphere, which can be pervasive at least locally^{39,40}. Alteration of olivine and orthopyroxene to serpentine and other hydrous minerals could release most of the ⁴⁰Ar to interstitial fluid and eventually to the atmosphere.

In any discussion of Ar loss from the solid Earth, it must be borne in mind that the average K concentration of neither the continental crust (~1–2 wt%)⁴¹ nor the bulk silicate Earth^{11,42,43} is precisely known (nor in fact is it certain that the core is devoid of K; ref. 44). Given these uncertainties, the dominance of the mantle over the crust as a producer of ⁴⁰Ar could range from less than a factor of two to almost a factor of five (in the distant geologic past, the relative contributions would be affected by the amount of continental crust existing at the time). If the correct ratio is close to the lower of these two values, and if the continents were formed early⁴⁵, then a significant fraction of all ⁴⁰Ar now in the atmosphere may have got there by processing of crustal materials through weathering⁴⁶, fluid–rock interaction, metamorphism and partial melting of potassic minerals such as alkali feldspar, micas or amphiboles. Deep-seated crustal fluids are considered to be in equilibrium with the atmosphere⁴⁷, which implies effective communication between these two Ar reservoirs.

The very high ⁴⁰Ar/³⁶Ar ratio of the martian atmosphere (~3,000) relative to that of the Earth (295.5) could be interpreted to mean that most of the Ar in the Martian atmosphere was produced by degassing of the near-surface through weathering processes, with most of the primordial ³⁶Ar (and ³⁸Ar) remaining sequestered deep in the planet.

In summary, it does not seem necessary to assume or conclude that the upper mantle of the Earth is essentially degassed of Ar, nor is significant degassing of the lower mantle a necessary consequence of mass exchange between the upper and lower mantle. The efficiency of mantle degassing may actually depend on the pervasiveness of shallow oceanic mantle hydration near divergent plate boundaries and the ease of gas escape to the ocean and atmosphere before and during eventual subduction. Our diffusion data rule out the significant contamination of relatively low-⁴⁰Ar/³⁶Ar mantle plume material by diffusive mixing during ascent with the high-⁴⁰Ar/³⁶Ar mid-ocean ridge basalt source.

At this juncture, the partitioning systematics and diffusion behaviour of most other noble gases relative to Ar are uncertain. Interestingly, the measured diffusion characteristics of Ar may place this element near the transition between equilibrium and disequilibrium behaviour during mantle melting and extraction at present-day rates (Fig. 6). Partitioning differences aside, the size variation of noble-gas atoms probably means that Kr and Xe diffuse more slowly than Ar in upper mantle phases, but Ne and He are probably faster. The possibility of diffusive fractionation of the noble gases during magmatic events thus seems almost certain⁴⁸.

Finally, we note that Ar degassing of olivine and orthopyroxene may be problematic in the laboratory as well as in nature. Unless very small diffusion domains govern Ar release in the laboratory, our diffusion data preclude complete outgassing in a reasonable time frame by any treatment short of melting (a week at 1,600 °C would result in only ~20% outgassing of a 2 µm domain).

Received 3 May; accepted 31 July 2007.

1. Staudacher, T. & Allègre, C. J. Terrestrial xenology. *Earth Planet. Sci. Lett.* **60**, 389–406 (1982).
2. Jacobsen, S. B. The HF–W system and the origin of the Earth and Moon. *Annu. Rev. Earth Planet. Sci.* **33**, 531–570 (2005).
3. Halliday, A. N. & Kleine, T. in *Meteorites and the Early Solar System II* (eds Lauretta, D., Leshin, L. & McSween, H. Jr) 775–801 (Univ. Arizona Press, Tucson, 2006).
4. Boyet, M. & Carlson, R. W. ¹⁴²Nd evidence for early (>4.5 Ga) global differentiation of the silicate Earth. *Science* **309**, 576–581 (2005).
5. Kurz, M. D., Jenkins, W. J. & Hart, S. R. Helium isotopic systematics of ocean islands and mantle heterogeneity. *Nature* **297**, 43–46 (1982).
6. Jochum, K. P., Hofmann, A. W., Ito, E., Seufert, H. M. & White, W. M. K, U and Th in mid-ocean ridge basalt glasses and heat production, K/U and K/Rb in the mantle. *Nature* **306**, 431–436 (1983).
7. Davies, G. F. Geophysically constrained mantle mass flows and the ⁴⁰Ar budget: a degassed lower mantle? *Earth Planet. Sci. Lett.* **166**, 149–162 (1999).
8. van der Hilst, R. D., Widiyantoro, S. & Engdahl, E. R. Evidence for deep mantle circulation from global tomography. *Nature* **386**, 578–584 (1997).
9. Anderson, D. L. The statistics and distribution of helium in the mantle. *Int. Geol. Rev.* **42**, 289–311 (2001).
10. Parman, S. W., Kurz, M. D., Hart, S. R. & Grove, T. L. Helium solubility in olivine and implications for high ³He/⁴He in ocean island basalts. *Nature* **437**, 1140–1143 (2005).
11. Porcelli, D. & Turekian, K. K. The history of planetary degassing as recorded by noble gases. *Treatise Geochem.* **4**, 281–318 (2006).
12. Porcelli, D. & Ballentine, C. J. in *Noble Gases in Geochemistry and Cosmochemistry* (eds Porcelli, D., Ballentine, C. J. & Wieler, R.) *Rev. Mineral. Geochem.* **47**, 411–480 (2002).
13. Klein, E. M. & Langmuir, C. H. Global correlations of ocean ridge basalt chemistry with axial depth and crustal thickness. *J. Geophys. Res.* **92** (B8), 8089–8115 (1987).
14. Hellebrand, E., Snow, J. E., Dick, H. J. B. & Hofmann, A. W. Coupled major and trace elements as indicators of the extent of melting in mid-ocean-ridge peridotites. *Nature* **410**, 677–681 (2001).
15. Watson, E. B. & Cherniak, D. J. Lattice diffusion of Ar in quartz, with constraints on Ar solubility and evidence of nanopores. *Geochim. Cosmochim. Acta* **67**, 2043–2062 (2003).
16. Thomas, J. B., Cherniak, D. J. & Watson, E. B. Lattice diffusion and solubility of Ar in forsterite, enstatite, periclase, quartz and corundum. *Chem. Geol.* (submitted).
17. Tsuchiyama, A. & Kawamura, K. in *Noble Gas Geochemistry and Cosmochemistry* (ed. Matsuda, J.) 315–323 (Terra Scientific Publishing, Tokyo, 1994).
18. Jambon, A., Weber, H. & Braun, O. Solubility of He, Ne, Ar, Kr and Xe in a basalt melt in the range 1250–1600 °C. Geochemical implications. *Geochim. Cosmochim. Acta* **50**, 401–408 (1986).
19. Lux, G. The behavior of noble gases in silicate liquids: Solution, diffusion, bubbles, and surface effects, with applications to natural samples. *Geochim. Cosmochim. Acta* **51**, 1549–1560 (1987).
20. White, B. S., Brearley, M. & Montana, A. Solubility of argon in silicate liquids at high pressures. *Am. Mineral.* **74**, 513–529 (1989).
21. Broadhurst, C. L. & Drake, M. J. Hagee, B. E. & Bernatowicz, T. J. Solubility and partitioning of Ar in anorthite, diopside, forsterite, spinel, and synthetic basalt. *Geochim. Cosmochim. Acta* **54**, 299–309 (1990).
22. Carroll, M. R. & Stolper, E. M. Noble gas solubility in silicate melts and glasses: New experimental results for Ar and the relationship between solubility and ionic porosity. *Geochim. Cosmochim. Acta* **57**, 5039–5051 (1993).
23. Shibata, T., Takahashi, E. & Matsuda, J. Solubility of neon, argon, krypton, and xenon in binary and ternary silicate systems. *Geochim. Cosmochim. Acta* **62**, 1241–1253 (1998).
24. Schmidt, B. C. & Keppler, H. Experimental evidence of high noble gas solubility in silicate melts under mantle pressures. *Earth Planet. Sci. Lett.* **195**, 277–290 (2002).
25. Batiza, R., Bernatowicz, T. J., Hohenberg, C. M. & Podosek, F. A. Relations of noble gas abundances to petrogenesis and magmatic evolution of oceanic basalts and related differentiated volcanic rocks. *Contrib. Mineral. Petrol.* **69**, 301–313 (1979).
26. Hiyagon, H. & Ozima, M. Noble gas distribution between basalt melt and crystals. *Earth Planet. Sci. Lett.* **58**, 255–264 (1982).
27. Hiyagon, H. & Ozima, M. Partition of noble-gases between olivine and basalt melt. *Geochim. Cosmochim. Acta* **50**, 2045–2057 (1986).
28. Brooker, R. A. et al. The “zero-charge” partitioning behaviour of noble gases during mantle melting. *Nature* **423**, 738–741 (2003).
29. Marty, B. & Lussiez, P. Constraints on rare gas partition coefficients from analysis of olivine-glass from a picritic mid-ocean ridge basalt. *Chem. Geol.* **106**, 1–7 (1993).
30. Valbrach, P. J., Honda, M., Staudigel, H., McDougall, I. & Trost, A. P. in *Noble Gas Geochemistry and Cosmochemistry* (ed. Matsuda, J.) 373–381 (Terra Scientific, Tokyo, 1994).
31. Poreda, R. J. & Farley, K. A. Rare gases in Samoan xenoliths. *Earth Planet. Sci. Lett.* **113**, 129–144 (1992).
32. McDougall, I. & Green, D. H. Excess radiogenic argon in pyroxene and isotopic ages on minerals from Norwegian eclogites. *Norsk Geol. Tidss.* **44**, 183–196 (1964).
33. Harrison, T. M. & McDougall, I. Excess argon in metamorphic rocks from Broken Hill, New South Wales: Implications for ⁴⁰Ar/³⁹Ar age spectra and the thermal history of the region. *Earth Planet. Sci. Lett.* **55**, 123–149 (1981).
34. Lanphere, M. A. & Dalrymple, G. B. Identification of excess ⁴⁰Ar by the ⁴⁰Ar/³⁹Ar age spectrum technique. *Earth Planet. Sci. Lett.* **32**, 141–148 (1976).
35. Hart, S. R. Equilibration during mantle melting: a fractal tree model. *Proc. Natl Acad. Sci. USA* **90**, 11914–11918 (1993).
36. Iwamori, H. A model for disequilibrium mantle melting incorporating melt transport by porous and channel flows. *Nature* **366**, 734–737 (1993).
37. Spieglerman, M. & Kenyon, P. The requirements for chemical disequilibrium during magma migration. *Earth Planet. Sci. Lett.* **109**, 611–620 (1992).
38. Cherniak, D. J. & Liang, Y. Rare earth element diffusion in natural enstatite. *Geochim. Cosmochim. Acta* **71**, 1324–1340 (2007).
39. Li, X.-P., Rahn, M. & Bucher, K. Serpentinites of the Zermatt-Saas ophiolite complex and their texture evolution. *J. Metamorph. Geol.* **22**, 139–177 (2004).

40. Korenaga, J. Thermal cracking and the deep hydration of the oceanic lithosphere: A key to the generation of plate tectonics. *J. Geophys. Res.* **112**, B05408, doi:10.1029/2006JB004502 (2007).
 41. Rudnick, R. L. & Fountain, D. M. Nature and composition of the continental crust: a lower crustal perspective. *Rev. Geophys.* **33**, 267–309 (1995).
 42. Allègre, C. J., Staudacher, T. & Sarda, P. Rare gas systematics: formation of the atmosphere, evolution and structure of the Earth's mantle. *Earth Planet. Sci. Lett.* **81**, 127–150 (1986).
 43. Lassiter, J. C. Role of recycled oceanic crust in the potassium and argon budget of the Earth: toward a resolution of the “missing argon” problem. *Geochem. Geophys. Geosyst.* **5**, doi:10.1029/2004GC000711 (2004).
 44. Murthy, V. R., van Westrenen, W. & Fei, Y. Experimental evidence that potassium is a substantial radioactive heat source in the planetary cores. *Nature* **426**, 163–165 (2003).
 45. Armstrong, R. L. The persistent myth of crustal growth. *Aust. J. Earth Sci.* **38**, 613–630 (1991).
 46. Turekian, K. K. The parameters controlling planetary degassing based on ^{40}Ar systematics. In *From Mantle to Meteorites* (ed. Gopalan, K.) 147–152 (Indian Academy of Sciences, Bangalore, 1990).
 47. McDougall, I. & Harrison, T. M. *Geochronology and Thermochronology by the $^{40}\text{Ar}/^{39}\text{Ar}$ Method* 1–269 (Oxford Univ. Press, New York, 1999).
 48. Burnard, P. Diffusive fractionation of noble gases and helium isotopes during mantle melting. *Earth Planet. Sci. Lett.* **220**, 287–295 (2004).
- Supplementary Information** is linked to the online version of the paper at www.nature.com/nature.
- Acknowledgements** We are grateful to F. M. Richter and K. K. Turekian for discussions about noble gas systematics and bulk-Earth model constraints, and to M. J. Drake for comments. This research was supported by the NSF.
- Author Contributions** E.B.W. ran exploratory experiments, developed the melting models and wrote the manuscript; J.B.T. performed most of the experiments and interpreted the data; D.J.C. conducted the Rutherford backscattering spectroscopy analyses and reduced the raw spectra.
- Author Information** Reprints and permissions information is available at www.nature.com/reprints. The authors declare no competing financial interests. Correspondence and requests for materials should be addressed to E.B.W. (watsoe@rpi.edu).

Postcranial evidence from early *Homo* from Dmanisi, Georgia

David Lordkipanidze¹, Tea Jashashvili^{1,2}, Abesalom Vekua¹, Marcia S. Ponce de León², Christoph P. E. Zollikofer², G. Philip Rightmire³, Herman Pontzer⁴, Reid Ferring⁵, Oriol Oms⁶, Martha Tappen⁷, Maia Bukhsianidze¹, Jordi Agustí⁸, Ralf Kahlke⁹, Gocha Kiladze¹, Bienvenido Martínez-Navarro⁸, Alexander Mouskhelishvili¹, Medea Nioradze¹⁰ & Lorenzo Rook¹¹

The Plio-Pleistocene site of Dmanisi, Georgia, has yielded a rich fossil and archaeological record documenting an early presence of the genus *Homo* outside Africa. Although the craniomandibular morphology of early *Homo* is well known as a result of finds from Dmanisi and African localities, data about its postcranial morphology are still relatively scarce. Here we describe newly excavated postcranial material from Dmanisi comprising a partial skeleton of an adolescent individual, associated with skull D2700/D2735, and the remains from three adult individuals. This material shows that the postcranial anatomy of the Dmanisi hominins has a surprising mosaic of primitive and derived features. The primitive features include a small body size, a low encephalization quotient and absence of humeral torsion; the derived features include modern-human-like body proportions and lower limb morphology indicative of the capability for long-distance travel. Thus, the earliest known hominins to have lived outside of Africa in the temperate zones of Eurasia did not yet display the full set of derived skeletal features.

Since 1991 hominin remains have been recovered from excavation blocks 1 and 2 at Dmanisi, Georgia. Three skulls (D2282/D211, D2700/D2735 and D3444/D3900), one cranium (D2280) and one mandible (D2600) have been described earlier^{1–7}. The well-preserved postcranial remains recovered from block 2 provide an insight into previously unknown aspects of early *Homo* morphology and also offer a new comparative perspective on key elements of the postcranial skeleton of the Nariokotome KNM-WT15000 subadult specimen⁸ and of *Homo floresiensis*⁹.

Stratigraphical context

The geological age of the bone- and artefact-bearing deposits at Dmanisi is approximately 1.77 million years (Myr)¹⁰. New palaeomagnetic analyses of block 2 deposits are fully concordant with the initial stratigraphical and palaeomagnetic studies of block 1 (Supplementary Information 1). Consideration of the overall mammalian fauna places the site close to the Plio-Pleistocene boundary and shows highest palaeozoogeographical similarity with the chronologically contemporaneous Late Villafranchian of Western Europe (Supplementary Information 2 and 3). Palaeoecological studies point to a remarkable variation in relief, humidity and vegetational character. The presence of fresh water and a variety of ecotones with different vegetal and animal resources nearby made Dmanisi an attractive locale for hominins (Supplementary Information 2–4). Analysis of the taphonomic signature of mammalian remains indicates that hominins were involved in meat acquisition, and that they had early access to carcasses, which suggests hunting or power scavenging. Carnivores were also active at the site, but did not damage bone to the degree found in many hyaena dens (Supplementary Information 5).

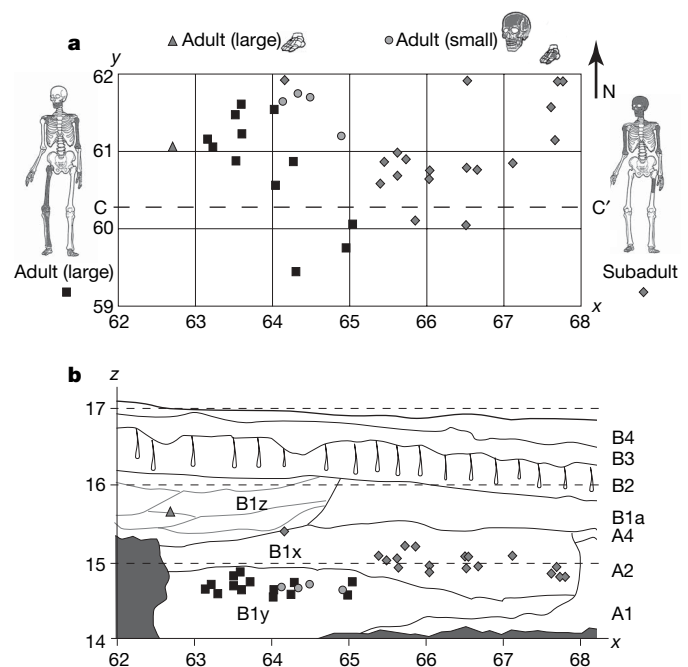


Figure 1 | Stratigraphy of the Dmanisi postcranial hominin remains recovered from block 2. **a**, Vertical projection (x - y excavation squares are 1×1 m; *in-situ* articulated cervical vertebrae D2673/D2674 are denoted by the double diamond). **b**, Lateral projection along y axis (profile section taken along C-C') and z axis (metres above zero level reference, see also Supplementary Fig. 1).

¹Georgian National Museum, 0105 Tbilisi, Georgia. ²Anthropologisches Institut, Universität Zürich, 8057 Zürich, Switzerland. ³Department of Anthropology, Peabody Museum, Harvard University, Cambridge, Massachusetts 02138, USA. ⁴Department of Anthropology, Washington University, St Louis, Missouri 63130, USA. ⁵Department of Geography, University of North Texas, Denton, Texas 76203, USA. ⁶Departament de Geologia, Universitat Autònoma de Barcelona, 08193 Bellaterra, Spain. ⁷Department of Anthropology, University of Minnesota, Minneapolis, Minnesota 55455, USA. ⁸ICREA, Institute of Human Paleoeology, University Rovira i Virgili, 43005 Tarragona, Spain. ⁹Senckenberg Research Institute, 99423 Weimar, Germany. ¹⁰Othar Lordkipanidze Center for Archaeological Research, 0102 Tbilisi, Georgia. ¹¹Dipartimento di Scienze della Terra, Università di Firenze, 50121 Firenze, Italy.

The new hominin skeletal elements from Dmanisi can be assigned to a minimum of four individuals: one adolescent and three adults (Figs 1 and 2). The postcranial remains of the adolescent individual are associated with skull D2700/D2735 (ref. 3). Attribution of all adolescent remains to one individual is based on their close stratigraphical proximity within layer B1x (Fig. 1) and equivalent developmental stages of cranial and postcranial elements (Supplementary Table 3). The spatial distribution pattern of these elements, their uniform stage 0/1 taphonomic condition¹¹, as well as the partial laminated infilling of the D2700 and D3444 cranial vaults⁷, indicate short-distance, low-energy dispersal followed by rapid burial (Supplementary Information 1).

Postcranial remains of three adult individuals, found in layer B1y, exhibit virtually no stratigraphical overlap with the adolescent remains (Fig. 1). These elements are provisionally attributed to one large and two small individuals. The large adult is represented by various elements of the appendicular skeleton. The right femur, tibia and patella exhibit fit in the knee joint, and the left talus, when mirrored to the right side, implies anatomical fit with the tibia. These postcranial remains are probably associated with the large mandible D2600 (ref. 4) found nearby in the same stratigraphical layer (Fig. 1

and Supplementary Fig. 1). Postcranial elements of one smaller adult individual comprise a right medial cuneiform and anatomically associated metatarsal I, and are presumably associated with the small skull D3444/D3900 (refs 5, 7) found nearby. A third adult individual is currently represented by a single metatarsal II found at a higher stratigraphical position (layer B1z; see Fig. 1). Measurements are provided in Table 1, Fig. 3 and Supplementary Information 7.

Upper limbs

D4166 is the lateral part of an adult right scapula comprising the glenoid cavity, and exhibiting some damage across the distal part of the coracoid process. The glenoid cavity is more cranially oriented relative to the midaxillary border than in modern humans, and thus closer to the condition found in australopiths (Sts7 and AL288-1)^{12,13} and African great apes. The narrow glenocoracoid angle, the relatively short coracoid process, and the high width-to-length ratio of the coracoid process are outside the range of variation found in modern humans, and are similar to great apes¹⁴, whereas the glenoid orientation relative to the spine and the breadth-to-width ratio of the spine are at the lower end of modern-human variation and similar to KNM-WT15000. D4161 and D4162 are left and right adult

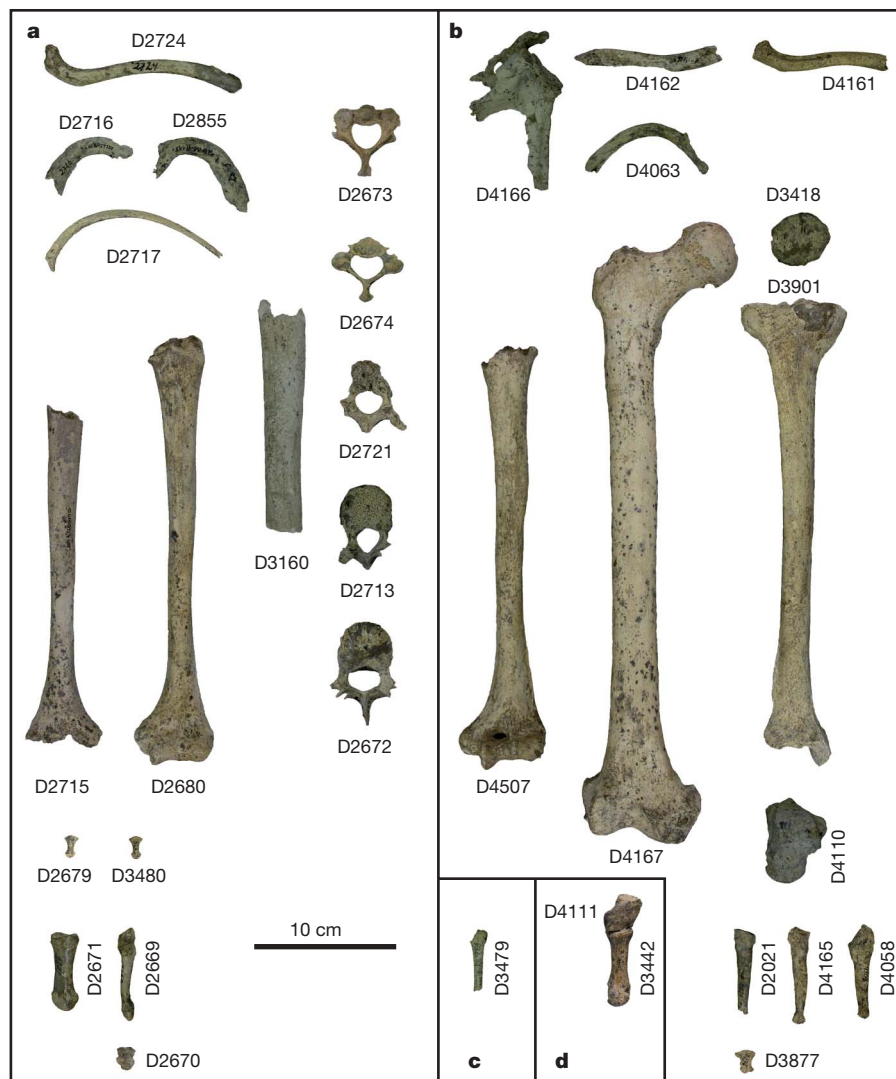


Figure 2 | Dmanisi postcranial elements. **a**, Remains of subadult individual. D2724, left clavicle; D2716/D2855, right/left first rib; D2717, eleventh rib; D2673/D2674/D2721/D2713/D2672, vertebrae C2/C3/Th3/Th10/L1; D2715/D2680, right/left humerus; D3160, left femur; D2679/D3480, distal phalanges of hand; D2671/D2669, right metatarsal I/IV; D2670, first distal phalange of right foot. **b**, Remains of large adult

individual. D4166, right scapula; D4162/D4161, right/left clavicles; D4063, right second rib; D4507, left humerus; D4167, right femur; D3418, right patella; D3901, right tibia; D4110, left talus; D2021/D4165, right metatarsals III/IV; D4508, left metatarsal V; D3877, distal phalange of foot. **c, d**, Remains of small adult individuals. D3479, right metatarsal III; D4111, right medial cuneiform; D3442, right metatarsal I.

clavicles, respectively. Both elements lack their sternal and acromial ends. D2724 is an almost complete subadult left clavicle with some damage at the epiphyses. The shaft is comparatively short, similar to Chk-B-2-81 (Zhoukoudian *Homo erectus*)¹⁵ and OH48 (*Homo habilis*)¹⁶, but within the range of variation displayed by subadult modern humans. In their mid-shaft and conoid tubercular cross-sectional shape, all Dmanisi clavicles are more similar to modern humans and Chk-B-2-81/OH48 than to KNM-WT15000, which has a greater antero-posterior than supero-inferior diameter. D2680 and D2715 are left and right subadult humeri; D4507 is a left adult humerus. In both individuals, the humeral shaft is almost straight, and the position of the lateral epicondyle in relation to the lateral condyle is comparatively high. This is different compared with the condition found in modern humans, but similar to Plio-Pleistocene hominins¹⁷ and African great apes. Humeral torsion in the Dmanisi sample is virtually absent, similar to australopiths (AL288-1, Sts7, KNM-ER739)¹⁸ and *H. floresiensis*¹⁹ (LB1), whereas the KNM-WT15000 humeri are at the lower end of variation of modern-human-like degrees of torsion.

Axial skeleton

The vertebral column of the subadult individual is represented by five elements: D2673 (cervical 2 (C2), axis), D2674 (C3), D2721 (thoracic ~3 (Th3)), D2713 (thoracic ~10 (Th10)) and D2672 (lumbar 1 (L1)). In C2, the superior articular process is sloping downwards mediolaterally, as in the great apes and australopiths, but the spinal process is short and narrow, similar to the condition found in modern humans and australopiths. Canal shapes of all vertebrae are wider transversally than dorso-ventrally, similar to AL333-101, KNM-WT15000 and modern humans. Zygapophyseal joint orientation of

C3, Th10 and L1 is like that in modern humans. The centra of Th10 and L1 are transversally extended; T10 exhibits anterior wedging, whereas L1 exhibits slight posterior wedging.

Lower limbs

The adult right femur, tibia and patella constitute the most complete lower limb of early *Homo* recovered so far. D4167 is a complete right femur with a well-developed linea aspera. The shaft is markedly more robust than that of KNM-ER1481a²⁰ (early *Homo*). The neck index is similar to australopiths and KNM-WT15000, but lower than in modern humans. As in all hominins²¹, the greater trochanter is less elevated than the head but is laterally prominent. In keeping with the low degree of anteversion (femoral torsion), the lesser trochanter is not carried far towards the medial margin of the shaft²². Like Asian and African *H. erectus*, the Dmanisi femur has a narrow medullary canal²¹ in comparison to modern humans. The shaft is straight in anterior view and displays the valgus orientation characteristic for hominins. The distal bicondylar angle is within the range of variation of australopiths and early *Homo*²³, and at the upper extreme of modern human variation. D3418 is a right patella. The medial surface is larger than the lateral surface, which is unusual in modern humans. The mediolateral breadth is slightly larger than that of the left patella SKX 1084 (ref. 24) from Swartkrans Member 2. D3901 is the first complete fossil hominin tibia. It is comparatively robust; the proximal and distal joint surfaces and the malleolus are large relative to diaphyseal length (Fig. 3a), but mid-shaft proportions are like those of early *Homo* (KNM-ER803b, KNM-ER741)^{25,26}. D3901 is similar to modern human tibiae in its degree of torsion, but clearly different in its degree of inclination. This latter feature is pronounced in humans, but not in great apes.

Table 1 | Postcranial dimensions of the Dmanisi hominins

Measurements	Australopiths	Earliest <i>Homo</i>	Dmanisi	KNM-WT15000	Modern humans
Shoulder girdle					
Olecranon orientation relative to midaxillary border (M17) (°)	115.0–116.0†	–	129.0	127.0	133.8–154.0
Glenohumeral angle (°)	–	–	55.0	59.5	60.0–94.5
Clavicular length (M1) (mm)	–	149.4‡	137.3 (L), 135.6 (R), 123.2	130.5	113.0–159.0, 113.0–139.0
Humerus					
Length (M1) (mm)	226.0–235.0§	–	295.0, 282.2	319.0	263.0–341.0, 255.0–334.0
Mid-shaft a–p diameter (mm)	19.0	–	37.1, 17.1 (L), 16.8 (R)	19.9	16.5–36.0, 12.5–24.3
Mid-shaft m–l diameter (mm)	15.0	–	34.8, 14.3 (L), 14.7 (R)	16.7	11.5–24.5, 13.3–31.4
Torsion (M18) (°)	111.0–130.0	–	110.0, 104.0	126.0	134.9–180.0, 138.2–160.7
Vertebrae					
C2 anterior angle of superior articular process (°)	107.0–120.0¶	–	111.0	–	129.1–147.2
C2/C3 zygapophyseal joint angle (°)	–	–	62.5	–	62.0–85.0
Th10 centrum area (M4*M7) (mm ²)	–	–	692.2	–	601.1–958.6
L1 centrum area (M4*M7) (mm ²)	–	–	777.8	803.4	706.3–1,288.9
Femur					
Length (M1) (mm)	280.0#	401.0–396.0☆	386.0	432.0	337.0–434.0
Head diameter (M19) (mm)	27.9–39.4**	40.0–42.0☆	40.0	46.0	42.7–55.1
Mid-shaft a–p diameter (M6) (mm)	22.0#	27.7–28.8☆	26.5	24.5	29.1–34.7
Mid-shaft m–l diameter (M7) (mm)	21.0#	26.4–25.6☆	22.2	24.3	26.1–29.9
Medial condylar breadth (M21c) (mm)	19.3–22.3††	20.7–21☆	24.2	–	27.6–40.3
Lateral condylar breadth (M21e) (mm)	17.9–22.1††	19.2–25.5☆	23.3	–	24.2–32.9
Bicondylar angle (M30) (°)	75.0–81.0‡‡	77.0–80.0☆	81.5	80.0	76.0–88.0
Tibia					
Length (M1a) (mm)	–	–	306.0	380	290.0–374.0
Mid-shaft a–p diameter (M8) (mm)	–	22.5–31.0§§	27.0	24.5	25.8–42.3
Mid-shaft m–l diameter (M9) (mm)	–	14.6–23.6§§	18.0	20.4	15.5–24.6
Angle of inclination (M13) (°)	–	–	82.0	–	89.1–111.7
Foot					
Neck angle of talus (M16) (°)	32.3	33.5¶¶	26.0	–	12.0–31.0
Estimates*					
Stature (cm)	110.0–151.0 (ref. 50)	125.0–157.0 (ref. 50)	144.9–166.2	150.5–169.1 (ref. 42)	–
Body mass (kg)	29.0–49.0 (ref. 50)	32.0–52.0 (ref. 50)	40.0–50.0	45.5–70.6 (ref. 42)	–
Encephalization quotient	2.4–3.1 (ref. 50)	3.1 (ref. 50)	2.57–3.13	2.71–3.78	6.3

Measurement ranges were used for australopiths and modern humans. Data for subadults are in italic font. a–p, antero-posterior; m–l, mediolateral. For measurement codes (M1, M7, and so on) see ref. 69 of Supplementary Information.

* See Supplementary Table 6 for details on estimation procedures. †Sts7, AL288-1. ‡OH48. §AL288-1, Bou-VP-12/1. ||AL288-1, ER739, Sts7, Omo119. ¶AL333-101, SK-854. #AL288-1. ☆KNM-ER1481, KNM-ER1472. **AL288-1, AL333-4. ††AL129, AL333-4, Sts34, TM1513. ‡‡AL288-1, AL129-1a, AL333-4, AL333w-56, Sts34, TM1513, ER993. §§OH35a, ER813a, ER741. ||||AL288-1, TM1517, ER1476a, ER813, ER1464, Stw573. ¶¶OH8.

Foot bones

D4110 is a well-preserved left talus. The neck is stout and expanded transversely but elongated compared to modern humans. The neck (horizontal) angle is small and similar to modern humans²⁷. The medial tubercle is strong and projecting, and the groove for the tendon of flexor hallucis longus is deep. This groove has a slightly oblique orientation, which is similar to great apes, whereas humans exhibit a more vertical orientation²⁸. D2671 and D3442 are subadult and adult right first metatarsals, respectively, with lengths at the lower end of modern human variation and elevated robusticity indices. The morphology of the head deviates from that known from apes and humans. It is spherical and exhibits a narrowing of the

dorsal breadth of the articular surface²⁹. Head torsion is in the range of variation of subadult and adult modern humans and of OH8 (*H. habilis*)³⁰. Two adult metatarsals III (D2021 and D3479) have a straight shaft, exhibit a high degree of torsion and have a dorso-ventrally elongated cross-sectional shape, as in modern humans. Metatarsals IV (adult D4165 and subadult D2669) exhibit an elevated degree of torsion and dorso-ventral elongation. Adult metatarsal V (D4508) is short and at the lower end of modern human variation for its mid-shaft dimensions.

Evolutionary and functional context

The postcranial morphology of the australopiths is best documented by the AL288-1 specimen³¹, indicating that their stature was small (105 cm) and their limb proportions between those of great apes and modern humans, suggesting terrestrial bipedalism with retained arboreal locomotor capabilities. Contrastingly, the postcranial morphology of earliest *Homo* (cf. *H. habilis*) is known from only a few fragmentary specimens (for example, OH35, OH62, KNM-ER3735 (refs 32–35)) dated between 1.75- and 1.9-Myr ago^{36,37}, such that inferences regarding the evolution of stature and limb proportions in this genus are a matter of ongoing debate^{38–40}. The first well-documented evidence for the postcranium of genus *Homo* comes from the KNM-WT15000 specimen, dated to approximately 1.55 Myr ago, the body proportions and stature of which are modern in almost every aspect⁸. Information about the transition from australopith-like to modern-human-like postcranial morphologies is thus rather limited, and the Dmanisi postcranial material fills significant gaps in our knowledge about this critical period of hominin evolution.

The presence of anatomically matching proximal and distal lower limb bones (D4167 and D3901) in the Dmanisi sample and the likely association of these elements with humerus D4507 can be used to infer stature and limb proportions. Stature and body mass of the Dmanisi individuals calculated from various independent long bone measurements yield estimates between 145–166 cm and 40–50 kg, respectively (Table 1 and Supplementary Information 8). Their small stature might be interpreted in two different, but non-exclusive, ways. On the one hand, it might represent a plesiomorphic character shared with earliest *Homo* (cf. *H. habilis*) (125–157 cm and 32–52 kg⁴¹), whereas the KNM-WT15000 specimen appears to be derived in this respect (150.5–169.1 cm and 45.5–70.6 kg)⁴². On the other hand, differences in stature between the Dmanisi and KNM-WT15000 hominins might reflect adaptation to different palaeo-ecological contexts. Limb proportions of the Dmanisi hominins, measured by femoral/tibial and humeral/femoral ratios (Fig. 3b, c and Table 1), were similar to those of modern humans, but also to those of earliest African *Homo* and to the BOU-VP-12/1 specimen dated to 2.5 Myr ago⁴³. Absolute hindlimb length of the Dmanisi hominins is greater than in australopiths and close to that of later *Homo* including modern humans. This may reflect selection for improved locomotor energy efficiency, as the cost of transport is inversely proportional to hindlimb length for terrestrial animals including bipeds⁴⁴.

Cranial capacities (roughly equivalent to brain volume) for the Dmanisi individuals vary from 600 to 775 cm³ (refs 2, 3, 7). These values overlap with *H. habilis* (614 ± 66 cm³; $n = 6$)⁴⁵, but are more than one standard deviation below the mean for *H. erectus* (904 ± 100 cm³; $n = 13$)⁴⁶. Combining cranial and postcranial dimensions, the encephalization quotient for the Dmanisi individuals is in the range of 2.6 to 3.1 (Table 1 and Supplementary Table 6), which is at the lower end of estimates for KNM-WT15000 (2.7–3.8) and more comparable to *H. habilis* (3.1) and australopiths (2.4–3.1).

Using modern human dental and postcranial developmental scores, the age difference between the Dmanisi and KNM-WT15000 specimens is around 2 yr (assuming individual ages of 11–13 and 8–10 yr, respectively), so these specimens are broadly comparable to each other. Overall vertebral morphology indicates

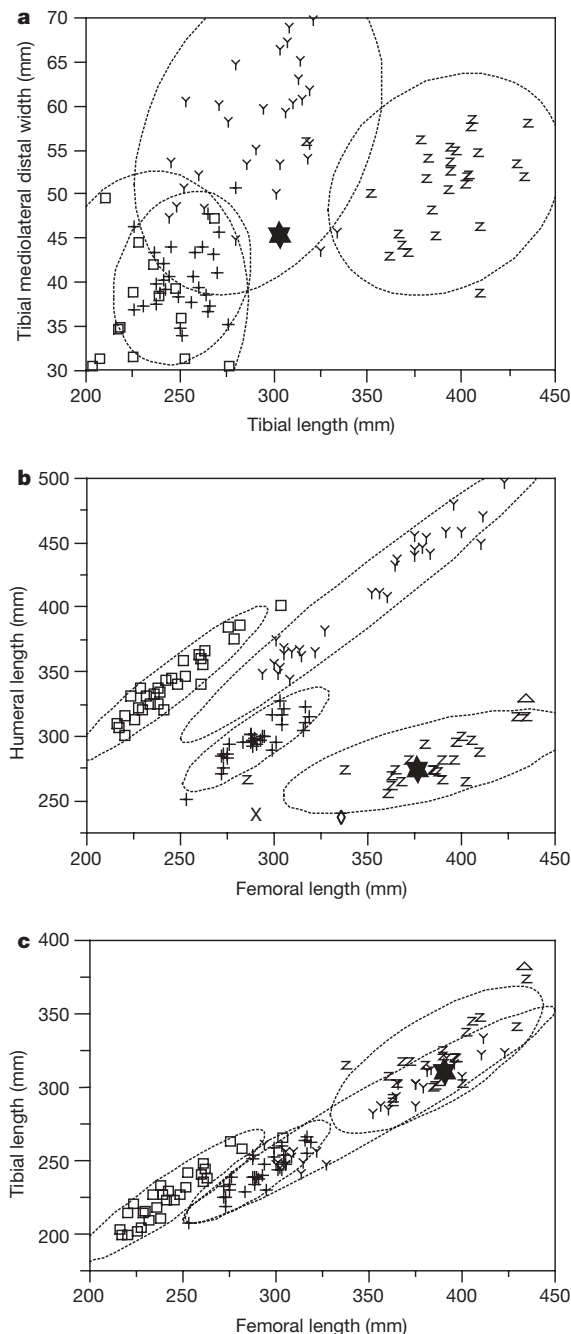


Figure 3 | Long-bone shape and proportions. **a**, Tibial mediolateral distal width versus maximum length. **b**, Humeral versus femoral length. **c**, Tibial versus femoral length. Stars, Dmanisi *Homo*; X, AL288-1 (*Australopithecus afarensis*); diamond, BOU-VP-12/1; triangle, KNM-WT15000 (*H. erectus*); Z, recent *Homo sapiens*; plus signs, *Pan troglodytes*; Y, *Gorilla gorilla*; squares, *Pongo pygmaeus*.

that the Dmanisi spine was more similar to that of early *H. erectus* and modern humans than to australopithecids. Vertebral wedging is indicative of lumbar lordosis; zygapophyseal joint orientation suggests expanded ranges of spinal flexion; and the relatively large vertebral cross-sectional areas are indicative of resistance to increased compressive loads characteristic of running and long-range walking⁴⁷.

Humeral torsion is an important variable that influences orientation and ranges of movement of the upper limb relative to the trunk. In modern humans, the high degree of torsion is seen as a compensation for the more dorsal position of the scapula¹⁸. The low degree of torsion in the Dmanisi sample could thus indicate a habitually more abducted/supine orientation of the arm, a more lateral position of the shoulder girdle, and also a diverse range of arm movement. Reduced torsion in the throwing arm of athletes requiring high upper limb mobility (external rotation)⁴⁸ suggests developmental plasticity, but because this feature is not lateralized in the Dmanisi subadult individual, it might be interpreted as part of a plesiomorphic configuration of the upper body that also includes a more cranial orientation of the glenoid cavity of the scapula, a short coracoid process and a narrow glenocoracoid angle. Following this line of argument, the Dmanisi hominins would have had a more australopithecine-like than human-like upper limb morphology⁴⁹, and absence of humeral torsion in *H. floresiensis*⁹ would provide support for the hypothesis of long-term continuity of this plesiomorphic trait in *Homo*.

Preservation in the Dmanisi remains of lower limb elements from the femur down to the metatarsals permits reconstruction of the positioning and orientation of the foot relative to the walking direction. The tibia exhibits slight medial torsion, and the talar neck angle is wide. This combination results in a more medial orientation of the foot, and a more equal load distribution on all rays than in modern humans. Although this configuration probably represents the plesiomorphic condition, various features of the Dmanisi foot are similar to modern humans and thus clearly derived: metatarsal torsion indicates the presence of a transverse arch; the wide base of the first metatarsal suggests a strong plantar ligament associated with a well-developed longitudinal arch²⁹; and the flat proximal articular surface of the first metatarsal indicates that the hallux had an adducted position.

The following preliminary conclusions can be drawn: the morphology of the upper and lower limbs from Dmanisi exhibits a mosaic of traits reflecting both selection for improved terrestrial locomotor performance and the retention of primitive characters absent in later hominins (Supplementary Table 8). The length and morphology of the hindlimb is essentially modern, and the presence of an adducted hallux and plantar arch indicate that the salient aspects of performance in the leg and foot, such as biomechanical efficiency during long-range walking and energy storage/return during running, were equivalent to modern humans. However, plesiomorphic features such as a more medial orientation of the foot, absence of humeral torsion, small body size and low encephalization quotient suggest that the Dmanisi hominins are postcranially largely comparable to earliest *Homo* (cf. *H. habilis*). Hence, the first hominin species currently known from outside Africa did not possess the full suite of derived locomotor traits apparent in African *H. erectus* and later hominins.

Received 16 April; accepted 30 July 2007.

- Gabunia, L. & Vekua, A. A. Plio-Pleistocene hominid from Dmanisi, East Georgia, Caucasus. *Nature* **373**, 509–512 (1995).
- Gabunia, L. *et al.* Earliest Pleistocene hominid cranial remains from Dmanisi, Republic of Georgia: Taxonomy, geological setting, and age. *Science* **288**, 1019–1025 (2000).
- Vekua, A. *et al.* A new skull of early *Homo* from Dmanisi, Georgia. *Science* **297**, 85–89 (2002).
- Gabunia, L., de Lumley, M.-A., Vekua, A., Lordkipanidze, D. & de Lumley, H. Découverte d'un nouvel hominidé à Dmanissi (Transcaucasie, Géorgie). *C.R. Palévol.* **1**, 243–253 (2002).
- Lordkipanidze, D. *et al.* The earliest toothless hominin skull. *Nature* **434**, 717–718 (2005).
- Rightmire, G. P., Lordkipanidze, D. & Vekua, A. Anatomical descriptions, comparative studies and evolutionary significance of the hominin skulls from Dmanisi, Republic of Georgia. *J. Hum. Evol.* **50**, 115–141 (2006).
- Lordkipanidze, D. *et al.* A fourth hominin skull from Dmanisi, Georgia. *Anat. Rec.* **288A**, 1146–1157 (2006).
- Walker, A. & Leakey, R. *The Nariokotome Homo erectus Skeleton* (Springer, Berlin, 1993).
- Brown, P. *et al.* A new small-bodied hominin from the Late Pleistocene of Flores, Indonesia. *Nature* **431**, 1055–1061 (2004).
- Gabunia, L., Vekua, A. & Lordkipanidze, D. The environmental contexts of early human occupation of Georgia (Transcaucasia). *J. Hum. Evol.* **38**, 785–802 (2000).
- Tappen, M., Ferring, R., Lordkipanidze, D., Vekua, A. & Kiladze, G. in *Current Topics on Taphonomy and Fossilization* (eds de Renzi, M. *et al.*) 161–170 (Ajuntament de Valencia, Valencia, 2002).
- Vrba, E. S. A new study of the scapula of *Australopithecus africanus* from Sterkfontein. *Am. J. Phys. Anthropol.* **51**, 117–129 (1979).
- Johanson, D. C. C. *et al.* Morphology of the Pliocene partial hominid skeleton (A.L. 288-1) from the Hadar formation, Ethiopia. *Am. J. Phys. Anthropol.* **57**, 403–451 (1982).
- Jashashvili, T. *Hominid Upper Limb Remains from the Paleolithic Site of Dmanisi*. PhD thesis, Georgian National Museum and Univ. Ferrara (2005).
- Weidenreich, F. Discovery of the femur and the humerus of *Sinanthropus pekinensis*. *Nature* **141**, 614–617 (1938).
- Day, M. H. in *Early Hominids of Africa* (eds Jolly, C. J.) 311–345 (St Martin's Press, New York, 1978).
- Senut, B. *L'humérus et ses articulations chez les Hominidés plio-pléistocènes* (CNRS, Paris, 1981).
- Larson, S. G. Estimating humeral torsion on incomplete fossil anthropoid humeri. *J. Hum. Evol.* **31**, 239–257 (1996).
- Morwood, M. J. *et al.* Further evidence for small-bodied hominins from the Late Pleistocene of Flores, Indonesia. *Nature* **437**, 1012–1017 (2005).
- Day, M. H., Leakey, R. E. F., Walker, A. C. & Wood, B. A. New hominids from East Rudolf, Kenya, I. *Am. J. Phys. Anthropol.* **42**, 461–475 (1975).
- Kennedy, G. E. A morphometric and taxonomic assessment of a hominine femur from the lower member, Koobi Fora, Lake Turkana. *Am. J. Phys. Anthropol.* **61**, 429–436 (1983).
- Lovejoy, C. O., Meindl, R. S., Ohman, J. C., Heiple, K. G. & White, D. T. The Maka femur and its bearing on the antiquity of human walking: Applying contemporary concepts of morphogenesis to the human fossil record. *Am. J. Phys. Anthropol.* **119**, 97–133 (2002).
- Tardieu, C. & Trinkaus, E. Early ontogeny of the human femoral bicondylar angle. *Am. J. Phys. Anthropol.* **95**, 183–195 (1994).
- Susman, R. L. New hominid fossils from the Swartkrans formation (1979–1986 excavations): postcranial specimens. *Am. J. Phys. Anthropol.* **79**, 451–474 (1989).
- Leakey, R. E. F. & Walker, A. C. New australopithecines from East Rudolf, Kenya (III). *Am. J. Phys. Anthropol.* **39**, 205–221 (1973).
- Day, M. H. & Leakey, R. E. F. New evidence of the genus *Homo* from East Rudolf, Kenya (III). *Am. J. Phys. Anthropol.* **41**, 367–380 (1974).
- Rhoads, J. G. & Trinkaus, E. Morphometrics of the Neandertal talus. *Am. J. Phys. Anthropol.* **46**, 29–43 (1977).
- Aiello, L. & Dean, C. *An Introduction to Human Evolutionary Anatomy* (Academic, London, 1990).
- Susman, R. L. & de Ruiter, D. J. New hominin first metatarsal (SK 1813) from Swartkrans. *J. Hum. Evol.* **47**, 171–181 (2004).
- Susman, R. L. & Stern, J. T. Functional morphology of *Homo habilis*. *Science* **217**, 931–934 (1982).
- Johanson, D. C. & Taieb, M. Plio-Pleistocene hominid discoveries in Hadar, Ethiopia. *Nature* **260**, 293–297 (1976).
- Leakey, L. S. B., Tobias, P. V. & Napier, J. R. A new species of the genus *Homo* from Olduvai Gorge. *Curr. Anthropol.* **6**, 424–427 (1964).
- Susman, R. L. & Creel, N. Functional and morphological affinities of the subadult hand (O.H. 7) from Olduvai Gorge. *Am. J. Phys. Anthropol.* **51**, 311–332 (1979).
- Johanson, D. C. *et al.* New partial skeleton of *Homo habilis* from Olduvai Gorge, Tanzania. *Nature* **327**, 205–209 (1987).
- Leakey, R. E. F., Walker, A., Ward, C. V. & Gausz, H. M. in *Hominidae* (eds Giacobini, G.) 167–173 (Jaka Books, Milan, 1989).
- Feibel, C. S., Brown, F. H. & McDougall, I. Stratigraphic context of fossil hominids from the Omo group deposits: Northern Turkana Basin, Kenya and Ethiopia. *Am. J. Phys. Anthropol.* **78**, 595–622 (1989).
- White, T. D. in *Encyclopedia of Human Evolution and Prehistory* (eds Delson, E., Tattersall, I., Van Couvering, J. A. & Brook, A. L.) 486–489 (Garland Publishing, New York, 2000).
- Haeusler, M. & McHenry, H. M. Body proportions of *Homo habilis* reviewed. *J. Hum. Evol.* **46**, 433–465 (2004).
- Richmond, B. G., Aiello, L. & Wood, B. Early hominin limb proportions. *J. Hum. Evol.* **43**, 529–548 (2002).
- Green, D. J., Gordon, A. D. & Richmond, B. G. Limb-size proportions in *Australopithecus afarensis* and *Australopithecus africanus*. *J. Hum. Evol.* **52**, 187–200 (2007).
- McHenry, H. M. Body size and proportions in early hominids. *Am. J. Phys. Anthropol.* **87**, 407–431 (1992).

42. Ruff, C. Body size prediction from juvenile skeletal remains. *Am. J. Phys. Anthropol.* **133**, 698–716 (2007).
43. Asfaw, B. *et al.* Remains of *Homo erectus* from Bouri, Middle Awash, Ethiopia. *Nature* **416**, 317–320 (2002).
44. Pontzer, H. Predicting the energy cost of terrestrial locomotion: a test of the limb model in humans and quadrupeds. *J. Exp. Biol.* **210**, 484–494 (2007).
45. Elton, S., Bishop, L. C. & Wood, B. Comparative context of Plio-Pleistocene hominin brain evolution. *J. Hum. Evol.* **41**, 1–27 (2001).
46. Rightmire, G. P. Brain size and encephalization in early to Mid-Pleistocene *Homo*. *Am. J. Phys. Anthropol.* **124**, 109–123 (2004).
47. Bramble, D. M. & Lieberman, D. E. Endurance running and the evolution of *Homo*. *Nature* **432**, 345–352 (2004).
48. Reagan, K. M. *et al.* Humeral retroversion and its relationship to glenohumeral rotation in the shoulder of college baseball players. *Am. J. Sports Med.* **30**, 354–360 (2002).
49. Stern, J. T. Jr & Susman, R. L. The locomotor anatomy of *Australopithecus afarensis*. *Am. J. Phys. Anthropol.* **60**, 279–317 (1983).
50. McHenry, H. M. How big were early hominids? *Evol. Anthropol.* **1**, 15–20 (1992).

Supplementary Information is linked to the online version of the paper at www.nature.com/nature.

Acknowledgements We acknowledge H. Herrmer for identification of cheetah remains from Dmanisi; M. Delfino for providing a revision of the amphibian and reptilian fauna; E. Trinkaus and M. Häusler for comments; G. Bumbiashvili and

N. Andriashvili for the photographs; and the excavation team for constant support. Palaeomagnetic measurements were carried out at the SCT of the Barcelona University. This work was supported by a grant of the Georgian National Science Foundation, a Rolex award for enterprise, BP Georgia, the National Geographic Society, a Dan David 2003 scholarship, the Swiss National Science Foundation, the Strategic Research Funds of the University of Zurich, Wenner-Gren Foundation short-term fellowships, the Fundación Duques de Soria, a CNRS international research project grant, ECO-NET (a joint international project of the French Ministry of Foreign Affairs between France, Georgia and Azerbaijan), The Italian Ministry for Foreign Affairs (DGPCC-V), the Spanish Ministry of Education and Science, the Consejería de Cultura de Andalucía, The National Science Foundation (USA) and the L. S. B. Leakey Foundation.

Author Contributions D.L. directs and coordinates research at Dmanisi; T.J., M.S.P.de L. and C.P.E.Z. performed comparative morphological/morphometric analyses, designed the paper and wrote the main text; G.P.R. and H.P. contributed to comparative descriptions; R.F. performed stratigraphical analyses; O.O. performed palaeomagnetic analyses; M.T. performed taphonomic analyses; G.K. organized fieldwork and prepared specimens; and A.V., M.B., J.A., R.K., B.M.-N., A.M., M.N. and L.R. performed fieldwork and provided comparative faunal analyses.

Author Information Reprints and permissions information is available at www.nature.com/reprints. The authors declare no competing financial interests. Correspondence and requests for materials should be addressed to D.L. (dlordkipanidze@museum.ge).

Structural insight into filament formation by mammalian septins

Minhajuddin Sirajuddin¹, Marian Farkasovsky^{1†}, Florian Hauer², Dorothee Kuhlmann¹, Ian G. Macara³, Michael Weyand¹, Holger Stark² & Alfred Wittinghofer¹

Septins are GTP-binding proteins that assemble into homo- and hetero-oligomers and filaments. Although they have key roles in various cellular processes, little is known concerning the structure of septin subunits or the organization and polarity of septin complexes. Here we present the structures of the human SEPT2 G domain and the heterotrimeric human SEPT2–SEPT6–SEPT7 complex. The structures reveal a universal bipolar polymer building block, composed of an extended G domain, which forms oligomers and filaments by conserved interactions between adjacent nucleotide-binding sites and/or the amino- and carboxy-terminal extensions. Unexpectedly, X-ray crystallography and electron microscopy showed that the predicted coiled coils are not involved in or required for complex and/or filament formation. The asymmetrical heterotrimers associate head-to-head to form a hexameric unit that is nonpolarized along the filament axis but is rotationally asymmetrical. The architecture of septin filaments differs fundamentally from that of other cytoskeletal structures.

Septins are conserved GTP-binding proteins discovered in the budding yeast *Saccharomyces cerevisiae*, where they organize into a ring at the bud neck^{1–4}. A parallel array of filaments is formed from hetero-oligomers of four septins, which interact asymmetrically with other proteins during cell division^{5,6}. The 13 human septin genes can be subdivided into 4 groups, which can, in principle, generate dozens of redundant heteromeric complexes^{7–9}. They have key roles in cell division, cytoskeletal dynamics and secretion¹⁰, and have been implicated in the pathogenesis of various diseases including neoplasia and neurodegenerative conditions¹¹. Missense *SEPT9* mutations were recently found to be responsible for hereditary neuralgic amyotrophy¹².

Not much is known about the structure of septins, the role of guanine nucleotide binding and GTP hydrolysis in septin function¹³. Mammalian septin complexes isolated from brain tissue or HeLa cells contain between three–five major isoforms^{14–17}. Purified septin complexes from *S. cerevisiae* with Cdc3–Cdc10–Cdc11–Cdc12 and from *Drosophila* with Pnut–Sep1–Sep2 have 2:2:2:2 and 2:2:2 stoichiometries^{18–20}, and contain 1 mol guanine nucleotide per polypeptide^{20–22}. Recombinant mammalian and yeast complexes with different numbers of septins contain bound nucleotides with varying affinities and stoichiometries^{22,23}, whereas the recombinant octameric yeast complex is fully saturated with tightly bound nucleotide^{21,22}. The trimeric SEPT2–SEPT6–SEPT7 complex, but not the dimeric human SEPT6–SEPT7 complex, forms filaments²³, whereas the *Caenorhabditis elegans* UNC-59 and UNC-61 gene products are sufficient for filament formation²⁴. Because a single recombinant Sept2 from *Xenopus laevis* and human SEPT2 expressed in insect cells can be reconstituted into filaments, a defined number of subunits is apparently not required for filament formation^{25,26}. Septin filaments have 7–9-nm width and various length, with a unit length of 25–32 nm observed under high salt concentration^{3,18,20,25}. As an approach to understand septin function better, we have determined the X-ray structure of the human SEPT2 G domain and the SEPT2–SEPT6–SEPT7 complex.

The SEPT2 G domain

Human SEPT2 lacking 46 residues of the predicted C-terminal coiled coil (SEPT2-315) was isolated as recombinant protein from *Escherichia coli*. It contains 50% bound GDP and elutes in several peaks during gel filtration, two of which correspond to apparent molecular masses of 36 and 72 kDa, respectively (Fig. 1a). In the presence of GDP, GppNHp (a slowly hydrolysing GTP analogue) or alkaline phosphatase, the monomer–dimer equilibrium is shifted towards the dimer or monomer, respectively, indicating that dimerization is influenced by the presence but not the nature of the nucleotide. SEPT2-315 was crystallized in the presence of excess GDP and the structure was solved using selenomethionine single-wavelength anomalous dispersion (SAD) to a resolution of 3.4 Å (Table 1). In the asymmetrical unit of the crystal, SEPT2 is dimerized via two different interfaces (Fig. 1b).

The basic structure of monomeric SEPT2 closely resembles the canonical G domain exemplified by Ras, with six β -strands and five α -helices (Fig. 1c and Supplementary Fig. 1). A unique feature of SEPT2 is the presence of four additional elements compared to Ras. These are the N-terminal helix $\alpha 0$ (to preserve the canonical G domain nomenclature), $\alpha 5'$ between $\alpha 4$ and $\beta 6$, the two antiparallel strands $\beta 7$ and $\beta 8$, and the $\alpha 6$ C-terminal helix that points away from the G domain at a 90° angle relative to the axis of interaction between subunits. The sequences of the additional elements are highly conserved. They contain residues that are invariant between SEPT2–SEPT6–SEPT7 and most other septins and are involved in contact to neighbouring subunits. GDP is bound in a conventional way, with the phosphates occupying the P-loop and the AKAD motif contacting the guanine base.

SEPT2 forms dimers via the nucleotide-binding site

Interface 1 of the septin dimer is along the nucleotide-binding site and forms the G-dimer, whereas interface 2 is mediated by the extra N- and C-terminal helices to form the NC-dimer (Fig. 1b and Supplementary Fig. 2a). The sizes of the interfaces are 1,851 Å² and

¹Abteilung Strukturelle Biologie, Max-Planck-Institut für molekulare Physiologie, Otto-Hahn-Strasse 11, 44227 Dortmund, Germany. ²Max-Planck-Institut für Biophysikalische Chemie, Am Fassberg 11, 37077 Goettingen, Germany. ³Center for Cell Signaling, Department of Microbiology, University of Virginia School of Medicine, Charlottesville, Virginia 22908-0577, USA. [†]Present address: Institute of Molecular Biology SAS, Dubravska cesta 21, 845 51 Bratislava, Slovak Republic.

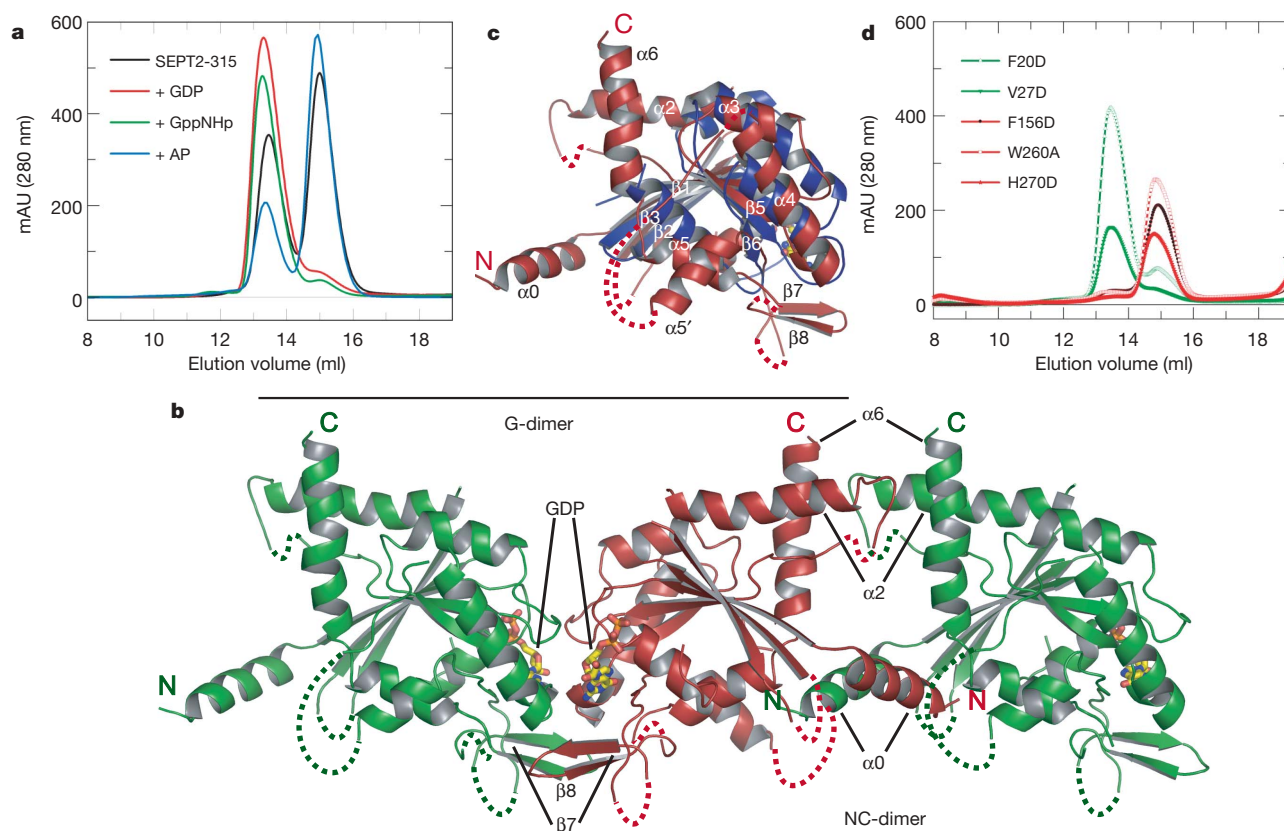


Figure 1 | Structure and dimerization of SEPT2. **a**, Gel filtration analysis of SEPT2-315 on a Superdex S-200 column. The elution profile shows a monomer–dimer equilibrium, which is shifted by the presence of excess GDP or GppNHp as indicated. In the presence of alkaline phosphatase (AP), which degrades nucleotides, the protein runs as a monomer predominantly. AU, absorbance units. **b**, Ribbon representation of three SEPT2-315

monomers found in the crystal, with two possible dimer interfaces labelled G- or NC-dimer, as indicated. Dashed lines represent disordered regions. **c**, Superimposition of the structures of SEPT2-315 (red) and Ras-GppNHp (blue) (Protein Data Bank 121P), indicating the extra secondary structure elements of the septin G domain. **d**, Gel filtration of mutant SEPT2 variants in the presence of excess GDP, analysed as described in **a**.

2,995 Å² for the G-dimer and the NC-dimer, respectively. To delineate which of these represents the solution structure, we mutated residues that are likely to contribute to the binding energy and are highly conserved (Supplementary Fig. 2b).

Phenylalanine 156 of SEPT2 interacts with Phe 156 from the other SEPT2 subunit and was mutated to Asp, whereas Trp 260 and His 270, which interact, were mutated to Ala and Asp, respectively. For the NC-dimer, Val 27 and Phe 20 were mutated to Asp. Dimer formation was analysed by analytical gel filtration in the presence of GDP (Fig. 1d). Whereas mutants of the NC-dimer interface showed the same equilibrium between monomer and dimer as wild-type SEPT2, the G interface mutants eluted as monomers. These results demonstrate that SEPT2 forms dimers across the nucleotide-binding site, with a face to face orientation of nucleotide-binding sites, similar to other GTP-binding proteins of the TRAFAC and SIMIBI classes²⁷ such as MnmE²⁸ and HypB²⁹, consistent with our observation that saturation with nucleotide favours dimerization (Fig. 1a).

Table 1 | X-ray refinement statistics

	SEPT2-315	Human septin complex
Resolution (Å)	20–3.4	49.15–4
$R_{\text{work}}/R_{\text{free}}$ (%)	27.9/31.3	37.5/39.2
Number of atoms		
Protein	3,650	4,575
Ligand/ion	56	87
B-factors		
Protein	80.27	78.3
Ligand	65.43	71.4
r.m.s deviations		
Bond lengths (Å)	0.012	0.057
Bond angles (°)	1.589	4.7

Structure of the human septin complex

The human septin complex consisting of full-length SEPT2–SEPT6–SEPT7 was isolated basically as described for the recombinant yeast complex²². Using gel filtration, the molecular mass of the complex was estimated as ~285 kDa, which accounts for a hexamer. It contains ~70% bound nucleotide relative to protein with a GDP:GTP ratio of >2:1. The structure of human septin complex was solved using the MIRAS (multiple isomorphous heavy-atom replacement using anomalous scattering) approach. The electron density reveals 4–5-nm-wide tubes, indicating that the human septin complex is polymerized under crystallization conditions (Supplementary Fig. 3). The asymmetrical unit of the crystal is a trimer rather than a hexamer. Subunit assignment of the trimer was guided by selenomethionine sites (Fig. 2a).

The final model of the SEPT2–SEPT6–SEPT7 repeating unit (Fig. 2b) shows that the filament in the crystal consists of an assembly of G domains; the G domains contact each other using the same conserved G and NC interfaces observed in the SEPT2 crystal. Surprisingly, no density is seen for the predicted C-terminal coiled coils, although there is sufficient space available between parallel filaments in the crystal. To exclude protein truncation during crystal formation, human septin complex crystals were dissolved and shown to contain full-length protein (not shown). Although the resolution of the structure is limited to 4 Å, we would expect to see density for the coiled coils because the density of the G domain is well defined. The location of the coiled coils can be deduced from the direction of helices α_6 , which protrude at a right angle to the filament axis and could in principle form parallel coiled coils, as predicted for SEPT6 and SEPT7 from fluorescence resonance energy transfer (FRET) data³⁰.

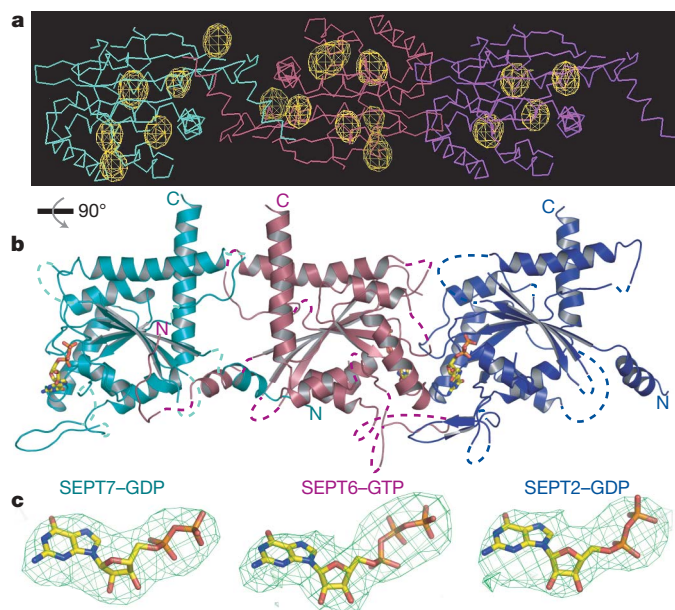


Figure 2 | Structural analysis of the human septin complex.

a, Superimposition of the molecular replacement solution using the SEPT2 G domain onto the selenomethionine anomalous map contoured at 5σ to assign the location of the SEPT2, SEPT6 and SEPT7 subunits in the asymmetrical unit. **b**, Ribbon model of the trimeric SEPT2-SEPT26-SEPT27 complex, with SEPT7 in cyan, SEPT6 in pink and SEPT2 in blue, with nucleotides in ball and stick representation. **c**, Positive $F_o - F_c$ electron density map, contoured at 3σ , around the nucleotide-binding sites of the respective septins, and the resulting nucleotide models, as indicated.

There is a continuing debate as to whether the nature of bound nucleotide determines septin complex or filament formation, and whether GTP hydrolysis has a role in the process. Nucleotides are

found in each septin active site. The $F_o - F_c$ electron densities of SEPT7 and SEPT2 are very consistent with a GDP nucleotide, whereas SEPT6 contains additional density that we tentatively assign to the γ -phosphate of GTP (Fig. 2c), consistent with biochemical findings^{7,20–22}.

Human septin complex is a linear hexamer

Electron microscopy of the human septin complex shows that the filament structure in the crystal also represents the structure in solution. Under low salt concentration, the heterotrimer forms filaments and rings of various dimensions with no consistent pattern. At high salt concentration, short pieces of uniform length become prevalent. Single-particle analysis shows a hexameric assembly consistent with a dimer of the trimeric asymmetrical unit of the crystal, with similar dimensions. It consists of six equally sized subunits, consistent with an array of G domains (Fig. 3a)¹⁵. No density corresponding to the C-terminal ends was observed after averaging. To confirm that the C termini are dispensable for complex formation, we found that a complex lacking coiled coils consisting of SEPT2(1–308), SEPT6(1–310) and SEPT7(1–305) could be isolated with the same purification procedure as wild-type human septin complex. We conclude that the coiled coils are not required for formation of a stable hexameric complex. Single-particle analysis did not reveal significant differences compared to the wild-type human septin complex (Fig. 3b).

Architecture of the hexamer

Although the electron microscopy studies show that the human septin complex forms a hexamer at high salt concentration, it is not possible to deduce, from the linear arrangement of subunits in the crystal, the boundaries of the solution particle. We thus analysed a complex between a maltose binding protein (MBP)–SEPT2 fusion and SEPT6–SEPT7, an intermediate of the purification scheme. Electron microscopy analysis (Fig. 3d) shows an extra density located at the centre of the particle. The fact that only one extra particle is

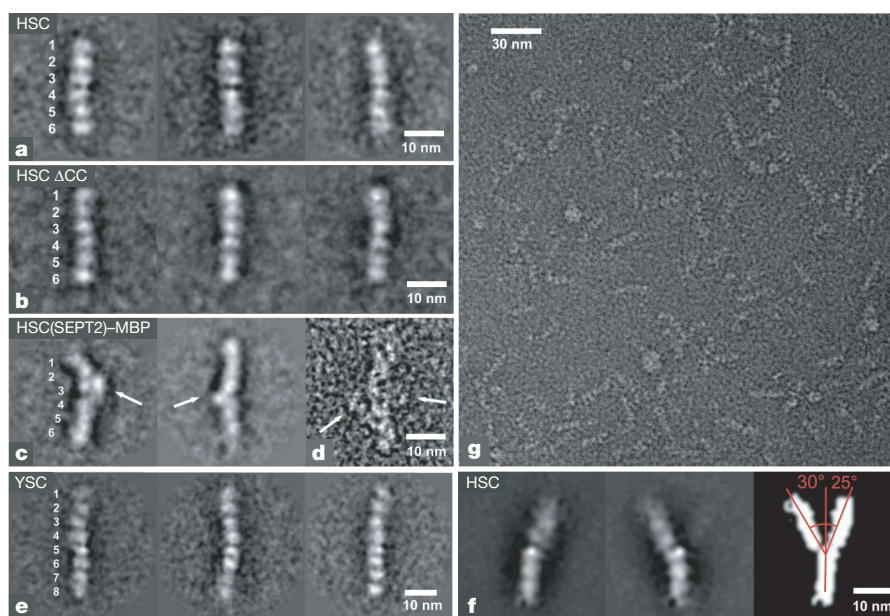


Figure 3 | Electron microscopic studies of septin complexes. **a**, Class averages of the negatively stained human septin complex (HSC) at high salt concentration obtained after reference-free alignment, MSA and classification. **b**, Class averages of the deleted coiled coil (Δ CC) human septin complex at high salt concentration showing the same hexameric arrangement and comparable density distribution as in **a**. **c**, Class averages of the MBP-fused human septin complex. Densities attributed to the fused MBP are indicated by an arrow and located close to the central part of the complex. **d**, Single-particle image of the MBP-fused human septin complex. Both MBP

fusion tags are visible as lateral protrusions highlighted by the arrows. **e**, Class averages of the Cdc3–Cdc10–Cdc11–Cdc12 yeast septin complex (YSC). In contrast to the human septin complex, the yeast septin complex forms an octameric complex. **f**, Class averages after alignment of the human septin complex using only the lower trimeric part as a reference to align the raw images. The upper trimeric part adopts different orientations, indicating the high level of flexibility of the hexamer. Bending is observed in the 25–30° range around a hinge formed by the central SEPT2 dimer. **g**, Raw electron micrograph of the human septin complex at high salt concentration.

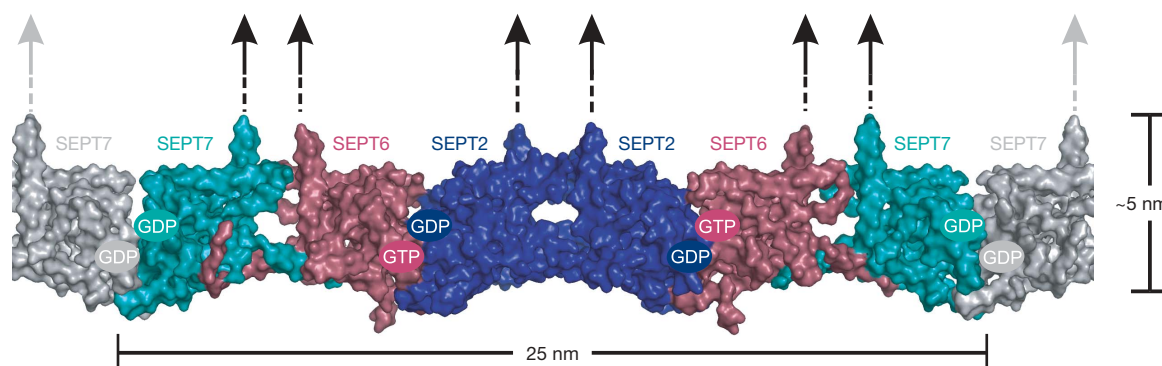


Figure 4 | The septin filament. Surface representation of the basic hexameric unit (in colour). The neighbouring hexamer makes longitudinal contact using SEPT7 (in grey), thereby forming septin filaments. The nature

of the nucleotide in the subunits is indicated. The presumed orientations of the C-terminal ends predicted to form coiled coils are shown schematically.

visible instead of two in most images (Fig. 3c) might be due to the flexible connection of the tag and/or the arrangement of particles on the grid. However, in combination with the X-ray data, the evidence for an arrangement of septins in the order 7-6-2-2-6-7 is unequivocal (Fig. 4). Thus, the SEPT7-SEPT6 interaction takes place by means of the NC interface, whereas the SEPT6-SEPT2 interaction is via the G interface. Notably, the SEPT2-SEPT2 interaction favours the NC interface rather than the G interface found for the isolated SEPT2 in solution, supporting the notion that septin interactions appear fairly promiscuous. Filament formation in the crystal and most likely in solution involves a SEPT7-SEPT7 G-dimer interaction, which should be sensitive to high salt concentration, whereas the G interface between SEPT2 and SEPT6 is not, arguing that the G-dimer interface of heterodimers is differentially sensitive or tighter than the G-dimer interface of homodimers.

Bending of filaments

By aligning all human septin complex particles against a linear trimer, flexibility of the hexameric complex is revealed by multivariate statistical analysis (MSA) and classification^{31,32} (Fig. 3f). Straight and kinked states are found in almost equal amounts within the particle population. The observed average flexibility of the hexamer can be described by bending one trimer with respect to the other by 25–30° around a hinge formed by the SEPT2-SEPT2 interface. This interface appears as an obvious hinge element, because it is connected by thinner density elements. Consistent with this, the upper half of the NC-dimer interface of SEPT2 near $\alpha 2/6$ is mediated mostly by charged residues (Fig. 1b and Supplementary Fig. 2a), which should be destabilized by the high salt concentration used in the electron microscopy analysis. This analysis indicates that septin filaments are not uniformly linear *in vitro*, consistent with observations that they can form ring-like structures *in vitro* and *in vivo*.

Discussion

The N-terminal extensions of the septin G domain upstream of $\alpha 0$ are usually fairly short, except for SEPT9 (also called MSF), and have no apparent secondary structure. The longer N terminus of SEPT6 makes additional contacts with SEPT7 and may thus be involved in tightening the interaction between the subunits. The C-terminal extensions have a strong coiled-coil probability and were expected to be structured and contribute to complex formation. Surprisingly, they were neither visible in the X-ray nor in the electron microscopy analyses. It could be that these regions are natively unstructured and only adopt structure by interacting with partner proteins such as the BORGs¹⁷ or other septin filaments. Alternatively, they might indeed adopt parallel coiled-coil structures as predicted³⁰, but are connected to the G domain via a flexible linker. Because such a break in the coiled-coil prediction does exist (Supplementary Fig. 1), the C-termini might indeed adopt numerous positions relative to the G

domain and are thus not visible. Thin strands projecting outwards from a rat oligomeric septin complex have been observed before¹⁵ and can also be identified in some of our electron microscopy images (Fig. 3g), but are lost on averaging. For the SEPT6-SEPT7 coiled coils, it was shown that they directly interact with each other³⁰. Although the G domain alone is sufficient to mediate complex and filament formation, the proximity of C termini of SEPT6-SEPT7 could indicate that the coiled coils, although not required, may further stabilize filament formation, consistent with results on recombinant coiled-coil-deleted *Xenopus laevis* Sept2 (ref. 25).

The 4–5-nm width of septin filaments from our crystal and electron microscopy analyses is about half the size of 7–9-nm septin filaments described in electron microscopic studies and consistently quoted in the literature. Although the nature of the discrepancy is not obvious, two single filaments tightly packed against each other would form such a particle. Paired filaments with varying space between them have been described, and the 8-nm filament could thus be a special case. The C-terminal regions may be involved in forming paired filaments or higher order structures seen *in vitro* and *in vivo*^{3,4,14,18,33}. Because C-terminal extensions of neighbouring filaments point into the same direction, the formation of paired filaments is prevented in the crystal.

The extended G domains of septins serve as universal building blocks for polymer formation, which is in contrast to published models. Polymers can be formed by a variable number of subunits using different combinations of septins. To show that this is a common design principle we analysed the recombinant yeast Cdc3-Cdc10-Cdc11-Cdc12 complex. Electron microscopy analysis shows a particle of 32-nm length and 4–5-nm width clearly composed of eight subunits (Fig. 3e), as predicted from previous biochemical analysis and consistent with the structural findings^{18,22,34}. The nature of the nucleotide indicates that it might have a role in oligomer and filament formation, because we observe that in the interface between SEPT6-GTP and SEPT2-GDP the switch regions are better defined than in the SEPT7-GDP interface. The data also show that the G-dimer interface between the homodimer SEPT7-SEPT7 can be dissociated using high salt concentration, but this is not the case for the G-dimer interface between the heterodimer SEPT6-SEPT2, possibly due to the nature of bound nucleotide. To decipher the rules of complex and filament formation, the role of nucleotide binding and GTP hydrolysis, and the function of the C-terminal extensions, more biochemical experiments and structural studies, possibly with higher resolutions, will be required. The structures presented here will provide powerful tools for the design of appropriate experiments.

METHODS SUMMARY

SEPT2-315 was isolated from *E. coli* using the glutathione S-transferase (GST) tag. Analytical gel filtration of SEPT2-315 was performed over a Superdex S-200

10/30 column (Amersham) with an ÄKTA explorer under different conditions. The GDP protein was prepared by incubating with 3× excess GDP; GppNHp protein was prepared by treating 5 units of alkaline phosphatase and 3× excess GppNHp for 4 h at 4 °C. Tris/HCl (50 mM) pH 7.5, 150 mM NaCl, 5 mM MgCl₂ and 5 mM dithioerythritol (DTE) was used as buffer throughout. Trimeric complex (human septin complex) was co-expressed in *E. coli* and co-purified using the His and MBP tags on SEPT7 and SEPT2, respectively. SEPT2-315 crystals were grown using 5% polyethylene glycol 6000, 0.1 M bicine pH 9.0, and 0.1 M glycine; crystals were transferred to cryoprotectant containing 25% ethylene glycol along with mother liquor and flash frozen in liquid nitrogen. Selenomethionine-labelled protein was crystallized as above and a SAD data set was used for structure determination. The structure of human septin complex was solved using a combination of five heavy-atom derivatives. All the samples for electron microscopy analysis were incubated in high salt buffer (20 mM HEPES pH 8.0, 800 mM NaCl, 5 mM MgCl₂, 10 mM dithiothreitol), except for human septin complex containing the MBP-SEPT2 fusion, which was centrifuged in a glycerol gradient (20 mM HEPES pH 8.0, 600 mM NaCl, 5 mM MgCl₂, 5–20% glycerol 5–20%) for 20 h at 92,000g. All samples were applied on a single carbon film on an electron microscopy grid and negatively stained with uranyl formate. Class averages of selected particles were reconstructed after reference-free alignment and subsequent MSA and classification. A more detailed description can be found in Methods.

Full Methods and any associated references are available in the online version of the paper at www.nature.com/nature.

Received 10 April; accepted 26 June 2007.

Published online 18 July 2007.

1. Versele, M. & Thorner, J. Some assembly required: yeast septins provide the instruction manual. *Trends Cell Biol.* **15**, 414–424 (2005).
2. Kinoshita, M. The septins. *Genome Biol.* **4**, 236 (2003).
3. Byers, B. & Goetsch, L. A highly ordered ring of membrane-associated filaments in budding yeast. *J. Cell Biol.* **69**, 717–721 (1976).
4. Haarer, B. K. & Pringle, J. R. Immunofluorescence localization of the *Saccharomyces cerevisiae* CDC12 gene product to the vicinity of the 10-nm filaments in the mother-bud neck. *Mol. Cell. Biol.* **7**, 3678–3687 (1987).
5. DeMarini, D. J. *et al.* A septin-based hierarchy of proteins required for localized deposition of chitin in the *Saccharomyces cerevisiae* cell wall. *J. Cell Biol.* **139**, 75–93 (1997).
6. Kozubowski, L. *et al.* A Bni4-Glc7 phosphatase complex that recruits chitin synthase to the site of bud emergence. *Mol. Biol. Cell* **14**, 26–39 (2003).
7. Kinoshita, M. Assembly of mammalian septins. *J. Biochem.* **134**, 491–496 (2003).
8. Macara, I. G. *et al.* Mammalian septins nomenclature. *Mol. Biol. Cell* **13**, 4111–4113 (2002).
9. Hall, P. A., Jung, K., Hillan, K. J. & Russell, S. E. H. Expression profiling the human septin gene family. *J. Pathol.* **206**, 269–278 (2005).
10. Kartmann, B. & Roth, D. Novel roles for mammalian septins: from vesicle trafficking to oncogenesis. *J. Cell Sci.* **114**, 839–844 (2001).
11. Hall, P. A. & Russell, S. E. H. The pathobiology of the septin gene family. *J. Pathol.* **204**, 489–505 (2004).
12. Kehlenbaumer, G. *et al.* Mutations in SEPT9 cause hereditary neuralgic amyotrophy. *Nature Genet.* **37**, 1044–1046 (2005).
13. Mitchison, T. J. & Field, C. M. Cytoskeleton: What does GTP do for septins? *Curr. Biol.* **12**, R788–R790 (2002).
14. Kinoshita, M., Field, C. M., Coughlin, M. L., Straight, A. F. & Mitchison, T. J. Self- and actin-templated assembly of mammalian septins. *Dev. Cell* **3**, 791–802 (2002).
15. Hsu, S. C. *et al.* Subunit composition, protein interactions, and structures of the mammalian brain sec6/8 complex and septin filaments. *Neuron* **20**, 1111–1122 (1998).
16. Surka, M. C., Tsang, C. W. & Trimble, W. S. The mammalian septin MSF localizes with microtubules and is required for completion of cytokinesis. *Mol. Biol. Cell* **13**, 3532–3545 (2002).
17. Joberty, G. *et al.* Borg proteins control septin organization and are negatively regulated by Cdc42. *Nature Cell Biol.* **3**, 861–866 (2001).
18. Frazier, J. A. *et al.* Polymerization of purified yeast septins — evidence that organized filament arrays may not be required for septin function. *J. Cell Biol.* **143**, 737–749 (1998).
19. Oegema, K., Desai, A., Won, M. L., Mitchison, T. J. & Field, C. M. Purification and assay of a septin complex from *Drosophila* embryos. *Methods Enzymol.* **298**, 279–295 (1998).
20. Field, C. M. *et al.* A purified *Drosophila* septin complex forms filaments and exhibits GTPase activity. *J. Cell Biol.* **133**, 605–616 (1996).
21. Vrabioiu, A. M., Gerber, S. A., Gygi, S. P., Field, C. M. & Mitchison, T. J. The majority of the *Saccharomyces cerevisiae* septin complexes do not exchange guanine nucleotides. *J. Biol. Chem.* **279**, 3111–3118 (2004).
22. Farkasovsky, M., Herter, P., Voss, B. & Wittinghofer, A. Nucleotide binding and filament assembly of recombinant yeast septin complexes. *Biol. Chem.* **386**, 643–656 (2005).
23. Sheffield, P. J. *et al.* Borg/septin interactions and the assembly of mammalian septin heterodimers, trimers, and filaments. *J. Biol. Chem.* **278**, 3483–3488 (2003).
24. Nguyen, T. Q., Sawa, H., Okano, H. & White, J. G. The *C. elegans* septin genes, *unc-59* and *unc-61*, are required for normal postembryonic cytokinesis and morphogenesis but have no essential function in embryogenesis. *J. Cell Sci.* **113**, 3825–3837 (2000).
25. Mendoza, M., Hyman, A. A. & Glotzer, M. GTP binding induces filament assembly of a recombinant septin. *Curr. Biol.* **12**, 1858–1863 (2002).
26. Huang, Y. W., Surka, M. C., Reynaud, D., Pace-Asciak, C. & Trimble, W. S. GTP binding and hydrolysis kinetics of human septin 2. *FEBS J.* **273**, 3248–3260 (2006).
27. Leipe, D. D., Wolf, Y. I., Koonin, E. V. & Aravind, L. Classification and evolution of P-loop GTPases and related ATPases. *J. Mol. Biol.* **317**, 41–72 (2002).
28. Scrima, A. & Wittinghofer, A. Dimerisation-dependent GTPase reaction of MnmE: how potassium acts as GTPase-activating element. *EMBO J.* **25**, 2940–2951 (2006).
29. Gasper, R., Scrima, A. & Wittinghofer, A. Structural insights into HypB, a GTP-binding protein that regulates metal binding. *J. Biol. Chem.* **281**, 27492–27502 (2006).
30. Low, C. & Macara, I. G. Structural analysis of septin 2, 6, and 7 complexes. *J. Biol. Chem.* **281**, 30697–30706 (2006).
31. Boehringer, D. *et al.* Three-dimensional structure of a pre-catalytic human spliceosomal complex B. *Nature Struct. Mol. Biol.* **11**, 463–468 (2004).
32. van Heel, M. & Frank, J. Use of multivariate statistics in analysing the images of biological macromolecules. *Ultramicroscopy* **6**, 187–194 (1981).
33. Chant, J. Septin scaffolds and cleavage planes in *Saccharomyces*. *Cell* **84**, 187–190 (1996).
34. Vrabioiu, A. M. & Mitchison, T. J. Structural insights into yeast septin organization from polarized fluorescence microscopy. *Nature* **443**, 466–469 (2006).

Supplementary Information is linked to the online version of the paper at www.nature.com/nature.

Acknowledgements Data collection was done at the Swiss Light Source, beam line X10SA, Paul Scherrer Institute, Villigen, Switzerland, and we thank the beam line staff for assistance. We would like to thank I. Vetter, I. Schlichting, T. Meinhardt, W. Blankenfeldt, N. Schrader, E. Hofmann, K. Kühnel, A. Scrima, R. Gasper and R. Rose for data collection and crystallographic advice. M.S. and F.H. thank the International Max Planck Research School for financial support. This work was supported by the 3D Repertoire project, within the EU Sixth Framework Program, and the Fondation Louis-Jeantet.

Author Contributions M.S. purified and crystallized SEPT2-315 and the human septin complex and solved the structures. M.F. made the human septin complex constructs, developed the purification procedure and purified the yeast septin complex used in the electron microscopy. F.H. and H.S. did the electron microscopy analysis. D.K. made SEPT2-315 mutants. M.W. assisted M.S. throughout data collection and structure determination. I.G.M. provided the clones for human septins, and valuable hints. A.W. supervised the project and wrote the paper. All authors discussed the results and commented on the manuscript.

Author Information The atomic coordinates of SEPT2-315 and the human septin complex are deposited in the Protein Data Bank with accession numbers 2QA5 and 2QAG, respectively. Reprints and permissions information is available at www.nature.com/reprints. The authors declare no competing financial interests. Correspondence and requests for materials should be addressed to A.W. (alfred.wittinghofer@mpi-dortmund.mpg.de).

METHODS

Purification and crystallization of SEPT2-315. Wild type and mutant human septin2-315 (amino acids 1–315) were expressed in *E. coli* BL21(DE3) as a GST-fusion protein. After overnight induction at 28 °C, the cell lysate was purified using GSTrap-FF columns (Amersham). SEPT2-315 was cleaved from the tag using PreScission protease and purified using a Superdex S-200 column. The low molecular mass fraction eluted in two peaks with apparent molecular masses of ~72 kDa and ~36 kDa. A large portion eluted in the size exclusion volume as higher oligomers, which was discarded. The monomer–dimer fraction was used for analytical gel filtration described in Methods Summary; the dimer fraction was used for crystallization. Standard buffer used throughout was 50 mM Tris/HCl pH 7.5, 150 mM NaCl, 5 mM MgCl₂ and 5 mM DTE. Selenomethionine protein was purified as above using cells grown in minimal media supplemented with selenomethionine.

Twenty milligrams per millilitre protein with 1 mM GDP was used for crystallization. Initial crystallization conditions were obtained by a semi-automatic nanolitre sitting-drop screening using commercial Qiagen/Nxtal screening kits, by combining protein and reservoir solution in a 1:1 ratio. Crystallization conditions were optimized by hanging-drop vapour diffusion in 24-well plates at 20 °C. Suitable crystals of SEPT2-315 were obtained in 2 weeks. The reservoir solution contained 5% polyethylene glycol 6000, 0.1 M bicine pH 9.0 and 0.1 M glycine. The crystals were transferred to a cryoprotectant solution containing 25% ethylene glycol together with the mother liquor and immediately flash-frozen in liquid nitrogen. A similar strategy was used to obtain selenomethionine protein crystals, and a SAD data set to 3.4 Å resolution was collected at beam line X10SA Swiss Light Source, Villigen, Switzerland at 100K. Data processing was carried out using the XDS software package³⁵. The crystals belonged to space group C2 with unit cell dimensions $a = 163$ Å, $b = 54$ Å, $c = 110$ Å, $\alpha = 90^\circ$, $\beta = 128^\circ$, $\gamma = 90^\circ$.

Structure determination of SEPT2-315. SAD data from the selenomethionine protein crystals were used to obtain phases. Eight selenomethionine sites were found using SHELXD³⁶ and these sites were fed into SOLVE³⁷ for phase calculation and subsequently RESOLVE³⁷ for solvent flattening. After a cycle of further density modification using the program DM of the CCP4 package³⁸, the electron density was used for manual building using COOT³⁹. Refinement was done with REFMAC5⁴⁰ and the final R_{work} and R_{free} values are 28% and 31.4%, respectively (see Table 1). The final model includes 469 amino acids out of 630 (for dimer), which were residues 20–62, 78–101, 116–139, 141–214, 224–246, 253–268 and 270–304. The model exhibits excellent geometry with 89.4% in favourable, 10.4% in allowed and no residues in disallowed regions of the Ramachandran plot (Supplementary Table 1). Buried surface areas were calculated with CNS⁴¹ using a default probe radius of 1.4 Å.

Purification and crystallization of the human SEPT2–SEPT6–SEPT7 complex. The human septin complex was purified from *E. coli* Rosetta carrying two plasmids as described for recombinant yeast septins²². SEPT6 and His-SEPT7 are expressed from a bicistronic vector and MBP–SEPT2 from a second compatible vector. After overnight induction at 28 °C, the human septin complex was purified using Ni-NTA and amylose columns with 25 mM sodium-phosphate pH 7.8, 8% glycerol, 300 mM NaCl, 5 mM MgCl₂ and 5 mM β -mercaptoethanol as buffer. Tags were cleaved using thrombin and final purification was via gel filtration using Sephacryl 400 with 20 mM HEPES pH 8.0, 500 mM NaCl, 5 mM MgCl₂ and 5 mM DTE as buffer. The hexameric fractions were collected, concentrated by ultrafiltration to 10 mg ml⁻¹ and stored at -80 °C. Selenomethionine protein complex was purified as above after growing the cells in minimal media supplemented with selenomethionine. Crystallization trials were done using wild-type human septin complex as well as a mutant in which 57 C-terminal residues of SEPT7 were deleted (human septin complex SEPT7-361). These complexes produced the same elution pattern, crystallized under the same conditions and produced a very similar diffraction pattern.

Crystals of the human septin complex were obtained at 20 °C by the hanging-drop vapour diffusion method with 1.5 μ l protein samples mixed with an equal volume of reservoir solution containing 1.4 M ammonium sulphate, 0.1 M Bis-Tris-propane pH 6.5 in 2–3 days. Crystals were collected after a week and transferred to a cryoprotectant solution containing glycerol along with the mother liquor. Transferring the crystals in the cryoprotectant using small gradual steps to a final concentration of 20% glycerol improved the diffraction quality of the crystals. Initial selenomethionine protein crystals were obtained by streak seeding with native crystals and additionally 10 mM TCEP was added to the mother liquor. These initial crystals were used for further micro- and macro-seeding to obtain diffraction quality crystals. Crystals were derivatized with 1–2 mM of the respective heavy atom compounds (see Supplementary Table 3) in the mother liquor over a period of 12–24 h. Several data sets were collected for the native-,

selenomethionine- and heavy-atom-soaked crystals at beam line X10SA SLS, Villigen, Switzerland at 100K. Crystals exhibited a high degree of anisotropy. Data processing was done using the XDS software package³⁵. Crystals belong to the $P4_322$ space group with unit cell constants $a = b = 252$ Å, $c = 156$ Å, $\alpha = \beta = \gamma = 90^\circ$ with a solvent content of 72% and Matthews' coefficient of 4.3 Å³ Da⁻¹ (estimated for one hexamer per asymmetric unit).

Structure determination of the human septin complex. Initial phases were obtained using SOLVE³⁷ and RESOLVE³⁷ from selenomethionine crystals. The program identified only 16 sites out of 82 (expected for one hexamer) and the resultant electron density looked like a tube mesh. Similar output was seen for Ta₆Br₁₄ crystals with one cluster per asymmetric unit. These weak phases were used for the cross validation of selenomethionine and Ta₆Br₁₄ phases and were also used to calculate an anomalous Fourier map from the SAD data sets collected from di- μ -iodobis(ethylenediamine) diplatinum(II) nitrate (PIP)-, HgCl₂- and K₂PtCl₄-soaked crystals (Supplementary Table 3). The sites were hand-picked manually and fed into SOLVE for phase calculation using the MIRAS approach with five derivatives along with native, which gave good experimental phases up to 5.5 Å, and the resultant electron density after RESOLVE showed the secondary structural elements (Supplementary Fig. 3a).

In another approach, molecular replacement was performed with the native 4 Å data using MOLREP³⁸ and a monomeric poly-alanine structure of SEPT2 as a search model. The resultant replacement solution contained three monomers where the trimeric model from MOLREP fitted very well with the experimentally phased electron density (Supplementary Fig. 3b), supporting the notion that a trimer not a hexamer occupies the asymmetrical unit. The crystals thus have an unusually high solvent content of 85.7% and Matthews' coefficient of 8.7 Å³ Da⁻¹.

In order to identify the position of each individual polypeptide, we used the information provided by selenomethionine, as the three septins contain different numbers of methionines in different positions of the polypeptide chain (Supplementary Fig. 1). The locations of SEPT2, SEPT6 and SEPT7 in the asymmetrical unit could be unequivocally identified (Fig. 2a). The initial trimeric model (molecular replacement output) was used to generate phases and the model-derived phases were combined with experimental phases and extended to 4 Å. CNS⁴¹ composite omit maps were generated to locate the missing parts. After several cycles of rebuilding, a model was generated where SEPT2 was taken from the SEPT2 G-dimer model, SEPT6 and SEPT7 were built using manual guidance by the replacement model and the methionine positions, side chains were placed confidently around the methionine positions, and the rest was built as poly-alanine stretches because the side chains were not visible. Initial refinement was done without nucleotide; where positive density was observed in the nucleotide-binding regions, nucleotides were placed in those densities and included in the final refinement. Refinement was done using REFMAC⁴⁰ with translation, libration, screw-rotation displacement (TLS) refinement, and the final R_{work} and R_{free} values were 37.5% and 39.2%, respectively (Table 1). Ramachandran statistics were obtained using PROCHECK (<http://www.biochem.ucl.ac.uk/~roman/procheck/procheck.html>). $F_o - F_c$ maps shown in Fig. 2c were calculated by removing the nucleotide from the respective subunit. Figures were generated using PYMOL⁴².

Electron microscopy. Human septin complex was incubated in high salt buffer (20 mM HEPES pH 8.0, 800 mM NaCl, 5 mM MgCl₂, 10 mM dithiothreitol). Human septin complex containing the MBP–SEPT2 fusion construct was centrifuged in a glycerol gradient (20 mM HEPES pH 8.0, 600 mM NaCl, 5 mM MgCl₂, glycerol 5–20%) for 20 h at 92,000g and 4 °C. After centrifugation and fractionation, samples were fixed in 0.05% glutaraldehyde to stabilize the complex and to obtain images suitable for image processing. Because complex formation capacity in the MBP–SEPT2 fusion complex is reduced, centrifugation and fixation at slightly lowered salt was necessary to obtain stable hexameric septin complexes. High salt conditions without gradient centrifugation and chemical stabilization did result in fragmentation of septin complexes containing the MBP–SEPT2 fusion complex. Lower salt conditions without gradient centrifugation and chemical stabilization, on the other hand, yielded a highly heterogeneous complex population (data not shown). The human septin complex lacking the coiled coils (ACC) and yeast septin complex consisting of Cdc3–Cdc10–Cdc11–Cdc12 was prepared for electron microscopy as described for the unmodified human septin complex. All samples were applied on a single carbon film on an electron microscopy grid covered with carbon support film (containing 1–4 μ m holes) and negatively stained with uranyl formate. Low-dose images were taken on a 4k \times 4k CCD camera in a Philips CM200 FEG electron microscope. Images of the yeast septin complex were recorded in a Philips CM120 electron microscope. Class averages of selected particles were computed after alignment by classification⁴³ and subsequent rounds of multivariate statistical analysis⁴⁴ and classification⁴⁵, and multi-reference alignment⁴⁶. The average number of members per class was 40 images. Most (~80%) particles were

intact hexamers. Within the data sets, 10–20% of class averages containing non-hexameric complexes were detected, which can be attributed to a remaining heterogeneous subpopulation of complexes and to flexibility of the SEPT2–SEPT6–SEPT7 complex. For image processing, IMAGIC-5 software was used⁴⁷. Image alignment was done by exhaustive alignment using re-sampling to polar coordinates⁴⁶. For particle statistics see Supplementary Table 4.

35. Kabsch, W. Automatic processing of rotation diffraction data from crystals of initially unknown symmetry and cell constants. *J. Appl. Cryst.* **26**, 795–800 (1993).
36. Schneider, T. R. & Sheldrick, G. M. Substructure solution with SHELXD. *Acta Crystallogr. D* **58**, 1772–1779 (2002).
37. Terwilliger, T. C. SOLVE and RESOLVE: automated structure solution and density modification. *Methods Enzymol.* **374**, 22–37 (2003).
38. CCP4. The CCP4 (Collaborative Computational Project Number 4) suite: programs for protein crystallography. *Acta Crystallogr. D* **50**, 760–763 (1994).
39. Emsley, P., & Cowtan, K. Coot: Model-building tools for molecular graphics. *Acta Crystallogr. D* **60**, 2126–2132 (2004).
40. Murshudov, G. N., Vagin, A. A. & Dodson, E. J. Refinement of macromolecular structures by the maximum-likelihood method. *Acta Crystallogr. D* **53**, 240–255 (1997).
41. Brunger, A. T. *et al.* Crystallography & NMR system: A new software suite for macromolecular structure determination. *Acta Crystallogr. D* **54**, 905–921 (1998).
42. DeLano, W. L. The PyMOL Molecular Graphics System (<http://www.pymol.org>) (2006).
43. Dube, P., Tavares, P., Lurz, R. & van Heel, M. The portal protein of bacteriophage SPPI: a DNA pump with 13-fold symmetry. *EMBO J.* **12**, 1303–1309 (1993).
44. van Heel, M. & Frank, J. Use of multivariate statistics in analysing the images of biological macromolecules. *Ultramicroscopy* **6**, 187–194 (1981).
45. van Heel, M. Classification of very large electron microscopical image data sets. *Optik* **82**, 114–126 (1989).
46. Sander, B., Golas, M. M. & Stark, H. Corrim-based alignment for improved speed in single-particle image processing. *J. Struct. Biol.* **143**, 219–228 (2003).
47. van Heel, M., Harauz, G., Orlova, E. V., Schmidt, R. & Schatz, M. A new generation of the IMAGIC image processing system. *J. Struct. Biol.* **116**, 17–24 (1996).

ARTICLES

Structure of acid-sensing ion channel 1 at 1.9 Å resolution and low pH

Jayasankar Jasti¹, Hiroyasu Furukawa^{1†}, Eric B. Gonzales¹ & Eric Gouaux^{1,2}

Acid-sensing ion channels (ASICs) are voltage-independent, proton-activated receptors that belong to the epithelial sodium channel/degenerin family of ion channels and are implicated in perception of pain, ischaemic stroke, mechanosensation, learning and memory. Here we report the low-pH crystal structure of a chicken ASIC1 deletion mutant at 1.9 Å resolution. Each subunit of the chalice-shaped homotrimer is composed of short amino and carboxy termini, two transmembrane helices, a bound chloride ion and a disulphide-rich, multidomain extracellular region enriched in acidic residues and carboxyl-carboxylate pairs within 3 Å, suggesting that at least one carboxyl group bears a proton. Electrophysiological studies on aspartate-to-asparagine mutants confirm that these carboxyl-carboxylate pairs participate in proton sensing. Between the acidic residues and the transmembrane pore lies a disulphide-rich 'thumb' domain poised to couple the binding of protons to the opening of the ion channel, thus demonstrating that proton activation involves long-range conformational changes.

Sensory perception, transduction and subsequent integration into the central nervous systems of mammals and other animals are processes mediated, to a large degree, by cell surface receptors. Acid-sensing ion channels (ASICs) are cation-selective, ligand-gated ion channels activated by protons and are an important family of receptor/ion channel proteins involved in the detection and processing of sensory information^{1,2}. Found in multicellular eukaryotes, ASICs are related in amino acid sequence to epithelial sodium channels (ENaCs), the degenerin channels (DEG) of *Caenorhabditis elegans* and the FMRF-amide peptide-gated channels (FaNaCh) of molluscs³. This amalgamation of diverse receptors is involved in the sensing of proton gradients (ASICs)^{3–5}, of mechanosensation (DEGs)⁶, of peptide neurotransmitters (FaNaCh channels)⁷ and in the regulation of sodium homeostasis (ENaCs)³.

Depolarization of neurons on brief excursions to low pH provided the first clues to the existence of proton-activated ion channels⁴, and subsequent cloning studies revealed four genes that give rise to six ASIC (also called ACCN) isoforms (ASIC1a, ASIC1b, ASIC2a, ASIC2b, ASIC3 and ASIC4)^{5,8–12} in mammals. ASICs are found throughout the mammalian central and peripheral nervous systems^{13–15} with ASIC1a, ASIC2a and ASIC2b present in the brain^{10,14,16}, and ASIC1a, ASIC1b, ASIC2a, ASIC2b and ASIC3 abundant in the sensory neurons of the peripheral nervous system^{10,13,17}. Consistent with the roles of ASICs in sensory perception and integration, ASIC1a participates in spatial learning and memory¹⁸, whereas ASIC3 mediates the sensation of ischaemic cardiac pain¹⁹. Mounting evidence suggests that activation of ASIC1a in the brain as a consequence of stroke leads to ischaemic cell death²⁰. Inhibition of ASIC1a by psalmotoxin 1 greatly ameliorates stroke-induced cell damage and death²⁰, implying that antagonists of ASIC1a hold promise as therapeutic agents.

Hallmarks of proton-activated ASIC gating are a steep dependence on proton concentration, block by amiloride, sodium selectivity and variations in the extents and rates of desensitization from subtype to subtype²¹. Calcium occupies a pivotal role in the gating of ASICs by stabilizing the closed, resting state and accelerating recovery from

desensitization^{22–24}. All subtypes except ASIC2b and ASIC4 assemble to form functional homomeric channels, although both heteromeric and homomeric channels are found under native conditions^{17,25,26}. Estimates of subunit stoichiometry for ASICs and the related ENaC, DEG and FMRF-amide ion channel proteins vary widely, ranging from complexes as small as tetramers²⁷ to assemblages of nine subunits²⁸. To define the architecture of ASICs and related receptors, and to elucidate the molecular principles of pH-dependent gating, we embarked on the crystallographic and electrophysiological studies described here.

Function and structure determination

Chicken ASIC1 (ref. 29) forms proton-activated ion channels with a pH₅₀ (pH of half-maximal activation) of ~6.7 and a Hill coefficient (*n*) of ~9 (Fig. 1a and Supplementary Fig. 1), and it also expresses robustly and exhibits a favourable, symmetric fluorescence-detection size-exclusion chromatography (FSEC) profile³⁰, which together indicate that it is a promising candidate for functional and crystallographic studies (Supplementary Fig. 2). On prolonged exposure to low pH the steady-state current is negligible, thus suggesting that chicken ASIC1 enters a thermodynamically favourable desensitized state. Crystallization of chicken ASIC1 requires low pH (pH 5–6) and the removal of 25 N-terminal and 64 C-terminal residues (hereafter referred to as ΔASIC1). Even though ΔASIC1 elicits abundant expression and forms a trimer (Supplementary Figs 2 and 3), like the full-length receptor, it does not elicit proton-induced currents in patch-clamp studies, perhaps because it is arrested in a closed, desensitized-like state.

ΔASIC1 crystallizes in space group *P*₂₁ with two trimers in the asymmetric unit. Most of the six subunits have strong electron density (Supplementary Fig. 4) starting at about residue 40 and ending near residue 460. The final refined structure has a conventional *R*-factor of 0.21 and *R*_{free} of 0.23 (Supplementary Table 1). In the Ramachandran plot, 90% of the residues are in the most favoured region with no residues in the disallowed region. The trimer composed of subunits A, B and C has the strongest electron density in

¹Vollum Institute and ²Howard Hughes Medical Institute, Oregon Health and Science University, 3181 SW Sam Jackson Park Road, Portland, Oregon 97239, USA. †Present address: Cold Spring Harbor Laboratory, 1 Bungtown Road, Cold Spring Harbor, New York 11724, USA.

comparison to the second trimer (subunits D, E and F), and thus we use trimer ABC in our analysis.

Architecture

The Δ ASIC1 structure has a chalice-like shape with a large extracellular domain protruding as much as 80 Å from the membrane plane, a slender transmembrane domain, and a broadened 'base' defined by the cytoplasmic N and C termini (Fig. 1b, c). In the crystal, the triangular extracellular domains are packed in tile-like, two dimensional layers, with interactions between the layers mediated by the transmembrane domains and the truncated N and C termini (Supplementary Fig. 5). Even though the subunits in the extracellular domain are related by a three-fold axis of molecular symmetry, this non-crystallographic symmetry breaks down in the transmembrane domains.

The transmembrane domain of Δ ASIC1 is defined by two long α -helices from each of the three subunits. On the cytoplasmic side of the membrane, the termini are frayed and we do not see well ordered protein structure, even though we know from amino acid

sequencing and mass spectrometry that additional disordered residues are present. Emerging from the extracellular side of the membrane, however, the ends of transmembrane segments 1 and 2 are well defined and the transmembrane helices are clearly coupled to long β -strands in the large extracellular domains. Surrounding this 'wrist'-like junction between the transmembrane and extracellular domains are well ordered 'loops' that probably have a key role in coupling conformational changes in the extracellular domain to the ion channel pore.

Shaped like a funnel, the trimeric extracellular domain is composed of a core of three large β -sheets, one per subunit, and decorating this central core are three smaller β -sheet and α -helical domains. The extracellular domain is replete with crevices and cavities, yet in this low-pH structure there is no continuous pore along the three-fold axis through which ions might pass, and thus ions may access the ion channel by way of fenestrations near the extracellular membrane surface. There are extensive contacts between subunits in both the extracellular and transmembrane domains, thus reinforcing our contention that ASICs, ENaCs and degenerin ion channel proteins are

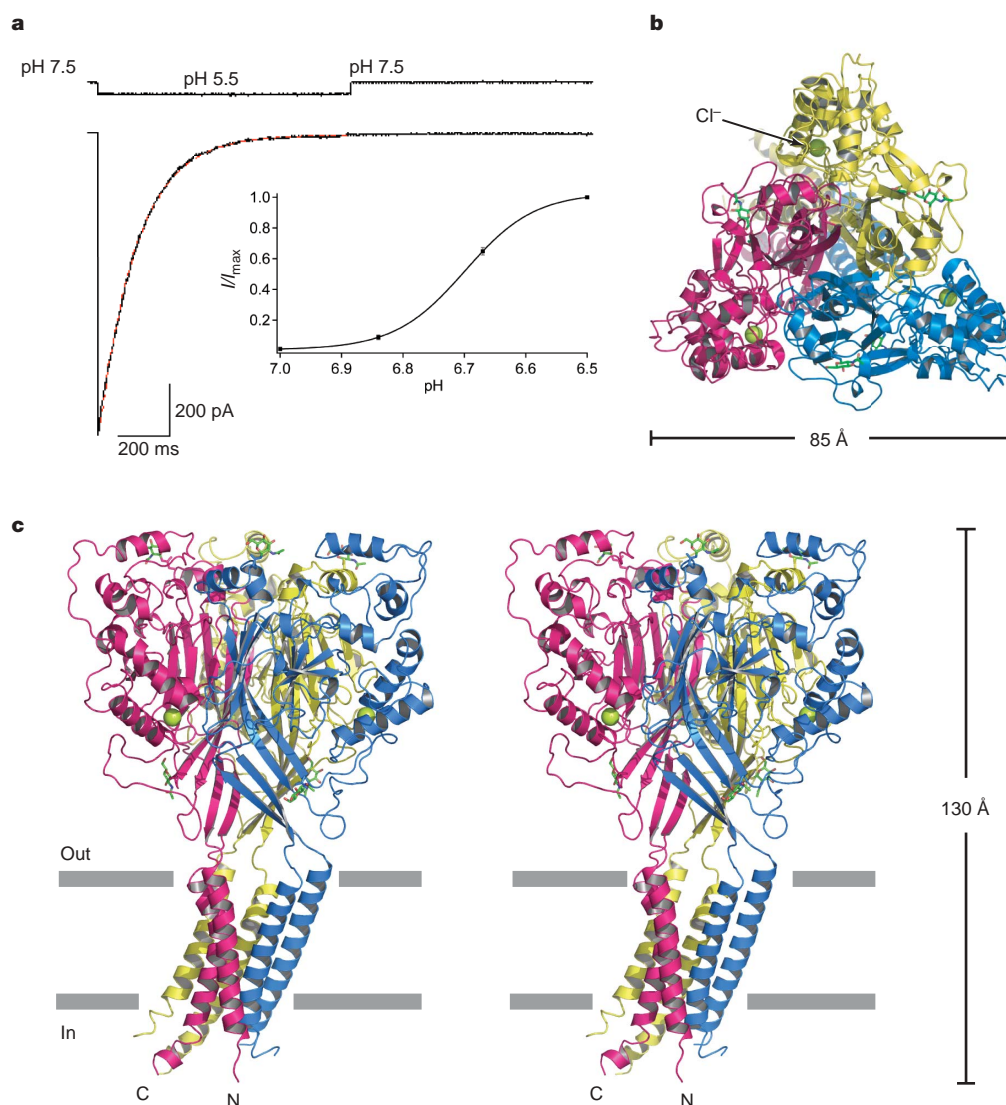


Figure 1 | Function and structure of chicken ASIC1. **a**, Outside-out, rapid solution exchange patch-clamp recording of currents from full-length chicken ASIC1. Shown in red is a fit of the current decay to a single exponential function. Inset shows dose-response analysis of currents elicited from chicken ASIC1 channels in outside-out patches. The mid-point of the titration (pH_{50}) is pH 6.7 and the curve has a Hill slope of about 9. Data points are from at least three patches and were fit to the Hill equation.

Uncertainties are expressed as standard error of the mean (s.e.m.). **b**, View of the homotrimeric Δ ASIC1 structure parallel to the molecular three-fold axis from the extracellular side of the membrane. Each crystallographically independent subunit is in a different colour, a single chloride ion per subunit is shown as a green sphere and N-linked carbohydrate is shown in stick representation. **c**, Stereoview of the homotrimeric Δ ASIC1 structure viewed parallel to the membrane plane.

trimers. Indeed, light-scattering and cross-linking studies on Δ ASIC1 (Supplementary Fig. 3), as well as a recent study on the epithelial sodium channel³¹, reinforce the realization that receptors in this superfamily are homo- or heterotrimers and not tetramers^{27,32} or higher ordered assemblages^{28,33}.

Protomer structure

The domain arrangement in Δ ASIC1 subunits resembles an up-right forearm and clenched hand, with the transmembrane, transmembrane–extracellular domain junction and the extracellular domain akin to the forearm, wrist and hand, respectively (Fig. 2a). The palm domain within the extracellular ‘hand’ is the central feature of each subunit. Not only does this seven-strand sheet span nearly the entire height of the extracellular domain, but it also directly connects to transmembrane 1 (TM1) and TM2 through β -strands 1 and 12, respectively, and to the thumb domain, by way of β -strands 9 and 10, connections that are likely to have pivotal roles in the conformational changes associated with channel gating. Above the palm domain are two short helices ($\alpha 6$ and $\alpha 7$; knuckle domain) together with a few short helices and non- α - and non- β -structure comprising what we refer to as the finger domain. The tip of the finger domain touches the disulphide-bond-rich thumb domain and these regions, together with the palm domain, surround the small 5-strand β -ball domain.

Rich in cysteine residues, the extracellular domain contains seven disulphide bonds in the thumb, palm and β -ball domains. The significance of these molecular staples is underscored by the fact that the associated cysteine residues are conserved throughout ASIC, ENaC, FaNaCh and DEG proteins (Supplementary Fig. 6). In the Δ ASIC1 thumb domain, the five disulphides are located such that one can draw a nearly straight line through all of the bridges, from the interface of the thumb and finger domains to a highly conserved Trp residue located at the wrist junction (Fig. 2a). We suggest that the disulphide bonds in the thumb provide structural integrity, thus facilitating faithful transduction of conformational changes to the transmembrane pore.

In electron density maps we clearly see the transition between the transmembrane domain and the β -strands of the extracellular palm domain, a structural feature present in other ligand-gated ion channels, such as the pre-TM1 ($\beta 10$) to M1 connection in the acetylcholine receptor³⁴. Even though only three and four residues are required in the transition between TM1 and $\beta 1$ (Leu 71–Pro 73) and $\beta 12$ and TM2 (Lys 423–Glu 426), respectively, these residues, together with their interacting neighbours, are probably crucial to the transduction of gating conformational changes.

The transmembrane domains of each subunit adopt markedly different conformations (Fig. 2b). Whereas the TM2 helices of subunits A and B have a substantial bend at Gly 435, the transmembrane helices of subunit C are nearly straight (Fig. 2b). Even though the asymmetry seen in trimer ABC is similar to that observed in the second crystallographically independent trimer DEF, the packing of the two trimers in the crystal lattice is also similar, and thus we cannot conclusively determine whether the asymmetry seen in the transmembrane domains is inherent to the trimer or is due to crystal lattice contacts.

Interfaces and cavities

Subunit–subunit interactions in the trimer are extensive and each subunit buries $\sim 4,852 \text{ \AA}^2$ of solvent-accessible surface area on trimer formation. The contacts between subunits are dominated by interactions between palm domains, between the palm domain of one subunit and the thumb of another, and to a lesser extent, between the knuckle and finger domains and between the palm and β -ball domain (Fig. 3a). The transmembrane domains also interact extensively, burying $\sim 1,071 \text{ \AA}^2$ of surface area, suggesting that the transmembrane domains also have an important role in the assembly and stability of the trimer. Because the intracellular termini are

disordered, we are limited in our understanding of how these regions contribute to subunit–subunit contacts.

There are three regions of subunit–subunit interaction in the extracellular domain that figure prominently in the structure (Fig. 3a). The first is near the wrist junction and involves intersubunit hydrogen bonds between Asp 79 of one subunit and His 74 and Gln 421 of an adjacent subunit. Previous studies have demonstrated that some of these residues shape the rate of desensitization in rat ASIC3 (ref. 35) and fish ASIC1 (ref. 36); in mouse ASIC2, mutation of the residue equivalent to His 74 to an alanine results in a receptor that is no longer activated by protons³⁷. A second prominent region involves multiple interactions between the loops of β -strands in the palm domain and the C terminus of helix $\alpha 5$ of the thumb domain in

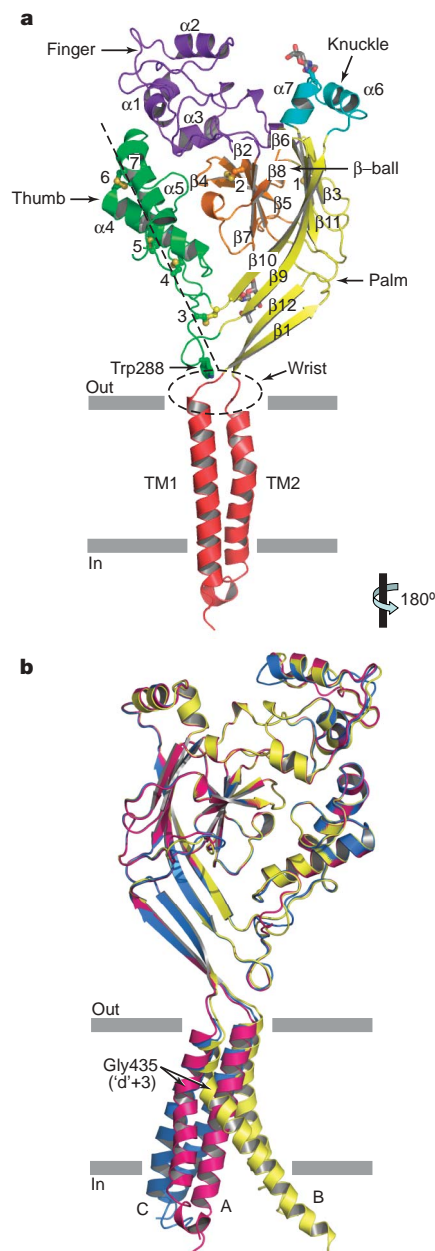


Figure 2 | Subunit structure and trimer assembly. **a**, Domain organization of a single subunit (A) and locations of disulphide bridges (labelled 1–7), glycosylation sites and Trp 288. **b**, Superposition of subunits B and C onto subunit A using main-chain atoms in the extracellular domains illustrates the asymmetry or variable conformation in the transmembrane domains. In parentheses is indicated the position of Gly 435 relative to the degenerin mutation position ('d'), equivalent to residue 432 in Δ ASIC1.

an adjacent subunit. Because the thumb is integral to pH-dependent gating (see below), we suggest that these palm-domain contacts are crucial to the allosteric conformational changes that accompany gating; Arg 176 caps $\alpha 5$ by hydrogen bonding to three consecutive carbonyl oxygens, and Lys 212 inserts deeply into the adjacent subunit to bind a buried chloride ion. The third series of interactions is near the 'top' of the extracellular domain and involves the envelopment of helix $\alpha 6$ from the knuckle by a concave surface on the neighbouring finger domain.

Solvent-filled cavities are unusual yet prominent features of the extracellular domain (Fig. 3b, c). The largest (approximately 233 \AA^3) is located on the molecular three-fold axis and is $\sim 15 \text{ \AA}$ above the extracellular end of the transmembrane domain (Fig. 3b). Three additional cavities (approximately 146 \AA^3), one per subunit, are located at about the same position along the three-fold axis, but displaced perpendicular to the three-fold axis by about 7 \AA (Fig. 3b). The cavities are lined primarily by polar or charged residues, together with a few hydrophobic amino acids (Fig. 3c), and are filled by ordered solvent. The cavity on the three-fold axis is replete with charged residues, as well as with close interactions between Glu 80 and Glu 417 (Fig. 3c). Chemical modification studies of rat ASIC3 show that the residue equivalent to Glu 80 of chicken ASIC1 becomes inaccessible on

receptor desensitization³⁵, thus suggesting that the cavity on the three-fold axis and the associated subunit–subunit interfaces undergo substantial conformational changes on receptor desensitization.

Transmembrane domain

The trimeric organization of ASICs distinguishes them from tetrameric glutamate receptors³⁸ and potassium channels³⁹, as well as from pentameric Cys-loop receptors⁴⁰, and raises the question of how the six transmembrane helices are arranged to form an ion-selective pore. The lipid-exposed, membrane-spanning region of Δ ASIC1 is composed of mostly aliphatic hydrophobic residues with interfacial regions defined by aromatic residues Phe 70 (outside) and Phe 51/Phe 453 (inside) (Fig. 4a). A V-shaped fenestration (Fig. 4a–c) between each subunit 'connects' bulk solution to the pore's extracellular vestibule, appears to extend $5\text{--}10 \text{ \AA}$ into the lipid bilayer, and is probably one route by which ions access the pore. Detergent headgroups occupy these crevices (Fig. 4d and Supplementary Fig. 7) and we suggest that in a lipid bilayer lipids form intimate interactions with the transmembrane helices, influencing the structure and gating of the ion channel.

The transmembrane domain has an hourglass-like shape with an overall, interior negative electrostatic potential (Fig. 4b), a feature that probably contributes to cation selectivity. The interior of the

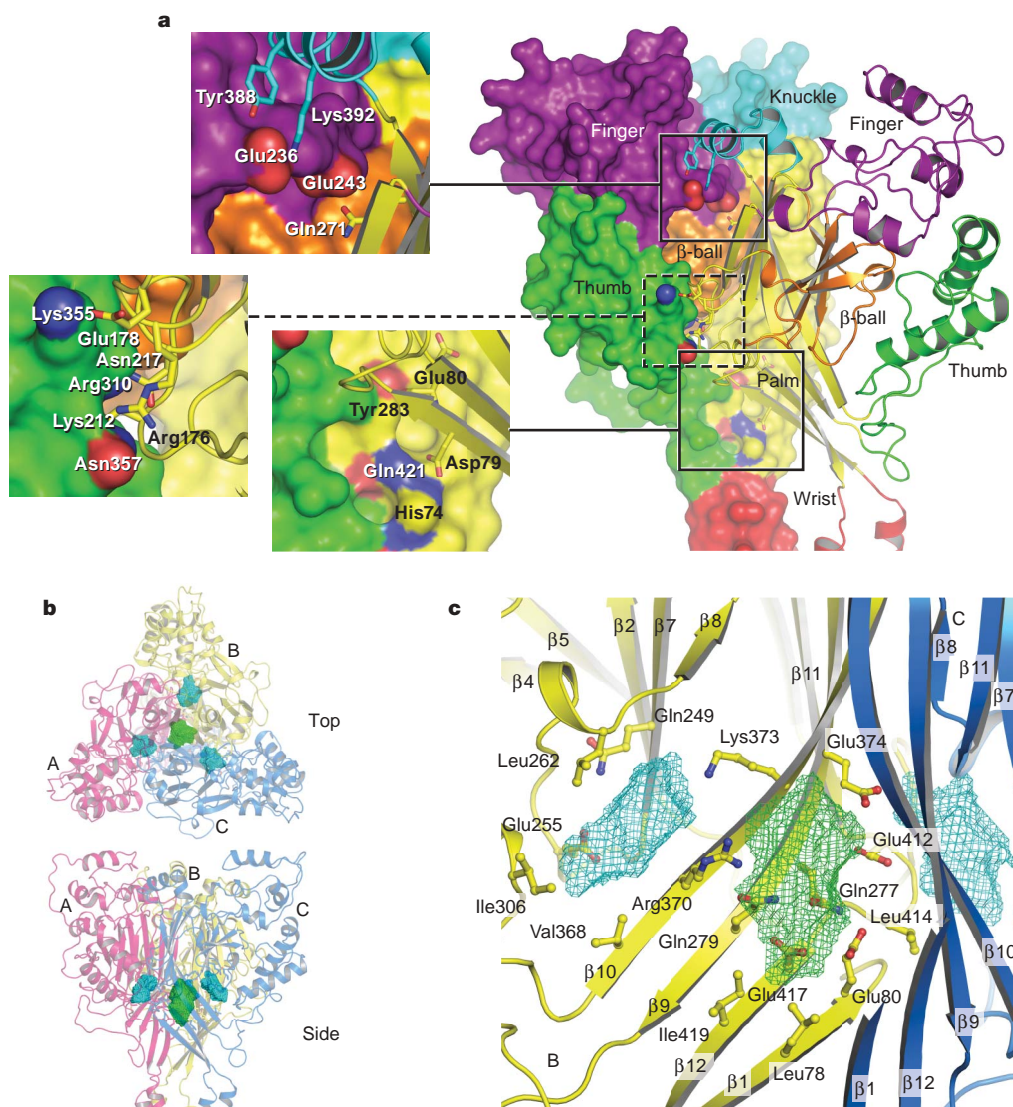


Figure 3 | Intersubunit interactions and solvent-filled cavities.

a, Intersubunit interactions between two subunits with one subunit shown in solvent-accessible surface and the other in ribbon representation, and with both subunits coloured according to domain as in Fig. 2a. Prominent

polar interactions are emphasized and illustrated in boxes. **b**, Views from the 'top' and the 'side' of the trimer showing the locations of one cavity in each subunit (cyan mesh) and between subunits, on the three-fold axis (green mesh). **c**, Close-up view of cavities and neighbouring residues.

pore is defined primarily by residues from TM2, although TM1 also lines portions of the pore, especially in the extracellular vestibule. At the extracellular side of the membrane the pore opens up to a diameter of about 12 Å and is lined by Tyr 425, Arg 65 and Asp 433, which together form an interacting triplet within each subunit (Fig. 4b, c). Glu 426 and Asp 433, implicated in open channel block by calcium⁴¹, are also located at the extracellular side of the transmembrane domain. Glu 426 is at the beginning of TM2 facing the extracellular medium, whereas Asp 433 faces towards the pore (Fig. 4c). Below the extracellular vestibule there are kinks in TM2 helices of $\sim 30^\circ$ and $\sim 33^\circ$ at Gly 435 of the A and B subunits, respectively. These kinks bring the TM2 helices closer together, causing the aliphatic side-chain atoms of Leu 440 to occlude the pore (Fig. 4c) near the conserved Gly-Ala-Ser motif in TM2. This region has an important role in ion selectivity in the ENaC/DEG family of ion channels⁴² and in Δ ASIC1 adopts a helical conformation that is completely different from the extended conformation of the Gly-Tyr-Gly region of the potassium channel selectivity filter⁴³. There is no evidence in electron density maps for bound ions, perhaps because the channel is trapped in a closed, desensitized-like state.

Below Leu 440, the pore opens up and conserved residues Trp 47 and Glu 451 face the putative ion permeation pathway (Fig. 4b, c), although the interactions of Trp 47 and Glu 451 with neighbouring residues vary from subunit to subunit because of the breakdown in the molecular three-fold axis of symmetry. Arg 44 also faces the pore, consistent with cysteine modification studies suggesting that this TM1 residue lines the ion channel⁴⁴.

ASIC, ENaC, FaNaCh and DEG proteins share many residues in common within TM2 (Supplementary Fig. 6) and therefore we suggest that these receptors have similar transmembrane architectures. Conserved residues are positioned either to the inside (towards the pore) or to the intra- and inter-transmembrane helix interfaces (Fig. 4c), contacts that are likely to change on channel gating. Indeed, the degenerin mutant phenotype, which results in a constitutively open ion channel, is the consequence of replacement of a conserved TM2 residue ('d' position) by bulky amino acids⁴⁵. In Δ ASIC1 the equivalent 'd' position residue, Gly 432, is located at an interface between TM2 and TM1 of adjacent subunits (Fig. 4d), indicating that introduction of large residues into this interface may profoundly perturb gating.

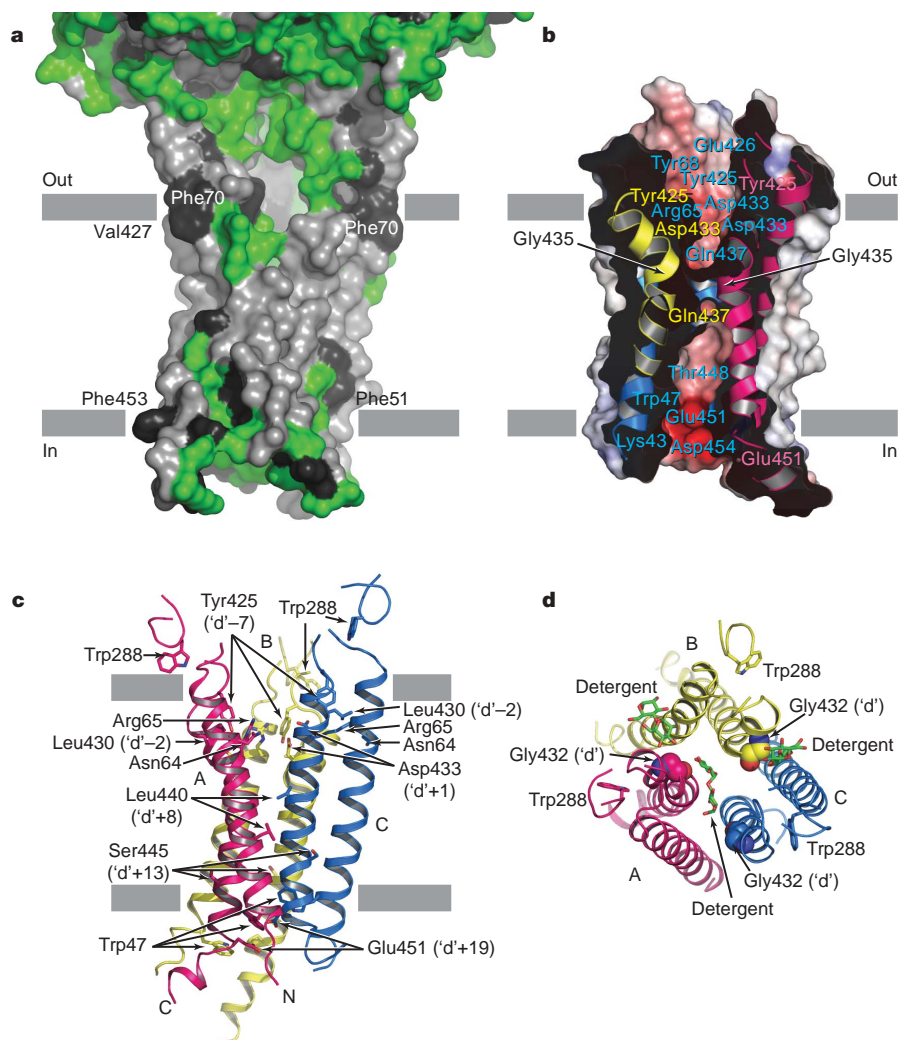


Figure 4 | Structure and key residues in the transmembrane domains.

a, Surface representation of the transmembrane region defining the membrane boundary. The aromatic residues are coloured in black, polar and charged residues in green, and aliphatic residues in grey. **b**, Surface potential representation of the transmembrane region sliced through the pore along the plane of membrane bilayer to show negative potential along the pore. Contours are from -8 (red) to $+8$ kT (blue) through 0 (white). **c**, View

parallel to the membrane plane. Carbon atoms of key residues are colour-coded according to subunit; oxygen atoms are red and nitrogen atoms are blue. Numbering in parentheses indicates residues in TM2 relative to the degenerin ('d') position. **d**, View from the extracellular side, along the pore axis, showing the location of Gly 432 ('d' position) and bound maltoside groups of detergent molecules.

Proton-binding sites

The Δ ASIC1 structure provides new clues to the location and molecular composition of the pH sensor in ASICs. Inspection of the electrostatic potential of Δ ASIC1 mapped onto the solvent-accessible surface reveals a highly negatively charged depression—deemed the acidic pocket—located far (~ 45 Å) from the transmembrane domain (Fig. 5a). This cavity is formed by intrasubunit contacts between the thumb, the β -ball and the finger domains, together with residues from the palm domain on an adjacent subunit.

Within the acidic pocket there are three pairs of unusually close (~ 2.8 Å) carboxyl-carboxylate interactions between the side chains of aspartate or glutamate residues (Fig. 5b). Two prominent pairs mediate interactions between the finger and thumb domains and are defined by contacts between Asp 238–Asp 350 and Glu 239–Asp 346. Glu 220 and Asp 408 (both located on palm of adjacent subunit) is a third pair in the acidic pocket and Glu 80 (palm) and Glu 417 (palm) define a fourth pair (Fig. 3c). Because Δ ASIC1 crystals diffract to 1.9 Å resolution and the extracellular domains are the most well ordered regions of the structure, the positions of these closely interacting acidic residues are accurately defined (Fig. 5b). Furthermore,

because the distances between the carboxyl groups of these residues are between 2.8–3.0 Å, at least one of the carboxyl groups must be protonated.

We suggest that the residues involved in these close carboxyl-carboxylate interactions define the primary sites for pH sensing in ASICs. Analysis of sequence alignments indicates that most of the residues involved in these close carboxyl pairs are conserved in ASICs but not in other members of the ENaC family (Supplementary Fig. 6). Carboxyl-carboxylate interactions are not uncommon in proteins⁴⁶, and from studies on the small molecules fumaric acid ($pK_a1 = 3.0$, $pK_a2 = 4.4$) and maleic acid ($pK_a1 = 1.9$, $pK_a2 = 6.1$), or on proteins such as the aspartyl proteases, positioning two carboxyl groups close in space shifts the pK_a of one carboxyl group 2–3 units more basic and the pK_a of the second carboxyl group 1–2 units more acidic. In ASICs there are multiple pairs of acidic residues, positioned close in space by way of the protein architecture, and the pK_a values of these residues are significantly perturbed from isolated aspartate and glutamate residues. At high pH, in the presence of calcium, some or all of these pairs may coordinate calcium, and in so doing stabilize the resting, closed state of the channel^{23,24,36,47}.

To test our hypothesis that the carboxyl-carboxylate interactions in the acidic pocket are involved in pH sensing, we neutralized one residue each in the Asp 238–Asp 350 and Glu 239–Asp 346 pairs. Neutralization of Asp 346 and Asp 350 had profound effects on either pH_{50} or apparent Hill coefficient (n), or both (Fig. 5c). Whereas the Asp 346 to Asn mutant shifts the dose–response curve to the right and reduces n from about 9 to 5, the Asp 350 to Asn mutation diminishes n to ~ 3 and has little effect on pH_{50} . These results confirm our identification of two key residues involved in proton sensing yet they also suggest that the pH sensor is distributed over multiple residues, perhaps including Glu 220 and Asp 408. Indeed, because the acidic residues identified here are also conserved in some proton-insensitive ASICs²⁹ (Supplementary Fig. 6), additional residues must participate in either proton binding or in subsequent conformational changes. Nevertheless, the protonation of at least one acidic residue in the Asp 238–Asp 350 and Glu 239–Asp 346 pairs, together with the observation that the ion channel is closed, supports our contention that this low-pH structure represents a desensitized or desensitized-like state.

Chloride-binding site

In $F_o - F_c$ maps we observed strong spherical electron density that we suspected might be a chloride ion, subsequently confirmed by anomalous difference Fourier maps calculated using data from bromide-soaked crystals (Supplementary Fig. 8). The chloride ion site is located in between the two helices ($\alpha 4$, $\alpha 5$) of the thumb domain and ~ 10 Å below Asp 350, one of the residues implicated in proton binding and pH-dependent activation (Fig. 5d). Coordination of the chloride is provided by Arg 310 (NE and NH1) and Glu 314 (OE2) from helix 4, via Lys 212 (NZ) from an adjacent subunit (Supplementary Fig. 8) and by van der Waals interactions from the side chains of Leu 352, Val 353 and Cys 360. What is the significance of the chloride site in ASICs? The conservation of residues involved in chloride coordination (Supplementary Fig. 6) suggests that the chloride site is important for channel function or assembly. Because Lys 212 from an adjacent subunit reaches deeply into the neighbouring subunit to bind to the chloride ion, and Lys 212 is near residues that have already been implicated in channel function, we suggest that chloride may have a crucial role in assembly and gating of ASICs.

Mechanism

This Δ ASIC1 structure yields multiple insights into the architecture and mechanism of ASICs and its orthologous ion channel relatives. First, subunit stoichiometry is trimeric, and thus the obligate heteromeric ENaCs are almost certainly trimers, defined by a $\alpha_1\beta_1\gamma_1$ stoichiometry. Second, the large extracellular portion of Δ ASIC1 polypeptide is composed of multiple domains that together form a

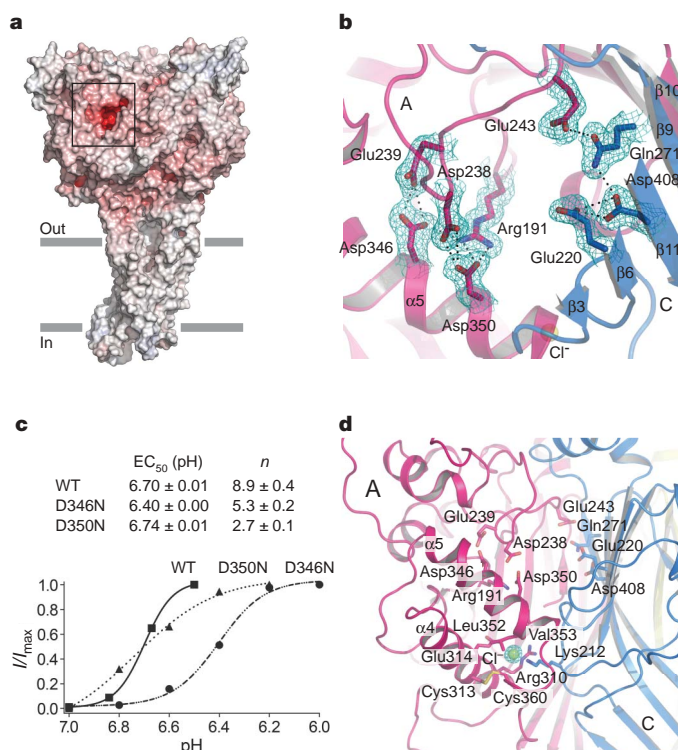


Figure 5 | Proton- and chloride-binding sites. **a**, Electrostatic potential mapped onto the solvent-accessible surface of the Δ ASIC1 trimer highlights a highly negative cavity in the extracellular domain (boxed region). Contours are from -40 (red) to $+40$ kT (blue) through 0 (white). **b**, Key acidic and interacting residues in the acidic cavity outlined in **a**. Electron densities for acidic residue pairs and neighbouring amino acids are shown in cyan mesh contours. Key interactions are shown as dotted lines. The map was calculated using $F_o - F_c$ coefficients and phases from the refined structure but with the residues omitted from the F_c calculation. The map is contoured at 2σ . **c**, pH dose–response curves for the wild type (WT), Asp 346 to Asn (D346N) mutant and Asp 350 to Asn (D350N) mutant obtained from outside-out patch-clamp recordings under conditions of rapid solution exchange. Data are from five and three separate patches for kinetic and dose–response experiments, respectively. Student's t -test analysis shows that the differences in pH_{50} and n for the wild-type and mutant channels are statistically significant (all P -values < 0.05). Uncertainties are expressed as s.e.m. **d**, The chloride-binding site is underneath $\alpha 5$, near acidic residues implicated in pH-dependent gating, and close to a subunit interface. Electron density (cyan mesh; 1σ) was calculated using $2F_o - F_c$ coefficients and phases from the final refined structure.

complex structure rich in cavities and protrusions, features probably present in ENaC, DEG and FaNaCh channels, and perhaps prominent 'hand-holds' for additional interacting proteins. Third, because the crystals of Δ ASIC1 diffract to high resolution, we identified multiple close acidic residue pairs as proton-binding sites, thus demonstrating that the pH-sensing sites are distributed in primary structure and three-dimensional space, far from the channel region.

How is proton binding at these distant sites translated into channel gating? We suggest that the disulphide-rich thumb domain undergoes movement on proton binding/unbinding and that these movements are transmitted to the ion channel transmembrane domain by way of primarily non-covalent interactions, mediated by residues at the base of the thumb (Fig. 6a, b, Supplementary Fig. 9 and Supplementary Movie). Trp 288 (thumb) may act like a ball sitting in a socket-like joint of the transmembrane domain and perhaps when the thumb domain moves, its movement is coupled to the transmembrane domain by way of this thumb–transmembrane domain ball-and-socket joint.

METHODS SUMMARY

Δ ASIC1 was expressed in Sf9 cells and purified using TALON and size-exclusion chromatography. Selenomethionine-labelled protein was purified with modifications of previously described protocol⁴⁸. Crystals were obtained in 100 mM

N-(2-acetamido)iminodiacetic acid (pH 6.5), 100 mM MgCl_2 and 10–14% PEG6000 (final pH 5.6). Phases were obtained from a platinum derivative and were improved by density modification. Patch-clamp recordings were done in HEK293 cells 24–48 h after transfection with plasmid-encoded chicken ASIC1.

Full Methods and any associated references are available in the online version of the paper at www.nature.com/nature.

Received 4 June; accepted 10 August 2007.

- Krishtal, O. The ASICs: Signaling molecules? Modulators? *Trends Neurosci.* **26**, 477–483 (2003).
- Lingueglia, E. Acid sensing ion channels in sensory perception. *J. Biol. Chem.* **282**, 17325–17329 (2007).
- Kellenberger, S. & Schild, L. Epithelial sodium channel/degenerin family of ion channels: a variety of functions for a shared structure. *Physiol. Rev.* **82**, 735–767 (2002).
- Krishtal, O. A. & Pidoplichko, V. I. A receptor for protons in the nerve cell membrane. *Neuroscience* **5**, 2325–2327 (1980).
- Waldmann, R., Champigny, G., Bassilana, F., Heurteaux, C. & Lazdunski, M. A proton-gated cation channel involved in acid-sensing. *Nature* **386**, 173–177 (1997).
- O'Hagan, R. & Chalfie, M. Mechanosensation in *Caenorhabditis elegans*. *Int. Rev. Neurobiol.* **69**, 169–203 (2006).
- Lingueglia, E., Deval, E. & Lazdunski, M. FMRFamide-gated sodium channel and ASIC channels: a new class of ionotropic receptors for FMRF-amide and related peptides. *Peptides* **27**, 1138–1152 (2006).
- Chen, C. C., England, S., Akopian, A. N. & Wood, J. N. A sensory neuron-specific, proton-gated ion channel. *Proc. Natl Acad. Sci. USA* **95**, 10240–10245 (1998).
- Price, M. P., Snyder, P. M. & Welsh, M. J. Cloning and expression of a novel human brain Na^+ channel. *J. Biol. Chem.* **271**, 7879–7882 (1996).
- Lingueglia, E. *et al.* A modulatory subunit of acid sensing ion channels in brain and dorsal root ganglion cells. *J. Biol. Chem.* **272**, 29778–29783 (1997).
- Waldmann, R. *et al.* Molecular cloning of a non-inactivating proton-gated Na^+ channel specific for sensory neurons. *J. Biol. Chem.* **272**, 20975–20978 (1997).
- Grunder, S., Geisler, H. S., Bassler, E. L. & Ruppersberg, J. P. A new member of acid-sensing ion channels from pituitary gland. *Neuroreport* **11**, 1607–1611 (2000).
- Alvarez de la Rosa, D., Zhang, P., Shao, D., White, F. & Canessa, C. M. Functional implications of the localization and activity of acid-sensing channels in rat peripheral nervous system. *Proc. Natl Acad. Sci. USA* **99**, 2326–2331 (2002).
- Alvarez de la Rosa, D. *et al.* Distribution, subcellular localization and ontogeny of ASIC1 in the mammalian central nervous system. *J. Physiol. (Lond.)* **546**, 77–87 (2003).
- Price, M. P. *et al.* The DRASIC cation channel contributes to the detection of cutaneous touch and acid stimuli in mice. *Neuron* **32**, 1071–1083 (2001).
- Bassilana, F. *et al.* The acid-sensitive ionic channel subunit ASIC and the mammalian degenerin MDEG form a heteromultimeric H^+ -gated Na^+ channel with novel properties. *J. Biol. Chem.* **272**, 28819–28822 (1997).
- Benson, C. J. *et al.* Heteromultimers of DEG/ENaC subunits form H^+ -gated channels in mouse sensory neurons. *Proc. Natl Acad. Sci. USA* **99**, 2338–2343 (2002).
- Wemmie, J. A. *et al.* The acid-activated ion channel ASIC contributes to synaptic plasticity, learning and memory. *Neuron* **34**, 463–477 (2002).
- Sutherland, S. P., Benson, C. J., Adelman, J. & McCleskey, E. W. Acid-sensing ion channel 3 matches the acid-gated current in cardiac ischemia-sensing neurons. *Proc. Natl Acad. Sci. USA* **98**, 711–716 (2001).
- Xiong, Z. G. *et al.* Neuroprotection in ischemia: blocking calcium-permeable acid-sensing ion channels. *Cell* **118**, 687–698 (2004).
- Hesselager, M., Timmermann, D. B. & Ahning, P. K. pH dependency and desensitization kinetics of heterologously expressed combinations of acid-sensing ion channel subunits. *J. Biol. Chem.* **279**, 11006–11015 (2004).
- Korkushco, A. O., Krishtal, O. A. & Nowycky, M. C. Steady-state characteristics of the proton receptor in the somatic membrane of rat sensory neurons. *Neurofiziologiya* **15**, 632–638 (1983).
- Immke, D. C. & McCleskey, E. W. Protons open acid-sensing ion channels by catalyzing relief of Ca^{2+} block. *Neuron* **37**, 75–84 (2003).
- Zhang, P., Sigworth, F. J. & Canessa, C. M. Gating of acid-sensitive ion channel-1: Release of Ca^{2+} block vs allosteric mechanism. *J. Gen. Physiol.* **127**, 109–117 (2006).
- Baron, A., Waldmann, R. & Lazdunski, M. ASIC-like, proton-activated currents in rat hippocampal neurons. *J. Physiol. (Lond.)* **539**, 485–494 (2002).
- Askwith, C. C., Wemmie, J. A., Price, M. P., Rokhlina, T. & Welsh, M. J. Acid-sensing ion channel 2 (ASIC2) modulates ASIC1 H^+ -activated currents in hippocampal neurons. *J. Biol. Chem.* **279**, 18296–18305 (2004).
- Coscoy, S., Lingueglia, E., Lazdunski, M. & Barbry, P. The Phe-Met-Arg-Phe-amide-activated sodium channel is a tetramer. *J. Biol. Chem.* **273**, 8317–8322 (1998).
- Snyder, P. M., Cheng, C., Prince, L. S., Rogers, J. C. & Welsh, M. J. Electrophysiological and biochemical evidence that DEG/ENaC cation channels are composed of nine subunits. *J. Biol. Chem.* **273**, 681–684 (1998).
- Coric, T., Zheng, D., Gerstein, M. & Canessa, C. M. Proton sensitivity of ASIC1 appeared with the rise of fishes by changes of residues in the region that

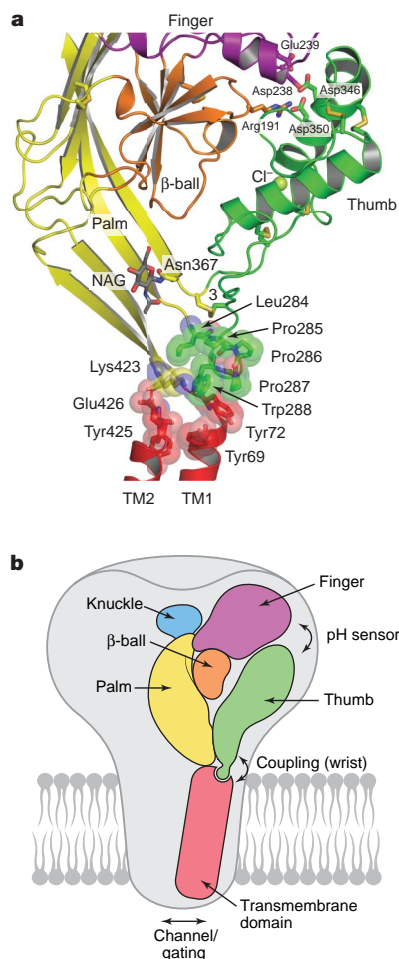


Figure 6 | Mechanism of pH-dependent gating. **a**, The disulphide-bond-rich thumb domain makes key contacts with the finger domain by means of interactions that include Asp 346–Glu 239 and Asp 350–Asp 238, and with the transmembrane domain via Trp 288 and residues on the extracellular ends of TM1 and TM2. **b**, Speculative model of how pH-dependent conformational changes between the finger and thumb domains might be coupled to ion channel gating via interactions between residues near Trp 288 and residues at the end or beginning of TM1 or TM2, respectively (see also Supplementary Fig. 9 and Supplementary Movie).

- follows TM1 in the ectodomain of the channel. *J. Physiol. (Lond.)* **568**, 725–735 (2005).
30. Kawate, T. & Gouaux, E. Fluorescence-detection size-exclusion chromatography for precrystallization screening of integral membrane proteins. *Structure* **14**, 673–681 (2006).
 31. Staruschenko, A., Adams, E., Booth, R. E. & Stockand, J. D. Epithelial Na⁺ channel subunit stoichiometry. *Biophys. J.* **88**, 3966–3975 (2005).
 32. Firsov, D., Gautschi, I., Merillat, A.-M., Rossier, B. C. & Schild, L. The heterotetrameric architecture of the epithelial sodium channel (ENaC). *EMBO J.* **17**, 344–352 (1998).
 33. Eskandari, S. *et al.* Number of subunits comprising the epithelial sodium channel. *J. Biol. Chem.* **274**, 27281–27286 (1999).
 34. Unwin, N. Refined structure of the nicotinic acetylcholine receptor. *J. Mol. Biol.* **346**, 967–989 (2005).
 35. Cushman, K. A., Marsh-Haffner, J., Adelman, J. & McCleskey, E. W. A conformational change in the extracellular domain that accompanies desensitization of acid-sensing ion channel (ASIC) 3. *J. Gen. Physiol.* **129**, 345–350 (2007).
 36. Coric, T., Zhang, P., Todorovic, N. & Canessa, C. M. The extracellular domain determines the kinetics of desensitization in acid-sensitive ion channel 1. *J. Biol. Chem.* **278**, 45240–45247 (2003).
 37. Baron, A., Schaefer, L., Lingueglia, E., Champigny, G. & Lazdunski, M. Zn²⁺ and H⁺ are coactivators of acid-sensing ion channels. *J. Biol. Chem.* **276**, 35361–35367 (2001).
 38. Rosenmund, C., Stern-Bach, Y. & Stevens, C. F. The tetrameric structure of a glutamate receptor channel. *Science* **280**, 1596–1599 (1998).
 39. MacKinnon, R. Determination of the subunit stoichiometry of a voltage-activated potassium channel. *Nature* **350**, 232–235 (1991).
 40. Reynolds, J. A. & Karlin, A. Molecular weight in detergent solution of acetylcholine receptor from *Torpedo californica*. *Biochemistry* **17**, 2035–2038 (1978).
 41. Paukert, M., Babini, E., Pusch, M. & Grunder, S. Identification of the Ca²⁺ blocking site of acid-sensing ion channel (ASIC) 1: Implications for channel gating. *J. Gen. Physiol.* **124**, 383–394 (2004).
 42. Kellenberger, S., Auberson, M., Gautschi, I., Schneeberger, E. & Schild, L. Permeability properties of ENaC selectivity filter mutants. *J. Gen. Physiol.* **118**, 679–692 (2001).
 43. Doyle, D. A. *et al.* The structure of the potassium channel: molecular basis of K⁺ conduction and selectivity. *Science* **280**, 69–77 (1998).
 44. Pfister, Y. *et al.* A gating mutation in the internal pore of ASIC1a. *J. Biol. Chem.* **281**, 11787–11791 (2006).
 45. Goodman, M. B. *et al.* MEC-2 regulates *C. elegans* DEG/ENaC channels needed for mechanosensation. *Nature* **415**, 1039–1042 (2002).
 46. Sawyer, L. & James, M. N. Carboxyl-carboxylate interactions in proteins. *Nature* **295**, 79–80 (1982).
 47. Todorovic, N., Coric, T., Zhang, P. & Canessa, C. M. Effects of extracellular calcium on fASIC1 currents. *Ann. NY Acad. Sci.* **1048**, 331–336 (2005).
 48. Bellizzi, J. J. III, Widom, J., Kemp, C. W. & Clardy, J. Producing selenomethionine-labeled proteins with a baculovirus expression vector system. *Structure* **7**, R263–R267 (1999).

Supplementary Information is linked to the online version of the paper at www.nature.com/nature.

Acknowledgements We thank all groups that provided us with ASIC DNAs. We thank T. Kawate for sharing the FSEC screening protocol, Gouaux laboratory members and E. McCleskey for discussions. We also thank the personnel at beamlines 8.2.1 and 8.2.2 of the Advanced Light Source and beamline X29 of the National Synchrotron Light Source. This work was supported by the NIH. E.G. is an investigator with the Howard Hughes Medical Institute.

Author Contributions E.G. and J.J. designed the project. J.J. performed cloning, cell culture, FSEC screening, purification and crystallography work. H.F. and E.B.G. did patch-clamp recordings. E.G. and J.J. wrote the manuscript.

Author Information Coordinates have been deposited with the Protein Data Bank under code 2QTS. Reprints and permissions information is available at www.nature.com/reprints. The authors declare no competing financial interests. Correspondence and requests for materials should be addressed to E.G. (gouauxe@ohsu.edu).

METHODS

Expression and purification. The protein construct used in the crystallographic studies includes chicken ASIC1 residues 26–463 (Δ ASIC1) and either an N-terminal (His)₈ or a (His)₈–GFP tag. Baculovirus-infected Sf9 cells were used for overexpression and were grown at 27 °C in serum-free media. Cells were harvested 3 days after infection and disrupted in 50 mM Tris (pH 8.0), 150 mM NaCl, 5 mM MgCl₂, 1 mM phenylmethylsulphonyl chloride with DNase 1 and protease inhibitor cocktail. Membranes were isolated by ultracentrifugation and solubilized with 40 mM *n*-dodecyl- β -D-maltoside (DDM) in 50 mM Tris (pH 8.0) and 150 mM NaCl. The resulting supernatant was loaded onto a metal affinity column and Δ ASIC1 was eluted in 20 mM Tris (pH 8.0), 150 mM NaCl and 1 mM DDM with 250 mM imidazole. Thrombin (10 U mg⁻¹ protein, 2 h at room temperature) was used to remove the purification tag and the protein was further purified by size-exclusion chromatography in 20 mM Tris (pH 8.0), 150 mM NaCl and 1 mM DDM, concentrated to 5 mg ml⁻¹, and used for crystallization. For preparation of selenomethionine (SeMet)-labelled protein, 24 h after infection, cells were collected by centrifugation and transferred into serum-free media devoid of methionine and supplemented with 150 mg l⁻¹ cystine. After 5 h SeMet was added (50 mg l⁻¹), the cells were harvested after 2 days and SeMet-labelled protein was purified as described above with 1 mM β -mercaptoethanol added to all buffers.

Crystallization. Crystals were obtained by vapour diffusion (4 °C) by mixing protein with a reservoir solution containing 100 mM *N*-(2-acetamido)iminodiacetic acid (pH 6.5), 100 mM MgCl₂ and 10–14% PEG6000 (final pH 5.6). Crystals were dehydrated by increasing the concentration of PEG6000 in 3% steps up to 33%, incubated overnight and flash frozen under liquid nitrogen. The platinum derivative was prepared by soaking the dehydrated crystals in 10 mM K₂Pt(NO₃)₄ for 6 h. The bromide data set was obtained by briefly soaking dehydrated crystals in 100 mM *N*-(2-acetamido)iminodiacetic acid (pH 6.5), 100 mM MgSO₄, 150 mM sodium bromide, 1 mM DDM and 33% PEG6000.

Structure determination. Diffraction data sets were collected at the Advanced Light Source (Supplementary Table 1) and were processed with HKL2000 and CCP4 programs. Phases were obtained by single-wavelength anomalous dispersion method from Pt derivative using the program SOLVE⁴⁹. The platinum phases were used to determine the positions of selenium atoms in anomalous difference Fourier maps using data measured from SeMet crystals. The initial platinum phases, together with non-crystallographic symmetry (NCS) operators determined from the selenium sites, were used in phase extension and density modification using the native diffraction data set using the program DM⁵⁰. The resulting electron density map showed clear density for the extracellular domains and the initial structure was automatically traced by Arp/wArp⁵¹. Because the transmembrane domains deviate from the three-fold NCS axis, they were not visible in these averaged maps. However, after iterated model building using the program O⁵² and refinement with CNS⁵³ in the absence of NCS restraints, density for the transmembrane helices was clearly visible and interpretable.

Water molecules were added using ARPP/REFMAC⁵¹ when the R_{free} dropped below 30% and were checked and adjusted for hydrogen-bonding distances.

Cross-linking and light scattering. Purified protein was dialysed against phosphate buffer saline containing 1 mM DDM (12 h) and treated with glutaraldehyde (1, 5 and 10 mM) for 15 min at room temperature. The reactions were stopped by adding 50 mM Tris (pH 8.0) and were analysed by SDS–polyacrylamide gel electrophoresis. For light scattering experiments, the protein was loaded onto a Superose 6 10/300 column coupled to light scattering, refractive index and ultraviolet detector system (Supplementary Fig. 3).

Electrophysiology. Rapid solution exchange patch-clamp recordings were done using HEK293 cells (TsA201 variant) 24–48 h after transfection with plasmids encoding chicken ASIC1 and GFP. The recording electrodes (3–6 M Ω resistance) were filled with 110 mM potassium gluconate, 2.5 mM NaCl, 5 mM BAPTA and 10 mM HEPES–KOH (pH 7.5). The wash solution contained 150 mM NaCl, 2 mM KCl, 2 mM CaCl₂, 5 mM HEPES and 5 mM MES (pH 7.5). The low-pH ‘activation’ solution (pH 5.5) was supplemented with 5 mM sucrose to increase visibility of the solution interface and with 14 mM NaCl to increase the amplitude of open-tip response. Outside-out patches were placed in front of a double-barrel theta tubing coupled to a piezoelectric device. Long (1 s) or brief (5 ms) pulses of the activation solution were applied at intervals of 1 min or 5 s, respectively, at a holding potential of –70 mV. The mean 10–90% rise time for the open tip response was typically 0.5–2 ms. Data points from three to five traces were averaged and fit to a single exponential equation, $I(t) = I_{\text{exp}}(-t/\tau)$, where I is the current amplitude and τ is the time constant for the current decay component. Typical amplitudes of peak currents were 500–1,000 pA and indistinguishable from currents recorded from CHO cells (data not shown). For the proton dose–response experiments, activation solutions with pH values between 6 and 7 were prepared with an increment of 0.2 pH units. The pH values were adjusted with *N*-methyl-D-glucosamine and for these experiments the high pH wash solution was adjusted to 8.0. A 500-ms pulse of activation solution was applied to outside-out patches containing wild-type or mutant chicken ASIC1 with 2-min intervals between recordings. Amplitudes of peak currents were measured, plotted and fit to the Hill equation.

49. Terwilliger, T. C. & Berendzen, J. Automated MAD and MIR structure solution. *Acta Crystallogr. D* **55**, 849–861 (1999).
50. Cowtan, K. & Zhang, K. Y. Density modification for macromolecular phase improvement. *Prog. Biophys. Mol. Biol.* **72**, 245–270 (1999).
51. Perrakis, A., Morris, R. & Lamzin, V. S. Automated protein model building combined with iterative structure refinement. *Nature Struct. Biol.* **6**, 458–463 (1999).
52. Jones, T. A., Zou, J.-Y. & Cowan, S. W. Improved methods for building protein models in electron density maps and the location of errors in these models. *Acta Crystallogr. A* **47**, 110–119 (1991).
53. Brunger, A. T. *et al.* Crystallography and NMR system: A new software suite for macromolecular structure determination. *Acta Crystallogr. D* **54**, 905–921 (1998).

LETTERS

Non-equilibrium coherence dynamics in one-dimensional Bose gases

S. Hofferberth^{1,2}, I. Lesanovsky³, B. Fischer¹, T. Schumm² & J. Schmiedmayer^{1,2}

Low-dimensional systems provide beautiful examples of many-body quantum physics¹. For one-dimensional (1D) systems², the Luttinger liquid approach³ provides insight into universal properties. Much is known of the equilibrium state, both in the weakly^{4–7} and strongly^{8,9} interacting regimes. However, it remains a challenge to probe the dynamics by which this equilibrium state is reached¹⁰. Here we present a direct experimental study of the coherence dynamics in both isolated and coupled degenerate 1D Bose gases. Dynamic splitting is used to create two 1D systems in a phase coherent state¹¹. The time evolution of the coherence is revealed through local phase shifts of the subsequently observed interference patterns. Completely isolated 1D Bose gases are observed to exhibit universal sub-exponential coherence decay, in excellent agreement with recent predictions¹². For two coupled 1D Bose gases, the coherence factor is observed to approach a non-zero equilibrium value, as predicted by a Bogoliubov approach¹³. This coupled-system decay to finite coherence is the matter wave equivalent of phase-locking two lasers by injection. The non-equilibrium dynamics of superfluids has an important role in a wide range of physical systems, such as superconductors, quantum Hall systems, superfluid helium and spin systems^{14–16}. Our experiments studying coherence dynamics show that 1D Bose gases are ideally suited for investigating this class of phenomena.

The starting point of our experiments is a 1D Bose gas of a few thousand atoms trapped in a highly elongated, cylindrical magnetic microtrap on an atom chip^{17,18} with typical transverse and longitudinal oscillator frequencies of $\nu_{\perp} \approx 4.0$ kHz and $\nu_z \approx 5$ Hz. Our trapped Bose gas is in the 1D quasi-condensate regime¹, which is characterized by both the temperature T and chemical potential μ fulfilling $k_B T, \mu < \hbar v_{\perp}$ (ref. 19).

After the initial preparation of this single 1D system, we perform a phase-coherent splitting along the transverse direction by means of a radio-frequency (r.f.) induced adiabatic potential¹¹. As shown in Fig. 1, the final system consists of two 1D quasi-condensates in a vertically orientated double-well potential²⁰. They are separated by a tunable potential barrier, the height of which is controlled by the applied r.f. fields. This splitting process initializes the system in a phase coherent state. Directly after the splitting, the phase fluctuation patterns of the two individual quasi-condensates are identical, resulting in a vanishing global relative phase. This is a highly non-equilibrium state of the split system, which will relax to equilibrium over time.

To study this time evolution of the phase coherence, the two 1D Bose gases are held in the double-well configuration for a varying time t before they are released and recombined during the time-of-flight. The resulting interference pattern is recorded using standard absorption imaging along the transverse direction of the system. The spatial variation of the relative phase between the two

quasi-condensates translates directly into local phase shifts in the interference pattern (Fig. 2).

If the two parts of the system are completely separated (see Methods), the equilibrium state consists of two uncorrelated quasi-condensates. Consequently, we observe an increasing waviness of the interference pattern with time, which in the end leads to a complete randomization of the relative phase $\theta(z, t)$ (Fig. 2a, b), where z is the spatial coordinate in the longitudinal direction of the system. This change in the interference pattern is a direct visualization of the dynamics of the phase fluctuations. Qualitatively similar behaviour was recently observed²¹ for elongated condensates with $\mu \approx 2\hbar v_{\perp}$ and $T \approx 5\hbar v_{\perp}$.

For a finite tunnel coupling (see Methods) between the two systems, we also observe an increase in the waviness of the interference. However, in contrast to the completely separated case, the final equilibrium state shows a non-random phase distribution (Fig. 2c, d). This is caused by the phase randomization being counterbalanced by the coherent particle exchange between the two fractions. The final width of the observed phase spread depends on the strength of the tunnel coupling^{22,23}.

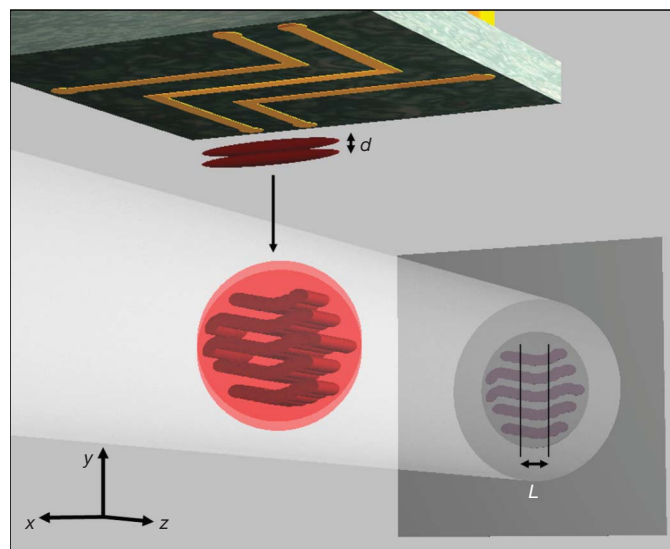


Figure 1 | Schematic of the experiment. A single 1D quasi-condensate is phase coherently split into two parts separated by distance d using r.f. potentials on an atom chip (top). A combination of two r.f. fields allows balanced splitting in the vertical direction²⁰, as indicated in the figure. After the separation, the system is held in the double-well potential for a variable time t and is then released from the trap. The resulting interference pattern (centre) is imaged along the transverse direction of the system onto a CCD camera (right). Thermal phase fluctuations in the two quasi-condensates can be directly observed as local shifts of the observed fringe profiles. Only the central area of length L of the interference pattern is included in the analysis.

¹Physikalisches Institut, Universität Heidelberg, Philosophenweg 12, D-69120 Heidelberg, Germany. ²Atominstitut der Österreichischen Universitäten, TU-Wien, Stadionallee 2, A-1020 Vienna, Austria. ³Institut für Theoretische Physik, Universität Innsbruck, Technikerstr. 25, A-6020 Innsbruck, Austria.

A quantitative measure of the fluctuations of the local relative phase is given by the coherence factor

$$\Psi(t) = \frac{1}{L} \left| \int dz e^{i\theta(z,t)} \right| \quad (1)$$

where L is the length of the analysed signal. We obtain the coherence factor from a single image by extracting the local relative phase $\theta(z, t)$ from the interference pattern in each vertical pixel slice. To account for variations in the 1D atomic density $n_{1D}(z)$ due to the longitudinal confining potential, we use only the central 40% of each image in our analysis. Over this range, $n_{1D}(z)$ varies by only $\sim 15\%$ from its peak value. In the following, we neglect this modulation and assume a homogeneous density, obtained by averaging over the density profile in this centre region.

We first investigate the time evolution of the coherence factor $\Psi(t)$ for the case of completely separated 1D quasi-condensates, separated by a potential barrier sufficiently high to suppress any tunnel coupling (Fig. 2a, b). The time evolution of the measured coherence factor for six different combinations of initial temperature T_{in} , 1D density n_{1D} , and transverse trap frequency ν_{\perp} is displayed in Fig. 3. In a time window of 1–12 ms, we observe a universal sub-exponential decay of the form

$$\Psi(t) \propto e^{-(t/t_0)^{\alpha}} \quad (2)$$

with decay time constants t_0 ranging from 5 ms to 9 ms (Table 1).

Our results can be directly compared with a recent theoretical study by Burkov *et al.*¹², based on a Luttinger liquid approach³, which predicts $\alpha = 2/3$ for the exponent in equation (2). For all the cases studied, we find α to be between 0.64 and 0.67 (Table 1), in very good agreement with the theoretical prediction. This agreement is even more remarkable because the approximations used by

Table 1 | Measured parameters after the splitting for the data shown in Fig. 3

T_{in} (nK)	n_{1D} (μm^{-1})	μ/h (kHz)	ν_{\perp} (kHz)	α	t_0 (ms)	T_f (nK)
82(28)	20(4)	0.7(1)	3.3	0.64(8)	9.0(4)	76(10)
133(25)	34(5)	1.2(2)	3.3	0.65(7)	5.5(3)	145(13)
171(19)	52(4)	1.8(1)	3.3	0.64(4)	6.4(3)	186(15)
81(31)	22(4)	0.9(2)	4.0	0.65(3)	8.1(2)	85(10)
128(23)	37(4)	1.5(2)	4.0	0.66(3)	5.9(2)	153(13)
175(20)	51(5)	2.1(2)	4.0	0.64(6)	6.1(4)	194(17)

Parameters measured from the coherence decay are the exponent α , decay time constant t_0 and final temperature T_f . Initial temperature T_{in} , density n_{1D} , and chemical potential μ are measured independently. Values in brackets indicate standard uncertainties of the measured values.

Burkov *et al.*¹² to obtain equation (2) and $\alpha = 2/3$ are only valid for $t > t_0$, whereas our data cover the full range from 0 up to $2 t_0$.

At our typical temperatures ($T_{in} \approx 80$ – 150 nK), the dynamics of the coherence factor is dominated by thermal phase fluctuations^{12,24}. Burkov *et al.* derive the decay of $\Psi(t)$ by assuming that the system of two 1D Bose gases can evolve into thermal equilibrium. The sub-exponential coherence decay then results from the fact that damping in a 1D liquid at finite temperature is always non-hydrodynamic, which in turn is caused by the breakdown of superfluid order in 1D on length scales longer than the temperature-dependent correlation length²⁵. The experimentally observed decay agrees with this non-trivial theoretical prediction, which is strong evidence that the final equilibrium state of our system is truly thermal equilibrium. In turn, this suggests the non-integrability of the experimentally realized system²⁶.

Following Burkov *et al.*¹², the decay time constant t_0 can be related to the parameters of the 1D quantum gas as follows:

$$t_0 = 2.61 \pi g n_{1D} K / T_f^2 \quad (3)$$

where $K = \pi \hbar [n_{1D}/(gm)]^{1/2}$ is the Luttinger parameter for the weakly interacting 1D Bose gas²⁷, $g = 2\hbar v_{\perp} a_s$ is the effective 1D coupling

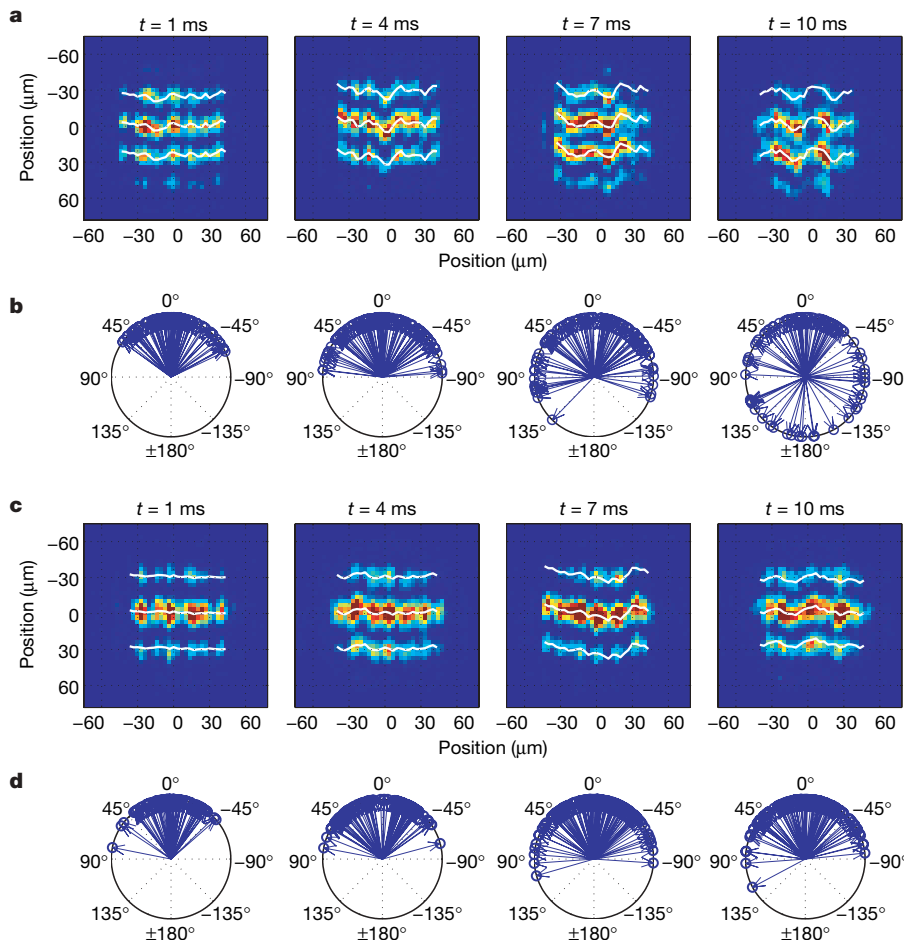


Figure 2 | Direct observation of the phase dynamics through interference. **a**, Example images of the observed interference patterns in the atomic density distribution for hold times $t = 1, 4, 7, 10$ ms in the case of isolated 1D systems (taken from the $T = 133$ nK data set in Fig. 3b). Blue areas indicate zero density, while red areas indicate high atomic density. The white lines show the position of the bright nodes of the local interference pattern, extracted from fits to the profiles in each vertical pixel slice. The randomization of the relative phase $\theta(z, t)$ over time leads to an increased waviness of the observed fringe patterns. **b**, Corresponding polar plots of the local relative phases from the central regions of five example images each. For the isolated systems, we find a complete randomization of the local relative phase over time. **c**, For a finite tunnel coupling through the potential barrier, the phase randomization is counterbalanced by particle tunnelling, resulting in a suppression of the fringe waviness (images correspond to Fig. 4c). **d**, This results in a non-random steady-state phase spread, whose width depends on the tunnel coupling and the temperature of the system.

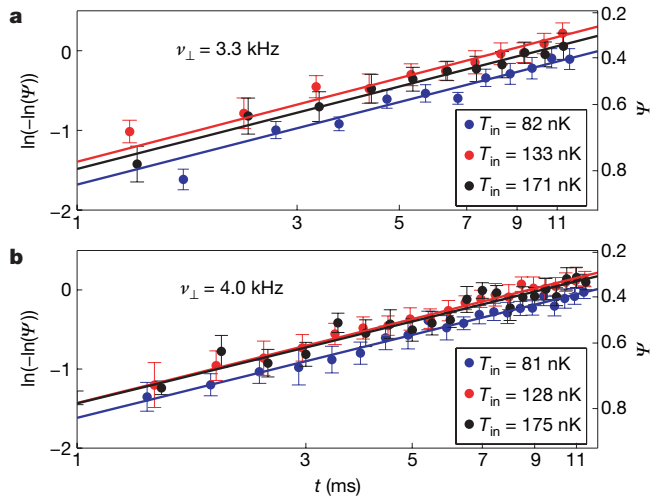


Figure 3 | Time evolution of the coherence factor for uncoupled 1D quasi-condensates. **a, b**, Double logarithmic plots of $\ln(\Psi)$ as a function of time t for transverse confinements of $\nu_{\perp} = 3.3$ kHz (**a**) and $\nu_{\perp} = 4.0$ kHz (**b**). Three different data sets corresponding to different initial temperatures (T_{in}) and line densities are shown for each configuration. Each data point is the average of 15 individual measurements. Error bars indicate the standard error of the mean. In this representation, the exponent of the decay function is given directly by the slope of the observed linear evolution of $\ln(\Psi)$. The lines shown are linear fits to the data, the obtained slopes are 0.64 ± 0.08 , 0.65 ± 0.07 and 0.64 ± 0.04 for **a**, and 0.65 ± 0.03 , 0.66 ± 0.03 and 0.64 ± 0.06 for **b**. All slopes show good agreement with the theoretical prediction of $2/3$.

constant, a_s is the s -wave scattering length, m the mass of the atoms, and T_f the final equilibrium temperature of the split system. T_f can be extracted from the decay constant t_0 following equation (3) using independently measured values of ν_{\perp} and n_{1D} . The results, together with an independently measured initial temperature of the unsplit system T_{in} from time-of-flight images, are compiled in Table 1. Within the error bounds, the temperatures T_{in} and T_f agree. Nevertheless, our data seem to indicate an increasing difference between T_{in} and T_f for increasing initial temperature.

This observation is in qualitative agreement with ref. 12, which predicts that the heating during the splitting will scale with $(T_{\text{in}}K)^{1/2}$. This is also supported by the observation that for identical T_{in} , we find the same temperature increase in the split system for both of the two different transverse confinements used in the experiment.

We note here that the temperature T_f is the temperature of the longitudinal excitations, and is measured on a timescale that is much shorter than the characteristic time given by the sound propagation through the sample—and very much shorter than the thermalization timescale. To check the universality of our experiments, we cut each sample in two and analysed each half separately. We obtained the same results within the statistical uncertainties.

We now turn to the case of (weakly) coupled 1D quasi-condensates realized when the potential barrier between the two 1D systems is only slightly larger than the chemical potential μ , and tunnelling between the two split systems is significant. In this case, we observe a qualitative change in the behaviour of the coherence factor $\Psi(t)$, as illustrated in Fig. 4. After an initial decay, the coherence factor saturates well above the value for random phases. This observation is a clear manifestation of a balancing between phase-locking due to coherent tunnelling and the local phase fluctuations in the 1D quasi-condensate¹³. It is the matter wave equivalent of injection-locking two lasers.

For a quantitative analysis, we use the results of ref. 13 for the energy spectrum and the mode functions, and express the final equilibrium coherence factor as:

$$\Psi = \Psi_q \times \exp\left(-\frac{1}{4\pi n_{1D}} \int dk \frac{S_k}{e^{\frac{\epsilon_k}{k_B T}} - 1}\right) \quad (4)$$

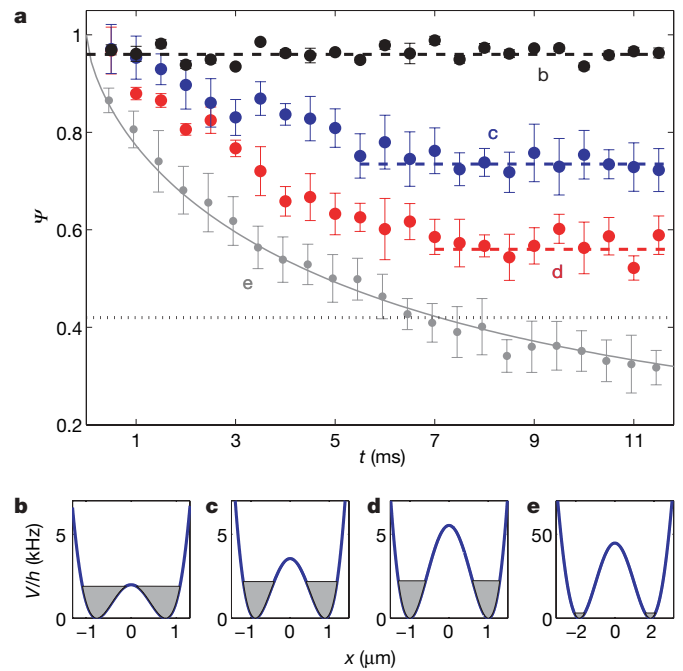


Figure 4 | Time evolution of the coherence factor for coupled 1D quasi-condensates. **a**, After an initial decay we observe a time-independent coherence factor determined by the strength of the tunnel coupling. Different colours correspond to the different transverse double-well potentials shown in **b–d** as indicated. Each data point is the average of 12 individual measurements. Error bars indicate s.e.m. The light grey points are the $T = 128$ nK data set from Fig. 3b, showing the sub-exponential decay in the case of uncoupled condensates for comparison. The corresponding transverse potential is shown in **e**. The dotted black line in **a** indicates the Rayleigh test confidence level above which the considered phase distribution of a single measurement can be identified as non-random with a 90% probability. In the coupled case, the final phase distribution in each realization can be clearly considered as non-random.

where Ψ_q (approximately 1 in our case) is the contribution of the quantum fluctuations, and

$$\epsilon_k = \sqrt{\left(\frac{\hbar^2 k^2}{2m} + 2\gamma\right) \left(\frac{\hbar^2 k^2}{2m} + 2\gamma + 2gn_{1D}\right)} \quad (5)$$

$$S_k = \sqrt{\frac{\frac{\hbar^2 k^2}{2m} + 2\gamma + 2gn_{1D}}{\frac{\hbar^2 k^2}{2m} + 2\gamma}}$$

are the energy eigenvalues and amplitudes of the Bogoliubov modes, respectively. γ thereby quantifies the tunnel coupling between the two 1D systems. Independent measurements of T and n_{1D} allow us to extract γ directly from the measured equilibrium coherence factors. For the red, blue and black data sets in Fig. 4, we obtain $\gamma/(gn_{1D}) \approx 0.003$, 0.01 and 0.2 , respectively. Comparison with numerical calculations of the tunnel coupling, based on the spatial overlap of the wavefunctions²⁸, yields qualitative agreement within a factor of three. This suggests that a two-mode model for the tunnelling dynamics is not sufficient to describe our experiments. Alternatively, if γ can be determined independently, the equilibrium coherence factor can be used for thermometry in the coupled system²³.

Particle exchange between the two condensates takes place on a timescale given by the inverse of the Josephson oscillation frequency¹³:

$$\omega_J = \frac{\sqrt{\gamma gn_{1D}}}{\hbar} \quad (6)$$

From our measured γ , we estimate $\omega_J \approx 2\pi \times 80, 200, 900$ Hz for the three presented data sets, which should be compared to the coherence

decay timescale of the order of 5 ms (Fig. 4). This suggests that the balancing process between coherent tunnelling and phase fluctuations stabilizes on timescales of the order of one (or a few) Josephson oscillation(s) in a coupled 1D system.

In summary, we have studied the non-equilibrium phase dynamics in a 1D Bose gas with the aid of matter wave interferometry. For completely separated systems, we observe the sub-exponential coherence decay predicted by Luttinger liquid theory¹². For coupled 1D Bose gases, the balance between decoherence and phase stabilization due to tunnelling establishes a finite coherence^{13,23}. In both examples, our experiments illustrate how the thermal equilibrium state of a phase-fluctuating 1D quasi-condensate^{1,4–7} is approached from the highly non-equilibrium situation of two phase coherent copies created by splitting a degenerate 1D Bose gas.

The above investigation demonstrates that with the exquisite control provided by atom chips, it is now possible to study in detail the non-equilibrium dynamics of coherence in a single quantum degenerate 1D system. This allows us to address the fundamental issue of thermalization in (almost) integrable systems²⁶. Our approach can easily be extended to study the dynamics of two- and three-dimensional quantum systems, and to include other factors, such as internal state dynamics. Moreover, it will be the starting point for detailed studies of coupled 1D quantum systems. One prominent example is the quantum sine-Gordon model, which plays an important role in many fundamental physics questions^{2,29–31}.

METHODS SUMMARY

Atom chips¹⁷ are devices where electric and magnetic fields for atom manipulation are created by microscopic wires and electrodes micro-fabricated on a carrier substrate. The precision and robust alignment of the fabricated structures allow well controlled quantum manipulation of ultracold neutral atoms.

Our experiments are performed with quantum degenerate samples of ⁸⁷Rb atoms magnetically trapped in the $|F=2, m_F=2\rangle$ state on such atom chips. A 1D degenerate Bose gas with $\mu, k_B T < \hbar v_\perp$ is prepared by tuning the evaporative cooling frequency between the ground state and the first excited transverse vibrational state in the highly elongated magnetic trap.

A crucial ingredient in the preparation of the initial state in the present experiments is the coherent splitting of a single 1D condensate by using radio frequency (r.f.) induced adiabatic potentials¹¹. To prepare two completely isolated 1D systems, we split to a large potential barrier (>50 kHz). To prepare two 1D systems with a variable tunnel coupling, we adjust the potential barrier to between 3 and 8 kHz. We use a multiple wire configuration first explored in ref. 20, which realizes a well compensated double-well potential in the vertical plane.

After releasing the atoms, the two expanding clouds form an interference pattern with fringes parallel to the atom chip surface (Fig. 1). We image the interference fringes in the atomic density using standard absorption imaging, and extract the local relative phase $\theta(z)$ by fitting a cosine function with a gaussian envelope to the observed density distribution in each individual vertical pixel slice (position z). This measured phase $\theta(z)$ is then used to calculate the coherence factor (equation (1)).

Full Methods and any associated references are available in the online version of the paper at www.nature.com/nature.

Received 14 June; accepted 2 August 2007.

1. Popov, V. N. *Functional Integrals in Quantum Field Theory and Statistical Physics* (Reidel, Dordrecht, 1983).
2. Giamarchi, T. *Quantum Physics in One Dimension* (Oxford Univ. Press, Oxford, 2003).
3. Haldane, F. Effective harmonic-fluid approach to low-energy properties of one-dimensional quantum fluids. *Phys. Rev. Lett.* **47**, 1840–1843 (1981).
4. Petrov, D. S., Shlyapnikov, G. V. & Walraven, J. T. M. Regimes of quantum degeneracy in trapped 1D gases. *Phys. Rev. Lett.* **85**, 3745–3749 (2000).

5. Dettmer, S. *et al.* Observation of phase fluctuations in elongated Bose-Einstein condensates. *Phys. Rev. Lett.* **87**, 160406 (2001).
6. Richard, S. *et al.* Momentum spectroscopy of 1D phase fluctuations in Bose-Einstein condensates. *Phys. Rev. Lett.* **91**, 010405 (2003).
7. Pricoupenko, L., Perrin, H. & Olshanii, M. *Quantum Gases in Low Dimensions* (Journal de Physique IV Proceedings, Vol. 116, EDP Sciences, 2004).
8. Paredes, B. *et al.* Tonks-Girardeau gas of ultracold atoms in an optical lattice. *Nature* **429**, 277–281 (2004).
9. Kinoshita, T., Wenger, T. & Weiss, D. S. Observation of a one-dimensional Tonks-Girardeau gas. *Science* **305**, 1125–1128 (2004).
10. Kinoshita, T., Wenger, T. R. & Weiss, D. S. A quantum Newton's cradle. *Nature* **440**, 900–903 (2006).
11. Schumm, T. *et al.* Matter wave interferometry in a double well on an atom chip. *Nature Phys.* **1**, 57–62 (2005).
12. Burkov, A. A., Lukin, M. D. & Demler, E. Decoherence dynamics in low-dimensional cold atoms interferometers. *Phys. Rev. Lett.* **98**, 200404 (2007).
13. Whitlock, N. K. & Bouchoule, I. Relative phase fluctuations of two coupled one-dimensional condensates. *Phys. Rev. A* **68**, 053609 (2003).
14. Blatter, G., Feigelman, M., Geshkenbein, V., Larkin, A. & Vinokur, V. Vortices in high-temperature superconductors. *Rev. Mod. Phys.* **66**, 1125–1388 (1994).
15. Shimshoni, E., Auerbach, A. & Kapitulin, A. Transport through quantum melts. *Phys. Rev. Lett.* **80**, 3352–3355 (1998).
16. Forte, S. Quantum mechanics and field theory with fractional spin and statistics. *Rev. Mod. Phys.* **64**, 193–236 (1992).
17. Folman, R., Krüger, P., Schmiedmayer, J., Denschlag, J. & Henkel, C. Microscopic atom optics: From wires to an atom chip. *Adv. At. Mol. Opt. Phys.* **48**, 263–356 (2002).
18. Fortagh, J. & Zimmermann, C. Magnetic microtraps for ultracold atoms. *Rev. Mod. Phys.* **79**, 235 (2007).
19. Bouchoule, I., Kheruntsyan, K. V. & Shlyapnikov, G. V. Interaction-induced crossover versus finite-size condensation in a weakly interacting trapped one-dimensional Bose gas. *Phys. Rev. A* **75**, 031606(R) (2007).
20. Hofferberth, S., Lesanovsky, I., Fischer, B., Verdu, J. & Schmiedmayer, J. Radio-frequency dressed state potentials for neutral atoms. *Nature Phys.* **2**, 710–716 (2006).
21. Jo, G. B. *et al.* Matter-wave interferometry with phase fluctuating Bose-Einstein condensates. Preprint at (<http://arxiv.org/abs/0706.4041v3>) (2007).
22. Spietz, L., Lehnert, K. W., Siddiqi, I. & Schoelkopf, R. J. Primary electronic thermometry using the shot noise of a tunnel junction. *Science* **300**, 1929–1932 (2003).
23. Gati, R., Hemmerling, B., Fölling, J., Albiez, M. & Oberthaler, M. K. Noise thermometry with two weakly coupled Bose-Einstein condensates. *Phys. Rev. Lett.* **96**, 130404 (2006).
24. Bistrizter, R. & Altman, E. Intrinsic dephasing in one dimensional ultracold atom interferometers. *Proc. Natl Acad. Sci. USA* **104**, 9955–9959 (2007).
25. Andreev, A. F. The hydrodynamics of two-dimensional and one-dimensional fluids. *Sov. Phys. JETP* **51**, 1038–1040 (1980).
26. Rigol, M., Dunjko, V., Yurovsky, V. & Olshanii, M. Relaxation in a completely integrable many-body quantum system: An ab initio study of the dynamics of the highly excited states of 1d lattice hard-core bosons. *Phys. Rev. Lett.* **98**, 050405 (2007).
27. Cazalilla, M. Bosonizing one-dimensional cold atomic gases. *J. Phys. B* **37**, S1–S47 (2004).
28. Ananikian, D. & Bergeman, T. The Gross-Pitaevskii equation for Bose particles in a double well potential: Two mode models and beyond. *Phys. Rev. A* **73**, 013604 (2006).
29. Bouchoule, I. Modulational instabilities in Josephson oscillations of elongated coupled condensates. *Eur. Phys. J. D* **35**, 147–154 (2005).
30. Gritsev, V., Polkovnikov, A. & Demler, E. Linear response theory for a pair of coupled one-dimensional condensates of interacting atoms. *Phys. Rev. B* **75**, 174511 (2007).
31. Gritsev, V., Demler, E., Lukin, M. & Polkovnikov, A. Analysis of quench dynamics of coupled one dimensional condensates using quantum sine Gordon model. Preprint at (<http://arxiv.org/cond-mat/0702343>).

Acknowledgements We thank A Burkov, V. Gritsev, E. Demler, R. Bistrizter and E. Altman for discussions. We also thank S. Groth for fabricating the atom chip used in the experiments. We acknowledge financial support from the Wittgenstein Prize and the European Union, through Atom Chips and FET/QIPC SCALA projects.

Author Information Reprints and permissions information is available at www.nature.com/reprints. The authors declare no competing financial interests. Correspondence and requests for materials should be addressed to J.S. (schmiedmayer@atomchip.org).

METHODS

Preparing a 1D Bose–Einstein condensate on an atom chip. We start by preparing a magnetically trapped ultracold ($T \approx 1 \mu\text{K}$) sample of ^{87}Rb atoms in the $|F=2, m_F=2\rangle$ state on the atom chip^{17,18} using our standard procedure of laser cooling, magnetic trapping and evaporative cooling³². The sample is then transferred to a highly elongated magnetic trap ($v_{\perp} \approx 4.0 \text{ kHz}$, longitudinal confinement $v_z < 5 \text{ Hz}$) at a distance of $75 \mu\text{m}$ from the atom chip surface and cooled to quantum degeneracy by tuning the evaporative cooling r.f. between the ground and first excited transverse trapping state. The resulting sample is effectively one-dimensional^{4,19} with $\mu, k_B T < \hbar v_{\perp}$ containing $(1-10) \times 10^3$ atoms.

Smoothness of the trapping potentials. Our atom chip wires³³ provide exceptionally smooth trapping potentials³⁴. The residual roughness due to current-flow perturbations in the trapping wire is much too small to be measured directly at our operation distance $h = 75 \mu\text{m}$ from the atom chip surface. An estimate based on the current flow pattern in the wire reconstructed from magnetic field microscopy measurements using 1D condensates at a short distance ($\sim 10 \mu\text{m}$)³⁵ shows that, for length scales below $40 \mu\text{m}$, the remaining potential perturbations are smaller than $1 \mu\text{G}$ (corresponding to $< 10^{-3} \mu$). Owing to the exponential damping of the higher spatial modes (wave vector $k = 2\pi/\lambda$) of the magnetic field variations with distance h from the chip surface (which follows $\exp(-kh)$), the disorder potentials will be even smaller on the short length scales corresponding to the phase coherence length or the healing length in the 1D Bose gas.

Preparing two phase-coherent 1D systems. To prepare two mutually phase coherent 1D systems, we use a combination of static and r.f. magnetic fields on our atom chip. Coupling electronic ground states of the magnetically trapped atoms results in dressed-state adiabatic potentials, whose versatility stems from the dependence of the potential on the angular orientation between the r.f. field and the static trapping field³⁶. In particular, one can create very robust double-well potentials, which allow the coherent splitting of a trapped Bose condensate¹¹. In the experiments presented here, we use a set-up similar to that in ref. 20, where the combination of two r.f. fields generated by auxiliary wires on the atom chip allows the realization of a compensated double-well potential in the vertical plane. For this double-well orientation, the observed interference fringes in the atomic density are horizontal, parallel to the atom chip surface. This allows us to image the interference pattern along the transverse direction of the system (Fig. 1).

Preparing two 1D systems with a variable tunnel coupling. To introduce a variable tunnel coupling between the two 1D systems, we adjust the potential barrier between 3 and 8 kHz by changing the amplitude of the r.f. fields (Fig. 4). The actual barrier height is determined from spectroscopic measurements of the r.f. potentials to a precision $< 1 \text{ kHz}$ (ref. 37). To evaluate whether the two samples in the resulting double-well potential can be considered as 1D, we compare the chemical potential μ and the thermal energy $k_B T$ of the trapped ensembles to the single-particle level spacing in the double well. In the case of large potential barriers, the transverse confinement of each individual well can be approximated by a harmonic oscillator, and the level spacing is given by the oscillator frequency v_{\perp} . For small barriers, this approximation fails and one has to numerically calculate the single particle states in the transverse double-well potential. For the configurations shown in Fig. 4b–d, we find energy separations between the ground-state doublet and first excited states of $\Delta = 2.8, 3.4$ and 3.8 kHz , respectively. Consequently, $\mu, k_B T \leq \hbar \Delta$ for all configurations, justifying the 1D treatment of the individual systems.

Measuring the interference pattern and extracting the local relative phase. We observe the interference pattern created by the two expanding, overlapping atomic clouds using standard absorption imaging. Using diffraction-limited optics, optimized light path and pulse duration, and a weak magnetic field to define a quantization axis, we achieve atom shot noise limited imaging with $3 \mu\text{m}$

resolution and a noise floor of ~ 3 atoms per $3 \times 3 \mu\text{m}$ pixel. We extract the local relative phase $\theta(z)$ by fitting a cosine function with a gaussian envelope to the observed density distribution in each individual vertical pixel slice. The free parameters of these fits are the relative phase θ , the contrast and the fringe spacing. The width, amplitude and centre position of the envelope are determined independently from a gaussian fit to the total integrated density pattern of the central area of each image. From the measured phases, the coherence factor is evaluated (compare equation (1)). This has to be contrasted to the methods used in refs 23 and 38, where the interference patterns are summed up and the contrast is analysed.

Evaluating the coherence decay constant. There are two considerations when evaluating the decoherence constant t_0 . First, the time $t = 0$ (when the tunnel coupling vanishes and the two condensates start to evolve independently) changes for different atomic densities and trap parameters, and has to be evaluated for each data set separately. Higher atomic densities³⁹, or stronger transverse confinement, lead to increased tunnel coupling as the overlap of the two matter waves in the tunnelling region becomes larger⁴⁰. The moment of the decoupling of the two systems can be estimated by numerically calculating the time-dependent tunnel coupling throughout the splitting. Experimentally, one observes a qualitative change in the detected interference patterns^{11,20,41} when the barrier becomes higher than the chemical potential. In the case of the widely split independent condensates, the uncertainty in the determination of $t = 0$ is much smaller than 1 ms.

The second consideration is that for a finite system length L , the coherence factor does not approach zero but converges to a finite value. The average coherence factor calculated from a limited number of samples is non-zero, even if these phases are totally random. Such a limited number of samples for a system of length L is given by the finite imaging resolution, and by the finite phase-coherence length itself⁸, which in our case is comparable to a single pixel width. This results in an additional offset in the equilibrium coherence factor, which can be determined from the number of data points used in the calculation of Ψ (ref. 42).

32. Wildermuth, S. *et al.* Optimized magneto-optical trap for experiments with ultracold atoms near surfaces. *Phys. Rev. A* **69**, 030901 (2004).
33. Groth, S. *et al.* Atom chips: Fabrication and thermal properties. *Appl. Phys. Lett.* **85**, 2980–2982 (2004).
34. Krüger, P. *et al.* Disorder potentials near lithographically fabricated atom chips. Preprint at (<http://arxiv.org/cond-mat/0504686>) (2004).
35. Wildermuth, S. *et al.* Sensing electric and magnetic fields with Bose-Einstein condensates. *Appl. Phys. Lett.* **88**, 264103 (2006).
36. Lesanovsky, I. *et al.* Adiabatic radio frequency potentials for the coherent manipulation of matter waves. *Phys. Rev. A* **73**, 033619 (2006).
37. Hofferberth, S., Fischer, B., Schumm, T., Schmiedmayer, J. & Lesanovsky, I. Ultracold atoms in radio-frequency dressed potentials beyond the rotating-wave approximation. *Phys. Rev. A* **76**, 013401 (2007).
38. Hadzibabic, Z., Krüger, P., Cheneau, M., Battelier, B. & Dalibard, J. Berezinskii-Kosterlitz-Thouless crossover in a trapped atomic gas. *Nature* **441**, 1118–1121 (2006).
39. Gerbier, F. Quasi-1d Bose-Einstein condensates in the dimensional crossover regime. *Europhys. Lett.* **66**, 771–777 (2004).
40. Smerzi, A., Fantoni, S., Giovanazzi, S. & Shenoy, S. R. Quantum coherent atomic tunneling between two trapped Bose-Einstein condensates. *Phys. Rev. Lett.* **79**, 4950–4953 (1997).
41. Röhl, A., Naraschewski, M., Schenzle, A. & Wallis, H. Transition from phase locking to the interference of independent Bose condensates: Theory versus experiment. *Phys. Rev. Lett.* **78**, 4143–4146 (1997).
42. Fisher, N. I. *Statistical Analysis of Circular Data* (Cambridge Univ. Press, Cambridge, UK, 1993).

LETTERS

Generating single microwave photons in a circuit

A. A. Houck^{1*}, D. I. Schuster^{1*}, J. M. Gambetta¹, J. A. Schreier¹, B. R. Johnson¹, J. M. Chow¹, L. Frunzio¹, J. Majer¹, M. H. Devoret¹, S. M. Girvin¹ & R. J. Schoelkopf¹

Microwaves have widespread use in classical communication technologies, from long-distance broadcasts to short-distance signals within a computer chip. Like all forms of light, microwaves, even those guided by the wires of an integrated circuit, consist of discrete photons¹. To enable quantum communication between distant parts of a quantum computer, the signals must also be quantum, consisting of single photons, for example. However, conventional sources can generate only classical light, not single photons. One way to realize a single-photon source² is to collect the fluorescence of a single atom. Early experiments measured the quantum nature of continuous radiation^{3,4}, and further advances allowed triggered sources of photons on demand^{5–11}. To allow efficient photon collection, emitters are typically placed inside optical or microwave cavities^{12–19}, but these sources are difficult to employ for quantum communication on wires within an integrated circuit. Here we demonstrate an on-chip, on-demand single-photon source, where the microwave photons are injected into a wire with high efficiency and spectral purity. This is accomplished in a circuit quantum electrodynamics architecture²⁰, with a microwave transmission line cavity that enhances the spontaneous emission of a single superconducting qubit. When the qubit spontaneously emits, the generated photon acts as a flying qubit, transmitting the quantum information across a chip. We perform tomography of both the qubit and the emitted photons, clearly showing that both the quantum phase and amplitude are transferred during the emission. Both the average power and voltage of the photon source are characterized to verify performance of the system. This single-photon source is an important addition to a rapidly growing toolbox for quantum optics on a chip.

When an atom or qubit is strongly coupled to a cavity, the spontaneous emission rate to the output mode of the cavity is enhanced, a process known as the Purcell effect²¹. This effect has been used for a triggered single-photon source^{14–16}. The underlying principle for this source is straightforward: each time the qubit is excited with a control pulse, it can emit one (and only one) photon when it decays. When the qubit is put in an arbitrary superposition state, this state is mapped onto a superposition of zero and one photon, thus transferring information from a stationary to a flying qubit. The challenge is to create a system where spontaneous emission dominates other relaxation channels. This spontaneous emission rate can be determined from the hamiltonian of the system, the well-known Jaynes–Cummings hamiltonian, $H = \hbar\omega_a\sigma_z/2 + \hbar\omega_c(a^\dagger a + 1/2) + \hbar g(a^\dagger\sigma_- + a\sigma_+)$. The first two terms represent a qubit with frequency ω_a described by Pauli operators σ_x , σ_y and σ_z and raising and lowering operators σ_+ and σ_- , and a single cavity mode of frequency ω_c described by the photon creation and annihilation operators a^\dagger and a . The final term represents a coupling of strength g between the qubit and the photon, which mixes the individual qubit and photon eigenstates. When far detuned ($\Delta = \omega_c - \omega_a \gg g$), the qubit acquires a small photonic component of the wavefunction, of

magnitude g/Δ . This opens up a new source of decay for the qubit, as the photonic component of the qubit can emit at the cavity decay rate κ , resulting in a new qubit decay rate $\gamma_\kappa = (g/\Delta)^2\kappa$. The qubit can be an efficient photon source if this new decay rate dominates over other non-radiative decay rates, $\gamma_\kappa > \gamma_{\text{NR}}$.

Verifying the single-photon output is a substantial challenge in on-chip microwave experiments. The simplest approach, that of looking for a photon each time one is created, is not currently possible; unlike in optical frequency experiments, no detectors can yet resolve single-microwave photon events in a single shot. Fortunately, several unique characteristics of the source are evident in the average signal generated by many single-photon events, together yielding a convincing verification even with noisy detectors. First, the output of the single-photon source is expected to be oscillatory in the amplitude of the control pulse applied to rotate the qubit. Second, the average amplitude produced should agree well with the expected value for a single photon. Third, and most importantly, if the output of the system depends only on the state of the qubit, state tomography measured for the photons should show complete agreement with that obtained from independent measurements of the qubit. The source reported here meets all three of these criteria.

The source is implemented in a circuit quantum electrodynamics system consisting of a superconducting transmon qubit²², an optimized version of the ‘Cooper pair box’²³, capacitively coupled to a half-wave transmission line cavity with fundamental frequency $\omega_c/2\pi = 5.19$ GHz (see Fig. 1). Two important design differences between this circuit and previous incarnations of circuit quantum electrodynamics^{1,24} are needed to achieve efficient single-photon generation. First, the cavity is asymmetric in that the capacitors (mirrors) at either end of the transmission line are no longer identical, resulting in asymmetric decay rates to the input and output ports ($\kappa_{\text{in}}/2\pi \approx 200$ kHz for the input side and $\kappa_{\text{out}}/2\pi = 44$ MHz for the output). As a result, photons generated in the cavity are emitted at the output port more than 99% of the time. In addition, the total decay rate for the cavity, $\kappa/2\pi = 44$ MHz, is substantially higher than in previous samples, a necessary change for spontaneous emission to be the dominant relaxation channel for the qubit. The qubit decay rate in the absence of spontaneous emission, γ_{NR} , is frequency-dependent, with $\gamma_{\text{NR}}/2\pi < 2$ MHz for all measured transmission frequencies between 4.3 and 7.3 GHz.

Transmission measurements are used to probe the energy spectrum of this system while the qubit frequency is tuned via an external magnetic field (see Fig. 2). When the qubit is far detuned from the cavity, only a single transmission peak is observed, centred at the cavity frequency with a lorentzian line shape and linewidth given by the bare cavity width. When the qubit and cavity are resonant, two peaks in transmission are seen, a phenomenon known as the vacuum Rabi splitting. Each peak corresponds to one of the two single-excitation eigenstates of the system, which are superpositions of the separate qubit and photon excitation states. The width of each

¹Departments of Applied Physics and Physics, Yale University, New Haven, Connecticut 06520, USA.

*These authors contributed equally to this work.

peak is the average of the qubit and photon decay rates, $(\gamma + \kappa)/2$. In the dispersive limit, where the detuning Δ is much larger than the coupling g , spontaneous emission is enhanced by the Purcell effect²¹, resulting in approximate decay rates $[1 - (g/\Delta)^2]\kappa + (g/\Delta)^2\gamma$ of the cavity and $[1 - (g/\Delta)^2]\gamma + (g/\Delta)^2\kappa$ of the qubit. The experimentally determined linewidths agree well with theoretical predictions (Fig. 2b), demonstrating our ability to tune the rate of radiative decay of the qubit by tuning its frequency.

It is this enhanced qubit decay due to the cavity that is used in generating single photons: the qubit line broadens when the decay of the photon-like part of the wavefunction dominates the non-radiative qubit decay. For the results presented here, the qubit was tuned to a frequency $\omega_d/2\pi = 4.68$ GHz. With a coupling $g/2\pi = 107$ MHz, the qubit wavefunctions had a $(g/\Delta)^2 = 4\%$ photonic nature, resulting in a spontaneous emission rate $\gamma_{\kappa}/2\pi = 1.9$ MHz. The measured relaxation rate of the qubit was $\gamma/2\pi = 1.8 \pm 0.1$ MHz, indicating that the observed relaxation could be mostly accounted for by spontaneous emission to the output transmission line to within our measurement accuracy. Because the lifetime of the qubit is short, the photon source is effectively reset in under 1 μ s, allowing for rapid repeated photon generation, for a peak source power of 3 aW.

To verify single-photon generation, we first show that the output of the cavity is an oscillatory function of the input drive, as at most one photon is generated, regardless of the magnitude of the input drive. A 12 ns gaussian control pulse rotates the qubit state by a Rabi

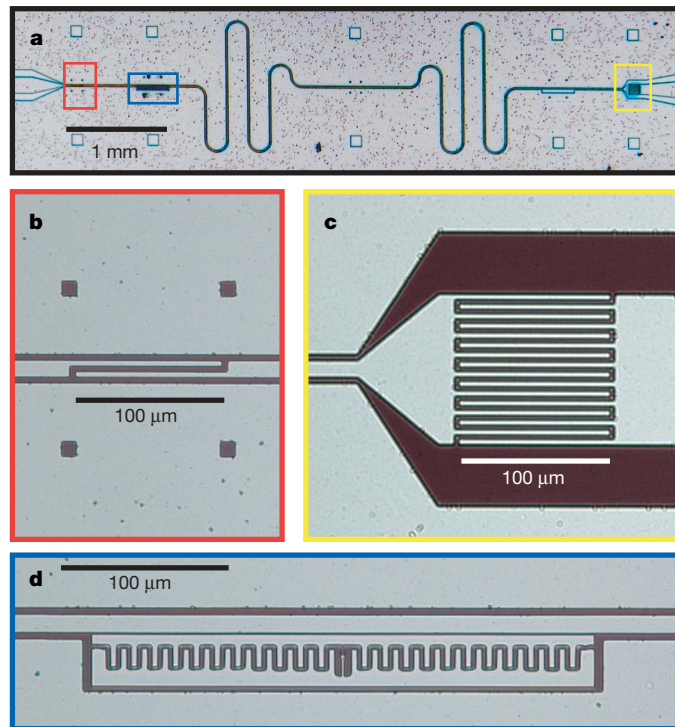


Figure 1 | The circuit quantum electrodynamics device for generating single photons. **a**, A transmission line cavity (180 nm Al on a SiO₂/Si substrate) is formed between two capacitors, with the input capacitor shown in **b** (red box in **a**) and the output in **c** (yellow box in **a**). Because the output capacitor is much larger, most radiation leaving the cavity leaves from this port, allowing efficient collection of light emitted from the cavity. **d**, Transmon qubit (100-nm-thick aluminium), an optimized ‘Cooper pair box’, at a voltage anti-node of the cavity (blue box in **a**). The qubit is characterized by a Josephson energy, tuned by an applied magnetic field with a maximum of $E_J^{\text{max}}/\hbar = 20.2$ GHz and a charging energy $E_C/\hbar = 0.37$ GHz. The coupling to the cavity is $g/2\pi = 107$ MHz at the qubit frequency primarily used in this paper, $\omega_d/2\pi = 4.68$ GHz, and has a slight dependence on the qubit frequency. The transition from the first to second excited state, $\omega_{12}/2\pi = 4.19$ GHz, is sufficiently different from ω_d to treat the qubit as a two-level system.

angle that is proportional to the pulse amplitude. The excited qubit will then relax, generating a new photon state at the qubit frequency (Fig. 3 inset). Because the control pulse leaves the cavity at a rate that is much faster than the rate of spontaneous emission, γ_{κ} , the control pulse and generated photons can easily be separated in time. As seen in Fig. 3a, the measured control signal increases monotonically, while the spontaneous emission oscillates as the qubit is rotated from the ground to the excited state and back, confirming that the spontaneous emission is proportional to the qubit state, not simply to the applied drive amplitude. This is the key to the experiment: a superposition of many photons incoming on one temporal mode give rise to one (and only one) photon on a distinct outgoing temporal mode. Moreover, because a single photon is the maximum output, the source is insensitive (to first-order) to fluctuations in the control pulse when generating one photon.

We characterize both the power and electric field of the single-photon source, using independent measurements of the qubit state made with dispersive readout techniques²⁵ to verify performance (Fig. 3). If the qubit state is mapped to the photon state, then an arbitrary superposition of the ground and excited states $\alpha|g\rangle + \beta|e\rangle$ will result in the same superposition of photon states: $\alpha|0\rangle + \beta|1\rangle$, where $|0\rangle$ and $|1\rangle$ refer to states with zero or one photon. The average photon number is proportional to the average qubit excitation probability, $\langle a^\dagger a \rangle = (\langle \sigma_z \rangle + 1)/2$, and has a maximum of one photon when the qubit is in the purely excited state. The two quadratures of homodyne voltage, on the other hand, are proportional to the x and y components of the qubit state: $\langle a + a^\dagger \rangle = \langle \sigma_x \rangle$ and $i\langle a^\dagger - a \rangle = \langle \sigma_y \rangle$. The measured homodyne voltage is therefore a $\pi/2$ rotation out-of-phase with the measured power, and the homodyne voltage is zero when a single photon is generated, because there is complete phase uncertainty in a photon Fock state.

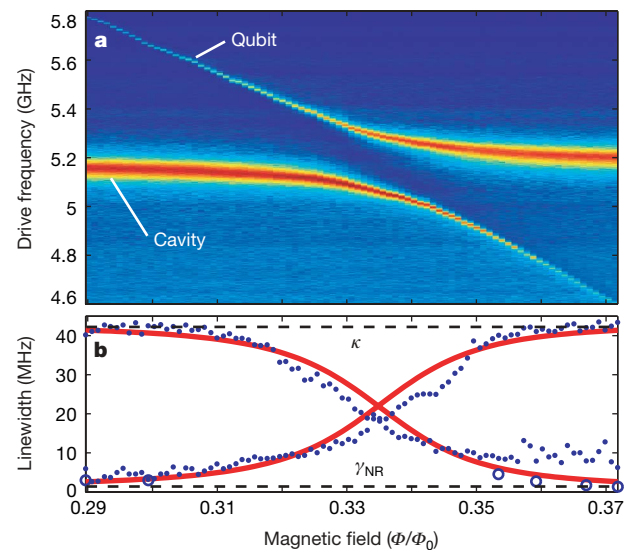


Figure 2 | Enhanced spontaneous emission through the Purcell effect.

a, Transmission through the cavity–qubit system at different applied fluxes (log scale). Two peaks are evident in transmission due to the vacuum Rabi splitting. Away from the avoided crossing, these peaks correspond to ‘mostly qubit’ and ‘mostly cavity’ states. The bare linewidth of the cavity, $\kappa/2\pi = 44$ MHz, is much larger than the bare qubit linewidth $\gamma/2\pi < 2$ MHz. **b**, Extracted linewidths from the data in **a** (blue dots) are compared with theoretical values (red lines). As the qubit and cavity peaks approach degeneracy, the qubit peak becomes broader owing to spontaneous emission to the cavity mode, while the cavity decay is suppressed. Extra dephasing present only at low frequencies (the right side of the graph) causes a non-Lorentzian line shape and excessive width. Measurements of the relaxation rate in the time domain (open blue circles) agree with theoretical estimates. Discrepancies arise due to flux noise and variations in non-radiative decay with frequency. The operating point for Figs 3–5 is $\Phi/\Phi_0 = 0.366$.

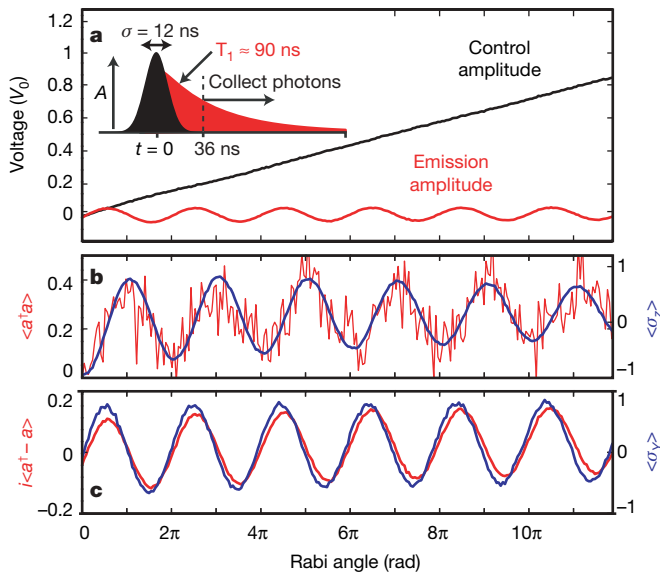


Figure 3 | Output of a single-photon source. Measurements of the qubit state are shown in blue, photon emission in red, and control signal in black. **a**, Measured drive (at $t = 0$ ns) and spontaneous emission voltage (at $t = 36$ ns) of cavity output, in units of zero-point voltage fluctuations $V_0 \approx 2 \mu\text{V}$. The inset shows the time sequence, with a gaussian pulse at the qubit frequency and subsequent photon emission with relaxation time T_1 . When the amplitude A of the drive rotating the qubit is linearly increased, the amplitude of the output voltage of the cavity is oscillatory. **b**, Photon number output of the cavity $\langle a^\dagger a \rangle$ (integrated from $t = 36$ ns to $t = 236$ ns) detected with a diode (left axis), and the measured qubit state $\langle \sigma_z \rangle$ (right axis). These peak when the qubit is in the excited state, after a π pulse; the agreement between qubit and photon states verifies the photon generation occurs as expected. After a π pulse, the integrated power is 38% of that expected for a single photon, setting the scale for the photon axis. Fits to the qubit decays are used to extrapolate the qubit polarization immediately after the control pulse, and are used to set the scale of the qubit axis. **c**, Integrated voltage of the output photons $i\langle a^\dagger - a \rangle$ (from $t = 36$ ns to $t = 104$ ns) compared with the qubit state $\langle \sigma_y \rangle$, measured with a Ramsey experiment. The agreement shows that the phase of superposition states is also transferred from qubit to photon. Only 12% of the voltage for the $\pi/2$ superposition is collected here, owing to non-radiative decay and qubit dephasing, setting the scale of the voltage axis. The qubit amplitude is again extrapolated to the time immediately following the control pulse.

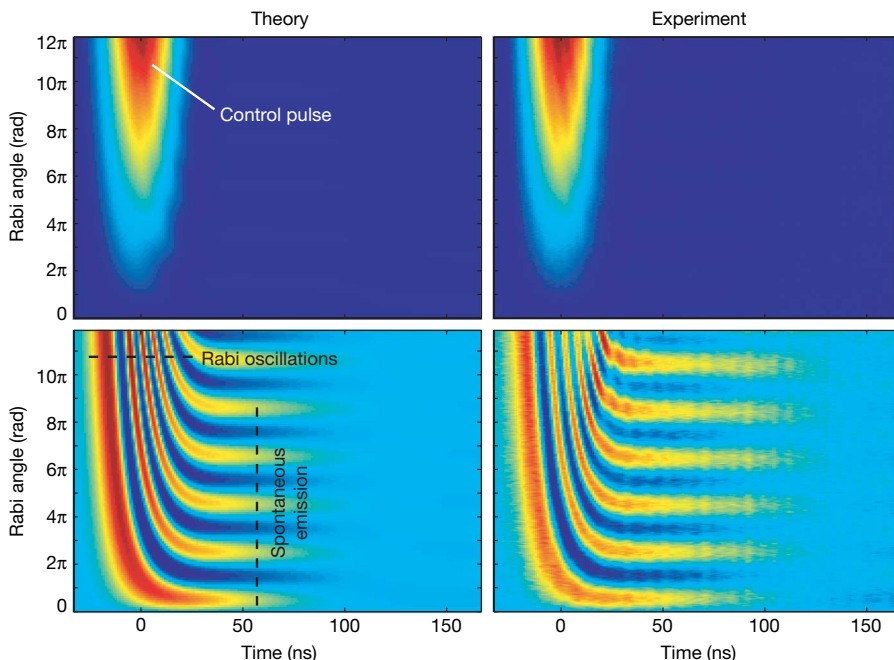


Figure 4 | Direct observation of the free induction decay of a superconducting qubit.

Theoretical predictions (left) for both quadratures of the homodyne voltage, both in-phase (top) and out-of-phase (bottom) with the drive, agree well with experimental measurements of the two phases (right). Because emission is always orthogonal to the rotation axis, the spontaneous emission and control signal are phase separable. The homodyne sine waves in Fig. 3c are calculated as integrals of horizontal slices through this data at different angles. The frequency of these oscillations, coupled with a gain known from measurements of the control pulse, provide a calibration, which is used to predict the experimental emission data. The qubit and drive are slightly detuned by a fluctuating amount due to flux instability (of the order of 3 MHz), so there is a slow beat note in the time direction. This fluctuating detuning is modelled by adding the predicted homodyne emission at two detunings, ± 1.5 MHz. The fast oscillations in the time domain are a direct measure of the Rabi oscillations of the qubit.

Using markovian master equation simulations, the complete time dynamics can be predicted with excellent accuracy, as shown for the homodyne voltage in Fig. 4. Several features of the time dynamics are striking. First, because the control pulse sets the rotation axis, and the qubit state sets the emission phase, the control and generated photons are orthogonal in phase, which allows the two signals to be completely separated in homodyne detection. In the generated photon quadrature, rapid time oscillations are apparent during the control pulse; this is a direct observation of the Rabi oscillation of the qubit through its spontaneous emission. After the pulse, the qubit emits with a phase that depends on its final state, resulting in oscillations in the control amplitude that smoothly connect to the time oscillations. Finally, there is a very-low-frequency oscillation in time. Photons are emitted at the qubit frequency, which is slightly detuned from the drive frequency. The result is a beating, with a half-period shown in both theory and data images, indicative of a frequency separation between the input and output photons in addition to the phase and time separations.

These simulations can also be used to calibrate the efficiency of the source. They are based on independently measured parameters of the system, with the only unknown parameter being the overall amplitude scaling. However, this scaling parameter is the same for both the measured control and measured emission photons. Therefore, comparison of the amplitude of the control pulse in theory and experiment yields a calibration for the single-photon emission, which allows a calculation of the efficiency of the sources.

Two metrics of efficiency characterize the performance of the system. The source efficiency is the fraction of time in which a photon is emitted after a control pulse. This depends on the final polarization of the qubit and the ratio of radiative to non-radiative channels. In generating a single photon, the π -pulse leaves the qubit 87% polarized, and nearly all decay is radiative ($\gamma_r/\gamma > 90\%$), giving source efficiency of more than 78%. For generating a superposition of zero and one photon, the quadrature phase of the photon must also be controlled. Here, the qubit is 77% polarized along σ_y , but a dephasing rate $\gamma_\phi \approx 1$ MHz leads to only $\gamma_r/(\gamma + 2\gamma_\phi) = 50\%$ radiative efficiency, giving a total source efficiency of 39%.

A second metric, the usable source efficiency, is somewhat lower in the current experiment, because the control pulse is slow and a delay is necessary to reject any control photons which could give a double-photon event. In the data of Fig. 3, collection of radiation begins after

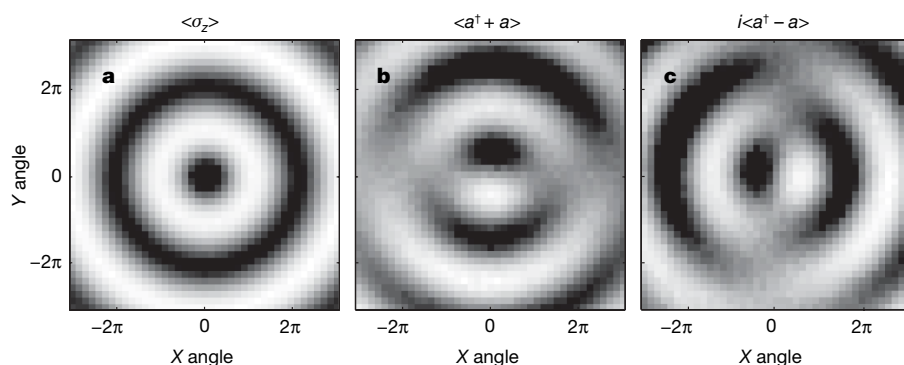


Figure 5 | Mapping the qubit state onto the photon state. **a**, Measurement of the qubit state $\langle \sigma_z \rangle$ after rotations by pulses of arbitrary amplitude and phase. Regardless of the phase of the pulse, the qubit oscillates to a peak after a π pulse. **b**, **c**, Fluorescence tomography. The amplitude of the voltage measured in each homodyne quadrature, $\langle a + a^\dagger \rangle$ and $i\langle a^\dagger - a \rangle$, agree with expectations for $\langle \sigma_x \rangle$ and $\langle \sigma_y \rangle$. Oscillations around the x-axis produce a signal in $i\langle a^\dagger - a \rangle$ and none in $\langle a + a^\dagger \rangle$. This shows the ability to map an arbitrary qubit state onto a photon state, as well as the ability to characterize a qubit state through spontaneous emission.

three standard deviations of the control pulse gaussian, making the likelihood of contamination by a control photon less than 0.01%. Integrating the measured spontaneous emission, the number of detected photons is measured directly, yielding an efficiency of 38% for the single-photon source, and 12% for the homodyne voltage of the superposition state, which is again lower, owing to dephasing. Even rejecting the emission contaminated by control pulse photons, which contains the high signal-to-noise part of the emission, a substantial fraction of one photon is recovered. If a less stringent rejection threshold of 1% is chosen, efficiencies rise to 46% for power and 16% for homodyne voltage. In future experiments, this could be improved further with faster pulses, longer coherence times, or fast tunability of the qubit frequency, achieving usable source efficiencies close to 100%.

Tomography presents an even more powerful tool for characterizing the transfer from qubit state²⁶ to photon state^{27,28} (Fig. 5). Here, qubit tomography is performed by applying control pulses of arbitrary phase and amplitude, and performing a dispersive measurement²⁵ of the qubit state $\langle \sigma_z \rangle$. This yields the expected concentric rings for a qubit initially in the ground state (Fig. 5a). Similarly, for the same set of control pulses, both quadratures of the output homodyne voltage are recorded (Fig. 5b, c). These show excellent agreement with the expected σ_x and σ_y components of the qubit state²⁶. This fluorescence tomography technique allows a full characterization of the qubit by looking at the spontaneous emission at the output, directly observing a superconducting qubit at its Larmor frequency. Moreover, this means that a qubit state at arbitrary points on the Bloch sphere can be transferred onto a photon state, thus moving information from a stationary qubit to a “flying qubit”, one of the DiVincenzo resources for quantum information processing²⁹.

The mapping of qubit states onto photon states allows for the use of microwave photons as a true resource for quantum information on a chip. These photons are generated on-demand with a high repetition rate, good spectral purity, and high efficiency. This is a convenient means of creating non-classical states of light to interact with atoms, in which the photon can be guided along the wires of an integrated circuit, allowing them to be shuttled around a chip. The generation of single photons, and superpositions of photon states, is an important step towards on-chip quantum optics experiments.

Received 6 February; accepted 24 July 2007.

- Schuster, D. I. *et al.* Resolving photon number states in a superconducting circuit. *Nature* **445**, 515–518 (2007).
- Oxborrow, M. & Sinclair, A. Single-photon sources. *Contemp. Phys.* **46**, 173–206 (2005).
- Clauser, J. F. Experimental distinction between the quantum and classical field-theoretic predictions for the photoelectric effect. *Phys. Rev. D* **9**, 853–860 (1974).
- Kimble, H. J., Dagenais, M. & Mandel, L. Photon antibunching in resonance fluorescence. *Phys. Rev. Lett.* **39**, 691–695 (1977).
- Diedrich, F. & Walther, H. Nonclassical radiation of a single stored ion. *Phys. Rev. Lett.* **58**, 203–206 (1987).
- Basche, T., Moerner, W. E., Orrit, M. & Talon, H. Photon antibunching in the fluorescence of a single dye molecule trapped in a solid. *Phys. Rev. Lett.* **69**, 1516–1519 (1992).

- Brunel, C., Lounis, B., Tamarat, P. & Orrit, M. Triggered source of single photons based on controlled single molecule fluorescence. *Phys. Rev. Lett.* **83**, 2722–2725 (1999).
- Lounis, B. & Moerner, W. E. Single photons on demand from a single molecule at room temperature. *Nature* **407**, 491–493 (2000).
- Kurtsiefer, C., Mayer, S., Zarda, P. & Weinfurter, H. Stable solid-state source of single photons. *Phys. Rev. Lett.* **85**, 290–293 (2000).
- Michler, P. *et al.* Quantum correlation among photons from a single quantum dot at room temperature. *Nature* **406**, 968–970 (2000).
- Darquie, B. *et al.* Controlled single-photon emission from a single trapped two-level atom. *Science* **309**, 454–456 (2005).
- Maitre, X. *et al.* Quantum memory with a single photon in a cavity. *Phys. Rev. Lett.* **79**, 769–772 (1997).
- Brattke, S., Varcoe, B. T. H. & Walther, H. Generation of photon number states on demand via cavity quantum electrodynamics. *Phys. Rev. Lett.* **86**, 3534–3537 (2001).
- Moreau, E. *et al.* Single-mode solid-state single photon source based on isolated quantum dots in pillar microcavities. *Appl. Phys. Lett.* **79**, 2865–2867 (2001).
- Santori, C., Fattal, D., Vuckovic, J., Solomon, G. S. & Yamamoto, Y. Indistinguishable photons from a single-photon device. *Nature* **419**, 594–597 (2002).
- Pelton, M. *et al.* Efficient source of single photons: A single quantum dot in a micropost microcavity. *Phys. Rev. Lett.* **89**, 233602 (2002).
- Kuhn, A., Hennrich, M. & Rempe, G. Deterministic single-photon source for distributed quantum networking. *Phys. Rev. Lett.* **89**, 067901 (2002).
- McKeever, J. *et al.* Deterministic generation of single photons from one atom trapped in a cavity. *Science* **303**, 1992–1994 (2004).
- Keller, M., Lange, B., Hayasaka, K., Lange, W. & Walther, H. Continuous generation of single photons with controlled waveform in an ion-trap cavity system. *Nature* **431**, 1075–1078 (2004).
- Blais, A., Huang, R.-S., Wallraff, A., Girvin, S. M. & Schoelkopf, R. J. Cavity quantum electrodynamics for superconducting electrical circuits: An architecture for quantum computation. *Phys. Rev. A* **69**, 062320 (2004).
- Purcell, E. M. Spontaneous emission probabilities at radio frequencies. *Phys. Rev.* **69**, 681 (1946).
- Koch, J. *et al.* Charge insensitive qubit design derived from the Cooper pair box. *Phys. Rev. A* (in the press); preprint at (<http://arxiv.org/cond-mat/0703002>) (2007).
- Bouchiat, V., Vion, D., Joyez, P., Esteve, D. & Devoret, M. H. Quantum coherence with a single cooper pair. *Phys. Scr.* **T76**, 165–170 (1998).
- Wallraff, A. *et al.* Strong coupling of a single photon to a superconducting qubit using circuit quantum electrodynamics. *Nature* **431**, 162–167 (2004).
- Wallraff, A. *et al.* Approaching unit visibility for control of a superconducting qubit with dispersive readout. *Phys. Rev. Lett.* **95**, 060501–060504 (2005).
- Steffen, M. *et al.* State tomography of capacitively shunted phase qubits with high fidelity. *Phys. Rev. Lett.* **97**, 050502 (2006).
- Smith, D. T., Beck, M., Raymer, M. G. & Faridani, A. Measurement of the Wigner distribution and the density matrix of a light mode using optical homodyne tomography: application to squeezed states and the vacuum. *Phys. Rev. Lett.* **70**, 1244–1247 (1993).
- Leonhardt, U. *Measuring the Quantum State of Light* (Cambridge Univ. Press, 1997).
- DiVincenzo, D. P. The physical implementation of quantum computation *Fortschr. Phys.* **48**, 771–783 (2000).

Acknowledgements This work was supported in part by the National Security Agency under the Army Research Office, the NSF, and Yale University. A.A.H. acknowledges support from Yale University via a Quantum Information and Mesoscopic Physics Fellowship.

Author Information Reprints and permissions information is available at www.nature.com/reprints. The authors declare no competing financial interests. Correspondence and requests for materials should be addressed to R.J.S. (robert.schoelkopf@yale.edu).

LETTERS

Increased terrestrial methane cycling at the Palaeocene–Eocene thermal maximum

Richard D. Pancost¹, David S. Steart², Luke Handley¹, Margaret E. Collinson², Jerry J. Hooker³, Andrew C. Scott², Nathalie V. Grassineau² & Ian J. Glasspool⁴

The Palaeocene–Eocene thermal maximum (PETM), a period of intense, global warming about 55 million years ago¹, has been attributed to a rapid rise in greenhouse gas levels, with dissociation of methane hydrates being the most commonly invoked explanation². It has been suggested previously that high-latitude methane emissions from terrestrial environments could have enhanced the warming effect^{3,4}, but direct evidence for an increased methane flux from wetlands is lacking. The Cobham Lignite, a recently characterized expanded lacustrine/mire deposit in England, spans the onset of the PETM⁵ and therefore provides an opportunity to examine the biogeochemical response of wetland-type ecosystems at that time. Here we report the occurrence of hopanoids, biomarkers derived from bacteria, in the mire sediments from Cobham. We measure a decrease in the carbon isotope values of the hopanoids at the onset of the PETM interval, which suggests an increase in the methanotroph population. We propose that this reflects an increase in methane production potentially driven by changes to a warmer^{1,6} and wetter climate^{7,8}. Our data suggest that the release of methane from the terrestrial biosphere increased and possibly acted as a positive feedback mechanism to global warming.

Although the PETM is not a direct analogue for future global warming because it occurs during a time when global temperatures were significantly higher than now⁹, it still allows the investigation of rapid warming comparable to that occurring today. A significant challenge in the investigation of terrestrial methane cycling at the PETM is the lack of appropriate sedimentary sequences. However, we have recently reported the identification of the PETM interval in lake and mire sediments from Cobham, southeast England⁵. The section, represented primarily by lignite through the PETM interval, provides a unique opportunity to study wetland microbial processes in a stratigraphically expanded and relatively complete continental section. The PETM is stratigraphically constrained (Methods) and characterized by a negative carbon isotope excursion (CIE) recorded by plant organic matter⁵ (Fig. 1). The pronounced CIE is one of the defining characteristics of the PETM^{6,9} and is typically attributed to the catastrophic release of ¹³C-depleted methane from marine gas hydrates.

Critically, at Cobham, the 2-m sequence between the top of the Upnor Formation and the base of the WSB (Woolwich Shell Beds) is entirely freshwater. The black slickensided clay at the base of the sand and mud unit contains leech cocoons, termite coprolites, pollen and spores, but lacks dinoflagellates. The overlying sand (sand and mud unit) contains continental and freshwater pollen and spores and lacks the *Ophiomorpha* burrows indicative of saline conditions that are present in the underlying Upnor Formation. The Cobham Lignite

Bed (lignites and included thin clay bands) contains an abundance of continental and freshwater aquatic pollen and spores and algal cysts, and lacks dinoflagellates^{5,10}; it is in this bed, with organic carbon contents ranging from 15 to 36 wt%, that the negative CIE has been recorded⁵ (Fig. 1). A similar sequence with a freshwater lignite (although a thinner one than at Cobham) followed by brackish shelly clays, has been described from the north French coast at Varengeville; like Cobham, the CIE is recorded in the lignitic beds¹¹, testifying to the extensive nature of the low-lying area of the southwest North Sea Basin at the time. Further to the east, in north Belgium, the Doel and Kallo boreholes, which are down dip from Kent in the North Sea Basin, show that the CIE occurs in a mixed freshwater and brackish sequence¹². Thus, the nearest occurrence of contemporaneous saline conditions is perhaps hundreds of kilometres from the Cobham Lignite studied here. Such a setting provides an ideal, perhaps even unique, opportunity to examine the biogeochemical response of a continental lacustrine/mire system to increased global temperature at the PETM.

Examination of microbially mediated biogeochemical processes in ancient sediments can be challenging, but biomarkers (organic compounds that can be structurally related to biological precursors) have proved to be useful in studying the ancient microbiology of, for example, the Permo-Triassic boundary¹³. In the Cobham Lignite, the hydrocarbon distribution is dominated by *n*-alkanes with an odd-over-even carbon number predominance indicative of a higher-plant origin¹⁴ and exceptional abundances of hopanes and hopenes (Fig. 2) derived from bacteria¹⁵. Triterpenes and sterenes of inferred higher-plant origin are also present but in subordinate abundances. In the polar fractions, which are discussed here only briefly, *n*-alkanols and sterols, also of inferred higher-plant origin, are predominant.

The hopanes are dominated by the C₂₉, C₃₀ and C₃₁ homologues (21-norhopane, hopane and homohopane, respectively), with the 17 α ,21 β (H), 17 β ,21 β (H) and 17 β ,21 α (H) isomers all present. The presence of abundant hopanes with the biological $\beta\beta$ configuration and the lack of hopanes with 22S stereochemistry, combined with high abundances of hopenes, indicate that the Cobham Lignite is relatively immature with regard to petroleum generation, which is consistent with vitrinite reflectance values ($R_o = 0.39 \pm 0.1$ (mean \pm s.d.))¹⁰. Traditionally, hopanes and their precursor hopanoids have been attributed to aerobic bacteria, but recent work has revealed an anaerobic origin for hopanoids as well¹⁶; consequently, the interpretation of hopanoid distributions and depth profiles is complex. In the Cobham Lignite, further complexity is imposed by marked variations in hopanoid distributions and stereochemistry, the latter possibly being due to changing environmental conditions during sediment deposition¹⁷.

¹Organic Geochemistry Unit, Bristol Biogeochemistry Research Centre, School of Chemistry, University of Bristol, Cantock's Close, Bristol BS8 1TS, UK. ²Department of Geology, Royal Holloway University of London, Egham, Surrey TW20 0EX, UK. ³Palaeontology Department, Natural History Museum, Cromwell Road, London SW7 5BD, UK. ⁴Department of Geology, The Field Museum, 1400 S. Lake Shore Drive, Chicago, Illinois 60605, USA.

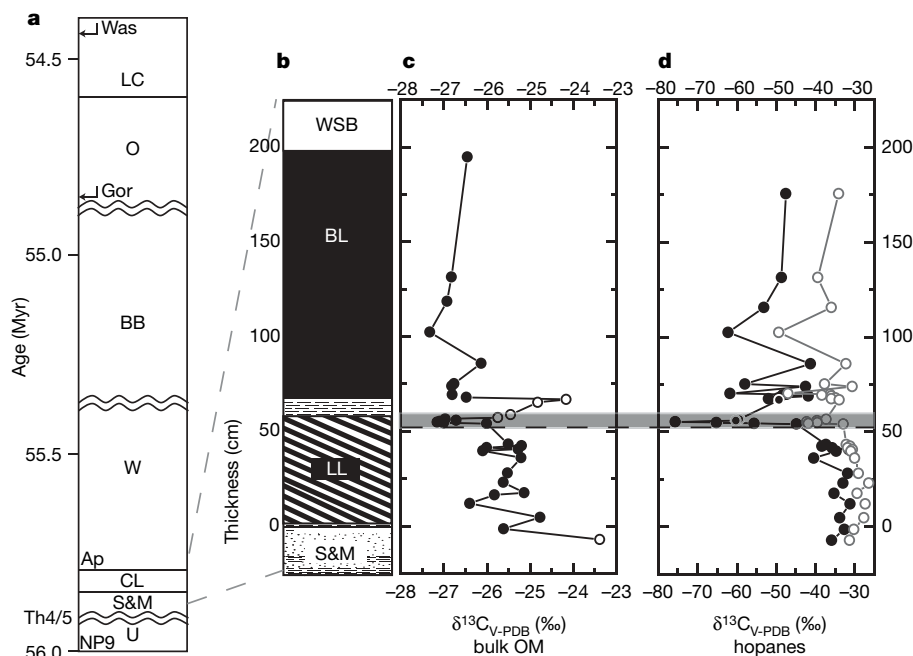


Figure 1 | Depth profile through the Cobham Lignite. **a**, Position of the profile in the temporally calibrated latest Palaeocene and Early Eocene East London Basin sequence. U, Upnor Formation; S&M, sand and mud unit; CL, Cobham Lignite; W, Woolwich Formation; BB, Blackheath Beds; O, Oldhaven Member; LC, London Clay Formation. Ap denotes *Apectodinium*, Gor and Was refer to dinocyst zones, and Th4/5 denotes a sequence boundary. For further details, see Methods. **b**, Lithologic log of the CL (BL, blocky lignite; LL, laminated lignite); WSB, lower Woolwich Shell Beds.

More specific biological source information can be obtained from the carbon isotopic composition of the hopanes (Fig. 1d). In the lower part of the lignite and the underlying sand and mud unit, $\delta^{13}\text{C}$ values of the C_{29} hopane ($17\beta,21\beta(\text{H})$ isomer) are about -36‰ and values of the C_{31} hopane ($17\beta,21\beta(\text{H})$ isomer) range from -31 to -30.5‰ . These values are slightly depleted relative to co-occurring bulk organic matter (-26 to -24.5‰) and higher-plant n -alkanes (-30.5 to -29.5‰). The carbon isotopic compositions of hopanes in some recent wetlands are typically enriched in ^{13}C relative to these values (-26 to -22‰) and relative to co-occurring higher-plant biomarkers¹⁷; this has been attributed to a heterotrophic ecology in which the source bacteria were consuming ^{13}C -enriched carbohydrates. In the Cobham Lignite, the lower $\delta^{13}\text{C}$ values suggest that the hopanes derive from a mixture of heterotrophic bacteria that

consumed higher-plant-derived organic matter and methanotrophs that were significantly depleted in ^{13}C (there is no biomarker evidence for cyanobacteria).

At the base of the PETM as indicated by a shift in bulk organic $\delta^{13}\text{C}$ values from -26 to -27.6‰ (Fig. 1c), hopane $\delta^{13}\text{C}$ values decrease markedly to -42‰ and -76‰ for the C_{31} and C_{29} hopanes, respectively. In fact, all hopane and hopene $\delta^{13}\text{C}$ values decrease significantly through this depth interval, but accurate values could be determined only for the components shown in Fig. 1 because of co-elution or peak size. Such a preponderance of hopanes with very low $\delta^{13}\text{C}$ values is unusual in the geological record, with reported occurrences limited to only a few methanogenic lacustrine settings^{18–20} and cold-seep carbonate deposits. We know of no other modern or ancient mire deposit characterized by such ^{13}C -depleted hopanoids.

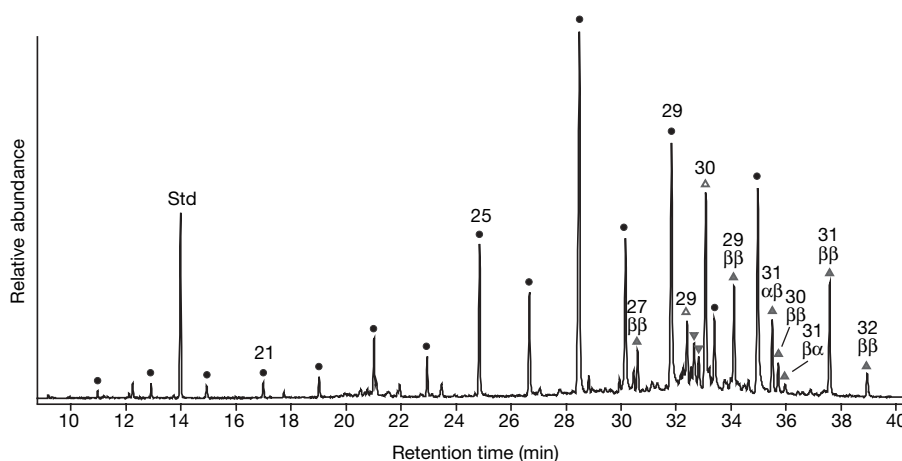


Figure 2 | Gas chromatogram of a typical Cobham Lignite apolar (hydrocarbon) fraction. The sample shown is from a depth of 55.3 cm, coinciding with the most negative hopanoid $\delta^{13}\text{C}$ values). Filled circles,

n -alkanes; filled triangles, hopanes with stereochemistry shown above; open triangles, hopenes; inverted triangles, C_{29} sterenes. In all cases, numbers indicate the number of carbon atoms in the molecule. Std, standard.

The shift in hopane $\delta^{13}\text{C}$ values could be due to a decrease in heterotrophic bacterial biomass or an increase in the total methanotroph biomass. In the Cobham Lignite, hopane concentrations vary significantly, but neither their absolute abundances (relative to total lignite) nor their abundances relative to higher-plant *n*-alkanes covary with their carbon isotopic compositions. In fact, abundances stay relatively constant during the most marked carbon isotopic shift, suggesting that the hopane CIE is not due solely to decreased inputs from heterotrophic bacteria but is instead a combination of decreased heterotrophic bacterial inputs coinciding with increased methanotroph inputs. As with all proxies, caution must be used when interpreting biomarker trends; for example, the decrease in $\delta^{13}\text{C}$ values could also indicate a change in the depositional environment that favours the preservation of methanotroph-derived hopanoids. Such an explanation seems unlikely because the shift in $\delta^{13}\text{C}$ values occurs before any major lithologic change (Fig. 1), and no ^{13}C -depleted compounds were observed before the PETM. The unusual dominance of ^{13}C -depleted hopanoids at the PETM is unlikely to be an artefact of a change in preservation that is unaccompanied by evidence for a change in depositional environment. Thus, we interpret the shift in hopane $\delta^{13}\text{C}$ values as evidence for increased methanotroph biomass and, possibly, decreased heterotroph biomass. Because methanotrophy generally tracks methane concentrations²¹, the increase in methanotroph hopanes was almost certainly a response to increased methane flux from deeper sediments; in fact, increased methanogenic organic matter degradation would also be consistent with the inferred decrease in hopane contributions from heterotrophic bacteria.

Although the Cobham Lignite is a unique deposit and comparable records have not yet been explored, it provides a useful analogue of how such settings might respond to the warming and associated climatic changes that occurred at the PETM. Higher temperatures increase the rate of methanogenesis in modern settings²²; consequently, warming could have exerted a direct control on methane release from the Cobham setting and similar environments. Alternatively or additionally, wetter conditions are also associated with elevated methane fluxes from wetlands, and there is evidence that the climate local to the Cobham Lignite became wetter at the PETM. The lower laminated lignite was deposited in a shallow lacustrine/mire setting, a situation that persisted through the base of the CIE and the corresponding shift in hopane $\delta^{13}\text{C}$ values. However, in the uppermost 2 cm of the laminated lignite, corresponding to the lowest hopane $\delta^{13}\text{C}$ values (as denoted by the horizontal grey bar in Fig. 1), there is a marked decrease in charcoal content and an increase in clay-rich laminae, which together have been interpreted as evidence for increased precipitation and/or humidity over the surrounding area²³. Deposition of the laminated lignite was followed conformably by a thin clay and then accumulation of the charcoal-poor blocky lignite. Because the change from laminated to blocky lignite lithology followed the negative shift in hopane $\delta^{13}\text{C}$ values, it seems to be an unlikely mechanism for increased rates of methanogenesis. Instead, changes in the hydrological regime (and possibly warming) could have brought about increased methanogenesis in the Cobham depositional setting. As there have been several studies suggesting elevated humidity⁷ or precipitation at the PETM^{8,24,25}, similar increases in methane cycling could have occurred at other locations. Potentially, such increased rates of methanogenesis and methanotrophy in continental settings could have contributed to changes in the global carbon cycle at the PETM.

Recent work, including new records of carbonate compensation depth shoaling²⁶ and higher-plant biomarker $\delta^{13}\text{C}$ values in Arctic sediments²⁷, has been used to argue for a greater input of carbon than that suggested by the methane hydrate model². Enhanced terrestrial methane inputs from Cobham and similar settings could have served as an additional source of carbon, but we consider this unlikely because increased methanogenesis would probably occur at the expense of CO_2 emissions, and the net carbon input into the

atmosphere would remain constant. However, wetlands are the dominant natural source of atmospheric methane on the Earth today²², and increased continental methane emissions could have been important. Continental methane sources are thought to be important components of glacial–interglacial changes in atmospheric methane concentrations, with enhanced methane production in tropical wetlands possibly accounting for 70% of the increase in atmospheric methane since the last deglaciation²⁸. Although this is equivalent to only about 250 Gt of methane, the magnitude of methane release from wetlands could have been greater at the PETM if large quantities of organic carbon had been sequestered in peatlands during the Palaeocene²⁹; indeed, previous workers have suggested that increased methane fluxes from wetlands could have contributed to warming at the PETM^{3,4,7}. In particular, it was argued³ that such an increased flux contributed to high-latitude warming by the formation of polar stratospheric clouds; given new data suggesting that sea surface temperatures in the Arctic Ocean were higher than models have predicted³⁰, the role of atmospheric methane as a positive feedback on climate change could have been significant.

Of course, caution is necessary when extrapolating our observations in the Cobham Lignite to a global scale: many previous workers have commented on the complex controls governing methane flux from wetlands and similar environments, with particular emphasis placed on not just changes in precipitation and temperature but also vegetation and the antecedent hydrological conditions. However, our work, especially when combined with globally diverse evidence for increasing precipitation or continental runoff at the PETM^{8,25}, suggests that terrestrial environments could produce more methane in response to global warming both at the PETM and in the future.

METHODS SUMMARY

In general, all of the East London Basin sequence from the latest Palaeocene to the Early Eocene was exposed at Cobham (Fig. 1a) with the sand and mud unit (S&M), Cobham Lignite (CL) and lower Woolwich Shell Beds (W) all shown in expanded view in Fig. 1b. Analytical methods employed in this study focused on the determination of both bulk and specific biomarker carbon isotopic compositions (expressed in $\delta^{13}\text{C}$ notation relative to Vienna Pee Dee Belemnite (V-PDB) carbonate standard). Carbon isotopic measurements on bulk samples were obtained with a high-resolution He-continuous flow mass spectrometry technique (EA-IRMS), and the reproducibility on the standards is better than $\pm 0.1\%$. For biomarker analyses, samples were gently washed with methanol, powdered and extracted by sonication; resultant lipid extracts were separated into three fractions on a column packed with (activated) alumina. GC–MS was performed with a Thermoquest Finnigan Trace GC interfaced to a Thermoquest Finnigan Trace MS, and GC-IRMS was performed with a ThermoFinnigan DeltaS. For both, a fused silica capillary column (50 m \times 0.32 mm) coated with CP-Sil-5 (film thickness 0.12 μm) was used with the following temperature programme: 40 $^{\circ}\text{C}$ to 140 $^{\circ}\text{C}$ at 20 $^{\circ}\text{C min}^{-1}$, then to 300 $^{\circ}\text{C}$ at 4 $^{\circ}\text{C min}^{-1}$, maintained at 300 $^{\circ}\text{C}$ for 22 min. For compound-specific carbon isotopic analyses, the reproducibility on the standards is better than $\pm 0.3\%$.

Full Methods and any associated references are available in the online version of the paper at www.nature.com/nature.

Received 12 December 2006; accepted 8 June 2007.

1. Zachos, J. C. *et al.* A transient rise in tropical sea surface temperature during the Paleocene–Eocene Thermal Maximum. *Science* **302**, 1551–1554 (2003).
2. Dickens, G. R. Rethinking the global carbon cycle with a large, dynamic and microbially mediated gas hydrate capacitor. *Earth Planet. Sci. Lett.* **213**, 169–183 (2003).
3. Sloan, L. C., Walker, J. C. G., Moore, T. C., Rea, D. K. & Zachos, J. C. Possible methane-induced polar warming in the early Eocene. *Nature* **357**, 320–322 (1992).
4. Sloan, L. C. & Pollard, D. Polar stratospheric clouds: A high latitude warming mechanism in an ancient greenhouse world. *Geophys. Res. Lett.* **25**, 3517–3520 (1998).
5. Collinson, M. E., Hooker, J. J. & Gröcke, D. R. in *Causes and Consequences of Globally Warm Climates in the Early Paleogene* (eds Wing, S. L., Gingerich, P. D., Schmitz, B. & Thomas, B.) 333–349 (Geol. Soc. Am. Special Paper 369, Boulder, Colorado, 2003).

6. Kennett, J. P. & Stott, L. D. Abrupt deep-sea warming, palaeoceanographic changes and benthic extinctions at the end of the Palaeocene. *Nature* **353**, 225–229 (1991).
 7. Bowen, G. J., Beerling, D. J., Koch, P. L., Zachos, J. C. & Quattlebaum, T. A humid climate state during the Palaeocene/Eocene thermal maximum. *Nature* **432**, 495–499 (2004).
 8. Crouch, E. M. *et al.* The *Apectodinium* acme and terrestrial discharge during the Palaeocene–Eocene thermal maximum: new palynological, geochemical and calcareous nannoplankton observations at Tawanui, New Zealand. *Palaeogeogr. Palaeoclimatol. Palaeoecol.* **194**, 387–403 (2003).
 9. Zachos, J., Pagani, M., Sloan, L., Thomas, E. & Billups, K. Trends, rhythms, and aberrations in global climate 65 Ma to present. *Science* **292**, 686–693 (2001).
 10. Collinson, M. E., Steart, D. C., Scott, A. C., Glasspool, I. J. & Hooker, J. J. Episodic fire, run-off and deposition at the Palaeocene–Eocene boundary. *J. Geol. Soc. Lond.* **164**, 87–97 (2007).
 11. Magioncalda, R. *et al.* L'excursion isotopique du carbone organique ($\delta^{13}\text{C}$) dans les paléoenvironnements continentaux de l'intervalle Paléocène/Eocène de Varengeville (Haute-Normandie). *Bull. Soc. Geol. Fr.* **172**, 349–358 (2001).
 12. Steurbaut, E. *et al.* Palynology, palaeoenvironments, and organic carbon isotope evolution in lagoonal Palaeocene–Eocene boundary settings in North Belgium. *GSA Spec. Pap.* **369**, 291–317 (2003).
 13. Xie, S. C., Pancost, R. D., Yin, H. F., Wang, H. M. & Evershed, R. P. Two episodes of microbial change coupled with Permo/Triassic faunal mass extinction. *Nature* **434**, 494–497 (2005).
 14. Eglinton, G. & Hamilton, R. J. Leaf epicuticular waxes. *Science* **156**, 1322–1334 (1967).
 15. Rohmer, M., Bouviernave, P. & Ourisson, G. Distribution of hopanoid triterpenes in prokaryotes. *J. Gen. Microbiol.* **130**, 1137–1150 (1984).
 16. Hartner, T., Straub, K. L. & Kannenberg, E. Occurrence of hopanoid lipids in anaerobic *Geobacter* species. *FEMS Microbiol. Lett.* **243**, 59–64 (2005).
 17. Pancost, R. D., Baas, M., van Geel, B. & Damste, J. S. S. Response of an ombrotrophic bog to a regional climate event revealed by macrofossil, molecular and carbon isotopic data. *Holocene* **13**, 921–932 (2003).
 18. Collister, J. W., Summons, R. E., Lichtfouse, E. & Hayes, J. M. An isotopic biogeochemical study of the Green River oil-shale. *Org. Geochem.* **19**, 265–276 (1992).
 19. Ruble, T. E., Bakel, A. J. & Philp, R. P. Compound-specific isotopic variability in Uinta Basin native bitumens—paleoenvironmental implications. *Org. Geochem.* **21**, 661–671 (1994).
 20. Schouten, S. *et al.* Molecular organic tracers of biogeochemical processes in a saline meromictic lake (Ace Lake). *Geochim. Cosmochim. Acta* **65**, 1629–1640 (2001).
 21. Inubushi, K. *et al.* Factors influencing methane emission from peat soils: Comparison of tropical and temperate wetlands. *Nutrient Cycling Agroecosyst.* **71**, 93–99 (2005).
 22. Christensen, T. R. *et al.* Factors controlling large scale variations in methane emissions from wetlands. *Geophys. Res. Lett.* **30**, 1414, doi:10.1029/2002GL016848 (2003).
 23. Steart, D. C., Collinson, M. E., Scott, A. C., Glasspool, I. J. & Hooker, J. J. The Cobham Lignite Bed: the palaeobotany of two petrographically contrasting lignites from either side of the Paleocene–Eocene carbon isotope excursion. *Acta Palaeobot.* **47** (1), 109–125 (2007).
 24. Schmitz, B. & Pujalte, V. Abrupt increase in seasonal extreme precipitation at the Paleocene–Eocene boundary. *Geology* **35**, 215–218 (2007).
 25. Gibson, T. G., Bybell, L. M. & Mason, D. B. Stratigraphic and climatic implications of clay mineral changes around the Paleocene/Eocene boundary of the northeastern US margin. *Sedim. Geol.* **134**, 65–92 (2000).
 26. Zachos, J. C. *et al.* Rapid acidification of the ocean during the Paleocene–Eocene thermal maximum. *Science* **308**, 1611–1615 (2005).
 27. Pagani, M. *et al.* Arctic hydrology during global warming at the Palaeocene/Eocene thermal maximum. *Nature* **442**, 671–675 (2006).
 28. Maslin, M. A. & Thomas, E. Balancing the deglacial global carbon budget: the hydrate factor. *Quat. Sci. Rev.* **22**, 1729–1736 (2003).
 29. Kurtz, A. C., Kump, L. R., Arthur, M. A., Zachos, J. C. & Paytan, A. Early Cenozoic decoupling of the global carbon and sulfur cycles. *Paleoceanography* **18**, doi:10.1029/2003PA000908 (2003).
 30. Sluijs, A. *et al.* Subtropical arctic ocean temperatures during the Palaeocene/Eocene thermal maximum. *Nature* **441**, 610–613 (2006).
- Acknowledgements** We thank I. D. Bull and R. Berstan of the Bristol Node of the NERC Life Sciences Mass Spectrometry Facility (LSMSF) for analytical support; Alfred McAlpine plc, AMEC and Channel Tunnel Rail Link for access to the Cobham Lignite Bed, and S. Rose for making arrangements; J. Skipper and S. Tracey for help with initial sample collection and field discussions; and L. Kump for critical comments and advice on the ideas proposed here. We acknowledge funding support for this research from the Leverhulme Trust, and studentship support for L.H. from the NERC.
- Author Contributions** R.D.P. and M.E.C. contributed equally to this paper. M.E.C., J.J.H. and A.C.S. initially characterized the Cobham Lignite, with I.J.G., and led the subsequent more detailed characterization of the sediments and fossils conducted by D.S.S. R.D.P. led the biomarker analyses at Bristol, with most of the preparation and analyses being conducted by D.S.S., with training and assistance from L.H. N.V.G. conducted bulk organic matter isotopic measurements. R.D.P. wrote the paper, and all authors discussed the results and commented on the manuscript.
- Author Information** Reprints and permissions information is available at www.nature.com/reprints. The authors declare no competing financial interests. Correspondence and requests for materials should be addressed to R.D.P. (r.d.pancost@bristol.ac.uk).

METHODS

Stratigraphy. Figure 1a shows a simplified East London Basin sequence from latest Palaeocene to Early Eocene calibrated to the latest geological timescale³¹. All of these units were exposed at Cobham. Figure 1a shows the positions of the sand and mud unit (S&M), Cobham Lignite (CL) and lower Woolwich Shell Beds (part of the Woolwich Formation, W), all of which are shown in expanded view in Fig. 1b. The Cobham Section (Fig. 1b) is underlain by the Upnor Formation (U), which is dated as latest Palaeocene by means of the occurrence of calcareous nannoplankton zone NP9 and magnetochron C25n in its lower part³². The Upnor Formation is separated from overlying units by a major unconformity marking the Th4/5 sequence boundary³³ (unconformities and missing strata are denoted in Fig. 1a by double undulating lines). The lower Woolwich Shell Beds, containing the *Apectodinium* acme (Ap), are overlain successively by the rest of the Woolwich Formation, the Blackheath Beds (BB), Oldhaven Member (O) and the London Clay Formation (LC). The last two are dated by means of the Early Eocene dinocyst zones Gor and Was^{33,34}. See ref. 5 for a full discussion of the dating.

The presence of calcareous nannoplankton and *Ophiomorpha* burrows indicates a marine depositional environment for the Upnor Formation. The sand and mud unit, and both the laminated and blocky lignites and the clay bands of the Cobham Lignite, were deposited in a freshwater environment as explained in the text. Furthermore, the sequence boundary (Th4/5) between the Upnor Formation and the sand and mud unit is major, such that there is no brackish transition between the two. The sand and mud unit thus represents the initial filling of an eroded topography during base level rise, saline conditions not returning until the lower Woolwich Shell Beds.

Analytical methods. The Cobham Lignite and related sediments were collected and stored as described previously^{5,10}. Carbon isotopic measurements on bulk samples were obtained with a high-resolution He-continuous flow mass spectrometry technique (EA-IRMS), by means of an elemental analyser EA-1500 (Fisons) coupled with an Optima GV-Micromass MS (described in ref. 35). The samples were cleaned in methanol in an ultrasonic bath for 10 min and then dried. The quantity analysed depended on the carbon content in the sample, with weights between 0.085 and 0.420 mg. Four standards were used to calibrate the results, two international standards (NBS 21 graphite and IAEA-CO9 barium carbonate), and two working minerals (a calcite and a graphite), covering a $\delta^{13}\text{C}$ range from -47 to $+3\text{‰}$. The reproducibility on the standards is better than $\pm 0.1\text{‰}$. The carbon isotopic composition is expressed also in conventional $\delta^{13}\text{C}$ notation as per-thousand (‰) variations relative to Vienna Pee Dee Belemnite (V-PDB) carbonate standard.

For biomarker analyses, samples were gently washed with methanol and powdered with a mortar and pestle. The powdered samples were extracted by sonication with a sequence of increasingly polar solvents (four times with dichloromethane (DCM), four times with DCM/methanol (1:1 v/v) and three times with methanol). The total lipid extracts were separated into three fractions by using a column packed with (activated) alumina by elution with hexane (apolar fraction), hexane/DCM (9:1 v/v; 3 ml) and DCM/methanol (1:2 v/v; 3 ml; polar fraction). GC-MS was performed with a Thermoquest Finnigan trace GC, equipped with an on-column injector and using helium as the carrier gas, interfaced to a Thermoquest Finnigan Trace MS. A fused silica capillary column (50 m \times 0.32 mm) coated with CP-Sil-5 (film thickness 0.12 μm) was used. Samples were injected at 40 °C and the oven was programmed to increase to 140 °C at 20 °C min⁻¹ and then to 300 °C at 4 °C min⁻¹, at which temperature it was held for 22 min. The mass spectrometer was operated with electron ionization at 70 eV and scanning a mass range of m/z 50–700 using a cycle time of 1.7 scans s⁻¹. The interface was set to 300 °C with the ion source at 240 °C. Carbon-isotopic ratios of individual compounds were determined by gas chromatography–isotope ratio mass spectrometry (GC-IRMS) with a ThermoFinnigan DeltaS and the same column and run conditions as described above. $\delta^{13}\text{C}$ values relative to V-PDB were calculated by comparison with a calibrated CO₂ gas; the uncertainties, determined by using co-injected standards, are $\pm 0.3\text{‰}$.

31. Gradstein, F. M., Ogg, J. G. & Smith, A. G. (eds) *A Geologic Time Scale 2004* (Cambridge University Press, Cambridge, 2004).
32. Ellison, R. A., Ali, J. R., Hine, N. M. & Jolley, D. W. in *Correlation of the Early Paleogene in Northwest Europe* (eds Knox, R. W. O'B., Corfield, R. M. & Dunay, R. E.) 185–193 (Geol. Soc. Lond. Special Publication 101, 1996).
33. Bujak, J. P. & Brinkhuis, H. in *Late Paleocene–Early Eocene Climatic and Biotic Events in the Marine and Terrestrial Records* (eds Aubry, M.-P., Lucas, S. G. & Berggren, W. A.) 277–295 (Columbia University Press, New York, 1998).
34. Powell, A. J. in *A Stratigraphic Index of Dinoflagellate Cysts* (ed. Powell, A. J.) 155–252 (Br. Micropalaeontol. Soc. Publ. Series, Chapman & Hall, London, 1992).
35. Grassineau, N. V. High-precision EA-IRMS analysis of S and C isotopes in geological materials. *Appl. Geochem.* 21, 756–765 (2006).

LETTERS

Calcineurin is required to release *Xenopus* egg extracts from meiotic M phase

Satoru Mochida¹ & Tim Hunt¹

Fertilization induces a transient increase in cytoplasmic Ca^{2+} concentration in animal eggs that releases them from cell cycle arrest in the second meiotic metaphase¹. In frog eggs, Ca^{2+} activates Ca^{2+} /calmodulin-activated kinase, which inactivates cytostatic factor^{2–5}, allowing the anaphase-promoting factor to turn on and ubiquitinate cyclins and securin, which returns the cell cycle to interphase⁶. Here we show that the calcium-activated protein phosphatase calcineurin⁷ is also important in this process. Calcineurin is transiently activated after adding Ca^{2+} to egg extracts, and inhibitors of calcineurin such as cyclosporin A (ref. 8) delay the destruction of cyclins, the global dephosphorylation of M-phase-specific phosphoproteins and the re-formation of a fully functional nuclear envelope. We found that a second wave of phosphatase activity directed at mitotic phosphoproteins appears after the spike of calcineurin activity. This activity disappeared the next time the extract entered M phase and reappeared at the end of mitosis. We surmise that inhibition of this second phosphatase activity is important in allowing cells to enter mitosis, and, conversely, that its activation is required for a timely return to interphase. Calcineurin is required to break the deep cell cycle arrest imposed by the Mos-MAP (mitogen-activated protein) kinase pathway^{4,5,9}, and we show that Fizzy/Cdc20, a key regulator of the anaphase-promoting factor⁶, is an excellent substrate for this phosphatase.

The cell cycle of *Xenopus laevis* eggs is arrested at meiotic metaphase II with a stable meiotic spindle carrying condensed chromosomes and high protein kinase activity due to Cdc2–cyclin B (ref. 10). At fertilization, a transient increase in cytoplasmic calcium activates Ca^{2+} /calmodulin-activated kinase (CaMKII), which phosphorylates Erp1, thereby making it a target for an E3 ubiquitin ligase, leading to its destruction by the proteasome^{3,11}. This Ca^{2+} -dependent degradation of Erp1 is the critical step that releases frog eggs from cell cycle arrest⁴, because Erp1 inhibits the anaphase-promoting factor (APC/C) E3 ubiquitin ligase. Once the APC/C is activated, a small set of proteins, including cyclins, securins and xKid, are ubiquitinated and degraded⁶. Sister chromatids separate, chromosomes decondense, the cell divides and the nucleus reforms.

We confirmed previous findings² that the addition of constitutively active CaMKII (CaMKII^{CA}) triggers cyclin destruction in *Xenopus* egg extracts, by measuring the disappearance of cyclin B2 and the phosphorylation status of Apc3, a component of the APC/C that undergoes a phosphorylation-dependent mobility shift during mitosis (Fig. 1a)¹². Addition of recombinant CaMKII^{CA} induced cyclin B2 destruction as expected², but whereas Apc3 dephosphorylation preceded cyclin destruction after adding Ca^{2+} , Apc3 was dephosphorylated after cyclin B2 disappeared, subsequent to the addition of CaMKII^{CA} (Fig. 1a). This result suggested that Ca^{2+} induces not only the activation of CaMKII but also additional rapid event(s) that lead to Apc3 dephosphorylation. Because non-degradable Erp1 constructs inhibit

cyclin destruction after the addition of Ca^{2+} to *Xenopus* egg extracts¹³, it was of interest to see whether Apc3 was dephosphorylated when Ca^{2+} was added under conditions in which the mitotic kinases remained active. We used a mutant Erp1 protein lacking its first 373 residues fused to glutathione S-transferase (GST–Erp1C) (Fig. 1b). As reported previously¹³, GST–Erp1C completely suppressed cyclin destruction (Fig. 1c). Significantly, however, Apc3 underwent a

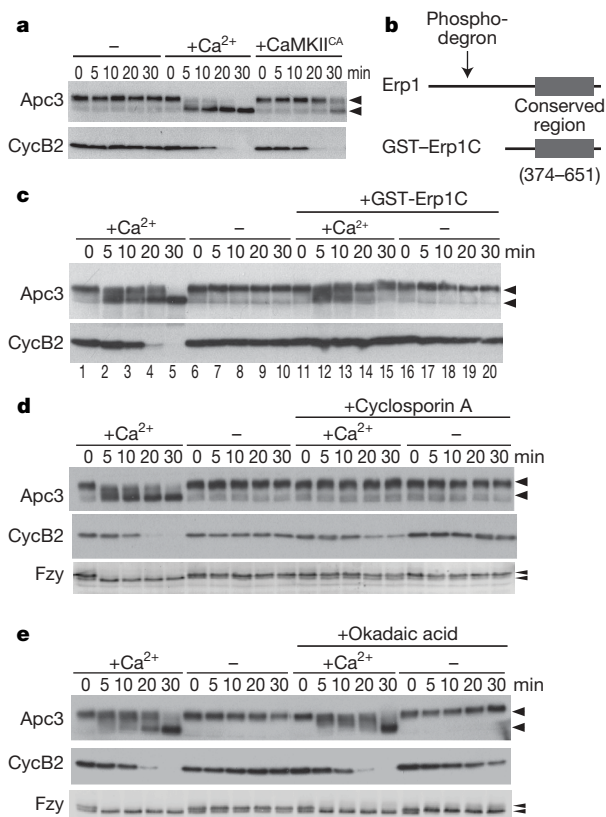


Figure 1 | Calcineurin is responsible for the dephosphorylation of Apc3 and Fzy induced by Ca^{2+} . **a**, CaCl_2 or constitutively active CaMKII was added to *Xenopus* CSF egg extract. Cyclin B2 and Apc3 were monitored by immunoblotting. Arrowheads indicate the positions of Apc3. **b**, Diagram of GST–Erp1C. A phosphorylation-dependent degradation signal (phospho-degron) is located at its amino terminus. **c**, GST–Erp1C inhibited cyclin destruction but not Apc3 dephosphorylation. **d**, CsA inhibited the Ca^{2+} -dependent dephosphorylation of Apc3 and Fzy, and delayed cyclin destruction. CsA (1 μM) or dimethylsulphoxide was added to the extract 10 min before Ca^{2+} . **e**, Okadaic acid (2.5 μM) did not inhibit the dephosphorylation of Apc3 or Fzy. Arrowheads in **c–e** indicate the positions of phosphorylated and dephosphorylated forms of each protein.

¹Cancer Research UK, London Research Institute, Clare Hall Laboratories, South Mimms, Hertfordshire EN6 3LD, UK.

transient mobility shift after Ca^{2+} addition, indicative of dephosphorylation, and reverted to the fully phosphorylated form by 30 min (Fig. 1c, lanes 12–14). We suspected that this reflected the transient activation of a Ca^{2+} -dependent protein phosphatase.

The most likely candidate for this activity is calcineurin/PP2B, considering that it is directly activated by Ca^{2+} /calmodulin¹⁴. We tested this by using two specific inhibitors of calcineurin, namely cyclosporin A (CsA) and FK506, which bind to endogenous immunophilins that then bind calcineurin and inhibit its phosphatase activity⁸. The CsA was added to cytosolic factor (CSF) extract 10 min before the addition of Ca^{2+} . CsA inhibited most dephosphorylation of both Apc3 and Fizzy (Fzy)/Cdc20 (another protein that changes its mobility at fertilization¹⁵) in the presence of Ca^{2+} (Fig. 1d; see Supplementary Fig. 1a for FK506). By contrast, 1 μM okadaic acid, an inhibitor of PP2A, did not inhibit the dephosphorylation of either Apc3 or Fzy after the addition of Ca^{2+} ; as reported previously¹⁶, okadaic acid showed signs of promoting cyclin degradation in the absence of Ca^{2+} after 30 min (Fig. 1e). These results support the hypothesis that calcineurin/PP2B is the phosphatase responsible for the mobility shifts of Apc3 and Fzy in response to the addition of Ca^{2+} . Figure 1d also shows that CsA delayed, but did not completely inhibit, cyclin destruction (Fig. 1d). This delay in cyclin proteolysis might reflect a sluggish destruction of the inhibitor Erp1; to test this, we compared the disappearance of Erp1 in response to added Ca^{2+} in the presence or absence of CsA. The timing of Erp1 mobility shifts and that of its disappearance in the presence of CsA were indistinguishable from those in the absence of the drug (Supplementary Fig. 1b). Thus, stabilization of Erp1 did not account for the delay in cyclin destruction when calcineurin inhibitors were present. Rather, there seemed to be a delay in the full and rapid activation of the APC/C.

Is calcineurin present in *Xenopus* egg extracts, and, if so, is it activated after the addition of Ca^{2+} ? We measured calcineurin activity by the $^{32}\text{PO}_4$ released from labelled substrate (inhibitor-1) in the presence of 2.5 μM okadaic acid¹⁷. Figure 2a shows that *Xenopus* egg extract arrested at meiotic metaphase II showed a very low phosphatase activity that increased transiently about 40–50-fold after Ca^{2+} addition (Fig. 2a). This phosphatase activity was almost completely suppressed by the addition of CsA, indicating that this assay measures the activity of calcineurin. We assume that the transience of the activity reflects the actual concentration of Ca^{2+} in the extract, which is rapidly decreased by pumps present in mitochondria and other vesicular components of the extract¹.

Because CsA inhibited the dephosphorylation of both Apc3 and Fzy (Fig. 1d), we next examined whether other proteins also lingered in their mitotic phosphorylation state in the absence of calcineurin activity. We used two phosphospecific antibodies to monitor these changes, namely MPM2 monoclonal antibody¹⁸ and an anti-(phospho-Ser-Pro) antibody. Figure 2b shows that the addition of CsA delayed almost all dephosphorylations detected by these antibodies. A similar result was obtained when the CSF extract was 'activated' by the addition of Ca^{2+} without CsA, or when GST-Erp1C was present when Ca^{2+} was added (in this case, of course, the mitotic kinase(s) remained fully active; see Supplementary Fig. 1d for cyclin B2 levels). This correlation was also true for the phosphorylation state of Cdc25, a protein that undergoes a large switch-like change in its phosphorylation state in M phase (Fig. 2b). These observations suggested that in CSF-arrested frog egg extracts, calcineurin makes a significant contribution by the reversion of global mitotic phosphoproteins to their interphase unphosphorylated or hypophosphorylated state.

The results shown in the previous section indicate that, although $\text{CaMKII}^{\text{CA}}$ efficiently triggered activation of the APC/C and brought about cyclin destruction and loss of mitotic kinase activity, the phosphoproteins in the extract returned only very slowly to their normal interphase state. To examine the biological importance of calcineurin activity in this process, we added *Xenopus* sperm chromatin to the extract and monitored its morphology. Transition into interphase

stimulated by Ca^{2+} is accompanied by the decondensation of chromatin and the formation of a functional nuclear envelope before DNA replication can begin¹⁹ (Fig. 3A, e and q). When CsA was present, the chromatin decondensed only partly compared with the control (Fig. 3A, e and f), and the formation of a nuclear envelope was considerably delayed (compare Fig. 3A, q with Fig. 3A, r). To assess the formation of a functional nuclear envelope, we measured the nuclear accumulation of green fluorescent protein (GFP) tagged with a simian virus 40 nuclear localization signal (GFP-NLS)²⁰. At 1 h after the addition of Ca^{2+} , the GFP-NLS signal localized together with DNA staining in the control (Fig. 3A, s). Addition of CsA delayed the nuclear localization of GFP-NLS by more than 30 min. If it is true that CaMKII is responsible for inactivating the mitotic kinases, and calcineurin is responsible for dephosphorylating certain of the mitotic phosphoproteins, then the combination of adding $\text{CaMKII}^{\text{CA}}$ and constitutively active calcineurin in the absence of Ca^{2+} ought to mimic the Ca^{2+} signal. To test this possibility, Ca^{2+} -independent constitutively active versions of calcineurin (calcineurin ΔC ; Supplementary Fig. 1c) and $\text{CaMKII}^{\text{CA}}$ were added to CSF extract. The combination of calcineurin ΔC and $\text{CaMKII}^{\text{CA}}$ induced the formation of a nuclear envelope that was morphologically, functionally and kinetically similar to the sample to which Ca^{2+} had been added (compare Fig. 3B, b, g and l with Fig. 3B, d, i and n, and see Fig. 3B, s). Calcineurin activity alone did not show any effect on nuclear morphology (Fig. 3B, c, h and m), whereas CaMKII activity alone showed slower morphological change and impaired nuclear import, similar to the sample with Ca^{2+} and CsA (compare Fig. 3B, e, j and o with Fig. 3A, f, l and r).

If activation of phosphatases is sufficient to induce the dephosphorylation of mitotic phosphoproteins, calcineurin ΔC might induce their dephosphorylation without having to inactivate the

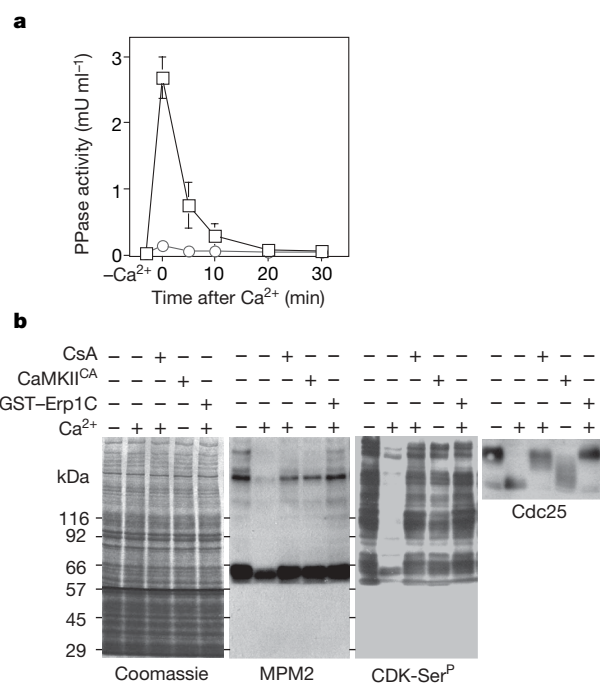


Figure 2 | Ca^{2+} activates calcineurin in *Xenopus* egg extracts. This activation is required for the global dephosphorylation of mitotic phosphoproteins at the metaphase–interphase transition. **a**, Inhibitor-1 phosphatase activity in egg extract. Squares, with Ca^{2+} ; circles, with Ca^{2+} in the presence of CsA. Results are means \pm range for three experiments. **b**, Egg extract 45 min after the addition of Ca^{2+} , CsA, CaMKII and/or GST-Erp1C were analysed by SDS-PAGE and immunoblotting. First panel, Coomassie blue stain; second panel, MPM2 immunoblot; third panel, anti-CDK phospho-(Ser) blot; fourth panel, anti-Cdc25 immunoblot. Arrowheads indicate phosphorylated (upper) and dephosphorylated (lower) forms of Cdc25.

mitotic kinases. To test this possibility, calcineurin ΔC or the catalytically inactive calcineurin ΔC^{H151A} complex was added to *Xenopus* egg extract. Calcineurin ΔC clearly induced the partial dephosphorylation of Apc3 (in the absence of added Ca^{2+}), whereas calcineurin ΔC^{H151A} did not (Fig. 3C, lanes 9–16). This dephosphorylation was not as complete as that induced by Ca^{2+} (Fig. 3C, lanes 5–8), even though the phosphatase activity was comparable to that in the presence of Ca^{2+} and sustained (because of its independence of Ca^{2+} (data not shown)). These data suggest that concomitant inactivation of kinases with the activation of phosphatase is required for exit from M phase. This speculation was supported by the addition of roscovitine, a cyclin-dependent kinase (CDK)-specific inhibitor²¹. In the presence of roscovitine, calcineurin ΔC promoted rapid dephosphorylation of Apc3 (Fig. 3C, compare lanes 9–12 and 17–20). Simply adding roscovitine, without the addition of Ca^{2+} or calcineurin ΔC , did not lead to the rapid dephosphorylation of Apc3, reinforcing the point that phosphatase activity in the CSF extract is low. Clearly, the phosphorylation state of Apc3 results from the balance of kinase and phosphatase activities. In contrast, cyclin destruction was never promoted by calcineurin and roscovitine, although cyclin B2 did become dephosphorylated (Fig. 3C, lanes 19–20).

Is calcineurin also required for exit from normal mitosis? This seemed unlikely, given the widespread use of calcineurin inhibitors as immunosuppressants²², but to examine this we added CsA to 'cycling' extracts of activated frog eggs¹⁰. The timing of entry into or exit from mitosis, as judged by the mobility of Apc3 and the

accumulation and destruction of cyclin B2, were completely unaffected by the drug (Fig. 4a). If phosphatases are shut off during mitosis to allow the complete conversion of mitotic phosphoproteins to their fully phosphorylated form, there must be a different mechanism for their reactivation that does not require calcium transients. To check whether 'anti-mitotic' phosphatase(s) are shut off in mitosis, as they seem to be in eggs, we prepared a substrate comprising maltose-binding protein (MBP) with 25 residues from *Xenopus* Fzy/Cdc20 fused to its carboxy terminus. Serine 50 is at the centre of this sequence, and it proved to be a good substrate for cyclin A–Cdk2 (data not shown). Figure 4b shows the surprising result of using MBP–Fzy–S50–³²PO₄ to assay phosphatase activity after the addition of Ca^{2+} to a frog egg extract. We observed the expected transient from calcineurin, which was abolished by the addition of CsA, but a second wave of phosphatase activity appeared shortly after the initial wave of calcineurin activity. The second activity was insensitive to CsA but was inhibited by okadaic acid (Supplementary Fig. 2a). The addition of CsA delayed the appearance of the second wave of phosphatase by roughly the same amount as it delayed the dephosphorylation of mitotic substrates in the experiments shown in Fig. 3. There

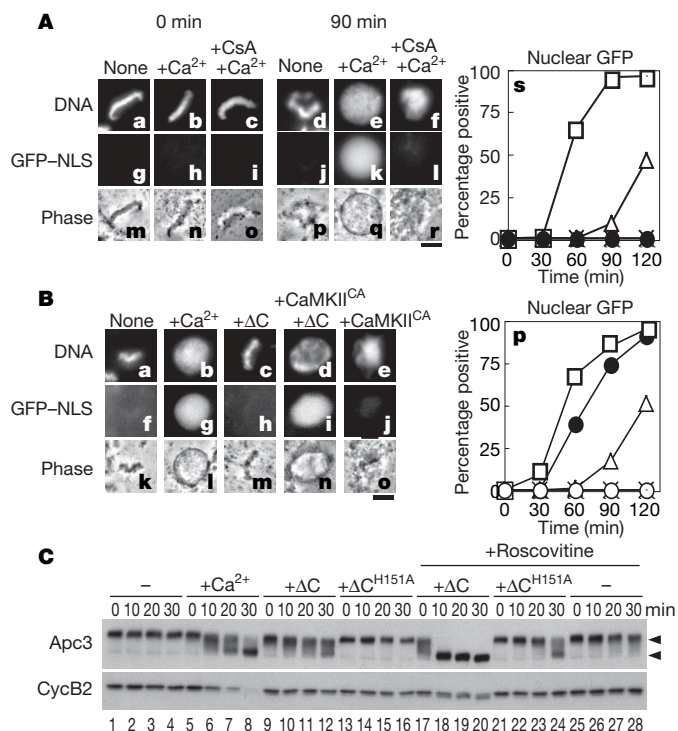


Figure 3 | Calcineurin and CaMKII activities together allow nuclear envelope formation. **A**, Chromatin morphology and import of GFP–NLS with CsA. Sperm chromatin morphology was monitored at 0 or 90 min after the addition of Ca^{2+} to egg extract. **a–f**, DNA stained with Hoechst 33342; **g–l**, GFP–NLS; **m–r**, phase contrast. **s**, Frequency of GFP co-localization with DNA. Open squares, with Ca^{2+} ; open triangles, with Ca^{2+} and CsA; filled circles, no treatment; crosses: with CsA. **B**, Similar experiment to that in **A** sampled at 90 min. Open squares, with Ca^{2+} ; filled circles, with calcineurin ΔC and CaMKII; open triangles, with CaMKII; open circles, no treatment; crosses, with calcineurin ΔC . **C**, Recombinant calcineurin (calcineurin ΔC or catalytically inactive calcineurin ΔC^{H151A}) was added to egg extract in the presence or absence of roscovitine (0.5 mM). Samples were analysed by SDS–PAGE and immunoblotting for Apc3 and cyclin B2. Arrowheads indicate the positions of phosphorylated and dephosphorylated Apc3.

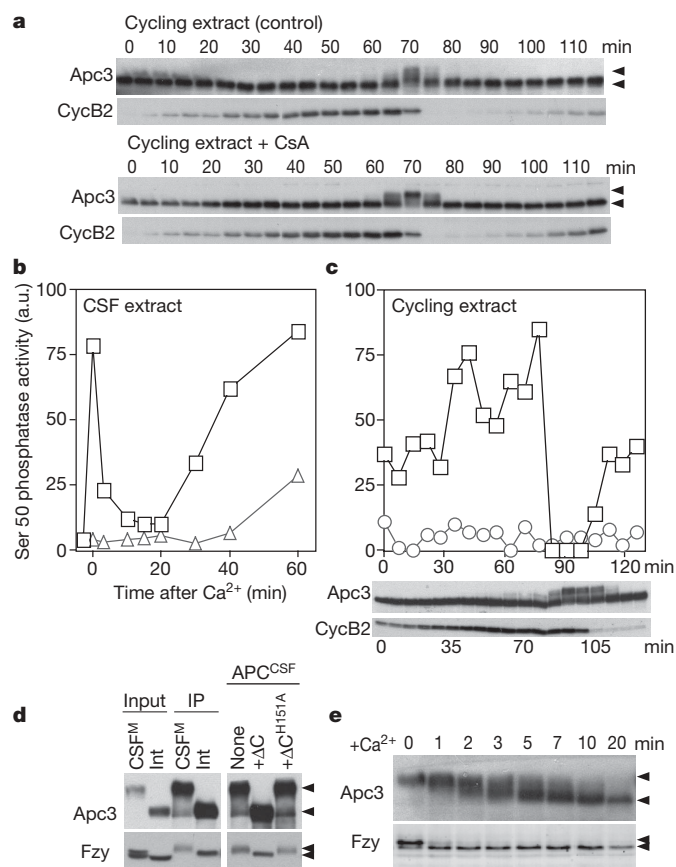


Figure 4 | Calcineurin is not required for mitotic cell cycles, but a second phosphatase activity appears after the calcineurin transient. **a**, CsA (lower panels) or dimethylsulphoxide (upper panels) was added to a 'cycling extract' of *Xenopus* eggs, which were analysed for Apc3 and cyclin B2 by immunoblotting. **b**, Phosphatase assays using Ser 50 of Fzy as substrate were performed after adding Ca^{2+} to CSF extract in the absence (squares) or presence (triangles) of CsA. **c**, A 'cycling extract' was analysed for Fzy Ser 50 phosphatase activity in the absence (squares) or presence (circles) of 2.5 μ M okadaic acid. The lower panel shows Apc3 and cyclin B2 at each time point analysed by immunoblotting. **d**, Calcineurin dephosphorylates Apc3 and Fzy *in vitro*. APC–Fzy complex was immunoprecipitated from egg extract (left panels), followed by incubation with buffer, calcineurin ΔC or calcineurin ΔC^{H151A} (right panels). IP, immunoprecipitation. **e**, Kinetics of Apc3 and Fzy dephosphorylation after the addition of Ca^{2+} . Arrowheads in **a**, **d** and **e** indicate the positions of phosphorylated and dephosphorylated forms of each protein.

are therefore two quite separate phosphatases capable of dephosphorylating mitotic substrates. We next used MBP-Fzy-S50- $^{32}\text{PO}_4$ to assay phosphatase activity in a cycling extract. Figure 4c shows that the activity responsible for releasing $^{32}\text{PO}_4$ from this substrate was high in interphase but was completely shut off as the extract entered mitosis, and it was reactivated concomitantly with the disappearance of cyclin at the end of mitosis. This phosphatase activity was inhibited by 2.5 μM okadaic acid. We prepared several similar substrates, of which most, but not all, behaved like this (Supplementary Fig. 2). Some substrates (for example lamin(B2 S16)) were not susceptible to calcineurin, and some were dephosphorylated by calcineurin but were poor substrates for the second phosphatase (for example Cdc6(S54)). In addition, one substrate, Fzy(T79), was dephosphorylated at a significant rate in the egg extract (although both calcium addition and the return to interphase increased phosphatase activity directed at this residue).

Many mitotic substrates thus become protected against dephosphorylation as the extract enters mitosis, but calcineurin is additionally required to release CSF-arrested egg extracts from M phase. What might be the special target(s) for calcineurin in the egg arrested in meiosis II? The obvious candidate(s) should be sites in the APC/C–Fzy pathway that are phosphorylated by protein kinases downstream of Mos, such as MAP kinase^{23,24} or p90rsk (ref. 25). To test this, immunoprecipitates of the APC/C from CSF or interphase extracts were incubated with recombinant calcineurin. This reversed the M-phase mobility shifts of both Apc3 and Fzy, which was present in these immunoprecipitates (Fig. 4d). We next followed the kinetics of the mobility shifts of Apc3 and Fzy after adding Ca^{2+} to a frog egg extract. The mobility of Fzy/Cdc20 changed very rapidly, within 1 or 2 min, well before Apc3 was fully shifted (Fig. 4e), which is consistent with the idea that calcineurin contributes to the activation of the APC/C by ‘unlocking’ Cdc20. There were also indications of a physical interaction between Fzy and calcineurin, because immune precipitates of calcineurin and calmodulin-Sepharose eluates both contained significant amounts of Fzy (Supplementary Fig. 3a, b) although anti-Fzy immunoprecipitates contained rather modest (although detectable) amounts of calcineurin. Given the evidence that Fzy is phosphorylated by MAP kinase¹⁵ and that phosphorylation seems to inhibit its activating function in respect of the APC/C^{15,26}, we suspect that failure to dephosphorylate Fzy when CsA is added to the egg extract may well contribute to the slow destruction of cyclin B2 that we observed in the presence of this calcineurin inhibitor. The resulting residual CDK activity in turn seems to delay the appearance of the second wave of anti-mitotic phosphatase activity (see Fig. 4b). Although two recent papers have shown that phosphorylation of Erp1 by p90rsk is important for its stability and activity as an inhibitor of cyclin degradation^{27,28}, this cannot account for the delay in cyclin destruction caused by CsA, because we found no effect of CsA on the disappearance of Erp1.

These observations raise questions about the regulation of phosphatases in mitosis and of their identity, multiplicity and substrate specificity. Until now, control of entry into mitosis has usually been seen in terms of a sudden increase in CDK activity, regulated by the balance of the Wee1/Myt1 protein kinase and the Cdc25 protein phosphatase²⁹. Yet in the rapid cell cycles that occur in fertilized frog eggs, it looks as though the inhibition of one or more protein phosphatases, or of protection of mitotic phosphoproteins against dephosphorylation, helps to promote entry into mitosis (Fig. 4c). At present we do not know the identity of this system or understand how it is regulated. Equally, details of the physiologically significant targets for calcineurin in breaking out of CSF arrest remain to be clarified.

METHODS SUMMARY

Materials were obtained from the following companies: calmodulin-conjugated Sepharose, Amersham; CsA, Calbiochem; FK506, rapamycin and okadaic acid, LC Laboratories; roscovitine, Calbiochem. Antibodies for immunoblotting were

obtained from the following companies: anti-Cdc27/Apc3, BD Bioscience; anti-CDK phospho-(Ser), Cell Signalling Technology. The anti-cyclin B2 (X121), anti-Fzy (BA8) and anti-Cdc25 antibodies were provided by J. Gannon. The MPM2 antibody was the gift of J. Kuang. Antibodies for immunoprecipitation: anti-Cdc27/Apc3 and AF3.1 were as described previously³⁰; anti-Fzy antiserum was a gift from H. Yamano.

Full Methods and any associated references are available in the online version of the paper at www.nature.com/nature.

Received 4 May; accepted 26 July 2007.

- Busa, W. B. & Nuccitelli, R. An elevated free cytosolic Ca^{2+} wave follows fertilization in eggs of the frog, *Xenopus laevis*. *J. Cell Biol.* **100**, 1325–1329 (1985).
- Lorca, T. *et al.* Calmodulin-dependent protein kinase II mediates inactivation of MPF and CSF upon fertilization of *Xenopus* eggs. *Nature* **366**, 270–273 (1993).
- Rauh, N. R., Schmidt, A., Bormann, J., Nigg, E. A. & Mayer, T. U. Calcium triggers exit from meiosis II by targeting the APC/C inhibitor XErp1 for degradation. *Nature* **437**, 1048–1052 (2005).
- Schmidt, A., Rauh, N. R., Nigg, E. A. & Mayer, T. U. Cytostatic factor: an activity that puts the cell cycle on hold. *J. Cell Sci.* **119**, 1213–1218 (2006).
- Liu, J., Grimison, B. & Maller, J. L. New insight into metaphase arrest by cytotostatic factor: from establishment to release. *Oncogene* **26**, 1286–1289 (2007).
- Peters, J. M. The anaphase promoting complex/cyclosome: a machine designed to destroy. *Nature Rev. Mol. Cell Biol.* **7**, 644–656 (2006).
- Stewart, A. A., Ingebritsen, T. S., Manalan, A., Klee, C. B. & Cohen, P. Discovery of a Ca^{2+} - and calmodulin-dependent protein phosphatase: probable identity with calcineurin (CaM-BP80). *FEBS Lett.* **137**, 80–84 (1982).
- Liu, J. *et al.* Calcineurin is a common target of cyclophilin-cyclosporin A and FKBP-FK506 complexes. *Cell* **66**, 807–815 (1991).
- Sagata, N., Watanabe, N., Vande Woude, G. F. & Ikawa, Y. The c-mos proto-oncogene product is a cytotostatic factor responsible for meiotic arrest in vertebrate eggs. *Nature* **342**, 512–518 (1989).
- Murray, A. W., Solomon, M. J. & Kirschner, M. W. The role of cyclin synthesis and degradation in the control of maturation promoting factor activity. *Nature* **339**, 280–286 (1989).
- Liu, J. & Maller, J. L. Calcium elevation at fertilization coordinates phosphorylation of XErp1/Emi2 by Plx1 and CaMK II to release metaphase arrest by cytotostatic factor. *Curr. Biol.* **15**, 1458–1468 (2005).
- Peters, J. M., King, R. W., Hoog, C. & Kirschner, M. W. Identification of BIME as a subunit of the anaphase-promoting complex. *Science* **274**, 1199–1201 (1996).
- Schmidt, A. *et al.* *Xenopus* polo-like kinase Plx1 regulates XErp1, a novel inhibitor of APC/C activity. *Genes Dev.* **19**, 502–513 (2005).
- Klee, C. B., Ren, H. & Wang, X. Regulation of the calmodulin-stimulated protein phosphatase, calcineurin. *J. Biol. Chem.* **273**, 13367–13370 (1998).
- Chung, E. & Chen, R. H. Phosphorylation of Cdc20 is required for its inhibition by the spindle checkpoint. *Nature Cell Biol.* **5**, 748–753 (2003).
- Lorca, T. *et al.* An okadaic acid-sensitive phosphatase negatively controls the cyclin degradation pathway in amphibian eggs. *Mol. Cell Biol.* **11**, 1171–1175 (1991).
- Stewart, A. A., Ingebritsen, T. S. & Cohen, P. The protein phosphatases involved in cellular regulation. 5. Purification and properties of a Ca^{2+} /calmodulin-dependent protein phosphatase (2B) from rabbit skeletal muscle. *Eur. J. Biochem.* **132**, 289–295 (1983).
- Westendorf, J. M., Rao, P. N. & Gerace, L. Cloning of cDNAs for M-phase phosphoproteins recognized by the MPM2 monoclonal antibody and determination of the phosphorylated epitope. *Proc. Natl Acad. Sci. USA* **91**, 714–718 (1994).
- Blow, J. J. & Laskey, R. A. A role for the nuclear envelope in controlling DNA replication within the cell cycle. *Nature* **332**, 546–548 (1988).
- Chatterjee, S., Javier, M. & Stochaj, U. *In vivo* analysis of nuclear protein traffic in mammalian cells. *Exp. Cell Res.* **236**, 346–350 (1997).
- Meijer, L. *et al.* Biochemical and cellular effects of roscovitine, a potent and selective inhibitor of the cyclin-dependent kinases cdc2, cdk2 and cdk5. *Eur. J. Biochem.* **243**, 527–536 (1997).
- Crabtree, G. R. Calcium, calcineurin, and the control of transcription. *J. Biol. Chem.* **276**, 2313–2316 (2001).
- Nebreda, A. R. & Hunt, T. The c-mos proto-oncogene protein kinase turns on and maintains the activity of MAP kinase, but not MPF, in cell-free extracts of *Xenopus* oocytes and eggs. *EMBO J.* **12**, 1979–1986 (1993).
- Haccard, O. *et al.* Induction of metaphase arrest in cleaving *Xenopus* embryos by MAP kinase. *Science* **262**, 1262–1265 (1993).
- Maller, J. L. *et al.* The pathway of MAP kinase mediation of CSF arrest in *Xenopus* oocytes. *Biol. Cell* **93**, 27–33 (2001).
- Yudkovsky, Y., Shteinberg, M., Listovsky, T., Brandeis, M. & Hershko, A. Phosphorylation of Cdc20/fizzy negatively regulates the mammalian cyclosome/APC in the mitotic checkpoint. *Biochem. Biophys. Res. Commun.* **271**, 299–304 (2000).
- Inoue, D., Ohe, M., Kanemori, Y., Nobui, T. & Sagata, N. A direct link of the Mos–MAPK pathway to Erp1/Emi2 in meiotic arrest of *Xenopus laevis* eggs. *Nature* **446**, 1100–1104 (2007).

28. Nishiyama, T., Ohsumi, K. & Kishimoto, T. Phosphorylation of Erp1 by p90rsk is required for cytosolic factor arrest in *Xenopus laevis* eggs. *Nature* **446**, 1096–1099 (2007).
29. Pomeroy, J. R., Kim, S. Y. & Ferrell, J. E. Jr. Systems-level dissection of the cell-cycle oscillator: bypassing positive feedback produces damped oscillations. *Cell* **122**, 565–578 (2005).
30. Yamano, H., Gannon, J., Mahbubani, H. & Hunt, T. Cell cycle-regulated recognition of the destruction box of cyclin B by the APC/C in *Xenopus* egg extracts. *Mol. Cell* **13**, 137–147 (2004).

Supplementary Information is linked to the online version of the paper at www.nature.com/nature.

Acknowledgements We thank H. Yamano and M. Dasso for gifts of the *Xenopus* Erp1 and GFP–NLS clones, respectively; C. Klee for advice about calcineurin biochemistry; T. Nishiyama and K. Ohsumi for anti-calcineurin A serum, anti-Erp1 antibody and sharing details of their parallel findings with us; S. Shenolikar for clones for inhibitor-1; H. Mahbubani and J. Kirk for care of frogs; and other members of the laboratory for advice and reagents. S.M. is supported by an EMBO long-term fellowship.

Author Information Reprints and permissions information is available at www.nature.com/reprints. The authors declare no competing financial interests. Correspondence and requests for materials should be addressed to T.H. (tim.hunt@cancer.org.uk).

METHODS

Preparation of egg extracts and cyclin destruction assays. 'CSF extracts' were prepared from unfertilized *Xenopus* eggs and frozen in liquid nitrogen as described³¹. Cyclin destruction assays were performed as reported³⁰ in the presence of cycloheximide (0.1 mg ml⁻¹). For cyclin destruction assays, a high-speed supernatant obtained after centrifugation for 18 min with a Beckman SW41Ti rotor at 25,000 r.p.m. at 4 °C were used, whereas nuclear envelope formation assays were performed with an equal mixture of high-speed and low-speed (centrifugation for 10 min with a Sorvall HB-6 rotor at 10,000 r.p.m. at 4 °C) supernatants.

Purification and use of recombinant proteins. Indestructible GST-Erp1 (ref. 3) was prepared from a complementary DNA of Erp1C (from the *EcoRI* site to the end) by subcloning into the appropriate pGEX vector. GST-Erp1C was purified on glutathione beads by following the manufacturer's protocol. The protein on beads was added to egg extract at 28 nM. CaMKII lacking its C terminus was expressed from pMAL-c2 vector (NEB) and purified on amylose resin. approx. 150 fmol of CaMKII was added per 1 µl of egg extract to induce cyclin destruction. GST-fused GFP-NLS was induced at room temperature (20–22 °C) for 16 h with 0.1 mM isopropyl β-D-thiogalactoside (IPTG) to enhance its solubility and fluorescence. All recombinant proteins were dialysed against 20 mM Tris-Cl pH 7.5 and 150 mM NaCl before use.

Nuclear envelope formation and GFP import assay. Approximately 1,000 demembrated sperm nuclei³², 0.1 µg of cycloheximide and 1 pmol of GST-fused GFP-NLS³ were added per 1 µl of extract before the addition of Ca²⁺ or other reagents. Because DMSO, the solvent for cycloheximide and CsA, decreased the efficiency of nuclear envelope formation, the amount of DMSO was kept to less than 2% of the total volume.

Calcineurin substrate. A histidine-tagged version of rat inhibitor-1 of protein phosphatase 1 was purified from bacteria as a heat-stable protein with Ni²⁺-nitrilotriacetate agarose (Ni²⁺-NTA agarose; Qiagen). Inhibitor-1 protein (100 µg) was incubated at 30 °C for 60 min with 1 µl of [γ -³²P]ATP (Amersham), 1 µl of 4 mM ATP, 20 µl of 2 × PKA buffer (40 mM Tris-HCl pH 7.5, 0.4 mM EGTA, 0.8 mM EDTA, 4 mM MgCl₂), 0.5 µl of PKA (NEB) and water in a final volume of 40 µl. The proteins were precipitated twice with NH₄SO₄ and were then mixed with 20 µl of Ni²⁺-NTA agarose beads to retrieve inhibitor-1 only. After cycles of washing to remove irrelevant materials, labelled inhibitor-1 was eluted from beads in 20 µl of elution buffer (20 mM Tris-HCl pH 7.5, 150 mM NaCl, 200 mM imidazole).

Calcineurin assay. Calcineurin was assayed as described³³. Extract (3 µl) was mixed with 1 µl of substrate and okadaic acid (final concentration 1.25 µM) and incubated for 3 min at 23 °C. The reaction was stopped by adding 20 µl of stop solution (10% trichloroacetic acid) and kept on ice until all samples had been prepared. After centrifugation, 20 µl of supernatant were vortex-mixed with 30 µl of 5% (w/v) ammonium molybdate in 0.5 M H₂SO₄ and 50 µl of water-saturated 2-methylpropan-1-ol/heptane (1:1). The radioactivity of the organic phase was measured with a liquid-scintillation counter.

Preparation and phosphatase assay of Fzy Ser 50 peptide. The DNA sequence encoding 25 amino acids surrounding Fzy Ser 50 was cloned into pMAL-c2

vector. The resulting fusion protein was expressed and purified from bacteria by using amylose resin. Protein-bound resin (20 µl) was phosphorylated with Cdk2-cyclin A complex in the presence of [γ -³²P]ATP in kinase buffer (20 mM Hepes pH 7.8, 10 mM MgCl₂, 15 mM KCl, 1 mM EGTA, 5 mM NaF, 20 mM sodium β-glycerophosphate, 0.1 mM ATP). After incubation at 37 °C for 2 h, the resin was extensively washed to remove the kinase and unincorporated [γ -³²P]ATP. Phosphorylated peptides were eluted with 40 µl of elution buffer (20 mM Tris-HCl pH 7.5, 150 mM NaCl, 10 mM maltose). The assay for Fzy Ser 50 phosphatase was performed as described above for the calcineurin assay. When a mutant substrate with Ser 50 replaced by Ala was used, there was less than 5% incorporation of labelled phosphate in comparison with the substrate with Ser 50, suggesting that more than 96% of the label resided in Ser 50-PO₄.

Expression and purification of recombinant calcineurin complexes. *Xenopus* calcineurin A and B cDNAs were amplified from an egg cDNA library and cloned into pMAL-c2 and pET16b expression vector, respectively. A phosphatase-dead mutation (H151 to A)³⁴ was inserted by site-directed mutagenesis using the oligonucleotides 5'-gtttttactacgtgggaatgctgaatgtagacatc-3' and 5'-gatgtctacattcagcattccacagtagtaaaac-3'. The constitutively active mutant was made by deleting the region after a *PstI* site. Expression of each protein was induced by adding 0.1 mM IPTG at 25 °C for 12–16 h. Total bacterial protein was extracted by sonication in degassed and N₂-aerated buffer A (20 mM Tris-HCl pH 7.5, 150 mM NaCl, 1 µM CaCl₂, 0.05% (v/v) Tween 20, 5 mM benzamidine, 1 mM PMSF, 1 mM dithiothreitol, 1 mg ml⁻¹ lysozyme and 10 mM sodium ascorbate), and the extract containing the A subunit was mixed with that containing the B subunit to form complexes, which were purified on 600 µl of amylose resin and washed three times with buffer A and once with buffer B (buffer A without Tween 20, benzamidine, PMSF and lysozyme). Calcineurin complexes were eluted with 600 µl of elution buffer (buffer B plus 10 mM maltose and 0.5 mM MnCl₂) for 20 min at 20 °C. The eluate was concentrated tenfold with Microcon 3 (Millipore), giving a 5 µg µl⁻¹ concentration for A subunit. A one-tenth volume of recombinant calcineurin was added to the extract, producing an activity equivalent to that just after the addition of Ca²⁺.

Dephosphorylation of APC complex *in vitro*. Immunoprecipitation of APC complex was as described³⁰. APC complex on magnetic beads (Dynal) from 30 µl of egg extract was mixed with 1 µg of recombinant calcineurin complexes in reaction buffer (80 mM Tris-HCl pH 7.5, 12 mM magnesium acetate, 32 mM sodium ascorbate, 200 mM NaCl, 1 µM okadaic acid, 0.2 mM CaCl₂, 1 mM MnCl₂, 1 mM dithiothreitol, 2 mg ml⁻¹ BSA) for 20 min at room temperature.

31. Murray, A. W., Solomon, M. J. & Kirschner, M. W. The role of cyclin synthesis and degradation in the control of maturation promoting factor activity. *Nature* **339**, 280–286 (1989).
32. Blow, J. J. & Laskey, R. A. A role for the nuclear envelope in controlling DNA replication within the cell cycle. *Nature* **332**, 546–548 (1988).
33. Mackintosh, C. & Moorhead, G. in *Protein phosphorylation: A practical approach* (ed. Hardie, D. G.) 153–181 (Oxford University Press, Oxford, 1999).
34. Mertz, P., Yu, L., Sikkink, R. & Rusnak, F. Kinetic and spectroscopic analyses of mutants of a conserved histidine in the metallophosphatases calcineurin and I protein phosphatase. *J. Biol. Chem.* **272**, 21296–21302 (1997).

Transient activation of calcineurin is essential to initiate embryonic development in *Xenopus laevis*

Tomoko Nishiyama¹, Norio Yoshizaki², Takeo Kishimoto¹ & Keita Ohsumi¹

At fertilization, an increase of cytosolic calcium ions (Ca^{2+}) triggers various activation responses in animal eggs^{1,2}. In vertebrates, these responses include exit from metaphase arrest in meiosis II (MII exit) and cortical remodelling initiated by cortical granule exocytosis. Although the essential requirement of Ca^{2+} /calmodulin-dependent protein kinase II for inducing MII exit has been documented³, a role of the Ca^{2+} /calmodulin-dependent protein phosphatase calcineurin in egg activation has not been investigated. Here we show, using cell-free extracts from unfertilized eggs of *Xenopus laevis*, that calcineurin is transiently activated immediately after Ca^{2+} addition to a concentration that induces MII exit. When calcineurin activation is inhibited, cyclin-dependent kinase 1 (Cdk1) inactivation by means of cyclin B degradation is prevented and sperm chromatin incubated in the extracts remains condensed. Similarly, if calcineurin is inhibited in intact eggs, MII exit on egg activation is prevented. In addition, the activation contraction⁴ in the cortex is suppressed whereas cortical granule exocytosis occurs. We further demonstrate that, when a high level of calcineurin activity is maintained after activation, growth of sperm asters is prevented in egg extracts and, consistently, migration of male and female pronuclei towards each other is hindered in fertilized eggs. Thus, both activation and the subsequent inactivation of calcineurin in fertilized eggs are crucial for the commencement of vertebrate embryonic development.

After fertilization, vertebrate eggs undergo marked changes in both their chromosomes and their cytoplasm. In fertilized eggs of the amphibian *X. laevis*, meiotic division, which in the unfertilized eggs was arrested in metaphase of MII by the action of cytotstatic factor (CSF)⁵, is completed. In addition, the contents of cortical granules are discharged to make the vitelline envelope impenetrable by sperm^{6,7}, and the cortical structure is remodelled through reorganization of cortical cytoskeletal filaments^{8,9}; the cortical remodelling appears as a pigment shift towards the animal pole, termed the activation contraction⁴. In the cytoplasm, an aster of microtubules is organized by the centrosome derived from the centriole of the fertilizing sperm, and the aster helps the haploid male and female pronuclei migrate towards each other to constitute the diploid genome of the zygote^{10–12}. These activation responses are caused by a transient increase in cytosolic Ca^{2+} , which is stored in endoplasmic reticulum and, on fertilization, is released into the cytosol by the action of inositol-1,4,5-triphosphate (ref. 1). Although the pivotal importance of the Ca^{2+} transient in egg activation has long been known^{13,14}, the downstream pathways leading to activation responses are largely unexplored.

Among Ca^{2+} -regulated enzymes, protein kinase C is known to be required for cortical granule exocytosis and the activation contraction¹⁵, although its mechanism is unclear. Recent studies^{16–18} have shown Ca^{2+} /calmodulin-dependent protein kinase II (CaMKII) to

have an essential role in the induction of cyclin B degradation, which is required for Cdk1 inactivation and MII exit. However, a role of calcineurin—an ubiquitous protein phosphatase, the activity of which is also regulated by Ca^{2+} /calmodulin (ref. 19)—has not been investigated in the context of egg activation, even though the phosphatase is expected to be activated by the Ca^{2+} transient after fertilization.

We first examined whether calcineurin is activated by the Ca^{2+} increase that initiates MII exit in extracts from CSF-arrested eggs (CSF extracts)^{20,21}. To measure calcineurin activity in egg extracts, we prepared a fusion of glutathione S-transferase (GST) and regulatory subunit II (RII) of mouse cyclic AMP-dependent protein kinase (PKA) (amino acids 80–120); this included the autophosphorylation site²², which was phospho-labelled *in vitro* with recombinant PKA. When phospho-labelled RII (p-RII) was incubated in CSF extracts diluted with buffer, the amount of the label released from p-RII increased with incubation time even though no exogenous Ca^{2+} was added, but the dephosphorylation could be inhibited almost entirely by the addition of 1 μM okadaic acid to the dilution buffer (Fig. 1a). However, when CaCl_2 was added to the extracts at a final concentration of 0.4–0.6 mM (the minimum amount needed to induce MII exit), the amount of the label released from p-RII increased even in the presence of 1 μM okadaic acid. The Ca^{2+} -dependent, okadaic-acid-insensitive increase of the label released from p-RII is caused by calcineurin activity in extracts.

We then examined the change of calcineurin activity in CSF extracts after Ca^{2+} addition. Calcineurin activity in CSF extracts increased immediately after Ca^{2+} addition, showing a peak of activity 2–4 min after Ca^{2+} addition, and then declined to a background level within 30 min (Fig. 1b). Immunoblot analysis revealed that the amount of calcineurin was constant during the rapid changes in activity (Fig. 1c). For comparison, we also examined the changes of CaMKII and Cdk1 activities of the same extracts using autocamtide-2 (ACT-2)²³ and histone H1 as substrates, respectively. The results confirmed that CaMKII was transiently activated immediately after Ca^{2+} addition, and showed that the transient activation of both calcineurin and CaMKII preceded Cdk1 inactivation by means of cyclin B degradation (Fig. 1b, d).

To examine whether calcineurin and CaMKII activation are interdependent, we inhibited calcineurin activity in egg extracts by adding a calcineurin fragment ($\text{CaN}^{420–508}$) containing the autoinhibitory domain of *Xenopus* calcineurin (amino acids 457–479)²⁴. When $\text{CaN}^{420–508}$ was added to CSF extracts, calcineurin activity was not detected following Ca^{2+} addition, although CaMKII was normally activated (Fig. 1e); essentially the same results were obtained with extracts supplemented with 2 μM cyclosporin A, a potent inhibitor for calcineurin. In contrast, when CSF extracts were combined with a peptide derived from CaMKII ($\text{CaMK}^{281–309}$), which specifically

¹Laboratory of Cell and Developmental Biology, Graduate School of Bioscience and Biotechnology, Tokyo Institute of Technology, 4259 Nagatsuta, Midori-ku, Yokohama 226-8501, Japan. ²Department of Animal Resource Production, United Graduate School of Agricultural Science, Gifu University, Gifu 501-1193, Japan.

inhibits CaMKII, CaMKII activation induced by Ca^{2+} addition was suppressed whereas calcineurin activation was not (Fig. 1e). Thus, calcineurin and CaMKII are activated independently in response to a Ca^{2+} increase in CSF extracts.

We next examined the change in the M-phase-specific Cdk1 activity after addition of Ca^{2+} to CSF extracts in which either calcineurin or CaMKII was inhibited. In control extracts to which a non-inhibitory peptide—the amino terminus of *Xenopus* calcineurin (CaN^{1-94})—had been added, Cdk1 activity dropped to a low level within 20 min after Ca^{2+} addition and remained at low levels afterwards (Fig. 2a). In CSF extracts in which calcineurin was inhibited with $\text{CaN}^{420-508}$, however, the decrease in Cdk1 activity was much lower than that in control extracts, and the activity soon returned to the original, high level. As shown in previous studies^{3,16,18}, when CaMKII was inhibited with $\text{CaMK}^{281-309}$, Cdk1 inactivation induced by Ca^{2+} addition was completely suppressed. Consistent with the changes of Cdk1 activity, sperm chromatin added to control extracts formed nuclei when Cdk1 activity became low, whereas sperm chromatin added to calcineurin- or CaMKII-inhibited extracts, which maintained high levels of Cdk1 activity, formed entangled chromosomes (Fig. 2b). Thus, both calcineurin-inhibited and CaMKII-inhibited extracts were not able to exit MII after an increase in

Ca^{2+} . We also examined the effect of calcineurin inhibition on MII exit in intact eggs, and obtained essentially the same results as those from extracts (Supplementary Fig. 1).

We further confirmed the requirement of calcineurin activity for MII exit by immunodepletion experiments. When CSF extracts were treated with anti-calcineurin antibody beads, calcineurin was mostly removed from the extracts (Fig. 2c). In calcineurin-depleted extracts, Cdk1 was not inactivated after Ca^{2+} addition (Fig. 2d). The potential to inactivate Cdk1 in response to a Ca^{2+} increase was restored by the addition of constitutively active calcineurin (calcineurin-CA), but not by the addition of its phosphatase-dead counterpart (calcineurin-PD) (Fig. 2d and Supplementary Fig. 2).

The requirement of calcineurin activity for MII exit seemed to be contradictory to a previous report that CaMKII activity is necessary and sufficient to induce MII exit in CSF extracts³. In this report, however, the MII exit in CSF extracts was induced by the addition of constitutively active CaMKII (CaMKII-CA), although, in fact, increased CaMKII activity is restricted to a short period during physiological egg activation (see Fig. 1d). We suspected that, when CaMKII activation is transient, calcineurin activity may be necessary to induce MII exit. To address this, we first confirmed that in CSF extracts Cdk1 was inactivated by the addition of CaMKII-CA in the

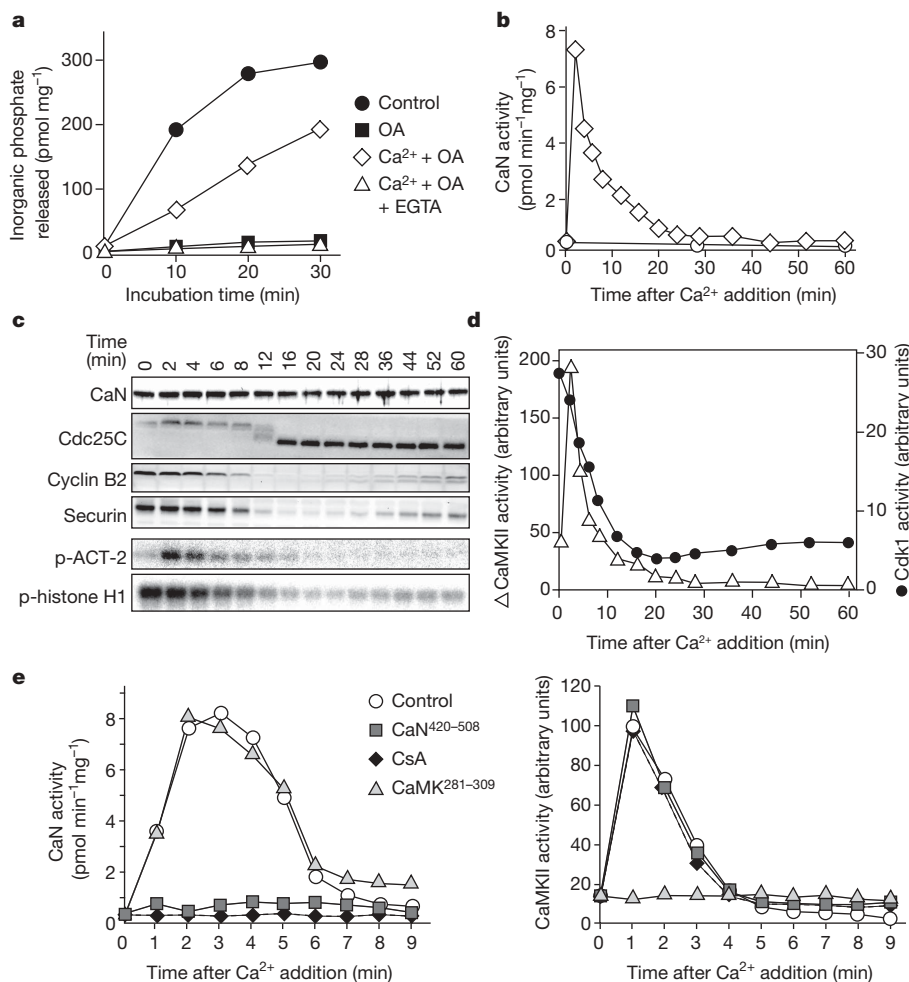


Figure 1 | Calcineurin is transiently activated in CSF extracts immediately after Ca^{2+} addition. **a**, Detection of Ca^{2+} -dependent, okadaic acid-insensitive protein phosphatase (calcineurin) activity in *Xenopus* egg extracts. CSF extracts before (filled symbols) and at 3 min after (open symbols) CaCl_2 addition were examined for phosphatase activity in the presence of okadaic acid (OA) alone or okadaic acid plus EGTA by using the ^{32}P -labelled RII peptide (p-RII) as a substrate. **b**, CSF extracts to which CaCl_2 was added (diamonds) or was absent (circles) were examined for calcineurin (CaN) activity at the indicated times after CaCl_2 addition. **c**, The same

CaCl_2 -added extracts were examined for changes in levels of calcineurin, Cdc25C, cyclin B2 and securin proteins by immunoblotting. **d**, They were also examined for CaMKII and Cdk1 activities by using ACT-2 and histone H1 as substrates, respectively. In **c**, the slower and faster migrating forms of Cdc25C reflect high and low Cdk1 activity, respectively. **e**, CSF extracts supplemented with inhibitory peptides from calcineurin ($\text{CaN}^{420-508}$), with those from CaMKII ($\text{CaMK}^{281-309}$) or with cyclosporine A (CsA) were activated by Ca^{2+} addition and examined for calcineurin and CaMKII activities at the indicated times.

absence of a Ca^{2+} increase (Fig. 2e; Supplementary Fig. 2). However, when CaMKII-CA was inhibited with CaMK^{281–309} 25 min after the CaMKII-CA addition, Cdk1 remained active during the following 60-min incubation period. In contrast, in CSF extracts to which calcineurin-CA had been added along with CaMKII-CA, Cdk1 was inactivated even when CaMKII-CA was inhibited after a 25-min incubation. It is noteworthy that Cdk1 inactivation induced by CaMKII-CA was significantly accelerated in the presence of calcineurin-CA (Fig. 2e). The addition of calcineurin-CA did not cause any change in Cdk1 activity in CSF extracts (data not shown). Thus, calcineurin activity, like CaMKII activity, is essential for MII exit on activation in *Xenopus* eggs.

Our additional data indicate that the incomplete inactivation of Cdk1 in calcineurin-inhibited extracts is caused by compromised degradation of Erp1, the anaphase-promoting complex/cyclosome inhibitor protein that induces MII arrest by means of suppression of cyclin B degradation^{25,26} (Supplementary Fig. 3). Our results also indicate that the recognition of Erp1 by β -transducin repeat-containing protein (also known as β -TrCP), which is an F-box protein that probably mediates Erp1 degradation^{25,27}, is enhanced by calcineurin activity, possibly through direct dephosphorylation of Erp1 by calcineurin (Supplementary Fig. 4).

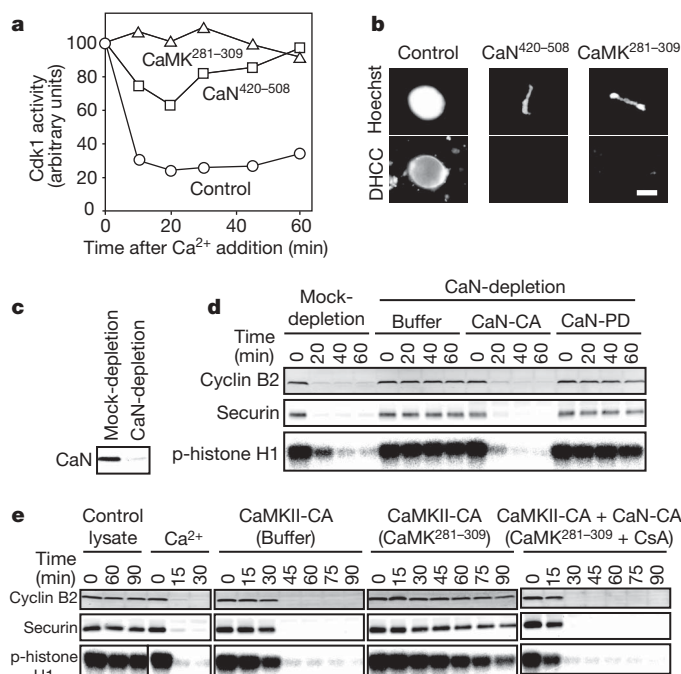


Figure 2 | Calcineurin activity is required for MII exit in response to a Ca^{2+} increase in CSF extracts. **a**, **b**, CSF extracts supplemented with the CaN^{420–508} or the CaMK^{281–309} peptide were activated by CaCl_2 addition and examined for the changes in Cdk1 activity. **a**, This was measured using histone H1 as substrate. **b**, The morphology of sperm chromatin that had been incubated in the extracts was examined 60 min after Ca^{2+} addition. Sperm DNA and membranes were stained with Hoechst and 3,3'-dihexyloxycarbocyanine iodide (DHCC), respectively. The scale bar represents 10 μm . **c**, **d**, CSF extracts were deprived of calcineurin by immunodepletion (**c**), followed by addition of calcineurin-CA or calcineurin-PD, and were examined for cyclin B2 and securin proteins as well as for histone H1 kinase activity at the indicated times after Ca^{2+} addition (**d**). **e**, Reticulocyte lysate, with which CaMKII-CA was synthesized, or both the lysate and the calcineurin-CA protein were added to CSF extracts, and, after a 25-min incubation, CaMKII-CA and calcineurin-CA were inhibited by the addition of inhibitors indicated in the parentheses. Extracts were examined for cyclin B2 and securin proteins as well as for histone H1 kinase activity at the indicated times after the enzyme addition. CSF extracts supplemented with control reticulocyte lysate and those activated by Ca^{2+} addition served as controls.

In fertilized or parthenogenetically activated *Xenopus* eggs, the activation contraction occurs in the cortex⁴. Before the activation contraction, cortical granule exocytosis occurs, resulting in perivitelline space formation. To investigate roles for calcineurin in these activation responses in the egg cortex, we examined cortical changes in eggs injected with CaN^{420–508}. Control eggs injected with the non-inhibitory peptide (CaN^{1–94}) exhibited a contraction of the pigmented area, accompanied by perivitelline space formation (Fig. 3a, b), 10 min after activation was induced by transfer of the eggs to the saline. In contrast, eggs injected with CaN^{420–508} did not show any marked changes in pigment distribution, but, nevertheless, formed

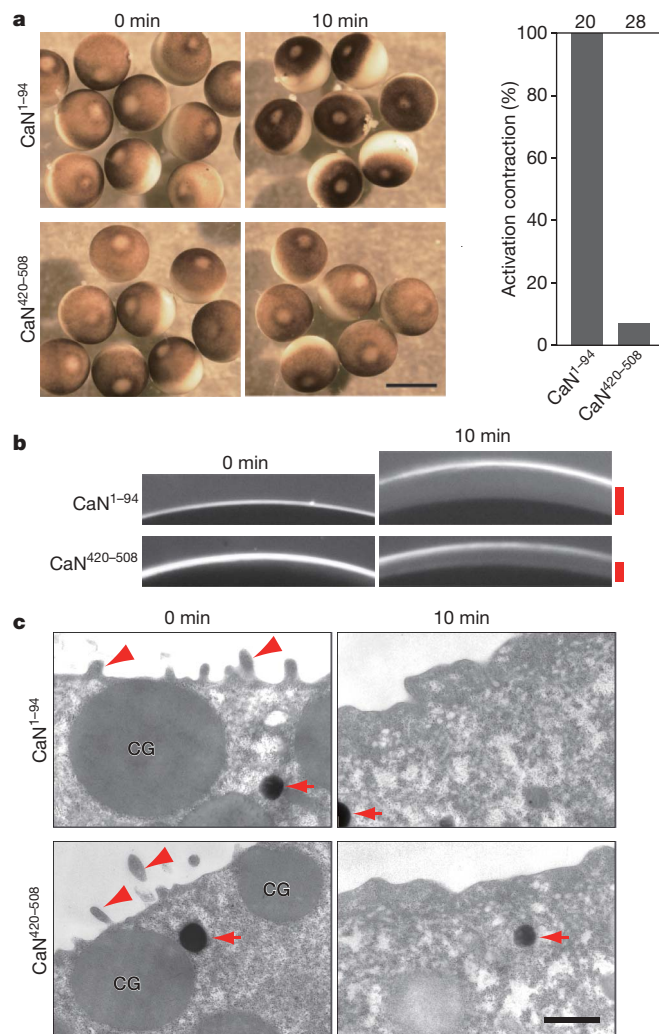


Figure 3 | Calcineurin activity is required for the activation contraction, but not for cortical granule exocytosis in activated eggs. Mature eggs were injected with either CaN^{1–94} or CaN^{420–508} in a low- Ca^{2+} buffer, and their activation was induced by transferring the eggs to a physiological saline. Eggs before (0 min) and after (10 min) activation were examined for the changes in the cortex using a dissecting microscope (**a**, **b**) and transmission electron microscopy (**c**). **a**, In 10 min after activation induction, CaN^{1–94}-injected eggs exhibited the activation contraction—a pigment shift towards the animal side—whereas CaN^{420–508}-injected eggs did not (left). The occurrence of the contraction in injected eggs after activation was examined for each group (right). The scale bar represents 1 mm. The numbers above the graph indicate the numbers of examined eggs. **b**, Dissecting microscopic observation through transmission light shows that CaN^{420–508}-injected eggs formed perivitelline space (bars on the right) after activation (10 min). **c**, Electron microscopic observation of egg cortex shows that, in eggs injected with CaN^{1–94} and in those injected with CaN^{420–508}, microvilli (arrowheads) and cortical granules (CG) in the egg cortex (0 min) disappeared after activation (10 min). The arrows indicate the pigment granules, and the scale bar represents 1 μm .

the perivitelline space after activation (Fig. 3a, b). This result indicated that cortical granule exocytosis had occurred in the calcineurin-inhibited eggs. We then observed the egg cortex by transmission electron microscopy. This demonstrated that, like control eggs, calcineurin-inhibited eggs underwent cortical granule exocytosis; it also revealed that the dense microvilli covering the surface of unactivated eggs disappeared 10 min after activation (Fig. 3c). Thus, calcineurin activity is required for the activation contraction, but not for cortical granule exocytosis or microvilli retraction in activated eggs.

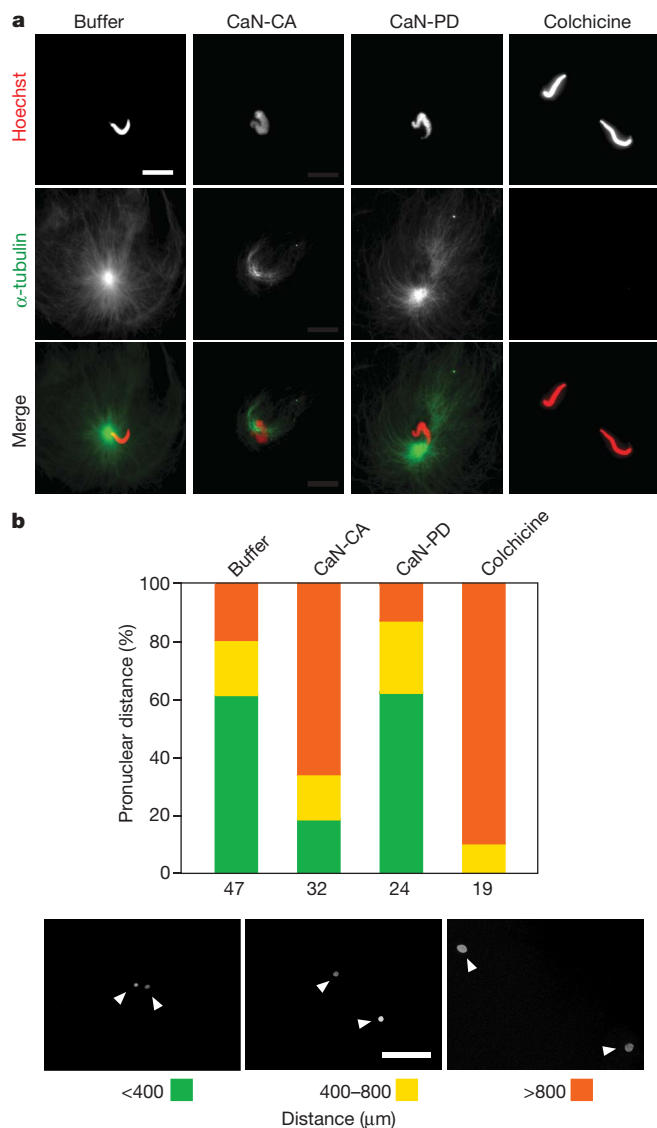


Figure 4 | Persistence of calcineurin activity after activation inhibits the growth of sperm asters and the coming together of the male and female pronuclei. **a**, Egg extracts activated by Ca^{2+} addition were supplemented with fluorescence-labelled α -tubulin as well as calcineurin-CA, calcineurin-PD or colchicine, followed by the addition of demembrated sperm. After incubation for 20 min, sperm asters were observed with a fluorescence microscope. DNA was counterstained with Hoechst. The scale bar represents 10 μ m. **b**, Fertilized eggs were injected with calcineurin-CA, calcineurin-PD or colchicine together with a GST–GFP fusion tagged with a nuclear localization sequence within 30 min after fertilization, and incubated in the presence of cycloheximide to inhibit M-phase entry. Injected eggs were fixed with formalin and were squashed by adding a coverslip 90–110 min after fertilization, and the distance between the fluorescence-labelled male and female pronuclei was determined. The numbers under the graph indicate the numbers of examined eggs, and the arrowheads in the images indicate pronuclei. The scale bar represents 400 μ m.

To examine whether calcineurin activity is involved in the regulation of sperm aster formation in fertilized eggs, we added either calcineurin-CA or calcineurin-PD together with fluorochrome-labelled α -tubulin protein and demembrated sperm to Ca^{2+} -activated extracts. In control extracts, large asters formed around sperm after a 20-min incubation, and aster formation was completely inhibited with colchicine (Fig. 4a). The size of sperm asters formed in activated extracts was greatly reduced in the presence of calcineurin-CA, but not of calcineurin-PD, indicating that sperm aster formation is negatively regulated by calcineurin activity. This result indicated that in fertilized eggs the coming together of the male and female pronuclei may be prevented in the presence of calcineurin activity. To examine this, we injected either calcineurin-CA or calcineurin-PD into fertilized eggs within 30 min of fertilization, along with GST–green fluorescent protein (GFP) tagged with a nuclear localization sequence. Following fixation at 60–90 min after incubation in the presence of cycloheximide to inhibit M-phase entry, we squashed the eggs to determine the distance between the two pronuclei, which had accumulated GFP. The results showed that the two pronuclei were much more distant from each other in calcineurin-CA-injected eggs than in buffer- or in calcineurin-PD-injected eggs (Fig. 4b). Thus, in fertilized eggs, the inactivation of calcineurin is critical for the haploid male and female pronuclei to come together to form the diploid zygote nucleus.

The present study implicates calcineurin in the regulation of various activation processes to initiate embryonic development in fertilized *Xenopus* eggs. Interestingly, Ca^{2+} -regulated protein kinases are also implicated in the activation responses that involve calcineurin: CaMKII in MII exit and protein kinase C in the activation contraction. Because protein phosphorylation and dephosphorylation are countervailing modifications, one may consider a differential, switch-like regulation between the kinases and the phosphatase. This type of differential regulation, however, is unlikely to operate during activation responses in eggs, because calcineurin and CaMKII are both activated quickly and are soon inactivated with similar kinetics following the Ca^{2+} transient. Thus, in egg activation, protein kinases and calcineurin seem to act collaboratively in response to the same Ca^{2+} signal to regulate an activation response, phosphorylating some substrates or sites and dephosphorylating others. The downstream targets of calcineurin in MII exit and cortical remodelling are worth investigation.

METHODS SUMMARY

Oocytes, mature eggs and fertilized eggs of *Xenopus laevis* were obtained as described²⁸. Electron microscopy was performed as described²⁹.

Full Methods and any associated references are available in the online version of the paper at www.nature.com/nature.

Received 21 May; accepted 26 July 2007.

- Stricker, S. A. Comparative biology of calcium signaling during fertilization and egg activation in animals. *Dev. Biol.* **211**, 157–176 (1999).
- Whitaker, M. Calcium at fertilization and in early development. *Physiol. Rev.* **86**, 25–88 (2006).
- Lorca, T. et al. Calmodulin-dependent protein kinase II mediates inactivation of MPF and CSF upon fertilization of *Xenopus* eggs. *Nature* **366**, 270–273 (1993).
- Palecek, J., Ubbels, G. A. & Rzehak, K. Changes of the external and internal pigment pattern upon fertilization in the egg of *Xenopus laevis*. *J. Embryol. Exp. Morphol.* **45**, 203–214 (1978).
- Masui, Y. The elusive cyostatic factor in the animal egg. *Nature Rev. Mol. Cell Biol.* **1**, 228–232 (2000).
- Hedrick, J. L. & Nishihara, T. Structure and function of the extracellular matrix of anuran eggs. *J. Electron Microsc. Tech.* **17**, 319–335 (1991).
- Larabell, C. & Chandler, D. E. Fertilization-induced changes in the vitelline envelope of echinoderm and amphibian eggs: self-assembly of an extracellular matrix. *J. Electron Microsc. Tech.* **17**, 294–318 (1991).
- Christensen, K., Sauterer, R. & Merriam, R. W. Role of soluble myosin in cortical contractions of *Xenopus* eggs. *Nature* **310**, 150–151 (1984).
- Capco, D. G., Tutnick, J. M. & Bement, W. M. The role of protein kinase C in reorganization of the cortical cytoskeleton during the transition from oocyte to fertilization-competent egg. *J. Exp. Zool.* **264**, 395–405 (1992).

10. Hamaguchi, M. S. & Hiramoto, Y. Analysis of the role of astral rays in pronuclear migration by the colcemid–UV method. *Dev. Growth Differ.* **28**, 143–156 (1986).
11. Navara, C. S., First, N. L. & Schatten, G. Microtubule organization in the cow during fertilization, polyspermy, parthenogenesis, and nuclear transfer: the role of the sperm aster. *Dev. Biol.* **162**, 29–40 (1994).
12. Reinsch, S. & Karsenti, E. Movement of nuclei along microtubules in *Xenopus* egg extracts. *Curr. Biol.* **7**, 211–214 (1997).
13. Jaffe, L. F. Sources of calcium in egg activation: a review and hypothesis. *Dev. Biol.* **99**, 265–276 (1983).
14. Sardet, C., Dumollard, R. & McDougall, A. Signals and calcium waves at fertilization. *Semin. Cell Dev. Biol.* **17**, 223–225 (2006).
15. Bement, W. M. & Capco, D. G. Protein kinase C acts downstream of calcium at entry into the first mitotic interphase of *Xenopus laevis*. *Cell Regul.* **1**, 315–326 (1990).
16. Rauh, N. R., Schmidt, A., Bormann, J., Nigg, E. A. & Mayer, T. U. Calcium triggers exit from meiosis II by targeting the APC/C inhibitor XErp1 for degradation. *Nature* **437**, 1048–1052 (2005).
17. Liu, J. & Maller, J. L. Calcium elevation at fertilization coordinates phosphorylation of XErp1/Emi2 by Plx1 and CaMK II to release metaphase arrest by cytosstatic factor. *Curr. Biol.* **15**, 1458–1468 (2005).
18. Hansen, D. V., Tung, J. J. & Jackson, P. K. CaMKII and Polo-like kinase 1 sequentially phosphorylate the cytosstatic factor Emi2/XErp1 to trigger its destruction and meiotic exit. *Proc. Natl Acad. Sci. USA* **103**, 608–613 (2006).
19. Rusnak, F. & Mertz, P. Calcineurin: form and function. *Physiol. Rev.* **80**, 1483–1521 (2000).
20. Lohka, M. J. & Maller, J. L. Induction of nuclear envelope breakdown, chromosome condensation, and spindle formation in cell-free extracts. *J. Cell Biol.* **101**, 518–523 (1985).
21. Murray, A. W., Solomon, M. J. & Kirschner, M. W. The role of cyclin synthesis and degradation in the control of maturation promoting factor activity. *Nature* **339**, 280–286 (1989).
22. Blumenthal, D. K., Takio, K., Hansen, R. S. & Krebs, E. G. Dephosphorylation of cAMP-dependent protein kinase regulatory subunit (type II) by calmodulin-dependent protein phosphatase. Determinants of substrate specificity. *J. Biol. Chem.* **261**, 8140–8145 (1986).
23. Hanson, P. I., Kapiloff, M. S., Lou, L. L., Rosenfeld, M. G. & Schulman, H. Expression of a multifunctional Ca^{2+} /calmodulin-dependent protein kinase and mutational analysis of its autoregulation. *Neuron* **3**, 59–70 (1989).
24. Colbran, R. J., Fong, Y. L., Schworer, C. M. & Soderling, T. R. Regulatory interactions of the calmodulin-binding, inhibitory, and autophosphorylation domains of Ca^{2+} /calmodulin-dependent protein kinase II. *J. Biol. Chem.* **263**, 18145–18151 (1988).
25. Schmidt, A. *et al.* *Xenopus* polo-like kinase Plx1 regulates XErp1, a novel inhibitor of APC/C activity. *Genes Dev.* **19**, 502–513 (2005).
26. Nishiyama, T., Ohsumi, K. & Kishimoto, T. Phosphorylation of Erp1 by p90rsk is required for cytosstatic factor arrest in *Xenopus laevis* eggs. *Nature* **446**, 1096–1099 (2007).
27. Guardavaccaro, D. *et al.* Control of meiotic and mitotic progression by the F box protein β -Trcp1 *in vivo*. *Dev. Cell* **4**, 799–812 (2003).
28. Iwabuchi, M., Ohsumi, K., Yamamoto, T. M., Sawada, W. & Kishimoto, T. Residual Cdc2 activity remaining at meiosis I exit is essential for meiotic M–M transition in *Xenopus* oocyte extracts. *EMBO J.* **19**, 4513–4523 (2000).
29. Sultana, F., Yokoe, A., Ito, Y., Mao, K. M. & Yoshizaki, N. The peri-albumen layer: a novel structure in the envelopes of an avian egg. *J. Anat.* **203**, 115–122 (2003).

Supplementary Information is linked to the online version of the paper at www.nature.com/nature.

Acknowledgements We thank S. Mochida and T. Hunt for sharing their unpublished findings with us and all the laboratory members for discussions. We thank M. J. Lohka for critical reading of the manuscript. This work was supported by grants from the Ministry of Education, Culture, Sports, Science and Technology of Japan to K.O. and T.K.

Author Information Reprints and permissions information is available at www.nature.com/reprints. The authors declare no competing financial interests. Correspondence and requests for materials should be addressed to K.O. (kohsumi@bio.titech.ac.jp).

METHODS

Eggs and extracts. *In vitro* matured eggs and fertilized eggs were obtained as described²⁸. When injected with peptides, mature eggs were incubated in low- Ca^{2+} buffer³⁰ to prevent injected eggs from being activated by pricking. Activation of mature eggs that had received an injection was induced by transferring them to the physiological saline MMR³¹ (100 mM NaCl, 2 mM KCl, 1 mM MgCl_2 , 2 mM CaCl_2 , 0.1 mM EDTA, 5 mM HEPES-NaOH, pH 7.5). CSF-arrested extracts were prepared as described in ref. 32 and immunoblot analyses of extracts and intact eggs were performed as described²⁸.

Plasmids and proteins. Complementary DNA for the RII subunit (80–120) of mouse PKA was isolated by polymerase chain reaction from NIH 3T3 total cDNA, mutated at Ser90, Thr93, Cys99 and Thr102 (S90G, T93D, C99A and T102A). RII cDNA was cloned into pGEX-4T3 (Amersham) to prepare GST–RII. To prepare GST–ACT-2, cDNA encoding the ACT-2 sequence (NLKKALRRQETVDALR) was ligated into pGEX-4T3. Full-length cDNA for *Xenopus* calcineurin A, a catalytic subunit, was isolated by PCR from total cDNA of *Xenopus* eggs, and its fragments encoding amino acids 420–508 ($\text{CaN}^{420-508}$) and 1–94 (CaN^{1-94}) were ligated into pET30a (Novagen) to prepare His-tagged $\text{CaN}^{420-508}$ and CaN^{1-94} , respectively. GST- and His-tagged fusion proteins were expressed in *Escherichia coli* strains BL21 and BL21(DE3) (Novagen), respectively, and purified according to the manufacturer's protocols. cDNA for constitutively active *Xenopus* calcineurin A (amino acids 1–390; calcineurin-CA) and its phosphatase-dead mutant (H151A; calcineurin-PD) in pMal-c2 and those for *Xenopus* calcineurin B, a regulatory subunit, in pET16b were provided by S. Mochida and T. Hunt. Maltose binding protein (MBP)-tagged calcineurin A and His-tagged calcineurin B were expressed in *E. coli* BL21 and BL21(DE3), respectively, and then the bacteria expressing calcineurin A and calcineurin B were mixed and washed with wash buffer (0.2 M NaCl, 10 mM ascorbic acid, 1 mM DTT, 20 mM Tris-HCl, pH 7.5). Fusion proteins were extracted in extraction buffer (0.2 M NaCl, 10 mM ascorbic acid, 1 mM DTT, 1 μM CaCl_2 , 0.05% Tween 20, 0.5 mg ml^{-1} lysozyme, 20 mM Tris-HCl, pH 7.5) supplemented with protease inhibitor cocktail Complete EDTA-free (Roche). Calcineurin A–calcineurin B complexes were bound to amylose resin (New England Biolabs), eluted with MBP elution buffer (0.2 M NaCl, 10 mM ascorbic acid, 1 mM DTT, 1 μM CaCl_2 , 10 mM maltose, 0.5 mM MnCl_2 , 20 mM Tris-HCl, pH 7.5), dialysed against egg extraction buffer (100 mM KCl, 5 mM MgCl_2 , 20 mM HEPES-KOH, pH 7.5) containing 10 mM ascorbic acid and 1 mM DTT, and then concentrated with Vivaspinn (Vivascience), aliquoted and frozen-stored. cDNA for rat CaMKII-CA (amino acids 1–290) in pT7G-4HA was provided by K. Tachibana. The plasmid was linearized with *Stu*I, and its transcription *in vitro* was carried out with mMESSAGE mMACHINE T7 (Ambion) according to the manufacturer's protocols. CaMKII(1–290)–4 \times haemagglutinin (HA) was translated from the transcript with rabbit reticulocyte lysate (Promega).

Antibodies. Anti-*Xenopus* calcineurin A sera were obtained by immunizing rabbits with a 6 \times His-tagged calcineurin A fragment (247–446), which had been expressed in *E. coli*, purified with Ni-NTA resins (Qiagen) under denaturing conditions, and dialysed against PBS. Anti-*Xenopus* cyclin B2 and securin antibodies were provided by J. Maller and M. Iwabuchi, respectively. Anti-*Xenopus* Cdc25C antibodies were obtained as described³³. Anti-human calcineurin antibody used for immunoblot analysis was purchased from BD Transduction Laboratories.

Calcineurin assay. To prepare a substrate for calcineurin, GST–RII bound to glutathione-sepharose 4B beads (Amersham) was phospho-labelled by incubation for 90 min at 25 °C with recombinant mouse PKA catalytic subunit (Calbiochem) in the reaction buffer (20 mM Tris-HCl, pH 8.0, 150 mM NaCl, 20 mM MgCl_2 , 10 μM ATP) containing $[\gamma\text{-}^{32}\text{P}]\text{ATP}$. After washing the beads, phospho-labelled GST–RII (p-RII) was eluted with GST elution buffer (50 mM Tris-HCl, pH 9.0, 25 mM glutathione, 10 mM DTT) and dialysed against egg extraction buffer. Calcineurin activity was measured according to the method used in ref. 34 with modifications. Egg extracts were diluted fivefold with egg extraction buffer containing p-RII and 1.0 μM okadaic acid, and were incubated for 15 min at 22 °C. Ten microlitres of reactions were combined with 25 μl of 10% trichloroacetic acid and were kept on ice. After centrifugation (15,000g, 5 min), 20 μl of the supernatant was mixed with 30 μl of 5% (w/v) ammonium molybdate in 0.5 M H_2SO_4 , and 50 μl water-saturated iso-butanol/heptane (1:1 mixture). The radioactivity of the organic phase was measured using a liquid

scintillation counter, and calcineurin activity ($\text{pmol min}^{-1}\text{mg}^{-1}$) was calculated, taking 390 c.p.m. as 1 pmol of p-RII.

CaMKII and Cdk1 assay. To measure CaMKII activity, egg extracts were diluted sevenfold with egg extraction buffer containing GST–ACT-2, $[\gamma\text{-}^{32}\text{P}]\text{ATP}$ and 6 mM ATP. After an incubation for 90 s at 22 °C, reactions were stopped by adding SDS sample buffer, and GST–ACT-2 was separated by SDS–polyacrylamide gel electrophoresis for autoradiography. CaMKII activity was quantified by the amount of $[\gamma\text{-}^{32}\text{P}]\text{ATP}$ incorporation into GST–ACT-2. Cdk1 activity of egg extracts was measured using histone H1 as a substrate as described³⁵.

Immunodepletion of calcineurin. Anti-calcineurin A serum was incubated with the same volume of protein G sepharose 4B-beads (Sigma) in TBS, and the beads were washed three times with egg extraction buffer. Egg extracts were treated with the equal volume of the immunobeads for 20 min on ice and, after removal of the beads by sedimentation, were supplemented with cycloheximide at a final concentration of 50 $\mu\text{g ml}^{-1}$.

Sperm aster formation. CSF-arrested egg extracts were supplemented with rhodamine- α tubulin (Cytoskeleton) at a final concentration of 120 $\mu\text{g ml}^{-1}$ and, after a 5-min incubation, the extracts were activated by the addition of 0.6 mM CaCl_2 along with demembrated sperm³⁵. Two minutes after CaCl_2 addition, either calcineurin-CA or calcineurin-PD was added to the extracts, followed by incubation at 22 °C. Extracts containing sperm were fixed and stained by mixing with 30% glycerol-egg extraction buffer containing 10% formalin, 10 $\mu\text{g ml}^{-1}$ Hoechst 33342 and 5 $\mu\text{g ml}^{-1}$ DHCC (Kodak), and microtubules and sperm chromatin morphology were observed with an epifluorescence microscope (Zeiss Axiovision).

β -TrCP binding assay. Full-length cDNA for β -TrCP was isolated by PCR from total cDNA of *Xenopus* eggs and was subcloned into pT7-G (UKII)³⁶ for 4 \times HA-tagged β -TrCP.

Its transcription and translation *in vitro* was carried out with a rabbit reticulocyte lysate system (Promega). For the β -TrCP binding assay, CSF extracts were supplemented with 1 mM MG115, a proteasome inhibitor, along with a 10% volume of reticulocyte lysate with which β -TrCP–HA was synthesized. The extracts were further supplemented with $\text{CaN}^{420-508}$, cyclosporin A or $\text{CaMK}^{281-309}$, and then activated by Ca^{2+} addition. After a 3-min incubation, the extracts were diluted fivefold with egg extraction buffer, and treated with anti-HA-antibody-conjugated protein-G beads for 1 h on ice. The beads were washed three times with egg extraction buffer containing 1% NP-40 and treated with λ -protein phosphatase, and their binding components including β -TrCP–HA were eluted with SDS sample buffer for immunoblot analysis.

***In vitro* dephosphorylation of Erp1.** MBP–Erp1 bound to amylose beads²⁶ were incubated for 30 min at 25 °C in diluted CSF extracts to which $[\gamma\text{-}^{32}\text{P}]\text{ATP}$ had been added. After washing with β -glycerophosphate buffer (80 mM β -glycerophosphate, 20 mM EGTA, 5 mM MgCl_2 , 20 mM HEPES-KOH, pH 7.5), MBP–Erp1 beads were incubated in egg extraction buffer containing 1 μM okadaic acid with calcineurin-CA or calcineurin-PD for 30 min at 22 °C, and then MBP–Erp1 was eluted with SDS sample buffer, separated by SDS–polyacrylamide gel electrophoresis and analysed by autoradiography.

- Wang, L. J. Injection of *Xenopus* eggs before activation, achieved by control of extracellular factors, improves plasmid DNA replication after activation. *J. Cell Sci.* **93**, 1–8 (1989).
- Newport, J. & Kirschner, M. A major developmental transition in early *Xenopus* embryos: I. characterization and timing of cellular changes at the midblastula stage. *Cell* **30**, 675–686 (1982).
- Murray, A. W., Solomon, M. J. & Kirschner, M. W. The role of cyclin synthesis and degradation in the control of maturation promoting factor activity. *Nature* **339**, 280–286 (1989).
- Yamamoto, T. M., Iwabuchi, M., Ohsumi, K. & Kishimoto, T. APC/C–Cdc20-mediated degradation of cyclin B participates in CSF arrest in unfertilized *Xenopus* eggs. *Dev. Biol.* **279**, 345–355 (2005).
- Mackintosh, C. & Moorhead, G. *Protein Phosphorylation: A Practical Approach* (ed. Hardie, D. G.) 153–181 (Oxford Univ. Press, Oxford, 1999).
- Ohsumi, K., Yamamoto, T. M. & Iwabuchi, M. Oocyte extracts for the study of meiotic M–M transition. *Methods Mol. Biol.* **322**, 445–458 (2006).
- Uto, K., Nakajo, N. & Sagata, N. Two structural variants of Nek2 kinase, termed Nek2A and Nek2B, are differentially expressed in *Xenopus* tissues and development. *Dev. Biol.* **208**, 456–464 (1999).

LETTERS

Generation of functional multipotent adult stem cells from GPR125⁺ germline progenitors

Marco Seandel^{1,3}, Daylon James¹, Sergey V. Shmelkov¹, Ilaria Falciani¹, Jiyeon Kim¹, Sai Chavala¹, Douglas S. Scherr², Fan Zhang¹, Richard Torres⁵, Nicholas W. Gale⁵, George D. Yancopoulos⁵, Andrew Murphy⁵, David M. Valenzuela⁵, Robin M. Hobbs^{4,6}, Pier Paolo Pandolfi^{4,6} & Shahin Rafii¹

Adult mammalian testis is a source of pluripotent stem cells¹. However, the lack of specific surface markers has hampered identification and tracking of the unrecognized subset of germ cells that gives rise to multipotent cells². Although embryonic-like cells can be derived from adult testis cultures after only several weeks *in vitro*¹, it is not known whether adult self-renewing spermatogonia in long-term culture can generate such stem cells as well. Here, we show that highly proliferative adult spermatogonial progenitor cells (SPCs) can be efficiently obtained by cultivation on mitotically inactivated testicular feeders containing CD34⁺ stromal cells. SPCs exhibit testicular repopulating activity *in vivo* and maintain the ability in long-term culture to give rise to multipotent adult spermatogonial-derived stem cells (MASCs). Furthermore, both SPCs and MASCs express GPR125, an orphan adhesion-type G-protein-coupled receptor. In knock-in mice bearing a GPR125- β -galactosidase (LacZ) fusion protein under control of the native *Gpr125* promoter (GPR125-LacZ), expression in the testis was detected exclusively in spermatogonia and not in differentiated germ cells. Primary GPR125-LacZ SPC lines retained GPR125 expression, underwent clonal expansion, maintained the phenotype of germline stem cells, and reconstituted spermatogenesis in busulphan-treated mice. Long-term cultures of GPR125⁺ SPCs (GSPCs) also converted into GPR125⁺ MASC colonies. GPR125⁺ MASCs generated derivatives of the three germ layers and contributed to chimaeric embryos, with concomitant downregulation of GPR125 during differentiation into GPR125⁻ cells. MASCs also differentiated into contractile cardiac tissue *in vitro* and formed functional blood vessels *in vivo*. Molecular bookmarking by GPR125 in the adult mouse and, ultimately, in the human testis could enrich for a population of SPCs for derivation of GPR125⁺ MASCs, which may be employed for genetic manipulation, tissue regeneration and revascularization of ischaemic organs.

The genetic and phenotypic profile of the specific subset of spermatogonial cells that converts into multipotent adult cells is poorly defined. We discovered a potential stem and progenitor cell surface marker (GPR125) expressed on the adult testis, while evaluating a large series of mouse knockouts³. The endogenous *Gpr125* locus was altered by joining the amino-terminal putative extracellular and first transmembrane domains to β -galactosidase (Supplementary Fig. 2). Homozygous mice were grossly normal and fertile. Histochemical examination of the post-natal testis with the β -galactosidase substrate X-gal (5-bromo-4-chloro-3-indolyl- β -D-galactoside) revealed that GPR125 expression was restricted to the seminiferous tubules and was confined within the first layer of cells

adjacent to the basement membrane of the peritubular cells (Fig. 1a–c). Immunohistochemistry revealed GPR125 expression only in spermatogonia (Fig. 1e).

As spermatogenesis proceeds along the length of the seminiferous tubule, characteristic sets of differentiating cell types are seen together in a given cross-section, allowing such cross-sections to be categorized into twelve stages⁴. Expression of GPR125 was greatest at later stages (that is, VII–VIII) with a nadir in earlier stages (that is, IV–V), as analysed either by promoter activity (X-gal) or by immunostaining (in wild-type mice; Fig. 1c–e). To quantify expression of GPR125-LacZ in the *Gpr125*^{LacZ/LacZ} spermatogonia, staining was performed with fluorescein di-D-galactopyranoside (FDG), followed by flow cytometry. Freshly dissociated adult *Gpr125*^{LacZ/LacZ} seminiferous tubules yielded ~35% LacZ⁺ cells (Fig. 1f). The high yield of LacZ⁺GPR125⁺ cells may be a result of our preparation of testicular tissue—in which contaminating interstitial somatic cells and spermatids are lost during washing steps—combined with the high sensitivity of the FDG assay⁵.

To determine whether LacZ⁺GPR125⁺ cells represent self-renewing spermatogonial cells with the capacity to generate MASCs, we sought to recapitulate *in vitro* the native niche that supports efficient self-renewal of these cells. We discovered that the LacZ⁺GPR125⁺ cells reside in close proximity to the CD34⁺ peritubular cells⁶, indicating that interaction of these two cell types may be essential for expansion of the GPR125⁺ SPCs (Fig. 1g and Supplementary Fig. 3a, b). To culture GPR125⁺ cells, we established primary mitotically inactivated adult mouse testicular stromal cells containing CD34⁺ putative peritubular cells (CD34⁺MTS), because our initial attempts using mouse embryo fibroblasts (MEFs) were unsuccessful. Amongst the CD34⁺ stromal cells were also α -smooth-muscle-actin-positive (ACTA2⁺) and vimentin-positive (VIM⁺) cells that together supported derivation and long-term proliferation of adult SPCs from mouse testes of various ages (up to 1 yr) and genetic backgrounds in >90% of attempts (Fig. 1g, inset and Supplementary Fig. 3c, d). The adult spermatogonial cultures displayed heterogeneous colony size, with frequent formation of massive proliferating colonies, exponential overall growth, and ~30% of cells in S phase (Fig. 1h, j, and Supplementary Fig. 4a–c). Adult SPC lines were also derived from mice displaying green fluorescence in all tissues (see ref. 7) and were serially passaged six times in typical fashion on CD34⁺MTS. This revealed expansion of SPCs and near total (>99%) depletion of any somatic green-fluorescent-protein-positive (GFP⁺) cells outside of the characteristic spermatogonial stem cell-like colonies, suggesting loss of the non-germline contaminants (Supplementary Fig. 4c). The SPC lines expressed typical

¹Howard Hughes Medical Institute, Department of Genetic Medicine, and ²Department of Urology, Weill Cornell Medical College, New York 10065, USA. ³Division of Medical Oncology, Department of Medicine, and ⁴Cancer Biology and Genetics Program, Department of Pathology, Memorial Sloan-Kettering Cancer Center, New York 10065, USA. ⁵Regeneron Pharmaceuticals, Tarrytown, New York 10591, USA. ⁶Cancer Genetics Program, Beth Israel Deaconess Cancer Center, Harvard Medical School, Boston, Massachusetts 02115, USA.

mouse germ-lineage markers, including germ-cell nuclear antigen (GCNA1), DAZL and MVH (also known as DDX4) (Supplementary Fig. 4d–f)^{8–10}. Notably, the colonies expressed the well-characterized marker PLZF (also known as ZBTB16), which identifies undifferentiated spermatogonia (Fig. 1i)^{11,12}. Evidence of bona fide stem cell activity within the SPC pool (cultured for more than one year) was revealed by the ability of cells to participate in reconstitution of spermatogenesis in busulphan-treated host mice (see Fig. 2)¹³.

Prior studies have found that embryonic stem cell (ESC)-like cells arose in culture either from neonatal testicular cells by spontaneous conversion in the presence of glial-cell-line-derived neurotrophic factor (GDNF) and leukaemia inhibitory factor (LIF) on MEFs¹⁴, or in adult spermatogonial stem cells (SSCs) maintained in the absence of GDNF within four weeks after the initiation of spermatogonial colonies¹. We found that long-term culture of adult SPCs generated distinct colonies of MASCs from cells that were originally cultured on the CD34⁺MTS feeder layers for more than three months (Fig. 1k, l). The emergence of MASC colonies was heralded

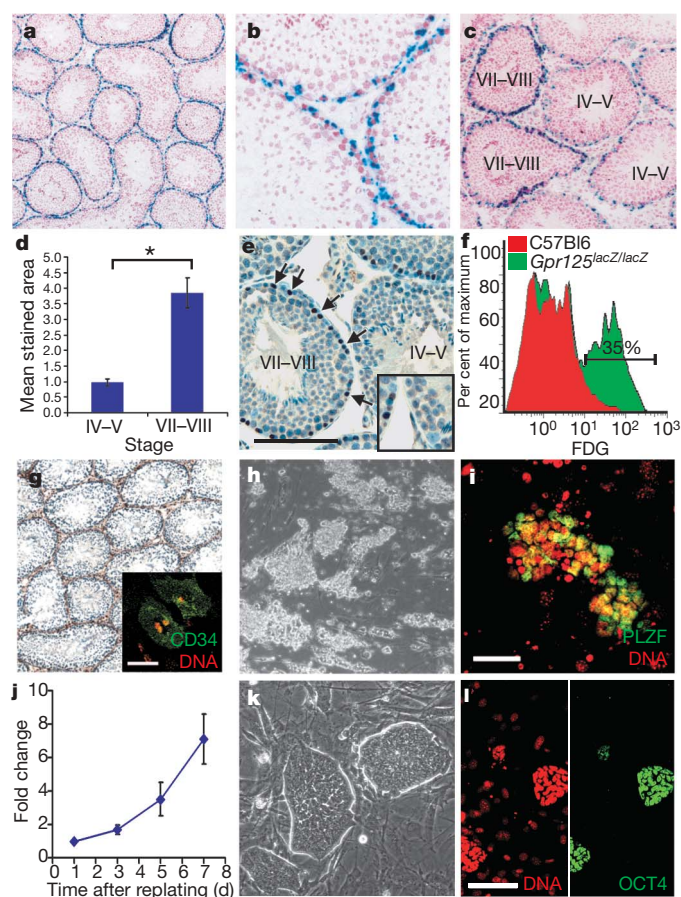


Figure 1 | Restricted GPR125 expression in adult mouse testis and derivation of multipotent cells from spermatogonial progenitor cells (SPCs). **a–c**, X-gal staining of adult GPR125-LacZ mouse testis. **d**, Quantification of X-gal staining (arbitrary units) in tubules grouped as stages IV–V (0.98 ± 0.11 (mean \pm s.e.m.); $n = 30$ tubules) versus stages VII–VIII (3.84 ± 0.49 ; $n = 28$; * $P < 0.001$ by Wilcoxon test). **e**, Anti-GPR125 staining (brown, arrows) of adult mouse testis. **f**, Flow cytometry on freshly dissociated adult *Gpr125^{lacZ/lacZ}* testis. Roman numerals in **c–e** denote approximate stages of the seminiferous tubules⁴. **g**, Anti-CD34 staining (brown) of peritubular/interstitial mouse cells, which remain CD34⁺ (inset, green staining) following *in vitro* expansion. **h**, **i**, Highly proliferative SPC colonies (**h**) that express PLZF (**i**, green staining) after expansion on inactivated CD34⁺MTS. **j**, The number (mean \pm s.d.) of SPCs doubled every ~2 days. **k**, **l**, The appearance of MASCs derived from *Gt(Rosa26)Sor-lacZ* SPCs following transfer to MEF for expansion and antibody staining, revealing OCT4 expression in the nucleus (green, right panel in **l**). Scale bars, 50 μm. Nuclei are shown in red (**a–c**, **i**, **l**) or blue (**e**, **g**).

by a distinct morphologic change in a subset of SPC colonies (Supplementary Fig. 4g). Putative MASC colonies, resembling ESCs, were mechanically transferred from CD34⁺MTS to MEFs for MASC expansion in the undifferentiated state (Fig. 1k, and Supplementary Fig. 1)¹⁵. Whereas the pluripotency marker OCT4 (also known as POU5F1) protein was undetectable in SPCs (data not shown), we found unequivocal OCT4 expression in the nuclei of MASCs that were expanded (15 passages before cryopreservation) on MEFs (Fig. 1l) and that were capable of differentiation into multiple lineages *in vitro*, including rhythmically contractile cardiogenic tissue (Supplementary Fig. 5a–d and Supplementary Movie 1). MASCs gave rise to teratomas (in 9/9 attempts) when injected subcutaneously in NOD-SCID mice

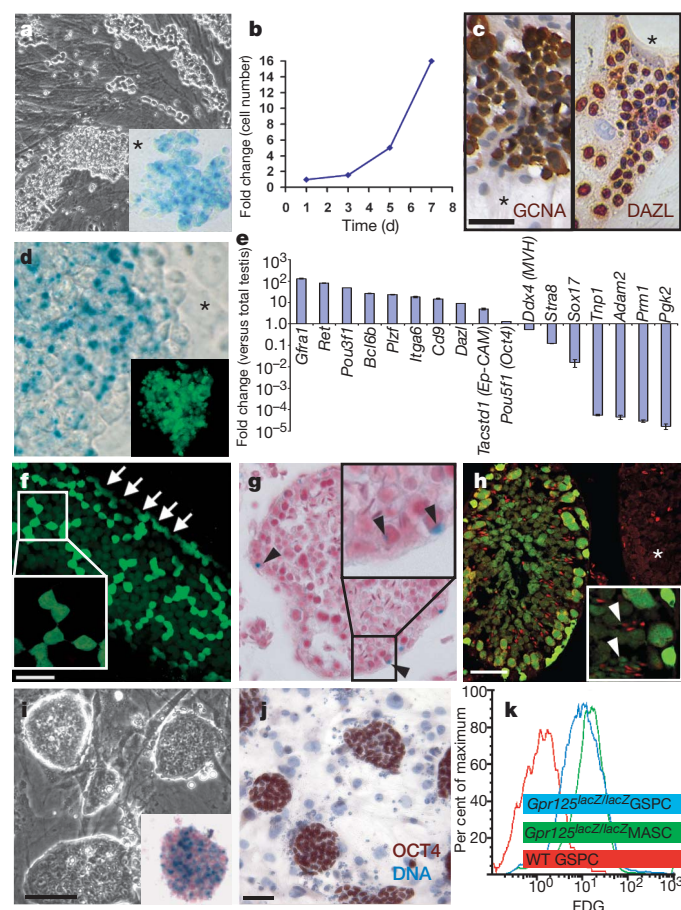


Figure 2 | Characterization and multipotent derivatives of *Gpr125^{lacZ/lacZ}* SPC lines **a**, Morphology of SPC colonies and expression of GPR125 by X-gal staining (blue, inset). **b**, Proliferation of GPR125⁺ SPCs (GSPCs) in culture. **c**, Immunolabelling by germ-cell markers GCNA (brown, left panel) and anti-DAZL (brown, right panel). Absent staining in feeders is denoted by asterisks. **d**, Expression of GPR125-LacZ in cloned GSPCs (tracked by GFP (green, inset), using lentivirus). **e**, Quantitative PCR of *Gpr125^{lacZ/lacZ}* GSPCs compared to *Gpr125^{lacZ/lacZ}* total testis. Bars depict fold change (\pm scaled s.d.) of gene expression (compared with total testis) of genes associated with GSPCs or differentiating spermatogenic cells. **f–h**, Engraftment of *Gpr125^{lacZ/lacZ}* GSPCs microinjected into busulphan-treated testes. **f**, Confocal slices (~1 μm, inset) distinguishing areas with GFP^{bright} spermatogonia along the basement membrane (arrows) from centrally located areas containing smaller, round GFP^{dim} differentiating cells, in the projection of 32 slices. **g**, GPR125 expression by X-gal staining (blue, arrowheads) present in engrafted cells along the basement membrane. **h**, Differentiation of donor-derived GFP⁺ cells and GFP⁺ non-engrafted tubules (arrowheads, spermatids; asterisk, non-engrafted tubule). **i**, Derivation of GPR125⁺ MASCs (blue staining in inset, X-gal) from GSPCs. **j**, Nuclear labelling by anti-OCT4 (brown). **k**, Flow cytometry for GPR125 expression in *Gpr125^{lacZ/lacZ}* MASCs or GSPCs by FDG staining (mean fluorescence intensity: 22.1 or 18.2, respectively, versus 2.2 in wild-type GSPC control). Scale bars, 50 μm.

(Supplementary Fig. 5e–h). The expression of LacZ in both *Gt(ROSA26)Sor-lacZ*⁶ MASCs, and the resultant teratomas, excluded the possibility of a multipotent mesenchymal cell originating from the wild-type, mitomycin-C-inactivated feeders. Furthermore, MASCs cloned from single cells were similarly competent to form tri-lineage teratomas and to contribute to chimaeric embryos on blastocyst injection (see Fig. 3).

To determine whether GPR125 is expressed on SPCs, testes from *Gpr125*^{+/lacZ} and *Gpr125*^{lacZ/lacZ} mice were used to derive SPC lines that were propagated on CD34⁺MTS. Refractile, cobblestone colonies reminiscent of SSCs appeared within one week, and large proliferative colonies were seen within 3–4 weeks that exhibited exponential clonal growth, and culture wells could be de-populated with complete re-growth of colonies (Fig. 2a, b). Maintenance of the germ-cell phenotype was confirmed by immunohistochemistry for GCNA and DAZL (Fig. 2c)¹⁷, but c-KIT was absent by flow cytometry

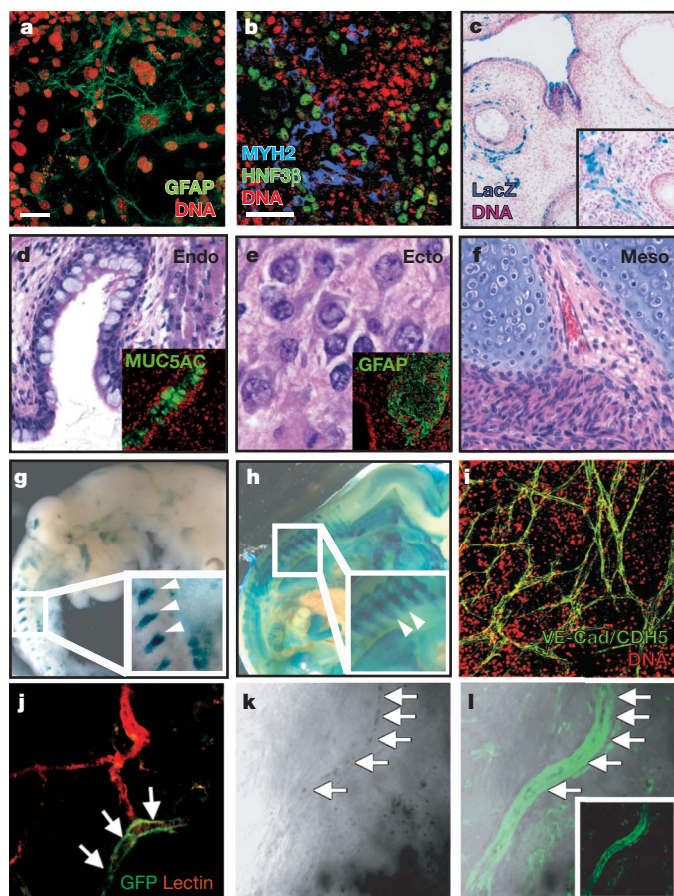


Figure 3 | GPR125–LacZ MASCs exhibit multipotency and can form functional vessels. **a, b**, Embryoid bodies differentiated *in vitro* and immunolabelled for neuroectoderm (anti-GFAP, green; **a**); mesoderm (anti-myosin heavy chain, myosin HC, blue; **b**); and endoderm or ectoderm (using anti-HNF3 β , green; **b**). **c**, X-gal-stained GPR125–LacZ MASC teratoma formed in NOD-SCID mice. **d–f**, Teratoma histology showing endodermal (**d**), ectodermal (**e**), and mesodermal (**f**) elements. Immunofluorescence (green) in insets: **d**, anti-Muc5ac; **e**, anti-GFAP. **g, h**, Whole-mount embryo X-gal staining. **g**, E13.5 GPR125–LacZ MASC chimaera formed by blastocyst injection. **h**, E14.5 full heterozygous *Gpr125*^{+/lacZ} embryo. **g, h**, Arrowheads denote putative ossification centres. **i**, GPR125–LacZ MASCs differentiated *in vitro* (22 days) and stained with anti-VE-cadherin/CDH5 (green). **j–l**, Cloned MASCs that were previously transduced *in vitro* with a VE-cadherin (*Cdh5*) promoter fragment driving GFP (green) in a lentiviral vector, form functional teratoma vessels *in vivo*, demonstrated by perfusion with mouse endothelial specific lectin (red in **j**) or by the presence of blood in GFP⁺ vessels (black in **k, l**; inset in **l** shows GFP alone). Arrows denote donor-derived vessels. Nucleic acid counterstain in **a–c, d** (inset), **e** (inset), and **i** is red. Scale bars, 50 μ m.

(Supplementary Fig. 6a). Strikingly, GPR125–LacZ SPCs maintained GPR125 expression after multiple passages *in vitro* (Fig. 2a, inset) and are hereafter referred to as GPR125⁺ SPCs (GSPCs). To determine the frequency of repopulating cells, limiting dilution analysis was performed using GFP-labelled GPR125–LacZ GSPCs (from *Gpr125*^{lacZ/lacZ} mice) on cells that were cultured beyond 9 months, revealing 0.23 (95% confidence interval, 0.19–0.27) colony forming units (c.f.u.) per cell or 1 c.f.u. for every 4–5 GSPCs (Fig. 2d). All emerging colonies derived from the testes of *Gpr125*^{lacZ/lacZ} mice expressed lacZ, suggesting that the GSPCs are clonogenic (Fig. 2d).

The molecular identity of *Gpr125*^{lacZ/lacZ} GSPCs in long-term culture was confirmed by quantitative PCR (Fig. 2e, and Supplementary Fig. 7). Among the transcripts expressed in *Gpr125*^{lacZ/lacZ} GSPC cultures were germ-cell-specific genes, including *Dazl* and *Mvh*^{10,17}. To rule out spontaneous spermatogenic differentiation of the cultured GSPCs¹⁸, we surveyed transcripts characteristic of differentiated germ cells and noted diminished or absent levels for transcripts such as *Sox17*, *Tnp1*, *Adam2*, *Prm1* and *Pgk2* (ref. 19). These data suggested that repopulating GSPCs were of germ-cell origin but remained undifferentiated. Even after *in vitro* propagation for over one year, GSPCs revealed a transcriptional profile highly reminiscent of spermatogonial stem cells (Fig. 2e, and Supplementary Fig. 7). Various cell surface markers used for isolation of SSCs were increased at the mRNA level in GSPCs: *Itga6* (~18-fold), *Tacstd1* (~5-fold), *Cd9* (~15-fold) and *Gfra1* (~128-fold)^{20–22}. Similarly, genes with preferential promoter activity in undifferentiated cells, including *Stra8* and *Oct4*, were detectable albeit at lower levels in the GPR125⁺ cells. Therefore, our culture technique yields undifferentiated spermatogonia, which like spermatogonia *in vivo*, express GPR125.

To interrogate the repopulating potential of GSPCs *in vivo*, we then evaluated the capacity of GFP-labelled *Gpr125*^{lacZ/lacZ} GSPCs to restore spermatogenesis within busulphan-treated C57Bl6 host mouse testes¹³. Within 2–3 months after transplantation, robust GFP⁺ *Gpr125*^{lacZ/lacZ} germ-cell colonies were detectable within the host seminiferous tubules (Fig. 2f, and Supplementary Fig. 8a). These colonies contained populations of GFP⁺ cells along the basement membrane, exhibiting typical spermatogonial morphology, and smaller round GFP⁺ cells located more centrally to tubular lumen (Fig. 2f, and Supplementary Fig. 8b–g). X-gal staining confirmed co-expression of GPR125 (LacZ⁺) in a small subset of the GFP-labelled, transplanted cells along the basement membrane (Fig. 2g, and Supplementary Fig. 9a–e), recapitulating the spatial expression pattern in the GPR125–LacZ testes (see Fig. 1). Importantly, GFP⁺ spermatids were seen in donor-colonized tubules but not in adjacent tubules containing residual, host-derived spermatogenesis, confirming the presence of true stem cell activity within the long-term *Gpr125*^{lacZ/lacZ} GSPC cultures (Fig. 2h, and Supplementary Fig. 8h). PCR for GFP detected donor-derived sperm in the epididymis draining the transplanted testis but not in negative controls (data not shown).

The origin of multipotent stem cells in the adult testis is not clear²³. Therefore, we sought to formally prove that GSPCs could indeed generate multipotent cells, even after long-term expansion *in vitro*. The spontaneous emergence of MASCs was observed in the *Gpr125*^{lacZ/lacZ} cultures that were initially propagated for more than 3 months. These *Gpr125*^{lacZ/lacZ} MASCs had a high nuclear-to-cytoplasmic ratio, formed refractile colonies, and could be split in a ratio of ~1:8 in mouse embryonic stem cell medium every 2–3 days (Fig. 2i; passaged >30 times before cryopreservation). The majority of cells had a normal karyotype, and no evidence of clonal cytogenetic abnormalities was found for either *Gpr125*^{lacZ/lacZ} MASCs or *Gt(Rosa26)Sor-lacZ* MASCs (data not shown). Notably, the majority of cells within the colonies were highly positive for GPR125 expression and also uniformly immuno-positive for OCT4 within the nucleus (Fig. 2j). FDG-labelling revealed more than 99% of both *Gpr125*^{lacZ/lacZ} GSPCs and MASCs to be GPR125⁺ by β -galactosidase

activity (Fig. 2k), suggesting that GPR125 is associated more universally with the stem- and progenitor-cell phenotype.

The multipotency of these *Gpr125^{lacZ/lacZ}* MASCs was first assessed by formation and differentiation of embryoid bodies *in vitro*²⁴. Within seven days after re-plating, embryoid bodies exhibited a distinct pattern of GPR125 expression, with distinct borders between GPR125⁺ and GPR125⁻ areas (Supplementary Fig. 10a, b). The resultant colonies contained HNF3 β ⁺ (FOXA2⁺) cells derived from endoderm or ectoderm, cytokeratin-positive (KRT⁺) or GFAP⁺ cells derived from ectoderm, and brachyury-positive or skeletal-muscle-myosin-positive (MYH2⁺) cells derived from mesoderm (Fig. 3a, b).

When GPR125^{lacZ/lacZ} MASCs were implanted subcutaneously in NOD-SCID mice, the resultant teratomas (14/14 attempts) similarly exhibited GPR125 expression in a lineage-specific manner, implying loss of GPR125 in certain differentiated cell types (Fig. 3c and Supplementary Fig. 11). In fact, these teratomas were reminiscent of GPR125–LacZ embryos, in which GPR125 expression is present in most but not all tissues and subsequently lost over time (see Fig. 3h, Supplementary Fig. 12). Lineage analysis of MASC teratomas demonstrated morphologic and immunologic evidence for tissue derivatives of all three germ layers, including mucin-positive (Muc5ac⁺) endoderm, GFAP⁺ neuroectoderm, and mesodermal chondrocytic, myoid, and vascular cells (Fig. 3d–f).

The ability to form chimaeric animals has been used to demonstrate multipotency of germ-cell derivatives². We therefore performed blastocyst injections with cloned *Gpr125^{lacZ/lacZ}* MASCs and found 8 chimaeric embryos out of 37 evaluated (22%). Importantly, the expression pattern of GPR125 in the C57Bl6 (host)/*Gpr125^{lacZ/lacZ}* (donor) chimaeric embryos partially recapitulated what was seen in heterozygous knock-in *Gpr125^{+/lacZ}* embryos, with prominent signal in developing ossification centres (Fig. 3g, h, and Supplementary Fig. 12e, f). In addition, LacZ⁺ cells were also detected in the chimaeric gut and other tissues that are known to harbour GPR125⁺ cells in non-chimaeric embryos (Supplementary Table 2 and Supplementary Fig. 12). These data indicate that generation of GPR125⁺ MASCs from GSPCs results in the maintenance of the expected global expression pattern of the *Gpr125* gene. As such, lineage-specific derivatives of MASCs may have the essential set of genetic and epigenetic instructions that are critical for autologous organ regeneration.

To this end, we examined the ability of MASCs to differentiate into endothelial cells. An extensive network of vessel-like, lumen-containing VE-cadherin⁺ (CDH5⁺) structures were formed *in vitro* from MASC embryoid bodies after 22 days of differentiation (Fig. 3i, and data not shown). To determine whether GPR125⁺ MASCs could differentiate into functional vessels *in vivo*, GPR125⁺ MASCs were transduced with a lentiviral vector expressing GFP under control of the promoter for the endothelial-specific marker VE-cadherin (ref. 25). Teratomas formed in NOD-SCID mice from such transduced MASCs contained donor-derived GFP⁺ blood vessels, continuous with the host circulation, as shown by perfusion-based staining and the presence of red blood cells within the vessels (Fig. 3j–l).

We asked next whether MASCs use the same molecular machinery for multipotency as ESCs. Expression analysis of *Gpr125^{lacZ/lacZ}* MASCs compared with mouse ESCs, GSPCs or MEFs revealed high levels of *Oct4*, *Nanog* and *Sox2* in both MASCs and ESCs (Fig. 4a). Minimal expression of typical SSC markers, including *Plzf*, *Ret* and *Stra8*, was seen in MASCs, which, as expected, were high in *Gpr125^{lacZ/lacZ}* GSPCs. Unexpectedly, certain key germ-lineage transcripts (for example, *Dazl*) were nearly absent in MASCs, as were some canonical mouse ESC transcripts (for example, *Gdf3*, *Esg1* (also known as *Dppa5*) and *Rex1*; Fig. 4b). The differences in expression of these genes and others (for example, *Nog* and *brachyury*) suggest that MASCs constitute a distinct stem cell type from that reported in ref. 1.

Here, we have identified GPR125 as a surface marker for self-renewing, clonogenic, cKIT⁺PLZF⁺ spermatogonial progenitor cells

(GSPCs), with the capacity for both repopulating the testis and generating GPR125⁺ MASCs. Recent evidence indicates that spermatogonial progenitor cells can manifest stem cell activity²⁶. This indicates that GPR125⁺cKIT⁺PLZF⁺DAZL⁺ GSPCs may not only be endowed with spermatogonial stem cell activity but may also perform as undifferentiated spermatogonial cells that can convert into GPR125⁺cKIT⁺PLZF⁺DAZL⁺OCT4⁺ MASCs. These data pinpoint GPR125⁺ spermatogonial cells as the cellular ancestors of MASCs (see Supplementary Fig. 1). Differentiation of GPR125⁺ MASCs into GPR125⁻ tissues qualifies GPR125 expression as a useful marker for tracking differentiation and lineage-specification of stem and progenitor cells.

The precise molecular and cellular pathways governing the emergence of MASC colonies remain unclear. Although MASCs and ESCs have identical morphological characteristics and are both multipotent, capable of giving rise to teratomas and chimaeric animals, there are major differences at the transcriptional level that distinguish these two cell types (Fig. 4c). Notably, unlike the ESC-like cells derived from STRA8⁺ SSCs¹, GPR125⁺ MASCs lack the molecular signature of ESCs but mimic other multipotent adult stem cells, such as multipotent adult progenitor cells (MAPCs)²⁷. Our data, therefore, imply that multipotency may be driven by multiple unique sets of signals, even in the absence of gene products typically associated with stem cells (for example, *Gdf3*, *Esg1* and *Rex1*). Also, in contrast to a prior report¹, the maintenance of long-term cultures of GSPCs was dependent on GDNF and was therefore necessary for the subsequent emergence of MASCs. Therefore, culture conditions may influence the ultimate multipotent phenotype.

GPR125 expression in undifferentiated cells and early progenitors and its subsequent downregulation on terminal differentiation raises the intriguing possibility of exploiting surface expression of GPR125

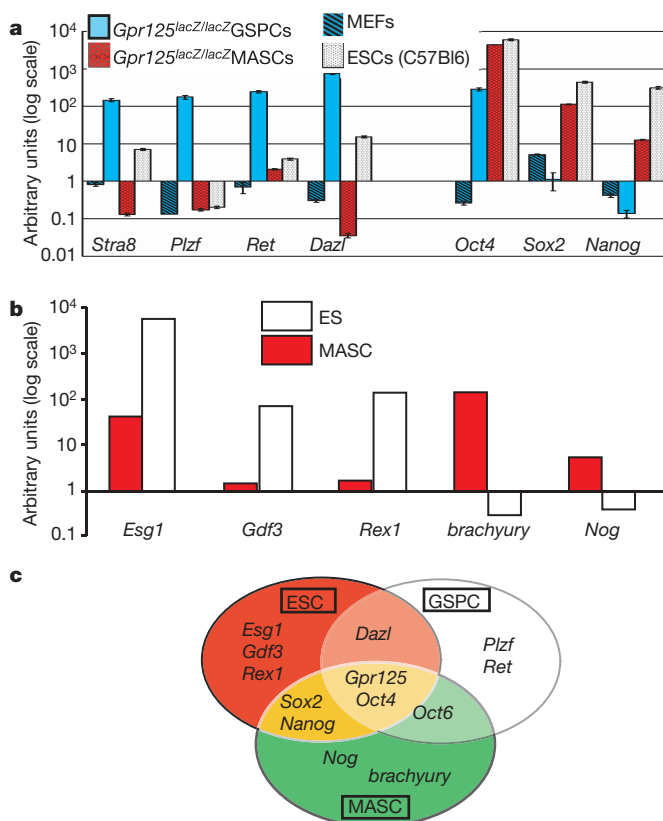


Figure 4 | *Gpr125^{lacZ/lacZ}* MASCs have an expression profile different from mouse embryonic stem cells. **a**, **b**, Quantitative PCR comparing expression of relevant genes *in vitro* in *Gpr125^{lacZ/lacZ}* MASCs versus wild-type ESCs, *Gpr125^{lacZ/lacZ}* GSPCs, and MEFs. **c**, Venn diagram illustrating transcripts unique or common to GSPCs, MASCs and ESCs.

to isolate human SSCs and GSPCs. Recent data demonstrated the *in vitro* differentiation of endothelium from multipotent cells derived from the neonatal testis²⁸. We extend these observations by showing that GPR125⁺ MASCs can generate functional vasculature *in vivo*. Taken together, these data indicate that GPR125⁺ MASCs could be used therapeutically for the generation of functional autologous vessels for revascularization. However, as germline stem and progenitor cells may have alterations in genomic imprinting in certain genes compared with adult somatic cells¹⁴, the use of these cells for therapeutic purposes should proceed with caution and extensive pre-clinical experimentation.

METHODS SUMMARY

SSC, MASC and feeder-cell culture. C57Bl6 mice aged 4–12 wks served as donors for mixed primary testicular feeder cells, which were expanded following enzymatic digestion of the seminiferous tubules. Feeder cells were treated with mitomycin-C before use for stem cell culture. Mouse GSPCs were obtained from enzymatically dissociated seminiferous tubules from mice aged 3 weeks to 8 months and were plated in StemPro-34 (Invitrogen) with the modifications of ref. 29. GSPCs were serially passaged onto fresh mitomycin-C-treated feeders every 2–8 wks. Morphologically atypical transitional colonies of GSPCs were mechanically removed from the plate after >2 wks in culture and re-plated in the same medium or embryonic stem cell (ESC) medium on mitomycin-C-inactivated MEF to obtain MASC lines.

GPR125–LacZ mice. VelociGene technology was employed for production of *Gpr125^{lacZ/lacZ}* mice as previously described³. Briefly, targeting vectors were generated using a bacterial artificial chromosome (BAC) and contained *Gpr125* in which exons 16–19 were deleted and replaced in-frame with *lacZ*, as a reporter gene, and neomycin, as a selectable marker. Targeting vectors were electroporated into ESCs. Clones that were properly targeted were confirmed by real-time PCR-based loss-of-native-allele assay³, using primers listed in Supplementary Information. Chimaeric mice were generated by blastocyst injection of ESCs and backcrossed to C57Bl6/J to produce heterozygote breeding pairs.

Additional methods. Additional methods, including histochemistry, immunostaining, flow cytometry following FDG-labelling, quantitative (q)PCR, lentivirus preparation and spermatogonial transplantation are presented in the Methods.

Full Methods and any associated references are available in the online version of the paper at www.nature.com/nature.

Received 1 June; accepted 27 July 2007.

- Guan, K. *et al.* Pluripotency of spermatogonial stem cells from adult mouse testis. *Nature* **440**, 1199–1203 (2006).
- Kanatsu-Shinohara, M. & Shinohara, T. The germ of pluripotency. *Nature Biotechnol.* **24**, 663–664 (2006).
- Valenzuela, D. M. *et al.* High-throughput engineering of the mouse genome coupled with high-resolution expression analysis. *Nature Biotechnol.* **21**, 652–659 (2003).
- Oakberg, E. F. A description of spermiogenesis in the mouse and its use in analysis of the cycle of the seminiferous epithelium and germ cell renewal. *Am. J. Anat.* **99**, 391–413 (1956).
- Fiering, S. N. *et al.* Improved FACS-Gal: flow cytometric analysis and sorting of viable eukaryotic cells expressing reporter gene constructs. *Cytometry* **12**, 291–301 (1991).
- Kuroda, N. *et al.* Distribution and role of CD34-positive stromal cells and myofibroblasts in human normal testicular stroma. *Histol. Histopathol.* **19**, 743–751 (2004).
- Schaefer, B. C., Schaefer, M. L., Kappler, J. W., Marrack, P. & Kedl, R. M. Observation of antigen-dependent CD8⁺ T-cell/dendritic cell interactions *in vivo*. *Cell. Immunol.* **214**, 110–122 (2001).
- Enders, G. C. & May, J. J. Developmentally regulated expression of a mouse germ cell nuclear antigen examined from embryonic day 11 to adult in male and female mice. *Dev. Biol.* **163**, 331–340 (1994).

- Schrans-Stassen, B. H., Saunders, P. T., Cooke, H. J. & de Rooij, D. G. Nature of the spermatogenic arrest in *Dazl*^{−/−} mice. *Biol. Reprod.* **65**, 771–776 (2001).
- Tanaka, S. S. *et al.* The mouse homolog of *Drosophila Vasa* is required for the development of male germ cells. *Genes Dev.* **14**, 841–853 (2000).
- Costoya, J. A. *et al.* Essential role of Plzf in maintenance of spermatogonial stem cells. *Nature Genet.* **36**, 653–659 (2004).
- Buaas, F. W. *et al.* Plzf is required in adult male germ cells for stem cell self-renewal. *Nature Genet.* **36**, 647–652 (2004).
- Brinster, R. L. & Zimmermann, J. W. Spermatogenesis following male germ-cell transplantation. *Proc. Natl Acad. Sci. USA* **91**, 11298–11302 (1994).
- Kanatsu-Shinohara, M. *et al.* Generation of pluripotent stem cells from neonatal mouse testis. *Cell* **119**, 1001–1012 (2004).
- Schatten, G., Smith, J., Navara, C., Park, J. H. & Pedersen, R. Culture of human embryonic stem cells. *Nature Methods* **2**, 455–463 (2005).
- Friedrich, G. & Soriano, P. Promoter traps in embryonic stem cells: a genetic screen to identify and mutate developmental genes in mice. *Genes Dev.* **5**, 1513–1523 (1991).
- Reijo, R. A. *et al.* DAZ family proteins exist throughout male germ cell development and transit from nucleus to cytoplasm at meiosis in humans and mice. *Biol. Reprod.* **63**, 1490–1496 (2000).
- Ehmcke, J., Hubner, K., Scholer, H. R. & Schlatt, S. Spermatogonia: origin, physiology and prospects for conservation and manipulation of the male germ line. *Reprod. Fertil. Dev.* **18**, 7–12 (2006).
- Wang, P. J., Page, D. C. & McCarrey, J. R. Differential expression of sex-linked and autosomal germ-cell-specific genes during spermatogenesis in the mouse. *Hum. Mol. Genet.* **14**, 2911–2918 (2005).
- Ryu, B. Y., Orwig, K. E., Kubota, H., Avarbock, M. R. & Brinster, R. L. Phenotypic and functional characteristics of spermatogonial stem cells in rats. *Dev. Biol.* **274**, 158–170 (2004).
- Kanatsu-Shinohara, M., Toyokuni, S. & Shinohara, T. CD9 is a surface marker on mouse and rat male germline stem cells. *Biol. Reprod.* **70**, 70–75 (2004).
- Shinohara, T., Avarbock, M. R. & Brinster, R. L. β 1- and α 6-integrin are surface markers on mouse spermatogonial stem cells. *Proc. Natl Acad. Sci. USA* **96**, 5504–5509 (1999).
- Seydoux, G. & Braun, R. E. Pathway to totipotency: lessons from germ cells. *Cell* **127**, 891–904 (2006).
- Keller, G. Embryonic stem cell differentiation: emergence of a new era in biology and medicine. *Genes Dev.* **19**, 1129–1155 (2005).
- Sun, J. F. *et al.* Microvascular patterning is controlled by fine-tuning the Akt signal. *Proc. Natl Acad. Sci. USA* **102**, 128–133 (2005).
- Simon, A. & Frisen, J. From stem cell to progenitor and back again. *Cell* **128**, 825–826 (2007).
- Jiang, Y. *et al.* Pluripotency of mesenchymal stem cells derived from adult marrow. *Nature* **418**, 41–49 (2002).
- Baba, S. *et al.* Generation of cardiac and endothelial cells from neonatal mouse testis-derived multipotent germline stem cells. *Stem Cells* **25**, 1375–1383 (2007).
- Kanatsu-Shinohara, M. *et al.* Long-term proliferation in culture and germline transmission of mouse male germline stem cells. *Biol. Reprod.* **69**, 612–616 (2003).

Supplementary Information is linked to the online version of the paper at www.nature.com/nature.

Acknowledgements This work was supported by the Howard Hughes Medical Institute, Ansary Stem Cell Center for Regenerative Medicine and Memorial Sloan Kettering Cancer Center T32 grant (M.S.), an AACR–Genentech BioOncology Fellowship for Cancer Research on Angiogenesis (M.S.), the Heed Foundation (S.C.), the International Retinal Research Foundation (S.C.) and National Heart, Lung and Blood Institute grants (S.R.). We thank M. Hardy, P. Schlegel, Marc Goldstein, A. Brivanlou and S. Noggle for critical input. We are grateful to G. Enders for providing anti-GCNA antibody. We thank D. S. Johnston, G. Linkov and G. Zlotchenko for technical assistance.

Author Information Reprints and permissions information is available at www.nature.com/reprints. The authors declare competing financial interests: details accompany the full-text HTML version of the paper at www.nature.com/nature. Correspondence and requests for materials should be addressed to S.R. (srafi@med.cornell.edu).

METHODS

Gene targeting. The primers to identify the 5' junction of the mutant *Gpr125* allele included forward primer ATGTTAGCTTAATGGACTGTC and reverse primer (*lacZ*) GTCTGTCTAGCTTCCTCACTG, and for the 3' junction, included forward primer (*neo*) TCATTCTCAGTATTGTTTGGC and reverse primer ATAGTAAATCCCAAGCTCAC.

Animals. Teratomas were generated by injecting $0.5\text{--}1 \times 10^6$ cells in Matrigel subcutaneously into 8-week-old NOD-SCID mice. *Gt(ROSA26)Sor-lacZ*, UBC-GFP, FVB, Steel Dickie and C57Bl6/129S mice served as donors for GSPCs. C57Bl6 mice served as hosts for spermatogonial cell transplantation. Mice were bred, manipulated and euthanized under the guidelines of the Institutional Animal Care and Use Committee.

Histology and immunostaining. Tissues were dissected from the mice and either snap-frozen in OCT (Tissue Tek) or fixed overnight in 4% paraformaldehyde (Alfa Aesar) in PBS at 4 °C, for paraffin embedding. X-gal staining for detection of galactosidase activity was performed on cryosections using an overnight incubation with substrate (Calbiochem) at 37 °C, as per the manufacturer's directions. For immunohistochemistry, paraffin sections were rehydrated and heated in Antigen Retrieval Solution (Dako). Primary antibodies used in this study included two rabbit polyclonal antisera against GPR125 peptides (Genesis Biotech), rat monoclonal anti-GCNA (courtesy of G. Enders), rat monoclonal anti-E-cadherin (R&D Systems), mouse anti-DAZL (Abcam), mouse anti- α smooth muscle actin (Dako), rat anti-mouse CD34 (Abcam), mouse anti-human CD34 (QBEND10), mouse anti-vimentin (Chemicon), mouse anti-OCT4 (R&D Systems), rabbit anti-VASA (Abcam), rabbit anti-mouse CD31 (RDI) anti-mouse HNF3 β (Santa Cruz), anti-mouse GFAP (Dako), and mouse anti-mucin 5AC (clone 45M1, Lab Vision). Primary incubation of antibodies was performed overnight. Monoclonal hamster anti-mouse PLZF was generated using a peptide corresponding to the PLZF hinge region, as will be described elsewhere. For immunohistochemistry, detection of primary antibodies was performed with biotinylated donkey anti-rabbit IgG (Jackson Laboratories) or biotinylated mouse anti-rat IgM (Zymed). Biotinylated secondary antibody was followed by streptavidin-horseradish peroxidase and amino-ethyl carbazole (AEC; Biomed Corporation). For immunofluorescence, primary antibodies were detected with FITC-conjugated goat anti-hamster antibody (eBioscience), cy2- or cy3-conjugated non-cross reacting donkey anti-rabbit, rat, or mouse antibody, or with biotinylated donkey secondaries (Jackson Laboratories) followed by Alexa546- or Alexa488-conjugated streptavidin (Invitrogen) for additional amplification. Staining of cells *in vitro* was performed identically except that permeabilization was carried out with 0.2% Triton X-100/10% normal donkey serum/PBS for 30 min before incubation with certain primary antibodies. Counterstaining was performed with TOPRO1 (Invitrogen) (for immunofluorescence), haematoxylin and eosin (Dako) for immunohistochemistry, or nuclear fast red (Vector Laboratories) for X-gal staining. Colour images of immunohistochemical or X-gal staining were captured using an Olympus microscope and contrast enhanced uniformly for images within each experiment using Adobe Photoshop 7.0. Immunofluorescent images were captured using the Zeiss LSM 510 Meta confocal microscope (Carl Zeiss) and pseudo-coloured after capture.

Cell culture. Primary mouse testicular stromal cells (MTS) were prepared from 4–12-wk-old C57Bl6 mice, as follows. Seminiferous tubules were collected from detunicated testes and minced. The tissue was washed and then enzymatically dissociated with agitation at 37 °C in a buffer containing 0.017% trypsin (Cellgro), 17 μM EDTA (Cellgro), 0.03% collagenase (Sigma-Aldrich), and DNase I (100 $\mu\text{g ml}^{-1}$; Sigma-Aldrich). The resultant cell suspension (non-filtered) was collected, plated in flasks coated with gelatin in a 50:50 mixture of alpha modified Eagle's medium/StemPro-34 (Invitrogen) supplemented with 20% FBS (Gibco) and expanded over two to seven passages. Cells were then cryopreserved for future use or plated in flasks coated either with Matrigel (BD Biosciences) diluted 1:40 (for the first 1–2 passages of GSPCs), to improve adherence of feeders to the plate) or gelatin (for subsequent passages) at $0.4\text{--}1.0 \times 10^6$ cells per 35 mm dish, and treated with mitomycin-C (10 $\mu\text{g ml}^{-1}$; Sigma-Aldrich) for 2–4 h, before use for stem cell culture. The population of cells in the MTS was heterogeneous, as depicted in Supplementary Fig. 3. Primary cultures of mouse spermatogonial stem cells were obtained as follows. Mice from 3 wks to 8 months of age, of the indicated genotypes, were euthanized. Seminiferous tubules were collected from 1 to 2 de-tunicated testes and minced. The tissue was washed in 50 ml of PBS/1% BSA (Sigma-Aldrich), centrifuged at 30g, and the pellet (containing only large tissue fragments) was enzymatically dissociated with agitation at 37 °C in a buffer (3 ml) containing trypsin, EDTA, 0.03% collagenase, and DNase I (100 $\mu\text{g ml}^{-1}$). The resultant cell suspension was collected and either cryopreserved or plated on the feeder cells described above in spermatogonial stem cell medium containing StemPro-34 (Invitrogen) and

supplements as follows: D(+)glucose, 33.3 mM (Sigma-Aldrich); BSA, 0.50%; MEM vitamin solution, $1 \times$ (Gibco); β -oestradiol, 110 nM (Calbiochem); progesterone, 190 nM (Calbiochem); fetal bovine serum, 1%; penicillin (100 U ml^{-1})/streptomycin (100 $\mu\text{g ml}^{-1}$)/amphotericin (0.2 $\mu\text{g ml}^{-1}$) (Mediatech); transferrin, 100 $\mu\text{g ml}^{-1}$ (Sigma-Aldrich); insulin, 25 $\mu\text{g ml}^{-1}$ (Sigma-Aldrich); human GDNF 10 ng ml^{-1} (R&D Systems), ESGRO (mLIF), 1,000 U ml^{-1} (Millipore); human bFGF, 10 ng ml^{-1} (Biosource), non-essential amino acid solution $1 \times$ (Gibco); L-glutamine, 2 mM (Mediatech); putrescine, 60 μM (Research Organics); sodium selenite, 30 nM (Sigma-Aldrich); pyruvic acid, 340 μM (Sigma-Aldrich); D(L)-lactic acid, 11 μM (Baker), β -mercaptoethanol, 50 μM (Gibco); ascorbic acid, 100 μM (EMD); D-biotin, 10 $\mu\text{g ml}^{-1}$ (Calbiochem); and mouse EGF, 20 ng ml^{-1} (BD Biosciences). Cells were maintained at 37 °C in 5% CO_2 and fed three times per week. Serial passaging was performed non-enzymatically by gentle trituration of colonies every 2–8 wks, to progressively isolate GSPCs from contaminating donor-derived stromal cells. Culture wells could be partially depopulated of GSPCs by gentle trituration of loosely adherent colonies without disturbing the feeder cells, with subsequent re-growth of colonies in the same wells after addition of fresh medium. In this way, a given well of feeders could support GSPC proliferation for up to 8 weeks. Subsequently, wells were then trypsinized for either cryopreservation or further passaging on fresh feeders. For limiting dilution analysis, gelatine-coated 96-well plates of feeders were prepared using an outgrowth cell line of the MTS that could be passaged continuously. Five 96-well plates of GSPCs were prepared by serial doubling dilution. The location of rows calculated to contain single cells was verified by phase and fluorescent microscopy to confirm the presence of a single cell per well. Plates were then maintained for 17 days at 37 °C and scored for the presence of single large colonies (greater than ~ 50 cells). The rows in which ~ 10 cells had been initially plated were employed for statistical analysis ($n = 60$ wells) to obtain normally distributed data on the frequency of colony-forming cells per total number of cells initially plated. To obtain MASC colonies, distinct clusters of GSPCs with atypical, transitional morphology were identified by phase microscopy, mechanically separated from the plate using Pasteur pipettes, and replated on mitomycin-C-inactivated CF1 MEF (Chemicon) in the same GSPC culture medium or ESC medium (see below). MASC were passaged with trypsinization every 2–4 days onto fresh inactivated MEF. C57Bl6 mouse ESCs were cultured using standard procedures. Mouse ESC culture medium consisted of KO-DMEM (GIBCO), 15% FBS, $1 \times$ non-essential amino acids, $1 \times$ penicillin/streptomycin antibiotic, 2 mM L-glutamine, 55 μM β -mercaptoethanol, and LIF at 1,000 U ml^{-1} . Embryoid bodies from MASC or ESCs were formed by the hanging drop method.

Quantitative polymerase chain reaction (qPCR). Total RNA was prepared from cultured cells using the RNeasy extraction kit (Qiagen) and reverse transcribed using Superscript II reverse transcriptase (Invitrogen), according to the manufacturer's instructions. Relative quantitative PCR was performed on a 7500 Fast Real Time PCR System (Applied Biosystems) using SYBR Green PCR mix (Applied Biosystems). Mouse-specific intron-spanning primer pairs used were as follows:

Stra8 ACAAGAGTGAGGCCAGCAT (fwd), CCTCTGGATTTTCTGAGTTGCA (rev.); *Plzf* TTTGCGACTGAGATGCATTTAC (fwd), ACCGCATTGATCACACACAAAG (rev.); *Ret* GGCTGTCCCGAGATGTTTATG (fwd), GACTCAATTGCCATCCACTTGA (rev.); *Dazl* AAATCATGCCAAACACCGTTTT (fwd), GGCAAAGAACTCCTGATTTTCG (rev.); *Oct4* TTGGGCTAGAGAAGGATGTGGTT (fwd), GGAAAGGGAGCTGAGTAGAGTGTGG (rev.); *Sox2* TTTTCGGTGATGCCGACTAGA (fwd), GCGCCTAACGTACCACCTAGAAGT (rev.); *Nanog* AAGAACTCTCTCCATCTCTGAACCT (fwd), TGCATCTCTCTTGGTTTTG (rev.); *Prr1* CCGCCGCTCATACACCATA (fwd), ACGCAGGAGTTTGTATGGACTT (rev.); *Pgk2* GGCAAAGTGAGTCTTAAGGGAAA (fwd), TTGGTTATCTTCATGGGAACGT (rev.); *Adam2* CTGAGTGGGCTGAGTGAACTT (fwd), TAATTTCTCACGAGTGCCTTCTGT (rev.); *Tnfr1* CGGAAGA-CGGTCTGTAAGG (fwd), CATTGCCGATCACAGATG (rev.); *Sox17* GGCCGATGAACGCCCTTT (fwd), ACGAAGGGCCGCTTCTCT (rev.); *brachyury* GCTGTGGCTGCGCTTCA (fwd), GAACATCCTCTGCCGTCTT (rev.); *Dkk1* TCAAAAATATATCACACCAAGGACAAG (fwd), GCCCTGCGGCACAGTCT (rev.); *Nog* AGCTGAGGAGGAAGTTACAGATGTG (fwd), CTAGGT-CATTCCACGCGTACAG (rev.); *Zfp42 (rex1)* CAGACGTCTCTGACACAG (fwd), GGGCACTGATCCGCAAAAC (rev.); *Pou3f1* GGAGCAGTTCGCCAAGCA (fwd), TGCGAGAACACGTTACCGTAGA (rev.); *Gfra1* TACCACAGCATGTCCAATGAA (fwd), GTAGCTGTGCTTGGCTGGAAGT (rev.); *Cd9* TGCATGTGGGATGTCTTCTC (fwd), GGCGCGCGCTATCTCAA (rev.); *Bcl6b* CGCCAGGAAGTGTGTTTTCA (fwd), GCTCCAGCCCCGATGAG (rev.); *Tacstd* (EPCAM) TGCTCCAACTGGCGTCTAA (fwd), TCCCAGACTTGTGTGAGTCA (rev.); *Esg1* GTGGGTGAAAGTTCCCTGAAGACCTGA (fwd), TGTTAGACATTCGAGAT-CCCTGTGG (rev.); *Gdf3* CTTCTCCCAGACACGGGTTTTT (fwd), CTGGAGACAGGAGCCATCTTG (rev.); *Irf6* ATGCAGATGGGTGGCAAGAC

(fwd), CTGCACCCCCGACTTCAC (rev.); and *Ddx4* (MVH) AGGACGAGATTTGATGGCTTGT (fwd), GGCAAGAGAAAAGCTGCAGTCT (rev.).

Cycle conditions were as follows: one cycle at 50 °C for 2 min, followed by 1 cycle at 95 °C for 10 min, followed by 40 cycles at 95 °C for 15 s and 60 °C for 1 min. Specificity of PCR products was tested by dissociation curves. Threshold cycles of primer probes were normalized to the housekeeping gene *Gapdh* or β -actin (*Actb*) and translated to relative values. Relative values of transcripts were derived using the equation, $2^{-\Delta\Delta Ct}$, where ΔCt is equal to the difference in threshold cycles for target and reference. In Fig. 2e, data are depicted as fold change of arbitrary units relative to total testis. Error bars were calculated as the range in fold change of SSC transcript levels (mean \pm standard deviation) relative to the mean of total testis transcript.

Flow cytometry. Flow cytometry was performed on either testis that had been freshly dissociated as described above or on cultured GSPCs or MASCs, following trypsinization. For fresh testicular cells, the washing and low speed (30g) centrifugation steps were employed to remove as many of the spermatozoa (which remained in the supernatant) as possible, but also probably depleted the preparation of small fragments of predominantly interstitial cells, whereas the larger fragments (in the pellet) were enzymatically dissociated for subsequent analysis. Dissociated cells were labelled with fluorescein di-D-galactopyranoside (FDG; Invitrogen), as per the manufacturer's protocol. Finally, cells were filtered through a 40 μ m mesh before analysis. For cell cycle analysis, cells were harvested, fixed in ethanol, incubated with 0.5 μ g ml⁻¹ RNase A (Sigma-Aldrich) and 50 μ g ml⁻¹ propidium iodide (Sigma-Aldrich) for 3 h at 4 °C. Cytometry for c-KIT was performed using phycoerythrin-conjugated rat monoclonal antibody 2B8 anti-c-KIT (BD Pharmingen). Cytometry was performed on a Beckman-Coulter FC500 Cytometer. Data were processed using FlowJo 7.1.2 (Tree Star). **Mouse VE-cadherin promoter.** The mouse VE-Cadherin promoter sequence (provided by L. Benjamin)²⁵ was subcloned into a lentiviral vector upstream of GFP (*mVE-CadPr-GFP*). Viral particles were produced as previously described³⁰ and used to generate MASCs with stable integration of the *mVE-CadPr-GFP* reporter construct. Mouse *VE-CadPr-GFP* MASCs were injected into NOD-SCID mice to form teratomas after 3–4 weeks, and contribution of GFP⁺ (VE-Cadherin⁺) cells to the vasculature was assessed by confocal microscopy, as described above.

Mouse embryo chimaeras. Either unlabelled *Gpr125*^{lacZ/lacZ} or *Gt(Rosa)Sor-lacZ* MASCs or *Gpr125*^{lacZ/lacZ} MASCs that had been previously stably transfected with either GFP or mCherry under control of the *Pgk* promoter by lentivirus^{30,31}, and then cloned, were employed for chimaerism experiments, using previously described protocols¹⁴. In brief, cells were injected into embryonic stage (E)3.5 C57Bl6 blastocysts and implanted into surrogate pseudopregnant female mice. Surrogate mothers were euthanized and embryos harvested at E10.5 to E18.5 for analysis by confocal microscopy (for GFP or mCherry labelled clones) or whole-mount X-gal staining.

Spermatogonial stem cell transplantation and analysis of recipient testes.

Adult C57BL/6 male mice were administered with a single intraperitoneal injection of busulphan (40 mg kg⁻¹ body weight) at 5–6 wks of age and used as recipients 4–8 wks later. *Gpr125*^{lacZ/lacZ} GSPC cultures stably transfected with GFP driven by the *Pgk* promoter (delivered by lentivirus) were transplanted. Cultured cells were dissociated using 0.05% trypsin/EDTA and resuspended in GSPC culture medium containing DNase I (30 μ g ml⁻¹) at a concentration of 8×10^6 cells ml⁻¹. Viability, evaluated by trypan-blue exclusion, was higher than 90%. Approximately 8 μ l (corresponding to $3\text{--}5 \times 10^4$ cells) of donor cell suspension were transplanted in each testis by efferent ducts³². Addition of trypan blue to cell suspensions revealed 70–95% filling of seminiferous tubules. Two to three months after transplantation, recipient testes were collected, detunicated and analysed fresh for GFP expression using fluorescent stereo or confocal microscopy. Each testis was then divided into fragments and processed for additional fluorescent imaging or for X-gal staining. Samples for whole-mount X-gal staining were fixed in 4% paraformaldehyde/PBS for 2 h at 4 °C. After washes in PBS, they were incubated overnight at 4 °C in LacZ buffer (0.2 M sodium phosphate, pH 7.3, 2 mM MgCl₂, 0.02% (v/v) NP-40, 0.01% (v/v) sodium deoxycholate, 20 mM potassium ferricyanide and 20 mM potassium ferrocyanide). The next day, staining was performed by incubating testes in LacZ-staining solution (LacZ buffer containing 1 mg ml⁻¹ of X-gal) for 4 h at 37 °C. After X-gal staining, samples were analysed for LacZ expression by light microscopy. Preservation of GFP fluorescence even after X-gal staining allowed concomitant visualization of GFP and X-gal in the same cells. This tissue was then processed for paraffin embedding, sectioned and stained with Nuclear Fast Red. For optimal GFP preservation, other tubule fragments were fixed overnight in 4% paraformaldehyde/PBS at 4 °C, washed and then imaged as whole tubules on the confocal microscope, or cryopreserved in OCT and sectioned.

Statistical analysis. Image analysis of X-gal-stained fields of *Gpr125*^{+/lacZ} testis was performed as follows. Colour images were captured using an Olympus microscope and converted to greyscale in Adobe Photoshop 7.0. ImageJ 1.36b (NIH) was used to perform thresholding (uniformly for all fields analysed) and measurement of the stained area within transverse cross-sections of tubules categorized as stage IV–V or stage VII–VIII. The Wilcoxon test for non-parametric data was performed using SPSS 9.0.

- Naldini, L. *et al.* In vivo gene delivery and stable transduction of nondividing cells by a lentiviral vector. *Science* **272**, 263–267 (1996).
- Shaner, N. C. *et al.* Improved monomeric red, orange and yellow fluorescent proteins derived from *Discosoma* sp. red fluorescent protein. *Nature Biotechnol.* **22**, 1567–1572 (2004).
- Ogawa, T., Arechaga, J. M., Avarbock, M. R. & Brinster, R. L. Transplantation of testis germinal cells into mouse seminiferous tubules. *Int. J. Dev. Biol.* **41**, 111–122 (1997).

Differential Notch signalling distinguishes neural stem cells from intermediate progenitors

Ken-ichi Mizutani^{1,2*}, Keejung Yoon^{1,2*,†}, Louis Dang^{1,3}, Akinori Tokunaga^{1,2} & Nicholas Gaiano^{1,2,3,4}

During brain development, neurons and glia are generated from a germinal zone containing both neural stem cells (NSCs) and more limited intermediate neural progenitors (INPs)^{1–3}. The signalling events that distinguish between these two proliferative neural cell types remain poorly understood. The Notch signalling pathway is known to maintain NSC character and to inhibit neurogenesis, although little is known about the role of Notch signalling in INPs. Here we show that both NSCs and INPs respond to Notch receptor activation, but that NSCs signal through the canonical Notch effector C-promoter binding factor 1 (CBF1), whereas INPs have attenuated CBF1 signalling. Furthermore, whereas knock-down of CBF1 promotes the conversion of NSCs to INPs, activation of CBF1 is insufficient to convert INPs back to NSCs. Using both transgenic and transient *in vivo* reporter assays we show that NSCs and INPs coexist in the telencephalic ventricular zone and that they can be prospectively separated on the basis of CBF1 activity. Furthermore, using *in vivo* transplantation we show that whereas NSCs generate neurons, astrocytes and oligodendrocytes at similar frequencies, INPs are predominantly neurogenic. Together with previous work on haematopoietic stem cells⁴, this study suggests that the use or blockade of the CBF1 cascade downstream of Notch is a general feature distinguishing stem cells from more limited progenitors in a variety of tissues.

The Notch signalling pathway is of fundamental importance to a wide variety of processes during embryonic development and in the adult^{5,6}. Of particular interest, is the fact that Notch signalling regulates stem cells in many different settings, including the nervous system, haematopoietic system, skin and gut⁷. The Notch receptors are transmembrane proteins activated by Delta and Jagged ligands⁶. On activation, the intracellular domain of Notch (NICD) is cleaved by γ -secretase and translocates into the nucleus to interact with the transcriptional regulator CBF1. In the developing nervous system, the NICD–CBF1 complex activates target genes such as *Hes1* and *Hes5* (ref. 8), which antagonize proneural genes and neuronal differentiation. Little is known about the specificity of Notch function in different proliferative neural cell types, although genetic evidence suggests that Notch signalling is not used uniformly in all telencephalic progenitors^{9,10}.

To characterize endogenous Notch signalling during brain development we generated a transgenic mouse line (TNR, for transgenic Notch reporter) expressing enhanced green fluorescent protein (EGFP) in cells with pathway activation. The transgene includes a CBF1-responsive element (CBFRE, four CBF1-binding sites and the basal simian virus 40 (SV40) promoter¹¹) upstream of EGFP (Fig. 1a). Proof-of-principle experiments (Supplementary Fig. 2), including short hairpin RNA (shRNA)-mediated knockdown of CBF1, and previous reports^{4,12,13}, indicate that the TNR transgene faithfully reports CBF1 activity. In the telencephalic ventricular zone (VZ),

EGFP is expressed together with the neural progenitor markers Nestin and CD133 (ref. 14) (Fig. 1b, c, and Supplementary Fig. 2i–k). On embryonic day (E) 10.5 most telencephalic VZ cells express EGFP (Supplementary Fig. 2h), whereas at E14.5 cell clusters express either high (EGFP^{hi}) or low (EGFP^{lo/neg}) levels of EGFP (Fig. 1c–f). Immunostaining revealed that both EGFP^{hi} and EGFP^{lo/neg} cells contain cleaved (activated) Notch1 (cIN1)¹⁵ (Fig. 1f), raising the possibility that not all cells activate CBF1 in response to Notch activation.

To characterize CBF1 activity in VZ cells, we performed DNA electroporation *in utero*. First, at E12.5 we electroporated a plasmid containing CBFRE–EGFP and also DsRed2 driven by the CAG promoter¹⁶ to permit the detection of all electroporated cells (CBFRE–EGFP–CAG–DsRed2; Fig. 1g). Consistent with the mosaic EGFP expression in the TNR VZ, only a subset of DsRed2⁺ VZ cells was EGFP^{hi} at E15.5 (Supplementary Fig. 3). Next, CBFRE–EGFP–CAG–DsRed2 was electroporated together with plasmids expressing NICD1 (constitutively active), or an activated CBF1 (CBF1 fused to the VP16 transactivation domain; CBF1–VP16 (ref. 17)) (Fig. 1g). At E15.5 most cells expressing NICD1 or CBF1–VP16 were in the VZ and subventricular zone (SVZ), which is consistent with the ability of Notch signalling to inhibit neurogenesis (Fig. 1h and Supplementary Fig. 4). However, whereas most VZ cells expressing CBF1–VP16 were EGFP⁺ (Fig. 1j), many cells expressing NICD1 were not (Fig. 1i). These data suggest that VZ cells are heterogeneous in their response to Notch activation, and that in a subset of cells NICD1 inhibits neurogenesis in a CBF1-independent manner.

Recent work has found that the neocortical VZ is heterogeneous², with radial glial NSCs driving gene expression from the glutamate–aspartate transporter promoter (GLASTp), and neurogenic INPs driving expression from the tubulin α 1 promoter (T α 1p)^{2,18}. To characterize CBF1 activity in those cell types, we electroporated CBFRE–EGFP, or a plasmid driving enhanced yellow fluorescent protein (EYFP) from the *Hes5* promoter¹⁹, together with GLASTp–DsRed2 or T α 1p–DsRed2 (Fig. 2a). Cells with CBF1 activity (EGFP⁺ or EYFP⁺) were largely GLASTp–DsRed2⁺ and T α 1p–DsRed2[–] (Fig. 2b, c, and Supplementary Fig. 5a). Similarly, in TNR embryos EGFP^{hi} VZ cells were largely GLASTp–DsRed2⁺ and T α 1p–DsRed2[–] (Supplementary Fig. 5b, c). CBF1 activity is therefore present in NSCs but not in INPs.

On the basis of the difference in CBF1 activity between NSCs and INPs, we tested whether a loss of CBF1 signalling could convert NSCs into INPs. After shRNA-mediated knockdown of CBF1 *in vivo* at E13.5, many electroporated cells migrated from the VZ to the SVZ and cortical plate, indicating that CBF1 knockdown promoted neurogenesis (Fig. 2h, i, and Supplementary Fig. 6a). Those cells remaining in the VZ after knockdown were largely T α 1p–DsRed2⁺ and incorporated bromodeoxyuridine (BrdU) (Fig. 2d–g), suggesting

¹Institute for Cell Engineering, ²Department of Neurology, ³Department of Neuroscience, and ⁴Department of Oncology, Johns Hopkins University School of Medicine, Baltimore, Maryland 21205, USA. [†]Present address: Division of Brain Diseases, Center for Biomedical Sciences, National Institute of Health, Tongil-Lo 194, Eunpyung-Gu, Seoul, 122-701, Korea. *These authors contributed equally to this work.

that blockade of CBF1 signalling promotes neurogenesis by converting NSCs into INPs.

Our findings that cIN1 is present in EGFP^{lo/neg} cells in the VZ (Fig. 1f), and that NICD1 inhibits the differentiation of INPs without activating CBF1 (Fig. 1h,i), suggested that INPs use CBF1-independent Notch signalling. Consistent with this idea was our observation that expression of NICD1 in cells with shRNA-mediated knockdown of CBF1 inhibited the exit of T α 1p–DsRed2⁺ cells (INPs) from the VZ or SVZ (Fig. 2h, i, and Supplementary Fig. 6). NICD1 did not inhibit cell migration from the VZ to the SVZ, which is consistent with the notion that INPs in the VZ give rise to those in the SVZ³. These data indicate that Notch signalling inhibits both NSC and INP differentiation. However, whereas CBF1-dependent Notch signalling promotes NSC character in the VZ, CBF1-independent Notch signalling promotes INP character in the VZ and SVZ. Experiments with a γ -secretase inhibitor to block ligand-dependent Notch processing have also provided evidence that Notch has a function in EGFP^{lo/neg} cells regardless of their CBF1 signalling status (Supplementary Fig. 7).

Although our *in vivo* data suggested that EGFP^{hi} cells are NSCs and that EGFP^{lo/neg} cells are neurogenic INPs, we tested this presumption directly. First, using fluorescence-activated cell sorting (FACS) we found that the neural progenitor markers CD133 (ref. 14) (Fig. 3a) and Nestin (Supplementary Fig. 8b) were expressed in both EGFP^{hi} and EGFP^{lo/neg} telencephalic cells from E14.5 TNR embryos. This finding was consistent with our observation that both EGFP^{hi} and EGFP^{lo/neg} cells are present in the telencephalic proliferative zone *in vivo*. Because CD133 is a cell surface marker, we were able to isolate CD133⁺/EGFP^{hi} cells (presumptive NSCs) and CD133⁺/EGFP^{lo/neg} cells (presumptive INPs) by FACS (Fig. 3a,b). Quantitative reverse-transcriptase-mediated polymerase chain reaction (RT-PCR) revealed that the former expressed higher levels of Notch receptors

and targets than the latter (Fig. 3c), although no differences were detected in the expression of *Rbpsiuh* (which encodes CBF1) or of the pathway inhibitors *Numb* and *Numblake*⁶ (not shown). We next used the neurosphere assay to examine the stem cell character of CD133⁺/EGFP^{hi} and CD133⁺/EGFP^{lo/neg} cells. In the presence of fibroblast growth factor 2 (FGF2), EGFP^{hi} cells generated more numerous and larger primary and secondary neurospheres than EGFP^{lo/neg} cells (Fig. 3d–f), suggesting that the former are indeed NSCs and the latter are INPs. Consistent with this notion was our observation that CD133⁺/EGFP^{lo/neg} cells generated neurospheres similar to those derived from CD133⁺/T α 1p–EGFP⁺ cells (compare Supplementary Fig. 9 and Fig. 3f). We used quantitative RT-PCR to compare gene expression in neurospheres generated from EGFP^{hi} and EGFP^{lo/neg} cells. Notably, the former continued to express higher levels of *EGFP*, *Hes1* and *Hes5*, whereas the latter expressed higher levels of *Mash1*, a gene antagonized by the *Hes* genes (Fig. 3d, e, g)⁸. The heritability of attenuated CBF1 signalling in EGFP^{lo/neg} cells (presumptive INPs) would explain why those cells are often found clustered in the VZ *in vivo* (Fig. 1c–f).

We next used adherent cultures to examine the developmental potential of presumptive NSCs and INPs separated by CBF1 activity. CD133⁺/EGFP^{hi} and CD133⁺/EGFP^{lo/neg} progenitors isolated from E13.5 neocortex or ganglionic eminences were cultured for two or five days in FGF2-containing medium. BrdU was added either after one day *in vitro* (DIV1) or four days *in vitro* (DIV4), and the cells were fixed one day later. Whereas on DIV2 about 60% of both populations were BrdU⁺, by DIV5 the EGFP^{hi} and EGFP^{lo/neg} cultures had decreased to 47% and 25% BrdU⁺, respectively (Fig. 4a). Concurrently, whereas TuJ1⁺ cells (neurons) in EGFP^{hi} cultures remained at about 25% from DIV2 to DIV5, TuJ1⁺ cells in EGFP^{lo/neg} cultures increased from 33% to 51% (Fig. 4a). After withdrawal of FGF2, EGFP^{lo/neg} cells generated mostly neurons (TuJ1⁺,

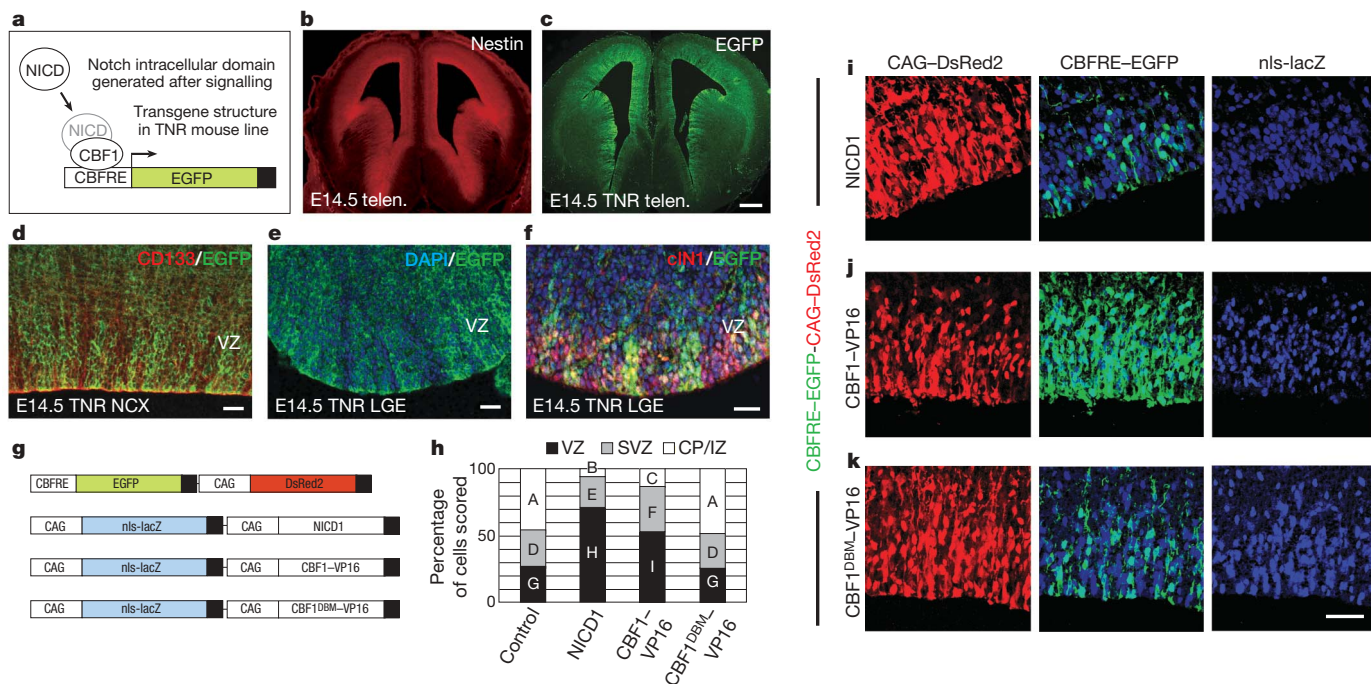


Figure 1 | CBF1 signalling heterogeneity in the telencephalic VZ. **a**, Strategy to detect CBF1 activation in the TNR line. **b**, **c**, Nestin (**b**) is expressed in the telencephalic (telen.) VZ, as is EGFP (**c**), in TNR embryos. **d**, **e**, EGFP^{hi} cells in the E14.5 neocortex (NCX, **d**) and lateral ganglionic eminence (LGE, **e**) are interspersed with EGFP^{lo/neg} cells. DAPI, 4,6-diamidino-2-phenylindole. **f**, Double labelling reveals that cleaved (activated) Notch1 (red) is present in cells expressing high and low levels of EGFP. **g**, CBFRE–EGFP–CAG–DsRed2 and plasmids expressing NICD1, wild-type or DNA-binding mutant (DBM) forms of CBF1–VP16, together with nucleus-localized β -galactosidase

(nls-lacZ). CP/IZ, cortical plate/intermediate zone. **h**, Quantification of cell position in the E15.5 neocortex after *in utero* electroporation at E12.5. **i**, NICD1 retains cells in the proliferative zone (VZ/SVZ) (Supplementary Fig. 4) but does not upregulate EGFP in all cells. **j**, CBF1–VP16 also retains cells in the proliferative zone but drives widespread EGFP expression. **k**, CBF1^{DBM}–VP16 does not retain cells in the proliferative zone or upregulate EGFP. Scale bars, 200 μ m (**b**, **c**), 25 μ m (**d**–**f**) and 50 μ m (**i**–**k**). In **h**, $P < 0.01$ for A–B, A–C, B–C, G–H, G–I and H–I comparisons, and $P < 0.03$ for E–F comparison; $n = 3$ for each.

whereas EGFP^{hi} cells generated mostly astrocytes (positive for glial fibrillary acidic protein (GFAP⁺); Fig. 4b, c, and Supplementary Fig. 10). These data support the idea that EGFP^{lo/neg} cells are indeed neurogenic INPs.

To compare the developmental potential of EGFP^{hi} and EGFP^{lo/neg} cells in a physiological setting we used *in vivo* cell transplantation. Donor cells were derived from TNR embryos containing a second transgene ubiquitously expressing human placental alkaline phosphatase (PLAP)²⁰ to permit morphological characterization after transplantation. CD133⁺/EGFP^{hi} and CD133⁺/EGFP^{lo/neg} cells were isolated by FACS from the ganglionic eminences of E14.5 double-transgenic embryos and were transplanted into the forebrains of E14.5 embryos *in utero* (Fig. 4d). Postnatal analysis revealed that whereas EGFP^{hi} cells differentiated into neurons, astrocytes and oligodendrocytes with similar efficiencies, EGFP^{lo/neg} cells differentiated predominantly into neurons and oligodendrocytes (Fig. 4e, f). This finding is consistent with previous work showing that Notch signalling promotes astrogliogenesis^{21–23} and with our finding that EGFP^{lo/neg} cells generate fewer astrocytes *in vitro* (Fig. 4b, c). Our data also support the existence of progenitors with primarily neuronal and oligodendroglial potential^{24,25} and suggest that INPs are these cells. Notably, many neurons generated from both EGFP^{hi} and EGFP^{lo/neg} cells incorporated BrdU after transplantation (40% and 29%, respectively) and were therefore derived from donor cell divisions in the host. All told, our *in vivo* and *in vitro* differentiation data show that telencephalic NSCs and INPs can be prospectively distinguished on the basis of CBF1 signalling.

Finally, whereas CBF1 knockdown *in vivo* promoted the conversion of NSCs into INPs (see Fig. 2f), the question remained: would forced activation of CBF1 in INPs promote their conversion back into NSCs? To test this possibility, we took advantage of the fact that NSCs generate predominantly astrocytes *in vitro*, and INPs generate predominantly neurons. CD133⁺/EGFP^{hi} and CD133⁺/EGFP^{lo/neg} cells were isolated by FACS, plated into FGF2-containing medium and transduced (with the use of lipofection) on DIV1 with plasmids expressing NICD1, CBF1–VP16 or nucleus-localized β -galactosidase. On DIV5, FGF2 was withdrawn and the cells were allowed to differentiate for one week, at which point lacZ⁺ cells were scored as either TuJ1⁺ or GFAP⁺. The introduction of NICD1 into EGFP^{lo/neg} cells had no significant effect on the percentage of differentiated cells expressing TuJ1 or GFAP (Fig. 2j and Supplementary Fig. 11). Although the expression of CBF1–VP16 did cause a modest shift towards astrocyte fate, as a population EGFP^{lo/neg} cells expressing CBF1–VP16 still differentiated mostly into neurons (Fig. 2j and Supplementary Fig. 11). Thus, once CBF1 signalling has been attenuated in INPs (EGFP^{lo/neg} cells), they become largely refractory to subsequent CBF1 activation.

Here we show that telencephalic progenitors are heterogeneous with respect to Notch signal transduction. Supplementary Fig. 1 summarizes the main result of this paper. In NSCs, Notch inhibits exit from the proliferative zone and activates CBF1 targets, whereas in INPs, Notch also inhibits exit from the proliferative zone but does not activate CBF1 targets. Knockdown of CBF1 promotes the conversion of NSCs into INPs, suggesting that the heritable blockade to

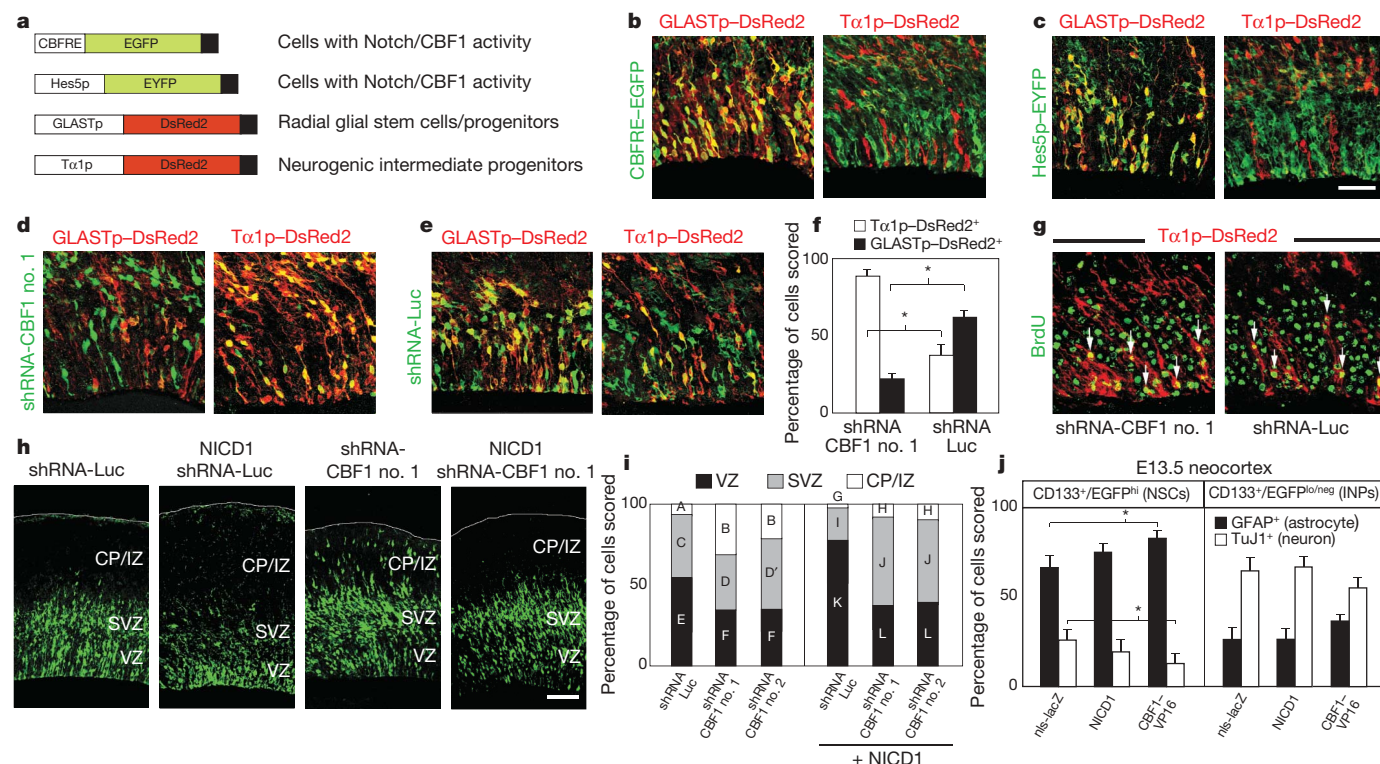


Figure 2 | Analysis of CBF1 function in NSCs and INPs. **a**, Plasmids used to identify cells with CBF1 activity, or with radial glial NSC or INP character. Hes5p, Hes5 promoter. **b**, **c**, After E12.5 co-electroporations, VZ cells with CBF1 activity (green) at E15.5, reported as expression from CBFRE–EGFP (**b**) or from Hes5p–EYFP (**c**), are predominantly GLASTp–DsRed2⁺ and Tα1p–DsRed2⁺. **d–f**, VZ cells with shRNA-mediated knockdown of CBF1 from E13.5 to E15.5 are predominantly Tα1p–DsRed2⁺ (**d**), indicating INP character, whereas controls are either Tα1p–DsRed2⁺ or GLASTp–DsRed2⁺ (**e**). **f**, Quantification of these data; the asterisk indicates $P < 0.01$; $n = 3$. **g**, Many Tα1p–DsRed2⁺ cells in the VZ were proliferating (BrdU⁺, arrows) after CBF1 knockdown. CP/IZ, cortical plate/intermediate

zone. **h**, shRNA knockdown of CBF1 promotes migration to the CP (third panel), which can be inhibited by NICD1 (fourth panel; see also Supplementary Fig. 6). shRNA-Luc to knockdown luciferase was used as a negative control (first and second panels). **i**, Quantification of the data in **h** and also Supplementary Fig. 6. **j**, Activation of CBF1 targets by using CBF1–VP16 was ineffective at shifting INPs towards an astroglial fate more consistent with NSC character (see also Supplementary Fig. 11). Asterisk, $P < 0.05$; $n = 3$. Scale bars, 50 μ m (**c**; also applies to **b–e**, **g**) and 100 μ m (**h**). In **i**, $P < 0.03$ for A–B, E–F, G–H, I–J, K–L, A–G, C–I, E–K, B–H and D–J comparisons; $n = 4$ for each. See Supplementary Fig. 13 for the individual channels. All error bars indicate s.d.

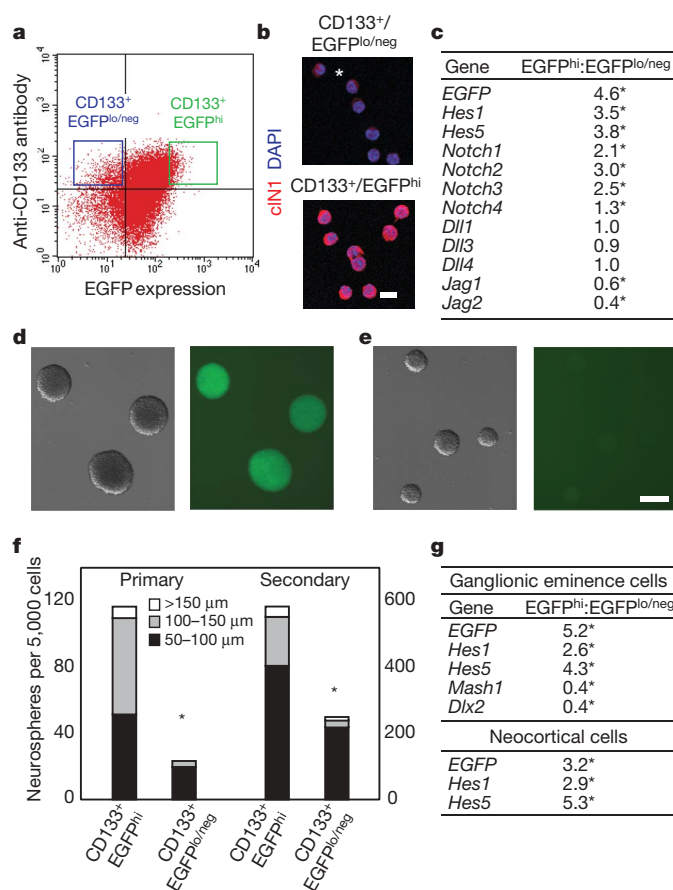


Figure 3 | *In vitro* analysis of EGFP^{hi} and EGFP^{lo/neg} cells. **a**, FACS plot of E14.5 TNR ganglionic eminence cells. **b**, Acutely isolated EGFP^{hi} cells (green box in **a**) expressed higher levels of cleaved Notch1 (cIN1) than EGFP^{lo/neg} cells (blue box in **a**), of which some expressed low levels (asterisk). Sorting gates were designed to limit overlap between distinct progenitor pools (see Supplementary Fig. 8). **c**, Primary EGFP^{hi} neocortical cells expressed higher mRNA levels of Notch receptors and targets (*Hes1*, *Hes5*) than EGFP^{lo/neg} cells at E14.5, as determined by quantitative RT-PCR. Asterisk, $P < 0.03$. **d–f**, EGFP^{hi} cells generated more numerous and larger neurospheres (**d**) than EGFP^{lo/neg} cells (**e**). **f**, Quantification of neurosphere frequency and size. Asterisk, $P < 0.002$; $n = 3$. Similar results were obtained with primary E14.5 neocortical neurospheres (Supplementary Fig. 12). **g**, Neurospheres derived from EGFP^{hi} cells expressed higher levels of *EGFP*, *Hes1* and *Hes5* mRNA than EGFP^{lo/neg} cells, but lower levels of *Mash1* and *Dlx2* (ref. 9) after one week *in vitro*, as determined by quantitative RT-PCR. Asterisk, $P < 0.01$; $n = 4$. Scale bars, 10 μ m (**b**) and 100 μ m (**d**, **e**).

CBF1 activation we have observed in INPs has a causal role in this transition. However, forced activation of CBF1 in INPs is ineffective at reverting them to NSC character, suggesting that INPs have limited plasticity. The importance of these findings beyond the nervous system has been supported by a recent haematopoietic stem cell (HSC) study using the TNR line: within a cell fraction highly enriched for HSCs, EGFP^{hi} cells were mostly HSCs, whereas EGFP^{lo/neg} cells were mostly unipotent progenitors⁴. The parallels between that work and the present study indicate that the differential use of Notch signalling, in particular with respect to CBF1 activation, may be a mechanism used to distinguish between stem and progenitor cell subtypes in many tissues.

METHODS SUMMARY

Animals. All mice were maintained in accordance with the Institutional Animal Care and Use Committee (IACUC) at Johns Hopkins University School of Medicine. The plug date was designated as E0.5. The TNR mouse line was generated by the Johns Hopkins Transgenic Core facility by pronuclear DNA injection, and is maintained and distributed by The Jackson Laboratory (<http://jaxmice.jax.org/strain/005854.html>).

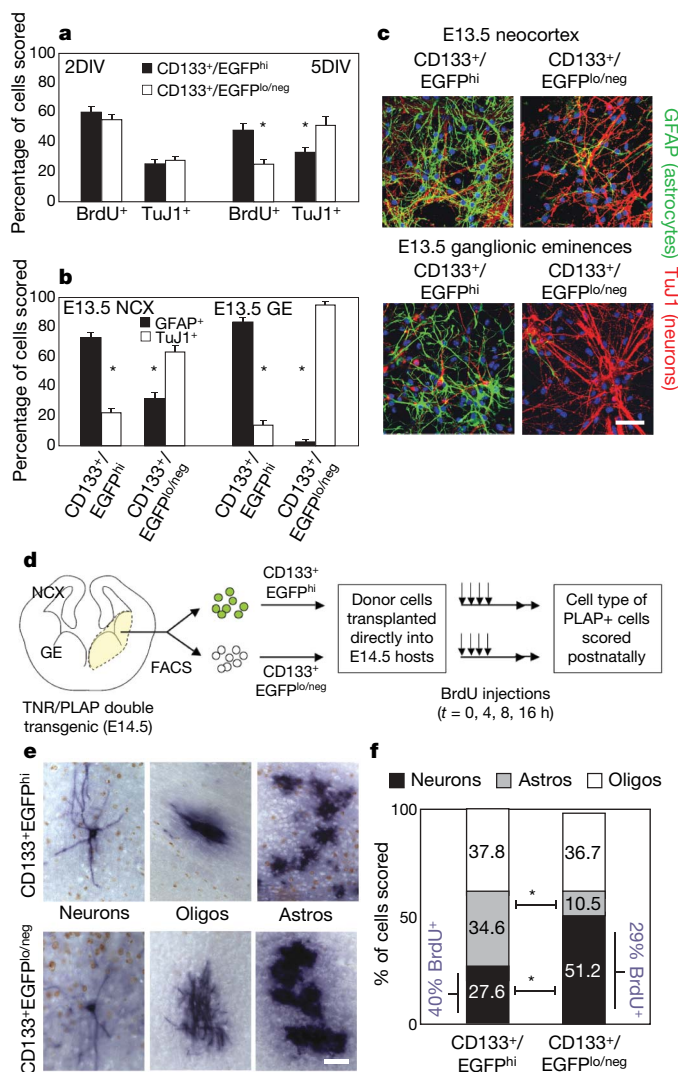


Figure 4 | Differentiation analysis of EGFP^{hi} and EGFP^{lo/neg} cells.

a, EGFP^{lo/neg} cells spontaneously differentiate into neurons in mitogenic culture containing FGF2. Asterisk, $P < 0.003$; $n = 3$. **b**, **c**, Differentiation of EGFP^{hi} and EGFP^{lo/neg} cells *in vitro* revealed that the former generate more astrocytes (GFAP⁺), and the latter more neurons (TuJ1⁺). **b**, Quantification of GFAP and TuJ1 expression status of EGFP^{hi} and EGFP^{lo/neg} cells. **c**, Representative images showing GFAP and TuJ1 stainings after *in vitro* differentiation. Similar results were obtained at E12.5 (Supplementary Fig. 10). Asterisk, $P < 0.001$; $n = 3$. **d**, The cell transplantation scheme used. **e**, The location and morphology of donor cells in the host tissue was determined by using PLAP histochemistry. **f**, After cell transplantation, EGFP^{lo/neg} cells generate more neurons and fewer astrocytes (astros) *in vivo* than EGFP^{hi} cells. Oligos, oligodendrocytes. Asterisk, $P < 0.01$; $n = 15$. Scale bars, 50 μ m. All error bars indicate s.d.

For cell transplantation, donor cells were isolated from E14.5 ganglionic eminences, and trypsin-EDTA was used during dissociation. Each E14.5 host received $(1-3) \times 10^4$ cells in about 1 μ l. Hosts were analysed at postnatal date (P) 21 or P30, and tissue sections were stained histochemically to detect PLAP⁺ donor cells. Cellular phenotype was evaluated by morphology, and a total of about 2,000 forebrain cells were scored.

Cell culture. Neurosphere and adherent progenitor cultures were established from the neocortex or ganglionic eminences (lateral and medial) of E12.5–E14.5 embryos. Dissected tissue was dissociated by trituration in the absence of

trypsin-EDTA. For adherent cultures, CD133⁺/EGFP^{hi} or CD133⁺/GFP^{lo/neg} cells were isolated by FACS and plated in eight-well chamber slides (Nunc). Cells were cultured in basal serum-free medium²⁸ including 10 ng ml⁻¹ FGF2. **CBF1 shRNA knockdown.** The target sequences used to knockdown CBF1 by shRNA interference were 5'-AAGAACTACTGCACAGCCAAA-3' (CBF1 no. 1), and 5'-AAGCAGACGGCATTACTGGAT-3' (CBF1 no. 2), and were first validated in NIH 3T3 cells. The target sequence of luciferase used for the control shRNA-Luc was 5'-CTTACGCTGAGTACTTCGATT-3'; it has previously been shown to knock down luciferase²⁹.

Full Methods and any associated references are available in the online version of the paper at www.nature.com/nature.

Received 28 May; accepted 12 July 2007.

Published online 26 August 2007.

1. Temple, S. The development of neural stem cells. *Nature* **414**, 112–117 (2001).
2. Gal, J. S. *et al.* Molecular and morphological heterogeneity of neural precursors in the mouse neocortical proliferative zones. *J. Neurosci.* **26**, 1045–1056 (2006).
3. Merkle, F. T. & Alvarez-Buylla, A. Neural stem cells in mammalian development. *Curr. Opin. Cell Biol.* **18**, 704–709 (2006).
4. Duncan, A. W. *et al.* Integration of Notch and Wnt signaling in hematopoietic stem cell maintenance. *Nature Immunol.* **6**, 314–322 (2005).
5. Bolos, V., Grego-Bessa, J. & de la Pompa, J. L. Notch signaling in development and cancer. *Endocr. Rev.* **28**, 339–363 (2007).
6. Yoon, K. & Gaiano, N. Notch signaling in the mammalian central nervous system: insights from mouse mutants. *Nature Neurosci.* **8**, 709–715 (2005).
7. Chiba, S. Notch signaling in stem cell regulation. *Stem Cells* **24**, 2437–2447 (2006).
8. Iso, T., Kedes, L. & Hamamori, Y. HES and HERP families: multiple effectors of the Notch signaling pathway. *J. Cell. Physiol.* **194**, 237–255 (2003).
9. Yun, K. *et al.* Modulation of the notch signaling by Mash1 and Dlx1/2 regulates sequential specification and differentiation of progenitor cell types in the subcortical telencephalon. *Development* **129**, 5029–5040 (2002).
10. Mason, H. A. *et al.* Notch signaling coordinates the patterning of striatal compartments. *Development* **132**, 4247–4258 (2005).
11. Hsieh, J. J. *et al.* Truncated mammalian Notch1 activates CBF1/RBPJk-repressed genes by a mechanism resembling that of Epstein-Barr virus EBNA2. *Mol. Cell. Biol.* **16**, 952–959 (1996).
12. Estrach, S., Ambler, C. A., Lo Celso, C., Hozumi, K. & Watt, F. M. Jagged 1 is a β -catenin target gene required for ectopic hair follicle formation in adult epidermis. *Development* **133**, 4427–4438 (2006).
13. Hellstrom, M. *et al.* Dll4 signalling through Notch1 regulates formation of tip cells during angiogenesis. *Nature* **445**, 776–780 (2007).
14. Lee, A. *et al.* Isolation of neural stem cells from the postnatal cerebellum. *Nature Neurosci.* **8**, 723–729 (2005).
15. Tokunaga, A. *et al.* Mapping spatio-temporal activation of Notch signaling during neurogenesis and gliogenesis in the developing mouse brain. *J. Neurochem.* **90**, 142–154 (2004).
16. Niwa, H., Yamamura, K. & Miyazaki, J. Efficient selection for high-expression transfectants with a novel eukaryotic vector. *Gene* **108**, 193–199 (1991).
17. Waltzer, L., Bourillot, P. Y., Sergeant, A. & Manet, E. RBP-Jk repression activity is mediated by a co-repressor and antagonized by the Epstein-Barr virus transcription factor EBNA2. *Nucleic Acids Res.* **23**, 4939–4945 (1995).
18. Sawamoto, K. *et al.* Direct isolation of committed neuronal progenitor cells from transgenic mice coexpressing spectrally distinct fluorescent proteins regulated by stage-specific neural promoters. *J. Neurosci. Res.* **65**, 220–227 (2001).
19. Ohtsuka, T. *et al.* Visualization of embryonic neural stem cells using Hes promoters in transgenic mice. *Mol. Cell. Neurosci.* **31**, 109–122 (2006).
20. DePrimo, S. E., Stambrook, P. J. & Stringer, J. R. Human placental alkaline phosphatase as a histochemical marker of gene expression in transgenic mice. *Transgenic Res.* **5**, 459–466 (1996).
21. Gaiano, N., Nye, J. S. & Fishell, G. Radial glial identity is promoted by Notch1 signaling in the murine forebrain. *Neuron* **26**, 395–404 (2000).
22. Tanigaki, K. *et al.* Notch1 and Notch3 instructively restrict bFGF-responsive multipotent neural progenitor cells to an astroglial fate. *Neuron* **29**, 45–55 (2001).
23. Gaiano, N. & Fishell, G. The role of notch in promoting glial and neural stem cell fates. *Annu. Rev. Neurosci.* **25**, 471–490 (2002).
24. He, W., Ingraham, C., Rising, L., Goderie, S. & Temple, S. Multipotent stem cells from the mouse basal forebrain contribute GABAergic neurons and oligodendrocytes to the cerebral cortex during embryogenesis. *J. Neurosci.* **21**, 8854–8862 (2001).
25. Battiste, J. *et al.* Ascl1 defines sequentially generated lineage-restricted neuronal and oligodendrocyte precursor cells in the spinal cord. *Development* **134**, 285–293 (2007).
26. Mizutani, K. & Saito, T. Progenitors resume generating neurons after temporary inhibition of neurogenesis by Notch activation in the mammalian cerebral cortex. *Development* **132**, 1295–1304 (2005).
27. Saito, T. & Nakatsuji, N. Efficient gene transfer into the embryonic mouse brain using *in vivo* electroporation. *Dev. Biol.* **240**, 237–246 (2001).
28. Nakashima, K. *et al.* Synergistic signaling in fetal brain by STAT3–Smad1 complex bridged by p300. *Science* **284**, 479–482 (1999).
29. Elbashir, S. M. *et al.* Duplexes of 21-nucleotide RNAs mediate RNA interference in cultured mammalian cells. *Nature* **411**, 494–498 (2001).

Supplementary Information is linked to the online version of the paper at www.nature.com/nature.

Acknowledgements We thank D. Hayward, D. Johns, E. Manet, T. Haydar, A. Ayoub and T. Ohtsuka for plasmids; J. Corbin for the PLAP mice; L. Blosser and A. Tam for cell sorting; R.-J. Zhao and J. Kim for technical assistance; and R. Wechsler-Reya, T. Reya, M. Starz-Gaiano, T. Haydar and S. Temple for discussions. K.M. was supported by a fellowship from the Japan Society for the Promotion of Science. This work was supported by grants from the Burroughs Wellcome Fund, the Sidney Kimmel Foundation for Cancer Research, and the National Institute of Neurological Disorders and Stroke (all to N.G.).

Author Contributions K.M. performed *in utero* electroporations, adherent and neurosphere cell culture experiments, quantitative RT-PCR analysis, γ -secretase inhibition and shRNA experiments. K.Y. generated and validated the TNR line, established flow cytometry staining protocols, performed γ -secretase inhibition and MEF experiments, and did the Nestin tissue staining. L.D. characterized the *in vivo* expression pattern of EGFP in the telencephalon of TNR embryos, performed *in vivo* cell transplantations, and did the CD133 tissue staining. A.T. performed cIN1, EGFP and CD133 immunostainings. N.G. conceived of the TNR line, oversaw the project, and prepared the manuscript.

Author Information Reprints and permissions information is available at www.nature.com/reprints. The authors declare competing financial interests: details accompany the full-text HTML version of the paper at www.nature.com/nature. Correspondence and requests for materials should be addressed to N.G. (gaiano@jhmi.edu).

METHODS

Animals. For gene transfer into CD1 or TNR mouse brains, 1–2 μ l of DNA solution in PBS (0.1–4.0 mg ml⁻¹, depending on the construct) was injected into the lateral ventricle of E12.5 or E13.5 embryos with the use of a mouth-controlled pulled capillary micropipette. Five square electric pulses (30 V for E12.5; 33 V for E13.5) were delivered at one pulse per second (50-ms pulse followed by 950-ms gap) to embryos through the uterus with forceps-type electrodes (CUY650P5, 5-mm diameter platinum round plates; Nepagene), while the uterus was kept wet with PBS.

Cell culture. Neurospheres were grown in serum-free medium containing B27 without vitamin A (Gibco) and 10 ng ml⁻¹ FGF2. Trypsin-EDTA was used to dissociate primary neurospheres for the generation of secondary neurospheres. Neurosphere frequency and size were scored after one week.

For adherent cultures, CD133⁺/EGFP^{hi} (the brightest 5% in the CD133⁺ range) or CD133⁺/GFP^{lo/neg} (the dimmest 10% in the CD133⁺ range) cells were isolated by FACS and plated at a concentration of 5×10^4 cells per chamber in eight-well chamber slides (Nunc) precoated with 15 μ g ml⁻¹ poly-(L-ornithine) (Sigma) and 1 μ g ml⁻¹ fibronectin (Sigma). Cells were cultured in basal serum-free medium²⁸ including 10 ng ml⁻¹ FGF2.

Cell staining and flow cytometry. FACS was performed at the Johns Hopkins Flow Cytometry Core facility with a Becton Dickinson FACS-Vantage. For CD133 staining, phycoerythrin-conjugated CD133 antibodies were used (from eBioscience at 1:20 dilution, or from Miltenyi at 1:50 dilution). Cells were incubated with antibody for 30 min on ice, washed three times with cold PBS and then sorted in cold PBS. For anti-Nestin (Developmental Studies Hybridoma Bank) staining of fixed cells a modified version of the Fix and Perm protocol (Caltag) was used.

Tissue and adherent culture staining. The antibodies used were mouse anti- β III-tubulin (TuJ1; Covance), rabbit anti-GFAP (Sigma), rat anti-BrdU (Accurate), goat anti-EGFP (Rockland), rabbit anti-DsRed (Clontech), goat anti- β -galactosidase (Biogenesis), rabbit anti-cleaved Notch1 (Cell Signalling) and mouse anti-CD133 (eBioscience and Miltenyi). Alexa Fluor-conjugated secondary antibodies (Molecular Probes) were used. For double immunostaining with DsRed2 and BrdU, BrdU was administered three times at 5-h intervals before harvesting of embryos. Sections were treated with 1 M HCl for 30 min at 37 °C, and signal amplification was used to detect BrdU. Stainings were revealed with a Zeiss Axioskop with an AxioCam, or a Zeiss LSM 510. Images were processed with Adobe Photoshop.

Quantitative RT-PCR. Total RNA was isolated from samples with the use of RNeasy (Qiagen) and was reverse transcribed into complementary DNA, which was then quantified with an ND1000 spectrophotometer (NanoDrop). Quantitative real-time PCR was performed with an ABI 7900 Sequence Detection System (Applied Biosystems) and the SYBR green labelling system (Applied Biosystems). Primer sequences used are available from the authors on request. GAPDH expression was used to normalize the samples, and each sample was run in triplicate.

CBF1 shRNA knockdown. Short hairpins designed to target sequences of luciferase were subcloned into the pSiren retroviral vector (Clontech), which includes the reporter gene ZsGreen. Versions were also made containing DsRed2 as the reporter. Retroviral infection was used to knock down CBF1 in neurospheres, whereas *in utero* electroporation of the retroviral plasmids was used *in vivo*.

Statistical analysis. Entire litters (10–15 embryos) were pooled for each *in vitro* experiment, and experiments were performed on at least three different days. Thus, whereas in some of the presented histogram data $n = 3$ for each class, each of those n values represents the mean value derived from a population. In cases where $n = 3$, P values were determined with a stringent two-tailed heteroscedastic t -test, which, although not ideal for such n values, uniformly yielded highly significant P values. To corroborate these we used a non-parametric two-tailed Mann–Whitney U -test and obtained the best possible P value with this test for $n = 3$ ($P = 0.1$). In cases where $n \geq 4$, the two-tailed Mann–Whitney U -test was used to generate the P values shown. To compare gene expression levels, log₂ fold changes were used.

LETTERS

ZEITLUPE is a circadian photoreceptor stabilized by GIGANTEA in blue light

Woe-Yeon Kim^{1,2*}, Sumire Fujiwara^{1*}, Sung-Suk Suh¹, Jeongsik Kim³, Yumi Kim³, Linqu Han¹, Karine David⁴, Joanna Putterill⁴, Hong Gil Nam³ & David E. Somers¹

The circadian clock is essential for coordinating the proper phasing of many important cellular processes. Robust cycling of key clock elements is required to maintain strong circadian oscillations of these clock-controlled outputs. Rhythmic expression of the *Arabidopsis thaliana* F-box protein ZEITLUPE (ZTL) is necessary to sustain a normal circadian period by controlling the proteasome-dependent degradation of a central clock protein, TIMING OF CAB EXPRESSION 1 (TOC1)^{1,2}. ZTL messenger RNA is constitutively expressed, but ZTL protein levels oscillate with a threefold change in amplitude through an unknown mechanism³. Here we show that GIGANTEA (GI) is essential to establish and sustain oscillations of ZTL by a direct protein–protein interaction. GI, a large plant-specific protein with a previously undefined molecular role, stabilizes ZTL *in vivo*. Furthermore, the ZTL–GI interaction is strongly and specifically enhanced by blue light, through the amino-terminal flavin-binding LIGHT, OXYGEN OR VOLTAGE (LOV) domain of ZTL. Mutations within this domain greatly diminish ZTL–GI interactions, leading to strongly reduced ZTL levels. Notably, a C82A mutation in the LOV domain, implicated in the flavin-dependent photochemistry, eliminates blue-light-enhanced binding of GI to ZTL. These data establish ZTL as a blue-light photoreceptor, which facilitates its own stability through a blue-light-enhanced GI interaction. Because the regulation of GI transcription is clock-controlled, consequent GI protein cycling confers a post-translational rhythm on ZTL protein. This mechanism of establishing and sustaining robust oscillations of ZTL results in the high-amplitude TOC1 rhythms necessary for proper clock function.

To understand how post-transcriptional stability of ZTL protein is achieved, we examined ZTL levels in mutants known to affect circadian period. Among these, *gigantea* (*gi*) mutations cause allele-specific effects on the period^{4–7}. We tested a wide range of *gi* alleles and all strongly reduce ZTL to near undetectable levels (Fig. 1a). Under light/dark cycles (Fig. 1b), continuous light and constant darkness (data not shown), *gi* mutations eliminate the normal 3–5-fold cyclic expression of ZTL³. Conversely, constitutive high expression of GI (GI-OX) increases ZTL abundance to constitutively high levels (Fig. 1a, b). In all *GI* backgrounds ZTL mRNA levels remain unchanged, indicating a post-transcriptional control of ZTL (Fig. 1a, b).

We also examined the effect of ZTL levels on *GI* expression. In plants expressing *GI-GI-TAP*⁸, GI-TAP (tandem affinity purification) protein levels were markedly diminished in the absence of ZTL (*ztl-103*) relative to wild type, with no effect on *GI-TAP* mRNA expression (Fig. 1c). These results indicate that GI is not a proteolytic substrate of the SCF^{ZTL} E3 ubiquitin ligase, but rather

that ZTL and GI proteins cooperatively stabilize each other. The phenotype of the double mutant supports this conclusion, as the period of *gi-2 ztl-103* is much longer than *gi-2* alone and nearly identical to *ztl-103* (Supplementary Fig. 1; ref. 6).

To determine whether sustained ZTL levels in GI-OX plants were due to increased ZTL stabilization, we performed cell-free *in vitro* degradation assays at times of most labile (ZT1; Zeitgeber Time1) and most stable (ZT13) ZTL³. At ZT1, high GI levels markedly reduce the ZTL degradation rate, indicating that GI acts post-translationally to stabilize ZTL protein (Fig. 1d). We next determined whether a direct interaction between GI and ZTL might be responsible for the stabilization. *In vitro* interaction tests between ³⁵S-labelled GI and glutathione S-transferase (GST)-tagged ZTL and the related family members, FLAVIN-BINDING, KELCH REPEAT, F-BOX (FKF1)⁹ and LOV KELCH REPEAT PROTEIN 2 (LKP2)¹⁰, showed a strong, specific interaction, when compared to GST alone or a negative control¹¹ (Fig. 2a). Quantitative two-hybrid assays with full-length ZTL confirmed this interaction (Fig. 2b). We observed a similar degree of interaction between GI and LKP2, but not between FKF1 and GI in this system (Fig. 2b). We tested different ZTL domains and found extremely strong binding of GI to the LOV domain (Fig. 2c), a flavin-binding region implicated in blue-light signalling in these and other molecules^{12–15}. Together these data indicate that all the necessary determinants for interaction reside in the GI and ZTL proteins.

To map more finely the interaction domains of ZTL, we carried out *in vivo* transient expression in *Nicotiana benthamiana*¹⁶. Expression constructs of ZTL were co-infiltrated with full-length green fluorescent protein (GFP)-tagged GI into *N. benthamiana*. ZTL interacts strongly with GI *in vivo* (Fig. 2d; compare lanes 1 and 9), as do FKF1 and LKP2 (Supplementary Figs 2 and 3). We extended these trials to test discrete domains of ZTL (LOV, Fkelch) and found that only the LOV polypeptide interacts with GI (Fig. 2d; compare lanes 10 and 11). These results support the *in vitro* and yeast findings, demonstrating that the ZTL N-terminal region contains the determinants for GI interactions *in planta*.

We next exploited an assemblage of *ztl* mutants to map further the ZTL interaction domain. All mutations tested diminish, or are predicted to reduce, ZTL activity or cause period-lengthening similar to a true *ztl* null¹⁷. Mutations in the F-box or kelch domains have little effect on the *in vivo* interaction between GI and ZTL (Fig. 2e). Because the double (L220A/L213A) and single (E203K) F-box mutations abrogate ZTL interaction with the *Arabidopsis* Skp1-like protein1 (ASK1)^{17,18} these results indicate that GI interaction with ZTL is independent of the larger SCF ligase complex. Additionally, because the two kelch mutations (D425N and G452D) reduce interaction with TOC1 (refs 2, 17), the GI–ZTL interaction does not require

¹Department of Plant Cellular and Molecular Biology/Plant Biotechnology Center, Ohio State University, 054 Rightmire Hall, 1060 Carmack Road, Columbus, Ohio 43210, USA.

²Environmental Biotechnology National Core Research Center (BK21 program), Gyeongsang National University, Jinju 660-701, South Korea. ³Department of Life Science, Pohang University of Science and Technology, Pohang, Kyungbuk 790-784, South Korea. ⁴School of Biological Sciences, University of Auckland, Private Bag 92019, Auckland, New Zealand.

*These authors contributed equally to this work.

the presence of a ZTL substrate. Attempts to isolate a GI–ZTL–TOC1 complex *in vivo* were unsuccessful, supporting this notion.

In contrast, three point mutations in the LOV domain strongly diminish GI–ZTL binding. The G46E mutation was recovered in a screen for suppressors of the arrhythmic phenotype of the ZTL over-expressor¹⁹ (Supplementary Fig. 4). This single amino acid change results in no detectable ZTL in GI immunoprecipitates (Fig. 2e). When expressed in *Arabidopsis* (Supplementary Fig. 4) or *N. benthamiana*, ZTL(G46E) protein migrates more slowly than wild type and other ZTL mutant proteins, suggesting aberrant folding (Fig. 2e). We introduced a mutation at the Cys82 residue (C82A) because it is predicted to interact with the flavin mononucleotide (FMN) moiety present within the ZTL LOV domain²⁰. The cognate cysteines in the phototropin LOV domains are essential to confer photochemical activity to these molecules^{12,21}. Strikingly, the C82A mutation diminishes the ZTL–GI interaction more than fivefold,

relative to the wild type (Fig. 2e). The G119D mutation (*ztl-21*), first identified in a screen for long period mutants¹⁷, also strongly reduces the ZTL–GI interaction (Fig. 2e). *ztl-21* protein cycling is reduced in amplitude, with peak levels reduced threefold (Fig. 2f). These reduced levels are expected if the GI interaction necessary for ZTL stabilization is diminished. Taken together, these results strongly demonstrate the necessary and sufficient role of the ZTL LOV domain in facilitating interaction with GI.

We next examined the ZTL–GI interaction in *Arabidopsis* using constructs expressing GI–TAP or GI–HA (haemagglutinin) from the native *GI* promoter. We first determined whether both proteins have overlapping spatial expression in the plant. ZTL is exclusively found in the cytosol, whereas GI–TAP or GI–HA is present both in the cytosol and the nucleus (Fig. 3a; Supplementary Fig. 5a, c). Hence, GI–ZTL interactions probably only occur in the cytosol *in planta*.

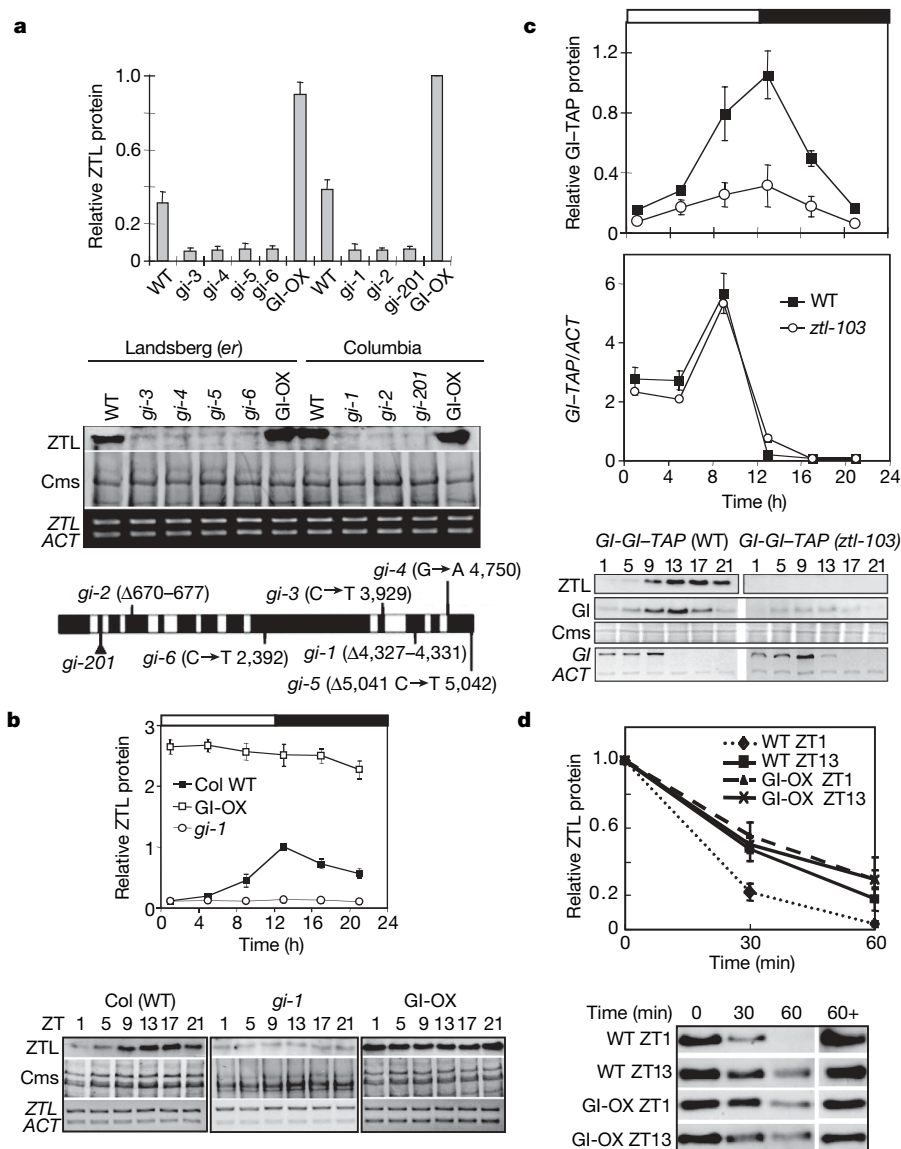


Figure 1 | GIGANTEA positively regulates ZTL protein abundance. **a**, ZTL protein and mRNA levels at ZT13 from the indicated genotypes grown under 12-h-light/12-h-dark (LD). **b**, Time course of ZTL protein and mRNA accumulation in *gi* and GI–OX plants in LD. **c**, Time course of protein and mRNA levels from wild-type and *ztl-103* mutant plants expressing the *GI-GI-TAP* transgene⁸ probed for GI–TAP and ZTL protein (upper gel panels) and mRNA (lower gel panel) abundances; quantification of GI levels is shown in the graphs above. **d**, Cell-free degradation of ZTL is reduced by GI. ZTL protein levels in extracts from wild-type (WT) and GI–OX plants

grown under LD cycles harvested at ZT1 and ZT13, and incubated as indicated. 60+, 60 min incubation with proteasome inhibitors. Periods of light and dark entrainment indicated by white and black bars, respectively, above each figure (**b**, **c**). ZTL and GI–TAP protein levels shown relative to Coomassie (Cms)-stained portion of gel and values normalized to GI–OX Col (**a**), WT Col (**b**) or WT ZTL and WT GI–TAP at ZT13 (**c**). Semi-quantitative RT–PCR shows ZTL (**a**, **b**) or GI–TAP (**c**) message relative to actin (ACT). All blots representative of each set of trials; means of three trials \pm s.e.m.

Co-operative stabilization implies a similar phase of expression, and peak expression of both GI and ZTL occur near early evening (\sim ZT11–13) in light/dark cycles (Fig. 3a). We next tested immunoprecipitates from *GI-GI-TAP* extracts⁸ for the presence of ZTL. During the light and dark periods, ZTL levels closely correlated with the increasing and decreasing steady-state level of GI (Fig. 3a; light/dark), showing that ZTL and GI exist in a complex together in proportion to their total abundances. We next asked whether the fraction of ZTL complexed with GI is light dependent. Although the amount of GI immunoprecipitated at ZT17 and ZT21, relative to ZT13, was similar in light/dark cycles and continuous light (Fig. 3b), the relative ZTL level was disproportionately higher in continuous light at ZT21,

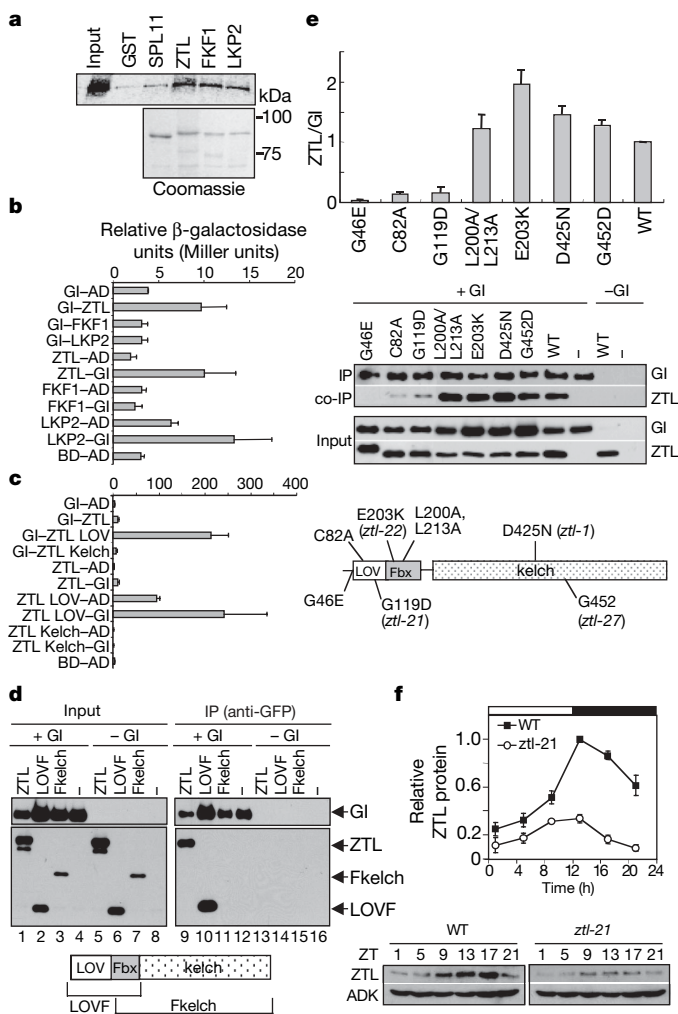


Figure 2 | Interactions of GI with ZTL require the LOV domain. **a**, *In vitro* interaction of ³⁵S-labelled GI with GST-tagged ZTL, LKP2 and FKF1. GST and SPL11-GST¹¹ are controls for binding specificity. Uppermost bands of Coomassie-staining show level of full-length proteins on resin. **b**, **c**, Two-hybrid interactions between GI and full-length ZTL family members (**b**), and GI and ZTL protein domains (**c**). **d**, *In planta* interactions between GI and ZTL. Protein extracts from *N. benthamiana* leaves transiently expressing full-length ZTL or LOVF polypeptides with GI-GFP show *in vivo* interaction (lanes 9, 10). —, no ZTL. **e**, GI-GFP and WT ZTL, or ZTL harbouring specific point mutations, were co-expressed as in **d** and harvested at ZT4–6. Input loadings are equal for GI and ZTL. Immunoprecipitate loadings adjusted to equalize GI levels among different ZTL alleles. Upper and lower portions of the same immunoblot were probed for immunoprecipitated GI (IP) or co-immunoprecipitated ZTL (co-IP), respectively. Quantification is relative to wild type. Diagram shows *ztl* mutations. **f**, *ztl*(G119D)/*ztl-21* shows reduced ZTL protein levels. Growth and extractions from wild-type and *ztl-21* as in Fig. 1c; normalized to WT ZT13 level. Adenosine kinase (ADK) shown as a loading control. **b**, **e**, **f**, Means of three trials \pm s.e.m. All blots representative of multiple trials. Fbx, F-box domain.

suggesting a light-enhanced interaction between ZTL and GI (Fig. 3b, compare ZTL light/dark and continuous light; Fig. 3a). We determined the effective wavelength by replacing the dark period with either red or blue light. Blue light caused a transient increase in the amount of immunoprecipitated GI at ZT17, but by ZT21 GI levels were similar under all conditions (Fig. 3b, c). In contrast, ZTL levels in the immunoprecipitates were consistently significantly higher under blue light (Fig. 3b; Fig. 3c compare co-immunoprecipitated light/blue (LB), light/red (LR) and light/dark (LD) cycles), indicating a blue-light-enhanced GI–ZTL interaction.

If blue-light activation of the LOV domain is responsible for this increased interaction, mutations in the LOV domain should diminish or eliminate blue-light-enhanced GI–ZTL binding. We determined the relative proportion of wild-type or mutant ZTL in GI immunoprecipitates from *N. benthamiana* extracts when expressed together under dark, white, red or blue light. The GI–ZTL interaction was enhanced fourfold in blue light, relative to dark or red light, and similar to results in white light (Fig. 3d). Kelch (D425N) and F-box (L200A, L213A) mutations showed blue-light-enhanced interactions very similar to wild type, indicating GI–ZTL light-enhanced interactions independent of these domains. Similarly, the G119D mutation has little effect on the blue-light-enhanced interaction and differences between dark, red and blue light remain

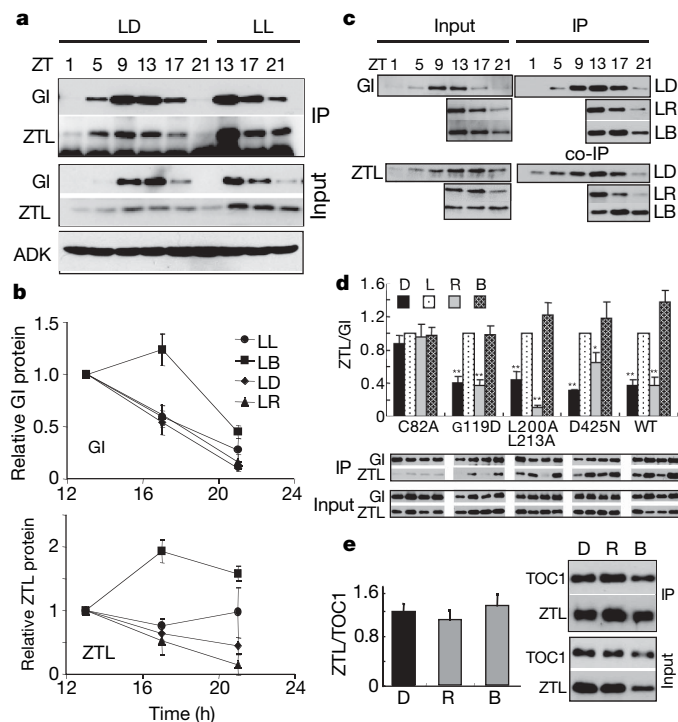


Figure 3 | Blue-light-enhanced binding of GI and ZTL. **a**, Time course of protein accumulation in *GI-GI-TAP* plants in light/dark cycles (LD) or continuous light (LL) (middle panel: input). TAP immune complexes probed for GI–TAP and co-immunoprecipitated ZTL levels (upper panel; IP). Adenosine kinase (ADK) used as cytosolic loading control (lower panel). **b**, Quantification of GI and ZTL levels in IPs of **a** and **c**. **c**, As in **a**, but plants transferred to 12 h of red (LR), blue (LB) light, or dark (LD) and sampled before and after transfer. **d**, As in Fig. 2e, except *N. benthamiana* grown under 12-h-light/12-h-dark after infiltration, transferred to dark (D), white (L), red (R) or blue (B) light at ZT12 and harvested at ZT18. Quantification relative to GI–ZTL interaction in white light for each allele; direct comparisons between alleles are not valid. Means of 4–5 trials \pm s.e.m. **e**, ZTL–TOC1 interactions are light-independent. TOC1–TAP and ZTL co-expressed in *N. benthamiana* and ZTL in TOC1–TAP immunocomplexes quantified as in **d**. **b**, **e**, Means of three trials \pm s.e.m.

significantly different, indicating that the mutation diminishes the GI–ZTL interaction in a similar manner across light conditions (compare with Fig. 2e). Strikingly, the C82A mutation entirely eliminates the blue-light-enhanced interaction. Although the GI–ZTL interaction was strongly reduced in white light by this mutation (Fig. 2e), ZTL was, similarly, weakly detectable in GI immunoprecipitates under all four light conditions (Fig. 3d). These results demonstrate that blue-light-enhanced binding between ZTL and GI requires a photo-activated LOV domain, which is abrogated by the C82A mutation. Notably, FMN is still bound to LOV domains with this mutation, indicating that photo-activation is necessary for complete function²¹.

Light absorption by the LOV domain may affect ZTL interactions with proteins outside the N terminus. Therefore, we next asked whether light also affects the binding of ZTL and TOC1. The amount of ZTL associated with the TOC1 immune complex was determined from *N. benthamiana* plants incubated in darkness, red or blue light. In strong contrast to the ZTL–GI interaction, there was no effect of light on the association of TOC1 and ZTL (Fig. 3e). Hence, among the known interaction partners of ZTL, the LOV domain seems dedicated to the control of the GI–ZTL interaction.

Because TOC1 is a proteolytic target of ZTL, an expected consequence of reduced ZTL in *gi* mutants is increased TOC1 levels. We compared the levels of TOC1–YFP (yellow fluorescent protein)² under light/dark cycles in *gi-2* and wild-type plants. We found a significant increase in TOC1 protein during the light period, and a moderate decrease during the dark period (Fig. 4a). This net result of reduced amplitude is consistent with reduced ZTL abundance. The amplitude and levels of TOC1–YFP message are unchanged in a GI-deficient background (Fig. 4b; ref. 6), suggesting that the weak residual cycling of TOC1 derives from the tracking of clock-regulated TOC1–YFP mRNA. These results directly link the circadian control of TOC1 to GI, by the control of ZTL protein levels.

Our data demonstrate a new and an unexpected relationship between ZTL, a component of an E3 ubiquitin ligase, and GI, an element of the photoperiodic flowering pathway and peripheral clock component, with a heretofore unidentified function. In this relationship, ZTL's role as a photoreceptor is to enhance its own stability at specific times during the circadian and photocycles. The blue-light-enhanced cooperative stabilization of GI and ZTL boosts the amplitude and refines and sharpens the circadian waveform of both proteins, allowing for their rapid deployment in the light, and accelerated loss in the dark, in which the ZTL–GI interaction is weakened. This interaction is critical for establishing the rhythm for ZTL and leads to amplification and sharpening of the expression profile of

TOC1 (Fig. 4a; Supplementary Fig. 6). The simultaneous in-phase expression of GI, ZTL and TOC1 in the cytoplasm, and the absence of ZTL from the nucleus, suggests that it is the dynamics of the cytosolic interactions of these three proteins that determines the levels of TOC1 in the nucleus, where it may act²².

These findings also define a new, third, function of the LOV domain in eukaryotes. The LOV domains of plant phototropin and *Neurospora* WHITE COLLAR 1 (WC-1) facilitate blue-light-dependent autophosphorylation and protein–DNA interactions, respectively^{13,23,24}. The ZTL LOV domain promotes blue-light-enhanced binding to GI, and this protein–protein interaction confers post-translational circadian regulation on ZTL. This new regulatory mechanism can be added to the growing list of post-translational processes (for example, phosphorylation and SUMOylation^{25,26}) that contribute to the essential robustness of the circadian system.

METHODS SUMMARY

Plant materials. Except where indicated, the Columbia ecotype of *Arabidopsis* was used. *gi-1*, *gi-2*, *gi-3*, *gi-4*, *gi-5*, *gi-6* (ref. 4), TOC1–TOC1–YFP², 35S–GI–OX (Ler)²⁷, GI–GI–TAP⁸, *ztl-21* (ref. 17) and 35S–ZTLOX¹⁹ have been described previously. The T-DNA insertion line in the *GI* gene is identical to *gi-t* (ref. 28) and *gi-201* (ref. 6). Double mutants of *GI–GI–TAP ztl-103* were obtained by crossing and genotyped by PCR⁶. Further details are found in the Methods.

Rhythm analysis. Bioluminescent imaging of free-running rhythms and subsequent period analysis was as previously described (cited in ref. 19).

Plasmid construction and two-hybrid analysis. Full details of constructs and two-hybrid analysis are found in the Methods.

Protein analysis. Immunoprecipitations were performed as described³ with modifications. See Methods for full details of protein extraction, GST pull-down assays, immunoblotting and immunoprecipitations.

Gene expression analysis and RT–PCR. RNA was extracted using Trizol reagent (Invitrogen) and quantified by spectrophotometer. Transcripts were quantified by reverse transcription (RT)–PCR followed by ethidium-bromide-staining. Reverse transcription was performed using SuperScript II RT (Invitrogen), oligo(dT)_{12–18} (Invitrogen), and 4 µg of total RNA according to the manufacturer's instructions. The PCR reaction was done with two different sets of primers: gene specific primers and actin (*ACT*) primers, in the same PCR. *ACT* was used to normalize the amount of complementary DNA. Different numbers of cycles (23, 21 and 23) were used for *ZTL*, *GI–TAP* and *TOC1–YFP*, respectively. See Methods for primer sequences and annealing temperatures.

Full Methods and any associated references are available in the online version of the paper at www.nature.com/nature.

Received 10 June; accepted 31 July 2007.

Published online 19 August; corrected 20 September 2007.

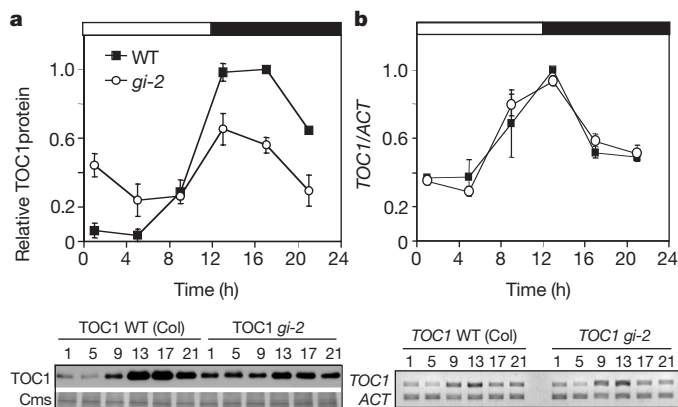


Figure 4 | Post-transcriptional control of TOC1 protein by GI. **a, b,** Time course of TOC1–YFP protein (**a**) and mRNA (**b**) accumulation in wild-type (WT)² and *gi-2* plants in LD. TOC1–YFP protein quantified relative to Coomassie (Cms)-stained gel portion, and semi-quantitative RT–PCR shows mRNA relative to *ACT*. Blots are representative of each set of trials; mean of three trials \pm s.e.m. Other features as in Fig. 1.

- Somers, D. E., Schultz, T. F., Milnamow, M. & Kay, S. A. ZEITLUPE encodes a novel clock-associated PAS protein from *Arabidopsis*. *Cell* **101**, 319–329 (2000).
- Mas, P., Kim, W. Y., Somers, D. E. & Kay, S. A. Targeted degradation of TOC1 by ZTL modulates circadian function in *Arabidopsis thaliana*. *Nature* **426**, 567–570 (2003).
- Kim, W. Y., Geng, R. & Somers, D. E. Circadian phase-specific degradation of the F-box protein ZTL is mediated by the proteasome. *Proc. Natl Acad. Sci. USA* **100**, 4933–4938 (2003).
- Fowler, S. et al. GIGANTEA: a circadian clock-controlled gene that regulates photoperiodic flowering in *Arabidopsis* and encodes a protein with several possible membrane-spanning domains. *EMBO J.* **18**, 4679–4688 (1999).
- Park, D. et al. Control of circadian rhythms and photoperiodic flowering by the *Arabidopsis* GIGANTEA gene. *Science* **285**, 1579–1582 (1999).
- Martin-Tryon, E. L., Kreps, J. A. & Harmer, S. L. GIGANTEA acts in blue light signaling and has biochemically separable roles in circadian clock and flowering time regulation. *Plant Physiol.* **143**, 473–486 (2007).
- Gould, P. D. et al. The molecular basis of temperature compensation in the *Arabidopsis* circadian clock. *Plant Cell* **18**, 1177–1187 (2006).
- David, K. M., Armbruster, U., Tama, N. & Putterill, J. *Arabidopsis* GIGANTEA protein is post-transcriptionally regulated by light and dark. *FEBS Lett.* **580**, 1193–1197 (2006).
- Nelson, D. C., Lasswell, J., Rogg, L. E., Cohen, M. A. & Bartel, B. *FKF1*, a clock-controlled gene that regulates the transition to flowering in *Arabidopsis*. *Cell* **101**, 331–340 (2000).
- Schultz, T. F., Kiyosue, T., Yanovsky, M., Wada, M. & Kay, S. A. A role for LKP2 in the circadian clock of *Arabidopsis*. *Plant Cell* **13**, 2659–2670 (2001).
- Zeng, L. R. et al. *Spotted leaf11*, a negative regulator of plant cell death and defense, encodes a U-box/armadillo repeat protein endowed with E3 ubiquitin ligase activity. *Plant Cell* **16**, 2795–2808 (2004).

12. Crosson, S. & Moffat, K. Structure of a flavin-binding plant photoreceptor domain: Insights into light-mediated signal transduction. *Proc. Natl Acad. Sci. USA* **98**, 2995–3000 (2001).
13. Froehlich, A. C., Liu, Y., Loros, J. J. & Dunlap, J. C. White Collar-1, a circadian blue light photoreceptor, binding to the *frequency* promoter. *Science* **297**, 815–819 (2002).
14. He, Q. *et al.* White Collar-1, a DNA binding transcription factor and a light sensor. *Science* **297**, 840–843 (2002).
15. Imaizumi, T., Tran, H. G., Swartz, T. E., Briggs, W. R. & Kay, S. A. FKF1 is essential for photoperiodic-specific light signalling in *Arabidopsis*. *Nature* **426**, 302–306 (2003).
16. Voinnet, O., Rivas, S., Mestre, P. & Baulcombe, D. An enhanced transient expression system in plants based on suppression of gene silencing by the p19 protein of tomato bushy stunt virus. *Plant J.* **33**, 949–956 (2003).
17. Kevei, E. *et al.* Forward genetic analysis of the circadian clock separates the multiple functions of ZEITLUPE. *Plant Physiol.* **140**, 933–945 (2006).
18. Han, L., Mason, M., Risseuw, E. P., Crosby, W. L. & Somers, D. E. Formation of an SCF complex is required for proper regulation of circadian timing. *Plant J.* **40**, 291–301 (2004).
19. Somers, D. E., Kim, W. Y. & Geng, R. The F-box protein ZEITLUPE confers dosage-dependent control on the circadian clock, photomorphogenesis, and flowering time. *Plant Cell* **16**, 769–782 (2004).
20. Imaizumi, T., Schultz, T. F., Harmon, F. G., Ho, L. A. & Kay, S. A. FKF1 F-box protein mediates cyclic degradation of a repressor of CONSTANS in *Arabidopsis*. *Science* **309**, 293–297 (2005).
21. Salomon, M., Christie, J. M., Knieb, E., Lempert, U. & Briggs, W. R. Photochemical and mutational analysis of the FMN-binding domains of the plant blue light receptor, phototropin. *Biochemistry* **39**, 9401–9410 (2000).
22. Strayer, C. *et al.* Cloning of the *Arabidopsis* clock gene *TOC1*, an autoregulatory response regulator homolog. *Science* **289**, 768–771 (2000).
23. Harper, S. M., Neil, L. C. & Gardner, K. H. Structural basis of a phototropin light switch. *Science* **301**, 1541–1544 (2003).
24. Christie, J. M. *et al.* *Arabidopsis* NPH1: A flavoprotein with the properties of a photoreceptor for phototropism. *Science* **282**, 1698–1701 (1998).
25. Lee, C., Etchegaray, J. P., Cagampang, F. R., Loudon, A. S. & Reppert, S. M. Posttranslational mechanisms regulate the mammalian circadian clock. *Cell* **107**, 855–867 (2001).
26. Cardone, L. *et al.* Circadian clock control by SUMOylation of BMAL1. *Science* **309**, 1390–1394 (2005).
27. Mizoguchi, T. *et al.* Distinct roles of GIGANTEA in promoting flowering and regulating circadian rhythms in *Arabidopsis*. *Plant Cell* **17**, 2255–2270 (2005).
28. Cheng, X. F. & Wang, Z. Y. Overexpression of *COL9*, a *CONSTANS*-LIKE gene, delays flowering by reducing expression of *CO* and *FT* in *Arabidopsis thaliana*. *Plant J.* **43**, 758–768 (2005).

Supplementary Information is linked to the online version of the paper at www.nature.com/nature.

Acknowledgements We thank S. L. Harmer for providing *ztl-103* in advance of publication, S. Kay for *TOC1-TOC1-YFP* and LKP2-OX seed, D. Bisaro for the adenosine kinase antibody and J. Na for excellent technical assistance. T. Mizoguchi provided *gi-3*, *gi-4*, *gi-5*, *gi-6*, and *GI-OX* (Ler). W.-Y. K. was supported in part by a grant from the MOST/KOSEF to the Environmental Biotechnology National Core Research Center (BK21 program grant), Korea. S.F. was funded in part by Support for Long-term Visit from the Yamada Science Foundation. Support is acknowledged from a Korea Science and Engineering Foundation (KOSEF) grant funded by MOST and the National Core Research Center for Systems Biodynamics (to H.G.N.), from the NZ Marsden grant (to J.P.), and from the NSF (IBN and MCB) to D.E.S.

Author Contributions W.-Y.K., S.F., S.-S.S., L.H., J.K. and Y.K. performed experiments. W.-Y.K. and H.-G.N. co-directed and designed experiments. J.P., K.D. and H.G.N. contributed novel reagents. J.P., S.F. and H.G.N. commented on and edited the manuscript. D.E.S. directed research, designed experiments and wrote the manuscript.

Author Information Reprints and permissions information is available at www.nature.com/reprints. The authors declare no competing financial interests. Correspondence and requests for materials should be addressed to D.E.S. (somers.24@osu.edu).

METHODS

Plant materials. To generate 35S-GI-GFP in *gi-2*, the 35S-GI-GFP plasmid was introduced into *Agrobacterium tumefaciens* (AGL1) by electroporation and transformed into *gi-2* plants²⁹. Two transgenic lines showing early flowering, short hypocotyls in constant red light, and altered leaf movement rhythm in constant light after entrainment in light/dark cycles (data not shown) were characterized and one used here.

The GI-GI-HA gene expression construct, consisting of the GI genomic region (from pPZP121-GI clone from E. Huq and P. Quail) including a 2.7-kb upstream region with a triple-HA epitope tag inserted upstream of the stop codon to create an in-frame GI-HA protein fusion, was transformed into *gi-2* plants. Details of the vector construction are available from the authors. The late flowering of the *gi-2* mutant was rescued in three lines, one of which was used here.

ztl (G46E) was isolated in a mutant screen for revertant rhythmic expressors of *cab2-luciferase* in a background of 35S-ZTL long hypocotyl, overexpressing plants (arrhythmic) (C24 ecotype). Seeds of a transgenic *Arabidopsis thaliana* line expressing 35S-ZTL were mutagenized with 0.3% ethyl methanesulfonate and assayed under white fluorescent light (30 μ m, 12-h-light/12-h-dark) for 7 to 10 days. Seedlings having shorter hypocotyls compared to the 35S-ZTL parent were transferred to new plates for period analysis. The mutation was confirmed by DNA sequencing of the ZTL transgene.

Plasmids and genes. To create the 35S-GI-GFP construct, the protein-coding sequence of the GI cDNA was generated by PCR with *Pfu* DNA polymerase (Stratagene), using the full length GI cDNA in pBluescript II SK(+) plasmid⁵ as template and the primers, GI-GFP-F: TGGTCTAGAAATGGCTAGTTCATCTTCATC and GI-GFP-R: TTTTCTAGATTGGGACAAGGATATAGTACA. The GI sequence in the final construct was confirmed by sequencing.

The 35S-GI-TAP construct was prepared using the LR recombination reaction (GATEWAY) starting with a pENTR 1A entry vector containing a GI cDNA clone generated by PCR from a full-length GI cDNA in pBluescript II SK(+) plasmid⁵ as template and cloned in by *EcoRI*/*NotI* using the primer sets: 5'-GAATTCTTATGGCTAGTTCATCTTC-3' and 5'-GCGGCCGCTGGGACAAAGGATATAGTACA-3'. The GI sequence was confirmed by sequencing and the final construct was established by LR recombination with the pC-TAPa vector³⁰.

The pTriEX GI construct (GST pull down) was generated by PCR with *Pfu* DNA polymerase, using the full-length GI cDNA as template and the primer sets, 5'-GGATCCGATGGCTAGTTCATC-3' and 5'-GGTACCATTGGGACAAGGATATAG-3'. PCR products were digested with *Bam*HI and *Kpn*I and ligated into the pTriEX-1 vector (Novagen).

ZTL cDNA sequence was subcloned into pGEX-KG to make the GST-FL ZTL construct as previously described⁵. For LKP2 and FKF1, full-length cDNA sequences were amplified using plasmid template containing the genomic DNA from LKP2-OX and FKF1 cDNA sequences, respectively, and subcloned into pGEX-KG. GST-SPL11 constructs were kindly provided by G.-I. Wang¹¹. The unique identifiers of the genes discussed are: ZTL, AT5G57360; TOC1, AT5G61380; ACT2, AT3G18780; GI, AT1G22770; SPL11, AY652590; LKP2, AT2G18915; and FKF1, AT1G68050.

GST pull-down assay. GST, GST-LKP2, GST-FKF1, GST-SPL and GST-ZTL were expressed in *Escherichia coli* BL21(DE3) and purified with glutathione-agarose (Sigma). ³⁵S-labelled GI protein was synthesized by using the T'nT *in vitro* transcription-translation system (Promega) according to the manufacturer's instructions. *In vitro* binding assays were according to (ref. 18) with minor modifications. Concentration of each fusion protein was determined by Coomassie staining. The amount of glutathione-agarose beads with bound GST, GST-LKP2, GST-FKF1, GST-SPL and GST-ZTL was adjusted to use equal amounts of fusion protein for the *in vitro* binding reactions. The beads were then washed twice with binding buffer and once with TBS buffer. The bound protein was eluted in 1× SDS sample buffer and size-fractionated on 8% SDS-PAGE along with 0.05 μ l ³⁵S-labelled GI as input. Detection was by autoradiography.

Yeast two-hybrid. The protein coding sequence of the GI cDNA was cloned into the pGilda vector (DupLEX-A) and pOST4-5, a modified vector for pJG4-5 containing the same multiple cloning sites as pGilda, for bait and for prey, respectively.

The bait and prey clones for the protein-coding sequence of ZTL, FKF1 and LKP2 were prepared using LR recombination reaction (GATEWAY). The final bait and prey constructs were established by LR recombination reaction using the ZTL, FKF1 or LKP2 entry clone and the Gateway version of pGilda or pOST4-5, according to the manufacturer's instructions. The bait or prey clones for the sub-domains of ZTL were prepared using LR recombination reaction (GATEWAY).

The protein-coding sequence of the KELCH and LOV domains in ZTL were generated by PCR with *Pfu* DNA polymerase, using the full-length ZTL cDNA clone (RAFL05-03-P09, RIKEN; refs 31, 32) as template and the primer sets:

5'-ATGACCACCCTTGAAGCT-3' and 5'-TTACGTGAGATAGCTCGCTA-3' for KELCH, and the primer sets: 5'-CTTCTGCAGATGGAGTGGGACAGTGGTTCC-3' and 5'-CTTAGGCCTTCATCGGAAACATTCCGCTCCC-3' for LOV, and the resulting clones confirmed by sequencing.

The final bait and prey constructs were established by LR recombination reaction using the entry clones for the subdomains of ZTL and the gateway version of pGilda or pOST4-5, according to the manufacturer's instructions. Expression of all proteins was confirmed by immunoblot analysis.

Vectors and strains of a LexA-based yeast two-hybrid system (DupLEX-A, OriGene Technologies) were used. Sets of constructs were co-transformed into EGY48 (*ura3*, *his3*, *trp1*, *leu::6 LexAop-LEU2*)-containing *lacZ* reporter plasmid pSH18-34 (ref. 33). Quantitative yeast two-hybrid interaction assays were performed according to published protocols.

Protein extractions. For detection of ZTL, GI-TAP, GI-HA, ADK and Histone H3 from *Arabidopsis*, extracts were prepared from 10-day-old seedlings grown in the indicated light conditions. Ground tissue was resuspended in extraction buffer by vortexing and clarified by centrifugation. Supernatant was concentrated by TCA precipitation and resuspended in urea/SDS loading buffer. Separation was on 8% (150:1, acrylamide:bis) or 10% (37.5:1, acrylamide:bis) SDS-PAGE and subjected to immunoblot analysis.

Immunoprecipitation and immunoblotting. Immunoprecipitations were performed according to ref. 3 with minor modifications. For immunoprecipitation of GI-GFP and co-immunoprecipitation of ZTL, anti-GFP mouse monoclonal antibody (anti-GFP, mAb 3E6; Molecular Probes) was pre-incubated with protein A agarose (Invitrogen) at 4 °C, after which protein extracts were incubated for 1 h with gentle rotation. Immune complexes were washed four times, resuspended in SDS-PAGE sample buffer, briefly heated and subjected to SDS/PAGE and immunoblotting.

For GI-TAP co-expressed with LKP2-GFP/ZTL-GFP and FKF1-TAP co-expressed with GI-GFP, supernatants were incubated with IgG-agarose (Sigma) and harvested immune complexes were washed twice with buffer, and elution from IgG beads performed using 3 C Protease (2 units μ l⁻¹, Precision Protease, Amersham Bioscience) for GI-TAP complexes, and AcTEV protease (10 units μ l⁻¹, Invitrogen), for FKF1-TAP complexes. Supernatant was collected after centrifugation, resuspended in SDS-PAGE sample buffer, briefly heated and subjected to SDS-PAGE and immunoblotting.

For GI-TAP expression analysis, *Arabidopsis* tissues were harvested as indicated and extracts were prepared in buffer by gentle vortexing and clarified by centrifugation. Immune complexes were purified and processed as above.

Protein was transferred to PVDF membrane (Bio-Rad) by standard techniques. For ZTL, ADK, GI-TAP, TOC1-TAP and histone H3, each immunoblot was incubated with the appropriate primary antibody (affinity-purified anti-ZTL antibody, 1:666; anti-ADK antibody, 1:1,000; peroxidase anti-peroxidase complex (PAP) (Sigma), 1:1,000; anti-histone H3 (Abcam), 1:1,000; anti-His6 (Abcam)) for 4 h at room temperature or over night 4 °C. GFP, HA and Thioredoxin h3 immunoblots were incubated with primary antibodies (anti-GFP rabbit polyclonal antibody (1:2,000) (Molecular Probes or Abcam); anti-HA antibody, (1:2,000) (Abcam); Thioredoxin h3, (1:3,000)). The membranes were developed using peroxidase-conjugated secondary antibody (1:3,000–5,000) (GE, UK or Sigma) by enhanced chemiluminescence (SuperSignal West Pico Chemiluminescent substrate; Pierce Biotechnology).

Cell fractionation. Cytoplasmic fractions were prepared with extraction, vortexed and clarified by centrifugation at 4 °C. For ZTL and GI-HA immunoblots, supernatant protein was concentrated by TCA precipitation as described above. Nuclei were isolated using CelLytic Plant Nuclei Isolation/Extraction Kit (Sigma) and stored at -70 °C. Cytoplasmic extract:nuclear extract were loaded with a ratio of 1:6 (GI-HA) and 1:2 (TOC1-YFP and ZTL).

RT-PCR conditions. The primer sequences and annealing temperatures used to amplify ZTL, GI-TAP, TOC1-YFP and ACT fragments are: ZTL, 50 °C, 5'-GATCTAAGCGCCGATGATGC-3' and 5'-GCTAACAGATGCAACGTCTC-3'; GI-TAP, 50 °C, 5'-GGAGTTGCAGCCTTGGATCG-3' and 5'-AAGGTACCTCAGGTTGACTTCCCCGC-3'; TOC1-YFP, 50 °C, 5'-CTTGACAGAAGAGAGGAAGC-3' and 5'-ACGCTGAACCTGTGGCCGTTTACG-3'; ACT, 50 °C, 5'-GTTGAACGGAAGGATTGAGAGT-3' and 5'-AAAACCACTTACAGAGTTCGTTCCG-3'.

29. Clough, S. J. & Bent, A. F. Floral dip: a simplified method for *Agrobacterium*-mediated transformation of *Arabidopsis thaliana*. *Plant J.* **16**, 735–743 (1998).
30. Rubio, V. et al. An alternative tandem affinity purification strategy applied to *Arabidopsis* protein complex isolation. *Plant J.* **41**, 767–778 (2005).
31. Seki, M. et al. Functional annotation of a full-length *Arabidopsis* cDNA collection. *Science* **296**, 141–145 (2002).

32. Seki, M., Carninci, P., Nishiyama, Y., Hayashizaki, Y. & Shinozaki, K. High-efficiency cloning of *Arabidopsis* full-length cDNA by biotinylated CAP trapper. *Plant J.* **15**, 707–720 (1998).
33. Ryu, J. S. *et al.* Phytochrome-specific type 5 phosphatase controls light signal flux by enhancing phytochrome stability and affinity for a signal transducer. *Cell* **120**, 395–406 (2005).

Loss of integrin $\alpha_v\beta_8$ on dendritic cells causes autoimmunity and colitis in mice

Mark A. Travis^{1†}, Boris Reizis², Andrew C. Melton¹, Emma Masteller³, Qizhi Tang³, John M. Proctor⁴, Yanli Wang¹, Xin Bernstein¹, Xiaozhu Huang¹, Louis F. Reichardt⁴, Jeffrey A. Bluestone³ & Dean Sheppard¹

The cytokine transforming growth factor- β (TGF- β) is an important negative regulator of adaptive immunity^{1–3}. TGF- β is secreted by cells as an inactive precursor that must be activated to exert biological effects⁴, but the mechanisms that regulate TGF- β activation and function in the immune system are poorly understood. Here we show that conditional loss of the TGF- β -activating integrin $\alpha_v\beta_8$ on leukocytes causes severe inflammatory bowel disease and age-related autoimmunity in mice. This autoimmune phenotype is largely due to lack of $\alpha_v\beta_8$ on dendritic cells, as mice lacking $\alpha_v\beta_8$ principally on dendritic cells develop identical immunological abnormalities as mice lacking $\alpha_v\beta_8$ on all leukocytes, whereas mice lacking $\alpha_v\beta_8$ on T cells alone are phenotypically normal. We further show that dendritic cells lacking $\alpha_v\beta_8$ fail to induce regulatory T cells (T_R cells) *in vitro*, an effect that depends on TGF- β activity. Furthermore, mice lacking $\alpha_v\beta_8$ on dendritic cells have reduced proportions of T_R cells in colonic tissue. These results suggest that $\alpha_v\beta_8$ -mediated TGF- β activation by dendritic cells is essential for preventing immune dysfunction that results in inflammatory bowel disease and autoimmunity, effects that are due, at least in part, to the ability of $\alpha_v\beta_8$ on dendritic cells to induce and/or maintain tissue T_R cells.

The critical pathways for activation of latent TGF- β at specific sites *in vivo* remain controversial. One important mechanism for activation of two of the three mammalian TGF- β isoforms (TGF- β 1 and TGF- β 3) is through interaction with members of the integrin receptor family^{5–7}. The *in vivo* importance of TGF- β activation by integrins has been recently demonstrated in mice with a mutated integrin-binding motif in TGF- β 1 (ref. 8). These mice completely phenocopy *Tgfb1*^{−/−} mice, which die from multi-organ inflammatory disease¹, showing that integrin-mediated TGF- β activation is vital to maintain immune homeostasis. However, the integrin(s) responsible for TGF- β activation in the immune system *in vivo*, where these integrins are expressed, and the mechanisms by which integrin-mediated TGF- β activation maintains immune homeostasis remain a mystery.

The integrin $\alpha_v\beta_6$ has previously been shown to activate TGF- β (ref. 6), but this integrin is restricted to a subset of epithelial cells and is not expressed on immune cells. Furthermore, the inflammatory phenotype of mice lacking $\alpha_v\beta_6$ is mild compared to mice lacking TGF- β 1 or TGF- β 3 (ref. 5). The $\alpha_v\beta_8$ integrin can also activate TGF- β (ref. 7). Mice completely lacking $\alpha_v\beta_8$ die before or shortly after birth from defects in brain vascular development⁹, so tissue-specific deletion was required to determine whether $\alpha_v\beta_8$ -mediated TGF- β activation has a function in regulating adaptive immunity. Polymerase chain reaction with reverse transcription (RT-PCR) analysis revealed that β_8 was expressed in total splenocytes, CD4⁺ T cells and dendritic cells (Supplementary Fig. 1a) but was present at very low or

undetectable levels in macrophages, CD8⁺ T cells, natural killer cells and B cells. To assess the *in vivo* significance of $\alpha_v\beta_8$ expression in the immune system, we produced mice with conditional loss of β_8 on leukocytes by crossing mice homozygous for a floxed β_8 (*Itgb8*) allele¹⁰ with mice expressing Cre recombinase under the control of the *Vav1* promoter¹¹ (hereafter called (*Vav1-cre*)*Itgb8*^{fl/fl}). Quantitative (q)RT-PCR revealed efficient knockdown (>98%) of *Itgb8* messenger RNA expression in CD4⁺ T cells and dendritic cells from (*Vav1-cre*)*Itgb8*^{fl/fl} mice (Supplementary Fig. 1b).

(*Vav1-cre*)*Itgb8*^{fl/fl} mice were phenotypically normal until 4–5 months of age, when they began to develop a progressive wasting disorder (Fig. 1a). (*Vav1-cre*)*Itgb8*^{fl/fl} mice also developed splenomegaly, massive enlargement of mesenteric lymph nodes (Fig. 1b) and accumulations of mononuclear cells adjacent to portal triads of the liver (Fig. 1c). By 10 months of age, all surviving (*Vav1-cre*)*Itgb8*^{fl/fl} mice developed severe colitis, characterized by cellular infiltration of the colonic wall with eosinophils and plasma cells, and formation of colonic cysts (Fig. 1d). These mice also developed high levels of auto-antibodies directed against double-stranded DNA and ribonuclear proteins (Fig. 1e). These findings are remarkably similar to phenotypes described for mice with a partial loss of TGF- β signalling in T cells as a result of expression of a dominant negative TGF- β receptor¹², and for mice lacking the key TGF- β signalling protein Smad4 in T cells¹³. Mice lacking Smad4 in T cells also had increased tumorigenesis¹³, a finding we did not observe.

PCR of stool samples revealed the presence of the common intestinal bacteria *Helicobacter hepaticus* and *Helicobacter ganmani* from all control and experimental mice tested. These organisms, endemic in our facility and in over 85% of mouse research colonies worldwide^{14,15}, are not pathogenic in most strains of mice, but have been reported to cause colitis and hepatic inflammation in some immunosuppressed strains¹⁶. We therefore cannot exclude the possibility that the presence of these organisms, or other unmeasured microbial flora, contribute to the severity of colonic and/or hepatic pathology in (*Vav1-cre*)*Itgb8*^{fl/fl} mice. Such a response could be relevant to inflammatory bowel diseases in humans, where abnormal responses to normally non-pathogenic intestinal flora have been suggested to have a role¹⁷.

Mice with impaired T-cell responsiveness to TGF- β were also shown to have increased numbers of activated peripheral T cells, increased circulating levels of IgA and IgG1, and increased numbers of T cells that produce interleukin-4 (IL-4) and/or interferon- γ (IFN- γ)¹². (*Vav1-cre*)*Itgb8*^{fl/fl} mice (4–6 months old) also had enhanced numbers of activated/memory CD4⁺ and CD8⁺ T cells (Fig. 2a), and increased numbers of CD4⁺ T cells producing IFN- γ and IL-4, and CD8⁺ cells producing IFN- γ (Fig. 2b and Supplementary Fig. 2).

¹Lung Biology Center, Department of Medicine, University of California San Francisco, 1550 4th Street, Room 545, San Francisco, California 94158, USA. ²Department of Microbiology, Columbia University, 701 West 168th Street, Room 609, New York, New York 10032, USA. ³Diabetes Center, Department of Medicine, 513 Parnassus Avenue, University of San Francisco, San Francisco, California 94143, USA. ⁴Howard Hughes Medical Institute, Department of Physiology, University of California, San Francisco, California 94158, USA.

†Present address: Wellcome Trust Centre for Cell-Matrix Research, Faculty of Life Sciences, University of Manchester, A3051 Smith Building, Oxford Road, Manchester M13 9PT, UK.

(*Vav1-cre*)*Itgb8*^{fl/fl} mice also had increased levels of circulating IgE, IgG1 and IgA (Fig. 2c), whereas levels of IgM, IgG2a, IgG2b and IgG3 were not significantly different (Supplementary Fig. 3). Again, these features were virtually identical to those described in mice with a partial loss of TGF- β signalling in T cells, suggesting that $\alpha_v\beta_8$ on leukocytes has an important role in activating TGF- β for presentation to T cells. This phenotype is not due to the mixed genetic background analysed in these initial experiments, because mice bred five generations to pure C57BL/6 background have a similar immune phenotype and also develop colitis (Supplementary Fig. 4).

We next assessed whether loss of $\alpha_v\beta_8$ on either dendritic cells or T cells was responsible for the *in vivo* phenotype observed in (*Vav1-cre*)*Itgb8*^{fl/fl} mice by crossing mice homozygous for the *Itgb8*-floxed allele with mice expressing Cre recombinase principally in T cells (CD4-Cre)¹⁸ or dendritic cells (CD11c-Cre)¹⁹. By qRT-PCR we saw a greater than 99% reduction in *Itgb8* mRNA levels in CD4⁺ T cells from *Itgb8*^{fl/fl} mice expressing CD4-Cre ((*CD4-cre*)*Itgb8*^{fl/fl}), with a modest reduction in dendritic cells (Supplementary Fig. 5a). Greater than 99% reduction in *Itgb8* mRNA levels was found in dendritic cells from *Itgb8*^{fl/fl} mice expressing CD11c-Cre ((*CD11c-cre*)*Itgb8*^{fl/fl}), with a modest reduction in CD4⁺ T cells (Supplementary Fig. 5b).

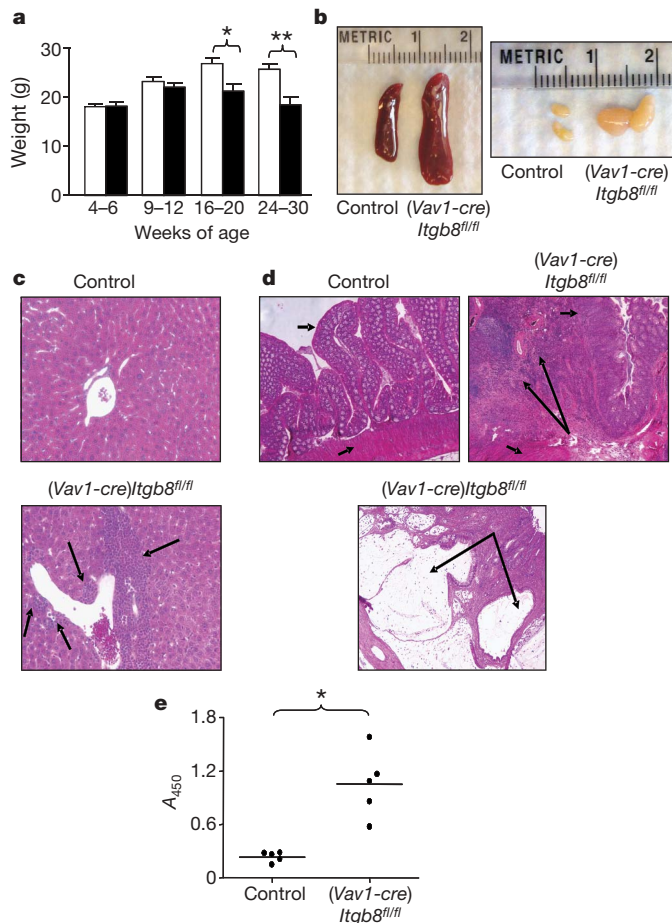


Figure 1 | (*Vav1-cre*)*Itgb8*^{fl/fl} mice develop age-related autoimmunity. **a**, Weight loss in control and (*Vav1-cre*)*Itgb8*^{fl/fl} mice (white, control; black, (*Vav1-cre*)*Itgb8*^{fl/fl}; $n = 7$ per group; asterisk, $P = 0.011$; double asterisk, $P = 0.0026$). Error bars represent s.e.m. **b**, Lymphoid organs of 5-month-old mice. **c**, Haematoxylin- and eosin-stained sections of livers (10 months, original magnification $\times 200$). Arrows show cellular infiltrates. **d**, Haematoxylin- and eosin-stained colon sections (9 months, original magnification $\times 50$). Short arrows, epithelium (top arrow) and smooth muscle (bottom arrow); large arrows, cellular infiltrates (top panel) and large cyst (bottom panel). **e**, ELISA for anti-dsDNA and anti-ribonuclear protein (9–12 months, $n = 5$, $P = 0.0013$).

Therefore, (*CD4-cre*)*Itgb8*^{fl/fl} mice completely lacked β_8 expression in CD4⁺ T cells, but only partially in dendritic cells, whereas (*CD11c-cre*)*Itgb8*^{fl/fl} mice completely lacked β_8 expression in dendritic cells, but only partially in CD4⁺ T cells.

By 4–6 weeks of age, (*Vav1-cre*)*Itgb8*^{fl/fl} mice already had increased numbers of activated/memory T cells, increased T-cell production of IFN- γ and/or IL-4, and increased circulating levels of IgE, IgG1 and IgA (Fig. 3). In contrast, (*CD4-cre*)*Itgb8*^{fl/fl} mice were indistinguishable from control mice, and showed no signs of illness up to at least 14 months of age. (*CD11c-cre*)*Itgb8*^{fl/fl} mice show an identical immunological phenotype to mice lacking β_8 integrin on all leukocytes, with significantly increased numbers of activated/memory T cells (Fig. 3a), increased T cells expressing IFN- γ and/or IL-4 (Fig. 3b), and increases in serum IgE, IgG1 and IgA levels (Fig. 3c).

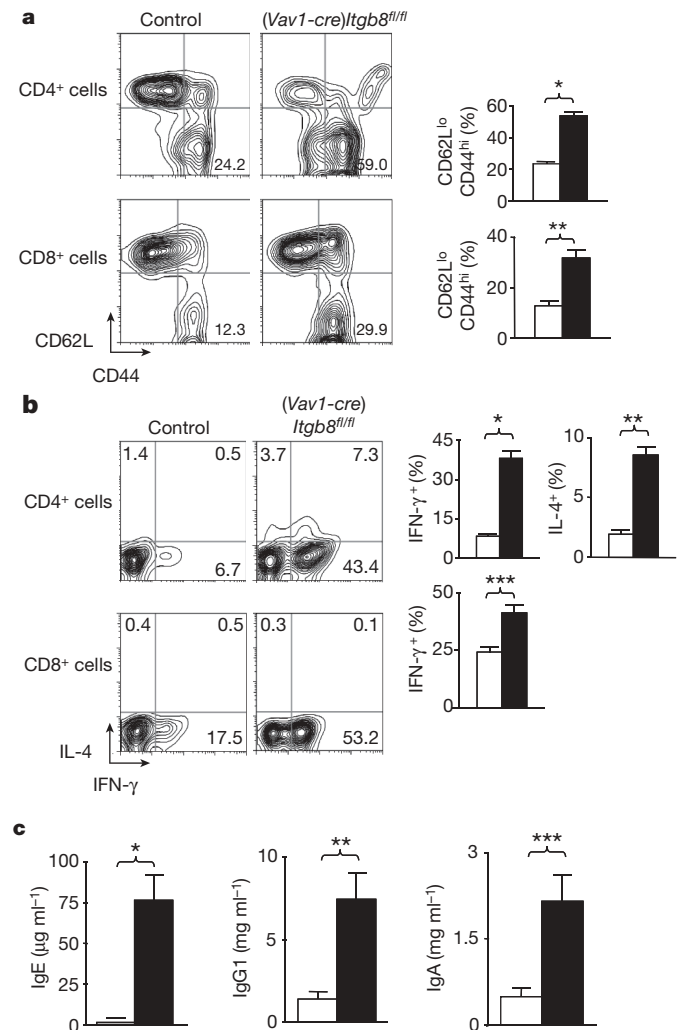


Figure 2 | (*Vav1-cre*)*Itgb8*^{fl/fl} mice develop enhanced numbers of activated/memory T cells expressing IL-4 and IFN- γ , and increased serum IgE, IgG1 and IgA levels. **a**, Activated/memory T cells from spleen (CD62L^{low}CD44^{high}, 4–6-month-old mice) were analysed by flow cytometry. Representative flow cytometry plots and plotted mean values are shown (white, control; black, (*Vav1-cre*)*Itgb8*^{fl/fl}; $n = 14$; asterisk, $P = 2.7 \times 10^{-11}$; double asterisk, $P = 4.9 \times 10^{-5}$). **b**, IL-4 and IFN- γ levels in T cells from spleen were analysed by intracellular flow cytometry. Representative flow cytometry plots and plotted mean values are shown (white, control; black, (*Vav1-cre*)*Itgb8*^{fl/fl}; $n = 9$; asterisk, $P = 1.8 \times 10^{-8}$; double asterisk, $P = 1.8 \times 10^{-7}$; triple asterisk, $P = 0.00048$). **c**, ELISA for IgE, IgG1 and IgA levels in sera (4–6-month-old mice; white, control; black, (*Vav1-cre*)*Itgb8*^{fl/fl}; $n = 4$; asterisk, $P = 0.0028$; double asterisk, $P = 0.011$; triple asterisk, $P = 0.016$). All error bars represent s.e.m.

Older $(CD11c\text{-}cre)Itgb8^{fl/fl}$ mice (6–7 months) manifested an identical phenotype to age-matched mice lacking β_8 on all leukocytes, with significant weight loss, enlarged spleen and mesenteric lymph nodes, infiltrates in portal triads of the liver, and development of colonic inflammation (Supplementary Fig. 6). These results suggest that expression of the $\alpha_v\beta_8$ integrin on dendritic cells is vital for the negative regulation of adaptive immunity. Loss of $\alpha_v\beta_8$ on T cells is not by itself sufficient to cause any aspects of this phenotype. However, because $CD11c\text{-}Cre$ did cause a modest reduction in β_8 expression in $CD4^+$ T cells, we cannot exclude a minor contribution from partial loss of $\alpha_v\beta_8$ on these cells.

Mice lacking T_R cells also develop severe autoimmunity²⁰, and recent work has shown an important role for TGF- β in the biology

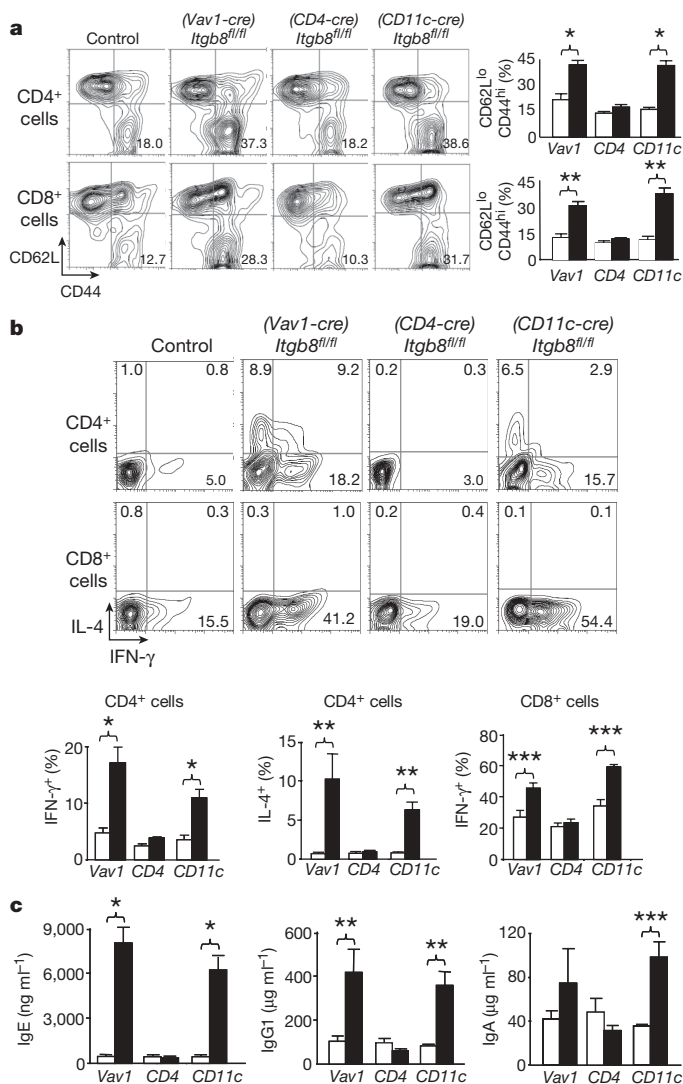


Figure 3 | Mice lacking integrin β_8 on dendritic cells develop an identical immune phenotype to mice lacking β_8 integrin on all leukocytes.

a, Activated/memory T cells from spleen ($CD62L^{low}CD44^{high}$, 4–6-week-old mice) were analysed by flow cytometry. Representative flow cytometry plots and plotted mean values are shown (white, control; black, $Itgb8$ conditional knockout; $n = 6$ per group; asterisk, $P < 8.2 \times 10^{-4}$; double asterisk, $P < 1.4 \times 10^{-4}$). **b**, IL-4 and IFN- γ levels in T cells from spleen were analysed by intracellular flow cytometry. Representative flow cytometry plots and plotted mean values are shown (white, control; black, $Itgb8$ conditional knockout; $n = 6$ per group; asterisk, $P < 0.0063$; double asterisk, $P = 0.0055$; triple asterisk, $P = 0.0045$). **c**, ELISA for IgE, IgG1 and IgA levels in sera (4–6-week-old mice; white, control; black, $Itgb8$ conditional knockout; $n = 6$; asterisk, $P < 0.0018$; double asterisk, $P < 0.016$; triple asterisk, $P = 0.0015$). All error bars represent s.e.m.

of T_R cells^{21–24}. We therefore examined the ability of control or β_8 -deficient dendritic cells to induce T_R cells from $CD4^+$ T cells in an *in vitro* T-cell activation assay. Both control and β_8 -deficient dendritic cells showed similar populations of myeloid ($CD11c^{high}CD8^-$), lymphoid ($CD11c^{high}CD8^+$) and plasmacytoid ($CD11c^{low}B220^+$) dendritic cells (Supplementary Fig. 7a), with comparable expression of the activation markers CD86 and major histocompatibility complex (MHC) class II (Supplementary Fig. 7b), indicating that lack of β_8 integrin does not affect the development or maturation of dendritic cells. In the presence of control dendritic cells approximately 3% of $CD4^+$ T cells converted to T_R cells (determined by expression of the T_R -cell-specific reporter gene $Foxp3\text{-}Gfp^{25}$) and induction was inhibited by an anti-TGF- β antibody (Fig. 4a). However, in the presence of β_8 -deficient dendritic cells, T_R cell induction was markedly reduced (Fig. 4a). Addition of active TGF- β to cultures containing either control or β_8 -deficient dendritic cells resulted in a similar induction of T_R cells (Fig. 4b). Co-culture with TGF- β -luciferase reporter cells also demonstrated decreased TGF- β activity generated by β_8 -deficient dendritic cells compared to control dendritic cells (Fig. 4c).

To determine whether there was a defect in T_R cell induction by β_8 -deficient dendritic cells *in vivo*, we analysed $CD4^+$ $Foxp3^+$ T_R cells in the spleen or colon of young (8–14 weeks) control or $(CD11c\text{-}cre)Itgb8^{fl/fl}$ mice. No difference in the proportion of T_R cells was observed in the spleens, but there was a greater than 50% reduction in the proportion of T_R cells recovered from the colonic lamina

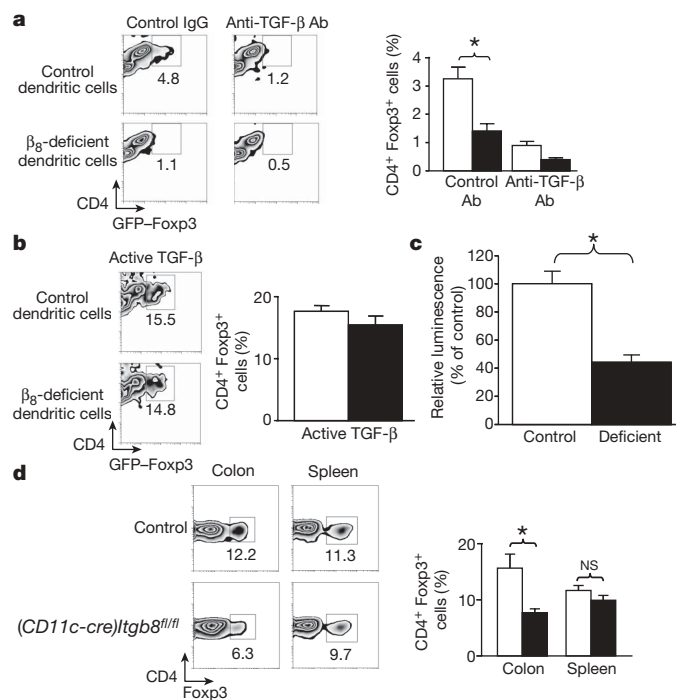


Figure 4 | β_8 -deficient dendritic cells fail to induce T_R cells *in vitro*, and $(CD11c\text{-}cre)Itgb8^{fl/fl}$ mice have reduced proportions of T_R cells in colonic tissue. **a**, **b**, Induction of T_R cells ($CD4^+$ $Foxp3^+$) by control or β_8 -deficient dendritic cells in the presence of control or anti-TGF- β antibody (**a**) or active TGF- β (**b**). Representative flow cytometry plots and mean data plots (expressed as percentage of $CD4^+$ cells that expressed GFP- $Foxp3$) are shown (white, control dendritic cells; black, β_8 -deficient dendritic cells; $n = 5$; asterisk, $P = 0.013$). **c**, TGF- β activation by control or β_8 -deficient dendritic cells, detected using mink lung reporter cells³⁰ (white, control dendritic cells; black, β_8 -deficient dendritic cells; $n = 6$; asterisk, $P = 0.0006$). **d**, T_R cell proportions present in spleen or colonic lamina propria. Representative flow cytometry plots and mean data plots (expressed as percentage of $CD4^+$ cells that expressed GFP- $Foxp3$) are shown (white, control; black, $(CD11c\text{-}cre)Itgb8^{fl/fl}$; $n = 6$; asterisk, $P = 0.012$). NS, not significant. All error bars represent s.e.m.

propria of *(CD11c-cre)Itgb8^{fl/fl}* mice (Fig. 4d). We cannot rule out the possibility that CD4⁺ effector cell expansion contributes to the observed reduction in the fractional number of T_R cells in the colon. However, taken together, our *in vitro* and *in vivo* results suggest that activation of TGF- β by $\alpha_v\beta_8$ on dendritic cells is important for the induction of T_R cells in peripheral tissues such as the colon, and that a defect in T_R cell induction and/or maintenance could contribute to the autoimmunity and colitis in *(CD11c-cre)Itgb8^{fl/fl}* mice.

Because the phenotype we observed is markedly similar to that of mice with impaired TGF- β signalling in T cells, and $\alpha_v\beta_8$ on dendritic cells activates TGF- β , our results suggest a key negative regulatory role for presentation of active TGF- β from $\alpha_v\beta_8$ on dendritic cells to T cells. Our findings further suggest that the aberrant immune homeostasis we observed may be explained by the known role of TGF- β in induction of Foxp3 expression²¹ and resultant differentiation of T cells to T_R cells. However, whereas T_R cells in the colon were decreased in *(CD11c-cre)Itgb8^{fl/fl}* mice, numbers of T_R cells in the spleen were normal. These results may be explained by a difference in the mechanisms underlying the generation of natural/innate T_R cells that are the primary contributor to T_R cells in the spleen, lymph nodes and circulation, and adaptive T_R cells that are critical for maintaining peripheral homeostasis and preventing diseases such as colitis^{26,27}. In addition to T_R cell abnormalities, the observed autoimmune phenotype could be partially explained by a role for dendritic cell $\alpha_v\beta_8$ -mediated TGF- β activation in the direct regulation of T-cell function, as it is known that TGF- β can also directly suppress effector T cells²⁸.

As described earlier, mutation of the RGD integrin-binding site in TGF- β 1 results in a more severe autoimmune phenotype reminiscent of loss of TGF- β 1 (ref. 8). Therefore, it is likely that activation of TGF- β by other integrins or cell types is also important for the maintenance of immune homeostasis. For example, the $\alpha_v\beta_6$ integrin on epithelial cells or the $\alpha_v\beta_8$ integrin on resident tissue cells might also contribute to T_R cell induction and immune suppression at specific sites. Notably, in the absence of the $\alpha_v\beta_8$ integrin on dendritic cells, mice demonstrate widespread evidence of immune activation, autoimmunity and colitis, suggesting that genetic or acquired abnormalities in $\alpha_v\beta_8$ might contribute to the development of inflammatory bowel disease or other autoimmune disorders.

METHODS SUMMARY

Mice. Mice expressing a floxed allele of *Itgb8* have been described¹⁰, and were maintained on a mixed CD1, FVB and C57BL/6 background. Vav1-Cre mice were a gift from D. Kioussis¹¹. CD4-Cre mice¹⁸ were purchased from Taconic. For some experiments, alleles were bred for five generations to C57BL/6 mice. CD11c-Cre mouse generation is described in a separate manuscript¹⁹. Foxp3-GFP mice were a gift from A. Rudensky²⁵. All mice were maintained under pathogen-free conditions, according to institutional guidelines.

Cell purification and flow cytometry. Cells were purified using magnetic beads (Miltenyi) or by flow cytometry. Flow cytometry data analysis was performed using FloJo software (Treestar).

Quantitative RT-PCR. RNA was isolated using an RNeasy mini kit (Qiagen), and reverse transcribed using Superscript II RT (Invitrogen). Quantitative PCR was performed using a Sybr Green qRT-PCR kit (Invitrogen). Primers used are detailed in the Methods.

Cytokine production assays. Splenocytes ($5 \times 10^6 \text{ ml}^{-1}$) were incubated with 50 ng ml⁻¹ PMA (Sigma) and 1 μM ionomycin (Calbiochem). For intracellular flow cytometry, cells were cultured for 2 h followed by addition of 2 μM monensin (eBioscience) and cultured for another 2 h. For ELISA analysis, cells were cultured for 24 h and supernatants harvested.

Regulatory T-cell induction assay. Briefly, non-T_R CD4⁺ cells (CD4⁺GFP-Foxp3⁻ T cells from GFP-Foxp3 mice²⁵) were incubated with CD11c⁺ dendritic cells in the presence of anti-CD3 antibody and either control antibody, anti-TGF- β antibody or active TGF for 3 days. T_R cell induction was measured by flow cytometry analysis of CD4⁺GFP-Foxp3⁺ cells. See Methods for full details of T_R cell induction and TGF- β activation assays.

Colon lamina propria cell preparation. Colonic lamina propria lymphocytes were isolated as described²⁹, with slight modification (see Methods).

Statistical analysis. All statistics were generated using a Student's *t*-test. All error bars in figures represent s.e.m.

Full Methods and any associated references are available in the online version of the paper at www.nature.com/nature.

Received 9 April; accepted 23 July 2007.

Published online 12 August 2007.

- Shull, M. M. *et al.* Targeted disruption of the mouse transforming growth factor- β 1 gene results in multifocal inflammatory disease. *Nature* **359**, 693–699 (1992).
- Marie, J. C., Liggitt, D. & Rudensky, A. Y. Cellular mechanisms of fatal early-onset autoimmunity in mice with the T cell-specific targeting of transforming growth factor- β receptor. *Immunity* **25**, 441–454 (2006).
- Li, M. O., Sanjabi, S. & Flavell, R. A. Transforming growth factor- β controls development, homeostasis, and tolerance of T cells by regulatory T cell-dependent and -independent mechanisms. *Immunity* **25**, 455–471 (2006).
- Annes, J. P., Munger, J. S. & Rifkin, D. B. Making sense of latent TGF β activation. *J. Cell Sci.* **116**, 217–224 (2003).
- Huang, X. Z. *et al.* Inactivation of the integrin β 6 subunit gene reveals a role of epithelial integrins in regulating inflammation in the lung and skin. *J. Cell Biol.* **133**, 921–928 (1996).
- Munger, J. S. *et al.* The integrin $\alpha_v\beta_6$ binds and activates latent TGF β 1: a mechanism for regulating pulmonary inflammation and fibrosis. *Cell* **96**, 319–328 (1999).
- Mu, D. *et al.* The integrin $\alpha_v\beta_8$ mediates epithelial homeostasis through MT1-MMP-dependent activation of TGF- β 1. *J. Cell Biol.* **157**, 493–507 (2002).
- Yang, Z. *et al.* Absence of integrin-mediated TGF β 1 activation *in vivo* recapitulates the phenotype of TGF β 1-null mice. *J. Cell Biol.* **176**, 787–793 (2007).
- Zhu, J. *et al.* β 8 integrins are required for vascular morphogenesis in mouse embryos. *Development* **129**, 2891–2903 (2002).
- Proctor, J. M., Zang, K., Wang, D., Wang, R. & Reichardt, L. F. Vascular development of the brain requires β 8 integrin expression in the neuroepithelium. *J. Neurosci.* **25**, 9940–9948 (2005).
- de Boer, J. *et al.* Transgenic mice with hematopoietic and lymphoid specific expression of Cre. *Eur. J. Immunol.* **33**, 314–325 (2003).
- Gorelik, L. & Flavell, R. A. Abrogation of TGF β signaling in T cells leads to spontaneous T cell differentiation and autoimmune disease. *Immunity* **12**, 171–181 (2000).
- Kim, B. G. *et al.* Smad4 signalling in T cells is required for suppression of gastrointestinal cancer. *Nature* **441**, 1015–1019 (2006).
- Bohr, U. R. *et al.* Prevalence and spread of enterohepatic *Helicobacter* species in mice reared in a specific-pathogen-free animal facility. *J. Clin. Microbiol.* **44**, 738–742 (2006).
- Taylor, N. S., Xu, S., Nambiar, P., Dewhirst, F. E. & Fox, J. G. Enterohepatic *Helicobacter* species are prevalent in mice obtained from commercial and academic institutions in Asia, Europe, and North America. *J. Clin. Microbiol.* **45**, 2166–2172 (2007).
- Whary, M. T. & Fox, J. G. Detection, eradication, and research implications of *Helicobacter* infections in laboratory rodents. *Lab Anim. (NY)* **35**, 25–36 (2006).
- Strober, W., Fuss, I. & Mannon, P. The fundamental basis of inflammatory bowel disease. *J. Clin. Invest.* **117**, 514–521 (2007).
- Lee, P. P. *et al.* A critical role for Dnmt1 and DNA methylation in T cell development, function, and survival. *Immunity* **15**, 763–774 (2001).
- Caton, M., L. Smith-Raska M. R. & Reizis, B. Notch-RBP-J signaling controls the homeostasis of CD8⁺ dendritic cells in the spleen. *J. Exp. Med.* **204**, 1653–1664 (2007).
- Sakaguchi, S. *et al.* Foxp3⁺ CD25⁺ CD4⁺ natural regulatory T cells in dominant self-tolerance and autoimmune disease. *Immunol. Rev.* **212**, 8–27 (2006).
- Chen, W. *et al.* Conversion of peripheral CD4⁺CD25⁺ naive T cells to CD4⁺CD25⁺ regulatory T cells by TGF- β induction of transcription factor Foxp3. *J. Exp. Med.* **198**, 1875–1886 (2003).
- Nakamura, K. *et al.* TGF- β 1 plays an important role in the mechanism of CD4⁺CD25⁺ regulatory T cell activity in both humans and mice. *J. Immunol.* **172**, 834–842 (2004).
- Fahlen, L. *et al.* T cells that cannot respond to TGF- β escape control by CD4⁺CD25⁺ regulatory T cells. *J. Exp. Med.* **201**, 737–746 (2005).
- Marie, J. C., Lettierio, J. J., Gavin, M. & Rudensky, A. Y. TGF- β 1 maintains suppressor function and Foxp3 expression in CD4⁺CD25⁺ regulatory T cells. *J. Exp. Med.* **201**, 1061–1067 (2005).
- Fontenot, J. D. *et al.* Regulatory T cell lineage specification by the forkhead transcription factor Foxp3. *Immunity* **22**, 329–341 (2005).
- Bluestone, J. A. & Abbas, A. K. Natural versus adaptive regulatory T cells. *Nature Rev. Immunol.* **3**, 253–257 (2003).
- Bluestone, J. A. & Tang, Q. How do CD4⁺CD25⁺ regulatory T cells control autoimmunity? *Curr. Opin. Immunol.* **17**, 638–642 (2005).
- Li, M. O., Wan, Y. Y., Sanjabi, S., Robertson, A. K. & Flavell, R. A. Transforming growth factor- β regulation of immune responses. *Annu. Rev. Immunol.* **24**, 99–146 (2006).
- Lefrançois, L. & Lycke, N. Isolation of mouse small intestine intraepithelial lymphocytes, Peyer's patch, and lamina propria cells. *Curr. Protocols Immunol. Unit* **3.19** doi:10.1002/0471142735.im0319s17 (2001).

30. Abe, M. *et al.* An assay for transforming growth factor- β using cells transfected with a plasminogen activator inhibitor-1 promoter-luciferase construct. *Anal. Biochem.* **216**, 276–284 (1994).

Supplementary Information is linked to the online version of the paper at www.nature.com/nature.

Acknowledgements We thank D. Kioussis for providing the Vav1-Cre mice and A. Rudensky for providing the GFP–Foxp3 mice. This work was supported by grants from the National Heart, Lung and Blood Institute (to D.S.), the National Institute of Allergy and Infectious Diseases (to J.A.B and B.R.) and funds from the Sandler Program for Asthma Research (to B.R.). M.A.T. was the recipient of an American Lung Association Research Fellowship.

Author Contributions M.A.T. performed all of the experiments described and wrote most of the manuscript; B.R. generated the CD11c-Cre mice and contributed to the design and interpretation of studies using those mice; A.C.M. contributed to the studies of colonic inflammation, colonic T_R cells and designed and performed

all of the qPCR studies described; E.M. helped design, perform and interpret the *in vitro* T_R cell induction assays; Q.T. helped to design, perform and interpret the studies analysing the nature of the immunological defects described; J.M.P. generated the conditional *Itgb8* knockout mice and helped in the design and interpretation of genotyping assays and crosses to Cre-expressing lines; Y.W., X.B. and X.H. helped in the design, performance and interpretation of all of the studies of tissue morphology; L.F.R. oversaw the generation of the conditional *Itgb8* knockout mice and contributed to the design and interpretation of studies using these animals; J.A.B. contributed to the design and interpretation of the studies characterizing the immunological abnormalities seen and analysing the contribution of T_R cells; D.S. oversaw the design and interpretation of all studies described and oversaw writing of the manuscript.

Author Information Reprints and permissions information is available at www.nature.com/reprints. The authors declare no competing financial interests. Correspondence and requests for materials should be addressed to D.S. (dean.sheppard@ucsf.edu).

METHODS

Cell isolation/purification. Cells were purified by positive selection using magnetic beads (Miltenyi Biotec) (typically >90% purity), or by sorting on a MoFlo cell sorter (DAKO) (typically >98% purity). CD11c⁺ dendritic cells were purified from spleens by digestion with collagenase D (2 mg ml⁻¹, Roche) and DNase I (50 U ml⁻¹, Roche) for 30 min at 37 °C, and subsequent positive selection using anti-CD11c magnetic beads (Miltenyi Biotec). Dendritic cells used were typically 90–95% pure.

Flow cytometry. For extracellular flow cytometry, cells were re-suspended in 100 µl PBS plus 4% FCS, containing 5 µg ml⁻¹ Fc block (BD Pharmingen), and incubated with 1.5 µg ml⁻¹ antibody for 20 min on ice. Cells were analysed on a FACS Calibur or FACSort (BD Pharmingen). Data were analysed using Flow-Jo (Treestar).

For intracellular flow cytometry, extracellular antigens were stained as above, and cells fixed and permeabilized using fixation/permeabilization buffer (eBioscience) for 30 min at 4 °C. Cells were washed twice and stained for 30 min at 4 °C with antibodies diluted in permeabilization buffer (at 1.5 µg ml⁻¹). Cells were analysed as described above.

The following antibodies were used in experiments, and were purchased from BD Pharmingen or eBioscience unless otherwise stated: anti-CD4 (clone RM4-5), anti-CD8 (clone 53-6.7), anti-CD62L (clone MEL-14), anti-CD44 (clone IM7), anti-IL4 (clone 11B11), anti-IFN-γ (clone XMG1.2), anti-B220 (clone RA3-6B2), anti-CD86 (clone GL1) and anti-MHC II (clone NIMR, Southern Biotech).

Primers used for RT-PCR and qRT-PCR. To detect expression of mouse *Itgb8* RNA by RT-PCR, the following primers were used: forward, 5'-CATTCTTGATCGGGTTGCTT-3'; reverse, 5'-CAGGCTTTCTCGTCGGTAG-3'. To detect mouse *Itgb8* RNA by qRT-PCR, the following primers were used: forward, 5'-CTGAAGAAATACCCCGTGGA-3'; reverse, 5'-AGACTGTATGCCTCCCAT-3'.

ELISA. For detection of auto-antibodies (against double-stranded DNA and ribonuclear proteins), mouse serum was diluted and analysed using a REAADS ANA ELISA kit (Corgenix) according to the manufacturer's instructions.

Levels of IgG1, IgG2a, IgG2b, IgG3, IgA and IgM in mouse serum were analysed using a Clonotyping ELISA kit (Southern Biotech) according to the manufacturer's instructions. Levels of IgE in mouse serum were measured by sandwich ELISA, using anti-mouse IgE as a capture antibody (clone R35-72, BD Pharmingen, 2 µg ml⁻¹ coating concentration) and biotinylated anti-mouse IgE antibody (clone R35-118, BD Pharmingen, 1 µg ml⁻¹) as a detection antibody. Wells were incubated with streptavidin-HRP (BD Pharmingen, 1:1,000), and wells were subsequently developed using TMB solution (BD Pharmingen), and absorbance read at 450 nm.

For detection of IL-4 and IFN-γ by ELISA, all antibodies were purchased from eBioscience. Anti-IL-4 antibody (clone 11B11, 2 µg ml⁻¹) or anti-IFN-γ antibody (clone AN-18, 1 µg ml⁻¹) was coated in 96-well ELISA plates. Supernatant from activated splenocytes (see below) was diluted and added to wells. Cytokine was detected by incubating wells with biotinylated anti-IL-4 antibody (clone BVD6-24G2, 1 µg ml⁻¹) or biotinylated anti-IFN-γ antibody (clone R4-6A2, 1 µg ml⁻¹) followed by streptavidin-HRP (BD Pharmingen, 1:1,000 dilution). Wells were developed with TMB solution, and absorbance measured at 450 nm. Concentrations of immunoglobulin/cytokine were calculated from standard curves using purified cytokine or specific immunoglobulin isotypes.

Regulatory T-cell induction assay. CD4⁺GFP-Foxp3⁻ T cells from GFP-Foxp3 mice²⁵ were purified to greater than 99.8% purity on a MoFlo sorter. Splenic CD11c⁺ dendritic cells from 2–4-month-old control or (*Vav1-cre*)/*Itgb8*^{fl/fl} mice were purified as described above. A total of 2,500 dendritic cells were incubated with 50,000 CD4⁺GFP-Foxp3⁻ T cells in the presence of 1 µg ml⁻¹ anti-CD3 antibody (clone 2c11, BD Pharmingen) and either 40 µg ml⁻¹ mIgG (Sigma), 40 µg ml⁻¹ anti-TGF-β antibody (clone 1d11, hybridoma purchased from ATCC), or 2 ng ml⁻¹ active TGF-β (R&D Systems). After 72 h, cells were stained with CD4 antibody, and analysed by flow cytometry for CD4⁺GFP-Foxp3⁺ cells (dead cells, identified by positive staining for 7-amino-actinomycin D, were excluded from analysis).

TGF-β activation assay. To determine TGF-β activity by dendritic cells, purified dendritic cells were cultured for 72 h in 96-well plates. A total of 100 ng ml⁻¹ lipopolysaccharide was added for the last 48 h, and mink lung epithelial cells stably transfected with a plasmid containing firefly luciferase cDNA downstream of a TGF-β-sensitive portion of the plasminogen activator inhibitor 1 promoter³⁰ were added for the last 24 h. TGF-β activity was calculated as the difference in luciferase activity between untreated wells and wells treated with a blocking antibody to TGF-β (1D11).

Colon lamina propria cell preparation. Colonic lamina propria lymphocytes were isolated using a previously described method²⁹, with slight modification. Briefly, colons were extracted and placed on ice in CMF buffer (Hank's Balanced Salt Solution (HBSS) plus 2% FCS plus 15 mM HEPES, pH 7.4). The colon was washed, chopped into small (0.5 mm) pieces with a razor blade, and washed six more times with ice-cold CMF. Colon pieces were then incubated with CMF plus 5 mM EDTA for 4 × 15 min at 20 °C with gentle stirring (100 r.p.m.) to remove intraepithelial lymphocytes. Remaining colon pieces were washed with complete RPMI (RPMI plus penicillin and streptomycin plus 10% FCS plus 10 mM HEPES) to remove residual EDTA, then incubated for 3 × 1 h in complete RPMI plus 0.5 mg ml⁻¹ collagenase D (Roche). Supernatants containing lamina propria cells were collected and analysed by flow cytometry for CD4 and Foxp3. Live cells were gated using forward and side scatter.

LETTERS

Insulin modulates gluconeogenesis by inhibition of the coactivator TORC2

Renaud Dentin^{1*}, Yi Liu^{1*}, Seung-Hoi Koo², Susan Hedrick¹, Thomas Vargas¹, Jose Heredia¹, John Yates III³ & Marc Montminy¹

During feeding, increases in circulating pancreatic insulin inhibit hepatic glucose output through the activation of the Ser/Thr kinase AKT and subsequent phosphorylation of the forkhead transcription factor FOXO1 (refs 1–3). Under fasting conditions, FOXO1 increases gluconeogenic gene expression in concert with the cAMP responsive coactivator TORC2 (refs 4–8). In response to pancreatic glucagon, TORC2 is de-phosphorylated at Ser 171 and transported to the nucleus, in which it stimulates the gluconeogenic programme by binding to CREB. Here we show in mice that insulin inhibits gluconeogenic gene expression during re-feeding by promoting the phosphorylation and ubiquitin-dependent degradation of TORC2. Insulin disrupts TORC2 activity by induction of the Ser/Thr kinase SIK2, which we show here undergoes AKT2-mediated phosphorylation at Ser 358. Activated SIK2 in turn stimulated the Ser 171 phosphorylation and cytoplasmic translocation of TORC2. Phosphorylated TORC2 was degraded by the 26S proteasome during re-feeding through an association with COP1, a substrate receptor for an E3 ligase complex that promoted TORC2 ubiquitination at Lys 628. Because TORC2 protein levels and activity were increased in diabetes owing to a block in TORC2 phosphorylation, our results point to an important role for this pathway in the maintenance of glucose homeostasis.

We monitored the activity of the TORC2 (also known as CRTC2) pathway in liver by *in vivo* imaging with a cAMP-responsive adenovirus—containing cAMP responsive elements (CREs) upstream of a minimal promoter—CRE-luciferase reporter (*Ad-CRE-Luc*)⁹. Fasting increased hepatic *Ad-CRE-Luc* activity 20-fold over that of re-fed mice (Fig. 1a; Supplementary Figs 1, 2). Amounts of de-phosphorylated and therefore active TORC2 were correspondingly elevated in livers of fasted mice, whereas re-feeding promoted TORC2 re-phosphorylation and degradation (Fig. 1b; Supplementary Fig. 2). RNA interference (RNAi)-mediated knockdown of TORC2 reduced *Ad-CRE-Luc* but not CREB-independent (*Ad-Rsv*(Rous sarcoma virus)-*Luc*) reporter activity in the liver (Fig. 1c; Supplementary Fig. 3)⁸. Moreover, gluconeogenic gene expression (*Pepck/Pck2*, *G6Pase/G6pc*) and fasting blood-glucose levels were decreased in *Ad-TORC2i* (adenovirus expressing TORC2 RNAi) mice compared to controls, indicating that TORC2 degradation during re-feeding may be sufficient to attenuate the gluconeogenic programme (Fig. 1d; Supplementary Fig. 4).

Having seen that hepatic TORC2 protein levels are downregulated during re-feeding, we wondered whether TORC2 activity is increased in insulin resistance. Consistent with their elevations in gluconeogenic gene expression and blood glucose concentrations, *db/db* diabetic mice had higher levels of *Ad-CRE-Luc* reporter activity and TORC2 protein in the liver, and re-feeding did not trigger

TORC2 phosphorylation or degradation (Fig. 1e, f; Supplementary Fig. 5).

On the basis of their roles in regulating hepatic glucose production, glucagon and insulin would be expected to modulate TORC2 activity in the liver. Intraperitoneal administration of glucagon stimulated hepatic *Ad-CRE-Luc* activity in mice; these effects were reversed by subsequent exposure to insulin, which also promoted the phosphorylation and degradation of hepatic TORC2 in fasted mice (Fig. 1g, h). Indeed, sequential exposure of cultured primary hepatocytes to forskolin and insulin (FSK/INS) also triggered the disappearance of TORC2 protein, whereas insulin alone did not (Supplementary Fig. 6). Indicating a potential role for ubiquitin-dependent degradation, treatment with the proteasome inhibitor MG132 blocked effects of FSK/INS on TORC2. Notably, exposure to the tris-phosphate kinase (PIK3) inhibitor LY294002 also disrupted TORC2 degradation, pointing to the involvement of PIK3 or other components of the insulin pathway such as AKT (Supplementary Fig. 7).

If insulin inhibits TORC2 activity by Ser 171 phosphorylation, then mutant TORC2(S171A) should be resistant to these effects. Supporting this idea, *Ad-CRE-Luc* activity, gluconeogenic gene expression, and blood-glucose concentrations were elevated in *Ad-TORC2(S171A)* mice relative to *Ad-TORC2* mice during re-feeding (Fig. 2a; Supplementary Fig. 8). Correspondingly, *Ad-TORC2(S171A)* was not degraded during re-feeding compared with wild-type *Ad-TORC2* (Fig. 2b; Supplementary Fig. 9). Indeed, *Ad-TORC2(S171A)* was similarly active in primary hepatocytes exposed to FSK/INS (Supplementary Fig. 10).

Previously, the salt inducible kinase 2 (SIK2; also known as SNF1LK2) has been found to inhibit TORC2 activity by promoting its Ser 171 phosphorylation¹⁰, prompting us to test the role of this kinase in the liver. RNAi-mediated knockdown of SIK2 (*Ad-SIK2i*) increased *Ad-CRE-Luc* activity during re-feeding compared with *Ad-USi*(unspecific RNAi) (Fig. 2c; Supplementary Fig. 11). TORC2 (Ser 171) phosphorylation was also disrupted in re-fed *Ad-SIK2i* mice, and TORC2 protein levels were consequently elevated (Fig. 2d). As a result, gluconeogenic gene expression and blood glucose concentrations were upregulated in *Ad-SIK2i* animals (Fig. 2c; Supplementary Figs 11, 12). *Ad-SIK2i* also increased TORC2 activity in primary hepatocytes; these effects were reversed by expression of an RNAi-resistant SIK2 (Supplementary Figs 13, 14).

We noticed that SIK2 contains a single conserved AKT phosphorylation site (RQRRPS) at Ser 358. Indeed, exposure of HEK293T cells to insulin increased the phosphorylation of wild-type but not the SIK2(S358A) mutant, by western blot assay with phospho-AKT substrate antiserum and by metabolic labelling with inorganic ³²P; these

¹Peptide Biology Laboratories, Salk Institute For Biological Studies, La Jolla, California 92037, USA. ²Department of Molecular Cell Biology, Sungkyunkwan University School of Medicine, 300 Chunchun-dong, Jangnan-gu, Suwon, 440-746, Gyeonggi-do, Korea. ³The Scripps Research Institute, 10550 North Torrey Pines Road, La Jolla, California 92037, USA. *These authors contributed equally to this work.

effects were blocked by addition of LY294002 inhibitor (Fig. 2e; Supplementary Figs 15, 16). Moreover, active recombinant AKT2 protein also catalysed wild-type but not SIK2(S358A) phosphorylation at a single site *in vitro* by phospho-amino-acid analysis and phospho-tryptic mapping (Supplementary Fig. 17).

To determine whether Ser 358 phosphorylation increases SIK2 catalytic activity, we performed *in vitro* kinase assays on SIK2 immunoprecipitates. Exposure to insulin increased wild-type SIK2 but not SIK2(S358A) auto-phosphorylation activity *in vitro* (Fig. 2f). Correspondingly, wild-type SIK2 was also more active in promoting TORC2 phosphorylation *in vitro*, indicating that insulin modulates TORC2 activity through the AKT-mediated phosphorylation of SIK2 at Ser 358.

Because phosphorylation often targets nuclear proteins for degradation by triggering their cytoplasmic export and polyubiquitination^{11–13}, we examined effects of fasting and feeding signals on TORC2 shuttling

in primary hepatocytes. Under basal conditions, TORC2 protein was phosphorylated and associated with 14-3-3 proteins in the cytoplasm; exposure to FSK promoted TORC2 dephosphorylation, dissociation from 14-3-3 proteins, and nuclear translocation (Fig. 3a; Supplementary Figs 18, 19)⁸. Exposure to insulin alone increased TORC2 phosphorylation and 14-3-3 binding; but it promoted TORC2 cytoplasmic export and degradation in cells exposed previously to FSK.

Consistent with these changes, sequential exposure of primary hepatocytes to glucagon and insulin stimulated TORC2 poly-ubiquitination

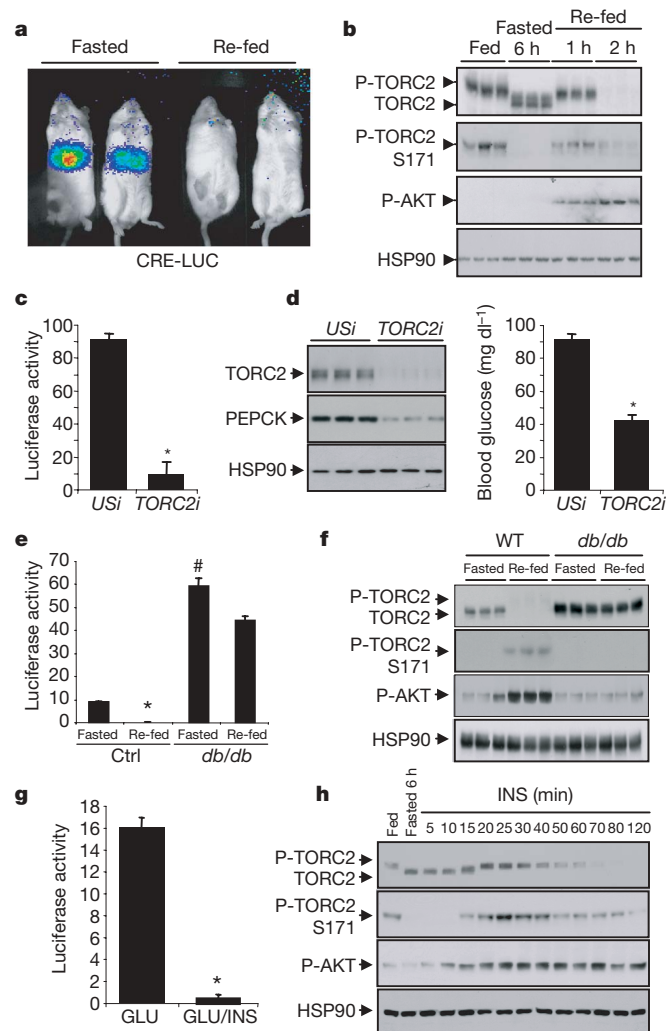


Figure 1 | Insulin inhibits TORC2 activity during re-feeding. **a**, Live imaging of hepatic CRE-luciferase (*Ad-CRE-Luc*) activity in fasted or re-fed mice. **b**, Immunoblot of phospho (Ser 171) and total hepatic TORC2 protein in *ad libitum* fed, fasted and re-fed mice ($n = 3$). **c**, Effect of control (*USi*) or *Ad-TORC2* RNAi on hepatic *Ad-CRE-Luc* activity ($*P < 0.001$; $n = 3$). **d**, Left panel, immunoblot showing effect of *Ad-TORC2i* on hepatic TORC2 and PEPCK proteins in fasted mice. Right panel, fasting glucose levels in *Ad-USi* and *Ad-TORC2i* mice ($*P < 0.02$; $n = 7$). **e**, *Ad-CRE-Luc* activity in wild-type and *db/db* diabetic mice under fasting or re-fed conditions. ($*P < 0.05$; $\#P < 0.01$; $n = 3$). **f**, Immunoblot of TORC2 in *db/db* and wild-type mice. **g**, Effect of glucagon (GLU) injection (i.p.), alone or followed by insulin (GLU/INS), on *Ad-CRE-Luc* activity. ($*P < 0.001$; $n = 3$). **h**, Immunoblot of TORC2 in fasted mice injected i.p. with INS. For **a**, **c–e** and **g**, data are means \pm s.e.m.

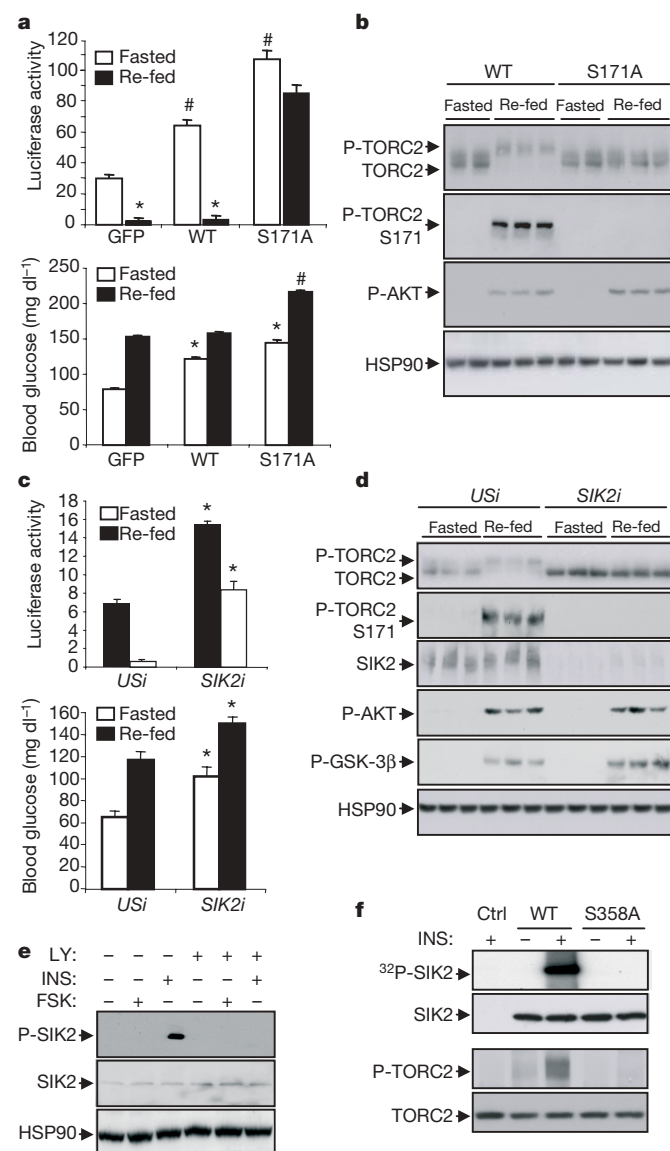


Figure 2 | SIK2 promotes TORC2 phosphorylation during re-feeding. **a**, *Ad-CRE-Luc* activity (upper panel) and blood glucose levels (lower panel) in mice expressing *Ad-TORC2*, mutant *Ad-TORC2(S171A)*, or green fluorescent protein (GFP) ($*P < 0.05$; $\#P < 0.01$). **b**, Immunoblot showing TORC2 protein amounts in mice expressing *Ad-TORC2* or *Ad-TORC2(S171A)*. **c**, Effect of *Ad-USi* or *Ad-SIK2i* on *Ad-CRE-Luc* activity (upper panel) and blood glucose levels (lower panel) in *Ad-USi* or *Ad-SIK2i* mice ($*P < 0.05$; $n = 3$). **d**, Immunoblot of phospho (Ser 171) and total TORC2 levels in *Ad-USi* or *Ad-SIK2i* mice. **e**, Immunoblot of SIK2 recovered from immunoprecipitates of anti-phospho AKT substrate antiserum prepared from primary hepatocytes exposed to INS or FSK. Effect of LY294002 inhibitor is shown. **f**, Upper panel, *in vitro* kinase assay with immunoprecipitates of wild-type or mutant SIK2(S358A) prepared from HEK293T cells that were exposed to INS (1 h) or vehicle. Lower panel, *in vitro* phosphorylation of TORC2 by SIK2; immunoprecipitates prepared from control or INS-treated cells as above (for **a** and **c**, data are means \pm s.e.m.). Ctrl, control.

in the cytoplasm, but only mono-ubiquitination in the nucleus (Fig. 3b). Indeed, TORC2 cytoplasmic export seemed critical for its polyubiquitination and degradation, because the constitutively nuclear and degradation-resistant TORC2(S171A) protein was selectively mono-ubiquitinated.

In proteomic studies to identify TORC2-interacting proteins, we recovered constitutive photomorphogenic protein-1 (COP1, also known as RFWD2) and DNA damage binding protein 1 (DDB1), components of an E3 ubiquitin ligase complex that recognizes substrates containing the consensus motif (D/E-D/E-X-X-V-P)^{14–17} (Supplementary Fig. 20). We confirmed the TORC2–COP1 interaction in co-immunoprecipitates of primary hepatocytes exposed to FSK/INS (Fig. 3c). TORC2 contains a conserved COP1 recognition motif (amino acids 209–215; EMDPKVP) that resembles a COP1-binding site in TRB3 (ref. 18; Supplementary Fig. 21). Indeed, mutation of Val and Pro residues in this motif (V214A, P215A) blocked the association of TORC2 with COP1 (Fig. 3d, left).

We tested the importance of COP1 in modulating TORC2 protein levels. *Ad-COP1* expression triggered TORC2 degradation and reduced glucose output from primary hepatocytes exposed to FSK (Fig. 3d, right; Supplementary Fig. 22). But COP1 was ineffective under basal conditions, suggesting that TORC2 nuclear import is

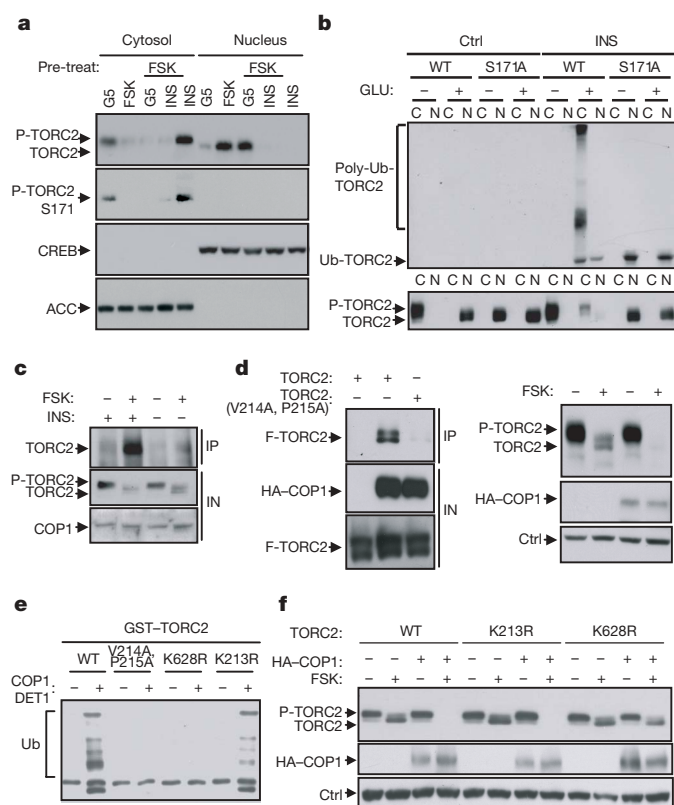


Figure 3 | COP1 promotes the ubiquitination and degradation of TORC2. **a**, Immunoblot of TORC2 in cytosolic and nuclear fractions from primary hepatocytes exposed to FSK, FSK/INS, or INS alone. **b**, Immunoblot of TORC2 proteins recovered from anti-ubiquitin immunoprecipitations of primary hepatocytes expressing *Ad-TORC2* or *Ad-TORC2(S171A)*. Sequential treatment with glucagon (GLU) and insulin (INS) indicated. Cytosolic (C) and nuclear (N) fractions labelled. Total amounts of TORC2 (bottom) shown. **c**, Immunoblot of TORC2 recovered from immunoprecipitations of COP1 in hepatocytes exposed to FSK and INS, as above. **d**, Left panel, immunoblot of wild-type and mutant TORC2(V214A, P215A) recovered from HA-COP1 immunoprecipitates. Right panel, effect of *Ad-COP1* on TORC2 protein amounts in hepatocytes exposed to FSK, as indicated. F, forskolin. **e**, Effect of COP1 and DET1 on *in vitro* ubiquitination of wild-type and mutant GST-TORC2 proteins. **f**, Immunoblot of wild-type and mutant TORC2 proteins in HEK293T cells co-transfected with HA-COP1 and exposed to FSK, as indicated.

required for its subsequent degradation by COP1. Indeed, COP1 protein was detected primarily in nuclear fractions by western blot analysis¹⁹ (Supplementary Fig. 21).

We performed mass spectrometry studies to characterize residues in TORC2 that undergo COP1-mediated ubiquitination. This analysis revealed one major (Lys 628) and one minor (Lys 213) site on TORC2 (ref. 20; Supplementary Fig. 23). To evaluate the relative importance of these sites, we performed *in vitro* ubiquitination studies. In the presence of relevant cofactors (DDB1, DET1), COP1 promoted the ubiquitination of wild-type but not COP1-interaction defective VP/AA TORC2 (Fig. 3e). COP1 also stimulated the ubiquitination of TORC2(K213R) but had no effect on TORC2(K628R), suggesting an important role for Lys 628 in this regard (Fig. 3e).

Consistent with its effects on TORC2 ubiquitination, COP1 enhanced the degradation of wild-type and TORC2(K213R) but not TORC2(K628R) or TORC2(V214A, P215A) proteins in HEK293T cells exposed to FSK (Fig. 3f; Supplementary Fig. 23). The K628R mutation in TORC2 seems specific for ubiquitination because TORC2(K628R) translocated to the nucleus and associated with COP1 comparably to wild-type TORC2, following exposure of

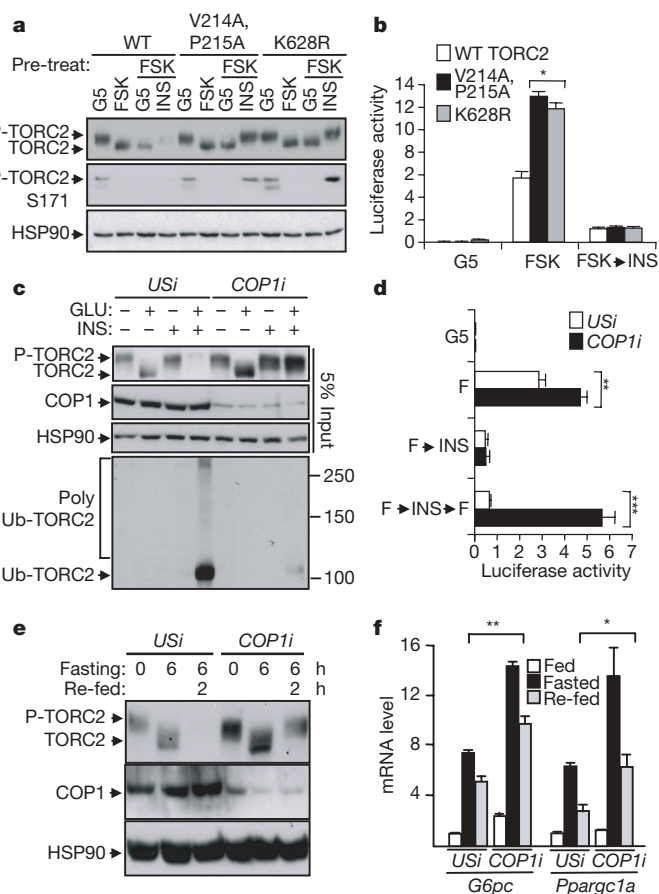


Figure 4 | TORC2 degradation by COP1 during re-feeding is required for glucose homeostasis. **a**, Immunoblot of wild-type and ubiquitination-defective (V214A, P215A; K628R) TORC2 proteins in hepatocytes exposed to FSK followed by FSK, INS or control medium (G5). **b**, Effect of wild-type and mutant TORC2 proteins on *Ad-CRE-Luc* activity in primary hepatocytes exposed to FSK and INS, as above. (* $P < 0.05$). **c**, Immunoblot showing effect of *Ad-USi* or *Ad-COP1i* on TORC2 ubiquitination and degradation in hepatocytes exposed sequentially to GLU and INS. **d**, Effect of FSK on *Ad-CRE-Luc* activity in *Ad-USi* and *Ad-COP1i* cells previously exposed to re-feeding signals (F→INS→F). Effect of FSK (F) or re-feeding (F→INS) relative to control (G5) is shown. (** $P < 0.002$; *** $P < 0.001$). **e**, Immunoblot of liver lysates showing the effect of *Ad-COP1i* on TORC2 degradation under *ad libitum* fed, fasted or re-fed conditions. **f**, G6Pase (*G6pa*) and PGC-1 α (*Ppargc1a*) hepatic mRNA levels in *Ad-USi* and *Ad-COP1i* mice (* $P < 0.05$; ** $P < 0.01$; $n = 3$; for **b**, **d**, **f**, data are means \pm s.e.m.).

HEK293T cells to FSK (Supplementary Figs 24, 25). Notably, Lys 628 is highly conserved in all mammalian TORC family members (Supplementary Fig. 26).

We suspected that ubiquitin-defective TORC2 proteins would also be resistant to degradation by re-feeding signals. Indeed, exposure of primary hepatocytes to FSK/INS decreased amounts of wild-type but not TORC2(K628R) or TORC2(V214A, P215A) protein (Fig. 4a). TORC2(K628R) and TORC2(V214A, P215A) were also more active in stimulating *Ad-CRE-Luc* activity, gluconeogenic gene expression, and glucose output from primary hepatocytes relative to wild-type TORC2 (Fig. 4b; Supplementary Fig. 27). Consistent with their ability to undergo Ser 171 phosphorylation and cytoplasmic export, however, both TORC2(K628R) and TORC2(V214A, P215A) were downregulated following insulin treatment.

On the basis of its ability to promote TORC2 degradation during re-feeding, COP1 may regulate the amplitude or timing of the gluconeogenic response to subsequent rounds of fasting. Supporting this notion, RNAi-mediated knockdown of COP1 reduced TORC2 ubiquitination and correspondingly increased amounts of TORC2 protein in primary hepatocytes exposed sequentially to glucagon and insulin (Fig. 4c; Supplementary Fig. 28). Consistent with a selective effect of *Ad-COP1i* on TORC2 degradation, exposure to the protein synthesis inhibitor cycloheximide did not block the effect of *Ad-COP1i* on TORC2 protein amounts (Supplementary Fig. 28). *Ad-CRE-Luc* activity and gluconeogenic gene expression were also elevated in *Ad-COP1i* hepatocytes, particularly in cells that had been previously treated with FSK/INS—when TORC2 is degraded—and then re-exposed to FSK (Fig. 4d; Supplementary Fig. 28).

We examined the role of COP1 in promoting glucose homeostasis *in vivo*. Similar to hepatocytes, *Ad-COP1i* mice had lower levels of ubiquitinated TORC2 and higher total amounts of hepatic TORC2 protein compared with *Ad-USi* mice (Fig. 4e; Supplementary Fig. 29). Gluconeogenic gene expression and blood glucose levels were also elevated in *Ad-COP1i* mice, revealing the importance of COP1 in this setting (Fig. 4f; Supplementary Fig. 29).

Glucose levels are maintained within a narrow range in mammals through counter-regulatory effects of pancreatic hormones on hepatic gluconeogenesis. We found that insulin suppresses hepatic glucose production during re-feeding by triggering the SIK2-mediated phosphorylation and COP1-dependent degradation of TORC2 (Supplementary Fig. 30). The inhibition of TORC2 in the re-fed state probably protects against further increases in blood glucose due to inappropriate induction of the gluconeogenic programme. By reducing the cellular pool of TORC2, COP1 may also determine the timing and amplitude of the gluconeogenic response with subsequent fasting. Future studies should reveal the extent to which defects in either SIK2 or COP1 signalling also contributes to insulin resistance and diabetes in humans.

METHODS SUMMARY

Adenoviruses were delivered by tail vein injection into 6–12-week-old male mice. For nutritional studies, mice were fasted for 6 h and then re-fed for 2 h. For *in vivo* imaging of adenoviral CRE-luciferase activity, mice were injected intraperitoneally (i.p.) with firefly D-luciferin. Anaesthetized mice were imaged and analysed using an IVIS 100 Imaging System (Xenogen). Luciferase activity was normalized to adenoviral β -galactosidase (β -gal) expression. Mouse hepatocytes were harvested, cultured and infected with adenoviruses or transfected with expression plasmids, as described²¹. Glucose production from primary cultured hepatocytes was determined enzymatically. Mass spectrometry studies were performed on immunoprecipitates of overexpressed TORC2 prepared from HEK293T cells, as reported¹⁸. *In vitro* ubiquitination assays on wild-type and mutant TORC2 proteins were performed using overexpressed COP1 and DET1 proteins in reactions containing ubiquitin, UbcH5b (also known as UBE2D2) and rabbit E1. To detect endogenous TORC2 ubiquitination, immunoprecipitates of anti-ubiquitin were prepared from primary hepatocyte or liver lysates followed by immunoblotting with anti-TORC2 serum. Metabolic labelling and phospho-tryptic mapping studies of TORC2 were performed as described¹⁰.

Full Methods and any associated references are available in the online version of the paper at www.nature.com/nature.

Received 22 March; accepted 27 July 2007.

Published online 5 September 2007.

1. Cho, H. *et al.* Insulin resistance and a diabetes mellitus-like syndrome in mice lacking the protein kinase Akt2 (PKB β). *Science* **292**, 1728–1731 (2001).
2. Nakae, J., Park, B. C. & Accili, D. Insulin stimulates phosphorylation of the forkhead transcription factor FKHR on serine 253 through a Wortmannin-sensitive pathway. *J. Biol. Chem.* **274**, 15982–15985 (1999).
3. Taniguchi, C. M. *et al.* Divergent regulation of hepatic glucose and lipid metabolism by phosphoinositide 3-kinase via Akt and PKC λ/ζ . *Cell Metab.* **3**, 343–353 (2006).
4. Herzig, S. *et al.* CREB regulates hepatic gluconeogenesis via the co-activator PGC-1. *Nature* **413**, 179–183 (2001).
5. Puigserver, P. *et al.* Insulin-regulated hepatic gluconeogenesis through FOXO1-PGC-1 α interaction. *Nature* **423**, 550–555 (2003).
6. Matsuzaki, H., Daitoku, H., Hatta, M., Tanaka, K. & Fukamizu, A. Insulin-induced phosphorylation of FKHR (Foxo1) targets to proteasomal degradation. *Proc. Natl Acad. Sci. USA* **100**, 11285–11290 (2003).
7. Cheng, A. & Saltiel, A. R. More TORC for the gluconeogenic engine. *Bioessays* **28**, 231–234 (2006).
8. Koo, S. H. *et al.* The CREB coactivator TORC2 is a key regulator of fasting glucose metabolism. *Nature* **437**, 1109–1111 (2005).
9. Suzuki, M., Singh, R. N. & Crystal, R. G. Regulatable promoters for use in gene therapy applications: modification of the 5'-flanking region of the *CFTR* gene with multiple cAMP response elements to support basal, low-level gene expression that can be upregulated by exogenous agents that raise intracellular levels of cAMP. *Hum. Gene Ther.* **7**, 1883–1893 (1996).
10. Screaton, R. A. *et al.* The CREB coactivator TORC2 functions as a calcium- and cAMP-sensitive coincidence detector. *Cell* **119**, 61–74 (2004).
11. Groulx, I. & Lee, S. Oxygen-dependent ubiquitination and degradation of hypoxia-inducible factor requires nuclear-cytoplasmic trafficking of the von Hippel-Lindau tumor suppressor protein. *Mol. Cell. Biol.* **22**, 5319–5336 (2002).
12. O'Keefe, K., Li, H. & Zhang, Y. Nucleocytoplasmic shuttling of p53 is essential for MDM2-mediated cytoplasmic degradation but not ubiquitination. *Mol. Cell. Biol.* **23**, 6396–6405 (2003).
13. Itahana, Y., Yeh, E. T. & Zhang, Y. Nucleocytoplasmic shuttling modulates activity and ubiquitination-dependent turnover of SUMO-specific protease 2. *Mol. Cell. Biol.* **26**, 4675–4689 (2006).
14. Holm, M., Hardtke, C. S., Gaudet, R. & Deng, X. W. Identification of a structural motif that confers specific interaction with the WD40 repeat domain of Arabidopsis COP1. *EMBO J.* **20**, 118–127 (2001).
15. Bianchi, E. *et al.* Characterization of human constitutive photomorphogenesis protein 1, a RING finger ubiquitin ligase that interacts with Jun transcription factors and modulates their transcriptional activity. *J. Biol. Chem.* **278**, 19682–19690 (2003).
16. Wertz, I. E. *et al.* Human De-etiolated-1 regulates c-Jun by assembling a CUL4A ubiquitin ligase. *Science* **303**, 1371–1374 (2004).
17. Dornan, D. *et al.* The ubiquitin ligase COP1 is a critical negative regulator of p53. *Nature* **429**, 86–92 (2004).
18. Qi, L. *et al.* TRB3 links the E3 ubiquitin ligase COP1 to lipid metabolism. *Science* **312**, 1763–1766 (2006).
19. Dornan, D. *et al.* ATM engages autodegradation of the E3 ubiquitin ligase COP1 after DNA damage. *Science* **313**, 1122–1126 (2006).
20. MacCoss, M. J. *et al.* Shotgun identification of protein modifications from protein complexes and lens tissue. *Proc. Natl Acad. Sci. USA* **99**, 7900–7905 (2002).
21. Dentin, R. *et al.* Hepatic glucokinase is required for the synergistic action of ChREBP and SREBP-1c on glycolytic and lipogenic gene expression. *J. Biol. Chem.* **279**, 20314–20326 (2004).
22. Konkright, M. D. *et al.* TORCs: transducers of regulated CREB activity. *Mol. Cell* **12**, 413–423 (2003).
23. Koo, S. H. *et al.* PGC-1 promotes insulin resistance in liver through PPAR- α -dependent induction of TRB-3. *Nature Med.* **10**, 530–534 (2004).

Supplementary Information is linked to the online version of the paper at www.nature.com/nature.

Acknowledgements We thank R. Crystal for *Ad-CRE-Luc* and *Ad-Rsv-Luc* reporters. We also thank J. Meisenheller for help with two-dimensional tryptic mapping and L. Vera for mouse tail vein injections. This work was supported by NIH grants. R.D. is a recipient of a post-doctoral fellowship from the Fondation pour la Recherche Médicale and is supported by the Bettencourt Schuller Foundation. Y.L. is a Hillblom Foundation Fellow. S.-H.K. was supported by a grant of the Korea Health 21 R&D Project, Ministry of Health & Welfare, Republic of Korea. M.M. is supported by the Keckhefer Foundation. This research was also supported in part by the Foundation for Medical Research, Inc.

Author Information Reprints and permissions information is available at www.nature.com/reprints. The authors declare no competing financial interests. Correspondence and requests for materials should be addressed to M.M. (montminy@salk.edu).

METHODS

Adenoviruses. Adenoviruses (1×10^8 plaque forming units (p.f.u.) *TORC2i*, *SIK2i*, *COP1i*, or *USi*; 5×10^7 p.f.u. *CRE-Luc* or *Rsv-Luc*; 2.5×10^7 p.f.u. *Rsv- β -gal*) were delivered to 6–12-week-old male mice (Jackson Labs) by tail vein injection. Mice were imaged on day 2–5 after adenovirus delivery. Wild-type TORC2, mutant TORC2(S171A), *TORC2* RNAi, and *SIK2* RNAi adenoviruses have been described⁸. *Ad-COP1* RNAi was constructed using the sequence: AGTCCAATGTGCTGATTGC.

In vivo imaging. Mice were fasted for 6–16 h or fasted and re-fed for 2 h before imaging. Intraperitoneal injections were performed with $100 \mu\text{g kg}^{-1}$ glucagon, (Sigma), insulin (1 U kg^{-1}) (Sigma), or PBS vehicle. For imaging, mice were injected (i.p.) with 100 mg kg^{-1} sterile firefly D-luciferin (Biosynth AG). After 10 min, mice were injected (i.p.) with 50 mg kg^{-1} Nembutal (Abbott Laboratories), imaged on the IVIS 100 Imaging System, and analysed with Living Image software (Xenogen).

In vivo analysis. Mouse tissues were sonicated at 4°C , centrifuged and supernatants were reserved for β -gal activity, protein determinations, and SDS–PAGE analysis. Blood glucose values were determined using a LifeScan automatic glucometer. Glucose tolerance tests were performed by glucose injection (i.p.; $1 \text{ g D-glucose per kg body weight}$) after overnight fasting on day 7 after injection with *Ad-USi* or *Ad-SIK2i* adenovirus. Plasma insulin levels were measured using ELISA kits from Mercodia (10115001).

Cell culture. Mouse hepatocytes, HEK293T, and HepG2 hepatoma cells were transfected, as previously described^{4,21,22}. For reporter studies, *Ad-CRE-Luc*-infected hepatocytes ($1 \text{ p.f.u. per cell}$) were exposed to FSK ($10 \mu\text{M}$) for 5 h, followed by exposure to control medium or insulin (10 nM) for 3 h. For MG132 studies, hepatocytes were pre-treated with MG132 ($10 \mu\text{M}$) and FSK ($10 \mu\text{M}$) for one hour and incubated with insulin (10 nM) for another hour. For experiments using LY294002 (Sigma), hepatocytes were cultured in serum-free M199 medium containing LY294002 ($10 \mu\text{M}$) with FSK ($10 \mu\text{M}$) or INS (10 nM). Glucose output from primary hepatocytes was determined enzymatically, following 1 h collection in glucose-free M199 media supplemented with 10 mM lactate and 1 mM pyruvate. Glucose production was expressed as nmol of glucose produced per hour per 10^6 hepatocytes.

Mass spectrometry and messenger RNA analysis. Mass spectrometry studies were performed as previously reported¹⁸. Total cellular RNAs from whole liver or from primary cultured hepatocytes were extracted using the RNeasy kit (Qiagen). Messenger RNA levels were measured as described²³.

Immunostaining. Cells were fixed in 4% paraformaldehyde, permeabilized with 0.1% Triton X-100, and stained with anti-TORC2 antibody. Slides were washed and mounted with coverslips using Vectashield mounting media containing DAPI.

TORC2 ubiquitination. For *in vitro* ubiquitination studies, haemagglutinin (HA)–COP1 and HA–DET1 were expressed and immunoprecipitated from HEK293T cells with anti-HA (Sigma) beads. COP1/DET1 beads were incubated with $1 \mu\text{g}$ wild-type or mutant GST (glutathione S-transferase)–TORC2 proteins in reactions (2 h, 30°C) containing $10 \mu\text{g}$ ubiquitin (Sigma), 300 ng of UbCH5b (Boston Biochem), and 20 ng of rabbit E1 (Boston Biochem), in 50 mM Tris, pH 7.5, 2 mM ATP, 5 mM MgCl_2 , $20 \mu\text{M}$ ZnCl_2 and 2 mM DTT. To detect endogenous TORC2 ubiquitination, primary hepatocytes were harvested in lysis buffer containing 0.1% SDS. To follow hepatic TORC2 ubiquitination, livers were homogenized in buffer containing 100 mM Tris–HCl, pH 8.0, and 6 M urea. Lysates were diluted; and anti-ubiquitin immunoprecipitates were prepared. Ubiquitinated TORC2 was detected by western blotting.

Immunoblot, in vitro kinase, and metabolic labelling. Western blot, immunoprecipitation and *in vitro* kinase assays were performed as described⁸. TORC2 antisera have been described⁸. For metabolic labelling studies, HEK293T cells were transfected with wild-type or mutant HA–SIK2 constructs. Cells were serum-starved and incubated for 18 h. with phosphate-free DMEM media containing 1 mCi of ^{32}P -orthophosphate ml^{-1} . Cells were exposed to insulin (500 nM ; 30 min), washed and harvested. Tryptic mapping was performed as described¹⁰.

Statistical analyses. Results are reported as mean \pm s.e.m. The comparison of different groups was carried out using two-tailed unpaired Student's *t*-test. Differences were considered statistically significant at $P < 0.05$.

naturejobs

JOBS OF THE WEEK

Readers may notice a familiar ring to this week's feature on Arizona's research boom (see page 372). It is a change fuelled by money from state and local governments, as well as from philanthropic organizations — money that is being used by researchers to make up a shortfall in federal funding. At the heart of the development are new interdisciplinary institutes that hope to capitalize on the combined expertise and perspectives of physicists, engineers, biologists and chemists. At the same time, institutes that are traditional rivals on the athletics field — Arizona State University in Tempe and the University of Arizona in Tucson — are searching for ways to collaborate. And the state's governor, Janet Napolitano, has given her wholehearted support to research as a way to amass a well-educated workforce in a state that is growing at a frenetic pace in terms of population and economy.

The changes are, in fact, remarkably similar to those occurring in Florida (see *Nature* **446**, 1112–1113; 2007), albeit on a smaller scale. In Florida, former governor Jeb Bush used surplus state funds to attract an impressive array of bioscience expertise, including new branches of the Scripps, Torrey Pines and Burnham institutes. The conditions, too, are similar: rivalry in college athletics affects collaborations between the University of Florida in Gainesville and Florida State University in Tallahassee. And researchers across Florida are using state and private funds to make up for a shortfall in federal funds.

It's a formula other states are keen to copy. Arizona and Florida have dared to encroach on funding and recruiting territory that is usually the preserve of institutions such as Harvard and Stanford. But can they succeed long-term? The build-up in biotechnology businesses that both states want could pose a problem, as the industry's profits are rare and there are already large established clusters in Boston, San Diego and San Francisco. More pertinent, perhaps, is that the state funds are unlikely to last for ever — and scientists and policy-makers must find long-term ways to sustain the research and infrastructure for which they have laid the foundations.

Gene Russo, acting editor of *Naturejobs*

CONTACTS

Acting Editor: Gene Russo

European Head Office, London

The Macmillan Building,
4 Crinan Street,
London N1 9XW, UK
Tel: +44 (0) 20 7843 4961
Fax: +44 (0) 20 7843 4996
e-mail: naturejobs@nature.com

European Sales Manager:

Andy Douglas (4975)
e-mail: a.douglas@nature.com
Business Development Manager:
Amelie Pequignot (4974)
e-mail: a.pequignot@nature.com

Natureevents:

Claudia Paulsen Young
(+44 (0) 20 7014 4015)
e-mail: c.paulsenyoung@nature.com

France/Switzerland/Belgium:

Muriel Lestringuez (4994)

Southwest UK/RoW:

Nils Moeller (4953)

Scandinavia/Spain/Portugal/Italy:

Evelina Rubio-Hakansson (4973)

Northeast UK/Ireland:

Matthew Ward (+44 (0) 20 7014 4059)

North Germany/The Netherlands:

Reya Silao (4970)

South Germany/Austria:

Hildi Rowland (+44 (0) 20 7014 4084)

Advertising Production Manager:

Stephen Russell
To send materials use London
address above.
Tel: +44 (0) 20 7843 4816

Fax: +44 (0) 20 7843 4996

e-mail: naturejobs@nature.com

Naturejobs web development:

Tom Hancock

Naturejobs online production:

Jasmine Myer

US Head Office, New York

75 Varick Street, 9th Floor,
New York, NY 10013-1917
Tel: +1 800 989 7718
Fax: +1 800 989 7103
e-mail: naturejobs@natureny.com

US Sales Manager:

Peter Bless

Japan Head Office, Tokyo

Chiyoda Building,
2-37 Ichigayatamachi,
Shinjuku-ku, Tokyo 162-0843
Tel: +81 3 3267 8751
Fax: +81 3 3267 8746

Asia-Pacific Sales Manager:

Ayako Watanabe
Tel: +81-3-3267-8765
e-mail: a.watanabe@natureasia.com

RAISING ARIZONA

Unburdened by tradition, funders are backing all kinds of innovative work in Arizona. **Gene Russo** looks at opportunities on the rise.



At first glance, misty Ireland and sunny Arizona seem to have little in common. But William Harris, former director-general of the government agency Science Foundation Ireland, believes that his country's science boom has important lessons for the desert state, where science is on the up. Harris, hailed as a leading architect of Ireland's economic and research success (see *Nature* **444**, 396–397; 2006), went to Arizona 18 months ago to help spur investment in the state. He now heads Science Foundation Arizona (SFAz), a non-profit organization that seeds promising research in biosciences, sustainability, and information and communications technologies. SFAz was set up last year with \$135 million in state funding over its first five years, much of which is likely to be matched by private money. It is part of a statewide funding and research surge that has brought new institutes, facilities and big companies to Arizona, and to Phoenix in particular — the fastest growing city in the United States.

Striving to replicate Ireland's success in Arizona, Harris notes that the economies are of a similar scale; state investment is plentiful; and both attract talented recruits. Yet the contrasts and challenges are many. Harris feels the US education system is inadequate at all levels up to the end of high school; on the other hand, he admires the much greater amount of philanthropic funding available in Arizona.

One of Harris's plans is to start a scholars programme to bring young talent to Arizona for three to six months, then convince them to stay. The state's higher-education sector is already blossoming. Arizona State University (ASU) in Tempe, not traditionally known

as a research institution, has started some thriving interdisciplinary programmes. Its president, Michael Crow, has a vision of the 'new American university' that embraces interdisciplinary science at every turn (see *Nature* **446**, 968–970; 2007). And ASU is just one of several institutions benefiting from a flurry of state and philanthropic investments.

Individual researchers such as Stephen Macknik at the Barrow Neurological Institute in Phoenix, are seeing the results. A few years ago, the US National Science Foundation (NSF) sent Macknik a strange message. His grant application had been successful but, because of budget cuts, the funding amount was for zero dollars. He turned to the SFAz, which kept his research going, and the following year he was finally awarded NSF funding.

Sales for science

Research initiatives have been buoyed by a state sales tax passed in 2000 that will generate about \$1.5 billion in research and science infrastructure money for state universities between 2002 and 2022. ASU and the University of Arizona (UA) in Tucson currently each get about \$30 million a year.

One major ASU initiative is the 32,500-square-metre Biodesign Institute, which has an interdisciplinary philosophy. Projects are chosen by institute members, then interdisciplinary teams are formed to tackle the challenges. Stephen Johnston, director of Biodesign's Center for Innovations in Medicine, says he enjoyed his previous job running the Center for Biomedical Inventions at the University of Texas Southwestern in Dallas, but lamented its lack of emphasis on translational research and the difficulty getting funding



Cutting edge: Phoenix's Biodesign Institute (above left) and, down the road in Tucson, BIO5 at the University of Arizona.

for his edgy ideas. Some potential funders even laughed. "I came here, and they may have laughed but they gave me the money to try it," Johnston says.

To come to ASU, you have to be something of an "intellectual cowboy," says Biodesign physicist Stuart Lindsay, a 28-year veteran of ASU. "You have to want to build something." You also have to like the desert and not mind the 43 °C summer heat. Occasionally, Lindsay notes, a recruit or spouse takes one look at the environment and says: "Oh my God, I could never live here." Still, the institute continues to grow, with two more buildings in the pipeline, and plans to hire two or three tenure-track faculty members and more than a dozen postdocs, according to Johnston. Current Biodesign projects include a vaccine against various cancers and a system to clean chemicals from drinking water.

ASU's innovative new School of Sustainability focuses on problems of urbanization, biodiversity, and energy and water use. It grew from ASU's Global Institute of Sustainability, set up in 2004 with \$15 million in start-up funds from chewing-gum tycoon turned philanthropist Julie Ann Wrigley, who added another \$10 million in June to recruit and provide seed money for researchers studying energy, business, climate and systems science.

A new ASU School of Earth and Space Exploration focuses on issues such as the origin of life, the distribution of life in the Universe and the formation of stars and galaxies. Founding director Kip Hodges — who joined from Massachusetts Institute of Technology last year after 23 years as a faculty member — relished the idea of building a new programme that all but requires collaborations among scientists and engineers. "We're going to forget about whether these are engineers or scientists," says Hodges. "We're training to solve big scientific problems." The school will be housed in a new 14,000-square-metre building. With 37 faculty members now, Hodges plans to almost double that number in the next five years.

Also in Phoenix, the International Genomics Consortium (IGC), started in 2001 with county and local government support, houses a biorepository of 1,900 patients' tumour samples. The IGC later created the Translational Genomics Research Institute, which, along with other organizations around the world, uses the IGC's tissue samples to research cancer. A spin-off called the Molecular Profiling Institute is attempting to

commercialize findings based on the samples. The three institutes combined have just 35 employees, but they plan to grow to about 90 in the next few years, says IGC founder Richard Mallery, who chose Arizona over several other candidate locations. "It didn't have many old institutions. We had a blank slate," he says. Arizona's established resources included strength in biology at UA, infectious-diseases research at Northern Arizona University in Flagstaff and bioengineering at ASU. "We took what was here and built on it," says Mallery.

And after much political wrangling (see *Nature* 446, 968–970; 2007), Phoenix will soon have a medical school, a UA–ASU collaboration that's an extension of UA's medical school in Tucson. At present, Phoenix is the only major US metropolitan area without one.

Research rivals?

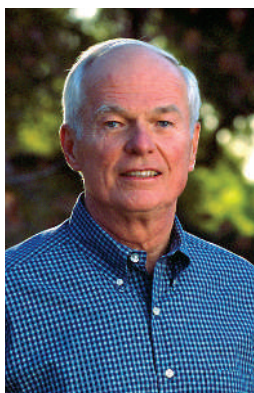
The state's traditional research powerhouse, UA, 185 kilometres southeast of Phoenix, boasts several good programmes, including optics and aerospace. It's a traditional rival of ASU, although the two are finding ways to collaborate. "I'm of the opinion that the rivalry should stay on the athletic field," says Vicki Chandler, director of BIO5, an interdisciplinary UA institute.

Like Biodesign, BIO5 was started with state funds. Most members are in other UA departments: the '5' represents science, agriculture, medicine, pharmacy and engineering. Recent BIO5 recruit Maggie So came from the Oregon Health and Science University, where she feared the administration was starting to devalue basic research. Soon after she arrived at BIO5, So, a microbiologist, established a collaboration with an engineer to examine the forces at work in bacteria during division. "It would've taken me years to find her if I'd been in the traditional campus setting," she says. So will be starting a pathogenesis programme at UA; she plans to hire about ten people in the next eight years.

In planetary and space science, collaborations can be trickier, says Jonathan Fink, director of ASU's Global Institute of Sustainability. ASU and UA have two of the country's top programmes and routinely compete for NASA funding.

"The University of Arizona used to be the only research institute in the state," says Fink. "Sharing that stage is new, and, for some people, uncomfortable." For now, it seems that stage can take multiple players. ■

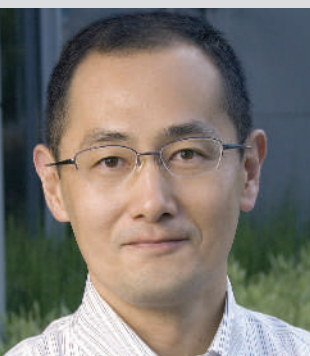
Gene Russo is acting editor of *Naturejobs*.



Vicki Chandler (top) and Richard Mallery.

MOVERS

Shinya Yamanaka, L.K. Whittier Foundation Investigator, Gladstone Institute, San Francisco



2004–present: Professor, Institute for Frontier Medical Sciences, Kyoto University, Japan

1999–2005: Associate and then full professor, Nara Institute of Science and Technology, Nara, Japan

1996–99: Assistant professor, Osaka City University Medical School, Osaka, Japan

Shinya Yamanaka, a rising star in stem-cell research, has taken a specially created post as a senior investigator at the Gladstone Institute in San Francisco, California. For Yamanaka, it's a homecoming of sorts.

As a young sports-player, Yamanaka's experience of injuries led him into a career as an orthopaedic surgeon. But he longed for intellectual conversations with colleagues. "If you do surgery every day, there's no time to make friends," he says. So he moved towards basic research, earning a PhD in pharmacology at Osaka City University. In 1993, he took a postdoctoral position at the Gladstone to work on knockout mice. "He exemplified qualities that often yield success in biology," says Robert Farese, who was a postdoc with Yamanaka and is now a senior investigator at the Gladstone. "Thoughtful intelligence and focus combined with an outstanding work ethic."

Yamanaka relished mingling with other scientists. His subsequent positions back in Japan, where labs are more isolated and the faculty more hierarchical, have offered less chance for discussion, he says: "Since I left the Gladstone, it has been my dream to come back to this place."

Although Yamanaka will direct a full-time team of about five postdoctoral fellows and technicians, he will still spend about three weeks a month at his current position at the Institute for Frontier Medical Sciences in Kyoto.

Yamanaka made headlines this June when his and two other laboratories revealed that they could transform mouse skin cells into cells essentially indistinguishable from embryonic stem cells (K. Okita, T. Ichisaka and S. Yamanaka *Nature* 448, 313–317; 2007). The technique was an advance on his breakthrough of last year, which showed that inserting four genes into differentiated mouse cells yields cells that can become most tissue types (K. Takahashi and S. Yamanaka *Cell* 126, 663–676; 2006). At the Gladstone, Yamanaka will move to human cells. His first postdoc, a colleague from Nara, has already begun experiments, he says. In Japan, Yamanaka would have had to wait at least a year to get permission to work with human embryonic cells.

Deepak Srivastava, one of the Gladstone's directors, says of Yamanaka's specially created position: "We wouldn't do it for everybody, but the magnitude of his discovery was worth the investment." Yamanaka says he will remain at Kyoto University for now so his family can stay in Japan and so as not to disrupt his graduate students. Eventually he plans to come to the Gladstone full-time. ■

Monya Baker

NETWORKS & SUPPORT

Nurturing physician-scientists

Many in the biomedical research community have voiced concern over a future shortage of physician-scientists in the United States. Tighter budgets at the National Institutes of Health and the escalating cost of medical education seem to be discouraging would-be investigators from committing to research careers.

Data describing the research activity of medical students provide additional insight. According to the Association of American Medical Colleges, nearly 80% of American medical students who were accepted to residency programmes in 2007 reported having actively participated in a research project. But as most of these will abandon research soon after, this statistic suggests that potential is being wasted — there is a need to fund more aspiring physician-scientists. In my view as a medical student, it also emphasizes the need for renewed commitment from investigators to mentor students and foster genuine enthusiasm for research early on.

Students and trainees know the biggest reason so many are engaged in research: it is perceived not as an end in itself, but as a means of gaining admission to medical schools, residencies and fellowships. When I told my college advisers that I was going to apply to medical school, they

said I needed "some kind of research experience" in medicine. Yet at the time, I had little interest in biomedical research — I was a history major — and doing so would have felt forced.

Good mentors can work against this perception. After a year working in a genetics lab during medical school, I developed such enthusiasm for basic-science investigation that I spent a year on a Sarnoff Fellowship in cardiovascular research. Both experiences were remarkable for how my mentors identified and nurtured my budding interests. They helped me understand not only the challenges of a research career but also its rewards. They shared with me their belief that the most exciting scientific discoveries in medicine are yet to come. Thanks in large part to mentors who invited me to try my hand at research, my new dreams of becoming a physician-scientist are coming to fruition.

I am fortunate in having had such proactive mentors. But if an imperative of the biomedical research community is to replenish its stocks with outstanding physician-scientists — and outstanding future mentors — I should not have to count myself as only one of an exceptionally lucky few. ■

Albert Luo is a third-year medical student at Case Western Reserve University in Cleveland, Ohio.

POSTDOC JOURNAL

Surviving public speaking

I stood on the stage, stared at the sea of faces before me, and felt the strong urge to run away, or at least to hide behind the podium. My heart was pounding, my mouth was dry, my breathing was shallow, and I clutched the pointer tightly in my cold, shaking hand. They say that an animal, when threatened, will exhibit the fight-or-flight response. As I poised myself to give my first oral presentation as a postdoc, I was clearly exhibiting all the physical symptoms of acute stress. Fortunately, I had gone to the ladies' room before my talk. I was no longer a composed postdoc who was confident in her data. Alone in the spotlight, looking at the international audience full of leading scientists in my new field, I felt like helpless prey, surrounded by predators.

Public speaking has always been a nerve-racking affair for me. Since my elementary-school spelling competitions, I have had the same deer-in-the-headlights feeling in front of large audiences. I sometimes wonder why I don't just tick the 'poster presentation only' box. But ideas are the currency of the scientific market, and our ability to communicate the importance of our work — to colleagues as well as to the public — is a necessity and a responsibility. And so, yet again, I stand my ground and fight my fear of public speaking. After all, it's a jungle out there and it's important to develop the right skills for survival. ■

Maria Thelma Ocampo-Hafalla is a research fellow at Cancer Research UK's London Research Institute.



NATUREJOBS PRESENTS A HIGHLIGHT ON FRANCOPHONE COUNTRIES

NATURE ISSUE: 4TH OCTOBER

AD DEADLINE:

US: 27th September, 2007

UK/EU/ROW: 28th September, 2007

Oui! Oui! Oui!

Naturejobs is pleased to present the **Highlight on Francophone Countries**, appearing in the 4th October issue of *Nature*.

This Highlight offers a remarkable opportunity for companies and organisations in all **French-speaking** countries to profile themselves and publicise their collaborations, research and activities to a superior audience.

If you're looking to showcase your positions to recruit top-tier scientific talent to your organisation or to simply raise your company's awareness amongst the global scientific community, you won't want to miss this issue.

This highlight will be marketed across all relevant NPG publications and web sites to draw readers' attention to this issue.

Learn more about advertising in the **Highlight on Francophone Countries** and contact a representative today!

NATUREJOBS FRANCE, BELGIUM, SWITZERLAND, LUXEMBOURG:

Muriel Lestringuez

T. +44 (0)20 7843 4994

F. +44 (0)20 7843 4996

E. m.lestringuez@nature.com

NATUREJOBS BUSINESS DEVELOPMENT MANAGER:

Amélie Péquignot

T. +44 (0)20 7843 4974

F. +44 (0)20 7843 4996

E. a.pequignot@nature.com

NATUREJOBS CANADA:

Lhea Copeland

T. +1 212 726 9261

F. +1 800 989 7103

E. l.copeland@natureny.com

NATUREEVENTS:

Claudia Paulsen Young

T. +44 (0)20 7014 4015

F. +44 (0)20 7843 4996

E. c.paulsenyoung@nature.com

WWW.NATUREJOBS.COM | WWW.NATUREEVENTS.COM

Supported by  **Île de France**
Agence Régionale de Développement

IN110939R

naturejobs

nature publishing group 

NATUREJOBS PRESENTS THE HIGHLIGHT ON IRELAND

DATE: 25 OCTOBER 2007

DEADLINE FOR ADVERTISING: 19 OCTOBER 2007

Naturejobs is pleased to present the Highlight on Ireland, appearing in the 25 October issue of *Nature*. If you're looking to recruit top-tier scientific talent to your organisation or raise your company profile amongst the European scientific community, you won't want to miss this issue.

This Highlight offers a unique opportunity for companies and organisations in Ireland to profile themselves and publicise their collaborations and activities to a high-quality audience.

If you'd like to learn more about advertising in the Highlight on Ireland, please contact one of our representatives.

Don't delay - the deadline for advertising is this issue is 19 October 2007.

T: +44 (0)20 7014 4059

E: m.ward@nature.com

If you are interested in advertising events in Ireland please call +44 (0)20 7014 4015 or e-mail c.paulsenyoung@nature.com

CALL TODAY TO ADVERTISE WITH NATUREJOBS!

WWW.NATUREJOBS.COM/CONTACTUS

naturejobs

nature publishing group **npg**

IN112580R



NATUREJOBS PRESENTS A HIGHLIGHT ON **MICHIGAN**

DATE: 1 NOVEMBER 2007 | AD DEADLINE: 25 OCTOBER 2007

Naturejobs is pleased to present the **Highlight on Michigan** in the November 1st issue of *Nature*.

The Highlight on Michigan offers a unique opportunity for scientific organizations within Michigan to profile themselves to an international high-quality audience as well as publicize their collaborations and activities in *Nature*. If you are looking to recruit top-tier scientific talent to your organization and to raise your profile in front of this audience, you won't want to miss this issue.

This Highlight is marketed to draw audience to this issue. Job advertisements will also receive a complimentary 60 days posting on naturejobs.com and will be matched to all relevant content across nature.com. Event advertisements will also receive a complimentary 60 days posting on natureevents.com – the events portal for *Nature*.

**TO PROFILE YOUR ORGANIZATION AND EVENTS TO POTENTIAL EMPLOYEES,
PARTNERS AND INVESTORS, PLEASE CONTACT:**

Helen Wu

T: 212-726-9347 / 800-989-7718

E: h.wu@natureny.com

WWW.NATUREJOBS.COM

naturejobs

nature publishing group **npg**



THE NATIONAL INSTITUTES OF HEALTH

OPPORTUNITIES @ NIH



**Department of Health and Human Services
National Institutes of Health
National Cancer Institute**

The Cell and Cancer Biology Branch at the National Cancer Institute is currently investigating various aspects of normal tissue stem cells, as well as the microenvironment-tumor relationship. This area of cancer research holds great promise in the treatment and prevention of cancer and a great deal remains to be learned about the identification and isolation of these cells. We are accepting applications for a Staff Scientist position. Incumbent will oversee the research activities of this Branch and specifically our efforts in defining the role of stem cells as a cancer initiator and determinant of the metastatic process. The applicant will have an MD or Ph.D. in biomedical science and a demonstrative record of strong leadership in addition to working in a collaborative setting. The salary range will be \$74,503 - \$162,371.

The Cancer and Cell Biology Branch (CCBB) is part of the Center for Cancer Research (CCR), which is the largest organization at the NCI dedicated to conducting basic, translational and clinical research on the discovery of the causes and mechanisms of cancer. The CCR is a highly interactive, interdisciplinary group of researchers who have access to new technology and the ability to participate in clinical investigations while maintaining a foundation for independent research.

As part of the Department of Health and Human Services (DHHS), which oversees the biomedical research programs of the National Institutes of Health and those of the NIH's research Institutes, NCI offers a vast array of resources and exciting opportunities for interlaboratory collaboration to our investigators. The NCI/NIH intramural research program provides an exceptionally rich environment for career development. Please send or email CV, cover letter and three references to: Simone John, Office of the Director, National Cancer Institute, 31 Center Drive, Room 11A19, Bethesda, MD 20892 or johnsi@mail.nih.gov. All applications must be submitted no later than October 15, 2007.



**HIV and AIDS Malignancy Branch
Center for Cancer Research**

Tenure Track or Tenure Eligible Position in Viral Oncogenesis

The HIV and AIDS Malignancy Branch (HAMB), NCI, is searching for a tenure track or tenure eligible investigator in the field of viral oncogenesis. It is anticipated that the investigator will establish an independent research program targeted to the study of viral-induced tumors, especially those associated with AIDS. The research program should be able to interface with the branch's existing clinical and basic programs in AIDS-associated malignancies. A particular interest will be for a research program in gammaherpesviruses, but other areas of viral oncogenesis will be considered as well. Current areas of laboratory research in HAMB focus on the molecular biology of Kaposi's sarcoma-associated herpesvirus (KSHV/HHV-8) and human papillomavirus (HPV), pathogenesis of tumors caused by these viruses, and the development of novel therapeutic interventions for HIV infection. The clinical research program in HAMB is primarily directed at AIDS-related malignancies. HAMB is located on the Bethesda campus of the NIH (<http://ccr.cancer.gov/labs/lab.asp?labid=63>). Candidates for the position should have an M.D./Ph.D., Ph.D., or M.D. and strong research credentials. Applicants for this position should submit a curriculum vitae including bibliography, a statement of research interests, a two-page outline of the proposed research program, and the names of three references to **Chairman, Search Committee, HAMB, NCI, Attention Jan Huque, 301-435-4627, fax 301-480-5955, Building 10, Rm. 6N106, 10 Center Drive, MSC, 1868, Bethesda, MD 20892-1868 no later than November 18, 2007.** You may also e-mail your application to: huquej@mail.nih.gov.



Today's Science Student Tomorrow's Leader

Recognized worldwide for our cutting-edge medical and scientific research, the National Institute of Allergy and Infectious Diseases (NIAID) has a responsibility to improve global health in the 21st century. Our basic and applied research programs are aimed at improving diagnosis, treatment, and prevention of immunological, allergic, and emerging and re-emerging infectious diseases.

Visit NIAID for its 5-day exploratory program:

Intramural NIAID Research Opportunities February 3–7, 2008

Explore NIAID's unique research training programs during INRO and

- Hear scientific lectures from some of the world's most talented investigators.
- Tour Institute laboratories and see the state-of-the-art science equipment.
- Interview with principal investigators for potential research training positions.

The open application period is from 8/15/07 – 10/15/07.

To learn more about INRO and submit your application, please visit

<http://www.niaid.nih.gov/labs/training/inro>



OPPORTUNITIES @ NIH THE NATIONAL INSTITUTES OF HEALTH

NW112738R

THE biodesign INSTITUTE

ARIZONA STATE UNIVERSITY

We've built our program around revolutionary concepts, attracting individuals who are unafraid to seek solutions in unfamiliar landscapes.

— George Poste, Director
The Biodesign Institute

THE BIG IDEA

The world's next great innovations – and career opportunities – will stem from a purposeful fusion of biotechnology, nanoscale engineering and advanced computing.

Arizona is fast becoming a leader in this technology convergence, and the Biodesign Institute at Arizona State University is leading the way. Our 600-person team is driven by a passion to address urgent problems on a global scale.

Opened in December 2004, we've rapidly become the largest generator of federal biomedical research funding in the Metro Phoenix area and have attracted more than 190 new faculty and researchers to Arizona State University.

DESIGNED FOR COLLABORATION, BUILT FOR SPEED

The Biodesign Institute fosters large team efforts aimed at delivering real-world solutions. It has launched major research initiatives to eradicate cancer, outpace infectious disease, clean the environment, generate alternative energy and rapidly detect disease.

We offer an outstanding work environment and competitive compensation. Named R&D Magazine 2006 Laboratory of the Year, our 350,000 sq. ft. facility is master-planned for growth to 800,000 sq. ft.

PLEASE VISIT OUR WEB SITE FOR CURRENT OPPORTUNITIES.

www.biodesign.asu.edu

See the April 26, 2007 issue of Nature for two articles on the bold approach being taken at Arizona State University

NW110483A

NEW!

The PhD Program in

BIOLOGICAL DESIGN at ASU

ASU's graduate program in Biological Design will prepare students to participate in the interdisciplinary research teams of the future while simultaneously providing training in core disciplines related to biology.

**CORE DISCIPLINES
AVAILABLE:**

MOLECULAR BIOLOGY

CHEMISTRY

BIOENGINEERING

BIOPHYSICS

MICROBIOLOGY

COMPUTATION

The research emphasis is on projects that are use-inspired, contributing directly to solutions for important societal challenges.

Engage in this highly mentored, personalized program of study and interact with a large, vibrant research community. Experience a new dimension of scientific exploration.

FOR INFORMATION OR TO APPLY:
www.biologicaldesign.asu.edu



NW112384R

**Postdoctoral Position in
Molecular Biology of
Prostaglandin Synthesis
St. Joseph's Hospital,
Phoenix, Arizona, USA**

We are looking a Postdoctoral Fellow/ Research Associate to study lipid mediators of fever and hypothermia in systemic inflammation in rats and mice (see PLoS Biol 4: e284, 2006). Highly motivated individuals with an enthusiastic interest in our research program are invited to apply. Background in molecular biology or immunohistochemistry/neuroanatomy is required. Working knowledge of the prostaglandin synthesis pathways is preferred, but the ability to think and work independently, dedication to work, and persistence in the face of failure are more important than the area of specialization. Mandatory requirements include an advanced degree, a track record of peer-reviewed publications, excellent computer skills, and good writing skills. To apply, send your curriculum vitae, reprints of full-length papers, a brief description of research interests and career goals, and names, e-mail addresses, and telephone numbers of at least two references to:

**Andrej A. Romanovsky, M.D., Ph.D.,
Director, Systemic Inflammation
Laboratory, St. Joseph's Hospital, 350
W. Thomas Road, Phoenix, Arizona
85013, USA; aromano@chw.edu**

NW112384R

THE UNIVERSITY OF ARIZONA.

Project Opportunities at Biosphere 2

Call for Proposals

Input from the international scientific community is being solicited to develop the programmatic thrust of the new B2 Institute at Biosphere 2. With this announcement, the B2 Institute Steering Committee is calling for program proposals in areas of scientific "Grand Challenges" where interdisciplinary activities, broadly defined, can result in significant progress or indicate new directions for progress on the major scientific questions of our day.

Proposals can be for programs and/or workshops which last from a few days to several months. Programs will be selected on the basis of their intellectual significance, timeliness, and opportunities for progress. The broader societal impact of the activity will be an important factor in selection.

There is no deadline for submission of proposals. Proposals will be considered by the B2 Institute Steering Committee and its International Advisory Board immediately following submission. Pre-proposal submissions consist of a working title, suggestions for program organizers and participants, and a brief description of the program and how it supports the mission of the Institute.

The B2 Institute organizes and hosts programs directed at the intensive study of scientific Grand Challenges in the natural sciences and related interdisciplinary areas. Building upon The University of Arizona's reputation as a trailblazer in interdisciplinary research, the B2 Institute serves as a center for research, outreach, teaching and life-long learning about Earth, its living systems, and its place in the universe. The goal of the B2 institute is to create extended programs and shorter, broadly attended conferences, as well as summer and winter schools for graduate students and postdoctoral fellows.

The B2 Institute also carries out significant outreach activities, including public lectures and teacher education days, and builds bridges via artist- and journalist-in-residence programs, art exhibits, and performing arts events.

Contact Pierre Meystre, B2 Institute Director at (520) 621-4651 or meystre@b2science.org for additional information.

Visit B2institute.org and click on the Call for Proposals promo.



B2 Institute

NW110660A



Photograph courtesy of Prof. LaiQiang HUANG (Tsinghua University Graduate School at Shenzhen), Prof. ZhongJian LIU and Ms. LiJun CHEN (National Orchid Conservation Center at Shenzhen)

NATUREJOBS PRESENTS A SPOTLIGHT ON SHENZHEN

30 years ago, Shenzhen, in southern China, was a small fishing village. Today it is China's fastest growing city and home to some of the country's most successful high-tech companies. Shenzhen also hosts graduate schools and research centres of the top universities in both China and Hong Kong, which is a short train ride away.

The city's economy has boomed since its designation as a Special Economic Zone in 1980 and it is a magnet for people from all over China and increasingly overseas. Local government is enthusiastically pursuing policies to provide a strong research base, not only to sustain the city's established record in IT but to foster the growth of life science and biotech industries. A culture of 'innovation' is actively promoted.

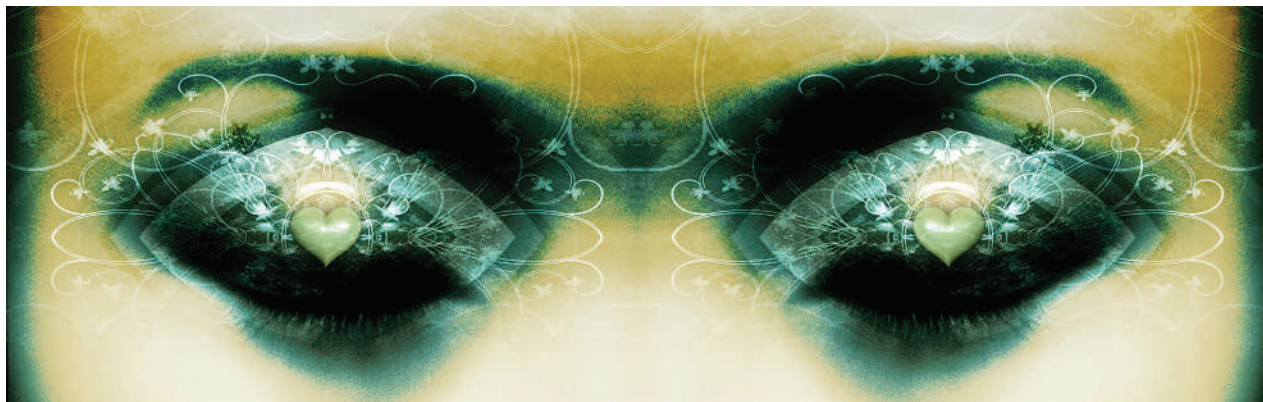
Shenzhen is fast becoming an attractive destination for individuals and businesses from abroad who appreciate the entrepreneurial and progressive environment the city offers.

READ MORE ABOUT SHENZHEN IN SPOTLIGHT ON SHENZHEN, PUBLISHING SOON IN NATURE AND ONLINE AT

WWW.NATUREJOBS.COM

naturejobs

nature publishing group **npg**



JACEY

Only in your dreams

It's a wonderful life.

Arran Frood

I'll miss this place. Clinical as it is, I've grown attached to how it makes me feel. I'm one of the stars, the brightest even, and this place makes me feel like I'm special. Maybe I am.

I won't miss the journey, the menacing building or the totalitarian security. I'll miss what it has become — the most wonderful personal adventure. It's not just a trial; it's an exploration of the nature of consciousness. Or is it the unconscious? Both, probably.

"I didn't think you were awake," says Mr Wonderful — another reason I'll miss this place — as he checks a bank of screens, keying in numbers until the machines hum in placid agreement. He looks very happy today.

"Oh I was just thinking about...the dreams...you know, and stuff," I reply. Best keep it casual. Don't give anything away, even though Mr Subject Liaison Officer will never know.

"What kind of stuff? About leaving?" We both know it's my last day. That's cute. He's so nice! I tell him I'm fine.

"Lie down then, and we'll get your last session sorted."

The routine begins — for the final time — I close my eyes and picture him last night.

"You know, you've really been a star around here," he continues, mindless to the real action. "You've pushed the project on like no one else has. Past the limits of what we, or they, thought was possible. It's just amazing."

He's right. I have been an excellent subject. I can tell from their faces; not just the professors, but everyone, that I'm important, cherished. And all I do is dream.

When I responded to the advertisement, I never thought it would go this far. Lucid dreamers wanted. Women of any age, Taurus, who had never taken drugs. Check, check, check. Sleep and get paid? You're on.

Divulge details of dreams in finest detail? A small price to pay for the money on offer.

That was seven years ago. Now the tests are faster, the corridors longer and the cheques larger. When I saw the first hazy, bitmapped images it was like seeing a part of myself that I always knew was there but was seen only by saints or devils. My dreams laid bare for the Readers.

It was two years before I even knew what was really going on. Symbols and diagrams to meditate on before a sleep; then objects, people and places; and now entire scenarios and plays. All before a reimagining with the Readers, so they could hone the technology that would read the dream from my nightly secretions.

"Relax. Perfect. I'm taking the pads off now," says Mr Wonderful. I'll miss the deference he shows each time he does the routine, like now, as I feel him gently peel away the tissues from my naked body. We never speak at this point. I feel him finish and open half an eye to see him securing my dreams in a sterile box like a genie in a lamp. A dreamie, even.

Mr Wonderful: you are a wonderful lover — a fair prince in this palace of plastic — even if I do make it all happen. I admit it will be embarrassing to recall and verify with my Reader (not for the first time) but she can keep a secret — my specialness has earned me a little leeway.

I am a Lucid 5. The first one, in fact, although I understand there are others. I don't know how it's done; I don't think they really do, but it will be a revelation — a revolution even — when it is finally unleashed upon the world.

I don't know the whole story, they can't tell me, but you hear things. For more than a century people knew the body produced natural hallucinogens in the tiniest amounts, but no one had looked at them. No one imagined they tuned our body clocks until migraine and something else

— cluster headache? — were cured all those years ago. That was the key. Our biorhythms, REM sleep, all dancing to the tune of a tiny gland barely even in the brain. Telepathy, déjà vu, the sixth sense... whatever you call it. Everything answered at a stroke. And they got there through the dreams. My dreams.

"Right. That's you done. Hello?"

Mr Wonderful's work is finished.

"Is that a wrap then?" I say.

"That's a wrap!" We both smile. The old ones are best.

"Wow. That's your last one. Historic, really. What was last night, a free dream wasn't it?"

"Yes it was a free dream," I say, and bite my lip. A little too free probably, but it was fun while it lasted. He's looking so pleased today. I ask why, and as soon as he speaks I wish I hadn't.

"Well, I shouldn't say anything but... well, since you're leaving... I got promoted!"

What?! Oh my God!

"I haven't signed yet, but the person who matters says it's a cert."

No, no, no, no. Please, no.

"I've passed the exams, and psychaptitude runs. This is it — I'm finally going to be a Reader."

I can't speak. That means he'll be able to see...

"It means I'll have access to the archives, your dreams, all the work we did together — everything."

Heart. Thump. Mouth. Dry. Head. Spin.

"You know it probably helped. Working with you, I mean. So...erm...well, thanks!"

"Brilliant!" I squeak.

My eyes are watering.

"There's a long way to go of course but, well, one day I'll learn to see it all."

And you will Mr Wonderful, you will. ■

Arran Frood is a freelance science and science-fiction writer based in London.